UNIVERSITAT DE BARCELONA

Departament
d'Astronomia i Meteorologia

Synthesis of proton flux profiles of SEP events associated with interplanetary shocks. The tool SOLPENCO

Memòria presentada per
Maria dels Àngels Aran i Sensat
per optar al grau de
Doctora per la Universitat de Barcelona

Barcelona, 25 juliol de 2007

Programa de Doctorat d'Astronomia i Meteorologia

Bienni 1998–2000

Memòria presentada per **Maria dels Àngels Aran i Sensat** per optar al grau de Doctora per la Universitat de Barcelona

Directors de la tesi

Dr. Blai Sanahuja Parera

Dr. David Lario Loyo

Als meus pares,

Agraïments - Acknowledgements

At the end of this thesis, I would like to express my gratitude to all the people that has contributed to make this project possible, directly or indirectly, during all these years. I have encountered many people during this travel that have given me advice and support, and from whom I have learnt a lot; I am grateful to all of them, and particularly to:

Dr. Blai Sanahuja, vull agrair la teva confiança al llarg d'aquesta dècada, la teva dedicació i guia i el teu ajut per dur aquesta tesi a terme. Sense tu no hauria estat possible. El teu formidable coneixement i estimació cap a la física de la relació Sol-Terra han estat una continua font d'inspiració. Gràcies per haver-me introduït en el nostre camp i per haver-me mostrat el camí a seguir.

Al Dr. David Lario perquè la teva feina ha fet possible aquest treball de tesi. Sense el teu model de transport de partícules, SOLPENCO no existiria. La comunicació a distància no és fàcil, així que et vull agrair les nombroses discussions per correu i telèfon, i el coneixement que m'has transmès.

My sincere thanks to Dr. Eamonn Daly, Dr. Alexi Glover, Dr. Giovanni Santin, Dr. Hugh Evans, and Dr. Petteri Nieminen, for supporting this project and for making my research stays at ESTEC warm and comfortable. I'm really thankful to L. Rosenqvist and to Dr. Alain Hilgers for unvaluable discussions about the development of SOLPENCO.

Vull agrair també la inestimable col·laboració del Dr. Vicente Domingo i de la Dra. Ada Ortiz en els primers anys d'aquest projecte, i a la Dra. Ana M. Heras per les discussions sobre el model i per haver-me fet sentir com a casa en les meves estades a ESTEC.

A la Neus Àgueda i la Rosa Rodríguez, per les nombroses converses mantingudes i especialment pel vostre suport i ajut en els darrers mesos d'aquest projecte. A l'Ada Ortiz, t'agraeixo un munt d'hores i situacions compartides.

Drs. Murray Dryer, Zdenka Smith, Tom Detman and Ghee Fry, for your kindness, encouragement and continuous support to our research. I'm really grateful to you, Marlene and Susan for making me feel like at home anywhere we meet.

To Dr. Rami Vainio for your kindness and valuable discussions on particle trans-

port; to Dr. Richard Marsden for providing the Phobos-2 data and Dr. Daniel Heynderickx for making possible the web access to SOLPENCO. También quiero agradecerle a la Dra. Consuelo Cid sus consejos, amabilidad y la oportunidad de haber trabajado en un proyecto del ISSI.

Als companys de departament, en especial a en JR pel seu continu suport i ànims. A l'Octavi, en Marc, l'Eduard, la Lola, l'Òscar i en David que m'heu ajudat resolent més d'un dubte al llarg d'aquest periple. I als diversos equips informàtics, el seu inestimable suport, en Jaume, en Rubèn, en Joaquim, en Gaby i en Jordi.

I als meus amics, pel seu suport, per les experiències compartides en diversos moments. Vull agrair a la Muntsa Guilleumas especialment la seva amistat i suport en els darrers anys; a la Ana Rosa, la Isabel i en Paolo per ser al meu costat fins l'últim moment; a en Dani Arteaga, pel seu inestimable ajut, gràcies; a l'Olga, l'Ignasi, en Jordi, en Joan, l'Albert, la Lidia, l'Emma, la Patri, la Maria Jesús, l'Anna, en Xevi i l'Alba, gràcies pel munt de sopars, dinars i berenars i més. També als meus companys de l'hora de dinar, en especial l'Albert, l'Edu i l'Adrià, gràcies per fer-me riure.

I a la meva familia, els meus pares, en Josep, la Isabel, en David, la Gemma i l'Anna, gràcies pel vostre suport incondicional, per haver-me fet costat en tot moment; sense vosaltres jo no hauria arribat fins aquí.

Aquesta tesi s'ha realitzat al departament d'Astronomia i Meteorologia de la Universitat de Barcelona. Agraeixo al departament tots els recursos dels que m'he pogut beneficiar durant la durada d'aquesta tesi. A tots el membres del departament, gràcies pels moments compartits.

I am grateful to the following research centers for their hospitality and for providing me with the necessary equipment during my research stays: ESTEC/ESA (Noordwijk, The Netherlands) and the SEC/NOAA (Colorado, USA).

A $\Phi(B)$,

"Quien se alza de puntillas no se mantiene en pie.
Quien alarga sus zancadas no consigue caminar.
Quien se exhibe ante los ojos de todos carece de luz.
Quien se da siempre la razón carece de gloria.
Quien se jacta de sus talentos carece de mérito.
Quien se enorgullece de sus méritos no está hecho para durar."

(Laozi, Daodejing 24)

Contents

Resum de la tesi:

1. Introducció

"Meteorologia espacial és l'estat físic i fenomenològic de l'entorn espacial. La disciplina associada té com a objectius l'observació, el seguiment, la modelització, i predicció de les condicions en l'entorn interplanetari i planetari, i de les pertorbacions conduïdes o no per activitat solar que els afecten. Tot depenent de les condicions prèvies de l'entorn, aquestes pertorbacions poden impactar sistemes tecnològics i biològics." Una definició de treball emprada per la COST Action 724 (Developing the scientific basis for monitoring, modeling and predicting space weather), 2007.

Els esdeveniments de partícules energètiques solars (SEP, Solar Energetic Particles) representen un dels perills més forts a l'entorn espacial. Aquests esdeveniments, de natura altament aleatòria, són més freqüents en els períodes d'activitat solar intensa, i poden produir dosis elevades de radiació en períodes curts de temps. Augments sobtats i esporàdics dels fluxos de partícules afecten directament les activitats de l'home, com ara la tecnologia aeroespacial o l'exploració de l'espai. Per a una part d'aquests efectes nocius, el paràmetre rellevant dels SEP és l'afluència total de partícules acumulada durant tota la missió, mentre que, per a una altra, ho és el màxim de la intensitat del flux de partícules observat en un esdeveniment aïllat. L'efecte del flux o l'afluència de partícules pot ser molt important per a la vida operativa de satèl·lits i les prestacions dels instruments embarcats a bord de la nau espacial. El camp magnètic de la Terra pot blindar parcialment els satèl·lits que estan en òrbites baixes, però al medi interplanetari, o fins i tot a gran altitud o gran altura a la Terra, les condicions de la radiació induïda poden produir un ambient hostil (Siscoe et al. 2000; Daly et al. 2005).

L'amenaça que els SEP representen per als vols tripulats espacials i les operacions

a l'espai els han revisat diferents autors (Feynman & Gabriel 2000, i referències que s'hi esmenten). Un element crític per al disseny de missions espacials és l'habilitat per aconseguir especificar i predir l'afluència d'un SEP i el pitjor cas possible de SEP, segons els requisits de la missió. Golightly et al. (2005), a partir d'aquí referit com a RWG05, i The Space Radiation Hazards and the Vision for Space Exploration, Baker et al. (2006), referit com a SRH06, fan una descripció actual del coneixement que es té pel que fa als riscos per a la salut en exposicions a la radiació espacial, al seguiment observacional i a la predicció en relació amb les missions tripulades. Ens adrecem a Koskinen et al. (2001) per a una descripció global dels efectes meteorològics espacials produïts pels SEP.

Les fonts més importants de fluxos SEP al medi interplanetari són les fulguracions solars i les ones de xoc conduïdes per ejeccions de matèria coronal (CMEs, Coronal Mass Ejections). Per a un observador situat a una distància heliocèntrica d'1,0 AU, els augments del flux de partícules produïts per aquests esdeveniments solars poden durar diversos dies i són difícils de predir. En termes de dosi total, els protons constitueixen l'element més important dels esdeveniments SEP, l'espècie iònica predominant. En conseqüència, excepte si s'esmenta explícitament, per "partícula" s'entendrà "protó" (amb energia fins a $\sim$1 GeV).

El coneixement que actualment es té sobre la generació, l'acceleració i la propagació d'aquestes partícules al sistema solar interior és incomplet a causa de la seva natura estocàstica i de la manca de coneixement de part de les lleis físiques que els governen; falta molt per tenir-ne una comprensió completa (Turner 2001; SRH06 Report). De fet, els models que hi ha per a la predicció de fluxos de SEP es basen en la hipòtesi que hi ha una relació directa entre les fulguracions i els SEP. Aquest és un conegut paradigma fals, les conseqüències operatives del qual encara no s'han revisat ni millorat per la dificultat intrínseca de desenvolupar nous models físics adients; vegeu, per exemple, els models PROTONS de la NOAA Balch (1999) i PPS de la USAF (Smart & Shea 1989).

La qüestió de fons rau en el fet que la presència dels xocs conduïts per CMEs té un paper fonamental en el desenvolupament dels SEP intensos, no sols pel fet de generar noves partícules energètiques, sinó també perquè controlen l'evolució dels fluxos detectats al medi interplanetari (Cane et al. 1988). La Figura 1.1 mostra el flux i l'afluència acumulada (dibuixos superior i inferior, respectivament) de protons de més de 30 MeV enregistrats durant l'esdeveniment SEP del 20 d'octubre de 1989.

La línia a traces fa referència a l'hipotètic cas d'un augment local de la intensitat associat al pas a l'altura de l'òrbita de la Terra del xoc interplanetari observat el dia 21 d'octubre a les 1650 UT, doy 293. Tal com es pot veure, la contribució a l'afluència total del component del flux associat al pas del xoc no és negligible. Els models predictius que no consideren els efectes del xoc interplanetari viatger, fallen a l'hora de predir fluxos i afluències, especialment en esdeveniments SEP intensos.

Les estratègies de gestió de riscos emprades per estudiar els efectes que les partícules solars energètiques produeixen i per predir-los es basen en tres maneres d'aproximar-se al problema: (a) emprar algorismes estadístics operacionals; (b) emprar codis numèrics per detallar el transport de les partícules, de manera similar a com es fa per descriure la propagació de la radiació cosmico-galàctica en medis ionitzats i magnetitzats, i (c) desenvolupar codis numèrics per estudiar els fenòmens magnetohidrodinàmics (MHD) a la magnetosfera terrestre i al medi interplanetari. En aquest treball farem servir codis numèrics per descriure el transport de partícules i una aproximació MHD per simular la propagació dels xocs interplanetaris des del Sol fins a la Terra (és a dir, els punts b i c abans esmentats). El nostre objectiu bàsic és l'estudi d'esdeveniments SEP aïllats que poden desenvolupar-se de forma inesperada en quasi qualsevol moment del cicle solar, però més freqüentment durant la part més activa d'aquest cicle (Lario et al. 2001).

Les missions espacials futures no estan restringides a l'entorn de la Terra. Hi ha plans de les diverses agències espacials per enviar missions tripulades a Mart i sondes interplanetàries a llocs més propers al Sol que Mercuri (e. g. Solar Orbiter, Inner Heliospheric Sentinels, BepiColombo). La determinació de la radiació ambient a aquestes distàncies heliocèntriques ha de partir dels models que es puguin construir, ja que les observacions fora d'1,0 AU són molt escasses, en el temps i en distàncies. Hi ha suggeriments d'extrapolacions en aquest sentit (Feynman & Gabriel 1988), però no són sempre aplicables, especialment en el cas d'esdeveniments SEP associats amb xocs (Smart & Shea 2003). D'altra banda, l'exploració de Mart ha fet sorgir un problema no considerat anteriorment: els astronautes i la nau espacial estaran exposats als efectes de l'activitat solar que es produeixi al costat del Sol no visible des dels observatoris de la Terra, o que hi estiguin propers. D'aquí les recomanacions fetes quant a aquest tema per l'US Space Weather Architecture Study Transition Plan (1999; Secció 4.2.2.8: Recomendation Robust R&D) i el Radiation Environment Models and In-Orbit Monitoring de l'ESA, Daly et al. (2005), que il·lustren la necessitat de tenir models que descriguin l'entorn de radiació per a

futures missions espacials.

Predir el flux i l'afluència d'esdeveniments SEP intensos, dies o hores abans que es produeixin és un repte immens. El procés global ha de ser quelcom com el següent: l'agent ha de predir: (a) on, quan i com es desenvoluparà un esdeveniment solar; (b) les característiques de la CME, com ara la situació, grandària, velocitat i capacitat per generar i conduir un xoc; (c) determinar l'eficiència del xoc generat per accelerar partícules a altes energies, com també la forma en què aquestes partícules s'injectaran en el medi interplanetari, i (d) predir com aquestes partícules i el xoc guiat per la CME viatjaran sobre el vent solar ambient.

És per aquesta raó que l'informe esmentat de l'ESA (Daly et al. 2005, Secció 9.4) estableix que el desenvolupament modelitzador ha d'incloure millors models estadístics de SEP, sistemes especialitzats per a l'anàlisi de dades, models per a la predicció de SEP basats en la millor física disponible i models físics per a la predicció de l'activitat solar.

En aquest treball es proposa l'ús d'un model compost que inclou ambdós aspectes dels esdeveniments SEP: un model MHD per simular l'evolució d'un xoc que es propaga pel medi interplanetari i un model per descriure el transport de partícules accelerades a prop del Sol i al xoc, que ressegueixi el camp magnètic interplanetari (IMF, Interplanetary Magnetic Field). Aquest model, conegut com el 'Shock-and-Particle model, l'ha desenvolupat el Grup de Física de la Relació Sol-Terra i Meteorologia Espacial (STP/SWG) de la Universitat de Barcelona, i l'ha aplicat a simulacions d'esdeveniments SEP observats per les sondes ISEE-3, Helios-1 i -2, i ACE, i pel satèl·lit IMP-8 (Heras et al. 1992, 1995; Lario et al. 1998; Aran et al. 2004). Aquest model ens permet construir una eina —útil per a aplicacions en meteorologia espacial— que simula els processos que donen lloc a determinats fluxos de perfils, espectres energètics i afluències per a esdeveniments SEP aïllats, especialment en els casos on l'acceleració de partícules està dominada pels processos d'acceleració en el medi interplanetari al front dels xocs conduïts per les CME.

L'objectiu principal d'aquest projecte és desenvolupar un codi d'enginyeria, conegut com **"SOLPENCO"** (acrònim de **P**article **EN**gineering **CO**de), per tal de caracteritzar esdeveniments SEP a llocs determinats de l'espai on se suposa que pot estar ubicat l'observador, des de la corona solar fins a l'òrbita de la Terra. Aquesta eina disposa d'una interfície gràfica senzilla que per a l'usuari genera ràpidament perfils temporals d'intensitat per a esdeveniments SEP en diferents escenaris inter-

planetaris. SOLPENCO no pretén resoldre el problema dels SEP; sols és un primer pas cap a una predicció fiable dels fluxos de partícules en esdeveniments SEP. Un segon objectiu —tan important com el primer— és la identificació de les variables físiques, com també les seves interdependències, que són rellevants per a la meteorologia espacial. D'aquesta manera, en un futur proper, serà possible millorar els models i orientar millor els objectius de protecció d'instrumentació embarcada o d'astronautes durant una EVA, per exemple.

Actualment hi ha un gran buit entre els models per predicció i la realitat de la propagació de xocs i l'acceleració de partícules en xocs; per tant, la fiabilitat d'aquests models és baixa. Millorar aquesta fiabilitat és una feina de futur que requereix una millor descripció de la formació de xocs per CME, una descripció tridimensional d'aquests fenòmens per al medi interplanetari, com també de la propagació de les partícules. Tal com s'ha dit, una tasca extraordinària. Mentrestant, l'única possibilitat raonable consisteix a determinar valors mitjans per al pic del flux i l'afluència total, a diferents energies, segons un conjunt no gaire gran de variables que caracteritzin l'escenari global. Aquesta tasca s'ha de fer de manera sistemàtica, per exemple, construint un conjunt d'esdeveniments SEP que verifiquin uns criteris fixats a priori, analitzant-ne les característiques més importants i, després, comparant-les amb les corresponents d'esdeveniments SEP sintètics equivalents produïts per SOLPENCO.

Aquest informe es desenvolupa de la manera següent. Al segon capítol es resumeixen les característiques principals dels esdeveniments SEP i dels models teòrics sobre els quals es construeixen els codis operatius. No es tracta d'un resum exhaustiu de la situació actual en aquest camp, sinó que està molt enfocat cap als aspectes necessaris per construir models i eines. Al tercer capítol s'expliquen les característiques principals del model i se'n discuteixen els punts febles, amb l'objectiu de tenir clar què cal millorar en el futur. Al capítol quart es presenten els esdeveniments SEP modelitzats per tal d'entendre millor les variables i els paràmetres emprats. Al capítol cinquè es descriu l'estructura de SOLPENCO, les característiques tècniques, la base de dades, i les interfícies d'entrada i sortida. Al capítol sisè es presenten i discuteixen diversos resultats derivats del codi, bàsicament lligats al pic del flux i a l'afluència, com també a la seva dependència radial heliocèntrica. Al capítol setè es comparen resultats de SOLPENCO amb observacions i es discuteixen els resultats. El capítol vuitè és una aplicació del model Shock-and-Particle a la predicció de perfils de fluxos de partícules a l'òrbita de Mart, a partir d'observacions fetes a 1,0 AU

que serveix per il·lustrar com de complicat és fer, actualment, prediccions raonables i fiables. El darrer capítol és el de les conclusions i comentaris sobre perspectives futures. Un seguit d'apèndixs contenen material complementari.

2. Esdeveniments de partícules solars energètiques

2.1 Característiques dels esdeveniments SEP. Esdeveniments graduals

L'inici dels esdeveniments SEP està associat amb diferents fenòmens lligats a l'activitat solar, com ara la desaparició de filaments, fulguracions, diversos tipus de radioemissió i, especialment, amb les CME. S'acostuma a distingir entre dos tipus d'esdeveniments SEP, els impulsius i els graduals. Al principi era una distinció basada en la composició química (Lin 1970, 1974 i van Hollebeke et al. 1975) i en la relació de la durada de l'emissió en raigs X tous per a la fulguració associada (Pallavicini et al. 1977) i en les abundàncies mostrades pels SEP (Kocharov et al. 1983; Cane et al. 1986). Els esdeveniments impulsius són unes 100 vegades més freqüents que els graduals al voltant del màxim del cicle solar, però també són de durada molt més curta i menys intensos que els graduals. En conseqüència, els esdeveniments impulsius tenen una incidència més petita en meteorologia espacial pel que fa al de pic de flux i l'afluència total. Les característiques d'ambdues classes s'han discutit i descrit profusament; vegeu, per exemple, les revisions de Reames (1999a) o de Cliver (2000).

La interpretació més acceptada és que els esdeveniments SEP impulsius estan generats per l'acceleració de partícules al lloc on es produeixen fulguracions de curta durada, probablement per processos de reconnexió magnètica. Els esdeveniments graduals, en canvi, es produeixen quan les partícules són accelerades en el xoc coronal o interplanetari guiat per la CME (Reames 1999a). Aquesta dicotomia s'ha esvaït perquè les mesures isotòpiques d'abundàncies, fetes per SAMPEX, SOHO i ACE, assenyalen l'existència d'un continu de possibilitats entre esdeveniments impulsius i graduals, els casos mixtos (Cane & Lario 2006). Enguany, al seu lloc, segons indiquen les observacions, sabem que hi ha dos mecanismes diferents prou efectius per produir l'acceleració de partícules solars: un d'associat a les fulguracions i un altre, als xocs

(e.g. Tylka et al. 2005). El que continua sent objecte de discussió intensa és fins a quin punt, i com, l'acceleració de partícules per fulguracions té un paper important en els esdeveniments graduals intensos (Klein & Trottet 2001; Tylka et al. 2005; Cane & Lario 2006; Klecker et al. 2006). Queda per veure encara, per exemple, si la fulguració concomitant amb la CME contribueix a l'esdeveniment SEP amb partícules accelerades per ella mateixa (**?**Li & Zank 2005) o no. L'estudi de von Rosenvinge et al. (2001) conclou que hi ha una dependència entre les abundàncies de ions pesats respecte a l'heliolongitud de la fulguració associada, i suggereix que, per esdeveniment magnèticament ben connectat, les partícules accelerades al lloc de la fulguració poden contribuir a les intensitats observades a la Terra. A una conclusió similar va arribar Cane et al. (2003), després d'estudiar la relació Fe/O en 29 esdeveniments SEP intensos.

La dependència del flux de partícules en funció de l'energia, la llei de potència (generalment definida per un índex espectral), d'un esdeveniment SEP individual és fàcil de caracteritzar, sigui per una llei de potència, una doble llei de potència o per una funció de Bessel. Ara bé, és difícil derivar una forma general per a aquesta dependència funcional per a un nombre gran de SEP. És freqüent adoptar una llei de doble potència amb un colze a una energia entre ∼5 MeV i ∼400 MeV (vegeu, per exemple, Xapsos et al. 2000 o Tylka et al. 2000), valor variable d'un esdeveniment a un altre. Aquest colze és conseqüència de la intensitat del xoc i de la intensitat de les ones autogenerades per les partícules accelerades a la part davantera del xoc, que varien en funció de l'energia. Partícules accelerades al xoc amb diferents energies escapen de la regió turbulenta a diferents distàncies i en diferents moments i, per tant, l'efecte sobre el transport de les partícules és diferent. El pendent de l'espectre del flux més enllà del colze és més pronunciat (dur) que abans, la qual cosa implica un decreixement més ràpid del flux en augmentar l'energia. La manca d'un espectre de l'energia que es pugui considerar com a representatiu per a una fracció important d'esdeveniments SEP és un problema greu si es volen derivar prediccions fiables. Per exemple, si el colze de l'espectre està a baixa energia, l'esdeveniment serà intens a baixa energia i feble a alta energia, però si el colze se situa cap a uns centenars de MeV, l'esdeveniment pot ser intens en un ampli rang energètic (i, per tant, més perillós).

Els esdeveniments graduals intensos són importants per dues raons: per les implicacions en meteorologia espacial (Kahler 2001a) i per la contribució dominant a l'afluència de les partícules al llarg del cicle solar (Shea & Smart 1996). Aquests

esdeveniments intensos estan correlacionats amb les CME ràpides (Kahler 2001a), tot i que a l'inrevés no és cert. Si les condicions són les apropiades, el xoc generat per la CME accelera partícules supratèrmiques del plasma del vent solar, o partícules més energètiques, accelerades en esdeveniments previs o per la fulguració concomitant a la CME, que poblen el tub de flux de camp magnètic. Una vegada accelerades, aquestes partícules s'injecten en el medi interplanetari, i es mouen cap endavant o cap endarrere, del xoc, al llarg de les línies de l'IMF. En general, els xocs interplanetaris acceleren més eficientment partícules a baixes energies ($\lesssim$ 5 MeV) que a altes (Forman & Webb 1985). Com a exemple, es pot veure a la Figura 2.3, un esdeveniment SEP observat per la sonda ACE el 29 d'octubre de 2000; a altes energies, una fracció important dels protons s'han accelerat a prop del Sol, mentre que per sota d'1 MeV el xoc és un accelerador força eficient a 1,0 AU.

Els detalls dels perfils de flux de protons a diferents energies i de llurs anisotropies (vegeu Sanderson et al. 1985a i l'apèndix A) són consistents amb la presència d'un xoc, conduï per una CME, que es propaga pel medi interplanetari tot injectant-hi contínuament partícules accelerades al seu front, amb una eficiència variable a mesura que es va expandint i allunyant del Sol (Heras et al. 1995). La forma dels perfils d'intensitat en un SEP pot ser molt diversa, (i.e. Heras et al. 1988, 1995; Cane et al. 1988; Lario et al. 1998; Kahler 2001b), segons: – l'heliolongitud de la regió font respecte a la posició de l'observador – la força del xoc i l'eficiència accelerant partícules – l'existència d'una població prèvia de partícules llavor, candidates a ser accelerades – l'evolució del xoc (velocitat, grandària, forma, etc.) – les condicions de propagació de les partícules pel medi interplanetari, i – l'energia considerada. La Figura 2.4 mostra diferents perfils de flux per a quatre esdeveniments SEP, observats per les sondes ACE i IMP-8; tal com es pot veure, les formes poden ser molt diferents. Cal notar que en aquesta Figura l'activitat solar que genera cadascun d'aquests esdeveniments es considera que té lloc en la direcció de la línia Sol–Terra per a un observador en posició del meridià central (W00 o CM). En conseqüència, els diferents panells s'han desplaçat en heliolongitud en un angle igual a l'heliolongitud de l'activitat solar progenitora.

El concepte de cobpoint (Connecting with the OBserver POINT), definit per Heras et al. (1995) com el punt del front del xoc que connecta magnèticament amb l'observador (vegeu les Figures 2.2 i 2.4), és molt útil per descriure els diferents tipus de perfils SEP:

- Els esdeveniments solars a l'hemisferi oest del Sol donen lloc a un augment inicial ràpid del flux perquè el cobpoint està a prop de la regió central del xoc. Aquest augment va seguit d'un decreixement gradual perquè el cobpoint es mou cap a l'ala est del xoc, i allí el xoc s'està debilitant (cas W69 i cas W27).
- Per a un esdeveniment al meridià central, el cobpoint està inicialment situat al flanc oest del xoc i es va movent progressivament cap a la regió central. Els fluxos de protons de baixa energia, normalment, presenten el pic a l'arribada del xoc.
- Per a esdeveniments originats a heliolongituds est, la connexió magnètica entre el xoc i l'observador s'estableix tan sols unes hores abans de l'arribada del xoc i el cobpoint es va movent des del flanc oest feble cap a la regió central més forta (cas E49).

Tot i el gran nombre de treballs que s'han dut a terme, que mostren que les CME estan a l'origen dels xocs interplanetaris (e. g. Cane et al. 1987), el coneixement actual sobre com les CME es generen a la corona solar és reduït. És molt important saber si els xocs interplanetaris són, o no, una extensió del xoc coronal. Diferents estudis de les explosions radiomètrica, decamètrica i kilomètrica de tipus II i dels esdeveniments SEP associats, i també en conjunció amb observacions coronogràfiques fetes des de l'espai (vegeu, per exemple, Gopalswamy et al. 1998; Cliver & Hudson 2002; Cliver et al. 2004 o Gopalswamy et al. 2005) no permeten donar encara una resposta única. Com a conclusió d'un d'aquests estudis, Cane & Erickson (2005) afirmen: "*The cause of this scenario is unclear*". L'evolució discontínua d'aquests xocs a la corona és conseqüència del perfil radial de densitat del medi en el si del qual evolucionen els xocs (Gopalswamy et al. 2001; Mann et al. 2003). En aquestes circumstàncies sols els xocs supersònics i superalfvènics generats per CME són capaços de produir protons d'alta energia (a més d'electrons i ions pesats) des de distàncies properes al Sol ($< 3\ R_{\odot}$) i seguir-ho fent al medi interplanetari (Kennel et al. 1985).

2.2 Models per a esdeveniments SEP graduals

Ja s'ha esmentat que modelitzar esdeveniments SEP requereix saber com les partícules i els xocs es propaguen pel medi interplanetari i com les partícules s'acceleren i s'injecten en aquest medi. Per tant, cal considerar: (1) Els canvis que es produeixen en

les característiques del xoc a mesura que es propaga pel medi interplanetari; (2) els diferents punts del xoc als quals l'observador es va connectant via el camp magnètic interplanetari, (3) i les condicions en què es propaguen les partícules.

Heras et al. (1992 i 1995; conegut com He925) va incloure per primera vegada un terme font dins de l'equació de transport amb focalització i difusió de (Roelof 1969). El terme font 'Q' representa el ritme d'injecció de partícules accelerades al xoc viatger; aquesta injecció es considera que es produeix al cobpoint. Per seguir l'evolució del cobpoint aquests autors van emprar un model MHD per simular la propagació del xoc des d'una distància límit propera al Sol fins a la posició de l'observador. Lario (1997) i Lar98 van refinar aquest model incloent-hi els efectes de la convecció deguda al vent solar i a la desacceleració adiabàtica en l'equació de transport amb focalització i difusió, com també l'efecte de la corotació de les línies de l'IMF. Aquest model s'ha utilitzat amb èxit per reproduir els fluxos i les anisotropies observats en diversos esdeveniments de protons de baixa energia ($<$20 MeV); Lar98. Un model del mateix tipus, però més senzill, el van desenvolupar Kallenrode & Wibberenz (1997) i Kallenrode (2001).

Ng et al. (1999a,b, 2001, 2003) han desenvolupat un model que inclou l'efecte de les ones d'Alfvén autogenerades pels protons accelerats, a la reunió davantera contigua al front del xoc (regió prexoc turbulenta). Aquests autors resolen consistentment l'equació de transport amb focalització i difusió i l'equació que descriu l'evolució de la intensitat de les ones. Aquest model permet una descripció millor dels processos de dispersió generats per les partícules de diferents espècies, però fan falta diverses hipòtesis simplificadores suplementàries (per exemple, per reduir el nombre de paràmetres lliures que descriuen la injecció de partícules) perquè el model sigui raonablement utilitzable en meteorologia espacial. Zank et al. (2000) han desenvolupat un model per a l'acceleració de partícules resolent l'equació de transport difusiva en una sèrie de capes al voltant del xoc que evoluciona i es propaga. Rice et al. (2003) generalitza el model per incloure-hi xocs de força arbitrària, és a dir, per a diferents condicions per a la difusió de partícules al voltant del xoc, emprant un model bidimensional 2D MHD. Els models de Zank et al. (2000) i Rice et al. (2003) suggereixen que en el cas de xocs molt forts, les partícules es poden accelerar fins a ($\lesssim$1 GeV quan el xoc encara està molt a prop del Sol. Tsurutani et al. (2003) indica que fa falta construir models tridimensionals 3D MHD amb dependència temporal per a les condicions a 1 $R_\odot$ i que s'estengui més enllà del punt crític per començar a disposar d'un model de simulació de xocs útil per a predic-

cions. Un model 3D d'aquesta mena hauria d'incloure una estructura fina del vent solar (perfils, per exemple) i mecanismes dissipatius realistes (Jacobs et al. 2005).

Aquests darrers anys, la disponibilitat efectiva de potència de càlcul en grans ordinadors de processament en paral·lel està permetent el desenvolupament de nous models 3D que tenen en compte més aspectes de la física i la geometria interplanetària del problema dels xocs interplanetaris que els models precedents. Ara ja comença a ser possible construir models de propagació de CME prou realistes com perquè tingui sentit comparar els resultats amb les observacions (vegeu, per exemple, Lionello et al. 2003 i Odstrčil et al. 2004). Manchester et al. (2004a,b) han desenvolupat un model 3D MHD que descriu l'evolució d'una CME des d'1 $R_\odot$ fins a 1,0 AU, sobre un vent solar estructurat. Manchester et al. (2005) fa servir aquest model per estudiar la regió posterior al front del xoc ja que el procés d'acceleració depèn fortament de la topologia d'aquesta zona. Wu et al. (2005a) ha desenvolupat un altre model 3D MHD per investigar els criteris d'iniciació d'un fenomen solar eruptiu que doni lloc a l'ejecció d'una CME. Un resum dels últims avenços pel que fa models de vent solar amb simulacions de CME superposades es pot trobar a Poedts & Arge (2005). Finalment, s'ha d'indicar que Sokolov et al. (2004), amb un model advectiu acoblat al model de Manchester et al. (2005), aconsegueix calcular la intensitat de les partícules accelerades en el xoc quan aquest es troba entre 4 i 30 $R_\odot$, i els resultats es poden comparar amb observacions del satèl·lit GOES-8, per a l'esdeveniment SEP del 2 de maig de 1989.

2.3 Dependències radials dels fluxos i afluències de partícules

La majoria de les observacions de partícules provenen d'observacions fetes a l'espai, de sondes i satèl·lits situats a la òrbita de la Terra. Per estimar l'impacte de la radiació deguda a aquest fluxos en missions espacials viatjant a diferents distancies radials del Sol, fa falta especificar la dependència radial dels fluxos i de les afluències de partícules. És un treball complex donat que les dependències radial i longitudinal estan entrelligades (Lar98) y, especialment, per que el nombre d'observacions fora d'1,0 AU és molt limitat. De fet, a efectes pràctics, sols existeixen les observacions fetes per les sondes Helios-1 i -2 entre 0,29 AU i 0,98 AU, entre 1975 i 1982. La situació actual és molt confusa, donat que no existeix cap model que pugui donar alguna dependència amb un cert grau de fiabilitat. A falta de rés millor, el protocol més utilitzat és el definit pel model JPL-91 (Feynman et al. 1993).

Lario et al. (2006) utilitza les dades de les dues sondes Helios i del satèl·lit IMP-8 (a 1,0 AU) per analitzar els pics d'intensitat i les afluències en 72 esdeveniments SEP observats simultàniament per dos o tres d'aquestes sondes. La conclusió més important és que el paràmetre dominant que determina el pic del flux i la afluència d'un esdeveniment no és la distancia radial heliocèntrica si no la distància angular entre la regió activa progenitora i el peu de la línia de camp magnètic que connecta l'observador amb el Sol. De l'ajust multi-paramètric fet a les observacions, es dedueix una dependència radial més feble que la deduïda a partir dels models de transport que utilitzen sols una equació difusiva (e.g. Hamilton 1988) i extrapolats a distàncies més petites que 1,0 AU. Vainio et al. (2007) han modelitzat un esdeveniment SEP gradual observat el 6 de juny de 2000 per ACE i IMP-8 a 1,0 AU i han derivat els perfils dels fluxos a 0,3 AU i 0,7 AU (vegeu la Figura 2.6), al llarg de la mateixa línia del camp magnètic interplanetari. La conclusió més important derivada és que les lleis per escalar la dependència radial heliocèntrica per a esdeveniments SEP graduals no té res a veure amb les lleis derivades emprant models simples de transport, perquè l'acceleració de partícules al xoc dóna lloc a una interrelació entre l'escenari interplanetari i la dependència temporal de la font de partícules.

Més recentment, Lario et al. (2007) han estudiat la dependència radial del pic d'intensitat i l'afluència d'esdeveniments SEP en el marc de l'equació de transport amb focalització i difusió, per al cas d'esdeveniments magnèticament ben connectats i amb la font fixa al Sol (p. ex. esdeveniments impulsius). Les conclusions més importants d'aquest estudi han estat: (1) la dependència radial augmenta a baixes energies i per recorreguts petits lliures de les partícules, i (2) com més baixa és l'energia, més gran és el decreixement de la intensitat del pic i de l'afluència amb la distància radial. Els índexs derivats per l'espectre de potències són menors que als fins ara recomanats a partir d'extrapolacions d'intensitats mesurades a 1,0 AU, la qual cosa pot permetre relaxar les condicions de protecció de la instrumentació embarcada en missions a l'espai interplanetari interior (<1 AU).

3. El model Shock-and-Particle

A He925 es descriuen els elements essencials del model Shock-and-Particle; es troben canvis i millores posteriors a Lario (1997) i Lar98 (apèndix B), i a les referències que s'hi donen. S'utilitza el concepte de cobpoint i les components bàsiques del model

són una descripció correcta d'ambdós del transport de les partícules accelerades pel xoc al llarg de les línies de l'IMF i de la propagació d'aquest xoc. El model no considera explícitament els processos que produeixen l'acceleració de partícules al xoc; de fet el model es comporta com una caixa negra perquè tan sols descriu la injecció de partícules accelerades en el medi interplanetari. El model s'ha aplicat a diferents esdeveniments SEP observats per sondes interplanetàries. Els resultats obtinguts han permès establir una dependència funcional entre el ritme d'injecció de partícules, Q, i el quocient normalitzat de velocitats, VR, davant del xoc respecte a darrere del xoc. Una limitació conceptual del model és que sols es pot aplicar a la part davantera del front del xoc.

El punt clau del model és que es pot comparar l'evolució de les variables MHD al cobpoint amb el ritme d'injecció de partícules, ja que: (1) els valors de les variables MHD provenen de la modelització de la propagació del xoc; (2) els valors del ritme d'injecció de partícules accelerades al xoc, al cobpoint provenen de l'ajust dels fluxos de partícules i de les anisotropies, a diferents energies. Com que ambdues simulacions es fan de manera independent, qualsevol relació empírica que es pugui trobar entre el ritme d'injecció i les variables MHD és independent del mecanisme que accelera les partícules al xoc. El model proporciona també l'espectre energètic del ritme d'injecció de partícules.

De la modelització de diferents esdeveniments (Lar98 i Capítol 4) és possible derivar una relació empírica entre la Q i la VR, relació que es coneix com la relació Q(VR). Una vegada s'estableix una dependència funcional del tipus Q(VR) és possible invertir el procediment i construir perfils sintètics de fluxos i anisotropies en altres situacions i escenaris interplanetaris, suposant que una relació d'aquesta mena segueix sent vàlida. Les Figures 3.2, 3.3 i 3.4 il·lustren un exemple de com es pot invertir el procediment de càlcul de la Q i, per tant, marquen un camí per construir un codi operatiu per a la predicció de fluxos (pic de fluxos i afluències) d'esdeveniments SEP.

Tot i que hi ha un gran consens sobre els punts bàsics del model, hi ha detalls que no estan completament aclarits o no estan quantificats: (1) com les condicions MHD al front del xoc es traslladen en una eficiència en l'acceleració de partícules i en la seva injecció en el medi interplanetari, i (2) com evoluciona aquesta eficiència a mesura que el xoc s'expandeix i es propaga pel medi interplanetari. Un altre paràmetre bàsic del model és el recorregut lliure mitjà de les partícules que

permet descriure'n la propagació emprant una equació de transport amb focalització i difusió; el valor del recorregut lliure mitjà s'ajusta tant com sigui possible a les observacions i a les prediccions teòriques, especialment l'evolució de l'anisotropia. L'elecció d'aquest paràmetre té una influència important en la descripció del transport i, per tant, en l'ajustament dels fluxos observats (per a més detalls, vegeu, Beeck et al. 1987; Beeck & Sanderson 1989, i les referències que s'hi donen.).

3.1 Simulacions MHD del xoc interplanetari

L'evolució del xoc interplanetari es descriu mitjançant el model 2.5D MHD (axisimètric respecte a un eix perpendicular a l'eclíptica) de Wu et al. (1983). Aquest model simula la pertorbació induïda per una CME dejectada del Sol sobre el plasma del vent solar, que es propaga pel medi interplanetari des de 18 $R_\odot$ fins 1,1 AU. Smith & Dryer (1990) donen detalls del mètode de computació, part d'ells es poden veure a He925 i a l'apèndix E de Lario 1997. Per a cada esdeveniment aquest model proporciona una simulació de la propagació del xoc; per tant, es pot estimar la força del xoc a cada instant i a cada punt al llarg del seu front, en particular al cobpoint.

La força del xoc es caracteritza per les variables VR i BR, el salt de velocitat normalitzat i el salt de camp magnètic de la part davantera del xoc respecte a la darrera, respectivament, i θ_{Bn}, l'angle entre l'IMF davanter i la normal al superfície del front del xoc al cobpoint (veure Armstrong et al. 1985; Scholer 1985, per més detalls). La Secció 3.3 de Lario (1997) descriu dos mètodes per calcular aquestes variables ('tall radial' i 'perfil temporal'; l'angle θ_{Bn} es calcula emprant dos mètodes descrits per Chao & Hsieh (1984) i acceptant la condició de coplanarietat dels punts.

La força MHD del xoc al cobpoint té una influencia determinant en la eficiència suposada als mecanismes d'acceleració de partícules. Aquesta força pot disminuir, a causa de l'expansió del xoc en el medi interplanetari o per que el cobpoint es mou cap a l'ala dreta del xoc, o augmentar, si el cobpoint es mou en sentit horari cap a la regió central del xoc. Llavors, és possible que una regió del xoc si capaç d'accelerar protons fins a 20 MeV a 0,1 AU, però que tan sols ho pugui fer fins a 500 keV quan arriba a 1,0 AU. Aquest escenari s'ha descrit qualitativament a partir d'anàlisis estadístiques d'esdeveniments SEP o de l'estudi d'esdeveniments SEP determinats (e.g. Cane et al. 1988; Domingo et al. 1989; Reames et al. 1996).

3.2 L'equació de transport per a partícules energètiques

Ruffolo (1995) va desenvolupar una forma explícita de l'equació de transport amb focalització i difusió per descriure el moviment dels raigs còsmics, incloent-hi els efectes de la desacceleració adiabàtica i de la convecció del vent solar, a partir de l'equació de transport de Roelof (1969). Aquest autor va aplicar l'equació per descriure el transport de protons des d'una font fixa (al Sol); ara bé, per modelitzar el transport de protons associats a un xoc, cal suposar una font mòbil de partícules accelerades. Aquest fet demana una aproximació diferent per a la resolució numèrica de l'equació de transport, tal com es pot veure a Lario (1997) i a Lar98 (Equació 3.1). Específicament, el valor del terme ritme d'injecció Q a l'equació de transport varia amb el temps i la posició de la font.

Per descriure l'IMF se suposa un règim de vent solar estable i un IMF descrit per una espiral de Parker. En aquestes condicions, i si se suposa una velocitat del vent solar constant, la topologia del camp magnètic queda totalment definida de manera analítica. Per a altres escenaris, un vent solar variable, per exemple, els valors de l'IMF a cada punt, s'han de donar de manera numèrica (o per a altres funcions analítiques que es puguin deduir).

La interacció entre les partícules energètiques i les irregularitats de l'IMF es descriuen per mitjà de l'aproximació de dispersió segons l'angle de batuda (pitch-angle). El coeficient de difusió PA per a l'angle de batuda es defineix en termes del model estàndard per a les fluctuacions de l'IMF, fluctuacions que se suposen petites respecte al valor de l'IMF global (aproximació QLT, Jokipii 1966). En aquesta situació el coeficient de difusió es pot parametritzar segons el recorregut lliure mitjà de les partícules paral·lel a l'IMF, $\lambda_{\parallel}$, que depèn indirectament de l'energia, ja que la dependència s'estableix per mitjà de la rigidesa, $\lambda_{\parallel}(R) = \lambda_{\parallel 0}(R/R_0)^{2-q}$ (Hasselmann & Wibberenz 1970 i Kunow et al. 1991).

En conseqüència, el model té dos paràmetres bàsics: (1) el recorregut lliure mitjà dels protons, escalat amb la seva rigidesa, i (2) el ritme d'injecció de partícules accelerades al xoc, Q, escalat amb l'energia $Q = Q(E)$, amb la dependència introduïda per mitjà de la funció $G(E) = G(E_0)(E/E_0)^{-\gamma}$ (vegeu-ne més detalls a Lar98), on E_0 és una energia de referència (0,5, 0,8 o 1,0 MeV, segons els canals d'energia de l'instrument). L'índex espectral per a la dependència de Q amb l'energia es dedueix dels ajustos dels fluxos observats a diferents energies.

Cal assenyalar que en determinats tipus d'esdeveniments fa falta considerar una regió davant del front del xoc amb un camp magnètic turbulent, a causa de l'acció de les ones alfvèniques generades pels mateixos protons accelerats al xoc. Aquesta regió és especialment necessària a baixa energia per reproduir el fort augment del flux a l'arribada del xoc (Figura 1.1) i l'anisotropia de la població de partícules, al qual està fortament isotropitzada. Hi ha observacions d'aquesta regió en diferents esdeveniments Kennel et al. (1982, 1986), Tsurutani et al. (1983), Viñas et al. (1984) o Sanderson et al. (1985b) tot i que no són gaire nombroses. En el model Shock-and-Particle, aquesta regió prexoc es caracteritza per una determinada grandària i un recorregut lliure mitjà molt més petit que el valor de $\lambda_{\parallel}$. El significat d'aquesta regió l'ha discutit Heras et al. (1992), Beeck & Sanderson (1989), Gordon et al. (1999) i més recentment Lee (2005) (la Figura 2 mostra un esquema d'aquest escenari).

3.3 El ritme d'injecció i la seva dependència energètica

Per a un esdeveniment SEP donat, el procediment és el següent. S'ajusten els perfils del flux i de l'anisotropia per a un determinat canal d'energia, E_0; de l'ajust es deriven els valors de λ_0 i Q_0, com també la seva evolució. Llavors, si se suposa la dependència funcional ja comentada de Q amb l'energia, es busca el millor ajust per als perfils de flux i anisotropies a totes les energies. D'aquest ajust es deriva el valor de l'índex espectral per a la injecció de partícules accelerades al xoc, γ, i la constant de normalització que permet donar els fluxos en unitats físiques (els detalls es poden veure a l'apèndix A de Lario 1997). L'experiència ens ha ensenyat que per ajustar simultàniament deu o més canals d'energia entre 50 keV i 50–100 MeV, el pendent de la dependència $Q \propto E^{-\gamma}$ a altes energies ($\gtrsim$2 MeV) ha de ser més gran (més negatiu) que la de a baixa energia. Aquest fet implica que l'eficiència del xoc com a injector de partícules decreix més ràpidament a altes energies que a baixes energies (vegeu la Secció 2.2).

L'evolució de Q varia d'un esdeveniment a un altre, depenent bàsicament de l'extensió angular del xoc, de la velocitat de trànsit i de la posició relativa de l'observador respecte a l'heliolongitud de l'activitat solar progenitora. Una vegada reproduïts els perfils d'intensitat i anisotropia observats a diferents energies, és possible comparar l'evolució del ritme d'injecció, Q amb l'evolució de les variables VR, BR i θ_{Bn} al cobpoint, derivades de la simulació MHD del xoc. Si s'elimina la dependència temporal entre aquestes dues dependències, és possible analitzar l'existència d'alguna

dependència funcional entre Q i les tres variables VR, BR i θ_{Bn}. Els resultats de les diverses simulacions de SEP mostren l'existència d'una relació del tipus

$$\log Q = \log Q_0 + k\mathrm{VR} \tag{1}$$

(vegeu, per exemple, la Figura 10 de Lar98; l'apèndix B mostra un cas representatiu). Els ajustos fets suggereixen també una relació entre Q i BR, però de manera menys nítida i sols en alguns dels esdeveniments modelitzats. No s'obté cap resultat per a Q i θ_{Bn}.

3.4 Millores del model

El valor del coeficient k en la relació Q(VR) varia amb l'energia de les partícules i per a cada esdeveniment. Fins on sabem, l'únic mètode per validar la relació Q(VR) (i possiblement estendre-la a BR) consisteix a modelitzar molts esdeveniments SEP, especialment entre les heliolongituds W50 i E10. Per tal de calibrar aquesta dependència i quantificar-la per obtenir codis operatius, aquests ajustos s'han de comparar amb els que es puguin sintetitzar amb el model assumint a priori en la relació Q(VR). D'altra banda, cal tenir en compte la gran varietat d'espectres energètics que hi ha entre els esdeveniments SEP, la qual cosa dóna lloc a una diversitat de valors per a k a partir d'altes energies ($\gtrsim$10 MeV). Per estendre aquesta relació a energies més altes (50 – 100 MeV), caldria tenir més estudis observacionals de l'evolució de l'anisotropia a aquestes energies; així s'aconseguiria imposar més restriccions als models teòrics i a les simulacions.

Per als propòsits de la meteorologia espacial és important estimar el flux de protons a energia lata ($\gtrsim$10 MeV). Es pot fer suposant una dependència funcional del ritme d'injecció de partícules accelerades al xoc extrapolant-la a aquestes energies, per exemple suposant una llei de potències ($Q \propto E^{-\gamma}$), que pot ser diferent a la de baixes energies. Aquesta dependència espectral podria llavors comparar-se amb les observacions. Desafortunadament, l'índex espectral és altament variable (vegeu la Secció 2.1.5) i no hi ha observacions sistemàtiques ni prou acurades com per poder derivar un valor raonablement representatiu per al conjunt d'esdeveniments SEP (o almenys, una gran part). Hi ha exemples de SEP generats per CME de característiques similars en els quals el flux a energies altes difereix en tres o més ordres de magnitud (e.g. Kahler 2001b).

A la Secció 2.2.3 s'ha discutit el poc coneixement que tenim sobre la formació de xocs a la corona solar i la seva transició al medi interplanetari. En conseqüència, la caracterització del xoc per a la velocitat inicial a 18 $R_\odot$ és tan poc significativa com emprar la velocitat mitjana de trànsit del xoc des del Sol fins a la Terra; cap de les dues és una variable observable en temps real. No hi ha encara indicadors quantificats de l'activitat CME i de les seves característiques; en general, cap indicador de l'activitat solar (proxy) és adequat per usar-se amb garantia. (Convé indicar que bona part de les crítiques que aquí es formulen són també aplicables als altres models breument descrits a la Secció 2.3.)

El flux de partícules en la regió posterior al pas del front del xoc pot romandre alta durant diverses hores, segons el tipus de SEP. L'evolució del flux de partícules en aquesta regió depèn de la topologia del camp magnètic i de la de la regió del front a la qual l'observador segueix connectat. Per a l'esdeveniment est, l'observador, després del pas del xoc, estableix connexió amb la part central del xoc i observa el pic del flux després del seu pas, freqüentment i també segons l'energia. En aquests casos la contribució d'aquesta regió posterior a l'afluència total pot ser no negligible (vegeu, per exemple, Rosenqvist 2003b). La modelització de la regió que segueix a l'arribada del front del xoc, abans del pas del conductor (driver o ICME) no és senzilla. La hipòtesi de vent solar estable no és vàlida i la presència de núvols magnètics (identificats amb l'ICME, per exemple) té efectes importants sobre el transport de les partícules, almenys, de dues maneres: (1) la distància al llarg de la línia de l'IMF que connecta dos punts és més llarga en el si del camp magnètic pertorbat que en el cas d'una espiral de Parker, i (2) la desviació de l'espiral estàndard modifica la longitud de l'enfocament de l'IMF (vegeu, per exemple, la Figura 1 of Kallenrode 2002). No hem inclòs aquesta regió en la versió actual del nostre model.

Reames (1989) suggereix que el recorregut lliure mitjà de les partícules varia amb el temps, a causa de la presència de les pròpies partícules accelerades que són capaces d'amplificar ones magnetohidrodinàmiques, les quals, al seu temps, ressonen amb altres partícules i n'augmenten la dispersió. Per tant, l'ús de $\lambda_\parallel$ com a paràmetre lliure s'ha de considerar com una feblesa del model. Ara bé, actualment, l'inclusiu d'aquestes ones de manera consistent comporta usar una equació de transport amb un llarg nombre de paràmetres lliures, com també aproximacions poc realistes (es poden veure més detalls a Ng et al. 2003), que la fan ser no operativa en meteorologia espacial.

Els models presentats assumeixen un únic tub de flux en el qual les partícules accelerades al xoc són successivament injectades i observades per una sonda interplanetària. La situació real és més complicada, ja que al llarg del desenvolupament d'un SEP, la sonda creua diferents tubs de flux, a causa de la propagació radial del vent solar i de les línies de l'IMF congelat. Cadascun d'aquests tubs conté una població diferent de partícules energètiques, corresponent a diverses històries dels paràmetres del xoc al cobpoint que els pertoca. Aquest efecte, conegut com a efecte de corotació (Kallenrode 1997; Lar98) pot ser important per a la modelització de SEP associats a xocs lents. D'altra banda, com més gran sigui la dependència longitudinal dels processos d'acceleració al llarg del front del xoc, més important pot ser l'efecte de corotació.

4. Modelització d'esdeveniments SEP per a aplicacions en meteorologia espacial

Per entendre la física que hi a la base dels models i codis de simulació, tenint en compte la complexitat de l'escenari solar i interplanetari en el qual es produeixen, cal modelitzar esdeveniments SEP de diferents tipus (oest, meridià central, est, ràpid, lent, etc.), tant amb propòsits generals (vegeu, per exemple, Kahler, 2001) o, en el nostre cas particular, per entendre millor la relació Q(VR). Tot i el gran nombre d'observacions d'esdeveniments SEP, sols una part reuneix les condicions adequades (evolució del vent solar, camp magnètic, fluxos de partícules a diferents energies, aïllament, etc.) que permeten modelar-los dins de les restriccions que acoten els models teòrics i les simulacions numèriques (es necessiten esdeveniments de llibre). D'altra banda, modelar un esdeveniment SEP amb cura és una tasca feixuga perllongada, si es vol fer amb les garanties necessàries per considerar la modelització com a prou detallada i acurada. Dins del període 1998 – 2000 s'ha fet una selecció de 10 esdeveniments SEP observats per ACE/EPAM i per IMP-8/CPME per modelitzar-se: (110 – 116)/1998, (236 – 240)/1998, (273 – 277)/1998, (47 – 51)/1998, (184 – 189)/1999, (95 – 100)/2000, (158 – 162)/2000, (248 – 252)/2000, (256 – 271)/2000 i (299 – 304)/2000. Les característiques observacionals d'aquests esdeveniments es poden veure en l'apèndix F d'Aran et al. (2004).

S'han modelitzat tres esdeveniments d'aquest conjunt, i els resultats s'han utilitzat, junt amb d'altres d'estudiats prèviament, per derivar els valors mitjans de

diverses variables emprades SOLPENCO (Capítol 5); són els que aquí es presenten: el tercer, 30 de setembre – 2 d'octubre de 1998 (Sep98); el sisè 4 – 6 d'abril de 2000 (Apr00), i el vuitè, 12 – 15 de setembre 2000 (Sep00). La metodologia de l'anàlisi i la modelització d'esdeveniments SEP ja s'ha descrit i comentat en els capítols anteriors. En aquest capítol sols es comenten breument les característiques de cada esdeveniment SEP i els resultats de la modelització rellevants per a l'aplicació SOLPENCO. Un altre exemple de modelització doble (Terra-Mart) es pot veure en el capítol vuitè, amb tot el detall de la complexitat. L'esdeveniment d'abril de 1998 també s'ha modelitzat, per tal de verificar un estudi anterior, com també l'esdeveniment del 6 – 8 de juny de 2000 (vegeu la Figura del Capítol 2), però com que els resultats d'aquestes modelitzacions no s'han considerat a l'hora de discutir els valors per a SOLPENCO, no s'han inclòs en aquest capítol.

Esdeveniment Apr00. Generat per una CME-halo observada el 14 d'abril a les 1632 UT en associació temporal amb una fulguració C9.7/2F (N18W66) amb màxim a les 1511 UT. Xoc detectat per ACE a les 1600 UT del dia 6 d'abril. Velocitat mitjana del trànsit Sol-Terra: 843 km s^{-1}. Modelització: assumeix un vent solar de 371 km s^{-1}, un pols d'injecció de 165° en la direcció W66, centrat a 10 $R_{\odot}$ i que es propaga a una velocitat inicial de 1510 km s^{-1}. Requereix una injecció solar durant 3,4 hores abans de t_c. El panell superior Figura 4.6 mostra l'evolució del ritme d'injecció de partícules accelerades obtingut de l'ajust, per a cinc canals d'energia entre 195 keV i 4,8 MeV. L'evolució obtinguda és semblant a la que correspon a un esdeveniment SEP oest ràpid (vegeu la Figura 7 de Lar98), amb diferències a causa que ni les velocitats ni les heliolongituds són exactament les mateixes. El panell inferior de la Figura 4.6 mostra el valor del ritme d'injecció Q segons l'energia, per a quatre intervals temporals diferents de l'esdeveniment. La Figura 4.7 mostra la dependència de Q en VR derivada, per als cinc canals d'energia que permet un ajust lineal i, per tant, derivar una dependència funcional senzilla.

Esdeveniment Sep98. Origen associat a una fulguració M2.8/2N (N32W81) amb màxim a les 1402 UT del dia 30 de setembre. Xoc detectat per ACE a les 0655 UT del dia 2 d'octubre. Velocitat mitjana del trànsit Sol-Terra: 1006 km s^{-1}. Modelització: assumeix un vent solar de 525 km s^{-1}, un pols d'injecció de 165° en la direcció W81, centrat a 1 $R_{\odot}$i que es propaga a una velocitat inicial de 1300 km s^{-1}. Requereix una injecció solar durant 4,0 hores abans de t_c.

Esdeveniment Sep00. Origen associat a una fulguració M1/2N (S17W09) amb

màxim a les 1131 UT del dia 12 de setembre. Xoc detectat per ACE a les 0400 UT del dia 15 de setembre. Velocitat mitjana del trànsit Sol-Terra: 651 km s^{-1}. Modelització: assumeix un vent solar de 317 km s^{-1}, un pols d'injecció de 165° en la direcció W09, centrat a $10\,R_{\odot}$ i que es propaga amb una velocitat inicial de 910 km s^{-1}. Requereix una injecció solar durant 5,2 hores abans de t_c.

La dependència funcional entre el ritme d'injecció Q i el salt de velocitat normalitzat, VR, per a cadascun d'aquests esdeveniments es mostra en les gràfiques 4.7, 4.14 i 4.20, respectivament, per als cinc canals d'energia per als quals s'ha fet l'ajust. En alguns casos, especialment a baixa energia, la contaminació a causa del flux d'electrons d'alta energia limita l'extensió de l'ajust en rang d'energia (cas Sep98). Les Taules 4.1, 4.2 i 4.3 llisten els valors de la constant Q_0 i de la constant k de l'ajust, deduïdes per a cada esdeveniment i per a cada energia considerada.

5. El codi SOLPENCO

L'objectiu a llarg termini és desenvolupar un codi per caracteritzar els SEP, per a un conjunt de posicions fixades a l'espai, des de l'exterior de la corona solar fins més enllà de l'òrbita de Mart. El model Shock-and-Particle serveix per analitzar i modelitzar esdeveniments SEP, però la complexitat dels processos físics involucrats en la formació dels perfils SEP el fa especialment difícil d'utilitzar per a no especialistes. A més, el temps de càlcul requerit per simular els perfils dels fluxos a diferents energies per a un esdeveniment donat, no permet que s'utilitzi per fer prediccions en temps real de l'esdeveniment SEP que s'està desenvolupant. Una possible solució consisteix a construir una base de dades de perfils de fluxos ja calculats per a determinats escenaris i deduir els perfils buscats per interpolació entre els perfils de la base de dades més propers a l'escenari descrit. Això és SOLPENCO: una eina per calcular perfils de fluxos de partícules en esdeveniments SEP ràpidament.

5.1 La base de dades

L'objecte primer de SOLPENCO és proporcionar la capacitat de predicció quantitativa de fluxos i afluències de protons d'esdeveniments SEP generats per xocs interplanetaris conduïts per CME. El conjunt de paràmetres emprats per generar

la base de dades s'ha seleccionat dins del possible interval de valors que poden tenir, si se suposen propietats mitjanes per a la propagació del xoc i el transport de partícules, tal com s'ha comentat al Capítol 3.

S'ha calculat el flux i l'afluència per a cada una de les següents possibilitats: (a) velocitat inicial del xoc, v_s: 750, 900, 1050, 1200, 1350, 1500, 1650 i 1800 (km s^{-1}); (b) amplada inicial del xoc, ω: 140° (fixat); (c) distància radial heliocèntrica, r: 0,4 AU i 1,0 AU; (d) heliolongitud de l'activitat solar progenitora: W90, W75, W60, W45, W30, W22.5, W15, W00, E15, E22.5, E30, E45, E60 i E75; (e) velocitat del vent solar: 400 km s^{-1}; (f) recorregut lliure mitjà (a 0,5 MeV), $\lambda_{\parallel 0}$: 0,2 AU i 0,8 AU; (g) regió prexoc: 'Yes/No' opció; (h) energia dels protons, E: 0,125, 0,250, 0,500, 1,0, 2,0, 4,0, 8,0, 16,0, 32,0 i 64,0 MeV. En conseqüència, per a un observador situat a un cert punt de l'espai (0,4 o 1,0 AU) la base de dades conté 14 valors per a l'heliolongitud, vuit valors per a la velocitat inicial del xoc i quatre possibles escenaris per a les condicions del transport de partícules, la qual cosa dóna 448 possibles escenaris interplanetaris. Finalment, cal afegir que per a cada escenari es tenen deu perfils del flux i de l'afluència. Tots aquests perfils s'emmagatzemen en dos fitxers, un per a cada distància heliocèntrica. Cada perfil a 1,0 AU està descrit per un vector de 10.000 elements i cada perfil a 0,4 AU, per un vector de 5.000 components. Com que els esdeveniments SEP poden tenir una durada que oscil·la entre 10 i 100 hores, part d'aquests vectors tenen components nul·les.

Es poden veure comentaris específics referents als valors adoptats per les diferents variables a la Secció 5.2.2, dels quals cal destacar els següents: el recorregut lliure mitjà, $\lambda_{\parallel}$, s'escala amb l'energia de les partícules via la seva rigidesa. Si se suposa vàlida l'aproximació QLT, llavors, $\lambda_{\parallel}$ (R) = $\lambda_{\parallel 0}$ $(R/R_0)^{0,5}$ on R_0 = 30,635 MV que correspon a la rigidesa dels protons de 0,5 MeV. La regió prexoc turbulenta es caracteritza amb un recorregut lliure mitjà $\lambda_{\parallel c}$ = 0,01 AU a $E = 0,5$ MeV, i una amplada de 0,1 AU; $\lambda_{\parallel c}$ s'escala amb l'energia com $\lambda_{\parallel c}(R) = 0,01\ (R/R_0)^{-0,6}$ on R_0 = 30,635 MV. L'energia de referència, E_0, és 0,5 MeV; els canals d'energia corresponents a cada valor de l'energia són Emin i Emax, els valors dels quals es llisten a la Taula 5.1.

Els diferents escenaris interplanetaris es resumeixen a les taules 5.2 i 5.3, per a observadors a 1,0 AU i 0,4 AU, respectivament. Cada taula dóna per a una determinada heliolongitud de l'observador respecte a l'activitat solar progenitora la informació següent: (1) l'heliolongitud de l'observador; (2) el temps de connexió,

t_c, el temps després de l'inici de l'activitat solar en el qual es produeix la connexió magnètica entre el front del xoc i l'observador per mitjà de l'IMF; (3) la distància heliocèntrica; (4) el temps de trànsit del xoc del Sol fins a l'observador; (5) la distància heliocèntrica, r_s (en $R_\odot$), al moment t_s, i (6) la velocitat mitjana de propagació el xoc del Sol fins a l'observador, $<v>$ (km s^{-1}).

5.2 La font de partícules accelerades

Per tal de produir perfils sintètics de flux i anisotropia, el model assumeix que el ritme d'injecció de partícules accelerades pel xoc està donat per $\log Q(t) = \log Q_0 + k\mathrm{VR}(t)$, amb $Q_0(E) = C\ E^{-\gamma}$. Els valors de k i γ modifiquen la forma i el valor absolut dels perfils sintètics de flux; aquests valors són diferents per a diferents intervals d'energia i, a més, també poden canviar amb el decurs del temps durant l'esdeveniment.

L'interval de possibles valors per a k no està ben establert ja que el nombre d'esdeveniments SEP fins ara modelitzats és limitat. A més la situació a altes energies ($\geq$ 10 MeV) és més complicada perquè la manca de mesures de les anisotropies no permet reduir el nombre de restriccions quan s'utilitza el model Shock and Particle per determinar aquest paràmetre a partir de les observacions. La contribució d'aquest treball en aquest punt ha estat estudiar i modelitzar un seguit d'esdeveniments SEP (Capítol 4) que permetin conèixer millor l'efecte del valor de k, però encara fan falta uns quants estudis més. L'apèndix D mostra tres exemples que il·lustren la dependència de l'evolució dels perfils respecte a k, de baixes a altes energies.

L'espectre en energia del flux diferencial, mesurat en diferents instants durant un esdeveniment SEP, es caracteritza freqüentment per una doble llei potencial amb un colze (vegeu Capítol 2). Com que l'espectre varia en cada esdeveniment, resulta complicat, per no dir sense gaire sentit, determinar un valor de l'índex espectral, γ, raonablement representatiu del conjunt de valors. Els estudis fets a baixa energia, $<$ 2 MeV, (van Nes et al. 1984; Reames et al. 1997a), energia mitjana, E $\geq$ 2 MeV, (Reames et al. 1997a; Torsti et al. 1999) i alta energia, E $\geq$ 10 MeV (Cane et al. 1988; Kahler, 2001b), per a l'espectre o per al pic del flux, mostren una gran dispersió de valors. Un exemple es pot veure a la Figura 5.1 (Figura 14 de Cane et al. 1998) on es pot apreciar la variació de l'índex espectral per a un conjunt d'esdeveniments segons la posició (longitud) de l'observador respecte a l'activitat solar progenitora.

D'aquests estudis i dels resultats de la modelització d'esdeveniments SEP fets fins ara, s'han assumit els valors següents per a l'índex espectral:

$$\gamma = \begin{cases} 2.0 & E < 2 \text{ MeV} \\ 3.0 & E \geq 2 \text{ MeV} \end{cases} \tag{2}$$

Alternativament, poden utilitzar-se altres expressions, com ara les derivades per Jones i Ellison (1991) o per Xapsos et al. (2000).

En el model Shock-and-Particle el ritme d'injecció de partícules accelerades al xoc en un determinat tub de flux està representat per la funció G (Secció 3.3), lligada al ritme d'injecció $Q(t, E)$ per a l'expressió $G(t, r, E) = A(r)Q(t, r, E)$, on $A(r)$ és l'àrea del tub de flux a la distància r on té lloc la injecció de partícules (p. ex. el cobpoint; vegeu-ne detalls a Lario 1997 o Lar98). El model de transport per a les partícules proporciona els perfils en unitats arbitràries que s'han de traduir a unitats físiques. Cal, per tant, un procés de calibratge amb observacions (és a dir, cal normalitzar els perfils de flux), segons es pot veure a l'apèndix A. Si $K(E)$ és la constant de normalització (que pot dependre de l'energia), llavors es té:

$$Q(t, r, E) = \frac{K(E)}{A(r)} G(t, r, E). \tag{3}$$

Com a primera aproximació hem considerat una única constant de normalització per a totes les distàncies heliocèntriques, posicions angulars i condicions interplanetàries per al transport de partícules, i suposem que depèn de l'energia com E^{-1} (que és la dependència entre el flux diferencial i la densitat columnar de partícules a l'espai de fases).

Els valors de Q_0 i k (definits a la Secció 3.4) es deriven d'esdeveniments SEP simulats (vegeu la Taules 4.1, 4.2 i 4.3 i l'Apèndix E). Després de l'estudi fet, i amb la idea de simplificar el nombre de paràmetres del model, s'han adoptat les hipòtesis següents: (1) usar un únic valor (mitjà) de k per a totes les energies, i (2) adoptar per a Q_0 valors típics per als esdeveniments oest i meridià central estudiats. D'aquesta manera la dependència espacial i temporal de Q queda determinada per la seva dependència funcional amb VR i la dependència de l'energia especificada per mitjà de Q_0. En conseqüència, cal fer una anàlisi i quantificació de la variació de Q_0 amb l'energia (el procés esta descrit en la Secció 5.3.3). L'últim pas d'aquest procés és seleccionar l'esdeveniment a partir del qual s'han de prendre els valors de

Q_0 i k per construir la base de dades. S'adopta l'esdeveniment W50 del 26 d'abril 1981 perquè la k mostra el comportament regular d'entre els esdeveniments oest i meridià central modelitzats. Conseqüentment, la base de dades s'ha construït prenent $k = 0,5$ per a totes les energies i la dependència de Q_0 amb l'energia ben donada d'acord amb l'ajust per a aquest esdeveniment (Figura 5.3); la Taula 5.4 dóna els valors de Q_0 per a cada valor de l'energia dels protons adoptada per la base de dades de SOLPENCO.

Per als esdeveniments en els quals l'observador està magnèticament ben connectat amb el lloc on l'activitat solar progenitora es desenvolupa, els tubs de flux que escombren la nau estan plens de partícules des de l'inici de l'esdeveniment. Atesa la condició límit interior (a $18\,R_\odot$), en aquest tipus d'esdeveniment fa falta introduir una injecció de partícules des de l'inici de l'esdeveniment. Aquesta injecció, simulada amb un perfil d'intensitat constant, permet considerar l'efecte d'un possible xoc coronal des de l'inici de l'esdeveniment fins a t_c, el temps de la primera connexió entre el front del xoc i l'observador.

5.3 El procediment SOLPENCO

La pantalla gràfica inicial de SOLPENCO és una finestra interactiva on l'usuari pot escollir les característiques de l'esdeveniment SEP que vol estudiar: velocitat inicial, distància heliocèntrica radial, posició angular relativa respecte a l'activitat solar progenitora, recorregut lliure mitjà de les partícules a 0,5 MeV, existència d'una regió magnèticament turbulenta davant del front del xoc (prexoc) i canal d'energia. Un exemple es pot veure a la Figura 5.5 i es pot recórrer a una versió en línia a l'European Space Weather Portal. The European gateway to Space Weather resources, http://www.spaceweather.eu/es. El procediment de SOLPENCO està escrit en llenguatge IDL i està disponible sota demanda a http://www.am.ub.es/∼blai/.

Per a un conjunt donat de paràmetres que defineixin uns esdeveniments, el programa calcula els fluxos i les afluències corresponents per interpolació entre els valors prèviament calculats més propers emmagatzemats a la base de dades. La interpolació és una senzilla interpolació lineal entre els quatre valors més propers. Si, per exemple, la parella (VS, WP) defineix un esdeveniment del qual cal calcular el flux, llavors, el corresponent valor es deriva fent una doble interpolació entre els casos: (VS1, WP1), (VS1, WP2), (VS2, WP1) i (VS2, WP2), on $\leq$ WP $\leq$ WP2 i VS1

$\leq$ VS $\leq$ VS2, són els valors més propers a WP i VS, respectivament, a la base de dades.

El problema bàsic d'aquestes interpolacions és que la durada de cada esdeveniment és diferent i, per tant, no se sap a priori en cada instant de temps entre quins punts del perfil del flux de cadascuna de les quatre gràfiques cal interpolar. Per resoldre el problema, els quatre perfils sobre els quals es durà a terme la interpolació es normalitzen a la velocitat de trànsit, $< v >$, del xoc entre el Sol i l'observador. És a dir, es multiplica la durada de cada esdeveniment per un factor homotètic que corregeix l'escala temporal de cada esdeveniment i unifica el temps d'arribada dels quatre xocs; sota aquestes condicions, la interpolació té sentit físic, almenys en primera aproximació. Una vegada duta a terme la interpolació es desfà el camí invers per tal de recuperar l'escala de temps original. Ara bé, aquest mètode implica determinar $< v >$ per a cada un dels quatre casos (diferent velocitat inicial i diferent heliolongitud). Aquesta velocitat es deriva a partir dels ajustos de les velocitats de trànsit derivades pels vuit xocs calculats amb el model MHD, per una funció polinòmica de segon grau (vegeu la Secció 5.2 i l'Apèndix F), que dóna els valors amb precisió suficient, per a observadors situats a 1,0 AU (Figura 5.7) i a 0,4 AU (Figura 5.8). Per exemple, si $<v>_1$ i $<v>_2$, llavors:

$$<v>=<v>_1 \frac{\mathrm{VS2}-\mathrm{VS}}{\mathrm{VS2}-\mathrm{VS1}}+ <v>_2 \frac{\mathrm{VS}-\mathrm{VS1}}{\mathrm{VS2}-\mathrm{VS1}}. \quad (4)$$

L'afluència acumulada es defineix com la integral de l'afluència des de l'inici de l'esdeveniment SEP fins a un moment determinat, i per sobre d'una energia llindar. L'afluència total és el valor de l'afluència calculada fins a l'arribada del xoc a la posició de l'observador. Un problema no resolt és el càlcul de la contribució a l'afluència de la regió posterior al front del xoc, ja que el model Shock and Particle atura la seva descripció a l'arribada del xoc. En molts casos aquesta contribució és negligible, però no sempre és així, especialment per als esdeveniments est intensos. Les afluències es deriven per integració dels valors de les afluències prèviament interpolats i emmagatzemats a la base de dades, de manera semblant al cas dels perfils de flux ja comentats. El flux de partícules per sobre 90 MeV (límit superior del model) s'estima suposant un espectre de potències per a aquesta regió donat per $\gamma = 3$. Una altra magnitud rellevant des del punt de vista de la meteorologia espacial és el pic del flux (e.g. Feynman et al. 2000), definit com el màxim del flux diferencial de partícules a cada energia. En conseqüència, per a cada esdeveniment SEP, el programa rastreja el màxim valor del flux i el temps al qual es produeix.

Finalment, SOLPENCO converteix a unitats físiques els valors dels fluxos i de les afluències resultants. Tal com es discuteix a l'apartat 5.3.3, la constant de normalització està donada per:

$$K(E) = \frac{j^{obs}(t_a, r_0, E_0)}{F^{arbi}(t_a, r_0, E_0)} \frac{A(r_0)}{mE} \tag{5}$$

on $j^{obs}(t_a, r_0, E_0)$ és el valor observat del flux diferencial de protons a l'energia E_0, mesurada a la distància heliocèntrica, r_0 a l'instant t_a; $\mathrm{F}^{arbi}(t_a, r_0, E_0)$ és el valor de la densitat columnar donat pel model (en unitats arbitràries) pels protons d'energia E_0-MeV a la mateixa distància i temps que el flux diferencial observat; $A(r_0)$ és la secció aerolar del tub de flux magnètic a r_0, m és la massa del protó en repòs (se suposa aproximació newtoniana) i E és l'energia cinètica dels protons (per a detalls, vegeu l'Apèndix A). Si se'n considera la discussió, feta a l'Apartat 5.3.3, la constant de normalització emprada a SOLPENCO és:

$$K(E) = \frac{2,4 \times 10^8}{E[\mathrm{MeV}]}. \tag{6}$$

Els resultats de l'execució de SOLPENCO poden tenir-se en forma de gràfics en format PNG (com les Figures 5.10 i 5.11 en forma de fitxers ASCII. Per a cada esdeveniment SEP computat es donen les variables d'entrada que caracteritzen l'esdeveniment (distància radial, posició angular de l'observador, velocitat inicial del xoc, regió prexoc, recorregut lliure mitjà i energia de les partícules), el temps de trànsit i la velocitat de trànsit des del Sol fins a la posició de l'observador, l'afluència total a l'arribada del xoc i el temps i la intensitat del pic de flux, com també la representació gràfica o numèrica del perfil del flux i del perfil de l'afluència. Un descriptor del tipus W450875W04[l02TN], per exemple, identifica cada esdeveniment SEP: W45 indica que es tracta d'un esdeveniment W45, amb una velocitat inicial de 875 km s^{-1}, per a un observador situat a 0,4 AU; els valors entre parèntesis són optatius i indiquen el recorregut lliure mitjà emprat (0,2 AU) i la no-presència (en aquest cas) d'una regió prexoc.

6. Fluxos i afluències derivades de SOLPENCO

Els resultats que produeix SOLPENCO depenen dels valors adoptats per l'escenari solar en el qual es desenvolupa l'esdeveniment SEP, tal com s'ha definit al Capítol

anterior. El que ara cal fer és estudiar la influència d'aquestes variables en el perfil de flux dels protons produïts per SOLPENCO i estudiar la coherència i el comportament del conjunt de perfils sintètics de fluxos i afluències produïts, els quals constitueixen la base del codi, segons les variables més importants pel que fa a les aplicacions en meteorologia espacial: el pic del flux (màxima intensitat) a una determinada energia, l'afluència total, i les variacions amb la distància radial heliocèntrica i l'heliolongitud de l'observador.

6.1 Perfils de flux: influència de les variables d'entrada

L'acceleració de partícules per xocs interplanetaris és més eficient a baixes energies que a altes; per tant, els esdeveniments SEP tenen fluxos més grans a baixa energia que a alta. A més, els perfils de flux poden mostrar dispersió en velocitat a l'inici de l'esdeveniment i, per a una energia donada, el recorregut lliure mitjà emprat pot fer que el perfil inicial creixi més ràpidament o menys. Aquest comportament en els diferents perfils, segons l'energia, del recorregut lliure mitjà es pot veure en els perfils de flux de dos SEP, W451200W10 i E300750W10, trets de la base de dades de SOLPENCO, que es mostren en les Figures 6.1 i 6.2, respectivament. Si se suposa (Figura 6.1) que $\lambda_{\|0} = 0{,}2$ AU (dreta) o 0,8 AU (esquerra). Tal com es pot veure, si es comparen aquestes figures, l'inici de l'esdeveniment en el primer exemple ocorre abans que en el segon perquè la connexió magnètica entre el front del xoc i l'observador (és a dir, el cobpoint inicial) es produeix més tard. També es pot comprovar que la influència del recorregut lliure mitjà en el perfil del flux és menys important que l'heliolongitud de l'activitat solar progenitora i que la velocitat de propagació del xoc interplanetari associat.

Bona part dels perfils de flux assoleixen el màxim a l'arribada del xoc, independentment de l'energia considerada. Ara bé, els esdeveniments oest observats mostren, en general, un màxim a prop de l'inici de l'esdeveniment, o bé un plateau durant un període dilatat de temps abans de l'arribada del xoc (p. ex. Cane et al. 1988; Tylka et al. 2000). Una futura versió de SOLPENCO haurà de tenir en compte la contribució al perfil de la injecció de partícules deguda al xoc, a partir de 4 $R_\odot$ i, potser, adoptar un valor més adaptat de la constant k de la relació Q(VR). Cal assenyalar que la dispersió en velocitat a l'inici d'un esdeveniment no sempre s'observa a causa de la presència de partícules de fons que poblen el tub de flux, de la contaminació dels canals de baixa energia per partícules d'alta energia o per

electrons, per saturació de l'instrument, o per algun canvi sobtat en la direcció de l'IMF, que fa que, de sobte, arribin partícules que ja estaven omplint el tub de flux al qual l'observador acaba quedant connectat.

L'existència d'una regió amb turbulència magnètica davant del front del xoc (el foreshock) té una influència rellevant en els perfils de flux. Segons se'n consideri l'existència o no (i les característiques), els perfils queden fortament afectats, especialment la posició i el valor del pic del flux, tal com es pot veure, per exemple, als panells de l'esquerra i de la dreta, respectivament, de les Figures 6.1 i 6.2. La Figura 6.3 il·lustra millor la situació, i presenta quatre casos segons si es considera i no l'existència d'un foreshock; la diferència rau, bàsicament, en el fet que si existís aquesta regió (caracteritzada per un recorregut lliure mitjà molt petit), les partícules en lloc d'escapar quedarien atrapades i emmagatzemades per davant del xoc; és a dir, els perfils es buiden a la regió intermèdia del perfil de flux de l'esdeveniment, i, en canvi, el pic del flux a l'arribada del xoc es fa més gran.

El perfil de flux d'un esdeveniment depèn, a part de la velocitat del xoc (que és un indicador de la força MHD), en bona mesura de la geometria de l'escenari interplanetari, és a dir, de la posició relativa de l'observador o detector respecte a l'heliolongitud de l'activitat solar progenitora. La Figura 6.4 mostra exemples de perfils de flux generats per vuit xocs amb diferents velocitats inicials (entre 750 i 1800 km s^{-1}) per a dos observadors a 1,0 AU, però col·locats en posicions angulars diferents (W45 a dalt, i E30, a baix), ambdós amb regió turbulenta i sense. La relació Q(VR) trasllada la velocitat del xoc al cobpoint en un ritme d'injecció de partícules, de manera que com més ràpid és el xoc, més eficient és el procés d'acceleració i, per tant (i a part d'altres factors), més alt és el flux sintetitzat. Els perfils en aquesta figura mostren un comportament variable i regular, essencialment, a causa de l'evolució del cobpoint al front del xoc. En el cas d'un esdeveniment W45 com el mostrat, l'augment ràpid inicial del flux es deu a que el cobpoint inicial està localitzat a prop de la regió central del xoc, la més eficient pel que fa a la injecció de partícules accelerades pel xoc. A mesura que el xoc s'expandeix, el cobpoint es va movent cap a l'ala est del xoc i, en conseqüència, el ritme d'injecció de partícules disminueix ja que VR decreix.

Per als esdeveniments est, la connexió magnètica entre l'observador i el front del xoc s'estableix tard, respecte al desenvolupament i l'expansió del xoc. A més el cobpoint inicial queda a prop de la regió més forta del xoc, la qual cosa produeix

un ràpid augment del flux, però tan sols unes quantes hores abans de l'arribada del xoc. La Figura 6.5 mostra un exemple d'un esdeveniment E30 (a 0,5 MeV), amb els mateixos valors per a les diferents variables que per a l'esdeveniment mostrat de la Figura 6.4, però per a un observador situat a 0,4 AU. Les diferències en els perfils de flux d'ambdós escenaris (a part de les velocitats inicials considerades, que corresponen al mateix conjunt) reflecteixen el fet que els observadors, tot i estar a la mateixa línia Sol-Terra, tenen una connexió magnètica amb el front del xoc diferent i una injecció al llarg de l'esdeveniment de diferent durada i intensitat. A més, l'amplada dels xocs simulats en SOLPENCO és gran, la qual cosa fa que un observador situat en longituds oest properes al meridià central estigui ben connectat amb el xoc des de l'inici de l'esdeveniment, mentre que un observador situat, per exemple, a E30 i 0,4 AU, no tingui una connexió magnètica tan bona amb el front del xoc i, per tant, que l'esdeveniment comenci més tard.

6.2 El pic del flux

Per a una posició angular donada de l'observador, sigui a 1,0 AU o a 0,4 AU, el pic del flux augmenta en créixer la velocitat inicial del xoc, és a dir, amb la força del xoc. La Figura 6.6 mostra aquesta tendència del valor del pic del flux, per a protons d'1 MeV d'energia, a 1,0 AU, per a 14 heliolongituds, agrupades en tres conjunts: esdeveniments oest (W90-W30), esdeveniments meridià central (W30-E30) i esdeveniments est (E30-E75). La Figura 6.7 mostra resultats semblants per a diferents combinacions d'energia (0,125, 1,0 i 8,0 MeV) i distàncies helioradials (1,0 i 0,4 AU), per a les mateixes heliolongituds. Hi ha excepcions en aquest comportament, per a valors extrems d'algunes d'aquestes variables, tal com s'explica al text, a causa de combinacions màximes o mínimes de factors com la velocitat del xoc (força del xoc), la posició del cobpoint sobre el front del xoc (heliolongitud de l'observador) i la presència o no d'una regió turbulenta davant del front. Aquesta última, per exemple, no produeix els mateixos efectes sobre esdeveniments SEP associats a xocs lents que sobre xocs ràpids, ja que en els primers l'acció dura poc temps, mentre que en els segons és perllongada.

La major part dels perfils calculats mostren el pic del flux a l'arribada del xoc: a 1 MeV, 100% a 0,4 AU i 97% a 1,0 AU (la proporció augmenta al 99,9% per a $E < 32$ MeV). En 94 casos d'un total de 4480, el pic es dóna entre 1 i 25 minuts abans de l'arribada del xoc, i en 40 casos, el pic es produeix poc després de l'inici

de l'esdeveniment. Aquests 40 casos corresponen a esdeveniments oest, tal com s'ha observat en molts esdeveniments oest, a energies similars (Cane et al. 1988). Per a altres escenaris interplanetaris i energies, es pot veure que el màxim del pic del flux es dóna en els esdeveniments W00, W15 i W22, per als quals el cobpoint es mou per la regió central del front del xoc (la part més forta, i la connexió magnètica s'estableix poc després d'iniciar-se l'esdeveniment). Els valors més intensos del pic del flux a 0,4 AU s'obtenen pels mateixos observadors (heliolongituds) que a 1,0 AU, afegint-hi el cas de l'observador situat a E15, per al qual també s'estableix una bona connexió magnètica.

És possible intentar derivar una correlació entre el valor del pic del flux i la velocitat inicial del xoc, de manera similar a com s'intenta derivar una dependència funcional (una llei del tipus, $f \propto v^{\alpha}$, entre el valor del pic del flux i la velocitat de la CME associada, observada en imatges coronogràfiques preses per SOHO/LASCO i SOLWIND (Reames 2000). El problema que sorgeix en intentar fer-ho amb els valors del pic del flux de la base de dades i de la velocitat del xoc, per després comparar-ho amb els valors deduïts de les observacions, és que no sabem quina és la relació (ni individual ni mitjana) entre la velocitat inicial del xoc a $18\,R_{\odot}$ i la velocitat observada de la CME associada. La Figura 6.8 mostra la correlació derivada (la recta d'ajust corresponent) per als perfils de flux i les velocitats inicials del xoc, de la base de dades de SOLPENCO, per a tres energies (0,5, 2,0 i 16 MeV) i per als tres conjunts agrupats d'esdeveniments (oest, meridià central i est). Les correlacions trobades es mostren en les Taules 6.1, 6.2 i 6.3. Els coeficients de correlació tendeixen a créixer amb l'energia quan es considera el conjunt total d'esdeveniments sintètics, que és el mateix tipus de correlació derivada per Reames (2000). Kahler i Vourlidas (2005) han estudiat els pics de flux de 116 SEP associats a CME; una part del seu conjunt d'esdeveniments es pot comparar amb els resultats mostrats en la Figura 6.8, assumint que el rang de velocitats de les CME és comparable al rang de velocitats inicials emprades a SOLPENCO i que a altes energies el flux segueix una llei de potències amb $\gamma = 3$. En aquestes condicions, els resultats de SOLPENCO estan d'acord amb els de Kahler i Vourlidas (2005), per als esdeveniments que mostren un pic de flux més alt. La raó és que els esdeveniments SEP intensos tendeixen a estar associats amb CME àmplies i intenses, com els esdeveniments de SOLPENCO, generats per xocs amplis i intensos.

6.3 L'afluència

Dos factors determinen l'afluència: la durada de la injecció de partícules accelerades al front del xoc, a mesura que aquest últim es propaga des del Sol, i l'eficiència del xoc com a accelerador de partícules, que depèn de la posició i de l'evolució del cobpoint. En conseqüència, s'ha estudiat la dependència de l'afluència segons la velocitat inicial del xoc i de l'heliolongitud de l'activitat solar progenitora, fent la mitjana dels valors que depenen del recorregut lliure mitjà i de l'existència o no d'un foreshock (l02/l08 i TY/TN). La Figura 6.9 mostra, de manera semblant a la Figura 6.7 per al pic del flux, la dependència de l'afluència total respecte a la velocitat inicial del xoc, per a observadors a 1,0 AU i a 0,4 AU, i per sobre de tres energies llindars d'1, 4 i 32 MeV. A 1,0 AU, com més llarga és la durada de l'esdeveniment, més gran és l'afluència. Els esdeveniments W45 mostren les afluències més altes a totes les energies (seguits dels W30, W22, W15 i W00). Hi ha excepcions, degudes a combinacions extremes de les variables que defineixen cada escenari (vegeu el text).

El temps de connexió, t_c, fa augmentar lentament els esdeveniments meridià central cap als esdeveniments est, per a cada xoc simulat, la qual cosa implica que la durada de la injecció disminueix a mesura que l'observador es connecta amb el xoc des de posicions situades més cap a l'est. Per aquesta raó l'afluència total decreix a mesura que l'observador es mou cap a longituds est per a una velocitat inicial del xoc donada. L'afluència comença a decréixer per a velocitats creixents, a partir dels esdeveniments E45 i E60, a totes les energies considerades. Per a aquests esdeveniments el cobpoint es troba a la regió més feble de l'ala esquerra del xoc i, per tant, el factor dominant és la durada de l'esdeveniment. Aquesta disminució augmenta amb l'energia perquè els xocs més lents són més ineficients a l'hora d'accelerar partícules d'alta energia.

A 0,4 AU la influència de la durada de la injecció de partícules és menys important que a 1,0 AU a causa del temps més curt de trànsit i a que molts observadors estan ben connectats al front del xoc des de l'inici de l'esdeveniment (d'E30 a W75). Per tant, la dependència de l'afluència amb la posició angular de l'observador situat a 0,4 AU està bàsicament determinada per l'eficiència en l'acceleració de partícules de la regió escanejada pel cobpoint. En conseqüència, les màximes afluències són les mesurades per observadors situats a W15 (l'observador està connectat a la part central del xoc) i W00 (el pic del flux s'observa al pas del xoc). Per a tots els esdeveniments ben connectats, l'afluència augmenta amb la velocitat inicial del xoc,

excepte en el cas W75, on el cobpoint ressegueix el feble flanc est del xoc i, llavors, la durada més gran de l'esdeveniment compensa l'efecte d'una eficiència més gran.

6.4 Variacions radials i longitudinals

La presència d'un xoc interplanetari dóna una contribució important a l'afluència d'un esdeveniment SEP, tant a 0,4 AU com a 1,0 AU, un factor entre 1,1 i 10 vegades, segons la velocitat inicial del xoc i l'heliolongitud considerada. Aquesta conclusió és força diferent de l'habitualment recomanada (però no provada) llei de variació amb l'invers del quadrat de la distància (Feynman et al. 1993) i amb més acord amb les dependències radials deduïdes del treball observacional de Lario et al. (2006).

S'ha comparat l'afluència total, F, d'esdeveniments SEP per a diversos parells d'observadors situats a 0,4 AU i 1,0 AU, aproximadament ubicats al mateix tub de flux de camp magnètic: E75 – E45, E60 – E30, E45 – E15, E30 – W00, E15 – W15, W00 – W30, W15 – W45, W30 – W60, W45 – W75 i W60 – W90. Si s'assumeix una dependència de la forma: $F \propto r^{\beta}$, es pot calcular per a cada parell d'observadors el quocient d'afluències $F(0,4)/F(1,0) = 0,4^{\beta}$ i, per tant, deduir l'índex radial β. Com que els observadors tenen cobpoint propers, tenen la mateixa història d'injecció de partícules accelerades pel xoc i, per tant, es poden eliminar tota la resta de factors comuns i fer una anàlisi estrictament de la dependència radial. La Figura 6.11 mostra els valors de β deduïts, segons la velocitat inicial del xoc, per a energies superiors a 2 MeV i a 32 MeV. Tal com es pot veure, β decreix a mesura que la velocitat inicial augmenta, per a aquells observadors que estan magnèticament ben connectats a la regió central del xoc. Hi intervenen dos factors: com més ràpid és el xoc, més petita és la diferència entre les durades de les injeccions de partícules respectives i, per tant, menys importants són les diferències dels SEP observats a 0,4 AU respecte a 1,0 AU. El pic del flux és més alt com més alta és la velocitat inicial del xoc, la qual cosa contribueix a reduir també les diferències entre les afluències calculades per als dos observadors.

Els valors de β derivats per a aquestes afluències no quadra amb els valors derivats per Lario et al. (2006). Hi ha tres raons: (1) cap dels 72 esdeveniments de l'estudi estadístic de Lario et al. (2006) té els observadors situats sobre la mateixa línia de camp magnètic; de fet la separació angular mitjana és de $73° \pm 44°$. (2) Sols nou d'aquests esdeveniments estan mesurats a $0,4 \pm 0,05$ AU. (3) SOLPENCO no

pot prendre en consideració la contribució a l'afluència de la regió posterior del xoc (important en algunes situacions i escenaris) ni la injecció de partícules quan el xoc encara està a prop del Sol.

Pel que fa al pic del flux, la dependència radial és menys clara que per a l'afluència, tal com es pot veure en la Figura 6.12. Els valors de β estan més escampats a mesura que es consideren energies més altes. El valor mitjà augmenta amb l'energia, però, per a esdeveniments individuals pot decréixer, tal com passa amb els esdeveniments lents magnèticament ben connectats amb el xoc.

La conclusió més important és que no es pot derivar una llei de dependència radial vàlida per a tots els tipus d'esdeveniments SEP, ni per a les afluències ni per als pics de flux. Les variacions d'aquestes quantitats amb la distància heliocèntrica depenen de: (1) l'eficiència del xoc, com a injector de partícules accelerades, a la regió escanejada pel cobpoint al llarg del seu front; (2) la força MHD del xoc (representada per la seva velocitat inicial), i (3) l'energia cinètica de les partícules. El primer d'aquests factors està d'acord amb les conclusions de Lario et al. (2006): és la distància angular entre el punt de connexió magnètica de la sonda a la superfície del Sol i la posició de l'activitat solar progenitora l'element bàsic, i és més rellevant que la distància radial heliocèntrica.

7. Comparació de fluxos i afluències observades amb prediccions

S'ha identificat l'origen solar de 115 xocs interplanetaris detectats per ACE, associats a esdeveniments SEP, entre gener de 1998 i octubre de 2001, per a diversos canals d'energia de protons entre 47 keV i 440 MeV (Apèndix I). Per assolir aquesta identificació s'ha fet un revisió acurada d'observacions d'aquests esdeveniments a la literatura, de les dades contingudes al Solar Geophysical Data i les contingudes als catàlegs de CME de SOHO/LASCO, per Yashiro et al. (2004).

En una primera aproximació ens hem centrat en l'anàlisi dels esdeveniments SEP del tipus meridià central (els generats per una activitat solar localitzada entre E30 i W30), perquè aquests esdeveniments produeixen els fluxos amb un pic d'intensitat i una afluència més grans. Les condicions imposades al conjunt de SEP són: (1) una

associació entre l'esdeveniment i l'origen solar única i ben establerta; (2) l'heliolongitud entre W30 i E30; (3) un augment important del flux per sobre del 25 MeV, i (4) que l'esdeveniment no estigui encavalcat en un esdeveniment previ (que estigui aïllat). El resultat és un subconjunt de vuit esdeveniments que es poden veure en la Taula 7.3, en la qual es donen totes les característiques de cada esdeveniment.

Conegudes les característiques de cada esdeveniment és possible derivar la velocitat del pols inicial a $18\,R_\odot$ (Aran et al. 2004); per a aquests vuit esdeveniments corresponen a: 1399, 1136, 1131, 1615, 740, 1222, 1348 i 1387 km s^{-1}, respectivament. Per a cada un d'aquests esdeveniments s'ha calculat el quocient entre el valor del pic del flux del flux sintètic calculat i el valor observat. Els panells de l'esquerral de la Figura 7.6 mostren aquesta relació per a quatre canals d'energia d'ACE/EPAM i d'IMP-8/CPME. Com que l'energia modelada per SOLPENCO i l'energia mitjana del canal corresponent no coincideixen, sols es comparen els més propers: els que corresponen a les dues energies que es corresponen amb SOLPENCO. Tal com es pot veure en aquesta figura, els valors predits i observats del pic del flux coincideixen millor a baixa energia que a alta; excepte en dos casos (esdeveniments 4 i 8), el factor és inferior a 10. Aquestes dues excepcions corresponen a un esdeveniment que mostra una gran component inicial a 440 MeV i per al qual el flux a 48 – 96 MeV es manté alt i constant fins a l'arribada del xoc corresponent.

El segon panell esquerre de la Figura 7.6 mostra la comparació entre els fluxos observats a 1,9 – 4,8 MeV i el flux sintètic derivat a 2,0 MeV i 4,0 MeV; tal com es pot veure, els valors a 2,0 MeV mostren uns pics de flux que s'ajusten millor que els corresponents a 4,0 MeV. El tercer panell mostra de la mateixa manera els valors observats en el canal 4,6 – 15,0 MeV amb els derivats a 4,0 MeV i 8,0 MeV; les prediccions a 4,0 MeV són clarament millors que les de a 8,0 MeV. És a dir, els valors observats concorden millor amb els valors calculats per a l'energia mínima del canal que per al corresponent valor mitjà de l'energia del canal. Una primera raó d'aquestes diferències és el fet que el límit inferior del model MHD, situat a $18\,R_\odot$, no permet una modelització millor de la contribució del xoc al flux de partícules d'alta energia. Una segona raó és el fet que el factor de proporcionalitat entre Q i VR ($k = 0,5$) es dedueix dels ajustos fets a diferents esdeveniments a baixa energia i s'assumeix que té el mateix valor a alta energia, la qual cosa no és necessàriament certa.

Un altre factor rellevant per a la meteorologia espacial és el moment en el qual

el flux de protons assoleix aquest màxim valor (el temps del pic del flux). En els panells drets de la Figura 7.6 s'ha dibuixat la diferència entre el temps observat i el temps predit, per a cada energia i per a cada esdeveniment. Sols es mostra un canal d'energia perquè per al canal 1,4 – 11,3 MeV el pic del flux es produeix sempre a l'arribada del xoc en la posició de l'observador. A baixa energia (∼0,4 MeV, panell superior), la predicció del temps del pic és correcta (menys de 5 hores) i coincideix amb l'arribada del xoc, excepte per a l'esdeveniment #5 de la Taula 7.3. A ∼8,0 MeV (tercer panell) les diferències són acceptables (inferiors a 10 hores, excepte per a #5). Finalment, a energies altes (∼67 MeV) les diferències són importants. La raó bàsica d'aquestes diferències creixents amb l'energia és el fet que el límit inferior del model MHD, situat a 18 $R_{\odot}$, no permet una modelització millor de la contribució del xoc al flux de partícules d'alta energia.

La Figura 7.7 mostra els valors de l'índex espectral γ del flux al pic del flux dels valors observats i dels derivats de SOLPENCO, si se suposa una llei de potències amb l'energia. El dos panells mostren els valors a baixa (de ∼0,1 MeV a ∼5 MeV) i alta energia (∼2 MeV ∼67 MeV), respectivament, per a cada esdeveniment de la Taula 7.3. Tal com es pot veure, SOLPENCO produeix un índex espectral quasi constant a baixa energia i a alta, independentment de la velocitat inicial del xoc. La raó és que SOLPENCO suposa el mateix espectre energètic per al ritme d'injecció Q de partícules accelerades pel xoc per a tots els esdeveniments, sigui quina sigui l'heliolongitud o la velocitat inicial del xoc. Un problema que cal resoldre és el fet que el nombre d'índexs espectrals observacionals a alta energia coneguts pel tipus d'esdeveniments que s'estan tractant és molt limitat. De fet, tal com s'ha comentat en el Capítol 5, els valors de γ a alta energia són molt dispersos, fins i tot sense prendre en consideració l'heliolongitud de la CME o la velocitat de propagació (p. ex. Cane et al. 1988). A més, les finestres energètiques dels canals d'alta energia són molt àmplies, la qual cosa evita poder fer comparacions realment fiables. Aquests factors fan que les prediccions dels índexs espectrals a alta energia siguin menys fiables.

Hem extès l'anàlisi a esdeveniments oest. Seguint els mateixos criteris que per els esdeveniments meridià central, hem seleccionat 8 esdeveniments amb heliolongituds entre W30 i W90 (Taula 7.5). De l'estudi de llurs pics de flux se'n dedueix que SOLPENCO prediu amb la mateixa cura que per als meridià centrals el valor del pic del flux per a $E < 2,0$ MeV. No obstant, la predicció del temps del pic falla per $E > 0,5$ MeV. Aquest fet és degut bàsicament que en aquests esdeveniments oest

la majoria de les partícules són accelerades quan el xoc és a pocs radis solars del Sol. Per tant, la conclusió és que per a obtenir una millora de les prediccions del codi a alta energia $E > 2,0$ MeV és necessari l'ús d'un model MHD que tingui unes condicions de contorn internes properes al Sol (entre $3-5\ R_{\odot}$), per tal de poder simular la propagació del xoc des del seu inici i per tant, poder donar compte de les partícules accelerades a l'inici de l'esdeveniment. També fóra necessari l'ús d'altres valors del coeficient k per a descriure la relació Q(VR) a alta energia.

8. Modelització i predicció de SEP a Mart. L'esdeveniment del 6 de març de 1989

Els esdeveniments SEP són importants a l'hora de preparar missions tripulades a Mart ja que el disseny d'aquestes missions ha incloure protocols bàsics de protecció dels astronautes i del material embarcat contra la radiació (Lanzerotti 2004). Fa falta saber quan es produirà un SEP, si afectarà la missió i si donarà lloc a un episodi de radiació intensa, quan i quina en serà la màxima intensitat i el valor de l'afluència total. Tots aquests paràmetres depenen de la posició, la velocitat, la força MHD i l'extensió de la font mòbil de partícules (el xoc interplanetari), com també de la complexitat de l'IMF quan es produeix l'esdeveniment. D'altra banda, pràcticament no hi ha estudis observacionals de la dependència del flux i de l'afluència amb la distància radial (vegeu Lario et al. 2006). Les recomanacions tècniques que actualment es fan servir per a l'extrapolació radial de les intensitats dels SEP a partir de mesures a 1,0 AU (Feynman i Gabriel 1988) són poc realistes, especialment quan l'evolució de la intensitat de les partícules està dominada pel xoc interplanetari.

La modelització d'esdeveniments SEP associats a xocs interplanetaris observats simultàniament per diferents sondes interplanetàries o satèl·lits situats al pla de l'eclíptica, requereix almenys models bidimensionals per descriure la propagació del xoc. La dependència longitudinal dels perfils temporals de la intensitat del SEP sols es pot reproduir si la connexió magnètica entre el xoc i l'observador es descriu correctament, per exemple, si se suposa una espiral de Parker però no un IMF radial. La hipòtesi que un mecanisme específic d'acceleració de partícules està funcionant en el xoc interplanetari es una sobresimplificació de la descripció de la realitat, atesa l'enorme varietat d'esdeveniments SEP observats amb el pas d'un xoc interplanetari

(van Nes et al. 1984; Tsurutani & Lin 1985; Lario et al. 2003a). Les variables que descriuen la injecció de partícules accelerades pel xoc i el seu escapament de la regió turbulenta formada davant del xoc, incrementen el nombre de paràmetres lliures utilitzats en els models d'esdeveniments SEP. Per aquesta raó, hem preferit fer servir un model senzill (e.g. Lario et al. 1998) que no té en compte explícitament els mecanismes d'acceleració pròpiament dits, i deixa per al futur l'ús d'aquest tipus de models per quan es tingui una millor comprensió de les condicions físiques que es donen on es produeixen els processos d'acceleració de partícules.

El model en qüestió s'aplica a l'únic esdeveniment SEP observat a Mart que reuneix les condicions mínimes per poder-se modelitzar. Mentre que les observacions d'esdeveniments SEP a l'òrbita de la Terra es poden fer de manera rutinària, des de fa tres cicles solars (Lario i Simnett 2004), les observacions a Mart sols han estat possibles en rares ocasions. Missions interplanetàries com la Phobos-2 i la Mars-Odyssey ens han ofert petites mostres d'esdeveniments SEP a l'entorn de Mart (Marsden et al. 1991; McKenna-Lawlor et al. 1991, i Cleghorn et al. 2004). En aquest capítol analitzem un esdeveniment SEP observat pel detector CPME (Charged Particle Measurement Experiment) a bord del satèl·lit IMP-8 (Sarris et al. 1976), a l'entorn de la Terra, i observat també pel detector LET (Low Energy Telescope) embarcat a la sonda Phobos-2 (Marsden et al. 1990), en òrbita entorn del planeta Mart. Phobos-2 va tenir una vida operativa de tan sols tres mesos; l'esdeveniment SEP del 6 de març de 1989 és un dels pocs que aquesta sonda va poder detectar, i és l'únic que es pot modelitzar amb un cert grau de fiabilitat, tot i que no es tracta, ni de lluny, d'un exemple de llibre, tal com es descriu al text.

Aquest esdeveniment SEP, junt amb els altres d'aquest mateix període, va ser produït pel trànsit de la regió activa NOAA AR 5395 sobre el disc solar. Diferents autors (e. g. Marsden et al. 1990 o Kurt et al. 2004) han associat aquest esdeveniment observat per IMP-8 el 6 de març i més tard per Phobos-2 amb una fulguració X15/3B localitzada a N35E69. IMP-8 va detectar el pas del xoc interplanetari a les $\sim$ 1800 UT del dia 8 de març, la qual cosa implica una velocitat de trànsit entre el Sol i la Terra de $<\mathrm{v}> = 798$ km s^{-1}. Marsden et al. (1990) identifiquen el pas del xoc per Phobos-2 a les 2015 UT del dia 9 de març, la qual cosa implica una velocitat de trànsit de $<\mathrm{v}> = 837$ km s^{-1}, si s'assumeix el mateix origen solar per a ambdues identificacions del xoc, tal com es discuteix en la Secció 2 d'aquest capítol.

8.1 Modelització de l'esdeveniment de partícules

Per modelitzar l'esdeveniment de partícules se segueix el mateix procediment descrit en el Capítol 3, aplicat als esdeveniments del Capítol 4. En primer lloc, per modelitzar la propagació del xoc interplanetari des de 18 $R_\odot$, primer fins a la Terra i després fins a Mart. Es fa servir el codi 2.5D MHD de Wu et al. (1983), segons es descriu a Smith i Dryer (1990). Les condicions inicials preses són les necessàries per ajustar l'arribada del xoc a IMP-8 i a Phobos-2 als valors observats i per ajustar el salt en velocitat i densitat del vent solar al pas del front del xoc (l'ajust del camp magnètic no es força), tal com es pot veure en la Figura 8.1. Amb aquest model es pot calcular la posició del cobpoint en cada instant de temps, tant per a IMP-8 com per a Phobos-2. A mesura que el xoc es propaga i expandeix, cadascun d'aquests cobpoint escombra regions diferents del front del xoc; en un moment donat, el cobpoint d'IMP-8 està sempre més cap a l'oest que el cobpoint de Phobos-2, tal com es pot veure en la Figura 8.2.

Per a cada cobpoint d'IMP-8 i de Phobos-2, per a cada interval de temps de la propagació del xoc des que la CME és ejectada fins que el xoc ultrapassa l'òrbita de Mart, es calcula la relació VR(salt de velocitat normalitzat a través del xoc) i BR(salt del camp magnètic a través del xoc: vegeu el Capítol 4). L'evolució de VR i BR és conseqüència del desplaçament del cobpoint al llarg del front del xoc (des del feble flanc oest cap la part central del xoc) i de l'afebliment del xoc a causa de la mateixa expansió i propagació. La Figura 8.3 mostra l'evolució d'aquestes variables segons la distància radial i l'angle heliocèntric per a cada una de les dues naus. El temps del primer cobpoint inicial no coincideix amb l'inici d'injecció de partícules, ja que s'assumeix que la VR ha de ser superior a un cert valor llindar, VR = 0,1.

Per reproduir les intensitats de partícules observades a diferents energies, s'ha seguit el mateix procediment emprat per Lario et al. (1998). El model assumeix que les partícules accelerades al front del xoc són injectades des del cobpoint de la línia de l'IMF que connecta el xoc amb l'observador. El ritme d'injecció està descrit per la funció $Q(r,t)$, descrita al Capítol 4, i que s'escala amb l'energia segons una llei de potències: $Q(E) = Q_0(E_0)(E/E_0)^{-\gamma}$, amb E_0 = 3,03 MeV (l'energia mitjana dels protons corresponent al canal d'energia 2,0 – 4,6 MeV, de l'instrument IMP8/CPME). La dispersió en angle de batuda es modela assumint un procés de dispersió segons la QLT, que es pot descriure per un recorregut lliure mitjà, $\lambda_{\|0}$ = 0,6 AU, amb una dependència amb l'energia donada per $\lambda_\| = \lambda_{\|0}(R/R_0)^{2-q}$

(Hasselman i Wibberenz, 1970), on R és la rigidesa de la partícula i q, l'índex espectral de les fluctuacions del camp magnètic (q = 1,5). L'ajust aconseguit per sis canals d'energia (0,5 MeV < E < 48 MeV) es pot veure en la Figura 8.4.

De l'ajust de les intensitats observades a IMP-8 es deriva l'evolució del ritme d'injecció Q, entre 0,50 MeV i 48 MeV i, per tant, es pot expressar el ritme de la injecció Q segons VR, després d'eliminar la variable t de l'evolució de Q i de VR. El panell inferior de la Figura 8.5 mostra la correlació entre Q i VR, amb les línies rectes que representen els ajustos lineals a una funció de la forma $\log Q = \log Q_0 + k\mathrm{VR}$. Aquesta és la relació $Q(\mathrm{VR})$ deduïda per Lario et al. (1998). La Taula 8.2 dóna els valors de Q_0 i de k, com també el coeficient de la regressió, ξ, obtingut per a cada canal d'energia. Com que VR augmenta amb el temps, tots els pendents, k, són positius. En la Secció 8.3.2 es discuteix el fet que el valor de la k per al canal 4,6 – 15,0 MeV és significativament més gran que els valors deduïts per als canals restants, ateses les conseqüències que aquest fet té al moment de fer les prediccions de les intensitats de protons que s'han de detectar a Phobos-2.

8.2 Modelització de l'esdeveniment de partícules a Mart

Les condicions del medi interplanetari per al transport de partícules energètiques són les usualment utilitzades i ja comentades, derivades de la modelització dels fluxos SEP i l'anisotropia de primer ordre. Ara bé com que ni IMP-8 ni Phobos-2 poden proporcionar mesures per determinar l'anisotropia, seria possible derivar diferents evolucions per a Q i del recorregut lliure mitjà que ajustessin els perfils de flux observat. Per restringir al màxim aquesta possibilitat, s'ha procedit a la modelització directa dels fluxos observats per Phobos-2 per tal de tenir una idea de com són les condicions de transport de partícules i del ritme d'injecció fins a l'òrbita de Mart. La Figura 8.6 mostra els perfils de la intensitat diferencial de protons per als quatre canals de Phobos-2/LET que s'han fet servir (0,9 – 1,2 MeV, 1,8 – 3,8 MeV, 3,8 – 8,0 MeV i 9,0 – 19,0 MeV). No s'ha considerat el canal d'1,2 – 3,0 MeV perquè se sobreposa amb els canals contigus.

Els perfils de flux derivats de l'ajust es mostren també en la Figura 8.6. El forat que hi ha a les dades poc després de l'inici de l'esdeveniment impedeix fer un ajust millor a l'esdeveniment per a aquest interval (per això està dibuixat de manera diferent). Per tal de simular la injecció de partícules abans del temps de

connexió, t_c = 12,6 hores, s'ha suposat una injecció del tipus Reid-Axford, similar a l'emprada en el cas d'IMP-8. Aquesta injecció permet ajustar les poques dades observacionals de què es disposa abans del període sense dades; és una injecció més intensa que la d'IMP-8 perquè Phobos-2 està més ben connectat amb la posició de l'activitat solar que IMP-8: $\sim 40°$ més cap a l'eix central del xoc que la connexió d'IMP-8 (si s'assumeix un vent solar de 434 km s^{-1} i un IMF descrit per una espiral nominal de Parker). El recorregut lliure mitjà derivat i la seva dependència amb la rigidesa són molt similars als derivats per IMP-8, excepte per a la descripció de la regió turbulenta que és més intensa; això també és una conseqüència que el cobpoint de Phobos-2 es trobi més cap a la zona central que el d'IMP-8 i, per tant, recorre una regió del front del xoc amb una turbulència més potent. De fet, fa falta que la dependència amb al rigidesa del recorregut lliure mitjà al foreshock sigui positiva, $R^{+0,2}$, per tal d'ajustar la rampa del flux just abans de l'arribada del xoc (Beck i Sanderson 1989).

8.3 Predicció de l'esdeveniment de partícules a Mart

El ritme d'injecció, Q, a Phobos-2 pot ser predit, si se suposa que la relació Q(VR) derivada de la modelització de l'esdeveniment SEP a IMP-8 és també vàlida per a tot l'esdeveniment i al llarg de front del xoc. Si s'accepta aquesta hipòtesi, llavors és possible sintetitzar els perfils dels fluxos que s'han d'observar a 1,58 AU per Phobos-2, ja que coneixem el valor de VR a cada cobpoint de Phobos-2, com també la relació Q(VR). Aquests perfils es poden comparar amb els observats i avaluar la bondat de la predicció.

Un problema important que sorgeix és el fet que els canals d'energia dels detectors Phobos-2/LET i IMP-8/CPME no cobreixen el mateix rang d'energies ni les finestres energètiques són similars. En conseqüència els valors de Q_0 i k s'han de recalcular (i extrapolar quan sigui necessari) per adaptar-los als canals d'energia de Phobos-2/LET, la qual cosa introdueix diferents opcions a l'hora de produir les prediccions dels perfils dels fluxos. Per tant, s'han definit tres prediccions, etiquetades respectivament com a Fc1, Fc2 i Fc3, que breument es descriuen tot seguit.

Predicció Fc1. La Figura 8.7 mostra dues prediccions per als perfils de flux, per al canal d'energia de 3,8-9,0 MeV: una correspon al valor de k derivat per al canal d'energia de 2,0 – 4,6 MeV d' IMP-8, i l'altra per al canal 4,6 – 15,0 MeV. També

s'hi poden veure dues prediccions del perfil del flux per al canal 9,0-19,0 MeV, ambdues calculades emprant el mateix valor de k, però suposant o no l'existència d'un foreshock davant del front del xoc. La raó és que per a aquest canal d'energia, no està clar si s'ha de considerar o no la regió esmentada, ja que el seu interval d'energia s'encavalca amb el dels canals de 4,6 – 15,0 MeV i el de 9,0 – 19,0 MeV d'IMP-8/CPME. Tal com es pot veure en la figura, les prediccions s'ajusten bé, a partir de $\sim$ 27 hores abans de l'arribada del xoc, però a la primera part els fluxos observats queden subestimats per un factor 2 a alta energia i $\sim$ 8 per al canal de més baixa energia.

Els factors responsables més importants d'aquest desajust de les prediccions a la primera part de l'esdeveniment són:

(1) La influència de les condicions MHD per a l'eficiència del xoc queda parcialment reflectida en la relació Q(VR) (Lario et al. 1998; Sokolov et al 2006).

(2) A mesura que el xoc s'expandeix i el cobpoint es mou cap a la part central del seu front, la geometria del xoc pot canviar cap a una configuració més obliqua, i afavorir un increment més gran dels processos de dispersió per a les ones d'Alfvén autogenerades davant del xoc, i esdevenir, per tant, més eficient del considerat.

(3) Les condicions de transport de les partícules al llarg de l'IMF poden ser diferents del Sol a IMP-8 o del Sol a Phobos-2, a causa de la distància radial i angular entre aquestes dues naus.

(4) La configuració de l'IMF no ha de ser necessàriament una espiral de Parker, la qual cosa faria variar les posicions del cobpoint (Cane et al. 2006).

(5) Pot haver-hi una població local de fons que actuï com a partícules llavors per a l'acceleració, de manera que aquesta esdevingui més eficient a Phobos-2 que a IMP-8, per exemple, a la primera fase de l'esdeveniment quan el xoc és més perpendicular (Tylka et al. 2005).

Predicció Fc2. Per tal de verificar els factors (2) i (3) s'han calculat els perfils predits a Phobos-2 suposant les condicions de transport derivades de la modelització de l'esdeveniment a Mart. Si es diferencien únicament de les calculades a IMP-8 per a la dependència de la rigidesa pel que fa al recorregut lliure mitjà adoptat per

la regió turbulenta, els perfils que s'obtenen són lleugerament més ajustats que els obtinguts per al cas Fc1, però són molt semblants. En conseqüència, es pot dir que la possible influència en els perfils de les diferents condicions de transport o del foreshock són petites, pel que fa a l'efecte en les prediccions dels fluxos del SEP observat a Mart.

Predicció Fc3. La població de partícules associades a la fulguració concomitant pot ser una font de partícules important, especialment en esdeveniments SEP intensos a altes energies. Per tal de simular una població d'aquesta mena, i la conseqüent acceleració i injecció des del xoc quan està a prop del Sol, s'ha suposat una injecció definida per a un perfil Reid-Axford caracteritzat per $\beta = 20$ hores i $\tau = 5$ hores, que s'escala amb l'energia com $E^{-2,5}$. La Figura 8.8 mostra els resultats d'aquesta predicció, suposant les mateixes condicions de transport i $Q(VR)$ que en el cas Fc2. Tal com es pot veure, les prediccions s'ajusten molt millor als valors observats; de fet a alta energia els valors pràcticament coincideixen, mentre que a baixa ($< 1{,}8$ MeV) energia queden sols lleugerament subestimats. Aquestes diferències menors es podrien ajustar si es considerés un espectre energètic menys fort per a les partícules injectades a prop del Sol, però no cal fer-ho ja que el resultat obtingut és ja prou il·lustratiu i acurat.

Aquest estudi és un clar exemple que no hi ha encara un model que pugui prendre en consideració tots els factors que poden aparèixer a l'hora de generar i modelitzar esdeveniments SEP, i que les prediccions que es puguin fer de fluxos a partir dels valors observats a 1,0 AU no estan lliures d'incerteses. Aquestes incerteses poden ser molt rellevants si el que es pretén és obtenir prediccions operatives dels fluxos de radiació utilitzables per al disseny de missions interplanetàries i per a la protecció de les tripulacions embarcades. Aquest punt s'il·lustra amb una quantificació dels fluxos i les afluències predites i els corresponents valors deduïts de les observacions, per a aquest esdeveniment a Mart.

8.4 Afluències i màxims del fluxos observats a Mart. Conclusions

Per pic del flux s'entén la màxima intensitat que pot assolir el flux diferencial de partícules, per a un interval d'energia determinat (segons la definició d'ECSS E.10.04 2000). L'afluència es defineix com la integral temporal de la intensitat diferencial,

des de l'inici de l'esdeveniment fins a un instant donat; si no s'especifica en un altre sentit, se sobreentén que es calcula fins a l'arribada del xoc.

La Taula 8.5 llista els diferents valors de l'afluència per als quatre canals d'energia considerats a l'instrument Phobos-2/LET, per als tres casos de prediccions Fc1, Fc2 i Fc3. La conclusió de la comparació d'aquests valors amb les observacions és que la predicció Fc3 ajusta bé les observacions, amb una lleugera subestimació del valor a baixa energia ($\sim$10%) i una lleugera sobreestimació a alta energia ($\sim$7%); cal indicar que no s'ha tractat de produir un millor ajust dels perfils observats introduint més paràmetres lliures al model, per exemple, suposant una dependència radial del recorregut lliure mitjà o de l'espectre d'injecció de partícules accelerades. Si es comparen els valors de les tres prediccions, en aquesta Taula es veu que la predicció millora en gran manera en considerar una injecció intensa de partícules a l'inici de l'esdeveniment. Això vol dir que un model que permeti simular l'evolució MHD del xoc des de més a prop del Sol (< 5 $R_\odot$) permetrà millorar les prediccions, especialment a alta energia.

La Taula 8.6 dóna els valors del pic del flux per als mateixos canals d'energia i casos descrits a la Taula 8.5. Per als dos canals més baixos d'energia el pic del flux es produeix uns 24 minuts després del pas del xoc per Phobos-2. Com que el model no permet simular els perfils de flux contracorrent (després del pas del xoc), sols podem comparar els valors predits al pas del xoc amb els observats a aquest moment. Aquesta situació que no és rellevant per a les afluències (< 4%), sí que ho és per als pics dels fluxos ja que les prediccions d'aquests valors al pas del xoc són, en mitjana, un $\sim$27% més petites que el valor real pel pic del flux. Per als dos canals de més alta energia el pic del flux s'observa al pas del xoc i la predicció Fc3 novament és la que dóna un millor resultat.

La dependència funcional suposada entre el ritme d'injecció al medi interplanetari de partícules accelerades pel xoc, Q, i la velocitat normalitzada al cobpoint, VR, ens permet construir perfils sintètics de fluxos per a observadors (sondes interplanetàries) situats a diferents llocs de l'espai. Aquesta idea ha donat lloc a la construcció de l'eina SOLPENCO, descrita als capítols anteriors. L'extensió d'aquest algorisme a Mart depèn de la validesa de les hipòtesis emprades, i la més important és la suposició que la relació funcional donada per Q(VR) segueix sent certa per a tota una varietat d'esdeveniments SEP (diferents ubicacions de l'activitat solar progenitora respecte als observadors interplanetaris, diferents règims del vent solar, CME impulsores de

xocs amb diferents velocitats, etc.). Moltes d'aquestes hipòtesis no es poden verificar atès l'escàs nombre d'observacions existents a distàncies diferents d'1,0 AU, ja sigui més a prop del Sol (Mercuri o de Venus) o més enllà de la Terra (Mart, per exemple).

En particular l'aplicació a l'esdeveniment SEP del 6 de maig de 1989, observat a 1,0 AU per IMP-8 i a 1,58 AU per Phobos-2, dóna suport a la validesa de la relació Q(VR), tot i el seguit de limitacions observacionals trobades per poder comparar les prediccions amb les observacions o, almenys podem dir que el model pot predir les observacions tot i que no es tracta d'un esdeveniment SEP que sigui fàcil de modelitzar. Aquesta dificultat il·lustra una qüestió més profunda: el fet que la Terra i Mart no sempre estaran ben col·locats a l'espai com per observar el mateix xoc i detectar les partícules accelerades per aquest xoc. A més, els esdeveniments SEP poden produir-se en sèrie a causa de l'activitat d'una regió solar activa complexa. En aquestes condicions, poden aparèixer nous factors (existència d'una població llavor de partícules, modificació temporal de l'estructura arquimediana de l'IMF) que facin que l'aplicació d'un model com l'usat esdevingui impossible (però tampoc n'hi ha cap altre, de moment). Esperem que les mesures de fluxos de partícules observats per les sondes STEREO ens donin l'oportunitat de modelitzar més esdeveniments per tal de poder avaluar l'aplicabilitat del model a la predicció d'esdeveniments SEP a l'entorn de Mart.

9. Conclusions i perspectives futures

Hem desenvolupat SOLPENCO, una eina d'enginyeria per produir prediccions ràpides del flux i l'afluència en SEP. Es tracta del primer codi predictiu operatiu que té en compte la contribució del xoc interplanetari al flux de SEPs, perquè està basat en el model shock-and-particle de Lario et al. (1998).

Hem emprat observacions de SEPs a 1,0 AU (d'IMP-8) com a línia de base per modelar i predir el perfil del flux de protons, afluències i pic del flux a 1,6 AU (a Phobos-2, en l'òrbita al voltant de Mart). Per aconseguir aquesta fita, hem aplicat, per primera vegada, la relació Q(VR) derivada a 1,0 AU al front del xoc escanejat pel cobpoint connectat a l'observador situat a 1,6 AU. Hem trobat una bona concordança entre les prediccions i les observacions, i hem discutit les dificultats més importants que han aparegut en el procés. Aquest estudi és un exemple clar de com de potent pot ser l'ús de la relació empírica Q(VR) en estudis de meteorologia

espacial.

Concretament:

1. Hem construït una base de dades, el nucli de SOLPENCO, que conté un gran nombre de perfils de fluxos de partícules energètiques precalculats, per a un conjunt de 448 escenaris interplanetaris diferents, per protons amb energies entre 0,1 i 90 MeV. Aquests escenaris estan bàsicament definits per la longitud de l'activitat solar progenitora (d'E75 a W90), i per dues posicions radials heliocèntriques de l'observador, 0,4 AU i 1,0 AU del Sol. SOLPENCO es pot fer servir en línia a http://www.spaceweather.eu/es/ model-access-interface i està disponible sota petició.

2. Hem modelitzat esdeveniments SEP graduals addicionals de diferents tipus, emprant el model shock-and-particle, amb l'objectiu d'aclarir i donar suport als valors de Q_0 i de k adoptats en la relació Q(VR) utilitzada per SOLPENCO. Tanmateix, el nombre d'esdeveniments SEP modelitzats és encara massa petit. La raó principal és el temps que pren la modelització acurada de cada esdeveniment i la verificació que es tracta de la millor elecció possible.

3. Hem fet una revisió de la literatura existent, per tal de definir al millor possible el rang de valors que poden tenir les diferents variables que apareixen a SOLPENCO i, en conseqüència, poder definir el valor representatiu més adequat perquè s'implementi al codi, les variables més importants dels quals són: l'índex espectral del ritme d'injecció de partícules accelerades al xoc, γ (a baixa i alta energia), i per la constant k de la relació Q(VR). Hem discutit detingudament la influència dels valors de la k i la γ en el perfil del flux , de l'afluència i del pic del flux.

4. Hem analitzat com depenen els perfils sintètics produïts per SOLPENCO de diferents variables bàsiques, ja que els perfils resultants poden mostrar una gran varietat de formes i detalls. Per tant, se n'ha estudiat la dependència de: (i) l'energia i el recorregut lliure mitjà considerat per les partícules; (ii) la presència o absència d'una regió prexoc turbulenta; (iii) la velocitat inicial del xoc, i (iv) l'heliolongitud de l'activitat solar progenitora, respecte a l'observador.

   Com a resultat general, es pot dir que no és possible descriure de manera senzilla la influència de tots aquests factors, ja que la contribució relativa de

cadascun d'ells al perfil final és molt variable, segons l'evolució del cobpoint. El resultat és una varietat de perfils de flux que reprodueixen moltes de les característiques dels diferents tipus de perfils de flux SEP observats.

5. Hem analitzat les característiques més importants del pic de flux i de l'afluència total, a la regió davantera dels esdeveniments SEP continguts a la base de dades de SOLPENCO, segons la velocitat inicial del pols del xoc i l'heliolongitud.

   Pel que fa al pic del flux, podem dir que: (i) una gran part dels perfils de flux mostren el màxim al pas del xoc; (ii) els valors màxims del pic de flux a 1,0 AU corresponen a observadors situats entre W22 i W00; aquest darrer valor s'estén fins a E15 per a observadors situats 0,4 AU; (iii) els valors calculats a 0,4 AU són més grans que els calculats a 1,0 AU, per als xocs més ràpids i posicions angulars entre W22 i E15, i (iv) hi ha una correlació entre el valor del pic del flux i la velocitat del pols inicial del xoc, correlació que queda ben quantificada pels esdeveniments meridians centrals.

   Pel que fa a l'afluència, podem concloure que: (i) per a un determinat xoc, l'esdeveniment més ben connectat mostra un afluència més elevada, sigui a 1,0 AU o a 0,4 AU; (ii) per a la mateixa heliolongitud i per als esdeveniments ben connectats de l'inici, com més ràpid és el xoc, més gran és l'afluència, i (iii) per als esdeveniments que tenen una connexió tardana, els esdeveniments associats a xocs lents tendeixen a mostrar afluències més grans que els esdeveniments ràpids.

6. L'anàlisi de les afluències i pic de fluxos derivats per a observadors situats a 0,4 AU i 1,0 AU no defensen la hipòtesi d'una dependència quadràtica inversa per a la relació funcional de l'afluència respecte a la distància radial heliocèntrica. La contribució de les partícules accelerades al xoc en el medi interplanetari entre 0,4 AU i 1,0 AU és important, entre un factor 1,1 i 10, segons la velocitat i l'heliolongitud considerades.

7. De l'ànalisi dels esdeveniments 4 – 6 d'abril de 2000 i 22 – 24 d'abril de 1979 podem concloure que SOLPENCO pot predir amb relativa precisió els perfils de flux per a diversos esdeveniments SEP, tot i la simplicitat de les hipòtesis en què es basa el codi. En general, les prediccions de SOLPENCO poden millorar amb la simulació de més esdeveniments SEP per tal d'estudiar la dependència de k amb l'energia de les partícules, d'obtenir l'espectre mitjà del ritme d'injecció i un valor mitjà per a la constant de normalització.

Hem començat el procés de verificació de SOLPENCO tot comparant els pics d'intensitat dels esdeveniments SEP isolats més importants esdevinguts entre gener de 1998 i octubre de 2001 amb els valors sintètics del pic de flux calculats pel codi.

Per esdeveniments meridià central, el pic del flux es predit per SOLPENCO per $E < 2,0$ MeV. Les prediccions són vàlides també per $E > 2,0$ MeV en aquells esdeveniments amb poca contribució de partícules accelerades en la fase inicial de l'esdeveniment, quan el xoc és encara prop del Sol. Per esdeveniments oest i meridià central que mostren una contribució important de partícules accelerades a l'inici de l'esdeveniment, SOLPENCO no en pot predir el pic del flux. En resum, per tal de millorar les prediccions del codi a alta energia, és necessari un codi MHD per a la propagació del xoc que tingui unes condicions inicials properes al Sol ($3-5\,R_{\odot}$) i diferents valors del coeficient k en la relació Q(VR).

8. Hem simulat la propagació d'un xoc interplanetari i els perfils de fluxos SEP associats observats per IMP-8 (que orbita la Terra) i Phobos-2 (que orbita Mart), durant l'esdeveniment del 6 de març de 1989. Tot suposant vàlida la relació Q(VR) al cobpoint, derivada de la simulació a IMP-8, hem predit el flux diferencial de protons observat a Phobos-2. És la primera vegada que es duu a terme una anàlisi d'aquestes característiques. La comparació entre els valors predits, modelitzats i observats dels perfils de flux a Mart, porta a la conclusió que la relació Q(VR) és adequada quan s'utilitza per a la predicció del pic de flux i de l'afluència per a cada canal d'energia. S'han discutit les limitacions del model i de l'escenari Terra-Mart pel que fa a les prediccions que es poden proporcionar.

Perspectives futures

1. Estudiar un nombre més gran d'esdeveniments SEP.
2. Aplicar el model shock-and-particle i SOLPENCO en observacions multisonda.
3. Investigar i modelitzar escenaris interplanetaris millorats, en els quals es consideri l'evolució del xoc coronal/interplanetari des de més a prop del Sol.
4. Millorar els algorismes emprats en la determinació del front del xoc i dels paràmetres del plasma al cobpoint.

5. Estendre el model shock-and-particle a l'escenari 3D.

6. Derivar perfils del flux a la regió contracorrent del xoc.

7. Analitzar els fluxos de partícules observats segons l'energia de les partícules, per tal de determinar la dependència energètica del flux, segons la distància angular a l'observador.

8. Incloure l'evolució de la població d'ions massius en el nostre codi.

9. Modelar la dependència de l'afluència i pic del flux d'un SEP segons la distància angular longitudinal i la distància heliocèntrica radial.

1 Introduction

> *"Space weather is the physical and phenomenological state of the space environment. The associated discipline is aimed at the observation, monitoring, modeling and prediction of the conditions in the interplanetary and planetary environments, and of the solar and non-solar driven perturbations affecting them. Depending on the prevailing conditions, these perturbations may impact biological and technological systems".* A working definition used by COST Action 724 (Developing the scientific basis for monitoring, modeling and predicting space weather), 2007.

Solar Energetic Particle (SEP) events present one of the most severe hazards in the space environment. Such events, highly random in nature, tend to occur during periods of intense solar activity, and can lead to high radiation doses in short time intervals. Sporadic increases in the energetic particle fluxes[1] can directly affect human endeavors like aerospace technology or space exploration. For many deleterious effects the relevant parameter of SEPs is the total fluence[2] of particles accumulated during a mission, while for others is the maximum particle intensity[3] observed during a single event. The effect of particle flux or fluence might have severe implications for the lifetime of the satellites and the performance of instruments onboard spacecraft. Earth's magnetic field can partially shield low-altitude Earth orbiting satellites, but in the interplanetary medium, or even at high altitude and high latitude Earth orbits, the radiation conditions can be hostile (Siscoe et al. 2000;

[1] Otherwise indicated, in this work 'particle flux' means the differential particle intensity derived from the measured count rate of particles detected by an instrument: the number of particles per unit of time, area, solid angle and energy in a given energy range [part. cm^{-2} s^{-1} sr^{-1} MeV^{-1} (or keV^{-1} in some cases)]; for more details see the reference E-10-04 (2000) of space standards.

[2] Fluence, cumulative fluence or total fluence, refers to the particle differential flux integrated over the solid angle, for a given time interval and above a certain threshold energy.

[3] Frequently referred as 'the peak flux of the event'.

Daly et al. 2005).

The threat that SEPs pose to manned spaceflights and to spacecraft operations has been reviewed by several authors (e.g. Feynman & Gabriel 2000, and references therein). Critical to the ability to design space missions, human and plan exploration missions, is the ability to precisely specify and predict the SEP fluence and the worst-case scenario for SEP radiation, as a function of the mission requirements. The Radiation Working Group Report from NASA (Golightly et al. 2005, hereafter RWG05) and The Space Radiation Hazards and the Vision for Space Exploration: Report of a Workshop (Baker et al. 2006, hereafter SRH06) present the state-of-the-art of our understanding about human health risks from space radiation exposure, and its monitoring and forecasting as related to exploration missions. We refer to Koskinen et al. (2001) for a global description of the space weather effects caused by SEP events.

The most significant sources of SEP fluxes in the interplanetary medium are both solar flares and shock waves driven by coronal mass ejections (CMEs). As observed from an heliocentric distance of 1 AU, the energetic particle flux enhancements produced by these solar events may last several days and are hard to predict in advance. In terms of total dose, protons are the primary radiation hazard posed by SEP events; in fact, protons are the predominant ion specie measured in large solar energetic particle events. Therefore, except otherwise indicated, by 'particle' here we will understand 'protons' (with energy up to $\sim$1 GeV).

Major SEP events are usually confined to a seven year period around the peak of activity of the solar cycle (Lario et al. 2001, and references therein), but they can also appear, although rarely, during the remaining four years of the solar cycle (Lario & Simnett 2004). The current understanding of the generation, acceleration, and propagation of these energetic particles in the inner solar system is incomplete because of their random nature and the insufficient knowledge of the physical principles ruling them (see Chapter 2). Our present ability to forecast SEP events in space is far from being satisfactory (Turner 2001; SRH06 Report). In fact, the current models to predict solar energetic particle fluxes are based on the assumption that there is a relationship between solar flare emissions and solar particle events. For example, the NOAA Space Weather Operations proton prediction model[4] assumes

[4]PROTONS model, validated by Balch (1999). Note that 'Validation' should not be confused with 'verification'; see for example, CMMI-SW v1.1, p.26 (http://www.sei.cmu/pub/documents/02reports/pdf/02tr029.pdf).

that the peak flux follows a power-law relationship with the time-integrated X-ray emission from the solar flare modified by correction factors for flare location and the previous occurrence of major flares. The USAF PPS model[5] utilizes radio (from 606 MHz to 2.8 GHz) and X-ray (from 0.5 Å to 8 Å) solar flare emissions to estimate the event-integrated fluence, the maximum peak flux, and the time delay between the occurrence of the flare and the time of the maximum flux.

However, the presence of a CME-driven shock plays a fundamental role in the development of large SEP events, not only in the acceleration of energetic particles but also in controlling the intensity-time histories of the energetic particle intensities recorded in the interplanetary medium (Cane et al. 1988). Figure 1.1 shows the >30 MeV proton flux (top panel) and cumulative fluence (bottom panel) measured during the 1989 October 20 SEP event. The dashed line in both panels considers the hypothetic case that the local intensity enhancement associated with the passage of an interplanetary shock observed at the Earth at 1650 UT on 1989 October 21, doy[6] 293, did not contribute to the measured flux and fluence. These intensity enhancements associated with passages of shocks are frequently known as Energetic Storm Particle (ESP[7]) events. As can be seen, the contribution of the ESP event into the peak flux and the total fluence of this event was not negligible at all. Prediction models that do not consider the effects of traveling interplanetary shocks fail to predict peak fluxes and total fluences, especially during the intense SEP events associated with shocks.

Risk management strategies to study and forecast the effects of energetic particles produced by solar and interplanetary sources are faced with three fundamental approaches: (a) the use of statistical operational algorithms presently operative at forecast centers; (b) the use of numerical codes for the transport of energetic particles that are currently applied to cosmic ray propagation in an ionized and magnetized environment; and (c) the development of numerical codes for the study of magnetohydrodynamic (MHD) phenomena in the corona and interplanetary medium that together with models of particle propagation will help us to describe the underlying physics involved in the development of large SEP events.

[5]PPS: Proton Prediction System (Smart & Shea 1989), only partially validated by Kahler et al. (2007b).

[6]Doy: day of year.

[7]ESP: this name is due to the historical association of the shock passage with the occurrence of a Sudden Storm Commencement in the Earth's magnetosphere.

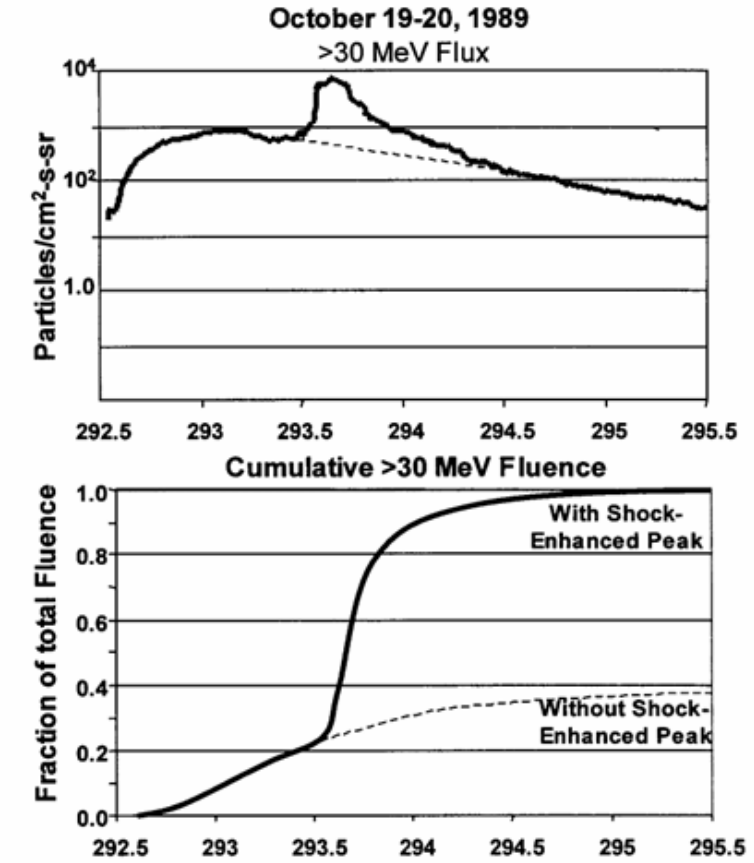

Figure 1.1: Flux and cumulative fluence of the October 20, 1989 particle event, as measured by the GOES satellite (from Turner 2001).

Point (a) refers to statistical models that estimate the cumulative exposure to solar protons over a period of time, by taking as input SEP event data from previous solar cycles. These probabilistic models for fluences and peak fluxes of SEP events (e.g. Feynman et al. 1993; Feynman et al. 2002; Nymmik 1998, 1999; Xapsos et al. 1998, 2004) are based on historical records of event occurrence frequency (and its dependence on solar activity cycle), the behavioral features of particle fluence, as well as estimations of the mean particle fluence, peak flux and spectra of historic SEP events. The JPL proton fluence model is extensively used for engineering consideration of time-integrated effects. The updated version of this model (Feynman et al. 2002) is based on data from two and a half solar cycles. Gabriel & Feynman (1996) and Feynman & Gabriel (1996) re-examined various aspects of this model, mainly focusing on the adequacy of the fits to predictions at high energy (1 – 60 MeV). Rosenqvist & Hilgers (2003) and Rosenqvist et al. (2005) discussed the sensitivity of the JPL-91 model to perform SEP event predictions with respect to the

fitting procedure, the fluence thresholds and the inclusion of different data sources. The SOLPRO model (Stassinopoulos 1975; Stassinopoulos & King 1974) was based on the analysis of SEP events during solar cycle 20 performed by King (1974) and it covered the energy range from 10 MeV to 100 MeV.

The Emission Solar Protons model (Xapsos et al. 2004, and references therein) used data from cycles 20, 21 and 22 and allows the computation of both the expected fluence and peak flux for time periods corresponding to space missions, extending the energy range up to 300 MeV. This model is currently used by the Naval Research Laboratory and the Space Environment and Effects Program of NASA. Since all these models are based on statistical approaches, a probability, confidence or risk level must be assumed. It must also be noted that:

- Extreme large events, such as the events in August 1972 and October 1989, may dominate the total fluence during a solar cycle. Therefore, this major events may determine the probabilistic functions used in the models. Those events tend to occur under very special conditions of the heliosphere (such as converging interplanetary shocks; Kallenrode & Cliver 2001; Lario & Decker 2001a, 2002). These conditions are difficult to predict and may not always be present in all solar cycles.
- Both the analysis of the SEP event development (i.e. the study of intensity and energy spectra time profiles) and the spatial dependence of the SEP events in terms of their location in the heliosphere are required before establishing probabilistic functions used in these models. This variability has implications for building probabilistic models of solar particle hazards. It is worth remembering that the goal of probabilistic models is to give engineers and mission designers confidence levels that reflect as much as possible the reality of the space environment[8].
- In certain cases, statistical forecasting can yield a false sense of security. For example, Turner (2001) showed that during the active solar period between 1989 and 1991, there were about 120 days with a SEP event in progress and about 970 days without any SEP event. From the analysis of this data, he concluded that if during this period a three-day-persistence criterion was used

[8]Tylka & Dietrich (1999) showed an example of the variability of the energy spectra from event to event and for different ion species. One of their conclusions was "*... complicate schemes that try to summarize this complexity in correlation functions of dubious physical and statistical validity can no doubt produce a wide range of behaviors. But whether that variability has anything to do with what astronauts will actually encounter in space is another question*".

for forecasting, the forecaster would have been right more than 90% of the time. However, this forecaster would also have had a 100% false sense of security about the prediction prior to each of the ∼30 SEP events that did occur.

In this work we will address the use of numerical codes for the transport of both MHD phenomena and energetic particles in the interplanetary medium (i.e. the points (b) and (c) above indicated). Our concern is the study of single SEP events that unexpectedly take place at almost any time during each solar cycle, but certainly more frequently during the most active periods of the solar cycle (Lario et al. 2001).

The largest SEP events observed during a solar cycle, such as the event shown in Figure 1.1, drive the design of spacecraft and onboard instrumentation. Space missions are not restricted to Earth's orbiting satellites. Future plans include manned missions to Mars and spacecraft located closer to the Sun (e.g. Solar Orbiter, Inner Heliospheric Sentinels[9]). Determination of the radiation environment at these heliospheric locations has to be model-based since observational data at distances different from 1 AU are limited. Extrapolations of 1 AU observations to other heliocentric radial distances have been suggested by Feynman & Gabriel (1988). However these extrapolations do not always apply, especially in the case of shock-associated SEP events (Smart & Shea 2003). In order to quantify the level of expected radiation for future missions at different radial distances, it is important the use of models that include the effects of traveling interplanetary shocks throughout the inner solar system. Furthermore, exploration to Mars raises a problem not previously considered: the astronauts and the spacecraft will be exposed to solar activity developing in the side of the Sun out of view from ground-based (or near-Earth orbiting) observatories.

Hence the recommendations of the US SWAST Plan (1999)[10] that guide the future investment, development and acquisition of space instrumentation and space-related Space Weather capabilities:

– "*Provide a robust Space Weather research and develop a program to implement*

[9]See, for example: http://mars.jpl.nasa.gov/; http://sci.esa.int/science-e/www/area/index.cfm?fareaid=45; or http://science.nasa.gov/headlines/y2006/01sep_sentinels.htm.

[10]SWAST Plan: Space Weather Architecture Study Transition Plan, paragraph 4.2.2.8: Recommendation Robust R&D.

and improve models, as well as provide options for further growth";

– "*Continue to leverage research and development of missions, and enhance operational products until new operational systems are ready.*"

The report "Radiation Environment Models and In-Orbit Monitoring" of the European Space Agency (Daly et al. 2005) also illustrates the need for models that will correctly describe the radiation environment for future missions. Three excerpts of Chapter 8 (Future Missions and Market Needs) of this report state:

– "*Current statistical models of solar particle radiation focus on provision of long-term radiation damage estimates. New requirements include the assessment of the temporal behaviors (durations, peaks, threshold durations, spectral variations) and sounder treatment of heavy ions in solar particle events...*"

– "*In addition, the variations of the solar energetic particle environment with position in the heliosphere need to be known for unmanned missions to the inner (< 1 AU) heliosphere and for manned missions beyond the near-Earth environment. However, the most extensive data sets on solar energetic particles are from spacecraft close to the Earth. Helio-radial variations are therefore very difficult to derive without recourse to models of solar particle acceleration and propagation since a significant proportion of the energetic particles are produced in interplanetary shocks.*"

– "*Tools have to be developed to predict the dose equivalent to astronauts for missions beyond LEO*[11]*. For the environment element of the problem this particularly implies establishment of models which include means of predicting event occurrence and magnitude based on solar precursors.*"

The prediction of the flux and fluence of large SEP events days or hours in advance of their occurrence is a formidable challenge. The whole process should accomplish a series of steps that will allow the forecaster to

(a) predict where, when and how a solar event will occur;

(b) specify the characteristics of the associated CME, such as location, size, speed, and its ability to drive a shock wave;

(c) determine the efficiency of the shock driven by the CME to accelerate particles to high energies, as well as how the particles will be injected into the interplanetary medium; and finally,

[11] LEO: Low Earth Orbit, see E-10-04 (2000).

(d) forecast how these particles and the CME-driven shock will travel through the interplanetary medium to reach spacecraft and/or astronauts.

This is the reason why the aforementioned ESA's report (Daly et al. 2005, Section 9.4) stated that new prediction tools should include models of SEP events with improved statistical representations of peak fluxes and fluences, systems for data-driven analysis, physics-based predictability of interplanetary particle acceleration and propagation as well as solar feature based modeling. The US National Space Weather Strategic Plan (1997) evaluated this situation and estimated a period of $10-15$ years before a reliable scientific model is achieved. Figure 1.2 displays the current situation (circa 2001) and estimates the future development of several items in relation to SEPs. In this context "reliable" means a model in which the scientific community can obtain quantitative and precise forecasting tools for SEPs. From this figure we can draw the conclusion that a reliable application with the aforementioned characteristics is difficult to achieve. At present, this conclusion still remains certain. In this sense, the SRH06 Report states:

– "*While continuing to provide insight into the understanding of the fundamental processes, research models have too many unknown input parameters for making the required space weather predictions.*" And,

– "*In some cases operational tools (i.e. tools for space operations) must be developed or adapted from scientific analytical tools and converted to real-time reporting tools; the transition from research to operations is a very challenging task.*"

We propose the use of a model that includes both MHD shock propagation in the interplanetary medium and energetic particle transport along the interplanetary magnetic field. This model (shock-and-particle model, described in Chapter 3) was developed by the Solar-Terrestrial Physics and Space Weather Group (STP/SWG) of the University of Barcelona and has been applied to the simulation of SEP events observed by the International Sun-Earth Explorer - (ISEE-3), the Helios and the Advanved Composition Explorer (ACE) spacecraft (Heras et al. 1992, 1995; Lario et al. 1998; Aran et al. 2004). This model allows us to build a code – useful for space weather purposes – that simulates the processes leading to specific intensity-time flux profiles, energy spectra evolution and fluences of individual SEP events, especially for those events where the acceleration of particles is dominated by acceleration processes in the interplanetary medium by CME-driven shocks.

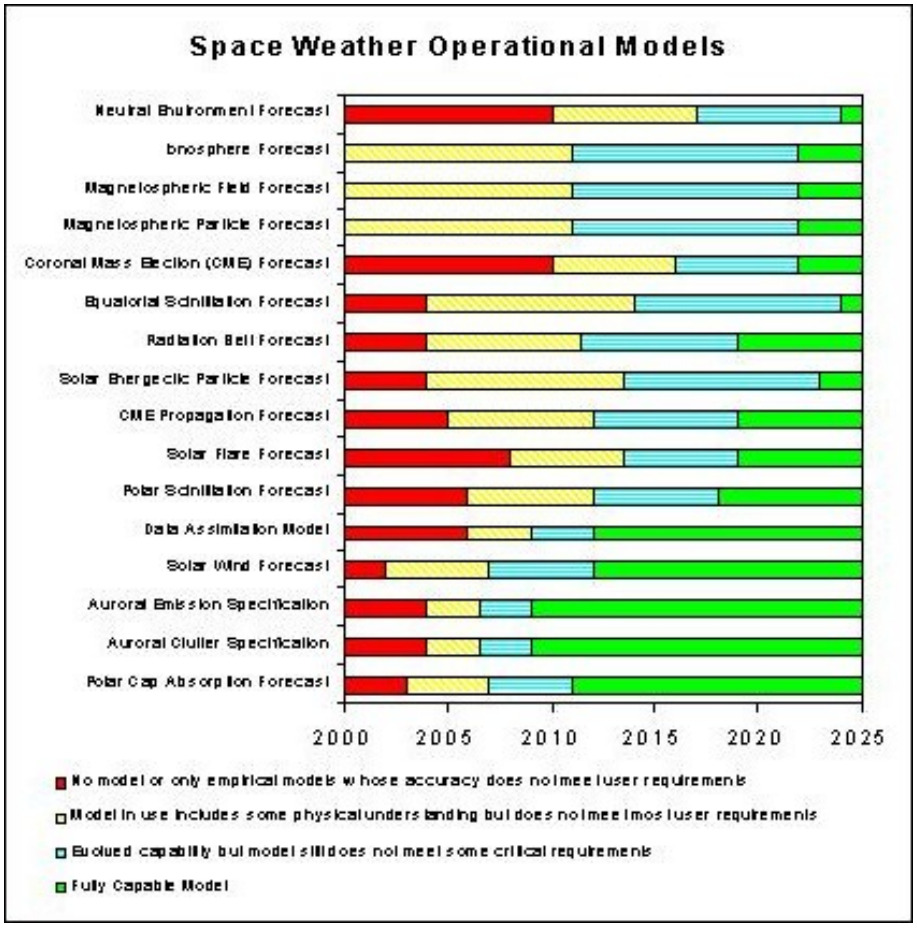

Figure 1.2: Tentative foresight for operational forecast of SEP events and CME models in space weather (NOAA/SEC 2001, private communication).

The main aim of the present work is the development of an engineering code named **"SOLPENCO"** (standing for **SOL**ar **P**article **EN**gineering **CO**de). The first objective of SOLPENCO is the characterization of SEP events at user-specified locations in space from outside the solar corona up to the orbit of the Earth. Figure 1.3 depicts the solar-terrestrial scenario where this code applies. SOLPENCO must allow us to estimate time-dependent proton fluxes and fluences as a function of the proton energy over the range from ∼100 keV to ∼90 MeV. This code provides a familiar user interface for running the engineering tool allowing a rapid generation of intensity-time profiles for SEP events in different interplanetary scenarios. At present, different groups are developing numerical simulation tools for modeling the effects of the solar activity, from the Sun to the ionosphere[12]. SOLPENCO does

[12]Lundsted (2005) estimated that it might take as long as 10 years before such models can be

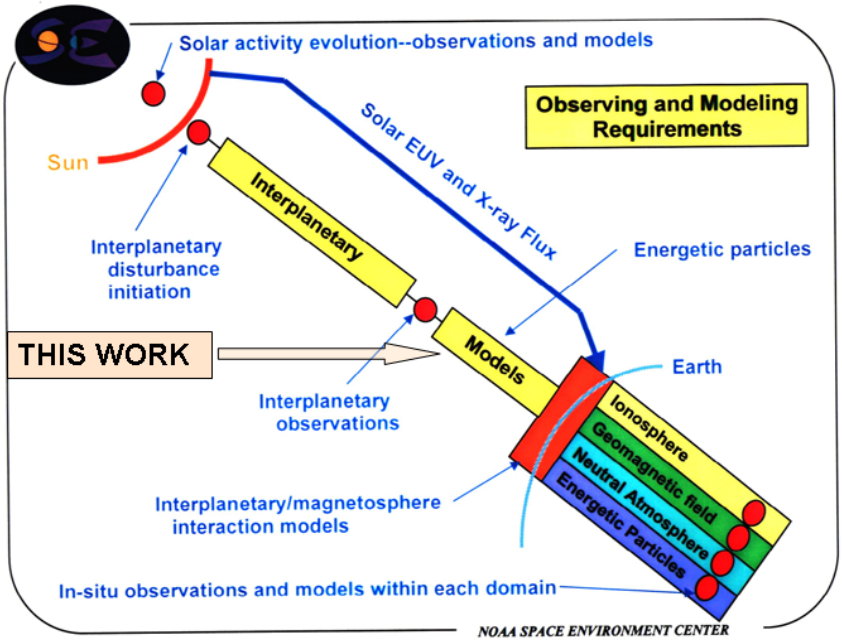

Figure 1.3: Sketch describing the Sun to Earth connection observing and modeling requirements (from NOAA/SEC 2001, private communication).

not intend to solve the overall problem; it is just a first step to the prediction of particle fluxes during SEP events. A second objective – as important as the first – is the identification of those physical variables, as well as their inter-dependences, that are relevant to space weather applications. This will allow us to both improve future modeling efforts and better orient the objectives for onboard space weather instrumentation.

Modeling SEP events for scientific purposes is a task different from performing statistical studies using the outputs of SOLPENCO and comparing the predicted fluxes or fluences with observations. Right now, there is a wide gap between what models can predict and the physics underlying in the processes of shock formation, propagation and particle acceleration by traveling shocks. In order to improve the model reliability we need a much better description of shock formation close to the Sun than the current available models can provide, as well as three dimensional descriptions of the shock propagation through the interplanetary medium. This is a task for the next future (i.e. the next decade, see Figure 1.2 or RWG05 Report). To our understanding it would even take a longer time to produce an operative code (for

good for space weather forecasting.

engineering purposes) based on such models. In the meantime, the only reasonable possibility is to look at average values of the peak fluxes and the total fluences of SEP events both simulated and observed as a function of a few initial variables characterizing the overall scenario. This task has to be undertaken in a systematic way, for example, building up sets of SEP events, verifying pre-defined selection criteria, analyzing their main features and comparing them with the corresponding synthetic SEP events produced by SOLPENCO. This is a necessary step to be performed in order to validate the code, although it is also very important to gain insights of the physics of the model and of the knowledge of the solar interplanetary scenario where the SEP events develop. Let us add that "whenever possible" because there are many aspects of the Sun-Earth scenario which still deserve much more scientific analysis before being useful for space weather purposes. This is the case, for example (see discussion in Section 2.3), of how to identify trustful proxy indicators of the solar activity (e.g. sigmoids, interplanetary scintillations measurements or metric type II radiobursts as indicators of the occurrence of a CME) and how to make them useful for space weather applications.

The outline of this dissertation is as follows. The second chapter summarizes the main characteristics of SEP events and outlines the main features of the existing theoretical models from which potential operational codes rely on. We do not intend to produce an exhaustive review of the state-of-the-art of the field, but only to describe the observational scenario assumed by the theoretical models of SEP events. We quote the main references to provide links to the reader interested in a more thorough lecture or review. The third chapter deals with the specific scenario and model in which our operational code is based. We describe the main features of the model and discuss its possible areas of improvement for the next future. We will point out that many of these flaws are common to all the current existing models of SEP events. In the fourth chapter we present the SEP events modeled in order to better understand the variables and parameters used; we outline the main conclusions and their effects in the code. The fifth chapter describes the structure of SOLPENCO, its technical characteristics, the data base and the input and output interface. In the sixth chapter we present and discuss various outputs of the code, mainly related to flux and fluence profiles and with their radial dependence. In the seventh chapter we compare the outputs of SOLPENCO with observations and we analyze its feasibility and robustness. The eighth chapter describes an application of the shock-and-particle model to the prediction of flux particle profiles at Mars' orbit from the SEP flux observed at 1 AU. This is a clear illustration of the difficulty in

producing a reliable prediction scheme of such type, right now. The ninth chapter gives the conclusions and comments the future perspectives. A set of nine appendices contains complementary material.

This work has been supported by the projects AYA2001 – 3304 and AYA2004 – 03022 of the Spanish Ministerio de Educación Ciencia, and by the ESA/ESTEC Contract 14098/99/NL/NM (2000 – 2003). We also acknowledge the computational support provided by the Centre de Supercomputació de Catalunya (CESCA).

2 Solar energetic particle events

The most abundant energetic particle population in interplanetary space are the Solar Energetic Particles (SEPs) and the Galactic Cosmic Rays (GCRs). For the energy range of interest in space weather (basically, protons between 500 keV to ∼100 MeV) the flux of SEPs prevails over the other particle populations of diverse origin, i.e. galactic, magnetospheric, or interplanetary in the form of corotating interaction regions (Mewaldt et al. 2002). GCRs are always present in the interplanetary medium and the factors that determine their flux and modulation over the different phases of the solar cycle are relatively well understood (Mewaldt et al. 1988). We will not discuss them further; more detailed information can be found elsewhere (i.e. Smart & Shea 1985; or Shea et al. 1989), and we refer to the RWG05 Report for details concerning the most used operative codes for space applications[1]. The prediction of SEP events is a big challenge because the underlying physical mechanisms involved in their production are neither well known nor fully understood (SRH06 Report). In this chapter we do not intend to produce a comprehensive review of the properties and models of SEP events. We only seek to highlight the main characteristics of both the SEP events and the physical mechanisms at work during their development. We also shortly comment[2] those aspects that in the near future can lead to improved versions of SOLPENCO. In other words, we will identify the flaws of the model and the code that – in the end – will allow us to say something like: "*These are some of the possibilities we will treat in our future investigations*" (Manchester et al. 2004a) or "*In a next step, we would like to use more complex CME models, and include a CME initiation scenario*" (Chané et al. 2005) or even the categorical comment "*The SEP models are not ready for the severe challenges posed by energy*

[1]For example, the CREME96 (Cosmic Ray Effects on MicroElectronics package) by Tylka et al. (1997a,b); the Moscow State University model (Nymmik 1999); or the more recent model by Davis et al. (2001) to study the influence of GRCs in the Near-Earth Radiation environment.

[2]Up to December 2005, plus several relevant more recent articles.

spectra, anisotropies and time profiles for electrons multiple ion species, and charge states for a complex variety of events with a variety of a magnetic connection geometries" (Mikić & Lee 2006). In particular, we do not proceed with lengthy discussions about the theory of shock-particle acceleration or about the compositional variation of the events, because at the present stage of development of SOLPENCO they do not yield any operative output. For a detailed description of SEPs characteristics, origin and modeling, we refer to the review papers by Lario & Simnett (2004), Lee (2005), Cane & Lario (2006), Klecker et al. (2006), and Mikić & Lee (2006).

2.1 Origin and characteristics of SEP events

2.1.1 Impulsive versus gradual events

The onset of SEP events is associated with many solar activity phenomena, such as filament disappearances, solar flares, and various forms of radio emission, as well as CMEs. In the late seventies, the three-spacecraft mission ISEE was launched with a very sensitive instrumentation. These spacecraft, especially ISEE-3, were able to measure low-energy particle fluxes and anisotropies, charge states elemental composition, not only in large SEP events but also in the far more numerous small events. Studies based on these data conventionally distinguish two basic types of SEP events: impulsive and gradual events. The origin of this separation was based on the bimodal distributions of elemental abundance compositions early suggested by Lin (1970, 1974) and van Hollebeke et al. (1975), as well as on the relationship between the duration of the associated soft X-ray flares (Pallavicini et al. 1977) and SEP abundances (Kocharov et al. 1983; Cane et al. 1986).

The conventional wisdom holds that SEPs in impulsive events are accelerated at the site of short-duration flares, probably by processes associated with magnetic reconnection, while SEPs in gradual events are accelerated by evolving coronal/interplanetary shocks driven by CMEs (Reames 1999a). There are several observational evidences suggesting that the dominant processes of particle acceleration in gradual events are associated with shocks driven by CMEs. First of all, there is a clear association between large gradual SEP events and fast CMEs (Kahler 2001a). SEP intensities in gradual events are correlated with CME speeds, although it is not uncommon to find SEP intensities that vary over a range of four orders of magnitude

for a given CME speed (Kahler 2001b).

Impulsive events are observed in a narrow cone of longitudes corresponding to observers magnetically well-connected to the site of the progenitor solar flare. For an observer near the Earth, these longitudes are clustered around W58, which corresponds to a nominal Parker spiral connection between the Sun and the Earth (assuming a solar wind speed of 400 km s^{-1}). Conversely, gradual events are observed in a wide-spread range of longitudes regardless of the associated solar flare location (Cane et al. 1986), if a flare can be identified at all (Sanahuja et al. 1983). This fact suggests that gradual events are associated with broad sources of particles. Impulsive events have charge state distributions characteristic of high-temperature plasma typical of solar flare sites, in contrast to the lower charge states observed in gradual events (Klecker et al. 1984; Luhn et al. 1987)[3]. Additionally, Cane et al. (1986) showed that impulsive events have a higher electron to proton ratio than gradual events.

Figure 2.1 shows two typical examples of impulsive and gradual SEP events. The left panel of this figure shows the impulsive event observed on 2000 May 1 (doy 122) that was associated with a M1.1 X-ray flare (Kahler et al. 2001). Enhanced proton intensities were observed for a period of only $\sim$12 hours with characteristic time profiles of rapid rise and relatively slow exponential decay. The right panel of the figure shows the gradual event with onset on 2000 April 4 (doy 95), with solar origin associated with a C9 X-ray flare and a fast (1188 km s^{-1}) halo CME as seen by the LASCO coronagraph onboard SOHO (Brueckner et al. 1995). Proton intensities were elevated for more than 3 days and < 5 MeV proton intensities peaked with the arrival of a CME-driven shock on doy 97. The event shown in the left panel of Figure 2.1 had low H/He ratios and high Fe/O and ^{3}He/^{4}He ratios characteristic of impulsive events (Kahler et al. 2001; Mason et al. 2002). The event shown in the right panel of this figure showed low Fe/O ratios and elemental abundances characteristic of gradual events (von Rosenvinge et al. 2001).

[3]The analysis of SAMPEX, SOHO and ACE data have shown that in several large gradual events high charge states are also measured, but while this feature is observed only in some gradual events it is systematically observed in impulsive events (see Klecker et al. 2006, and references therein). In addition, these authors claim that, in small impulsive events, high charge states should be taken as tracers for particle acceleration sources low in the corona, rather than an indication of high temperatures at the acceleration site, since plasma for these events may be far for thermodynamic equilibrium.

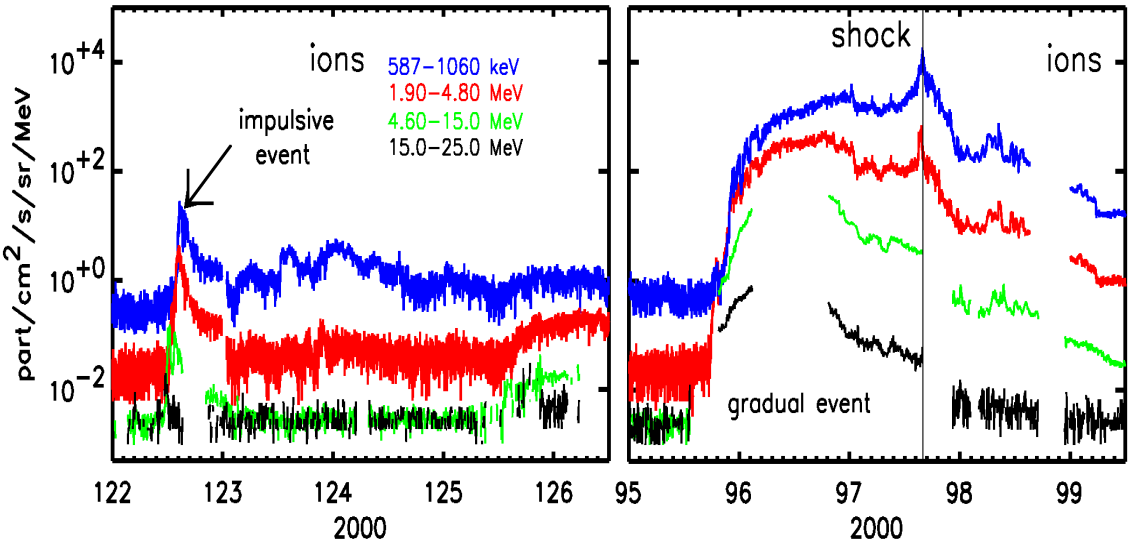

Figure 2.1: Intensity-time profiles of ions for an impulsive (left) and a gradual (right) SEP event of the year 2000 as measured by ACE/EPAM (Gold et al. 1998; hereafter Gol98). The two lower traces (high energy channels) are proton observations from IMP-8/CPME (Sarris et al. 1976; hereafter Sar76).

Impulsive events are about hundred times more frequent than gradual events at the maximum of the solar cycle, but they have typical durations of the order of hours and are less intense than gradual events. Therefore, impulsive events have weak space weather effects in terms of total fluence and peak flux intensities. The detailed characteristics and properties of these two types of events have been described elsewhere; see, for example, the reviews by Reames (1999a) and Cliver (2000). This dichotomic paradigm of SEP events has been controversial (e.g. Cliver et al. 2002). The current usage of these terms have been critically reviewed by Cliver & Cane (2002), we refer to that paper for a description of the usefulness and limitations of them. Expanded classifications including hybrid events have been proposed by Kallenrode et al. (1992), Cliver (1996) and Ruffolo (2002). Charge state and abundance measurements gathered during solar cycles 22 and 23 together with the fact that intense electron events are also associated with CMEs have blurred the two-class paradigm of SEP events (Cane & Lario 2006). Instead, measurements lead to conclude that there are two not exclusive mechanisms for accelerating energetic particles, one associated to flares and the other to shocks (Tylka & Lee 2006). What

remains a matter of intense debate is to what extend (dependent on energy) and how – directly (e.g. Klein & Trottet 2001) or indirectly (e.g. Tylka et al. 2005) – flare-accelerated particles play a role in large gradual SEP events (e.g. Cane & Lario 2006 and Klecker et al. 2006).

2.1.2 Energetic particle acceleration

Several mechanisms of particle acceleration at flares have been proposed. They include both resonant wave-particle interactions (Roth & Temerin 1997) and stochastic acceleration with a complex spectrum of cascading waves (Miller & Viñas 1993). These processes occur in connection with the magnetic reconnection at the time of the flare and are confined to the site where the flare takes place.

Mechanisms of particle acceleration at interplanetary shocks include the followings: [1] The shock drift acceleration that takes advantage of the electric induction field existing in the shock front and the motion of particles that drift along the shock front (e.g. Hudson 1965; Sarris & van Allen 1974; Armstrong et al. 1977). [2] The diffusive shock acceleration mechanism where particles undergo repeated reflections between converging scattering centers formed by magnetohydrodynamic waves such as Alfvén waves propagating in the vicinity of the shock (e.g. Parker 1965; Lee & Fisk 1982; Jokipii 1982; Lee 1982). During the wave-particle interactions there is an energy transfer between the wave and the particle as well as a change in the direction of motion of the energetic particle[4]. [3] Stochastic acceleration in the turbulent medium existing downstream of the shock. Particles moving in this region may interact with uncorrelated magnetic inhomogeneities moving in arbitrary direction resulting in a net energy gain if a strong downstream turbulence exists (e.g. Campeanu & Schlickeiser 1992; Schlickeiser et al. 1993; Vainio & Schlickeiser 1998, 1999).

The relative contribution of these three shock-acceleration mechanisms depends on the properties of the shock (Jokipii 1982). Shock parameters such as shock speed, compression ratio, alfvénic Mach number, and the angle between the upstream mag-

[4]The net gain of energy by particles interacting with propagating waves results from the fact that the scattering centers move together with the upstream and downstream medium (it depends on the relative speed between particle and wave), and as the particles move back and forth across the shock, head-on collisions are favored and hence the increase in particle energy.

netic field and the normal to the shock, θ_{Bn}, as well as the existence of turbulence in the vicinity of the shock are all factors that can influence the relative contributions of the particle acceleration (e.g. Lee & Fisk 1982; Tsurutani & Lin 1985; Lario et al. 1998 hereafter Lar98; Sokolov et al. 2006).

2.1.3 Flare/CME-driven shock-particle acceleration. Contribution to SEP events

The typical gradual event shown in the right panel of Figure 2.1 shows that particle acceleration in gradual events are dominated by the CME-driven shock, especially at low ($\lesssim$ 20 MeV) proton energies. The distinction between the acceleration processes that contribute to the intensity enhancements at the onset of the event is difficult. Fast CMEs tend to occur in association with flares (Harrison 1995; Nitta & Akiyama 1999), hence the difficulty to distinguish what process contributes (and with which percentage) to the development of a SEP event. To rule out the possibility that flares and CME-driven shocks contribute to a given energetic particle event, it is essential to find pure cases of gradual events not associated with solar flares. Those events are usually associated with filament eruptions (Domingo et al. 1981; Sanahuja et al. 1983, 1991; Kahler et al. 1986) and in one case with a huge X-ray arcade (Kahler et al. 1998). These events are usually observed at $E \lesssim 50$ MeV. Cane et al. (2002) suggested that for the most energetic event associated only with disappearing filaments (i.e. Kahler et al. 1986) there are also signatures of flare activity that contributed to the SEP event (see discussion in Cane et al. 2002). It has to be mentioned that there are impulsive SEP events, such as the event shown in the left panel of Figure 2.1, which are associated with narrow CMEs (Kahler et al. 2001).

Reames (2002) proposed that impulsive events result from resonant stochastic acceleration in magnetic reconnection regions that incorporate open magnetic field lines, allowing both accelerated particles and hot plasma to escape into the interplanetary medium in the form of beam of particles and narrow CMEs or jets, respectively (Kahler et al. 2001). By contrast, in large gradual events, magnetic reconnection occurs on closed field lines beneath closed flux ropes formed in the solar corona. The acceleration and injection of particles able to propagate along open interplanetary magnetic field (IMF) lines only occurs when the flux rope expands through the corona and the interplanetary medium being able to drive a shock wave efficient accelerator of particles from the ambient plasma of the corona and solar

wind. Therefore, according to Reames (2002), energetic particles observed in gradual SEP events are accelerated solely by the CME-driven shock, and flares play no role in the production of SEPs. This simple scenario may be disturbed by the wide variety of conditions and processes that may occur during the eruption of a flux rope (Klimchuck 2001), including dynamic flare processes that may open temporary and locally the field, possible magnetic connectivity of the flare site to open field lines (Aschwanden 2002), and also some magnetic reconnection processes that involve open field lines, such as the magnetic breakout model proposed by Antiochos et al. (1999). Kocharov & Torsti (2002) emphasized the importance of coronal liftoff processes during the occurrence of flares and CMEs, as well as the aftermath configuration resulting from the CME liftoff. Both processes allow these authors to explain the existence of hybrid SEP events (i.e. those mixing gradual impulsive and gradual composition characteristics).

The separation between impulsive SEP events from flares and gradual events from interplanetary CME-driven shocks is also challenged by the composition measurements from the ACE spacecraft. Gradual SEP events show on average charge state distributions consistent with temperatures of the order of $\sim 1.8 \times 10^6$ K supporting their coronal origin (Tylka et al. 1995). However, Cohen et al. (1999) showed that for $E > 10$ MeV/nucleon certain gradual events have compositions and charge states typical of impulsive events. Mewaldt et al. (2002) showed that most SEPs with $E > 5$ MeV/nucleon are not simply an accelerated sample of the average solar wind as observed at 1 AU, but a population of particles accelerated within a few solar radii of the Sun. Furthermore, SEP events associated with interplanetary CME-driven shocks may have ^{3}He ion enhancements with abundances substantially larger than those measured in the solar wind and typically assumed for gradual events (Desai et al. 2001). Actually, it was proposed that CME-driven shocks not only accelerate particles from the coronal and solar wind pool of particles but also from a suprathermal remnant of particles originated in prior impulsive flares (Mason et al. 1999).

It remains to clarify whether the concomitant flare (i.e. the flare that occurs in temporal association with the CME liftoff) contributes to the SEP event with impulsive or flare-type particles (Cane et al. 2003; Li & Zank 2005). A pertinent study was performed by von Rosenvinge et al. (2001) who found a dependence of the heavy ion abundances with respect to the longitude of the site of the associated

solar flare[5], suggesting that, for magnetically well-connected events, flare-associated particles may contribute to the particle intensities observed at Earth. Zhang et al. (2001) analyzed four CMEs in detail and their respective X-ray emission, demonstrating that the main energy release of associated flare occurs almost simultaneously in time (see also Zhang et al. 2004). Cane et al. (2003) studied the Fe/O ratios of 29 intense SEP events observed in the energy range 25 – 80 MeV/nucleon; their main conclusion was that the observed ratios are consistent with a population of flare-accelerated particles in most of the major SEP events, suggesting that the associated flare does indeed contribute to the SEP event.

On the other extreme of non-contribution at all from the concomitant flare, Tylka et al. (2001, 2002) suggested that CME-driven shocks are responsible for the acceleration of all energetic particles observed in gradual events, and only the presence or absence of a suprathermal remnant flare-type seed particle population from prior impulsive events distinguishes the compositional characteristics of the event. In order to explain the different spectral characteristics of the Fe/O ratio observed in SEP events, Tylka et al. (2005) suggested that selective acceleration processes by CME-driven shocks are responsible for the different spectral properties. Quasi-perpendicular shocks efficiently accelerate particles that already have elevated energies or high rigidity (suprathermal protons or heavy ions, respectively).

Tylka et al. (2005) suggested that large SEP events with typical impulsive compositional signatures result from re-acceleration of flare-type remnants by quasi-perpendicular shocks, whereas large SEP events with gradual compositional signatures result from acceleration by quasi-parallel shocks of coronal or solar wind seed particle populations[6]. The conclusion of the present discussion on the classification of SEP events as gradual or impulsive is that the current paradigm is not sufficient to determine either the origin of the particles, or the mechanism that accelerates them, or the acceleration history of the solar energetic particles (Ruffolo 2002)[7].

[5]Usually shortened to "solar longitude of the flare" or "helilolongitude of the flare".

[6]However, this distinction between shock acceleration mechanisms as responsible for the gradual and impulsive signatures of the SEP events requires a specific geometry of the shock, geometry that changes as the shock propagates; for more details, see the aforementioned paper.

[7]In that sense, Li & Zank (2005) point out: "*If CMEs and flares are indeed not distinct processes, but rather different manifestations of the same process, then the traditional paradigm for SEP events requires some modification.*"

2.1.4 Flare/CME-driven shock-relativistic particle acceleration

One of the concerns of the shock-acceleration origin of SEPs in gradual events is the ability of the shocks to accelerate coronal and solar wind particles rapidly to GeV energies (Cliver et al. 2002). Shock acceleration may be fast if either an energetic seed particle population is already existent in the case of quasi-perpendicular shocks or if a region in the vicinity of quasi-parallel shocks is highly turbulent allowing the energetic particles to interact several times with the traveling shocks (Lee 2005). The question is whether [1] a suprathermal particle population is already present before the shock develops, [2] the shock-associated turbulence is already existent, or [3] there are enough streaming particles to amplify waves upstream of the shock enhancing the turbulence, hence reducing the diffusion coefficients of the particle transport around the shocks, and thus allowing particles to interact many times with the shocks. At some distance ahead of the shock, energetic particles may escape from the upstream turbulent medium, reaching 1 AU. Models of shock formation in the solar corona estimate that diffusive shock acceleration may account for the prompt production of protons up to 10 GeV (e.g. Roussev et al. 2004).

SEP events that reach relativistic energies and that are magnetically well connected with the Earth are observed by ground-level neutron monitor stations and thus called Ground Level Events (GLEs). The origin of most of these GLEs is associated with both fast CMEs and flares producing gradual X-ray bursts, long-lasting soft X-ray and centimetric-decametric radio emission. A key issue to determine when energetic particles start being injected is to compare flare emissions with the release time of energetic particles. Many of these GLEs show rapid onsets, within tens of minutes of the associated flare, and exponential decays (timescales of a few hours) indicating impulsive injections of relativistic particles into interplanetary space. The observed delays between CME launch times and the estimated release times of both near-relativistic electrons and relativistic (>400 MeV) protons (Kahler 1994; Krucker & Lin 2000; Simnett et al. 2002; Lee 2005) indicate that the injection of energetic particles begins when CMEs are already at a heliocentric radial distance between $2\,R_\odot$ and $5\,R_\odot$ (see also Kahler et al. 2003). The acceleration of these GeV-protons may continue up to $\sim 30 R_\odot$ if the CME-driven shocks are still strong enough to accelerate particles to these high (relativistic) energies.

Kocharov et al. (2005) have modeled the diffusive shock acceleration of protons

(up to tens of MeV) in a turbulent layer at the base of the solar wind. They found that protons can be emitted from the trailing turbulent layer behind the shock and released into the interplanetary medium in a few tens of minutes after the CME liftoff, demonstrating that coronal shocks can explain many properties of the post-impulsive phase acceleration of SEPs.

Alternative scenarios to the flare and CME-driven shock particle acceleration suggest that at the time of the CME liftoff, it is possible to produce simultaneously soft X-ray flares as well as coronal shocks which initiate particle acceleration in regions apart from the flare site (Torsti et al. 2001). Particle injection from coronal sites widely separated from the flare site and delayed with respect to the main flare phase and CME launch has also been inferred from radio, optical and extreme ultraviolet observations (Klein & Trottet 2001, and references therein). These observations suggest that particle acceleration may occur in the post-phase of solar eruptions and in broad regions of the corona distant from the solar flare site. However, Kahler et al. (2000) rebutted this possibility of post-eruptive coronal arcades contributing to gradual SEP events. In order to clarify the origin of energetic particles and the mechanism able to accelerate them, it is essential to study the relationship between flares and CMEs, the timing between the temporary opening of coronal magnetic fields within flaring regions, the occurrence of interplanetary type III bursts, the processes that accelerate particles to high energies, and the coronal altitude where shocks form and particle acceleration occurs. Cane et al. (2002) suggested that flare-accelerated electrons may have access to open filed lines; if this is true, it is reasonable to assume that ions accelerated during the flare process may have also access into interplanetary space (Cane et al. 2003). Therefore, depending on the interplanetary magnetic connection between the Sun and the observer, some SEP gradual events can also show a flare-accelerated particle component (Cane et al. 2006).

2.1.5 Energy spectrum of SEP events

The energy spectrum of individual SEP events is relatively easy to characterize, either by a power-law, a double power-law, or a Bessel function. However, it is difficult to derive general features of these spectra that simply and accurately describe the energy dependence of the flux for a large fraction of SEPs. Figures 1 to 4 of Xapsos et al. (2000), for example, suggest that many SEPs spectra can be described

by means of a double power-law with a "knee"[8] somewhere between ~ 5 MeV and ~ 400 MeV (see also Tylka et al. 2000). This means that there is a bend in the energy spectra, although the energy at which such knee appears is highly variable from event to event. The existence of this knee has been interpreted as a consequence of the strength of the shock and the intensity of the upstream self-generated waves. Above this energy there are not enough particles to generate MHD waves to resonate with, therefore, particles do not interact with the shock anymore and escape freely from its vicinity. The energy spectrum becomes steeper due to a greater decrease of the flux with increasing particle energy. The energy spectrum of shock-accelerated particles is continuously changing due to the energy dependence of the particle scattering processes and the expansion and propagation of the shock.

There are many suggestions to describe the energy spectra of SEPs based upon empirical or theoretical grounds. These include: an exponential function in energy (King 1974); a lognormal distribution in magnetic rigidity (Goswami et al. 1988); or a Bessel function expression derived from stochastic acceleration arguments (McGuire & von Rosenvinge 1984). Xapsos et al. (2000) adopted an exponential-potential function on the energy of the flux or the fluence, in order to characterize SEP spectra for radiation effects applications. This approach succeeds in representing the observed differential flux for SEP events that extends in energy up to 300 MeV, but it needs two parameters to define the hardness of the spectrum (as in the case of assuming a double power-law). From shock-acceleration models, Ellison & Ramaty (1985) suggested for the spectra of GLEs events a power-law times an exponential function in energy (energy/nucleon, for ions) which works well over several orders of magnitude in intensity (see also Lovell et al. 1998). Tylka et al. (2000) and Tylka (2001) found that this type of function fits reasonable well the energy spectra of 10 elements (H, He, C, O, Fe, etc.) in two large SEP events, but that these fits are not entirely consistent with those of Ellison & Ramaty (1985), and may even be improved by an exponential that is not linear with the energy (Lee 2005).

The conclusion drawn from this literature survey is that it does not exist a simple functional dependence of the flux with the energy that can be considered representative of this dependence for a large fraction of SEP events. This is an important problem for space weather predictions. For example, if the knee in the energy spectrum is at low energies, the SEP event may be intense at low energies

[8] Also known as the "rollover energy".

but weak at high energies; on the contrary, if the knee lies at high energies, then the SEP event may be considered intense throughout abroad range of energies. Energy spectra up to several tens of MeVs have been compiled from old space data sets, but their extension to higher energies for a given event is risky when the energy of the knee remains unknown.

2.2 Large gradual SEP events

Large long-lasting SEP events are important mainly for two reasons: their space weather implications (Kahler 2001a) and their dominant contribution to the fluence of energetic particles observed throughout a solar cycle (Shea & Smart 1996). Large SEP events are well correlated with fast CMEs (Kahler 2001a), although the converse is not true, there are fast CMEs without associated SEP event. The presence of fast CMEs propagating into a slower medium involves the existence of a shock wave. Regardless of the primary processes initiating the acceleration and injection of energetic particles, the scenario adopted to describe the large gradual SEPs assumes that the acceleration and injection of particles throughout the SEP event are dominated by the processes of shock acceleration. Therefore, we will assume that the initial perturbation generated as a consequence of the solar eruption is able to drive a shock wave that propagates across the solar corona and through the interplanetary medium.

If the conditions are appropriate, this shock is able to accelerate particles from the ambient plasma (or from contiguous or previous solar flare processes). These accelerated particles stream out along the IMF lines en route to Earth or to spacecraft located in the interplanetary medium. Figure 2.2 sketches this scenario; it shows how the shock propagates away from the Sun, expanding in the interplanetary space and how its front intersects the IMF lines. Once shock-accelerated particles escape from the vicinity of the shock, they are injected into the interplanetary medium, and propagate upstream (as indicated in the figure) or downstream of the shock, along the IMF lines. In particular, those particles moving upstream of the shock that reach the spacecraft will constitute the observed SEP event prior to the shock arrival (or "the upstream part of the SEP event").

In general, interplanetary shocks accelerate particles more efficiently at low than at high energies (Forman & Webb 1985). When the observer is located at 1 AU from

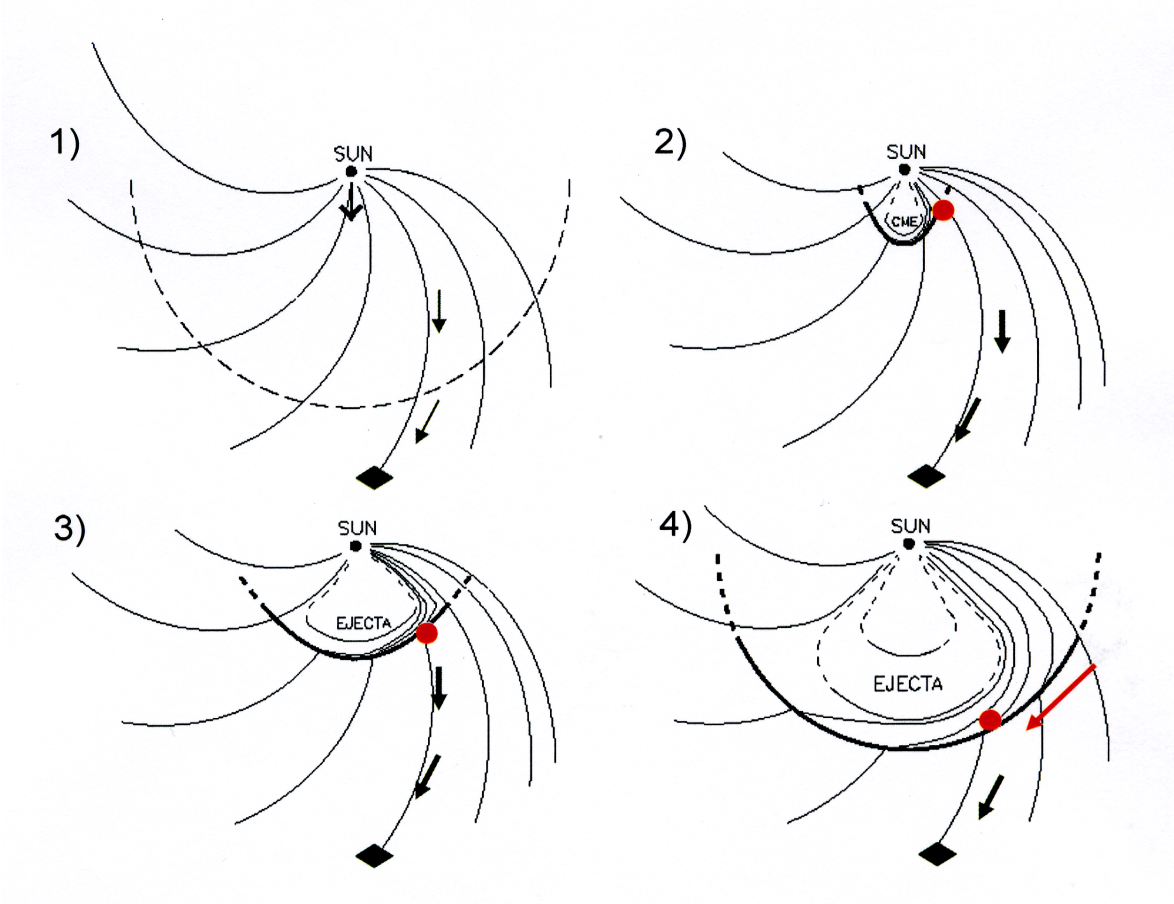

Figure 2.2: Sketch of a CME-driven shock propagating away from the Sun and expanding in the interplanetary medium. Its front intersects the IMF and shock-accelerated particles stream away along them (upstream, black arrows). The red point identifies the cobpoint; i.e. the point of the shock front that magnetically connects to the observer (identified by a black diamond). The red arrow indicates the direction followed by the cobpoint as it moves along the shock front. In the case shown, the cobpoint moves toward the nose of the shock as the shock approaches the observer.

the Sun, it is quite usual to see a small peak (less than one order of magnitude) or not increase at all for the 1 MeV proton flux at the shock passage, while a jump from one to three orders of magnitude can be observed in the proton flux at ~ 100 keV. Figure 2.3 shows, for a specific SEP event, the proton differential flux for ten energy channels between 115 keV and 96 MeV, observed at 1 AU by the ACE and IMP-8 spacecraft. This SEP event was associated with an interplanetary shock that reached ACE on 2000 October 28 (doy 302). Above 5 MeV, most of the protons were already observed before the shock passage, suggesting that a large

fraction of them protons were already accelerated when the shock was close to the Sun. At lower energies (<1 MeV), however, the shock was still an efficient particle-accelerator when it arrived at 1 AU. The energy dependence of the intensity-time profiles results from the evolution of the CME-driven shock as a particle accelerator and as it moves away from the Sun. It is reasonable to assume that as the shock expands in the interplanetary medium, it weakens, therefore, becoming less and less efficient at accelerating particles to high energies.

Low-energy proton fluxes usually peak at the arrival of the shock (Lario et al. 2003a) (the ESP part of a SEP event; see also the diagram in Figure 1 of Lee 2005) or sometimes later, depending on the energy and the heliolongitude of the event (Sanahuja & Domingo 1987). For certain SEP events (as in Figure 1.1) the shock-enhanced peak, the ESP may account for over the sixty per cent of the total fluence measured during the event. This value is highly dependent on the energy considered and the type of SEP event.

In order to explain SEP events observed simultaneously by a number of spacecraft at different locations in the heliosphere and magnetically connected to distant regions of the Sun[9], it is necessary to assume, in some cases, that the particle source, i.e. the shock in the corona, may extend up to 300° in longitude (Cliver et al. 1995). Interplanetary shocks observed at 1 AU extend at most 180° in longitude (Cane 1988); therefore, the angular width of the shock able to accelerate particles must decrease as it moves out from the Sun. In addition, the extension of the shock front able to efficiently accelerate particles depends on the energy considered, becoming smaller as the energy of the particles considered increases.

2.2.1 Energetic particle anisotropies

The presence of shock-accelerated particles in large SEP events can be also tracked from the evolution of the first-order anisotropy (A1/A0)[10] of the particle population. The definition of the A1/A0 anisotropy can be found in Sanderson et al. (1985a); first part of Appendix A presents a short summary of the different coefficients. The evolution of A1/A0 at either the upstream part of the SEP event (ahead of the

[9]hereafter, shortened to "multiple spacecraft observations"

[10]A0 is the isotropic part of the distribution.

A1/A0 (or A10/A0) is also quoted as 'parallel anisotropy' or 'normalized first order anisotropy'.

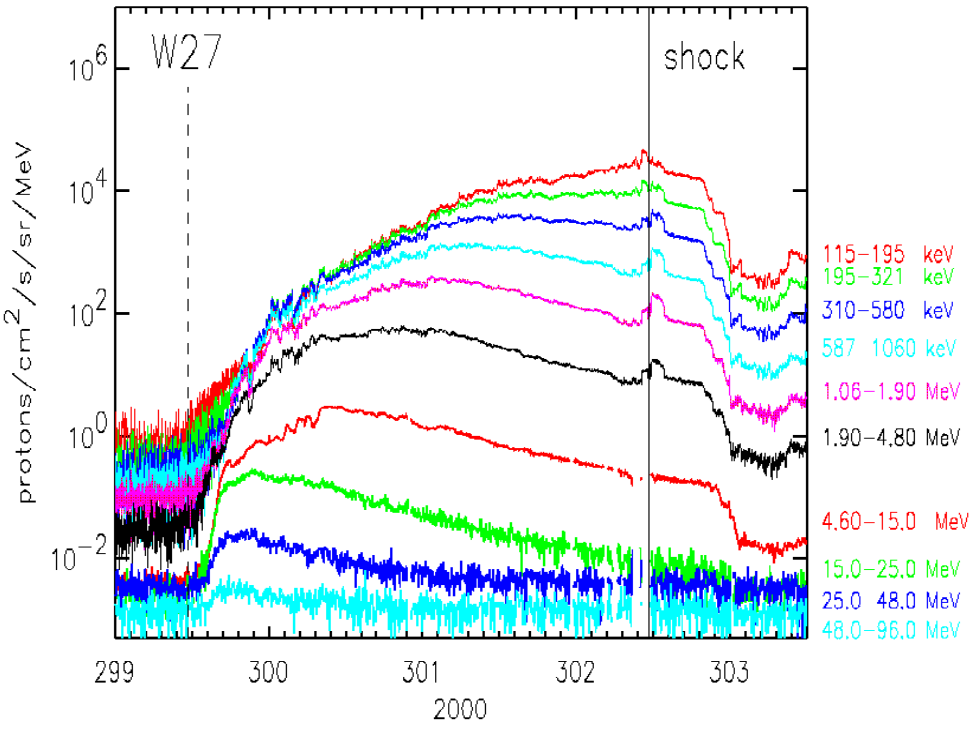

Figure 2.3: Intensity-time profiles of the SEP event of 29 October 2000 (ACE/EPAM, Gol98; and IMP-8/CPME, Sar76). It is worth to realize the different evolution of these profiles at low and high energy, which reflects the different contribution to the flux of shock-accelerated particles (see text).

shock) or at the time of the shock passage shows evidence of the CME-driven shock as particle accelerator. Heras et al. (1994) demonstrated that large SEP events can show very high anisotropies ($A1/A0 > 0.2$) for long-lasting periods of time; from the onset of the event and lasting between 5 and 36 hours, depending on the heliolongitude of the solar source triggering the SEP event. The first two figures of Appendix A (see Heras et al. 1994, for more details) illustrate the case. Figure A.1 shows three different SEP events that were generated from different solar longitudes and displayed large and long-lasting anisotropies. Figure A.2 shows the dependence of the anisotropy on the heliolongitude of the parent solar event. Owing to the influence of both the particle transport and particle acceleration processes on the behaviour of the particle flux anisotropy, this is an observational variable that must be taken into consideration and be fitted when modeling particle events.

2.2.2 Influence of the shock in shaping the SEP time-flux profiles

As the shock propagates away from the Sun, it crosses many IMF lines and may be responsible for accelerating particles out of the solar wind or out of remnant particles from either previous SEP events or the contiguous solar flare (Desai et al. 2001). These energetic particles propagate along the IMF lines flowing outward from the shock. The details of the proton flux and anisotropy profiles during these gradual SEP events are consistent with the presence of a traveling CME-driven shock that continuously injects energetic particles as it propagates away from the Sun (Heras et al. 1995). In general, the factors that determine the shape of the intensity-time profiles of the SEP events take different forms (i.e. Heras et al. 1988, 1995; Cane et al. 1988; Lario et al. 1998; Kahler 2001b) are:

- the heliolongitude of the source region with respect to the observer's location,
- the strength of the shock and its efficiency at accelerating particles,
- the presence of a seed particle population to be further accelerated,
- the evolution of the shock (its speed, size, shape and efficiency in particle acceleration),
- the conditions for the propagation of shock-accelerated particles, and
- the energy considered.

Figure 2.4 shows the dependence of the shapes of the intensity-time profiles on the heliolongitude of the parent solar flare associated with the origin of the SEP event, for four events observed by the ACE and IMP-8 spacecraft; this figure is an adaptation of Figure 15 of Cane et al. (1988). Those flux profiles are typical of the SEP events generated from different solar longitudes relative to the observer. Dashed and solid vertical lines in each one of the panels indicate, respectively, the occurrence of the parent solar event and the arrival the associated CME-driven shocks.

Note that in the representation shown in Figure 2.4, the solar activity which generates the CME-driven shock is assumed to take place always in the Sun-Earth line, i.e. in a central meridian position (CM or W00). As a consequence, the different panels have been displaced over the figure the value of the heliolongitude of the corresponding solar event. In other words, for an observer at 1 AU, the heliolongitude

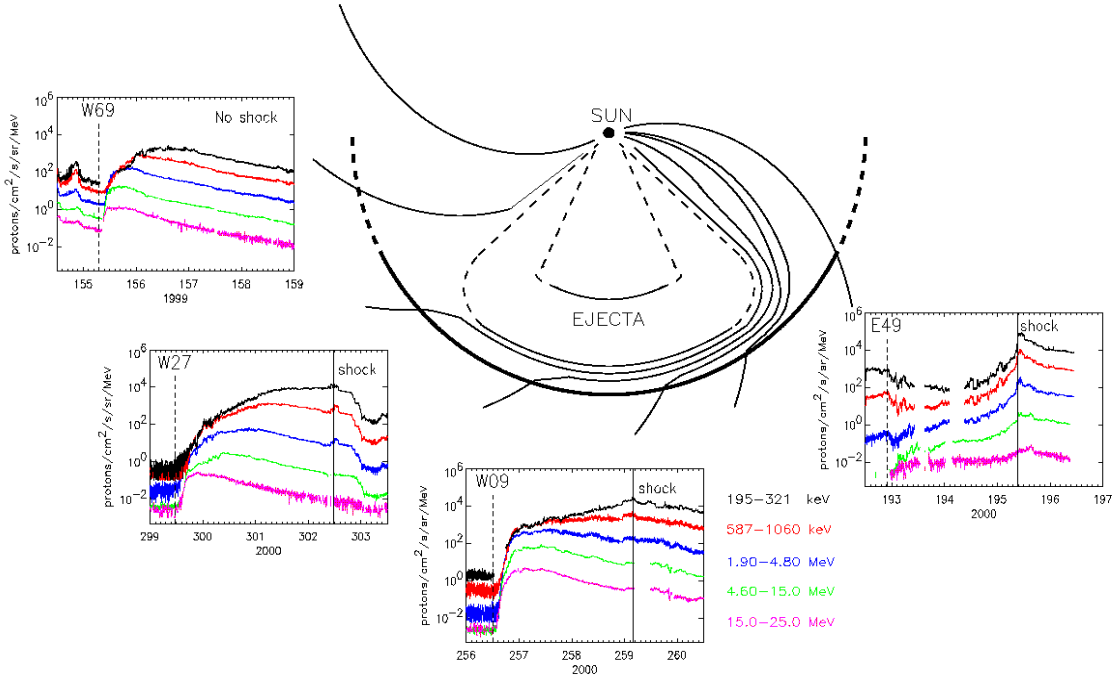

Figure 2.4: Particle intensity-time profiles for four different SEP events (ACE/EPAM, Gol98; and IMP-8/CPME, Sar76). Those profiles are typical of SEP events generated from different solar longitudes relative to the observer (W69, W27, W09 and E49, as indicated). Dashed vertical lines mark the occurrence of the parent solar event and solid vertical lines the arrival of the interplanetary shock. (D. Lario, private communication, 2002)

of the parent solar event is interpreted as if the observer rotates this heliolongitude value but in the opposite sense, keeping the solar activity and the CME-driven shock always centered in CM position. Therefore, in this representation, western events (generated by solar activity in the right side of the disk as seen from the Earth, W65 or W27 in Figure 2.4) appear in the left side of the figure. The opposite is true for eastern events. In western events, the observer quickly connects with the front of the shock (when it is still close to the Sun) via the IMF, that on nominal conditions takes the shape of a Parker spiral. If the magnetic connection between the observer and the traveling shock keeps stable, it can be maintained until the shock arrival, more than one and a half day after the launch of the CME at the Sun. For eastern events, the magnetic connection takes place only several hours before the shock arrival. This is a sketchy characterization of SEP events in terms

of the relative position of the observer with respect to the parent solar activity (see also Figure 2.2). To quantify the influence of the heliolongitude in shaping the flux-profiles is hard because of the contribution of other relevant factors in the process, such as how wide and fast the shock is or the stability of the upstream IMF and, it is basically valid for an observer located at 1 AU from the Sun or near by.

The concept of "cobpoint" (Connecting with the OBserver POINT), defined by Heras et al. (1995) as the point of the shock front that magnetically connects to the observer (see Figures 2.2 and 2.4), is useful to describe the different types of SEP flux profiles:

- Solar events from the western hemisphere have rapid rises to maximum because, initially, the cobpoint is close to the nose of the shock near the Sun. These rapid rises are followed by gradual decreasing intensities because the cobpoint moves toward the eastern flank of the shock just where and when the shock is weaker. The observation of the shock at 1 AU in these western events depends on the width and strength of the shock. These are the cases W69 and W27 in Figure 2.4.
- For near central meridian events the cobpoint is initially located on the western flank of the shock and progressively moves toward the nose of the shock. Low-energy proton fluxes usually peak at the arrival of the shock, being part of the ESP component. This is the case W09 in Figure 2.4, as well as the case sketched in Figure 2.2[11].
- For events originating from eastern longitudes, connection with the shock is established just a few hours before the arrival of the shock and the cobpoint moves from the weak western flank to the central part of the shock. Connection with the shock nose is only established when the shock is beyond the spacecraft and, usually, it is at this time when the peak particle flux is observed. This is the case E49 in Figure 2.4.

The evolution of the low-energy (<5 MeV) ion flow anisotropy profiles throughout the SEP events reflects the cobpoint motion along the shock front (e.g Cane et al. 1988; Domingo et al. 1989; Heras et al. 1995; Kahler 2001b). Moreover, it can also reveal the flow pattern of particles through the front of the shock. In many large

[11]Depending on the characteristics of the solar flare or the extension of the shock in the corona. Central meridian events can also show a particle component at the onset of the event that is not directly associated with the interplanetary shock.

SEP events, the first-order anisotropy reverses its sense at the shock passage or some time later depending on the heliolongitude of the event (see Sanahuja & Domingo 1987 or Domingo et al. 1989). This observational fact represents a further constraint for SEP models trying to describe particle fluxes in the downstream region of shocks (Kallenrode & Wibberenz 1997; Lario et al. 1999; Kallenrode 2002).

Since the arrival of SEPs at the spacecraft is modulated by transport processes, the *in situ* observation of shocks and particles is essential to understand the physical mechanisms involved in the particle acceleration at CME-driven shocks. Analysis of these observations have revealed a wide variety of shock structures and different types of ESP events (e.g. Tsurutani & Lin 1985; Lario et al. 2003a). Only one particular event extensively analyzed, the 12 November 1978 event (Kennel et al. 1986), yielded relatively good agreement with the set of predictions of the diffusive shock-acceleration theory (Lee 1983). The diversity of observed events, however, suggests that different shock acceleration mechanisms and different physical processes contribute to the formation of SEP events. Kallenrode (1995) showed that at energies ($\sim$5 MeV) proton observations could be inconsistent with the predictions of the diffusive shock acceleration theory.

The ESP component of SEP events seems to be the most dangerous part of these events (Reames 1999b) and hence the importance of their study. Most ESP events are usually confined to ion energies less than a few MeV (Kallenrode 1995). Nevertheless, a few unusual events may extend to energies higher than 100 MeV under special conditions (and not necessarily associated with local shock-particle acceleration) (Lario & Decker 2001b).

Barouch & Raguideau (1970) already described the influence that intervening structures (located between the particle source and the observer) have on the propagation of SEPs and shaping the observed intensity-time profiles. These structures may be constituted by either CMEs previously ejected from the Sun and traveling through the interplanetary medium, or by shocks formed between the observer and the shock. The presence of an additional traveling interplanetary shock may also influence the acceleration of energetic particles in the interplanetary medium. Kallenrode & Cliver (2001) pointed out the possibility that two converging CME-driven shocks as a necessary condition to produce long-lasting high-intensity particle events. Gopalswamy et al. (2002) proposed that the presence or absence of an interaction with one or more previous CMEs, within $\sim 50\,R_\odot$ of the Sun, is an important

discriminator between large CMEs associated with SEP events and those that are not. The first shock could provide enhanced intensities of energetic seed particles ready to be efficiently re-accelerated by the second shock. Nevertheless, Richardson et al. (2003) concluded that these interactions do not play a fundamental role in the formation of major SEP events. Gopalswamy et al. (2004) further analysed this issue concluding that large SEP events are mainly associated with fast and wide CMEs that are preceded (within a day) by other wide CMEs from the same source region.

2.2.3 Shocks in the corona

An important problem that lies deep in the root of this discussion (in spite of the numerous studies showing that CMEs are the sources of interplanetary shocks, e.g. Cane et al. (1987)) is our poor knowledge about how CMEs are generated in the corona. An important issue is whether or not interplanetary shocks are extensions of coronal shocks. Gopalswamy et al. (1998) investigated the relationship between metric type II and kilometric type II radio bursts, respectively generated by shocks propagating in the corona and by interplanetary shocks propagating in the interplanetary medium, and found that they seem to be two different populations (see also Cliver & Hudson 2002)[12]. Cliver et al. (2004) made a statistical study of metric type II bursts and the associated SEP events observed by the WIND spacecraft. The main conclusion of this study was that $\sim$20 MeV protons of solar origin observed near Earth are accelerated by coronal shock waves, but only $\sim$50% of coronal shocks are 'SEP-effective'. The coronal shocks strong enough to produce decametric-hectometric type II emission (i.e. $> 3\,R_{\odot}$) are the ones with a higher chance to be followed by SEPs observed at 1 AU. Cane & Erickson (2005) examined radio data from the WAVES experiment on WIND spacecraft in conjunction with ground-based data, in order to investigate the relationship between the shock responsible for metric type II radio burst propagating in the corona and the shocks in front of CMEs. Their interpretation is that these bursts are not caused by the CME-driven shock, literally, "*The cause of this scenario is unclear*". At the same time, Gopalswamy et al. (2005) reported on a study of type II radio burst emission from WIND/WAVES in conjunction with the white-light CME observations from

[12]A description of the types and main characteristics of radio observations related to CMEs can be found in Vourlidas (2004) and in Gopalswamy (2004a,b).

SOHO/LASCO. The main result of this study is that the majority (78 %) of CME events showing radioburst counterparts from metric to kilometric wavelength domains were associated with SEP events; the remaining cases correspond to events magnetically poorly connected to the near Earth observer. Also, Gopalswamy et al. (2005) interpret that only CMEs fast enough are able to produce first metric type II in the corona and later kilometric type II in interplanetary space; these CMEs are the only ones able to drive shocks that produce SEPs.

Mann et al. (2003) analyzed the typical spatial and temporal scales of the formation and development of shock waves in the corona. Their main conclusions are that shocks waves in the corona can become super-Alfvénic between 1.2 and $3\,R_{\odot}$, and later at distances beyond $6\,R_{\odot}$. The discontinuous evolution of these shocks is a result of the radial profile of the background medium where these shocks evolve (Gopalswamy et al. 2001; Mann et al. 2003). Under such circumstances, only supercritical CME-associated shocks are able to produce highly energetic protons, electrons and ions (Kennel et al. 1985) from distances very close to the Sun ($<3\,R_{\odot}$) and continue in the interplanetary medium. Slower CMEs will have a discontinuous evolution from $1.2-3\ R_{\odot}$ up to $6\ R_{\odot}$, if they can still drive a shock at these farther distances. Chen & Krall (2003) concluded that one mechanism is sufficient to explain flare – and prominence – related CMEs. In addition, for a given event there may be various shock fronts driven by the flare/CME association. It is no clear yet whether Moreton waves, coronal shocks (that produce metric II bursts) and interplanetary shocks (that produce kilometric type II bursts) are different manifestations of the same shock or different shocks. Cargill & Schmidt (2002) discussed the present state of modeling CMEs using MHD simulations. One of their points is that "*a lack of knowledge of the coronal magnetic field makes such simulations of little use in space weather forecasts that require knowledge of the ICME*[13] *magnetic field strength*". Lee (2005) pointed out that there are many features of the coronal shocks that are not well known but that play a key role in the acceleration of SEPs. These include the formation of the coronal shock, its shape, its propagation through the coronal streamer belt, the existence of MHD turbulence in its vicinity, or even the possible

[13]ICME: Interplanetary counterpart or extension of a CME, also known as ejecta or driver. ICMEs have been identified by observations of interplanetary perturbations (frequently in the downstream part of a interplanetary shock) showing smooth magnetic field, low-β regions, enhanced charge state ratios of specific chemical elements, enhanced helium abundances and composition anomalies of solar wind ions (see, e.g. Zurbuchen & Richardson 2006); although these signatures do not occur at the same time, do not show up in all events and may vary from event to event. See also Richardson & Cane (2004) or Cane & Lario (2006).

existence of multiple shocks driven by the flare/CME association[14].

Finally, it is worth to remember that electrons are also a constituent of the SEP gradual events. Although electron events have potential as predictors of the onset of SEP events[15] interplanetary shocks are inefficient accelerators of electrons due to their small gyroradii. The electrons move adiabatically through transition of interplanetary shocks, without undergoing any acceleration process. In addition, the high-frequency turbulence required for the scattering of low-energy electrons by the diffusive shock-acceleration mechanism is often not present in interplanetary shocks and is not readily excited by the electrons themselves (Lee 1997). Therefore, diffusive shock-acceleration mechanism is thought to be inefficient for electrons and, consequently, the effects that shocks produce on electrons are usually minor. Nonetheless, several cases of low-energy (< 50 keV) shock-accelerated electrons at 1 AU have been clearly observed (Tsurutani & Lin 1985; Lario et al. 2003a). A different question is whether the unknown properties of the shock in the corona are adequate for electron acceleration[16].

Recently, RHESSI[17] observations made possible to relate SEP observations in interplanetary space to the accelerated particle population existing at the flare site[18]. Comparisons between the spectra of energetic protons producing γ-ray line at the Sun and the spectra of energetic protons observed at 1 AU suggest that the γ-rays and the energetic protons may have a common origin (Lin 2005). On the other hand, Krucker et al. (2004) found a correlation between the spectral index of hard X-ray photons and the spectral index of the in-situ electrons, suggesting a common

[14]In this sense, Lee (2005) reads: *"All these complexities and variations create temporal and spatial variations in interplanetary space and at the observing spacecraft depending on the field line connection."*

[15]Haggerty & Roelof (2001, 2002) studied the properties of a large set of near-relativistic beam-like electrons (38 – 315 keV) observed by ACE. They found that these electrons are released, on average, with a $\sim$10 minutes delay with respect to the start of the flare-associated electromagnetic emissions.

[16]Simnett et al. (2002) compared the electron release time in the Sun with CME observations from SOHO, concluding that these near-relativistic electrons are accelerated by the shock driven by the CME and released in the corona at heights of 2 – 3 $R_{\odot}$. See, however, Kahler et al. (2005) for a criticism of this study and Cane & Erickson (2003) for alternative SEP injection scenarios.

[17]RHESSI: Ramaty High Energy Solar Spectroscopic Imager. A hard X-ray and γ-ray observatory with imaging and spectroscopic capabilities, launched in February 2002.

RHESSI web page: http://hesperia.gsfc.nasa.gov/hessi/

[18]Those interacting particles result from the flare process and do not escape into interplanetary space. Precipitating electrons, for example, are able to produce γ-rays and neutron emission.

accelerating mechanism.

2.3 Models of gradual SEP events

The first models for SEP events assumed that particle injection occurs in spatial and temporal conjunction with the associated solar flare. However, flare activity lasts, at most, just a few hours while low-energy ion events may last for several days. In addition, gradual SEP events are observed even when the associated flare takes place at longitudes poorly connected with the observer. These two observational facts led modelers to suggest that energetic particles may remain stored in the solar corona and diffuse across the coronal field to reach widespread ranges of heliolongitudes. Algorithms or codes based on such models (e.g. Smart & Shea 1992; Heckman et al. 1992) failed to include the effects of shocks because their predictions for particle intensities were based on the characteristics of the associated solar flare (such as its location, X-ray and radio bursts intensity). Apart from their inability to reproduce ESP events (see Section 2.2), particle transport through the interplanetary medium was based on simple static diffusion models.

As mentioned before, the current scenario proposed to account for gradual SEP events involves the presence of fast CMEs able to drive shocks efficient accelerators of energetic particles. The simulation of these particle events requires knowledge of how particles and shocks propagate through the interplanetary medium, and how shocks accelerate and inject particles into interplanetary space. The modeling of particle fluxes and fluences associated with SEP events has to consider:

- the changes in the shock characteristics as the shock travels through the interplanetary medium,
- the different points of the shock where the observer is connected to, and
- the conditions under which particles propagate through the interplanetary medium.

Owing to the predominance of ions over electrons in gradual events, most of the attempts to model these events have been applied only to ions. Each model presents its own simplifying assumptions in order to tackle the series of complex phenomena occurring during the development of SEP events. Two main approximations have been used to describe the particle transport: the cosmic ray diffusion equation

(Jokipii 1966) and the focusing-diffusion transport equation (Roelof 1969; Ruffolo 1995).

To describe the shock propagation, approximations range from considering a simple semicircle centered at the Sun propagating radially at a constant velocity, to fully developed magnetohydrodynamic (MHD) models. Lee & Ryan (1986) adopted an analytical approach to solve the time-dependent cosmic ray diffusion equation for an evolving interplanetary shock which was modeled as a spherically-symmetric blast wave propagating into a stationary surrounding medium. The application of the diffusion approximation outside the shock region and some other strong assumptions were needed to retain a tractable model[19]. None of them is especially well supported observationally in the inner heliosphere (Zank et al. 2000).

2.3.1 One and a half decade of modeling efforts

Fifteen years ago[20] Heras et al. (1992 and 1995, hereafter jointly identified as He925) included for the first time in the focused-diffusion transport equation, a source term, Q, representing the injection rate of particles accelerated at the traveling shock. The use of the focused-diffusion transport equation (Roelof 1969) is more adequate to describe the transport of particles between the Sun and 1 AU since it includes the effects of focusing in the diverging IMF, allowing us to reproduce the large and long-lasting anisotropies usually observed in gradual SEP events (Heras et al. 1994; Appendix A, figures A.1, A.3 and A.4). The injection of particles is considered to take place at the cobpoint. To track this point with time, the authors used a MHD model that describes the shock propagation from a given inner boundary close to the Sun up to the observer's location. The IMF is described upstream of the shock by a nominal Parker spiral. This model had been refined by including solar wind convection and adiabatic deceleration effects into the particle transport equation and the corotation of the IMF lines (Lario 1997 and Lar98). It has been successfully applied to reproduce low-energy (<20 MeV) proton flux and anisotropy profiles of

[19]For example, very high blast waves velocities and a radial mean free path of the energetic particles that increases with r^2 (r, the radial heliocentric distance).

[20]Take it as a rough time-mark. Before the early 90's there was practically nothing in the field of shock-and-particle modeling of gradual events. A dramatic improvement in SEP monitoring has occurred since then (even over twenty years, starting with ISEE-3 and Helios spacecraft). Nevertheless, the accuracy of a few-days-forecast of SEPs is not much different today than at that time.

a number of SEP events simultaneously observed by several spacecraft (He925 and Lar98).

Kallenrode & Wibberenz (1997), Kallenrode & Hatzky (1999) and Kallenrode (2001) adopted the same scheme as the previous works. However, these authors use a semicircle propagating radially from the Sun at constant speed to describe the shock. They also parameterize the injection rate Q in terms of a radial and azimuthal variation which represents the temporal and spatial dependences of the shock efficiency in accelerating particles. This model allows particle propagation in the downstream region[21] of the shock, just by changing the magnitude of the focusing length. Nevertheless, these authors did not modify the IMF topology behind the shock (still an unperturbed Parker spiral). Different topologies of the shocked IMF field lines may lead to different effects in the particle transport, thus different results (Lario et al. 1999). Torsti et al. (1996) and Anttila et al. (1998) adopted a similar scheme as the above-mentioned works but assuming, in order to locate the cobpoint, that the distance of the cobpoint to the observer along the IMF line connecting with the observer decreases linearly with time. They also used a complex parametric function to describe the injection rate of shock-accelerated particles, including energetic, temporal and spatial dependences. Differences among the above models have been described in Sanahuja & Lario (1998) and Kallenrode (2001).

Ng et al. (1999a,b, 2001, 2003) developed a numerical model where the particle transport includes the effect of self-generated Alfvén waves by the streaming protons. Whereas the above-described models assume that the scattering of particles may be parameterized by a given mean free path (which may depend on the particle energy and time), Ng et al. (1999b) consistently solved the focused-diffusion transport equation for the particles and the equation describing the evolution of differential wave intensity. Assuming that particles are accelerated out of a constant source plasma with a specific composition, Ng et al. (2001) described the evolution of ion abundance ratios in some SEP events but no quantitative agreement of the predicted wave spectrum has yet been presented (Tsurutani et al. 2002). The shock was assumed to travel radially away from the Sun at a constant speed and the injection rate of shock-accelerated particles was also parameterized to account for temporal, radial and rigidity dependence. Ng et al. (1999b, 2003) assumed a five

[21] By downstream region of the shock, here we mean the region left behind by the shock and between its front and the discontinuity (contact, tangential or reverse shock) that separates the shocked solar wind material from the ICME.

parameter expression for the injection rate of particles that depends on time, radial distance and particle energy (a time varying power-law). This model allows for a better description of self-generated scattering processes throughout the transport of particles of different species. However, several simplifying assumptions are needed in order to render the model tractable[22].

Many efforts to incorporate the mechanisms of shock-acceleration of particles into traveling interplanetary shocks have been made. They are based on the assumption that traveling shocks accelerate particles via the diffusive shock acceleration mechanism, although *in situ* observations of shocks and particles suggest that multiple acceleration processes may occur (van Nes et al. 1984; Tsurutani & Lin 1985; Lario et al. 2005c). Zank et al. (2000) developed a dynamical time-dependent model of particle acceleration by solving the diffusion transport equation in a series of shells around an evolving and propagating shock. The time-dependent shock-accelerated particle distribution is derived in a self-consistent way by computing the shock strength, which in turn determines the accelerated energetic particle spectra. Zank's model assumes a spherically symmetric solar wind into which a blast wave propagates, from a inner boundary located at $\sim 21\, R_{\odot}$ from the Sun. Both the wind and shock are modeled numerically using hydrodynamic equations and assuming a Parker spiral for the IMF. The local characteristics of the shock, such as the shock strength or the Mach number, are dynamically computed, and they are used to determine the distribution of particles injected into the diffusive shock acceleration mechanism. In this model, shock-accelerated particles propagate diffusively in the vicinity of the shock generating resonant alfvénic waves, and at a certain distance from the shock, they are able to escape from the shock complex and propagate toward the observer[23].

Rice et al. (2003) generalized Zank et al. (2000) model to include shocks of arbitrary strength (i.e. different conditions for particle diffusion around the shock) by

[22]The most important are a radial magnetic field, non-interacting waves, the omission of non-linear effects and the consideration of only Alfvén waves propagating parallel or anti-parallel to the magnetic field. Particularly, the use of radial IMF does not allow the reproduction of the longitudinal dependence shown in Figure 2.4. Moreover, observation of shock speeds in different directions (Cane 1988) and dynamic studies from MHD simulations (Smith & Dryer 1990) have shown a decrease of the shock speed toward its flanks and a weakening of its front as it expands, indicating that the shock cannot be represented by a semicercle at constant speed.

[23]See Lee (2005) for a criticism of this model, being a relevant point the fact that this approach cannot be easily adapted to compare with observations of specific events.

using a two-dimensional MHD model for the shock simulation and assuming that particles are accelerated by the diffusive shock-acceleration mechanism, taking the upstream wave intensity as predicted by Gordon et al. (1999). The transport of particles outside the shock complex is modeled by a ballistic projection between the shock and the observer. It is noteworthy to point out that this model assumes the shock formation at $21\,R_{\odot}$, and therefore the initial injection of particles (that occurs when the shock is still closer to the Sun) has to be artificially incorporated by a mechanism different than shock-acceleration. On the other hand, it remains to be seen both whether the diffusive shock-acceleration is the only mechanism actually working at interplanetary shocks (Kallenrode 1995) and whether the signatures predicted by this model have been actually observed in shocks. Li et al. (2003) combined the results of Rice et al. (2003) with a Monte Carlo solution for the focused-diffusive transport of particles escaping from the shock complex along a Parker spiral magnetic field. In this model, the mean free path of the particles is considered an arbitrary parameter and the Alfvén waves generated by the streaming of particles (Ng et al. 2003) is not taken into account. Whether the Alfvén waves generated by the streaming protons have a relevant effect on the transport of energetic particles remains uncertain; it might be that the number of particles is not enough to amplify the necessary upstream alfvénic waves to have a significant effect on the evolution of the SEP event (Vainio 2003).

Li et al. (2005) studied the influence of the charge/mass ratio on the observed SEP spectrum at 1 AU, by modeling two species of ions (CNO-type particles and iron) for two shocks of different strength. The shock simulation they used is based on the earlier work of Zank et al. (2000) and Rice et al. (2003), with the CME-driven shock introduced at 0.1 AU. They took into account the coupling between the streaming proton population and the stimulated upstream turbulence. Particles diffused ahead of the shock front can propagate along the IMF subject to pitch-angle scattering processes, and their transport is followed using a Monte Carlo code (Li et al. 2003). The simulations performed provide a theoretical basis for comparison with observations, and yield some general features (e.g. Fe/O ratio, the energetic particle power-law spectra for weak shocks) that are often observed in SEP events. Li & Zank (2005) used a similar code (but with the CME starting at 5 $R_{\odot}$) to study the relative contribution of a CME-driven shock and the associated flare to the SEP flux profile. The results obtained showed that the relative contribution of both processes depend on the time between the end of the flare process and the formation of the CME shock because such contribution can come from two populations, [1]

those particles coming from the ambient solar wind and being shock-accelerated, and [2] those particles accelerated during the flare process but that have been absorbed and re-accelerated by the shock.

An interesting point of the Zank et al. (2000) and Rice et al. (2003) models is that, for extremely strong shocks, particle energies of the order of 1 GeV can be achieved when the shock is still close to the Sun. As the shock propagates outward, the maximum accelerated particle energy decreases sharply. This issue has been cast in doubt because the short span of time ($\sim$20 minutes) after the onset of the CME. Other shock acceleration models (Berezhko et al. 2001) also suggested the possibility that 1 GeV protons can be accelerated when extremely strong shocks are close to the Sun ($<3\ R_{\odot}$). Evidence has been reported (Lee 2005, and references therein) that these particles are accelerated at coronal shocks, where the shocks are particularly strong, based on the delay of the particle onset as a function of the energy and the energy spectrum. Roussev et al. (2004) modeled the passage of a driven shock through a coronal model, using as input data synoptic magnetic field observations for a specific event displaying >2 GeV fluxes. They estimated that the shock was strong enough to diffusive-shock accelerate protons up to ~ 10 GeV, but they did neither consider the upstream escape nor the observed SEP flux profiles at 1 AU. Kocharov et al. (2005) suggested that the trailing turbulent layer behind the shock may be the region where >10 MeV-particle acceleration occurs, and concluded that the direction of the shock propagation has little influence in the formation of the particle spectrum.

Lee (2005) presented an analytical quasi-linear theory for the evolution of gradual events consisting in particles accelerated at an evolving coronal shock, later transformed into interplanetary shock. The upstream particle transport accommodates the large streaming anisotropies observed near the onset of these types of events. This model is able to reproduce the onset, the flux plateau with particles showing large anisotropies, the flux increase prior the shock arrival (the ESP component) and the decaying invariant phase downstream[24]. The particle transport equation and a wave kinetic equation are solved together for the coupled behavior of the waves and energetic protons. It treats the transition from a scatter-dominated sheath adjacent to the front of the shock to the near-scatter free particle transport in interplanetary space, but neglects adiabatic deceleration of particles (which is important at low

[24]The decaying phase with small spatial gradients and invariant power-law energy spectra is the last phase of many SEP events; see definition and details in Reames et al. (1997b).

energies) and the shock is assumed to be spherical symmetric. The downstream transport of particles is treated under two extreme assumptions: vanishing diffusive transport or effective diffusive transport. This latter hypothesis allows reproducing the invariant spectra, spatial gradients and exponential decay in the late phase of the event. The author points out some discrepancies with observations, concluding that they could substantially modify the predicted wave intensity.

A major problem to be solved to obtain reliable warnings and forecasts of SEP events is to know where, when and how the SEP events originate in the solar atmosphere. That means to improve our knowledge of the physical mechanisms that generate the interplanetary shock in the corona (Section 2.2.3), and its propagation in the interplanetary medium. We do not know yet too much what characteristics of the CME or the ambient medium are dominant in the development of a SEP event (Kahler 2001b). For example, CME propagation models often superpose a density or velocity perturbation on a given solar wind background. Odstrčil & Pizzo (1999) showed that the motion of a CME in interplanetary space – and hence the front of the driven shock, i.e. the source of accelerated particles – is affected by its interaction with the heliospheric pattern. Chané et al. (2005) derived a similar conclusion with respect to the magnetic field orientation of the solar wind parcel on top of which the perturbation propagates. Tsurutani et al. (2003) precisely indicated that appropriate three dimensional 3D MHD model with full-time dependent boundary conditions at one solar radius and that extends beyond all critical points – useful for space weather predictions – does not exist yet. In that sense, it is necessary to create 3D MHD models that include a fine structure, realistic dissipation and an adequate solar wind profile (see, for example, Jacobs et al. 2005).

2.3.2 The last three years of modeling efforts

Important new developments have occurred these last years. The US National Space Weather Program has revitalized studies of CME-driven shock propagations, since these shocks contribute to geomagnetic disturbances. The availability of CPU power and computer memory enables more advanced modeling, taking into account new physical and geometrical effects. This has allowed CME modelers to start incorporating observational data as boundary conditions, and the simulations are becoming realistic enough to compare simulation results in detail with observations. Two examples: Lionello et al. (2003) developed a 3D MHD model of the solar corona,

incorporating thermal conduction along the magnetic field, radiation losses and heating into the energy equation; and Odstrčil et al. (2004) developed a coupled coronal-solar wind model where the solar wind features are derived from coronal models utilizing photospheric magnetic field observations, and input for transient disturbances are derived from coronograph observations of CMEs. More relevant is that these modelers and researchers form part of recently developed general frameworks for space weather modeling that joins people from different institutions[25]. Two groups, the Center for Space Environment Modeling (CSEM) and the Center for Integrated Space Weather Modeling (CISM)[26], are developing coupled models of the inner heliosphere. These models aim to extend from the solar corona to beyond the orbit of Earth or Mars, including the global magnetosphere, radiation belts and ionosphere.

Manchester et al. (2004a,b) developed a 3D MHD model describing the evolution of a CME from the solar corona (at $1\,R_\odot$) up to 1.0 AU into a structured solar wind. The CME is driven by magnetic pressure and buoyancy of a flux rope in an initial state of force imbalance (see details of the flux rope modeling in Manchester et al. 2004a). Manchester et al. (2005) used this model to explore the sheath region that forms behind the shock because particle acceleration processes strongly depend on the topology of such region. They concluded that the sudden postshock increase in magnetic field strength is effective in accelerating particles to the GeV range and – the most importantly – that "*this simulation represents and ongoing effort to develop global space weather models that can track and resolve shocks to accurately derive MHD quantities from which SEP properties are calculated*". Jacobs et al. (2005) tried to quantify the effect of the background solar wind models (three 2.5D MHD models) on the evolution of a simple CME model. Then, Chané et al. (2005) studied the effect of the CME initiation parameters on the CME evolution, particularly the polarity of the initial magnetic flux rope. They also pointed out that the comparison between the results of different CME models is a serious problem, because different background wind models and different CME initiation models are used. Chané et al. (2006) extended the study of Chané et al. (2005) up to 1 AU. They concluded that the initial magnetic polarity of the CME is strongly related to its geo-effectiveness

[25]General frameworks are becoming important in numerical simulations of complex phenomena. These frameworks are reusable modular systems that allow the integration, extension, modification and use of the coupled models more efficiently than in monolithic codes. Independent models are coupled via standardized interfaces.

[26]CSEM, University of Michigan. http://csem.engin.umich.edu; see Tóth et al. (2005).

CISM, Boston University. http://www.bu.edu/cism/index.html; see Luhmann et al. (2004).

and also influences its arrival time at the observer's location.

Wu et al. (2005a) developed a 3D MHD model to investigate the criteria for initiating a solar eruptive phenomena. The relevant innovation of this model is that it can incorporate realistic photospheric dynamics together with the differential rotation and meridional flow. Further numerical simulations show that solar surface conditions play an important role on determining the type of resulting CME (see Wu et al. 2005b, for more details). The latest developments in relation to the solar wind models and the superposed CME simulations, triggering in the solar corona and propagation in the interplanetary medium, can be found in Poedts & Arge (2005) and a review of the current knowledge about CME theory and modeling in Forbes et al. (2006).

Sokolov et al. (2004) presented a field line advection model for particle acceleration coupled with the global MHD code of Manchester et al. (2005), then it is possible to follow the proton-shock accelerated flux as the shock advances, from the Sun to the Earth[27]. Sokolov et al. (2004) computed particle intensities of the shock-accelerated particles via the diffusive shock acceleration mechanism for a shock traveling from 4 to 30 $R_{\odot}$. The resulting profiles were compared with GOES-8 measurements of the SEP event on May 2, 1998 showing good agreement with GOES measurements for six of the available energy channels (from >5 MeV to >100 MeV). Kóta et al. (2005)[28] are developing a numerical model for particle propagation based on the coupled solution of the focused transport equation and the wave kinetic equation, similar to the approach of Ng et al. (2003), but including shock acceleration by imposing a boundary condition on the transport equation at the shock. This model also uses one or more IMF lines advected with the plasma, the geometry of these field lines and the plasma parameters along them are obtained from the CME model.

[27] A conclusion of this work is "*... what is important to know from the CME model is when (or if) the shock wave forms on the magnetic field line connecting the Sun with the Earth*"; in fact, the cobpoint concept, Heras et al. (1995).

[28] Private communication to Tóth et al. (2005); quoted there as "submitted manuscript to The Astrophysical Journal (2005)". For preliminary results of their model see e.g. Kóta, Manchester, & Gombosi (2005).

2.4 Radial dependence of particle fluxes and fluences

The vast bulk of energetic particle observations in interplanetary space come from spacecraft close to the Earth's orbit ($\sim$1.0 AU). In order to estimate the impact of SEPs on interplanetary missions traveling at different radial distances it is necessary to specify the radial dependence of particle intensities and fluences. The variation with radial distance of SEP intensities and fluences changes from event to event; its study can be approached via observational or modeling efforts. This is a hard observational task because the scarcity of observational data at several heliocentric distances and because of both radial and longitudinal dependences are interrelated (Lar98). Moreover, there is little information about particle flux environment close to the Sun due to the lack of spacecraft operating in this region. Basically, only Helios-1 and Helios-2 spacecraft made observations from 0.29 AU to 0.98 AU that can be used to compare with observations at 1.0 AU. Therefore, very few data from large particle events are available to asses the radial dependence of SEP events in the inner most part of the heliosphere, in spite that this is a critical information for missions going close to the Sun (e.g. Bepi Colombo, Solar Orbiter, Solar Probe or the Inner Heliospheric Sentinels). The standard for space environment adopted by ESA (E-10-04 2000) recommends to scale the proton flux prediction from JPL-91 model (Feynman et al. 1993) with an inverse square law. However, the expected radial variation of flux during the SEP events depends on the way in which the energetic protons are produced and the energy considered, and this dependence is not the same for flux, fluence or peak flux.

Existing models do not help too much since their interest has been focused on the 1 AU scenario and furthermore, the scarce number of multispacecraft studies performed (e.g. Beeck et al. 1987; Hamilton 1977) are based on analytical solutions of the diffusion transport equation for protons, without considering either particle acceleration by propagating shocks or the focusing effect dominating the transport of energetic particles within 1 AU. The current situation is confusing, because an empirical rule or theoretical expression that can be applied with a certain degree of confidence does not exist for either fluxes or fluences. For example, an usual recommendation to scale peak fluxes with distance is using a scaling factor r^{-3} for the inner interplanetary medium, $r < 1$ AU, and a factor r^{-2} for outer space, $r > 1$ AU (Feynman et al. 1988). Nevertheless, the JPL-91 model suggests using the inverse

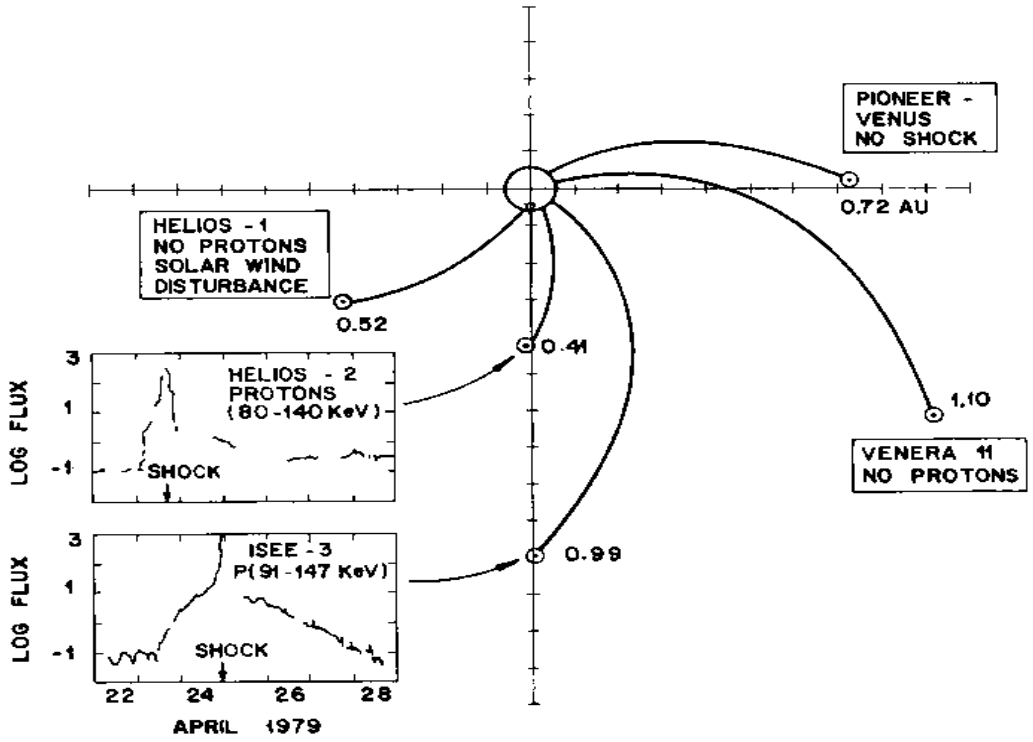

Figure 2.5: Location of different spacecraft in interplanetary space between the Sun and the Earth (not to scale) at time of a solar filament eruption in April 22, 1979. Spacecraft distances are in AU. The insets show proton flux observations at ISEE-3 and Helios-2 (from Sanahuja et al. 1983)

quadratic radial dependence for all heliocentric distances (Feynman et al. 1993). The key point here is that this recommendation is solely based on the work of Hamilton (1988) which, as mentioned before, does not take into account either the effect of the propagating shock or the focusing effect, and was based on its application to SEP events mostly observed beyond 1 AU.

Different studies dealing with comparative multispacecraft observations show that a key parameter is the connection angle between the observer and the particle sources; in other words, the cobpoint for gradual events, or the magnetic footpoint for impulsive events. Figure 2.5 (from Sanahuja et al. 1983) shows an example of a SEP event observed by different spacecraft in 22 – 28 April 1979. The proton flux intensity observed by ISEE-3 and Helios-2, both close to the Sun-Earth line, were similar, although the two spacecraft were at 1.0 AU and 0.4 AU, respectively. A plausible explanation is that the effect of the distance (that means more time for particle

shock-acceleration) is compensated by the fact that the cobpoint of Helios-2 is closer to the central part of the shock (a more efficient region for particle-acceleration) than the cobpoint of ISEE-3. In addition, to complete this picture, Helios-1, located at 0.5 AU and slightly more to the east than Helios-2, and Venera 11, at 1.1 AU but more to the west than ISEE-3, did not detect any particle enhancement at the same time. Rosenqvist (2003b) presented other examples of multispacecraft SEP observations (also involving Helios-1 and -2, and ISEE-3). If the radial dependence of the flux depends on the efficiency of the shock as particle-accelerator, this implies that it also depends on the energy considered. For example, Figure 4 of Kallenrode (1996) shows that the relative fraction of particles accelerated by interplanetary shocks decreases with increasing energies; therefore, the higher the energy of the particles the higher the fraction of particles accelerated near the Sun, and hence a different radial dependence for each energy.

Rosenqvist (2003b) used Helios proton data to re-examine the radial dependence of the SEP fluxes, deriving a trend according to which the SEP integral fluxes vary from $r^{-0.77}$ for >4 MeV protons to $r^{-1.0}$ for >51 MeV protons, thus rebutting a r^{-2} dependence. This conclusion, however, should be taken cautiously because of the meager number of events considered in the study. Rosenqvist (2003b) also developed an heuristic geometric model to provide indications of the impact of various simple hypothesis (basically, the inclusion of a mobile source and type of particle propagation) on the fluence of SEP events, reaching conclusions similar to those discussed in the former paragraph, and stressing the fact that the main problem to face is the lack of continuous data from radial distances close to the Sun. Reames & Ng (1998) used GOES $4.2-8.7$ MeV proton data to analyze the "streaming limit" of proton flux at 1 AU. Comparison of the GOES data with similar Helios $\sim 1-10$ MeV proton observations (Reames 1990), reveals that radial variation of the streaming-limit intensity[29] is consistent with a dependence on the radial distance as $\sim r^{-3}$, although it only applies to the intensity of streaming particles, not to those accelerated locally or convected out by the shock.

Recently, we (Vainio et al. 2007) have modeled a gradual proton event observed on the $6-8$ of June 2000 by ACE and IMP-8 spacecraft ($0.58-48.0$ MeV). Top left panel in Figure 2.6 shows the fitted differential flux profiles (black traces) of the measurements at 1 AU (gray traces). The calculated proton intensity-time histories

[29]This limit is occasionally exceeded in large events, as shown by Lario et al. (2001) and Lario & Simnett (2004).

derived for observers located at 0.3 AU and 0.7 AU – along the same IMF line – for three of the simulated energies are displayed in the top right panel of Figure 2.6, together with those fitted at 1.0 AU. From these profiles they calculated the peak intensities, differential fluence and the time-integrated net flux reached at each observer. The bottom panels of Figure 2.6 show the dependence of these quantities as a function of the radial distance from the Sun. Their conclusion is that scaling laws for radial dependence in gradual events do not show any similarity to laws deduced from simple analytical diffusion modeling, because there is an interplay between the interplanetary scenario and the time dependence of the source. Ruzmaikin et al. (2005) reached the same conclusion after computing the variation of the 1 MeV- and 100 MeV-particle flux profiles with radial distance, using the model developed by Li et al. (2003) for a strong shock.

Lario et al. (2006) use energetic proton data from the IMP-8 and the two Helios spacecraft, for two energy channels, to analyze the peak intensities and fluences of 72 SEP events observed simultaneously by at least two of these spacecraft located at different radial distances. The main conclusion of this study is that the dominant parameter that determines the peak intensity and fluence of the SEP events is not the heliocentric radial distance, r, but rather the angular distance between the parent active region and the footpoint of the magnetic field line connecting the observer to the Sun, ϕ. They perform a multiparameter fit of these two variables[30], for the peak intensities and fluences measured during those events, concluding that their radial dependence show variations that range from $r^{-2.7}$ to $r^{-1.9}$ for 4 – 13 MeV and 27 – 37 MeV proton peak intensities, respectively, and from $r^{-2.1}$ to $r^{-1.0}$ for the respective proton fluences. These radial dependences are weaker than those inferred from diffusion transport models (e.g. Hamilton 1988) and than those recommended to extrapolate these quantities to radial distances within 1.0 AU from measurements at 1.0 AU (Feynman & Gabriel 1988). Applications of these results should be taken cautiously because these are values averaged over the ensemble of SEP events.

Most recently, we (Lario et al. 2007) have studied the radial dependence of peak intensities and fluences of SEP events in the framework of the focused transport theory (see Chapter 3). It was assumed a fixed source of particles at the base of an

[30]The radial and longitudinal distributions of peak intensities or fluences, j, of the ensemble of events follow the functional form $j = j_0 r^{-\alpha} exp[-k(\phi - \phi_0)^2]$, where r is the heliocentric radial distance of the spacecraft, ϕ is the longitudinal angular distance between the footpoint of the field line connecting the observer to the Sun and the site of the active region that generated the event, and ϕ_0 is the centroid of the peak flux or fluence distributions.

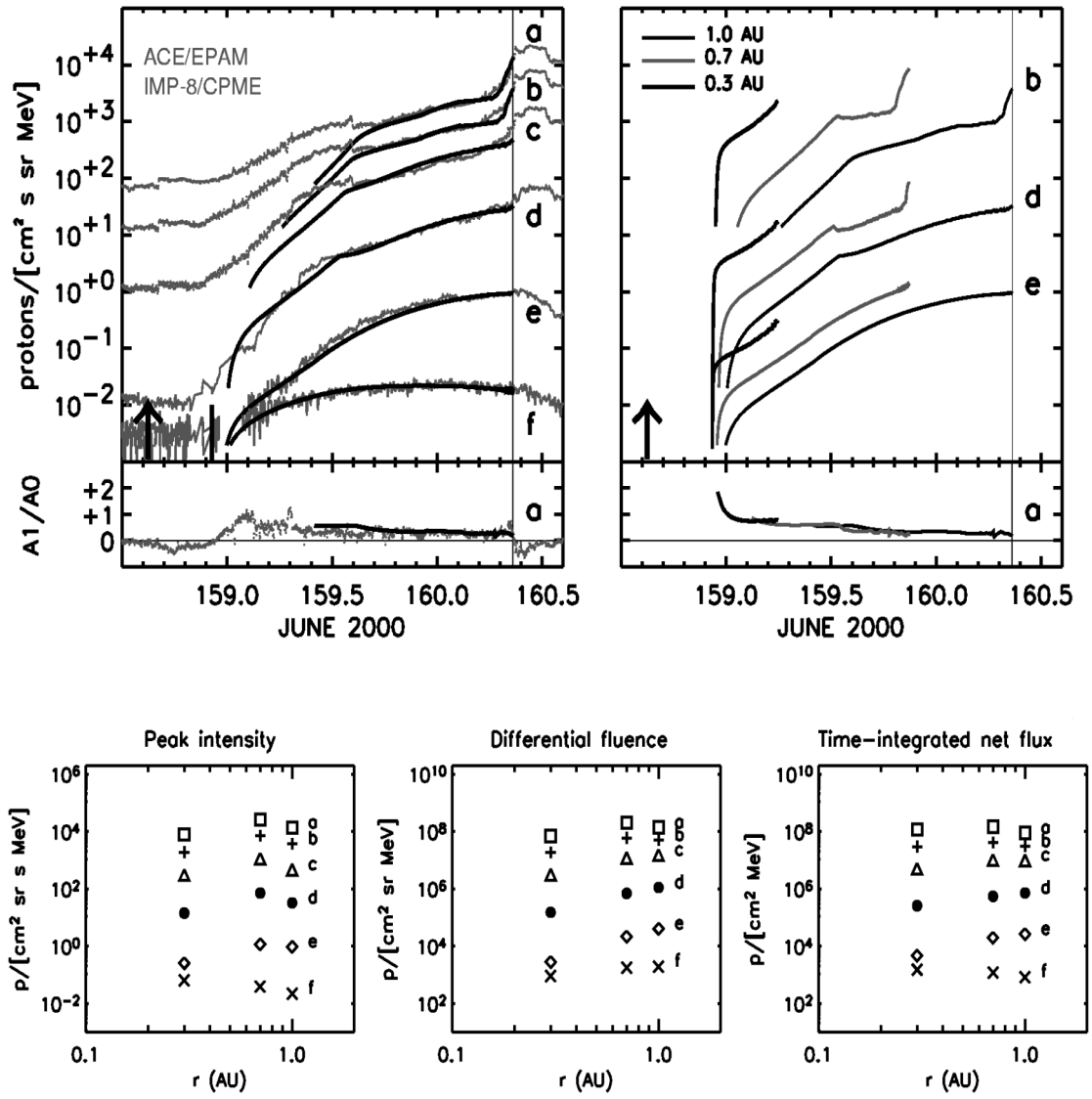

Figure 2.6: Top panels: Gradual SEP event of 6−8 of June 2000 as observed by ACE/EPAM and IMP-8/CPME. The observed (gray traces) and fitted proton intensities and anisotropies at 1 AU (left panel, black traces) are given in addition to the modeled ones at 0.3 AU and 0.7 AU (right panel). The energy channels are denoted with labels a−f: a: 0.58−1.06 MeV, b: 1.06−1.90 MeV, c: 1.90−4.80 MeV (from ACE/EPAM, Gol98); d: 4.6−15.0 MeV, e: 15.0−25.0 MeV and f: 25.0−48.0 MeV (from IMP-8/CPME, Sar76). Bottom panels: Peak intensities, differential fluences and time-integrated net flux of this proton event as a function of radial distance for the same energy channels a−f (symbol coded). Figure adapted from Vainio et al. (2007).

Archimedian spiral IMF line and a particle injection rate is represented by a Reid-Axford[31] profile. Energetic particles propagate along the field line where several observers are located at radial distances ranging from 0.3 to 1.6 AU. Figure 2.7 shows one of the four cases studied by Lario et al. (2007). The left panel of this figure shows the evolution of the 8.3 MeV proton intensity assuming a particle injection rate characterized by the parameters: $\beta = 1.5$ hours and $\tau = 0.2$ hours. The value of the proton mean free path along the field line, $\lambda_{\parallel} = 0.1$ AU, is assumed to be constant in time and energy. Circles denote the peak intensity reached at each one of the 10 observers considered. The right panel shows the power-law radial dependence of the peak intensity (black traces) and event fluence (gray traces).

Transport processes undergone by energetic particles as they propagate away from the Sun contribute to the decrease of peak intensities and fluences with radial distance. Pitch-angle scattering and adiabatic deceleration processes are dominant over the focusing and solar wind convection effects at low energies, large heliocentric distances and when mean free paths are small. Hence, the larger values of the power-law indices, α, of the radial distance are deduced for heliocentric distances between 1.0 AU and 1.6 AU for low energy particles and with small mean free paths. The dependence of α with the energy of the particles and the adopted values of $\lambda_{\parallel}$ shows that (1) the smaller the mean free path of the particles, the larger the decrease of both peak intensities and fluences with radial distance, and (2) the smaller the energy of the particles, the larger the decrease of both peak intensities and fluences with radial distance. When particle injection at the base of the flux tube extends over a long time interval, peak intensities do not decrease so fast with radial distance as when particle injections are of short duration.

The radial dependence of the total event fluence does not vary with the duration of the particle injection (if the rest of transport parameters are kept constant). The power-law dependences derived from this study are, in general, less steeper than those recommended for radial extrapolation of intensities observed at 1.0 AU (Feynman & Gabriel 1988), especially within 1 AU of the Sun and for large mean free paths and high proton energies. The derived values of α are closer to those deduced observationally by Lario et al. (2006), suggesting that the framework of

[31]The Reid-Axford profile is a phenomenological parametrization of the source (Reid 1964; see also Beeck et al. 1987): $I(t) = (N/t)exp(-\beta/t - t/\tau)$. This injection profile shows a fast rise to maximum intensity, followed by a monotonic decay, over a finite amount of time; the respective rates depend on the values assumed for β and τ.

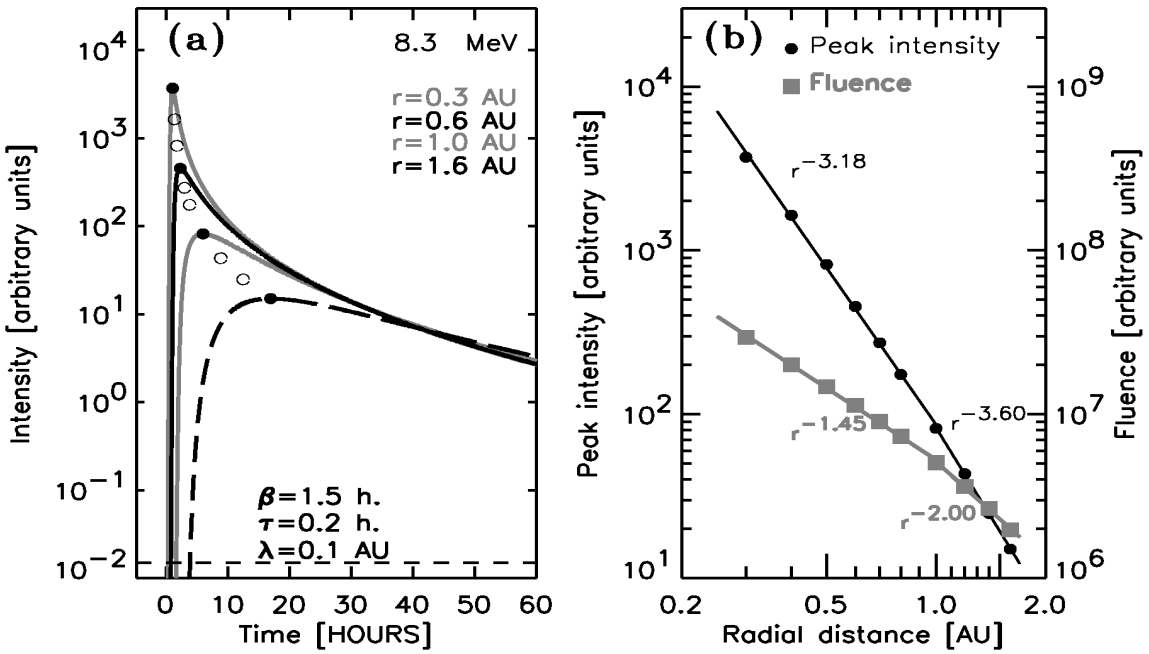

Figure 2.7: (a) intensity-time profiles of the 8.3 MeV protons as observed at 0.3, 0.6, 1.0 and 1.6 AU. The source of particles is fixed at the Sun and the injection rate is described by a Reid-Axford profile characterized by $\beta = 1.5$ hours and $\tau = 0.2$ hours; the proton mean free path is assumed to be constant, $\lambda_{\parallel} = 0.1$ AU (see text for details). Solid circles indicate the peak intensity observed at these radial distances, whereas the open circles indicate the maximum intensity at 0.4, 0.5, 0.7, 0.8, 1.2 and 1.4 AU. The horizontal dashed line indicates the value above which the event fluence is computed. (b) Radial dependence of peak intensities (black dots) and event fluences (gray squares) (from Lario et al. 2007).

the focused-diffusion transport is more appropriate to describe particle propagation than a pure-diffusion models, especially within 1 AU of the Sun.

In the outer interplanetary medium ($r > 1$ AU), Hamilton et al. (1990) examined multiple spacecraft observations of five well connected 10 – 20 MeV SEP events. They found that peak intensities decrease with the heliocentric distance as $r^{-3.3}$ whereas event fluences decrease as $r^{-2.1}$. Lario et al. (2000a,b) compared SEP events observed by the Wind spacecraft with those detected at Ulysses during 1997 and 1998 when Ulysses was near the ecliptic plane at a distance between 5.2 AU and 5.4 AU. Figure 1 of Lario et al. (2000a) shows a rough correspondence between the major SEP events at the two spacecraft at either ~ 2 MeV and ~ 10 MeV

proton intensities, despite the fact that the connection longitudes of each spacecraft to the source shocks varied significantly throughout the study period. Comparing the fourth largest event at each spacecraft, Kahler (2001a) suggested that the peak intensity for those events decrease by a factor $r^{-3.75}$ and that the decrease in the fluence would be less because of the longer duration of the SEP events at Ulysses. This result is consistent with the work of Hamilton et al. (1990). Lario et al. (2005b) studied the SEP events observed by ACE, GOES-11, Ulysses, Cassini and Voyager-2 spacecraft resulting from the solar activity period of 19 October to 12 November 2003. From those events these authors derived a power-law radial dependence of the proton fluence of $r^{-2.5}$. These dependences found by Kahler (2001a) and Lario et al. (2005b) appear to be consistent with those found by Hamilton et al. (1990) and distances beyond 1.0 AU.

2.5 Observational data

A large fraction of energetic particle, solar wind and interplanetary magnetic field data used in this work comes from the Advanced Composition Explorer (ACE) spacecraft, launched in August 1997 (Stone et al. 1998; and [w1]). ACE orbits the Sun-Earth L1 libration point, at ~ 0.99 AU from the Sun (see Figure 4 of Stone et al. 1998), ahead the Earth in the Sun-Earth line, and it has enough propellant on board to maintain that orbit until $\sim$2019. Since January 1998, NOAA and the ACE project opened up the ACE Real Time Solar Wind monitoring capability (Zwickl et al. 1998; and [w2]) to provide 24 hours coverage of the solar wind parameters and energetic particle intensity. The Electron, Proton, and Alpha Monitor (EPAM; Gol98) onboard ACE measures ion and electron fluxes over a broad range of energies (from $\sim$50 keV to $\sim$5 MeV). EPAM configuration consists of five solid-state detector systems mounted on four telescopes: The Low-Energy Magnetic Spectrometers (LEMS30 and LEMS120) measure ions, and the Low-Energy Foil Spectrometers (LEFS60 and LEFS150) measure both ions and electrons. Another detector, the Composition Aperture (CA), measures the elemental composition of the ions (He, C, N, O and Fe). The telescopes use the spin of the spacecraft to sweep the sky into different sectors; the LEMS30 and the LEFS60 telescopes, for example, sweep out an annulus centered at 30° and 60°, respectively, to the ACE spin axis. LEMS30 accumulate data in four sectors of 90° every 3 seconds; LEFS60 has eight 45° wide sectors that accumulate data every 1.5 seconds. For more details, see Gol98 or [w3].

The magnetic field and solar wind data used in this work essentially come from ACE. The magnetometer (MAG; Smith et al. 1998) on ACE measures the local IMF direction and magnitude. MAG establishes the large scale structure and fluctuation characteristics of the IMF as a function of time, providing continuous data at 3, 4 or 6 vectors/sec, although only 12 seconds data are publicly available; see [w4] for more details. The Solar Wind Electron, Proton and Alpha Monitor experiment (SWEPAM; McComas et al. 1998) provides measurements of electron and ion (H and He) distribution functions in three dimensions over all of the velocity space needed to characterize the bulk flow and kinetic properties of the solar wind (density, velocity and temperature); see [w5] for more details.

We have frequently used high-energy proton data from the CPME instrument onboard the IMP-8 satellite. This satellite was the last of ten IMP (Interplanetary Monitoring Platform) launched by NASA to measure magnetic fields, plasmas and energetic charged particles in geospace and the nearby region. IMP-8 was a spin-stabilized spacecraft, launched in October 1973 and that has been fully operative until recently (November 2006). It described a near-circular 12-day orbit around the Earth, spending about two thirds of the time in the solar wind, out of the bow shock, and the rest in the magnetosheath and magnetosphere; see [w6] for a general description. The Charged Particle Measurement Experiment (CPME; Sar76) consists of a number of particle detector assemblies with many of them with their fields of view centered in the ecliptic plane, so that fairly comprehensive angular distributions in this plane can be obtained. Particularly, the proton data relevant to our work come from five energy channels ranging from 4.6 MeV to 96 MeV. More details (energy pass-bands, flux conversion factors, and data formats) can be found in Sar76 and in [w7].

We have also used energetic proton, solar wind and magnetic field data from the ISEE-3 spacecraft (1978 – 1982, the first spacecraft in a halo orbit around the Sun-Earth L1 point). The low-energy proton detector (DFH/EPAS; Balogh et al. 1978 and van Rooijen et al. 1979) allowed detection of ions with energies between 35 keV and 1600 keV with three-dimensional capability. For more details about this spacecraft and other instruments onboard, see [w8] and the IEEE Transactions on Geoscience Electronics (vol.3, July 1978), issue devoted to the ISEE-3 spacecraft. Information about CME parameters and flares can be found in [w9] and [w10], respectively.

Web addresses:

[w1] Advanced Composition Explorer (ACE)

http://www.srl.caltech.edu/ACE/ace_mission.html

[w2] ACE Real Time Solar Wind

http://sec.noaa.gov/ace/ACErtsw_home.html

[w3] EPAM/ACE instrument

http://sd-www.jhuapl.edu/ACE/EPAM

[w4] MAG instrument on ACE

http://www-ssg.sr.unh.edu/mag/ACE.html

[w5] SWEPAM instrument on ACE

http://swepam.lanl.gov/paper.html

[w6] IMP-8 satellite

http://nssdc.gsfc.nasa.gov/space/imp-8.html

[w7] CPME/IMP-8 instrument

http://sd-www.jhuapl.edu/IMP/imp_cpme_info.html.

[w8] ISEE-3 and DFH instrument

http://nssdc.gsfc.nasa.gov/database/MasterCatalog?sc=1978-079A

[w9] CME parameters

http://cdaw.gsfc.nasa.gov/CME_list

[w10] Flare parameters

http://www.ngdc.noaa.gov/stp/SOLAR/sgdintro.html

3 The Shock-and-Particle model

3.1 An overall view

In chapter 2 we described the basic components required to model gradual SEP events associated with interplanetary shocks. Three basic components are required:

- a suitable description of the propagation of protons along the interplanetary magnetic field;
- an adequate simulation of the evolution of the interplanetary shock where protons are accelerated; and
- a survey of the mechanisms that accelerate particles at the shock, as it expands and moves away from the Sun.

He925 described the essential details of the combined interplanetary shock-and-particle propagation model. Further improvements and relevant changes can be found in Lario (1997) and Lar98 (Appendix B), and references quoted there. We use the concept of cobpoint: particles accelerated at this point of the shock propagate through the magnetic flux tube defined by the magnetic line connecting the observer and the shock. As the shock propagates through the interplanetary medium, the cobpoint moves along the front of the shock, where shock-accelerated particles are assumed to be injected. The cobpoint describes different paths along the shock front, depending on the heliolongitude of the parent solar activity that generates the shock; or in other words, on the angular position of the observer with respect to the leading direction of the shock.

The basic components of the model used in this work are a correct description of both the energetic particle transport along the IMF lines and the propagation

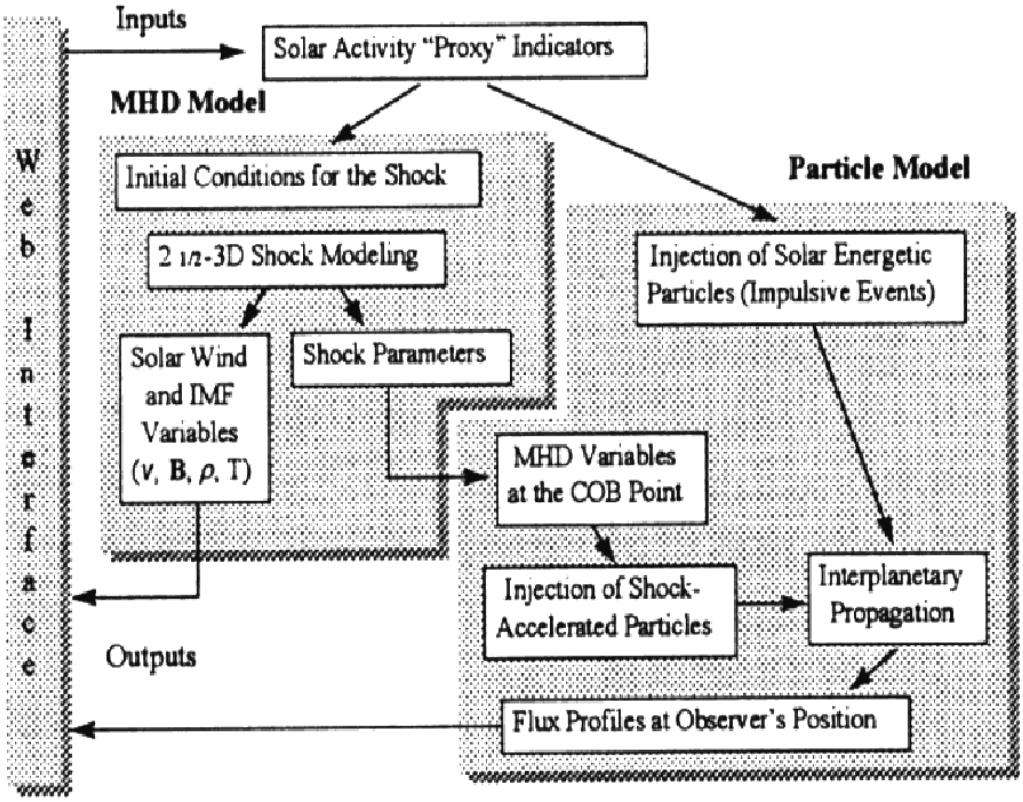

Figure 3.1: Basic blocks and interfaces of the shock-and-particle model (M. Dryer, 2002, private communication)

of the traveling interplanetary shock. However, we do not consider explicitly the processes of particle acceleration at the shock. In that sense, this model behaves as a black box model because it only describes the injection of shock-accelerated particles into the interplanetary medium; it does not specify either the mechanism that accelerates the particles at the shock or how this mechanism depends on the properties of the shock. Figure 3.1 sketches the two basic blocks of this compound model: the MHD model and the particle model (to be commented in the following sections) together with the user interface (described in Chapter 5) that allows the insertion of the input parameters and obtaining the outputs of the model.

This model has been applied to several particle events detected by the ISEE-3 spacecraft, as well as the Helios-2 spacecraft, for proton energies between 56 keV and 50 or $\sim$100 MeV (depending on the event), and currently it is used to interpret SEP

events observed by ACE. The results obtained permit us to establish a functional dependence between the injection rate of particles and the normalized velocity ratio of the shock at the cobpoint (Lar98). The results are not conclusive for the magnetic field ratio of the shock at the cobpoint. Improvements of the model include accounting for the effect of corotation and a better identification of the shock front at the wings where its strength (i.e. its density compression ratio) is weak. Both factors could be important when extending the model beyond the orbit of Mars, as well as when considering either wider or weaker shocks.

A conceptual limitation of this model is that it can only be applied to the upstream part of the SEP events (i.e. ahead of the shock). The shock front is a mobile source of particles that can inject them into both the upstream and the downstream regions. However, the post-shock region is highly modified by the shock itself and evolves rapidly as the shock moves away from the Sun. Therefore, the assumption of a Parker spiral IMF for the downstream region of the shock may not be valid. In addition, particle propagation through the shock involves processes of reflection and energy exchange that have not been included in the model. The simulation of particle fluxes and anisotropy profiles when the shock propagates beyond the observer location may be included in the near future, but it would require a more realistic MHD description of the downstream region of the shock and of the particle transport in this region.

The key point of the model is that it allows us to compare the evolution of the MHD variables at the cobpoint with the injection rate of shock-accelerated particles:

- The values of the MHD variables come from modeling the shock propagation (Section 3.2),
- The injection rate values of shock-accelerated particles at the cobpoint come from fitting the energetic particle flux and anisotropy profiles of SEP events observed at different energies (Section 3.3).

Since both simulations are worked independently, any empirical relation found between the injection rate and the MHD variables is independent of the mechanism that accelerates particles at the shock. The model also provides the energy spectrum of the injection rate of shock-accelerated particles for a range of energies. From modeling different SEP events (Lar98 and Chapter 4) we have been able to derive an empirical relation between the injection rate of shock-accelerated particles at the

front of the shock, Q, and the MHD velocity jump across the front of the shock, VR. We call this relation "the Q(VR) relation" (Section 3.4).

Once a functional dependence between the injection rate of shock accelerated particles and the MHD variables at the cobpoint is established, it is possible to invert the procedure. That is, for a given solar event that triggers a shock:

(i) The MHD simulation of the shock propagation model provides the parameters of the shock (i.e. the velocity, density and magnetic field compression ratios), all along its front and throughout its travel time toward the observer, and in particular at the cobpoint;

(ii) this allows us to evaluate the number of particles to be injected onto the IMF line rooted at the cobpoint. And, finally,

(iii) the effects of the propagation of these particles through the interplanetary medium, along the IMF, are estimated by means of the particle transport equation.

The outputs of the model are flux and anisotropy profiles which can be compared with observations, or used as fiducial profiles. Presently the code has been used to derive the injection rate and its evolution for different events, and to test its reliability. First applications to synthesize flux profiles were presented in Lario et al. (1995b) and Lar98.

Figures 3.2, 3.3 and 3.4 illustrate an example of how we can invert the procedure in such a way that the model can yield to an operational code useful for SEP flux predictions. These figures show six snapshots of how the proton flux-profiles are built up while a CME-driven shock is propagating from the Sun to Earth. Each box displays the flux to be detected by five different observers at 1.0 AU, located at different longitudes with respect to the dashed straight line representing the Sun-Earth line (i.e. E45, E22.5, CM, W22.5 and W45). The first five plots refer to the evolution of 1 MeV particle flux while the sixth is the final flux profile for 8 MeV protons. The central plot represents the position of the shock front (thick curved line), with upstream IMF lines connecting to the different observers. Each observer has a different cobpoint, therefore the rate of accelerated particle is also different (see Section 3.3).

This shock-and-particle model, in which the operational code (Chapter 5) is based, is fully described in Lario (1997) and Lar98, and the conceptual scenario

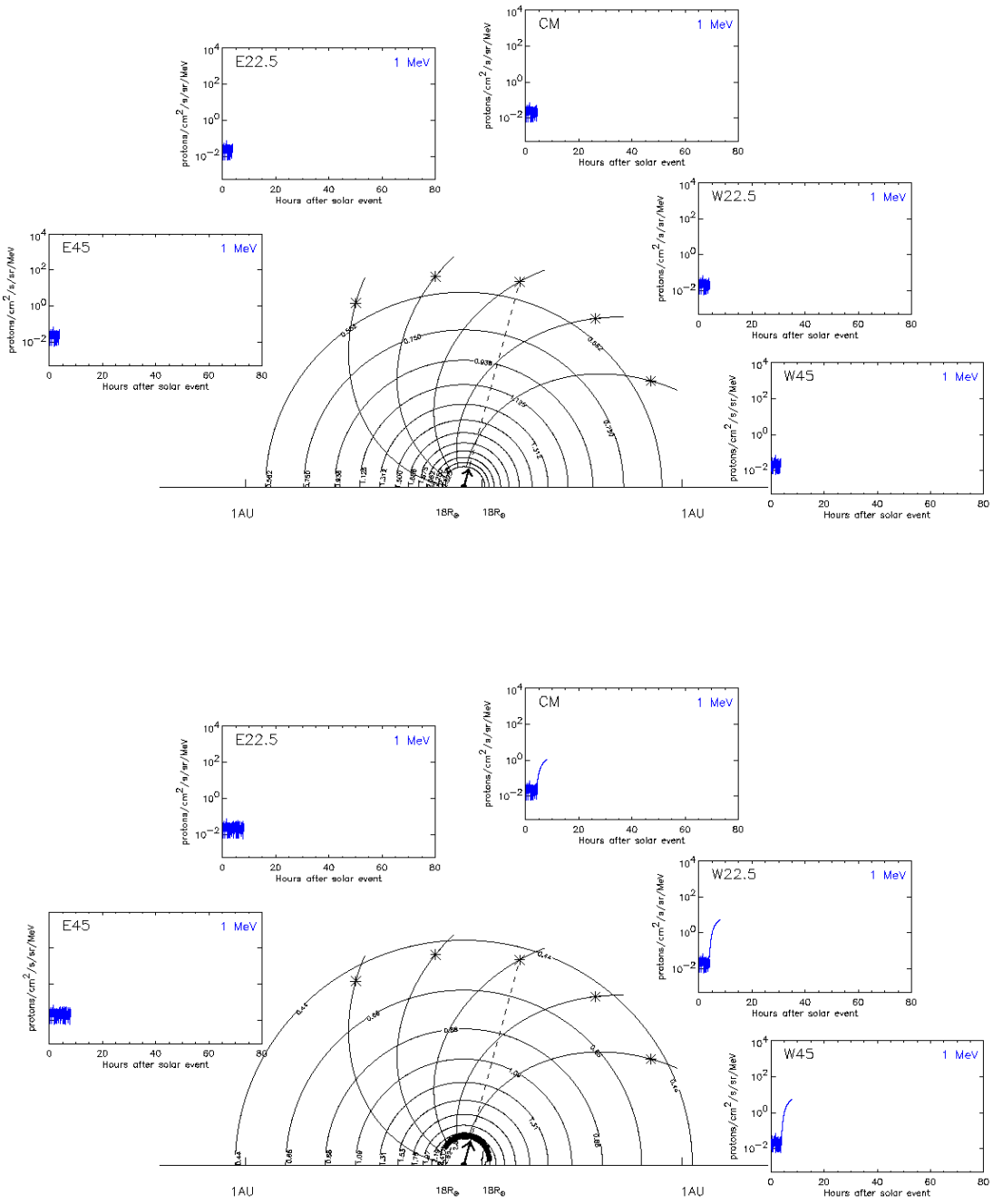

Figure 3.2: Snapshots of the simulation of an interplanetary shock propagating from the Sun up to 1.0 AU, showing the 1 MeV proton flux profiles synthesized as seen for observers located at different angular positions (from E45 to W45). The dashed line marks the orientation of the solar source (CM position). Top plot represents the initial situation, just before the CME-driven shock is launched from the Sun. Bottom plot shows the growing flux profiles 5 hours later.

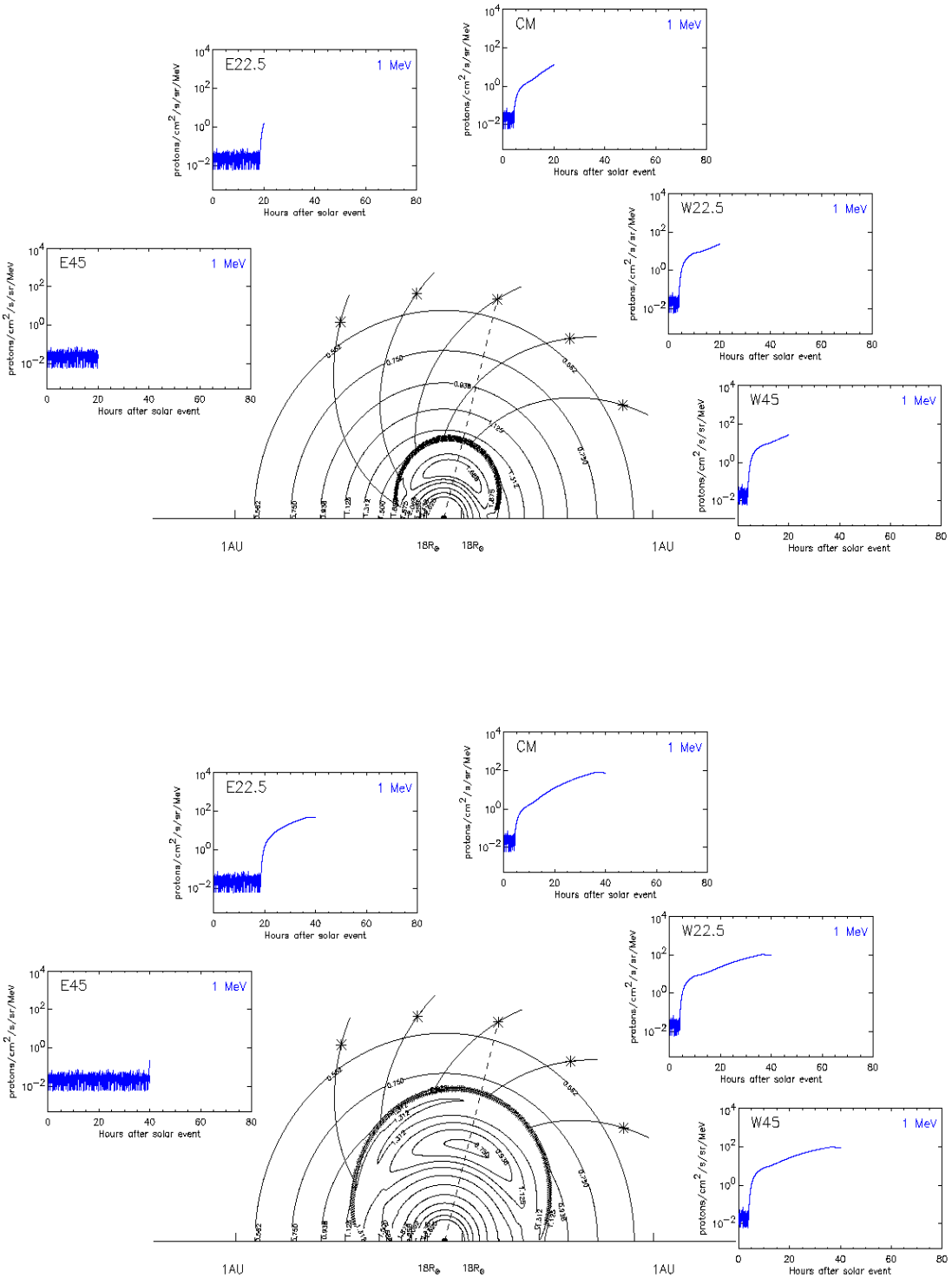

Figure 3.3: The same as in Figure 3.2, but 20 (top) and 40 (bottom) hours later, respectively.

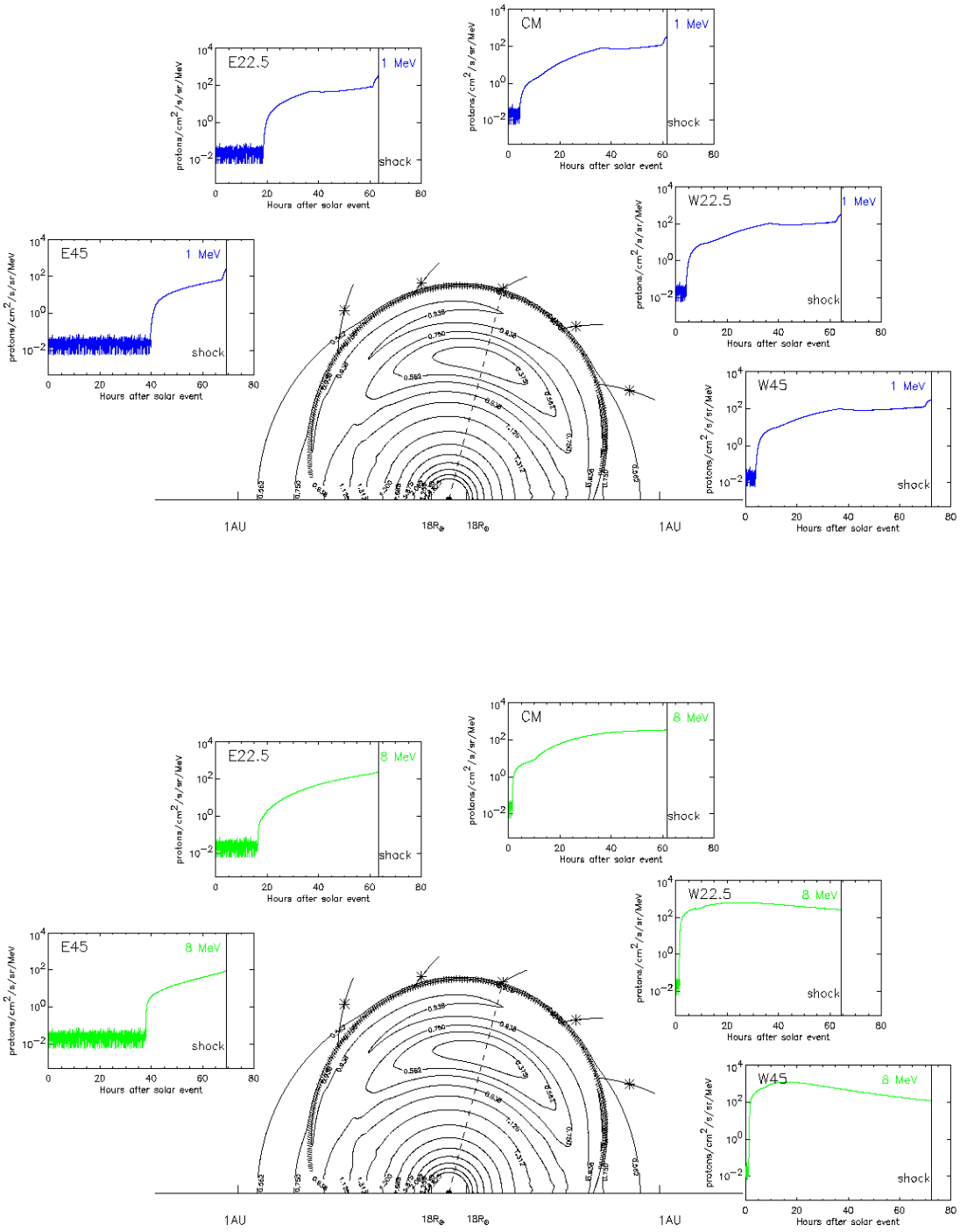

Figure 3.4: Top plot: Snapshot of the same simulation when the shock arrives at 1.0 AU (indicated by the vertical line inside each box), showing the 1 MeV proton flux profiles as in the former plots. Bottom plot: the same as in the top plot but for the 8 MeV proton flux profiles.

has been already described in Chapter 2. In order to derive the injection rate of shock-accelerated particles, it is necessary to remove the effects of the particle journey from the cobpoint to the observer's position. Particle flux and anisotropy profiles are modulated by the transport effects that particles undergo during their propagation through the interplanetary medium.

Apart from theoretical analysis, mechanisms of particle acceleration can only be studied by in situ observations of CME-driven shocks and associated energetic particle events (the ESP component of the SEP events). Detailed comparisons of ESP events with the theoretical predictions of the shock-acceleration mechanisms have been relatively successful (van Nes et al. 1984; Sanderson et al. 1985b). Only one specific event (Kennel et al. 1986) has shown significant agreement with the complete set of predictions of the diffusive shock-acceleration theory (Lee 1983), whereas other events show only partial agreement. Although the "general consensus" establishes that shock-drift acceleration works at quasi-perpendicular shocks and diffusive shock acceleration at quasi-parallel shocks, the comprehensive study of shocks and associated energetic particle events reveals a rich variety of shock structures and events (Tsurutani & Lin 1985). It is possible to find signatures of diffusive shock acceleration at quasi-perpendicular shocks and signatures of drift acceleration at quasi-parallel shocks (Richter et al. 1985; Lario et al. 2005a). The common idea that diffusive shock-acceleration is the dominant mechanism in the interplanetary medium and usually adopted in numerical models (e.g. Zank et al. 2000; Lee 2005) is unsatisfactorily sustained by detailed observations at 1.0 AU. Therefore, we decided not to assume any mechanism for shock-acceleration, that would also depend on additional parameters such as the existence (and characteristics) of both seed particle populations and magnetic turbulence in the vicinity of the shock.

The observed flux and anisotropy profiles of SEP events depend on both how efficiently the shock-accelerated protons are injected onto the IMF lines, and how the IMF irregularities modulate this population during its journey toward the observer. Lario et al. (1995a) showed examples of particle flux profiles that can be adjusted in different ways if only one of those aspects is considered. The MHD strength of the shock at the cobpoint has also a dominant influence on the efficiency of the mechanisms of particle acceleration. This strength may either diminish, because of the shock expansion in the interplanetary medium (or because the cobpoint slides clockwise from the central part of the shock to its right wing), or increase, when the cobpoint moves from the left wing to the central region of the shock. Then, it is

possible that a region of the shock could accelerate protons up to 20 MeV at 0.1.0 AU, but only to 500 keV when it reaches 1.0 AU. This scenario for particle acceleration at the shock and their further propagation upstream was also qualitatively inferred from either statistical studies or multi-spacecraft analysis of specific events (e.g. Cane et al. 1988; Domingo et al. 1989; Reames et al. 1996).

Although there is an extended consensus about these ideas, the details on both [1] how the MHD conditions at the front of the shock translate into "efficiency" in particle acceleration and injection into the interplanetary medium, and [2] how the particle acceleration efficiency evolves as the shock propagates, are neither completely clear nor quantified yet. Therefore, we focus on the analysis of the efficiency of the shock as an injector of protons. We represent the efficiency of the shock in both accelerating particles and injecting them into the IMF by a parameter Q that gives the injection rate of particles of a given energy at a given time and at a given position. The other main parameter of the model is the mean free path of the particles, $\lambda_{\parallel}$, that describes the propagation of particles in a diffusive-focused transport. The mean free path is tuned to fit the observations and theoretical predictions, specially the evolution of the anisotropy. We refer the reader to other studies on the influence of $\lambda_{\parallel}$ on the interplanetary transport of protons (e.g. Beeck et al. 1987; Beeck & Sanderson 1989, and references therein).

3.2 The MHD simulation of interplanetary shocks

The evolution of the interplanetary shock is described by means of the 2.5D MHD time-dependent model of Wu et al. (1983). This model simulates plasma disturbances that propagate through the interplanetary medium, keeping symmetry with respect to the equatorial plane (i.e. there are no meridional effects; for this reason it is called "2.5 dimensional"). The domain of the shock propagation simulation extends from close to the Sun (18 $R_{\odot}$) up to 1.1 AU[1] (see details in He925 and in Appendix E of Lario 1997). Smith & Dryer (1990) gives details of the method of computation, the input pulse and the steady-state background medium where shocks propagate. Figure 3.5 shows a snapshot of one of these MHD simulations of an interplanetary shock about 22 hours after the onset of the event[2].

[1] For a later application to reproduce and predict SEP intensities at the orbit of Mars (1.6 AU), the domain of integration have been extended up to 2.0 AU (see Chapter 8).

[2] A complete movie with the results of this simulation can be found in

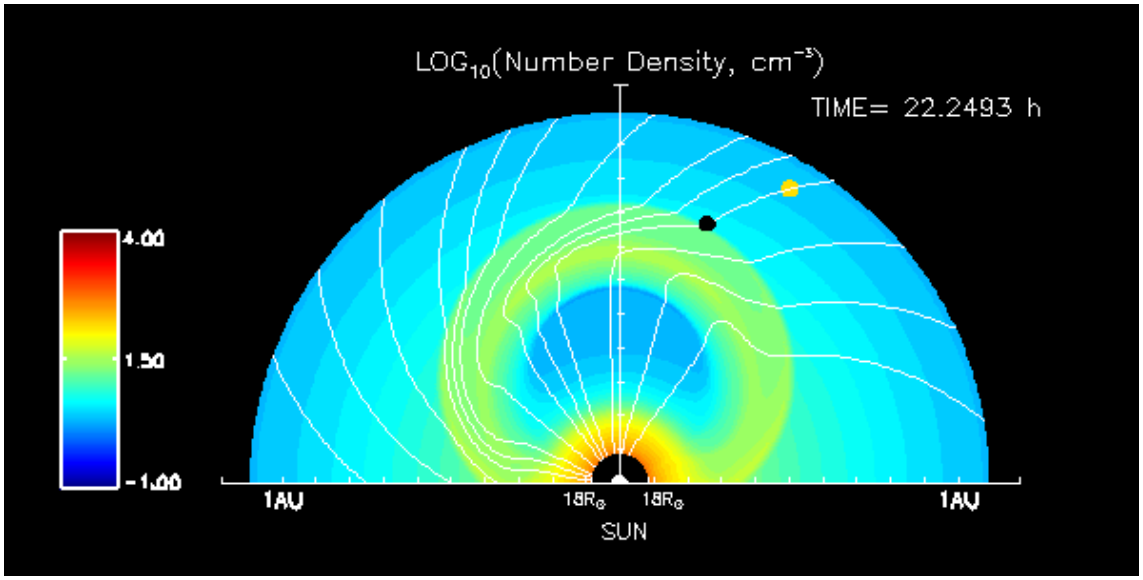

Figure 3.5: Snapshot of the MHD simulation of an interplanetary shock generated by a CME centered in the CM position. Density contours are represented by the color bar, where red represent high densities and blue low densities. White curved lines are IMF lines. The yellow dot marks the position of the observer and the black dot the location of the cobpoint in the shock front.

For each event, this MHD model provides a simulation of the shock propagation; thus we can estimate the strength of the shock at each time and for every point along the shock front and in particular at the cobpoint. We characterize this strength by the downstream/upstream normalized velocity ratio, VR $= (V_{r_d} - V_{r_u})/V_{r_u}$ and the magnetic field ratio, BR $= |B|_d/|B|_u$ (where subscripts u and d stand for upstream and downstream of the shock, respectively). The angle between the IMF upstream of the shock and the normal of the shock front, θ_{Bn}, gives the character of quasi-parallelism or quasi-perpendicularity related to the mechanisms of particle acceleration at shocks (see the reviews by Armstrong et al. 1985; Scholer 1985). A non trivial problem is to identify in the numerical simulated data, the regions downstream and upstream where to measure the plasma values necessary to calculate these shock parameters. Section 3.3 of Lario (1997) describes the two methods (*radial cut* and *time profile*) used routinely. The angle θ_{Bn} is calculated using both the method proposed by Chao & Hsieh (1984) and the coplanarity theorem (e.g. Appendix C of Lario 1997). The evolution of these variables is followed once the

http://www.lmsal.com/∼schryver/Public/homepage/movies/Lario_CME.html or in http://www.am.ub.es/∼blai/enginmodel/SEP_Abstract.html.

magnetic connection between the observer and the shock is established up to the passage of the shock by the observer's position (see, for example, Figure 2 of Lar98). Variable initial steady conditions for the solar wind can be also included by using the model developed by Vandas et al. (1995) for the propagation of magnetic clouds or the full 3D MHD extended model (see Dryer 1994, for further references).

As already commented in Chapter 2, the transition of a shock from the corona to the interplanetary medium is not well determined. Therefore, it is difficult to establish the initial conditions of the shock at the inner boundary (18 $R_{\odot}$). The assumptions considered here to initiate the simulation of the shock (a pulse where the Rankine-Hugoniot conditions are satisfied) are the initial pulse speed and width, the time of the pulse-injection plus the time spent by the shock to travel up to the inner boundary, as well as the heliolongitude where the central part of the shock is launched (its direction of propagation). Plasma and magnetic field observations from spacecraft, when available, are used to secure adequate initial conditions for shock propagation, reproducing the time of the shock arrival at the spacecraft and the discontinuity of the plasma variables at the shock passage. The prediction of shock characteristics soon after the onset of the CME requires a realistic model of the magnetic field and plasma in the inner corona and a realistic model of how the CME is initiated.

3.3 The energetic particle transport equation

The transport equation used by He925 to describe the propagation of protons was the focused-diffusion transport equation derived by Roelof (1969); Appendix A shows two examples of such fits (Figures A3 and A4). The diffusion-convection approximation (Parker 1965) is not applicable to the description of large SEP events because it neglects the focusing effect that dominates the particle transport between the Sun and 1.0 AU. SEP events observed at 1.0 AU often show high anisotropies in the upstream region, not only at the onset of the event but also for many hours before the shock passage (Heras et al. 1994), indicating that particle distributions are far from being isotropic; hence for, the diffusion-convection equation is not useful for a description of SEP events observed at distances smaller than 1.0 AU.

The effects of adiabatic deceleration or convection by the solar wind were not taken into account in the focused-diffusion equation used by He925. These ef-

fects may be important below 800 keV, thus the values of injection rates of shock-accelerated particles derived by He925 at low energies ($\sim$100 keV) had substantial uncertainty because of the inclusion of arbitrarily positive (high-energy) or negative (low-energy) contributions due to adiabatic deceleration. A similar discussion involving the determination of the mean free path, $\lambda_{\parallel}$, can be found in Ruffolo (1995). Solar wind convection may have also an important influence on determining the onset of an event and the occurrence of the maximum of flux, especially at low energies. For that reason, the focused-diffusion equation should be used judiciously below 500 keV. Ruffolo (1995) developed an explicit equation for the focused-diffusion transport of solar cosmic rays, including adiabatic deceleration and solar wind convection effects. This equation is more appropriate to describe the transport of low-energy particles than Roelof (1969) approximation. Ruffolo (1995) applied the equation to the transport of protons from a fixed source. However, for modeling SEP events associated with traveling shocks it is necessary to assume a mobile source of accelerated particles.

The injection rate of shock accelerated particles is described in the model by adding a source term to the focused-diffusion transport equation, the function Q mentioned above. We identify Q with the "efficiency" of the shock as a particle accelerator, which comprises [1] the effectiveness of the shock in accelerating protons, and [2] the efficiency of the shock injecting these protons into the interplanetary space. The injection rate depends on the conditions around the shock, for example, the presence of a turbulent wavy foreshock region, or a large background of protons acting as a seed particle population. The function Q is considered to be zero everywhere except at the cobpoint position.

The energetic particle transport equation that considers the effect of particle streaming along the IMF, solar wind convection, adiabatic deceleration, pitch-angle scattering and focusing is the following (Ruffolo 1995):

$$\frac{\partial F(t,\mu,r,p)}{\partial t} = -\cos\psi \frac{\partial}{\partial r}\left\{ v\mu F(t,\mu,r,p) \right\} - \qquad \text{(streaming)}$$

$$-\cos\psi \frac{\partial}{\partial r}\left\{ \left(1-\mu^2\frac{v^2}{c^2}\right) v_{sw} \sec\psi F(t,\mu,r,p) \right\} - \qquad \text{(convection)}$$

$$-\frac{\partial}{\partial \mu}\left\{ \frac{v}{2L(r)}\left[1+\mu\frac{v_{sw}}{v}\sec\psi - \mu\frac{v_{sw}v}{c^2}\sec\psi\right](1-\mu^2)F(t,\mu,r,p) \right\} + \qquad \text{(focusing)}$$

$$+\frac{\partial}{\partial\mu}\left\{v_{sw}\Big(\cos\psi\frac{d}{dr}\sec\psi\Big)\mu(1-\mu^2)F(t,\mu,r,p)\right\}+ \qquad \text{(differential convection)}$$

$$+\frac{\partial}{\partial\mu}\left\{\varphi(\mu)\frac{\partial}{\partial\mu}\left\{\Big(1-\mu\frac{v_{sw}v}{c^2}\sec\psi\Big)F(t,\mu,r,p)\right\}\right\}+ \qquad \text{(scattering)}$$

$$+\frac{\partial}{\partial p}\left\{pv_{sw}\Big[\frac{\sec\psi}{2L(r)}(1-\mu^2)+\Big(\cos\psi\frac{d}{dr}\sec\psi\Big)\mu^2\Big]F(t,\mu,r,p)\right\}+ \qquad \text{(deceleration)}$$

$$+G(t,\mu,r,p) \qquad \text{(source of particles)}$$

$$(3.1)$$

We have expressed this equation using mixed coordinates, where p is the particle momentum, μ the pitch-angle cosine, v is the particle velocity, r the heliocentric distance, t the time, ψ is the angle between the radial direction and the magnetic field, $\mathbf{B}$, L is the focusing length (see definition in Roelof 1969), $\varphi(\mu)$ is the diffusion coefficient in the μ-space, and v_{sw} is the solar wind radial speed. The coordinates p, v and μ are referred to the local solar wind frame, comoving with the inhomogeneities of the IMF. On the other hand, r and t are referred to a frame fixed at the Sun.

The distribution function of particles inside a magnetic flux tube, F, of cross-sectional area $A(r)$ depends on the particle distribution function in the phase space, f, as $F(t,\mu,r,p) = A(r)f(t,\mu,r,p)$ (Ng & Wong 1979). The mobile source of particles is given by the function G that represents the local source of particles per unit area of the flux tube; thus $G(r,t) = A(r)Q(r,t)$, with $A(r)$ computed at the cobpoint, and $Q(r,t)$ being the injection rate of shock-accelerated particles in phase space.

For the description of the IMF we assume a stable solar wind regime and an IMF described by a Parker spiral. Under these conditions, we have $\tan\psi = \Omega r/v_{sw}$, $A(r) = A(r_0)r^2/(1+\tan^2\psi)^{1/2}$ and $L = r/\cos\psi(1+\cos^2\psi)$, where Ω is the angular rotation rate of the Sun and r_0 is a given radial distance. Assuming a constant value for the solar wind speed, $A(r)$, ψ and L are unequivocally determined. For other scenarios, such as a variable solar wind regime or in the downstream shock region, these values have to be given in numerical form (or any other analytical function).

To describe the interaction between energetic particles and IMF irregularities, we adopt the approximation of pitch-angle scattering. The pitch-angle diffusion coefficient is defined in terms of the standard model for IMF fluctuations and the magnetic field fluctuations are assumed to be small compared to the large-scale magnetic field (i.e. the quasi-linear theory (QLT) approximation; Jokipii 1966).

Under these approximations, $\varphi(\mu)$ can be parameterized in terms of the mean free path of the particles parallel to the magnetic field, $\lambda_\parallel$, that depends on the rigidity of the particles as $\lambda_\parallel(R) = \lambda_{\parallel 0}(R/R_0)^{2-q}$ (Hasselmann & Wibberenz 1970). The particle rigidity is defined as $R = pc/\tilde{q}$, where $\tilde{q}$ is the particle charge. The index q is the spectral index of the magnetic field fluctuations and $\lambda_{\parallel 0}$ and R_0 are the mean free path and the particle rigidity, respectively, at a specific given energy E_0. The model assumes a typical value for q as deduced from IMF observations ($q = 1.5$; see, for example, Kunow et al. 1991). The influence of the adopted value of q in the results is minimal (Lario 1997).

Therefore, the two basic parameters of the energetic particle transport model are: [1] the mean free path of the protons, $\lambda_\parallel$; and [2] the injection rate of shock-accelerated particles, Q[3]. The relation $\lambda_\parallel(R) = \lambda_{\parallel 0}(R/R_0)^{2-q}$ allows us to scale the mean free path with the energy of the particles. The model also assumes a power-law dependence of the injection rate with the energy, $Q = Q(E)$; this assumption is introduced via the intermediate function G (for more details, see Lar98), with $G(E) = G(E_0)(E/E_0)^{-\gamma}$. The energy of reference (or fiducial energy) E_0 is 0.5, 0.8 or 1 MeV, depending on the characteristics of the energy channels of the used detector. From fitting the observed flux and first-order anisotropy profiles of protons at a given energy E_0, we determine Q_0 and $\lambda_{\parallel 0}$, as well as their evolution until the shock arrives at the spacecraft. The energy dependence of Q is deduced from fitting the observed fluxes at different energies.

It must be pointed out that for some events, a turbulent magnetic foreshock region is required in order to reproduce the isotropic proton flux enhancement observed in association with the arrival of the shocks, usually at low-energy, $E \lesssim 500$ keV (i.e. the ESP component of the events as observed for example in the event shown in Figure 1.1). This foreshock is a region adjacent to the front of the shock where, accelerated protons excite cyclotron-resonant waves which in turn produce short scattering mean free paths, allowing the particles to change its direction of propagation and interact many times with the shock (but remaining confined in the vicinity of the shock). We characterize this turbulent foreshock region with a given width in front of the shock, and a mean free path smaller than the mean free path in the rest of the upstream medium. Scattering mean free paths from $\sim$0.001 AU to 0.1 AU are inferred from proton gradients in ESP events (Fisk 1971; Tan et al. 1989; Bamert et al. 2004).

[3]The units of Q are $\mathrm{cm}^{-6}\ \mathrm{s}^{3}\ \mathrm{s}^{-1}$.

Observations of enhanced magnetic field fluctuations at interplanetary traveling shocks are very limited. Kennel et al. (1982, 1986), Tsurutani et al. (1983), Viñas et al. (1984) and Sanderson et al. (1985b) documented such turbulent enhancements upstream of several shocks. They have been observed mostly at quasi-parallel shocks. Low-frequency MHD turbulence associated with fast-shocks had been also observed by Helios-1 magnetic field and plasma instruments (Luttrell et al. 1984) and by Venera 13 and 14 spacecraft (Morozova et al. 1984). The significance of this turbulent foreshock region had been discussed by Heras et al. (1992), Beeck & Sanderson (1989), Gordon et al. (1999) and more recently by Lee (2005). Figure 2 of Lee (2005) sketches the scenario proposed, where enhanced fluctuations and restricted particle propagation (thus, particle storage) only exists in the vicinity of the shock.

We will not consider here the possible perpendicular diffusion of particles in turbulent plasma. Analytical models for the perpendicular diffusion (i.e. Giacalone & Jokipii 1999; Mace et al. 2000) yield results that do not agree with observations. Matthaeus et al. (2003) improved the former theoretical model by assuming that perpendicular transport is governed by the velocity of gyrocenters that follow the IMF lines. Zank et al. (2004) used an approximation of this model to evaluate the particle acceleration timescale for diffusive shock acceleration at perpendicular shocks (among other applications), concluding that the radial diffusion coefficient is dominated by the parallel diffusion coefficient and that "*the injection of low-energy particles into the diffusive shock acceleration mechanism for perpendicular shocks remains a problem*". Furthermore, observations of SEP events by Ulysses during its solar maximum orbit above the solar poles has shown that particle anisotropy flows are aligned with the IMF, indicating that no net flow across the local magnetic field happens (Sanderson et al. 2003). Therefore, we will only consider particle transport along the IMF lines.

3.4 Deriving the injection rate and its energy dependence

For a given SEP event, the procedure is as follows. We fit the flux and anisotropy profiles for one energy channel, E_0. This yields $\lambda_{\parallel 0}$ and Q_0, as well as their evolution. Then, assuming the functional dependence described for Q and $\lambda_{\parallel 0}$ on the energy, we derive the best fit for fluxes and anisotropies at all energies. As the model yields the

differential flux profile in non-scaled units, it has to be normalized, thus translating them to physical units. That means choosing a period of time during which the flux does not oscillate sharply. The mathematical details are described in Appendix A (from Lario 1997).

Experience in modeling SEP events has shown us that in order to simultaneously fit ten or more proton energy channels between 50 keV and 50 – 100 MeV, it is necessary that the slope of the power law $Q \propto E^{-\gamma}$ at high energies ($\gtrsim 2$ MeV) should be different than at low energies (Lar98). That means that the efficiency of the shock as a particle injector decreases more rapidly as higher energies are considered (see comments in Section 2.2). It is important to bear in mind that the "efficiency" of the shock as an injector of shock-accelerated particles in the interplanetary medium is not directly equivalent to the "efficiency" of the shock as a particle accelerator. The function Q gives only the rate at which shock-accelerated particles are injected into interplanetary space and not how the shock acceleration mechanisms evolve in time and energy.

The lack of a satisfactory model for the formation of the CME-shock at the corona (Chapter 2), as well as of its evolution to the interplanetary medium, together with the inner boundary of the MHD shock-model, obliges to assume, in certain cases, an injection of particles below this boundary and before the time when the simulated shock establishes magnetic connection with the observer. This time is known as the connecting time, t_c (Heras925 and Appendix B; see also chapter 4)[4]. In average, it is possible to say that the shortest elapsed time for the injection of protons corresponds to western fast events, and increases toward central meridian events, being the largest for eastern events. Other features of the injection rate for different type of events, and for the energy spectral dependence can be found in Lar98. The evolution of Q is different from event to event, basically depending on the angular extension of the shock, its transit velocity and the relative position of the observer with respect to the heliolongitude of the parent solar activity.

Once the model has reproduced the intensity-time profiles of flux and anisotropy observed at different energy channels, it is possible to compare the evolution of

[4]For an observer located at 1.0 AU on the Sun-Earth line (i.e. Central Meridian position), shocks generated by solar events occurring on the western hemisphere of the Sun establish magnetic connection with the observer shortly after of their launch (small t_c), whereas shocks generated by solar events occurring on the eastern hemisphere take a longer time to connect with the observer (large t_c).

the injection rate Q with the evolution of the variables VR, BR and θ_{Bn} at the cobpoint inferred from the shock MHD modeling. We then analyze whether there is a functional dependence among the shock parameters (i.e. VR, BR and θ_{Bn}) and Q. Figure 10 of Lar98 (Appendix B) shows a representative example of the Q(VR) relation found for four events: two western events (fast and slow cases), one central meridian event and one eastern event (more examples are shown in Chapter 4). A relation of the type $\log Q = \log Q_0 + k\text{VR}$ was inferred from the simulation of these specific SEP events. Similar fits were suggested for Q and BR, although only partially sustained during the evolution of the events modeled. It was not possible to derive a similar relation between Q and θ_{Bn}. The relevant features of the Q(VR) fits and the reason why they did not work for BR and θ_{Bn} were thoroughly discussed in Lario (1997); particularly, its Appendix G lists the full set of Q_0 and k values derived, resumed in Table 2 of Lar98, for the four SEP events modeled.

A first application of this Q(VR) relation was performed in Lar98 (see their Figure 13), deriving a synthetic flux profile for ~ 120 keV protons for Helios-2 spacecraft, and comparing it with the observed flux. A rather simple application of the same type was formerly developed in Lario et al. (1995b). None of them was thought in terms of space weather applications but only to show the potential predictive capacity of such a result.

3.5 Necessary improvements of the model

3.5.1 Initial conditions near the Sun

In Section 2.2.3 we discussed the present poor knowledge on the formation of shocks in the solar corona and their transition to the interplanetary medium. Therefore, in order to characterize the CME-initiated shock, the initial velocity of the shock at $18\,R_\odot$ is as meaningless as the mean transit velocity of the shock from the Sun to the Earth. None of them are real-time observable variables. Nevertheless, the mean transit velocity can be useful for posterior analysis of SEP events (see Chapter 4). Right now it is not possible to do have actual quantified indicators of CME activity and, in general, of any solar activity suitable to be used as a proxy of a

shock formation[5]. In the past, metric type II burst emission was used to infer the initial shock speed, but it does not seem to be a reliable tool to characterize the interplanetary shocks (Cane 1997; Gopalswamy et al. 1998). This prevents us from a quantitative improvement of the initial conditions assumed by the model. It is not possible to replace the velocity of the input pulse velocity, nor the mean transit speed, by any observable. A possibility, is the use of the plane of sky speed of the CME, derived from coronagraph observations (i.e. LASCO onboard SOHO)[6]. However, to be useful as a proxy indicator, additional assumptions are needed such as the expanding direction of the ejecta, a correct projection of the measured speed to this projected direction, and the further location of the CME-driven shock (not only its leading edge but all its longitudinal extent). Schwenn et al. (2001) introduced the concept of the lateral expansion of a CME and further studies (e.g. Zhao et al. 2002; Michałek et al. 2003) can reproduce some useful geometric and kinematic properties of CMEs[7].

Tsurutani et al. (2003) have presented a self-consistent, global axisymmetric MHD model with an initial state consisting of a streamer and flux-rope embedded in a model solar wind. This model is capable of predicting the location and strength of the CME induced shock and shows that the fast forward shock may form very close ($\sim 3.2\ R_{\odot}$) to the surface of the Sun. They demonstrate the capability to produce quantitative descriptions of the undisturbed and disturbed physical parameters of simulated CME shocks that propagate from the Sun to the Earth environment, as well as of the relevant shock parameters to be considered in connection with particle shock-acceleration[8]. To our understanding, this model by Tsurutani et al. (2003), together with the 3D MHD models mentioned in Subsection 2.3.2 and the model presently being developed by Jacobs et al. (2006), point toward the direction to follow in the near future.

[5]It is worth to point out that many of the comments in this subsection are also largely applicable to other models shortly described in Section 2.3.

[6]Unfortunately, the most interesting (to our purposes) CMEs, halo and partial-halo CMEs, are the most difficult to measure their speed. That is why the STEREO mission (operational in early 2007; web page: http://stereo.gsfc.nasa.gov/) is so important.

[7]For example, that the average corrected speeds only differ $\sim$20% from the projected speeds.

[8]Quoting them: "*The results also suggest that the shock conditions (i.e. Mach number, absolute magnetic field and velocity jump) along the global shock are, as suggested by Heras et al. (1995), relevant to any study of the efficiency of shock energization processes*".

3.5.2 The Q(VR) relation and the proton intensity at high energy

The value of the coefficient k in the Q(VR) relation varies with the energy of the particles and from event to event. As far as we know, the unique way to asses the validity of the Q(VR) relation (and probably extending it to BR) is modeling a large set of various types of SEP events, mainly originated from solar longitudes between W50 and E10. In order to calibrate this dependence and to quantify it for operative purposes, these fittings must be compared to those synthesized by the model assuming the previous Q(VR) relation. Moreover, to extend this relation to higher energies (50 – 100 MeV), it would be also very helpful to study the evolution of the anisotropy at these high energies, because of the further constraints that can impose on theoretical models and simulations. Owing the large variety of energy spectra from event to event, there is a diversity of values of k at high energies ($\gtrsim$10 MeV).

For space weather purposes it is important to estimate the proton flux at high energy ($\gtrsim$ 10 MeV). Currently, this can be done in our model by assuming an energy dependence of the injection rate of shock-accelerated particles that can extend from low ($\lesssim$ 10 MeV) to high energies (i.e. assuming an index of the power law dependence $Q \propto E^{-\gamma}$ that can be different from that assumed at low energies). The assumed spectral-energy dependence can then be compared with observations; unfortunately it happens that the observed slope of the energy spectrum is highly variable from event to event (see Section 2.1.5). To our knowledge it does not exist enough adequate observations from which derive averaged values of fluxes at high energy for different types of SEP events. There are documented cases of SEP events generated by CMEs of similar characteristics that show high energy fluxes differing in three or four orders of magnitude (e.g. Kahler 2001b).

3.5.3 The proton flux in the downstream region

Modeling propagation of energetic particles in the sheath region formed immediately behind the shock, i.e. the post-shock period just after the shock passage and the arrival of the driver (that on average at 1.0 AU lasts for $\sim$12 hours), is not easy. The characteristics of the region downstream of the shock depend on the steady state

medium where the shock runs into, as well as on the properties of the propagating shock; there, the particle flux can remain high for several hours. The evolution of the particle flux in this region depends on the magnetic field topology of this region and that of the shock front's region to which the observer establishes magnetic connection. For eastern events, the observer may establish connection with the central part of the shock through its downstream region and thus observe the peak flux after the shock passage. In these cases, the flux measured in the downstream region may represent a significant contribution to the total fluence. Rosenqvist (2003b) evaluated the case of the SEP event on February 14, 1978 (E59), concluding that the downstream flux of <2 MeV protons can account for up to the 35% of the cumulative fluence.

A full description of the compressed downstream region (plasma and magnetic field spatial changes and evolution) is difficult and, as a consequence, a reasonable modeling for the propagation of energetic particles in this region is not straightforward[9]. Usually, the downstream region is characterized by a slow exponential decay of the SEP intensity. Reames et al. (1997b) showed that in the decay phase the particle flux frequently shows invariant energy spectra. Reames et al. (1996) and Lee (2005) explained, although with slight differences, the e-folding decay time of SEP intensities in terms of the combination of two processes: the trapping of particles between the back of the shock and the Sun, and the adiabatic deceleration due to the expansion of the downstream volume. Lario et al. (1999) started from the modeled draping of the downstream IMF around a magnetic cloud[10] and described the focusing effects of the resulting IMF configuration. These authors emphasized the effects that the distortion of the IMF around the magnetic cloud produces on the energetic particle transport.

Kallenrode (2002) addressed the case of the variations of the IMF structure due to the presence of a propagating magnetic cloud, although the method performed does not allow the simulation of energetic particle transport inside the cloud. The presence of a magnetic cloud and the distortion of the IMF it produces influences the particle transport in two ways: the path between two points along a field lines is in general longer along the disturbed field line than along the undisturbed Parker spiral (see Figure 1 of Kallenrode 2002); and the changes in the magnetic field

[9]Tan et al. (1992) proposed a sketchy qualitative explanation for one specific case.

[10]Magnetic clouds are a subset of ejecta in interplanetary space where flux-rope magnetic field configurations are observed (Burlaga et al. 1990, and references quoted there).

magnitude around the cloud modify the focusing length. The generic conclusions of Kallenrode (2002) are that [1] if there is a cloud following the shock, the upstream $\gtrsim$10 MeV flux intensity slightly increases with respect to the case without magnetic cloud; [2] this increase becomes larger as lower energies are considered; and [3] the downstream intensities reduces. We have not yet attempted to include this region in our modeling effort.

3.5.4 The scenario and simplifications of the model

In He925 and Lar98, the propagation of the shock is described by means of a magnetohydrodinamic model. The model assumes an initial shock pulse that propagates in a given steady state background medium (Wu et al. 1983). The propagation of this shock is controlled by the MHD equations of mass, momentum and energy conservation, together with the induction equation. The success of this model in reproducing the actual shock will depend on how accurate both the input pulse and the assumed background medium are. The fact that interplanetary shocks can only be detected by in situ observations of solar wind plasma and magnetic field at the spacecraft locations keeps us in the dark about the evolution of their large-scale structure, as well as of the interplanetary conditions under which they propagate. The formation of shocks in the solar corona at the time when a CME takes place is a controversial subject (Gopalswamy et al. 1998; Cliver 2000; Srivastava et al. 2000). The present available data and our observational capabilities do not allow us to discern the origin and formation of the shocks close to the Sun (see Section 2.2.3).

In our simulation of actual events we are forced to choose the initial input shock that better reproduces the arrival time and speed of the shock at the observer, as well as the jump of the plasma parameters observed at the arrival of the shock at the spacecraft location. The situation gets worse when observations come from only a single spacecraft, or from two or more spacecraft in geospeace, i.e. too close to infer the large-scale structure of the shocks in interplanetary space.

We use a focusing-diffusion transport equation (see Section 3.3) to model the particle propagation along the IMF lines. This equation includes the main effects that the IMF and the solar wind produce to the energetic particles (Ruffolo 1995). It assumes that energetic particles propagate in a given flux tube determined by

the large-scale structure of the IMF that, in steady conditions, turns out to be a Parker spiral. Throughout their propagation, energetic particles undergo the effects of focusing with the magnetic field, pitch-angle scattering by the magnetic field irregularities, solar wind convection and adiabatic deceleration. In the present state of our model, the pitch-angle scattering is described by the quasi-linear theory, which assumes that magnetic field irregularities are represented by waves of small amplitude with respect to the background IMF. That allows us to parameterize the pitch-angle scattering process by a mean free path of the particles, $\lambda_{\parallel}$. The simultaneous observation of the proton flux anisotropy and the particle intensity throughout the development of a SEP event allows us to determine $\lambda_{\parallel}$ (i.e. its energy dependence and its time evolution).

Reames (1989) suggested that the mean free path of the particles is a time-dependent variable which is self-regulated by the presence of energetic particles able to amplify magnetohydrodinamic waves which, in turn, resonate with other particles and thus increasing their scattering. The use of $\lambda_{\parallel}$ as a free parameter may be considered as a drawback of our model. However, at present, the consistent evaluation of the mean free path in terms of the instantaneous flux of particles all along the flux tube requires a series of non-realistic approximations (for example, the assumption of a radial magnetic field, non-interacting waves, etc., see Ng et al. 2003). The inclusion of self-generated waves in a more realistic scenario (i.e. Parker spiral for the IMF, wave-wave interaction, cascading and decaying of waves, inclusion of nonlinear effects, etc.) leads to particle and wave transport equations with a large number of free parameters, and not ready to use for space weather purposes.

The results presented in this project assume only one flux tube where particles are successively injected and observed by the spacecraft. The real situation is that throughout the development of a SEP event several flux tubes will cross the spacecraft, due to the radial propagation of the solar wind and the freezing of the IMF lines in the solar wind and the rotation of the Sun. Each one of these flux tubes contains a different population of energetic particles with a distinct history of shock parameters. The history of a SEP event is the result of the successive samples of flux tubes seen by the spacecraft. This effect is known as the corotation effect (Kallenrode 1997; Lar98). For slow shocks (or longer transit times for the shock to travel from the Sun to the spacecraft), this effect becomes important. The bigger the longitudinal dependence of the acceleration mechanisms along the shock front, the more important the effect of corotation.

Another important aspect in particle propagation is the effect that the shock may produce to the energetic particle population and vice-versa. Obviously, the interaction of a particle with a shock may induce changes in its energy or its transport direction, depending on its gyroradius and pitch-angle. In our case, the consideration of an absorbing boundary of particles just behind the shock (He925) forces us to include in the injection rate $Q(r,t)$ not only those particles accelerated by the shock but also those particles which could be reflected. The inclusion of other type of boundaries, such as completely reflecting or partially absorbing, will be studied in a next future.

The arrival of the shock at the observer is usually accompanied by an isotropic population of particles that produces an increase in the particle flux. We reproduce this flux enhancement by assuming a small mean free path in a given region around the shock front. This region of high scattering is able to confine a significant amount of energetic particles in the vicinity of the shock. Obviously, we only know of its existence at the arrival of the shock at the spacecraft (Tsurutani et al. 1983; van Nes et al. 1984; Beeck & Sanderson 1989). Details about its longitudinal extent or its temporal evolution is beyond the present observational capabilities. Assumptions about its existence and effects throughout the event should be made in order to reproduce this effect. The simulation of this region by self-generated waves will also be studied in the future, although this description will still be deficient because of the inherent turbulence associated with the own shock.

The dependence of Q with the plasma velocity ratio VR at the shock front implicitly considers its time and longitudinal dependence as the shocks expands and as the cobpoint moves along the shock front. The dependence of Q with the energy of the particles is determined by a power-law and by different coefficients of proportionality in the Q(VR) relation. We note that Q includes not only those particles accelerated by the shock but also those reflected at the shock front; therefore, a simple dependence between Q and VR should be thought only as a convenient way to quantify the time evolution and longitudinal dependence of Q by relating them to the dynamic expansion of the shock. Other shock parameters, different than VR, play also a role in the production of energetic particles at shocks. In our case, these parameters are the angle between the upstream magnetic field and the normal to the shock, θ_{Bn}, the magnetic field ratio across the shock, BR, as well as the background particle population acting as a seed for the acceleration mechanisms (Tsurutani & Lin 1985). These pre-existing particles can be of quite different origin for different

events: [1] the suprathermal tail from the quiet-time solar wind (Gloeckler et al. 2000); [2] suprathermal particles from concomitant flare activity (Mason et al. 1999; Tylka et al. 2001); or [3] the population remaining from former impulsive or gradual SEP event. In that sense, Kahler & Vourlidas (2005) confirm that SEP event peak intensities are higher when the associated driver is preceded within a day by wide CMEs at the same locations.

So, our knowledge of the quantitative dependence of Q on those variables is far from being definitive. For example, Tylka et al. (2005) illustrates the case of two similar large SEP events, triggered by very similar solar progenitors, but whose respective spectral characteristics and elemental composition are highly variable and different. More realistic approaches for the injection rate Q are required in order to fully link the shock evolving properties with its efficiency in particle acceleration and injection. In other words, and talking about these dependences, Tylka et al. (2005) paper concludes: "*We suggest additional studies for testing this hypothesis*". But the situation can be even worst. Recently, Sokolov et al. (2006) have revisited the diffusive shock acceleration theory of charged particles by shock waves, concluding that "*the quantitative model of particle acceleration at shock waves is more tightly coupled to the models of the background solar corona and the CME than is usually assumed. Apart from the compression ratio, other important factors that determine the particle production at shocks are the shock angle* θ[11]*, the Alfvén Mach number, and the level of turbulence, along with its power spectrum and extent anisotropy*[12]*.*"

3.6 How we have proceeded

To simplify the description we will assume here a spacecraft fixed in a point in space at the heliocentric distance of 1.0 AU (thus, we neglect its possible movement). For a given SEP event the observed intensity-time profiles result from the evolution of the particle population in a set of flux tubes that sweep over the observer. These particles are produced by a number of dynamic processes occurring on the Sun and at the front of the CME-driven shock, whereas their arrival at the spacecraft depends on the dynamic transport processes occurring in the interplanetary medium.

[11] θ_{Bn} in our nomenclature.

[12] Our group has been considering many of these factors, particularly in the empirical shock-and-particle model, since 1992 (He925).

Spacecraft observations are, therefore, averages over time and space of the particle population propagating within the individual flux tubes that cross the spacecraft. The relative fraction of particles of different energies within these flux tubes varies with the different physical mechanisms at work. For the sake of simplicity, SEP modelers solve relative simple equations that reasonably reproduce the observations under different simplifying assumptions. Relevant to the study and discussions in the next chapters, we assume that:

(i) Once the relative flux derived at a given energy is fixed by comparison with the observed profile, the corresponding profiles for other lower and higher energies are scaled automatically by assuming energy dependences of Q, $\lambda_{\parallel}$ and k. Even if this is not the case (this is what happens with very simple models), additional fittings of either the anisotropy or the relative ratio of abundances of different ion species will constraint the input parameters, the output fits and will give more physical sense to the results.

(ii) Numerical procedures to solve the transport equation introduce ambiguities like numerical diffusion, absorbing or reflecting boundaries either at the shock or at the inner and outer limits of the numerical domain of integration. The influence of these numerical 'artifacts' on the outputs of the model is usually evaluated, but their existence does not allow us to track from the beginning to the end of the solving process the precise value of the number of particles injected, thus the absolute flux values. Therefore, we will care more about the absolute value of the flux profiles yield by the model and then scale them as indicated in the point above[13].

(iii) Our poor knowledge of the real physical conditions at the origin of the SEP events, about the corotation of the flux tubes over the spacecraft, and the influence of the possible cross-field diffusion of the particles, can also induce similar consequences to those described in the latter point.

A problem in space data analysis is the possibility to separate time and space variations of a given phenomena. Another reason why it is necessary to model as many observed SEP events as possible is the necessity to derive general features of the physical mechanisms involved in the development of the SEP events, and therefore,

[13]Monte Carlo methods applied to solve the transport equation (e.g. Li et al. 2003; Kocharov et al. 2005; Agueda et al. 2007) might be able to alleviate this situation; but even then, the transport parameters used in the model make difficult to compute the estimation of the number of particles injected by the traveling shock.

estimate the variables of interest for space weather applications (in our case, for prediction of SEP fluxes, peak fluxes and fluences). At present, we only have a vague idea about these variables and their averaged values for a prescribed set of scenarios. Consequently, we have proceeded in three directions:

[1] modeling more SEP events (Chapter 4),

[2] analyzing the coherence of the flux profiles produced by SOLPENCO and how we can solve their absolute calibration for space weather purposes (Chapter 6) and

[3] comparing these synthetic flux profiles with observational flux data for as much as possible interplanetary scenarios at 1.0 AU, and whenever possible at smaller radial distances from the Sun (Chapters 6 and 7).

To progress in this latter direction, it is necessary to perform a comprehensive statistical analysis of SEP events developed under different conditions and assume that the same factor may be applicable to those fluxes calculated by the model at inner heliocentric distances. Afterward, it will be necessary to check the results obtained using these assumptions with the observational data available at distances < 1.0 AU. This kind of analysis has several inherent difficulties, the most relevant being the following:

(i) The number of SEP events observed at 1.0 AU is large, however the fraction of specific interplanetary scenarios is small (i.e. different observer locations, disparate shock velocities, etc.).

(ii) SEP events show a widespread range of flux values for similar interplanetary scenarios (Kahler 2001b). This range depends also on the energy considered.

(iii) Up to now, there are too few particle observations at distances of $\lesssim 0.5$ AU that for a reasonably range of energies (i.e. from 0.5 MeV to 40 MeV) can be used or assumed as "typical values" of SEP events. Moreover, the number of SEP events whose flux observations at ~ 0.4 AU can be directly related to SEP events observed at 1.0 AU is limited (~ 8 SEP events at this distance have been related to 1.0 AU observations using $4-37$ MeV proton data from the Helios-1, Helios-2 and IMP-8 spacecraft, see Lario et al. 2006).

Caminante son tus huellas
el camino, y nada más;
caminante, no hay camino
se hace camino al andar.
Al andar se hace camino
y al volver la vista atrás
se ve la senda que nunca
se ha de volver a pisar.
Caminante no hay camino,
sino estelas en la mar

Antonio Machado, poet (1875 – 1939)

4 Modeling SEP events for space weather purposes

4.1 Introduction

We have already commented the importance of modeling a large number of SEP events in order to understand the set of processes involved in the development of SEP events and how they can be simulated by the Shock-and-Particle model. Nonetheless, this is an arduous task owing to the complexity of the scenario. In fact, only a handful of events have been completely modeled (Lar98, Appendix B). The fourth final recommendation of Rosenqvist (2003a, Section 6.3 point4) states that *"A large number of events would help to support statistical studies such as the heliocentric dependence of the fluence value"*. This recommendation applies to our case and more widely to the whole study of SEP events in the heliosphere (SRH06 Report). For example, we need to further investigate the domain of scenarios where the Q(VR) relation is applicable, and characterize the energy dependence of the coefficient k of this relation and its average value over the modeled events. It is also important to gain insights on those aspects of the model that can be improved (Section 3.5).

In this context, we have modeled three SEP events that were selected from observations recorded by the ACE and IMP-8 spacecraft, both at 1.0 AU from the Sun. Our selection criteria were based on the solar wind and IMF conditions observed throughout the event, and the proton differential intensity-time profiles of the event measured at several energy channels (from 47 keV to 440 MeV). These conditions have to fit into or approach to the rather simple scenario assumed in our model, i.e. we require: [1] the solar wind speed and magnetic field profiles throughout the

upstream part of the SEP event to be the most stable as possible, and [2] the particle flux profiles not to show upstream irregular shapes or enhanced particle pre-event backgrounds. From a large set of SEP events, ten potential candidates were identified (see Appendix F in Aran et al. 2004) from which we have selected the following cases:

- Sep98: 30 September – 2 October 1998 (doys 273 – 277)
- Apr00: 4 – 6 April 2000 (doys 95 – 100)
- Sep00: 12 – 15 September 2000 (doys 256 – 261)

As described in Section 2.5, proton data come from the EPAM instrument on board the ACE spacecraft (Gol98) and from the CPME instrument on board the IMP-8 spacecraft (Sar76). Interplanetary magnetic field and solar wind plasma measurements come from the magnetometer (MAG; Smith et al. 1998) and the solar wind experiment (SWEPAM; McComas et al. 1998) on board ACE. For each studied event, this set of data is represented in plots as that shown in Figure 4.1 for the Apr00 event. The top panel of this figure shows the proton intensity-time profiles measured at the following 16 energy channels (color coded), from top to bottom: (1) 68 – 115 keV (black), (2) 195 – 321 keV (red), (4) 310 – 580 keV (dark green), (6) 587 – 1060 keV (navy blue), (8) 1.1 – 1.9 MeV (cyan) and (9) 1.9 – 4.8 MeV (pink) of the ACE/EPAM/LEMS120 instrument; and (3) 0.29 – 0.50 MeV (orange), (5) 0.50 – 0.96 MeV (clear green), (7) 0.96 – 2.00 MeV (emerald), (10) 2.0 – 4.6 MeV (blue), (11) 4.6 – 15.0 MeV (purple), (12) 15 – 25 MeV (deep red), (13) 25 – 48 MeV (dark gray), (14) 48 – 96 MeV (clear gray), (15) 96 – 145 MeV (yellow) and (16) 145 – 440 MeV (olive green) of IMP-8/CPME. As can be seen in this figure, the flux profiles measured by the two spacecraft at similar energy windows closely overlap. The second, third and fourth panels respectively show the evolution of the proton velocity, density and temperature of the solar wind. The last three panels show the evolution of the intensity, and of the latitudinal and azimuthal IMF components in GSE coordinates, respectively. Figures 4.9 and 4.15 are the same plots corresponding to the Sep98 and Sep00 events.

In this chapter we briefly analyze the observational characteristics of these events and present the results of their simulations. The methodology of both analysis and modeling follows the procedure already described in Chapter 3. We will only describe in detail the interplanetary shock modeling and the fitting of the flux and anisotropy profiles for the Apr00 event (Section 4.2). For the remaining two SEP

events we will outline the main characteristics of their simulation, focusing on the results obtained for the injection rate of shock accelerated particles, its evolution and energy dependence. The main objective of this analysis is to obtain the $Q(\mathrm{VR})$ relation that will allow us to derive average conditions for predicting flux profiles of different SEP events (e.g. Lario et al. 1995b). For that reason we will not refine each parameter of the model to adjust every particular feature of the SEP events. Several interesting details concerning these fittings are shortly addressed in Appendix C.

During the time interval when the Helios spacecraft were operative (1976 – 1982 for Helios-1 and 1976 – 1980 for Helios-2), two-point and three-point observations were used to constraint the three parameters used to characterize the input pulse of the MHD shock propagation model (Smith & Dryer 1990; He925). However, this is not the case for the present events (from 1998 to 2006) since operative spacecraft within 1 AU are very close to each other (either at the Sun-Earth L1 point or orbiting the Earth). Hopefully, we expect that the twin STEREO mission with two identical spacecraft orbiting at 1 AU, ahead and behind the Earth, will provide multi-point observations of individual CME-driven shocks that will constraint the shock propagation models.

In the meantime, we use only one-point observations recorded at ~ 1 AU from the Sun. We realize that the characteristics and location of the initial pulse and the background solar wind of the MHD model can be slightly modified in order to improve the fitting of the observed solar wind plasma and IMF values at the shock arrival. Taking advantage of this, the SEP events studied in this chapter have been modeled twice: first, by assuming the initial shock pulse used by Smith & Dryer (1990), Lario (1997) and Lar98, and second, by using a slightly modified initial conditions for the MHD model.

Smith & Dryer (1990) used a wide arch of a semicircle centered at the Sun as shock input pulse injected at $18\,R_{\odot}$, with shock speed scaled as a symmetric sine profile. The plasma jump parameters at the shock were computed solving the Rankine-Hugoniot conditions using the fact that the normal to the shock was radial, and hence the shock was parallel. In the second ensemble of MHD shock simulations, we assume shock input pulses not centered at the Sun but at a few solar radii off the center (which is not a physically implausible situation). This simple adjustment implies a non radial shock and permits an improvement of the fittings of both the measured plasma speed and magnetic field jumps. In addition, for each event, the

background solar wind has been modified in order to match the upstream observed average values of the plasma density, speed and IMF intensity. To shorten the description of the fittings of the SEP events, in this chapter, we always refer to this "off-center" shock simulation (labeled with a subindex 'n' when there is any possibility of confusion); otherwise, it will be indicated. The outputs from the two sets of shock simulations that are relevant to the development of SOLPENCO have been summarized in the last section of this chapter.

4.2 The 4 – 6 April 2000 Event (Apr00)

A full halo CME was observed by SOHO/LASCO at 1632 UT on April 4 (doy 95), in temporal association with a C9.7/2F flare in AR 8933 region (N18 W66). The onset of the 1 – 8 Å X-ray emission was at 1511 UT on the same day. A strong interplanetary shock reached ACE at 1600 UT on April 6. Therefore, the transit time of the shock, measured from the X-ray flare onset up to the shock arrival, is 48.82 hours and the shock transit speed[1] is 842.7 km s^{-1}. This event is interesting because it triggered a strong geomagnetic storm (e.g. Huttunen et al. 2002) contrary to what it is expected from events originating in the western solar hemisphere[2]. In fact, this event was selected as a special ISTP[3] science event. We refer to a recent paper Kahler et al. (2007a) for a description of the near-relativistic electron emission and of the radio bursts associated with this event.

Figure 4.1 shows the proton flux profiles for the selected energy channels of ACE and IMP-8, as well as the evolution of the solar wind and IMF. The first vertical line, at 1600 UT on doy 97, indicates the passage of the aforementioned forward shock. The time of the shock arrival delimits the upstream part of the event; we only model this time interval because the interplanetary conditions for shock and particle propagation agree with the assumptions made in the model. The solar wind and the IMF keep reasonably stable throughout this upstream region. The second vertical line, located about half a day later, marks the passage of a second shock by

[1]The Sun-ACE distance divided by the shock transit time.

[2]This event, together with the 6 – 8 June 2000 SEP event (Section 2.4) and the Sep00 event, pose a challenge to forecasting the geoeffectiveness of events based on their solar origin (Zhukov et al. 2006; http://cost724.obs.ujf-grenoble.fr/General/ESWW3/ESWW3_Zhukov.pdf).

[3]ISTP: International Solar Terrestrial Physics project of NASA (see details at http://www-istp.gsfc.nasa.gov/istp/events).

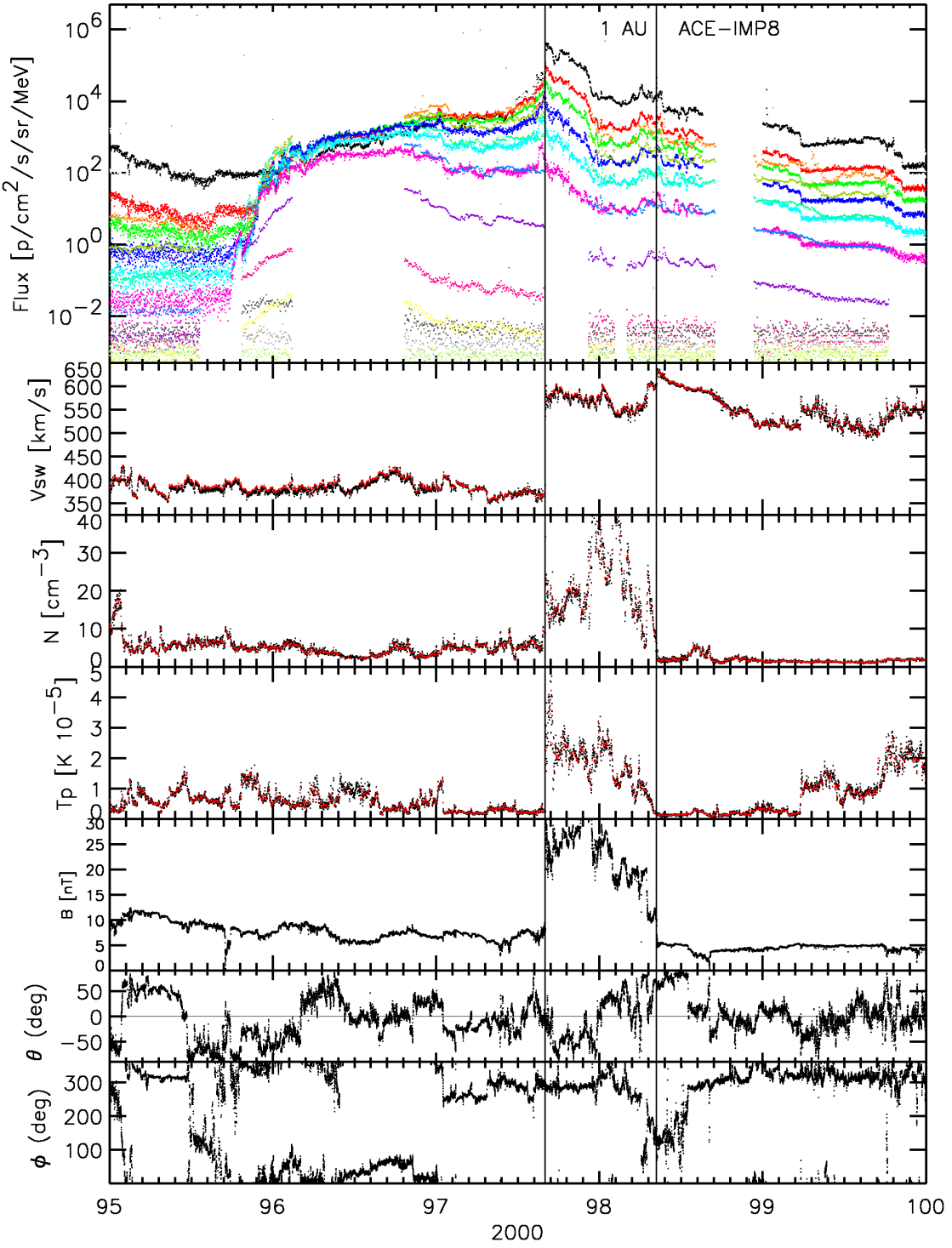

Figure 4.1: Apr00 event. Evolution of the proton flux profiles measured by several energy channels, and evolution of the solar wind and interplanetary magnetic field variables. See text for details.

ACE. This is a reverse shock that indicates the ending of the turbulent downstream region (i.e. the region where the IMF, solar wind density and temperature keep elevated).

4.2.1 Simulation of the shock propagation

With the aim of obtaining a correct description of the solar wind and magnetic field values measured before the shock arrival at ACE we have slightly modified the steady-state background medium of the MHD code given by Smith & Dryer (1990). The resulting values at 1.0 AU of the solar wind speed, density and magnetic field magnitude are 371 km s^{-1}, 5.7 cm^{-3} and 7.5 nT, respectively. The semicircular input pulse at 18 $R_\odot$ is centered at W66 and at 10 $R_\odot$ from the Sun. The parameters characterizing this input pulse are the same as those used by Smith & Dryer (1990) with initial speed $v_s = 1510$ km s^{-1}, initial width $\omega = 165°$, and piston-driving time $\tau = 1$ hour. This set of input values (selected after several trials) are our best choice in order to fit the shock arrival time and the plasma and IMF parameters measured at 1.0 AU. The transit time of the simulated shock is 48.85 hours and its transit speed is 842.2 km s^{-1}.

Figure 4.2 shows the evolution of the measured solar wind density, radial velocity and temperature together with the IMF intensity (dotted lines) and the corresponding values resulting from the MHD shock modeling (solid thick lines). The simulated shock reproduces the jump in speed and magnetic field intensity at the shock arrival (bottom panels of this figure). As commented in Chapter 3, these are the two main variables to be fitted in order to infer the evolution of the injection rate of shock-accelerated particles at the cobpoint position. In this case, we point out that the simulated density and temperature overestimate the observed jump (top panels).

The downstream to upstream normalized radial velocity ratio, VR, and the magnetic field ratio, BR, at the shock are shown in Figure 4.3. As can be seen, the observed values (dotted lines) are closely fitted by the simulation (solid lines). It is worth noting that the sudden increase of any of these variables at the shock arrival (the jump) is tracked by the corresponding modeled value although the latter presents a less steep slope than the actual jump due to the finite grid used in the MHD model ($\Delta r = 0.5\,R_\odot$ in radial distance and $\Delta\varphi = 0.75°$ in azimuth). The fitting could have been improved by reducing the size of the grid cells; however, this

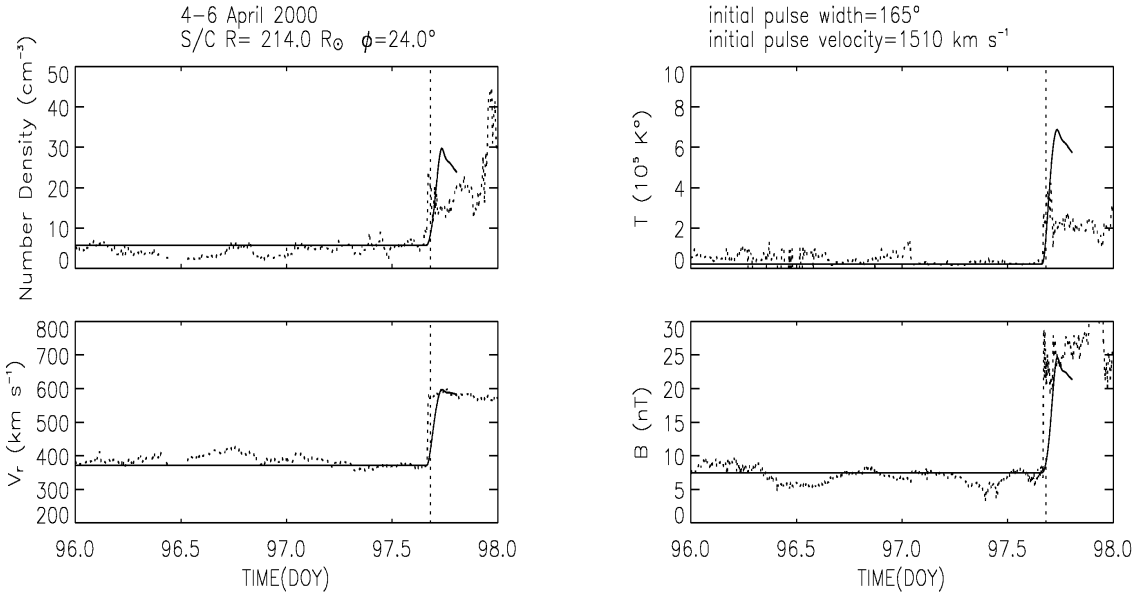

Figure 4.2: Apr00 event. Observed (dotted lines) and MHD-modeled (thick solid lines) solar wind density (top left panel), radial velocity (bottom left) and temperature (top right) and IMF magnitude (bottom right). The dashed vertical line in each plot marks the time of the shock arrival at ACE. See text for details.

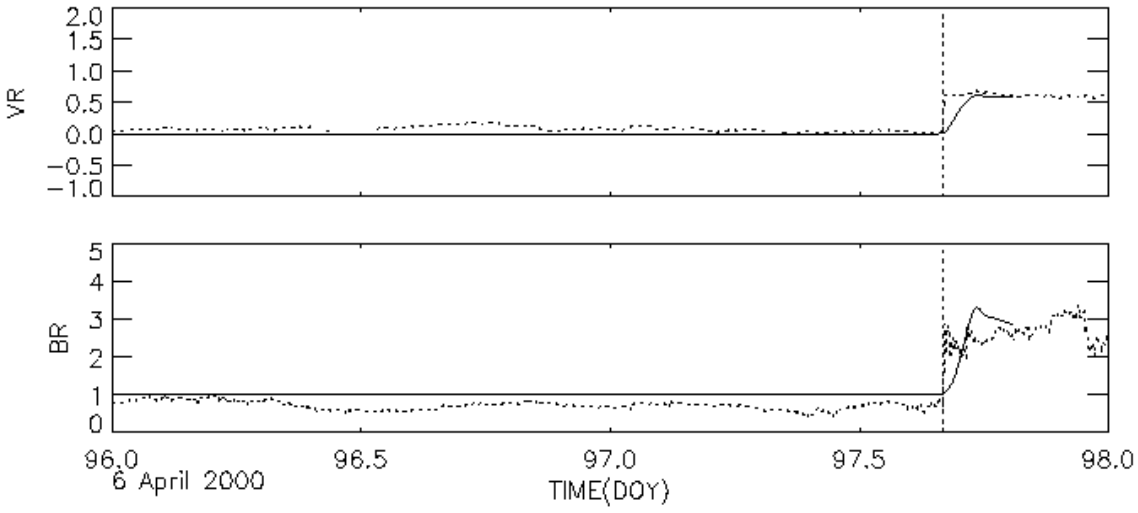

Figure 4.3: Apr00 event. The observed (dotted lines) and computed (solid lines) radial velocity, and the magnetic field downstream-to-upstream ratios, VR (top panel) and BR (bottom panel), respectively.

would have implied to spend a much larger computing time in each simulation. The adopted values represent a balance between resolution and computing time.

From the shock simulation we can derive the evolution of the parameters VR and BR (and also θ_{Bn}, although not commented here) at the cobpoint. These values depend on both the parameters used to define the shock input pulse (determined to fit 1.0 AU observations) and the location of the cobpoint on the shock front. The two bottom panels of Figure 4.4 show the resulting position of the cobpoint obtained from the time at which the magnetic connection between the observer and the front of the shock is established ($t_c = 3.4$ hours) up to the shock passage by the observer's location ($t_s = 48.85$ hours). The bottom panel displays the heliocentric radial distance of the cobpoint (in solar radii). The third panel shows the evolution of the angle between the leading direction of the shock propagation (i.e. the pulse central meridian direction, 'PCM') and the Sun-cobpoint vector. In this notation, the angular position of the Sun-Earth(or ACE) direction is $-66°$. The radial distance of the cobpoint from the Sun increases (as a consequence of the shock expansion) almost linearly with time, while the cobpoint slides along the eastern wing of the shock front (i.e. the angular position changes from $-10°$ at t_c down to $-66°$ at t_s). In other words, the evolution of the cobpoint implies that shock-accelerated particles detected by the observer come from far distant points of the shock front.

The temporal evolution of BR and VR at the cobpoint are plotted in the top two panels of Figure 4.4. VR decreases with time, from 2.4 down to 0.6, because of the combination of two factors: (i) the cobpoint displacement along the shock front, from close to the nose of the shock (the PCM) toward the eastern flank (a weaker region than the PCM in terms of MHD strength); and (ii) the weakening of the shock resulting from its expansion while traveling away from the Sun. In contrast, the magnetic field ratio (BR) increases with time; thus indicating that the magnetic field becomes more compressed along the eastern wing of the shock as it expands into the interplanetary medium. Appendix C.1 shows, for comparison, the evolution of these two variables derived from the simulation of this shock by using the original input pulse and background solar wind of the MHD model.

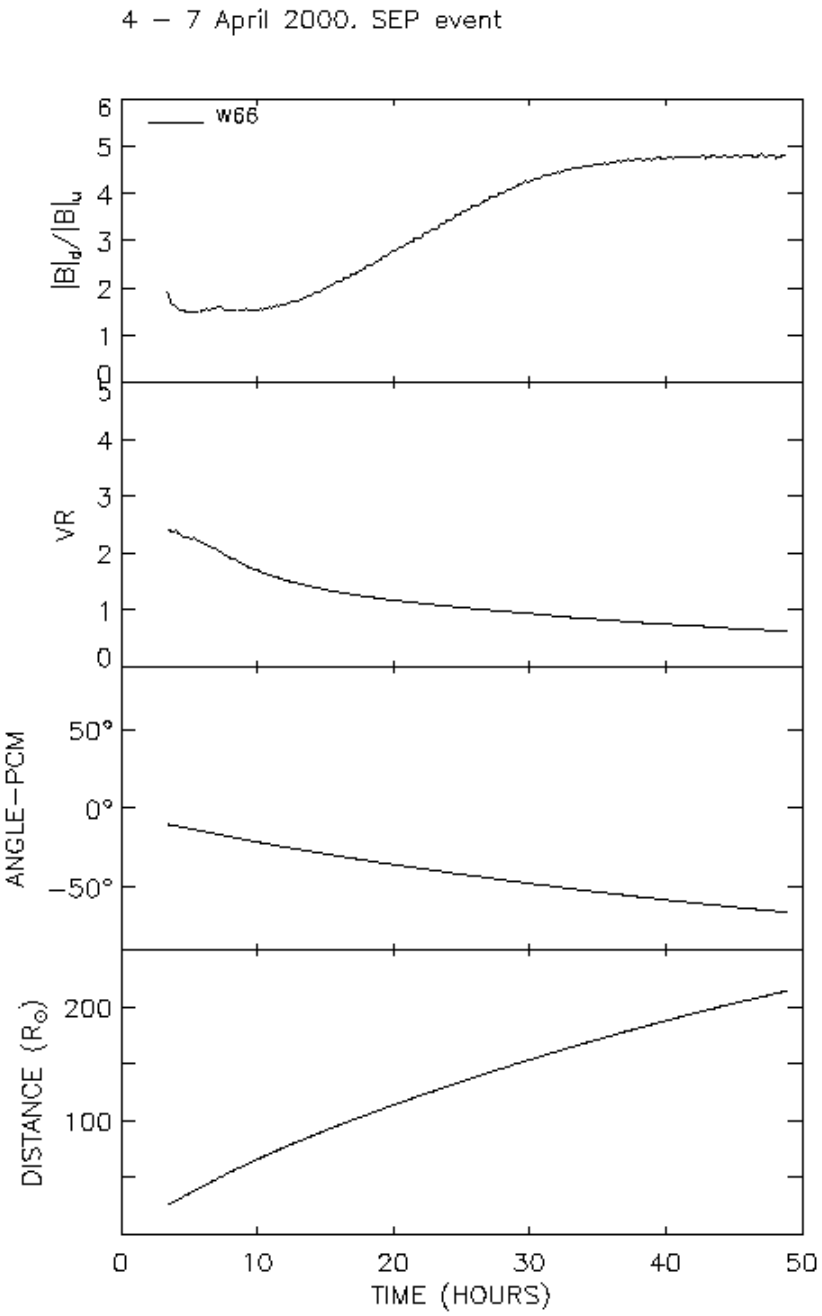

Figure 4.4: Apr00 event. Two upper panels: evolution of the BR (first panel) and VR (second) parameters. Two lower panels: evolution of the position of the cobpoint at the shock front, identified by the angle of the cobpoint with respect to the central meridian position, PCM, (third) and by its radial distance from the Sun (fourth).

4.2.2 Fitting the proton flux and anisotropy profiles

Figure 4.5 shows the observed proton flux data for five energy channels between 195 keV and 4.8 MeV of the ACE/EPAM LEMS120 and LEMS30 telescopes[4]. The data for each energy channel is represented in two panels: the top panel shows the omni-directional component of the particle intensity (A0) and the bottom panel, the parallel component of the first order anisotropy (A1/A0). We have calculated this first order anisotropy along the IMF, in the solar wind frame, following the method by Sanderson et al. (1985a), as described in Appendix A (and references quoted there and in Lario et al. 2004a). The vertical arrow marks the onset of the solar event, the vertical solid line the arrival of the shock at ACE, and the small vertical dotted line the time when energetic particles start being injected from the cobpoint (t_c).

After a rapid flux increase at the onset of the SEP event, particle intensities below 1.1 MeV (left panels of Figure 4.5) keep smoothly increasing for twelve hours (up to doy 97), then remain quasi-constant for a long plateau of about twenty hours, followed by a sudden increase that peaks at the shock arrival. For energies above 1.1 MeV (the two upper right panels), the particle intensities show a plateau following the prompt phase until doy 97, then slightly decrease to sharply increase again just before the shock passage. The intensities attained at the shock (and during the plateau) decrease with increasing proton energy. Hence, we deduce that the efficiency of the shock as a particle accelerator when it arrives at 1.0 AU decreases with increasing energy. The first order anisotropy remains high (> 0.5) at the onset and during large part of the event; but it smoothly decreases to zero at the passage of the shock, where the sense of particle flow rapidly reverses. The bottom left panel and the three lower right panels of Figure 4.5 display the evolution of the solar wind speed and magnetic field components, respectively, as in Figure 4.1.

Proceeding as in former events (e.g. Lar98), first, we fit both the intensity and the anisotropy profiles measured by a given energy channel, in this case the 580 – 1060 keV channel (geometric mean energy, $E_0 = 0.8$ MeV)[5]. From the fitting of

[4]EPAM instrument cannot distinguish between protons and other ions; nevertheless, the collected particle intensities are largely dominated by protons (Lario et al. 2004a).

[5]We solve the particle transport equation by applying the finite differences technique using a finite grid of energies. Therefore, we have to consider discrete values of the energy to describe a given energy window.

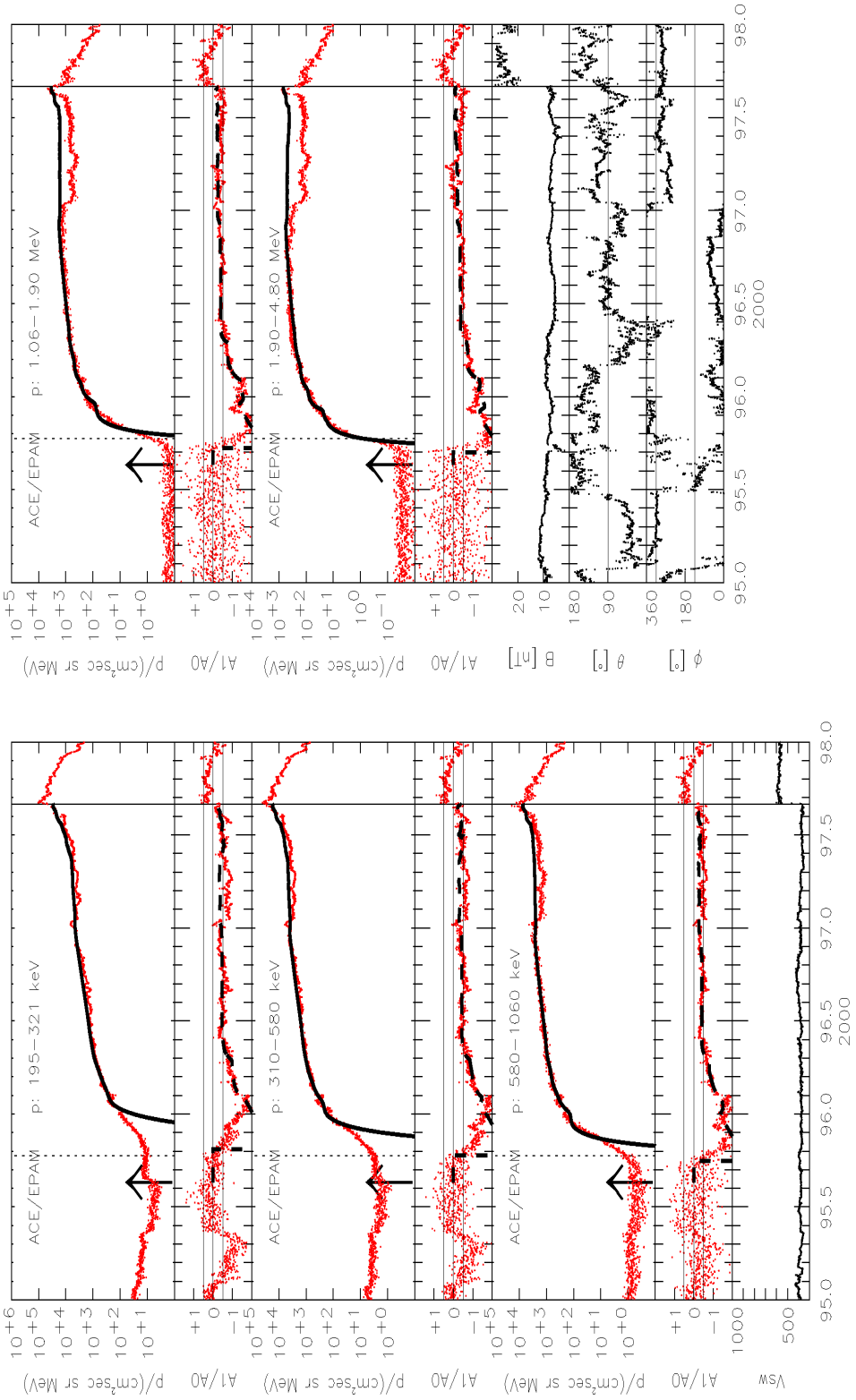

Figure 4.5: Apr00 event. Flux and anisotropy profiles in the upstream region of the event, for five energy channels, from 195 keV to 4.8 MeV. Observed values are shown as red dots, computed values are represented by black lines. Bottom left panel shows the evolution of the solar wind speed and the three lower panels to the right display the evolution of the IMF components. The vertical arrow marks the onset of the solar event.

this channel we derive the evolution of the injection rate, Q, the value of the 0.8 MeV proton mean free path, $\lambda_{\parallel 0}$, and determine the existence or absence of the turbulent foreshock region (described below). Then, we proceed to model and adjust simultaneously the six considered energy channels, from 115 keV to 4.8 MeV. By fitting together the five energy channels we derive the spectral index (at low and at high energy) of the injection rate, γ and the variation of the characteristics of the turbulent region with the energy. We iterate the process in order to globally improve the fittings at different energies as much as possible. The resulting flux and anisotropy profiles are shown in Figure 4.5 as black lines overlapping the observations.

It has to be mentioned that the observed first < 580 keV proton intensity enhancement at the time of the solar flare (vertical arrow in Figure 4.5)is due most probably to near-relativistic electrons or high energy ions contaminating the low-energy channels of the LEMS120 and LEMS30 telescopes of EPAM (Lario et al. 2004a). Additionally, the background population observed prior to and close to the onset of the event can also be modeled by including a background isotropic population filling the flux tube that would also account for the slow increase (in absolute values) of the anisotropy observed between doys 95.7 and 96.0 (see for example, the WF-event in Lario 1997). Since this feature is not relevant to our purposes and it has no influence on the determination of the Q(VR) relation, we have not included it here.

The values of the mean free path adopted for $\lambda_{\parallel 0}$ are 0.8 AU for $t < 11$ hours, 0.4 AU for $11 \leq t < 15.8$ hours, and 0.2 AU for $15.8 \leq t < 48.85$ hours. In fact, this precise evolution of the values of the mean free path is not necessary for our modeling purposes, since by assuming a constant $\lambda_{\parallel 0} = 0.2$ AU near identical fittings are obtained, with only slightly less precision at fitting the prompt phase of the flux profiles. The proton mean free path is scaled with the particle rigidity as $\lambda_{\parallel}(R) = \lambda_{\parallel 0}(R/R_0)^{2-q}$, where $q = 1.5$ (Section 3.3). The turbulent region is characterized by a width of 0.07 AU and starts acting from $t > 30.18$ hours (i.e. from 18.7 hours prior the shock arrival). The derived mean free path within this region is $\lambda_{\parallel 0c} = 0.02$ AU and it depends on the particle rigidity, R, through $\lambda_{\parallel c}(R) = \lambda_{\parallel 0c}(R/R_0)^{-0.6}$ where $R_0 = 38.5$ MV is the proton rigidity corresponding to E_0. The particle injection rate function, G, scales with the energy as a power law, $G(E) = (E/E_0)^{-\gamma}$. The values of the spectral index are $\gamma = 1.0$ for $t < 40.0$ hours and $\gamma = 1.5$ for $t \geq 40.0$ hours. In the simulation presented here, we have not tried to fit the 1.06 – 1.90 MeV and 1.90 – 4.80 MeV flux profiles in the period from 97.0 to 97.5 but the peak flux at

the shock arrival. The particle injection rate for $t < t_c = 3.4$ hours is assumed to follow a Reid-Axford time profile with $\beta = 7$ hours and $\tau = 3$ (see footnote 31 in Chapter 2) and it depends on the particle energy as $E^{-1.5}$.

It is important to keep in mind that each SEP event has its own specific features. Thus, each event must be carefully analyzed, specially when these features can determine the inferred evolution of the shock injection $Q(t)$. As an example, in Appendix C.2 we comment the different $Q(t)$ evolution when trying to fit the $E \geq$ 1 MeV proton intensity decrease observed at 97.0 doy. Finally, we would like to point out that the particle transport conditions and the values of γ derived from the fitting of this SEP event when using the cobpoint position obtained from the MHD shock modeling using the original input pulse, are the same as those described here obtained using the modified shock input pulse shape.

4.2.3 Evolution and spectrum of the injection rate Q

The top panel of Figure 4.6 displays the evolution of the injection rate of shock-accelerated protons at the cobpoint, Q, for the five energy channels modeled between 195 keV – 4.8 MeV (color coded) shown in Figure 4.5. The values of Q are obtained directly from the values of G determined by solving the transport equation to fit the particle event and then scaling it by the cross-sectional area of the magnetic flux tube at the cobpoint (Section 2.4) and converting the values into physical units as described in Appendix A.1. The first point of each curve is the value of the injection rate at the connecting time, t_c, while the last point is the value of Q just before the shock passage by ACE. As can be seen, the injection rate of shock-accelerated particles decreases for all energies up to $\sim$30 hours prior to the shock arrival. This reduction indicates that the shock is more efficient at injecting particles at the beginning of the event and becomes less efficient as it moves away from the Sun and as the cobpoint slides from the nose of the shock front toward its eastern flank. This is the expected behavior for a well-connected western event like the Apr00 event.

We note that at low-energy (< 0.58 MeV; traces a and b in Figure 4.6) Q starts to increase just before the arrival of the shock while at higher energies (traces c, d and e of this figure) Q keeps decreasing and at a higher rate as higher energies are considered. This behavior is due to the combined effects of the presence of a

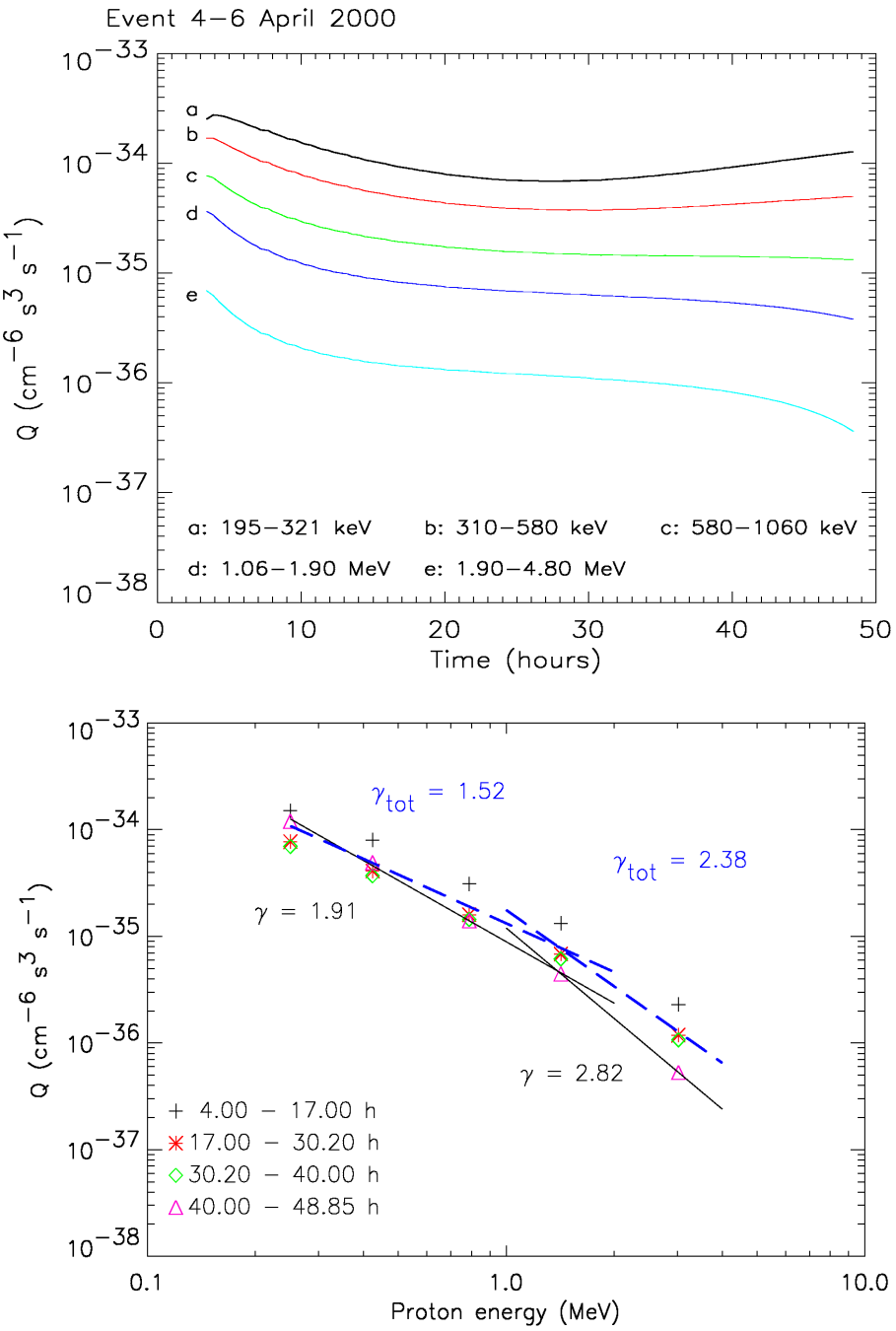

Figure 4.6: April00 event. Top panel: evolution of the particle injection rate, Q, for five energy channels, as labeled. Bottom panel: Spectra of Q over the periods indicated in the inset. The black solid lines are the fittings to the points at low and high energies for the last period (triangles), prior to the shock passage. The blue dashed line show the fittings to the average value over all time intervals.

foreshock region approaching the observer, the value of the particle mean free path assumed in this region, the higher efficiency of the shock at injecting particles at low (< 0.58 MeV) than at high (> 1.06 MeV) energy, i.e. $G(E) = (E/E_0)^{-\gamma}$, and the fact that the model assumes an absorbing boundary moving behind the shock front (Section 3.2). The turbulent foreshock region keeps particles trapped in front of the shock and particles of low energies are trapped easily within this region because of their smaller mean free path; thus, enhancing the low-energy particle population suitable to be injected into the magnetic flux tube by the shock and the consequent increase of Q for $E < 0.58$ MeV up to the shock arrival. On the other side, it is possible to fit more precisely the high-energy flux (as performed in Appendix C.2) but the only effect is a higher decrease of Q with time for $E > 0.58$ MeV. The evolution of Q deduced here for the 0.58 – 1.06 MeV channel (trace c) resembles that obtained for the WF event (W50) modeled by Lar98 (see Figure 7 of this paper) for the 0.62 – 1.0 MeV channel of ISSE-3/DHF instrument.

The bottom panel of Figure 4.6 shows the energy dependence of the injection rate, Q, averaged over four time intervals (symbol coded) as indicated in the inset (to be compared with Figure 8 of Lar98). We have calculated the average value of Q for the same energy channels shown in the top panel. The value of the energy assumed for each channel is the geometric mean of the window. As can be seen, the energy dependence becomes steeper as the shock is approaching the observed (i.e. the last period marked by triangles). This is mainly due to both the effect of the foreshock region, that results in a increase of the injection rate at low-energy (< 0.58 MeV) and the inefficiency of the shock at injecting high-energy particles for $t > 40.0$ hours, resulting in a decrease of the injection rate with the particle energy and with time. For this period, the spectral index of Q is $\gamma = 1.91$ ($E < 2$ MeV) and $\gamma = 2.82$ ($E > 1$ MeV). These values are comparable to those adopted for SOLPENCO (2.0 and 3.0, respectively, see next chapter).

The spectral indices $\gamma_{tot} = 1.52$ and $\gamma_{tot} = 2.38$ (at low and high-energy, respectively) are the event-average spectral indices that result from fitting the average value of Q over the time interval that the shock-injection lasts and for each energy channel considered. The equivalent values derived when using the MHD simulation with the original shock input pulse centered at the Sun ('Sun-centered' simulation), are $\gamma_{tot} = 1.45$ and $\gamma_{tot} = 2.33$. For the period prior to the shock arrival, the derived spectral indices are similar to those obtained from the off-center simulation: $\gamma = 1.85$ at low-energy and $\gamma = 2.77$ at high-energy.

4.2.4 Dependence of Q on VR and BR

Since we know the temporal evolution of Q, VR and BR at the cobpoint, we can derive how Q varies as a function of VR and BR. Figure 4.7 shows the dependence of Q on VR for the five energy channels analyzed here (from 195 keV up to 4.8 MeV, color coded). Due to the discretization of the finite differences technique used in the model, each point in Figure 4.7 represents a time step at which the position of the cobpoint has been calculated and hence is at which the particle shock-injection occurs. In this figure time runs from right to left. The first point at the right of the figure corresponds to t_c, while the last point to the left corresponds to the shock arrival time. The solid lines are the linear fit corresponding to the Q(VR) relation for each energy channel: $\log Q = \log Q_0 + k\text{VR}$. The values of Q_0 and k are listed in columns 3 and 4 of Table 4.1 (labeled as Q_{0n} and k_n); and column 5 gives the value of the regression coefficient ξ_n. The values of this coefficient are higher than 0.95, except for the two lower energy channels; the deviations from the linear fit at low-energy correspond to the effect of the foreshock region commented in the former paragraph.

Columns 6 – 8 of Table 4.1 list the values of Q_0, k and the regression coefficient, ξ, corresponding to the Q(VR) relations obtained when using the evolution of VR from the Sun-centered MHD shock simulation. As can be seen, the values of k and Q_0 obtained from both simulations are very similar. The small differences come from the slightly different range of values of VR deduced from each shock simulation (see the left panel of Figure C.2 in Appendix C): $\text{VR}_n \in (0.6, 2.4)$ and $\text{VR} \in (0.5, 2.8)$.

Proceeding in the same way with the magnetic field ratio, BR, instead of VR, we can try to derive a Q(BR) relation: $\log Q = \log Q_0 + k\text{BR}$. Figure 4.8 shows the evolution of the injection rate as a function of BR for the same set of energy channels. Since BR increases with time (Figure 4.4), now time runs from left to right. The straight lines represent the obtained linear fits that show a high value for the regression coefficient $\xi > 0.88$ for $E > 0.58$ MeV. However, in this case we cannot extract any clear conclusion about the validity of the derived $Q(BR)$ relations because about 70% of the points are concentrated around BR = 1.5 or BR = 4.8, at both extremes of the range of the values of BR (see the top panel of Figure 4.4)[6]. Additionally, at both ends of the curves of Figure 4.8, the points

[6]We note that the magnetic field vector downstream of the shock is most likely unrealistically determined due to the input pulse used in the MHD code (Smith & Dryer 1990). This comment

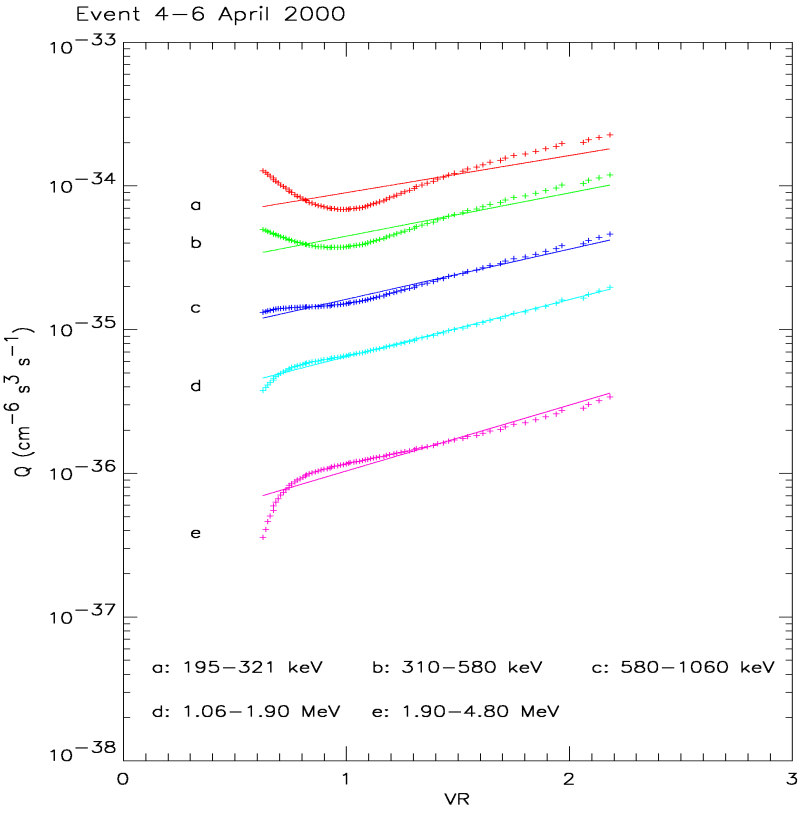

Figure 4.7: April00 event. Functional dependence of the injection rate, Q, on the normalized radial velocity ratio, VR. The straight lines represent the linear fits for each energy. Time runs from right to left.

Table 4.1: Q_0 and k coefficients values for the $Q(\mathrm{VR})$ relation derived from the off-center (labeled with 'n') and from the Sun-centered MHD shock propagation modeling.

E (MeV)	$<E>^a$	Q_{0n} (cm^{-6} s^3 s^{-1})	k_n	${\xi_n}^b$	Q_0 (cm^{-6} s^3 s^{-1})	k	ξ^b
0.195 – 0.321	0.250	5.0×10^{-35}	0.26	0.74	3.6×10^{-35}	0.26	0.88
0.310 – 0.580	0.424	2.2×10^{-35}	0.30	0.89	1.8×10^{-35}	0.29	0.94
0.580 – 1.060	0.789	7.3×10^{-36}	0.35	0.98	6.6×10^{-36}	0.32	0.98
1.06 – 1.90	1.419	2.6×10^{-36}	0.40	0.99	2.4×10^{-36}	0.35	0.98
1.90 – 4.80	3.020	3.6×10^{-37}	0.46	0.95	3.7×10^{-37}	0.39	0.98

[a] Geometric mean energy of each channel.
[b] Regression coefficient of the linear fit.

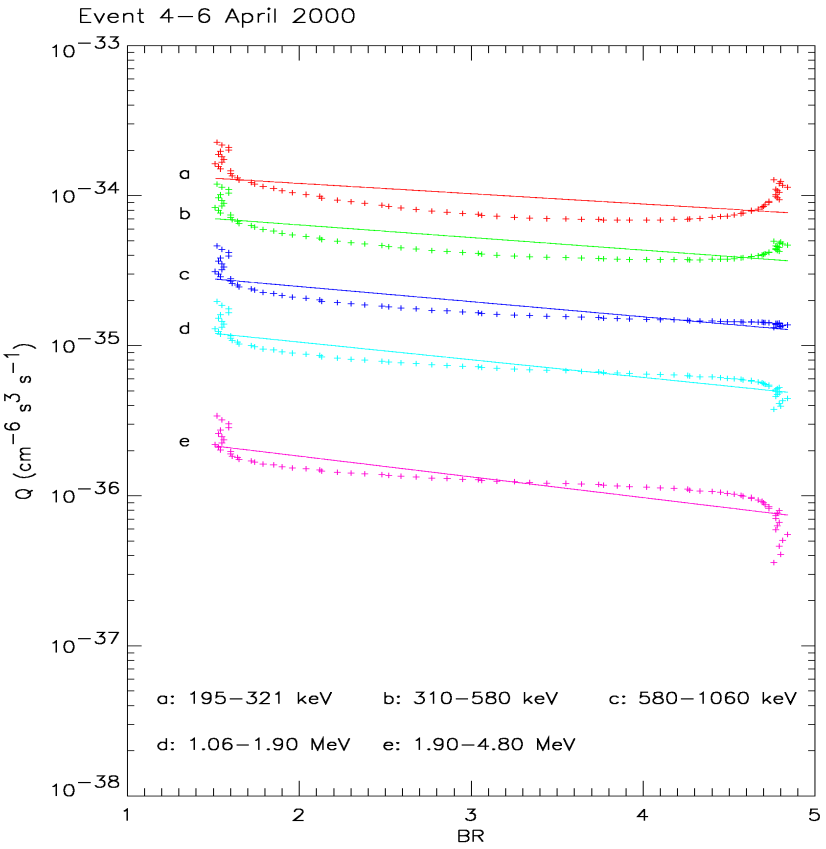

Figure 4.8: April00 event. Functional dependence of the injection rate, Q, on the magnetic field ratio, BR. The straight lines represent the linear fit for each energy channel. Time runs from left to right.

are not completely well ordered in time, because of numerical artifacts of the MHD code when determining the downstream magnetic field vector used to compute BR. Similar results are found when applying this relation to the Sep98 and Sep00 events. Therefore, if there is any dependence of Q on BR, it is too weak to be detected with the present version of the MHD model (either the modified or the original version). The situation is even worse for θ_{Bn} (not shown) because the dispersion of values is much larger than for BR and without defining any temporal sequence (Lar98 discuss this situation for other modeled SEP events).

also applies to the simulation commented in Appendix C.

4.3 The 30 Sep. – 2 Oct. 1998 event (Sep98)

4.3.1 Observations and modeling

The solar event associated with the origin of the Sep98 SEP event is an M2.8/2N flare starting at 1402 UT on 1998 September 30, from the NOAA active region AR 8340 (N32 W81). SOHO/LASCO was not operational at that time and no coronal activity was detected by the Mark III K coronameter at Mauna Loa Solar Observatory (Lario et al. 2000b). ACE detected the passage of an interplanetary shock at 0655 UT on October 2 (doy 275; the vertical line in Figure 4.9). Lario et al. (2000b) associated the SEP event with the W81 flare and the passage of of the eastern flank of a shock presumably driven by a CME temporally related to the solar events observed on doy 273. Assuming that this shock originated at the time of the W81 flare, its transit time is 40.88 hours with an average transit speed of 1006 km s^{-1}. Figure 4.9 shows the proton flux profiles of this SEP event, as well as the main features of the solar wind and IMF[7].

In order to model the propagation of the associated traveling shock, we have assumed that the steady-steady state solar wind velocity, density and IMF values at 1.0 AU are 525 km s^{-1}, 4.3 cm^{-3} and 6.2 nT, respectively. The initial shock pulse is characterized by: v_s = 1300 km s^{-1}, $\omega = 165°$, and τ = 1 hour. The pulse is centered at 1 $R_\odot$ from the center of the Sun and oriented toward the W81 direction. The shock transit time derived from the simulation is 40.74 hours and the transit speed 1010 km s^{-1}. As can be seen in Figure 4.10 the simulated disturbance reproduces the shock arrival time and the jumps in the plasma radial speed and temperature (bottom left and top right panels, respectively) and in the magnetic field intensity (bottom right panel). The simulated jump in density, however, is ∼5 times higher than that observed.

Figure 4.11 shows the position of the cobpoint and the evolution of VR and

[7]Several authors have studied different observational features of this event, for example: Lario et al. (2000b) study the proton intensities collected by WIND; Reames et al. (2000) and Reames et al. (2001) study the spectra of ions at the onset and the particle streaming as a function of plasma β; Kahler et al. (2007a), and references therein, study the radio signatures and electron emission associated with this event; and Tan et al. (2007) the bulk flow speed of different ions as seen by WIND.

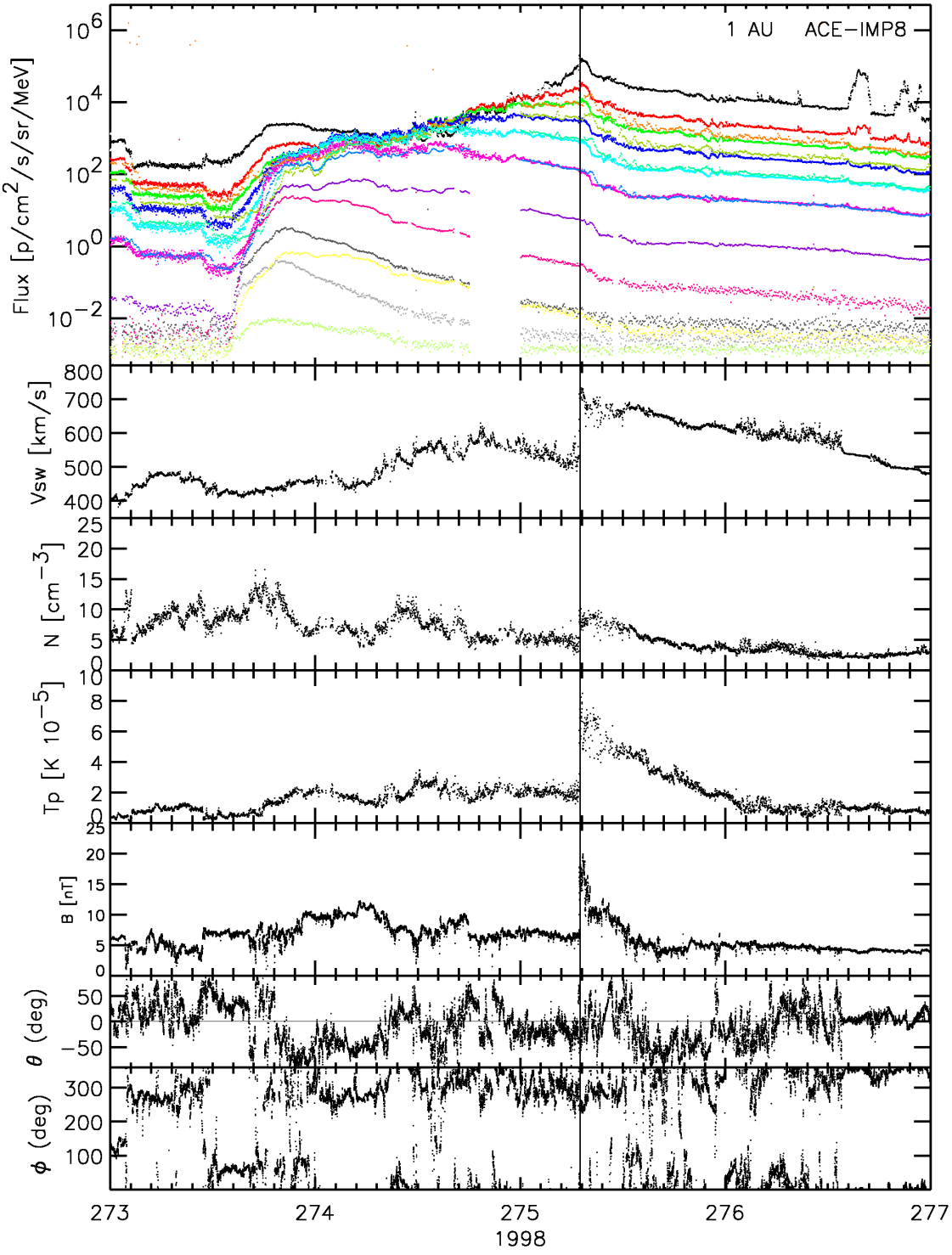

Figure 4.9: Sep98 event. The same as Figure 4.5.

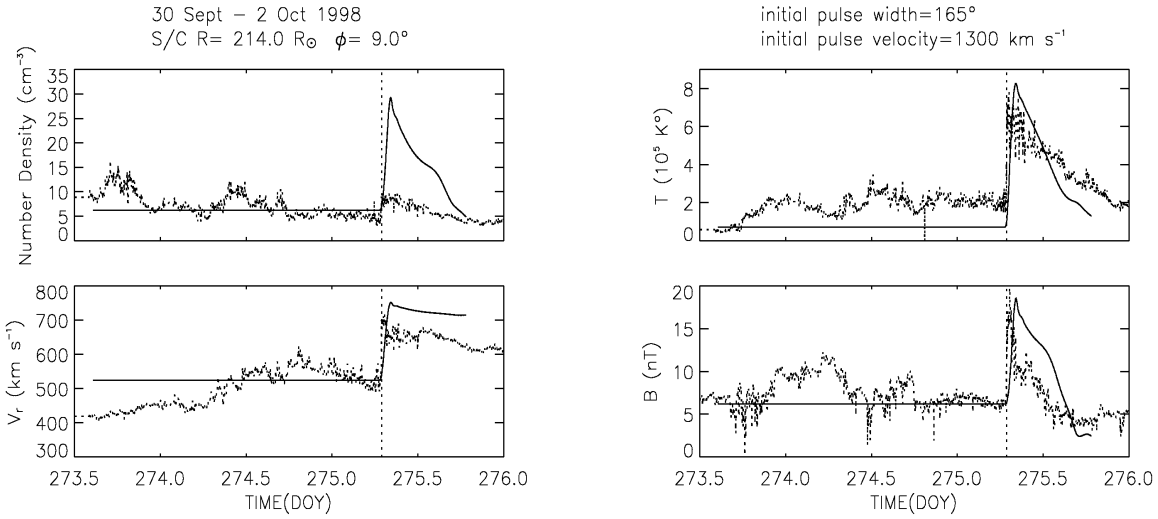

Figure 4.10: Sep98 event. The same as Figure 4.2.

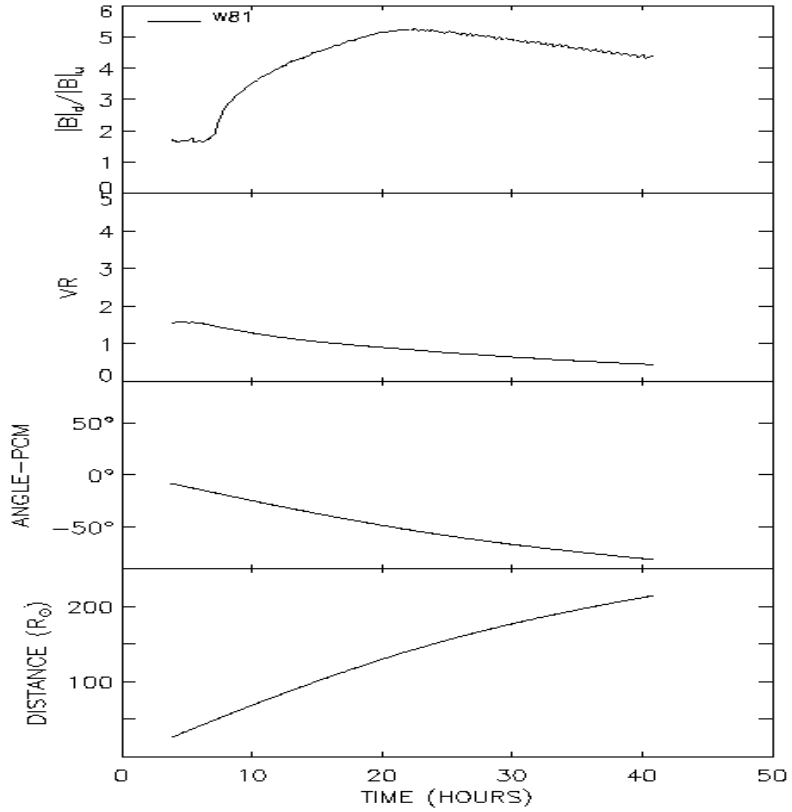

Figure 4.11: Sep98 event. The same as Figure 4.4.

BR as described in Figure 4.4. Since this is a western event (like the Apr00 event) VR decreases with time, from the time of connection, $t_c = 4.0$ hours, up to the shock arrival, $t_s = 40.74$ hours. VR decreases from 1.6 to 0.5. These values are lower than those obtained for the Apr00 event because the cobpoint scans a more distant region of the eastern wing of the shock and the input pulse speed is lower than for the Apr00 event. For comparison, the evolution of VR obtained with the Sun-centered MHD shock simulation is shown in Appendix C.1.

The resulting fittings of the particle flux and first order anisotropy for the six energy channels between 115 keV and 4.80 MeV of ACE/EPAM are shown in Figure 4.12. This figure is similar to Figure 4.5 but it includes the lowest energy channel modeled (top left panel). This panel displays the 38 – 53 keV electron intensity profile (orange trace) measured by the ACE/EPAM/LEMS30 telescope (Section 2.5) with the purpose to show that the associated electron event at the onset of the event (marked by a black arrow) strongly dominates the low-energy (< 1.1 MeV) proton channels[8]. In order to illustrate that the enhanced ion intensity observed by the low-energy channels before doy 274 is not a prompt component of the SEP event, we mark the minimum flying time of the particles for the lowest and highest proton energies, of each energy channel (vertical blue lines). A deeper analysis of the data available at the onset of the event should be performed in order to discard or confirm whether there is another particle population contributing to this elevated low-energy intensity; this, however, is beyond the scope of the present work.

The values of the proton mean free path at $E_0 = 0.8$ MeV (scaled with the particle rigidity as for the previous event) derived from the modeling are: 0.3 AU for $t < 16.8$ hours, 0.2 AU for $16.8 \leq t < 20.4$ hours, and 0.1 AU for $20.4 \leq t < 40.74$ hours. In this case, as for the Apr00 event, similar fittings are obtained when a constant value of $\lambda_{\parallel 0} = 0.2$ AU is assumed. For $E < 0.58$ MeV a thin (0.04 AU wide) turbulent foreshock region is assumed from $t > 20.0$ hours with $\lambda_{\parallel 0c} = 0.02$ AU and the same energy dependence as for Apr00. The injection rate before t_c depends on the proton energy as $E^{-1.5}$ and its magnitude is assumed to be constant[9].

[8]The ion channels of the ACE/EPAM instrument can suffer from electron contamination (Keeney 1999), specially at the onset of large SEP events, before low-energy ions arrive to the spacecraft and an elevated intensity of electrons is already recorded (Lario et al. 2004a), as in the case shown here.

[9]The contamination of the low-energy channels at the onset of the event does not allow to refine these values.

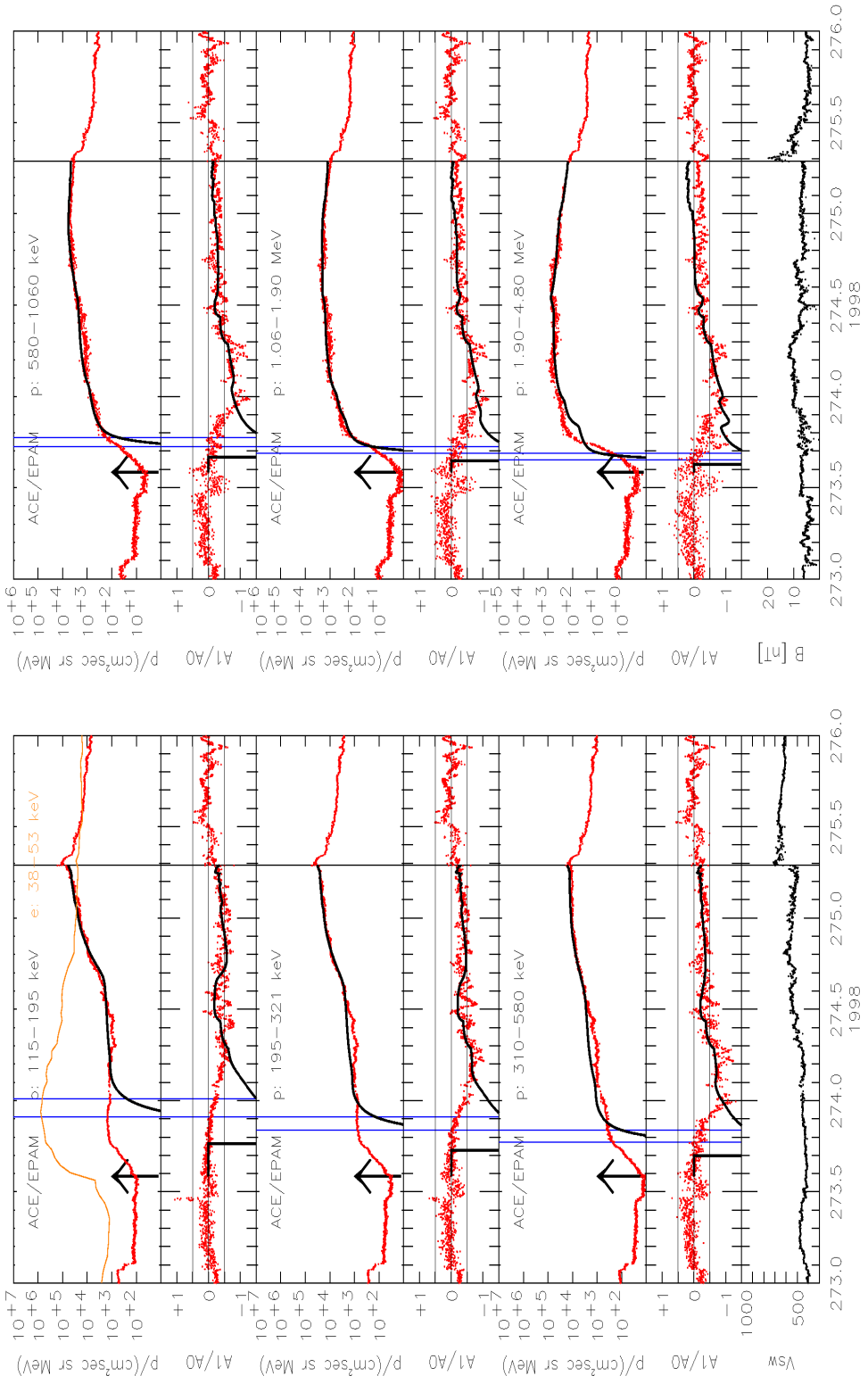

Figure 4.12: Sep98 event. Proton flux and anisotropy profiles in the upstream region of the event, for six energy channels. Observed values are shown as red dots, fitted values are represented by black lines. Bottom left panel displays the evolution of solar wind velocity while the bottom right panel shows the IMF magnitude. The yellow trace in the top left panel is the 38 – 53 keV electron flux. See text for details.

The energy dependence derived for $G(E)$ yields a spectral index $\gamma = 0.5$ for $t < 19.50$ hours. This flat spectrum of the injection rate is in accordance to the flat energy spectrum of the proton intensity observed at this time interval for protons $E < 2$ MeV (cf. Figure 2 of Reames et al. 2000). Later, $\gamma = 1.75$ for $19.5 \leq t < 33.6$ hours and $\gamma = 2.0$ for $t > 33.6$ hours. The values of these parameters are equal to those obtained when using the position of the cobpoint derived with the original (Sun-centered) MHD shock propagation model.

4.3.2 The spectral index and the Q(VR) relation

The values derived for the spectral index of the injection rate Q of this SEP event are shown in Figure 4.13. The inset in the plot indicates the periods of time over which the injection rate Q has been averaged. This figure is similar to the bottom panel of Figure 4.6. As for the Apr00 event, we have calculated the energy spectra from 195 keV to 2 MeV and from 1 MeV to 4.8 MeV; the energy assumed for each channel is the geometric mean of the interval. As can be seen in Figure 4.13, the values of the injection rate Q for protons with $E > 0.58$ MeV decrease with time, indicating that the shock becomes less efficient at accelerating particles as it approaches the spacecraft and as the cobpoint slides toward the eastern flank of the shock front. For protons with $E < 0.58$ MeV, this evolution is not observed because of the presence of the turbulent foreshock region that enhances the values of Q.

Consequently, as the shock expands the spectrum of Q becomes steeper both at low and high energies. Its value prior to the shock arrival (time interval indicated by triangles) is: $\gamma = 2.62$ at low-energy (< 2 MeV) and $\gamma = 3.31$ at high-energy (> 1.0 MeV). The equivalent values for γ (during this last period) derived from the Sun-centered MHD simulation are: $\gamma = 2.66$ at low-energy and $\gamma = 3.42$ at high-energy.

The functional dependence of the injection rate Q on VR has been derived as for the Apr00 event. Figure 4.14 shows this dependence for the same energy channels indicated in Table 4.1. Time runs from right to left. For $E < 0.58$ MeV, in order to avoid the contribution to the derived values of Q of the electron contamination, we have only considered the values of Q from $t > 20.0$ hours (doy 274.4) (Figure 4.12) up to t_s. For the remaining energy channels, the first point represents the values of Q and VR at t_c. The solid lines in Figure 4.14 correspond to the derived Q(VR)

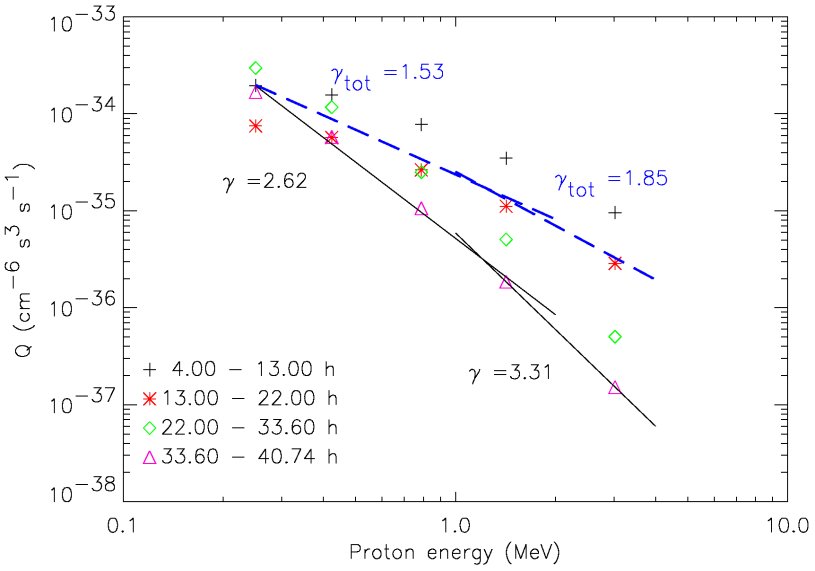

Figure 4.13: Sep98 event. Spectra of Q over the periods indicated in the inset for five energy channels between 195 keV and 4.8 MeV. Black solid line: fit to the points at low and high energies for the last period (triangles), prior to the shock passage. Blue dashed line: fit to the average value over all time intervals.

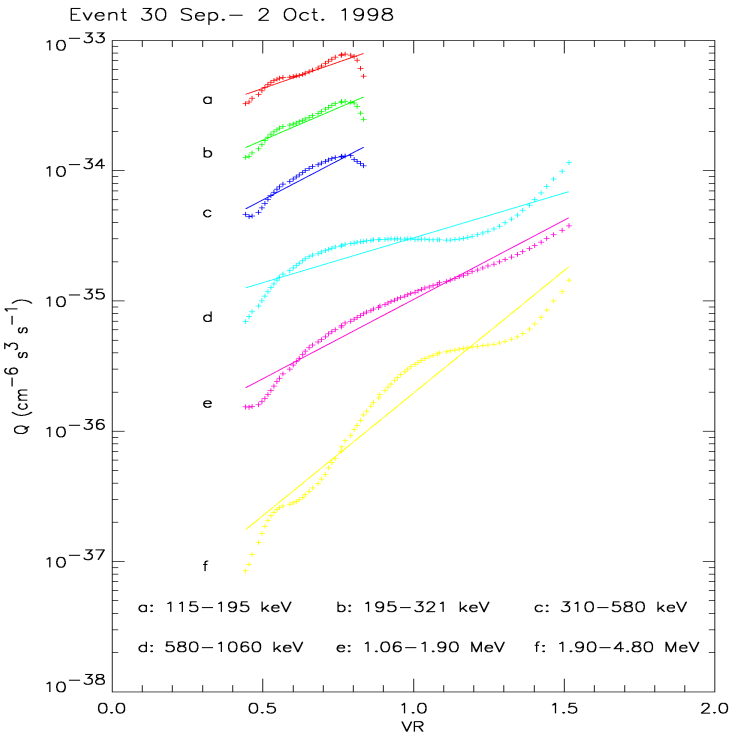

Figure 4.14: Set98 event. The same as in Figure 4.7.

Table 4.2: Sep98 event. Q_0 and k coefficients values for the $Q(\mathrm{VR})$ relation derived from the off-center (labeled with 'n') and from the Sun-centered MHD shock simulation.

E (MeV)	$<E>^a$	Q_{0n} (cm^{-6} s^3 s^{-1})	k_n	${\xi_n}^b$	Q_0 (cm^{-6} s^3 s^{-1})	k	ξ^b
0.195 – 0.321	0.250	*5.5 × 10^{-35}* [c]	*0.99*	*0.92*	*2.0 × 10^{-34}*	*-0.13*	*0.24*
0.310 – 0.580	0.424	*1.5 × 10^{-35}*	*1.21*	*0.93*	*2.1 × 10^{-35}*	*0.48*	*0.74*
0.580 – 1.060	0.789	6.3×10^{-36}	0.69	0.90	9.2×10^{-36}	0.22	0.75
1.06 – 1.90	1.419	6.2×10^{-37}	1.22	0.98	1.3×10^{-36}	0.46	0.92
1.90 – 4.80	3.020	2.3×10^{-38}	1.88	0.96	6.5×10^{-38}	0.47	0.92

[a] Geometric mean energy of each channel.
[b] Regression coefficient of the linear fit.
[c] Values in italics indicate the energy channels with electron contamination.

relation at each energy channel. The values of Q_0 and k are shown in columns 3 and 4 of Table 4.2, labeled as Q_{0n} and k_n, respectively; as well as the regression coefficient, ξ_n. Columns 6 – 8 of this table list the values of the same coefficients but derived from the particle flux fitting and the shock propagation results when using the original MHD model. The differences between both sets of values come from the resulting different evolutions of VR: $\mathrm{VR}_n \in (0.5, 1.6)$ and $\mathrm{VR} \in (0.6, 3.7)$ (see Appendix C.1).

4.4 The 12 – 15 September 2000 event (Sep00)

4.4.1 Observations and modeling

Figure 4.15 shows the proton intensity-time profiles and the main features of the solar wind and IMF (as depicted for Figure 4.5) for the 12 – 15 September 2000 central meridian SEP event. On September 12 (doy 256) a full Halo CME was detected by the SOHO/LASCO/C2 coronagraph at 11:54 UT in temporal association with a M1/2N flare, starting at 1131 UT on the same day and located at S17 W09. The ACE spacecraft detected the passage of an interplanetary shock at 0400 UT on September 15 (doy 259; the vertical thick line in Figure 4.15). The CME driving the shock was directed toward the South and no trace of an ICME is observed just after the shock passage (Zukhov, Cid and Cremades, private communication, 2005).

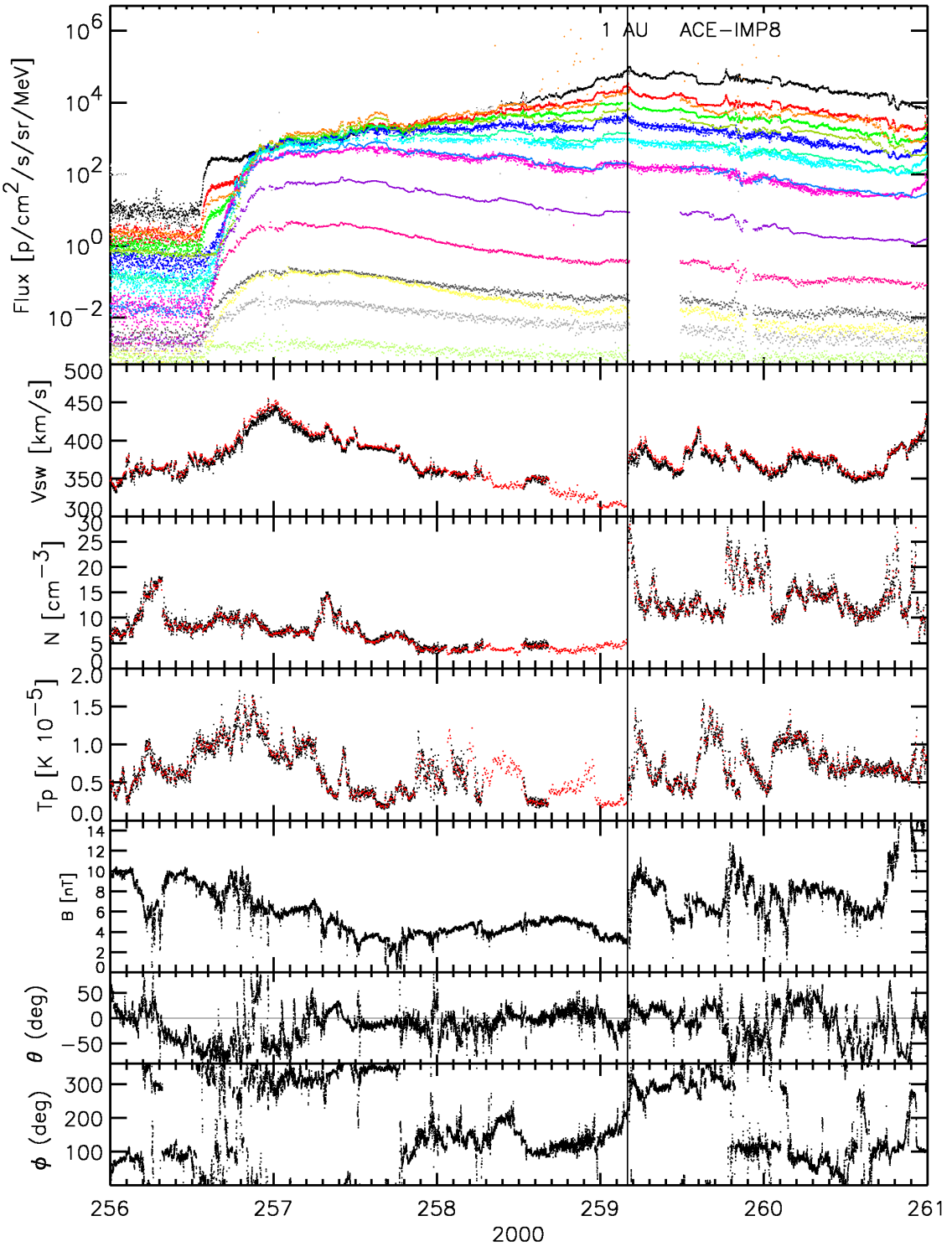

Figure 4.15: Sep00 event. The same as Figure 4.5.

The transit time of the shock is 63.79 hours and the transit speed is 651 km s^{-1}. The onset of the particle event for $E > 0.58$ MeV presents velocity dispersion whereas the lower proton energy channels (from 68 keV to 0.58 MeV) show some contamination due to by-passing electrons (top panel of Figure 4.15)[10].

We have assumed that the 1.0 AU background (undisturbed) solar wind velocity, density and IMF values are 317 km s^{-1}, 5.0 cm^{-3} and 3.4 nT, respectively. The initial pulse shock is characterized by: $v_s = 910$ km s^{-1}, $\omega = 165°$, and $\tau = 1$ hour. The pulse is centered at $10\,R_\odot$ from the center of the Sun and oriented toward the W09 direction. As can be seen in Figure 4.16, the simulated shock fits the shock arrival time at ACE (the derived transit time is 63.77 hours and the transit speed 652 km s^{-1}). The simulated shock reproduces the observed jumps in plasma density (top left panel of this figure) and in magnetic field intensity (bottom right panel). In this case, the obtained jump in the plasma radial speed (bottom left panel) is 1.2 times higher than the observed solar wind speed jump and the temperature jump has been largely overestimated.

From this MHD shock simulation, the observer establishes magnetic connection with the shock front at $t_c = 5.2$ hours. Figure 4.17 shows the position of the cobpoint (two lower panels). At t_c the observer is connected to right wing of the shock front, and hence the initial lower values of VR (second panel of this figure) at this time than to those values derived for the western Apr00 and Sep98 SEP events. As the shock expands into the interplanetary space, the cobpoint slides from the right wing of the shock front toward its nose, resulting in values of VR that smoothly decrease with time, from 1.1 to 0.5. As for the previous events, the time profile of VR obtained from the Sun-centered MHD shock simulation is shown in Appendix C.1. The evolution of BR (top panel) shows a similar profile as that of the April 1979 central meridian SEP event modeled by Lario (1997).

Figure 4.18 shows the fittings of the particle flux and anisotropy performed for the same five energy channels of ACE/EPAM as for the Apr00 SEP event. The blue vertical line indicates the shock arrival time and the vertical dashed line the time of connection t_c. As can be seen, the 0.195 – 1.06 MeV flux profiles (left panels of this figure) smoothly increase up to the shock arrival, without showing a strong ESP component (which is quite different to what is expected to happen in a central

[10]Recently, Cane et al. (2006) have studied the Fe/O abundances of this event. They obtain very low Fe/O abundance values at 3.0 – 10 MeV; thus suggesting that below 10 MeV the SEP event is dominated by shock-accelerated particles, as we assume here.

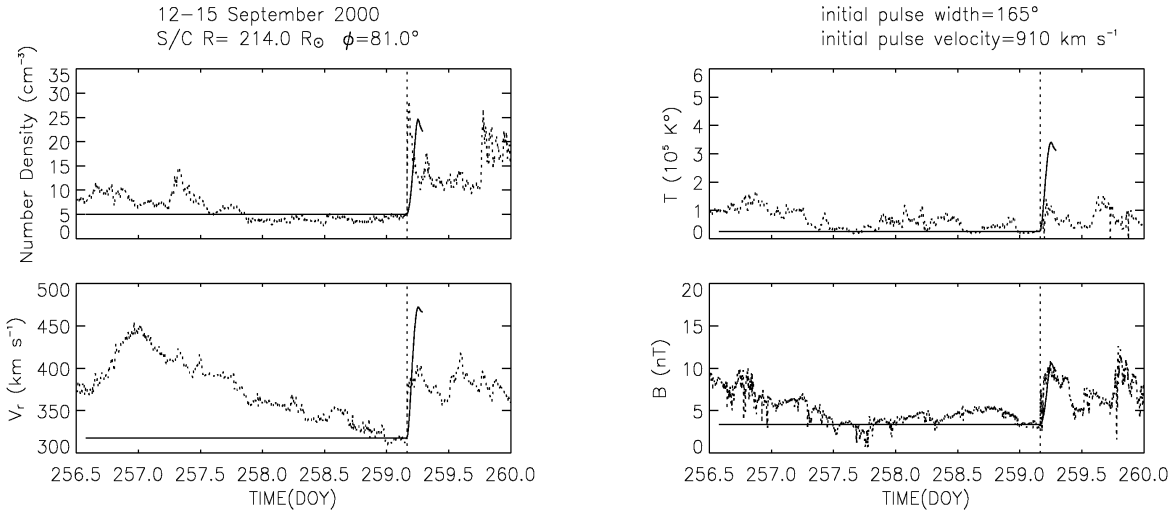

Figure 4.16: Sep00 event. The same as Figure 4.2.

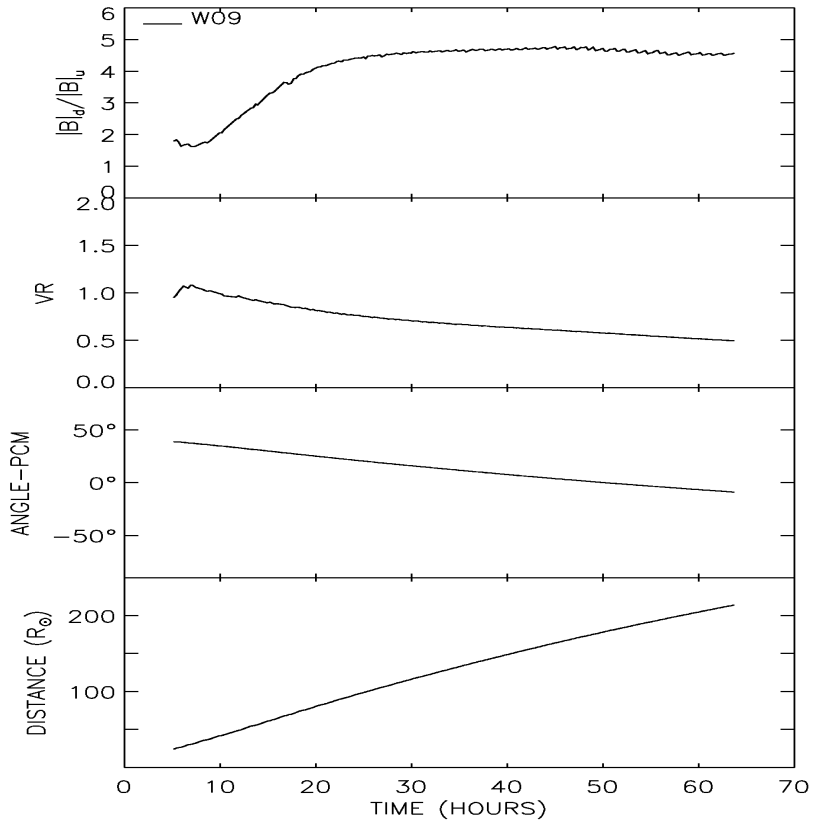

Figure 4.17: Sep00 event. The same as Figure 4.4.

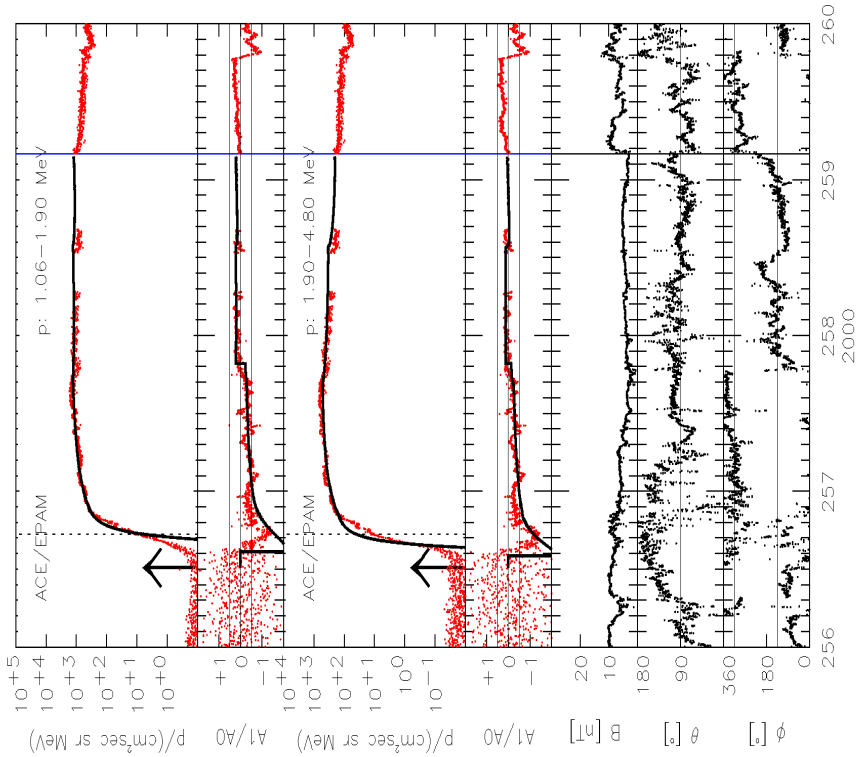

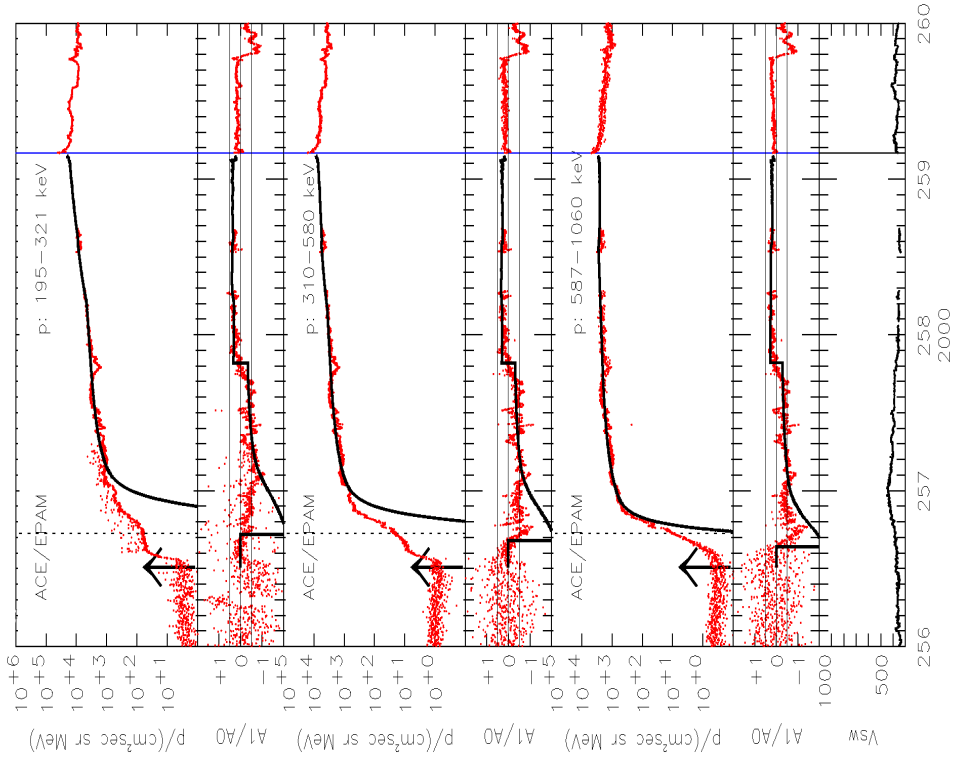

Figure 4.18: Sep00 event. The same as Figure 4.5.

meridian event). To simulate the particle intensities and anisotropies at this energy range, we have assumed a thin (0.04 AU wide) foreshock region from $t >$ 48.0 hours. The proton mean free path within this region is given by $\lambda_{\|c}(R) = 0.01(R/R_0)^{-0.6}$ AU where $R_0 = 38.5$ MV is the proton rigidity at $E_0 = 0.8$ MeV.

The derived proton mean free path is constant throughout the duration of the upstream event, $\lambda_{\|0} = 0.2$ AU, and scales with the particle rigidity as in the previous events. The values derived for the spectral index of $G(E)$ are $\gamma = 1.0$ for $t <$ 31.2 hours, $\gamma = 1.5$ for $31.2 \leq t < 48.0$ hours and $\gamma = 2.0$ for $t > 48.0$ hours. The injection rate before t_c follows a Reid-Axford time profile with $\beta = 7$ hours and $\tau = 2$ hours, and scales with the energy as $E^{-1.5}$. The fittings computed by using the outputs from the original MHD shock propagation model for the same energy channels are shown in Figure 2 of Aran et al. (2005a). The values of the proton mean free path and the spectrum of the injection rate G are the same as the aforementioned values, but the foreshock region is assumed to be active from $t > 36.12$ hours, for all energies, and with $\lambda_{\|0c} = 0.2$ AU.

4.4.2 The spectral index and the $Q(\mathrm{VR})$ relation

Figure 4.19 shows the evolution of the injection rate Q as a function of the geometric mean energy of the modeled differential channels; the format is the same as in the bottom panel of Figure 4.6. The evolution of Q indicates that the interplanetary shock becomes less efficient at injecting high-energy (> 0.58 MeV) protons at the cobpoint as the shock travels away from the Sun (and with increasing particle energy) despite the cobpoint movement toward the leading edge of the shock front. Thus, the slow shock associated with this central meridian event is a poor shock-accelerated particle injector, as suggested by the derived evolution of VR (second panel of Figure 4.17). The values of the spectral indices derived for the interval prior to the shock arrival are: $\gamma = 2.48$ at low-energy ($E < 2$ MeV) and $\gamma = 3.10$ at high-energy ($E > 1.0$ MeV). The corresponding values derived from the Sun-centered MHD modeling are 2.50 and 3.18, respectively.

The linear fits $\log Q = \log Q_0 + k\mathrm{VR}$ to the Q-VR points are shown in Figure 4.20 (solid traces), for five of the modeled energy channels covering the particle energy range between 195 keV and 4.8 MeV. As in the preceding cases, time runs from right to left, and the first point at the left of the figure corresponds to t_s and the

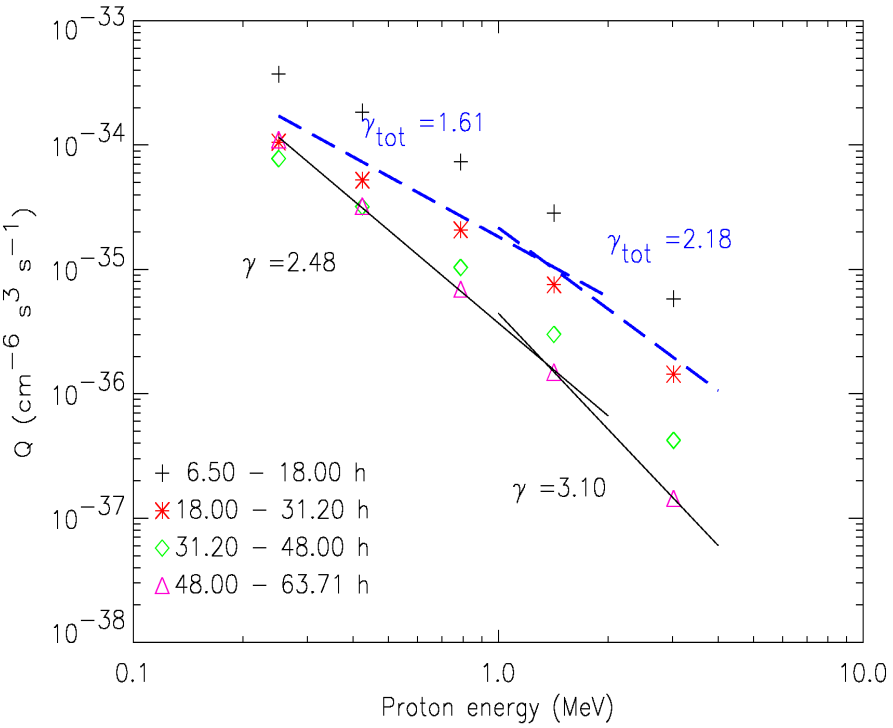

Figure 4.19: Sep00 event. The same as Figure 4.6.

last point at the right to t_c. The values of Q_0, k and ξ derived from these fittings are given in columns 3 – 5 of Table 4.3, respectively. As can be seen in column 5, the regression coefficients obtained for $E > 0.58$ MeV are close to 1. This is not the case for $E < 0.58$ MeV) where the effect of the thin foreshock region during the last 15.8 hours causes the values of Q to oscillate prior to the shock arrival (see Figure 4.20).

Columns 6 – 8 show the values of the Q_0, k and ξ coefficients derived when using the Sun-centered MHD shock simulation output. Again, the derived Q(VR) relations present a higher correlation at high energies than at low energies. The range of values of k obtained for this set of relations (column 7) is larger than that shown in column 4. This is mainly due to the different range of values of VR obtained from the two MHD shock simulations: $\mathrm{VR}_n \in (0.5, 1.1)$ and $\mathrm{VR} \in (0.4, 0.6)$ (see Appendix C.1).

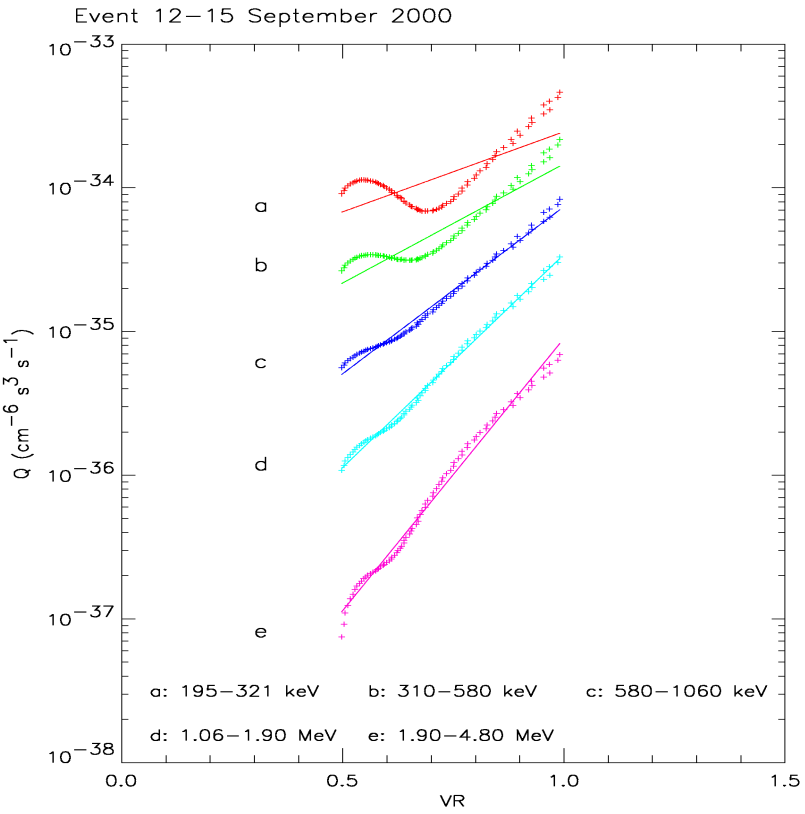

Figure 4.20: Sep00 event. The same as Figure 4.7.

Table 4.3: Sep00 event. Q_0 and k coefficients values for the $Q(\mathrm{VR})$ relation derived from the off center (labeled with 'n') and from the Sun-centered MHD shock propagation modeling.

E (MeV)	$<E>^a$	Q_{0n} (cm^{-6} s^3 s^{-1})	k_n	${\xi_n}^b$	Q_0 (cm^{-6} s^3 s^{-1})	k	ξ^b
0.195 – 0.321	0.250	1.9×10^{-35}	1.11	0.84	1.1×10^{-35}	2.19	0.68
0.310 – 0.580	0.424	3.2×10^{-36}	1.66	0.95	1.1×10^{-36}	3.39	0.85
0.580 – 1.060	0.789	3.5×10^{-37}	2.32	0.99	6.4×10^{-38}	4.81	0.93
1.06 – 1.90	1.419	3.7×10^{-38}	2.96	0.99	4.0×10^{-39}	6.12	0.96
1.90 – 4.80	3.020	1.5×10^{-39}	3.79	0.99	7.6×10^{-41}	7.83	0.98

[a]Geometric mean energy of each channel.
[b]Regression coefficient of the linear fit.

4.5 Summary

We have reproduced the 0.195 – 4.8 MeV proton differential intensities and the first order parallel anisotropies of three gradual SEP events by assuming that the associated interplanetary shocks are the main sources of accelerated particles that contribute to the observed intensities. These shocks have been modeled twice by considering two different initial conditions for the MHD propagation model developed by Wu et al. (1983) (both for the steady-state background and the input pulse location and properties). Both simulations assume wide initial input pulses; for the Sun-centered (or original) MHD shock simulation (Smith & Dryer 1990) we assume $\omega = 140°$ (see Appendix C.1) whereas for the off-center MHD shock simulation we assume $\omega = 165°$. We have chosen a wide input pulse because two of the events (Apr00 and Sep98) were originated from western longitudes and the associated shocks were well observed at 1.0 AU. In addition, the Apr00 and the Sep00 events were triggered by full Halo CMEs; thus, it is reasonable to assume that the shock wave generated ahead of the CME was also wide. For the Sep98 event we have considered the same width in order to obtain the resulting Q(VR) relations under the same conditions as for the other two events.

From the three events modeled here, we can conclude that the Q(VR) relation still may hold for [1] SEP events associated with wide shocks[11] and for proton energies between 0.2 MeV and 4.8 MeV, and [2] central meridian events slightly west orientated (i.e. $< 10°$ from the Sun-Earth line) and western events with parent solar origins westward than W66, since this is the first time that SEP events at these locations have been modeled to obtain the Q(VR) relation.

One of the major concerns when deriving an average Q(VR) relation applicable to a large number of different type of SEP events is the fact that the values of k vary with the particle energy and from event to event (see Appendix E and Tables 4.1, 4.2 and 4.3). From the modeled seven events, we can infer that the shorter the range of VR values, the larger the range of values of k, as well as the higher the values obtained for this coefficient (see Table 4.3 and Table E.1); in Chapter 5 we will come back to this point. Consequently, if we assume that the MHD parameters at the cobpoint determining the injection of shock accelerated particles do not depend on

[11] Note that among the former SEP events modeled, Appendix E, the widest input pulse has $\omega = 90°$.

the particle energy (i.e. VR is independent of the particle energy), it is important to derive an average functional energy dependence of Q that hold for as many SEP events as possible. Obviously, this functional dependence may be refined by modeling a large number of events.

5 The code SOLPENCO

5.1 Introduction

Our long-term objective is the development of an engineering code for characterizing SEP events at user-specified locations in space, from outside the solar corona to beyond the orbit of Mars. This code should estimate time-dependent proton fluxes and fluences of SEP events as a function of the energy over the range 50 keV – 100 MeV, with a friendly user interface. The purpose is to develop an engineering tool for SEP flux and fluence predictions. This aim is hard to achieve, basically because, as already commented, our knowledge of the underlying physics in SEP events is still immature and observational data at different points in space are still scarce. Therefore, the overall strategy adopted is proceeding step by step. We also adopted a modular scheme that allows us to replace different parts of the model and of the operative code as soon as either new updates of the model become available or improvements in knowledge of the underlying physics are achieved so that the different assumptions made in the operative code can be corrected or modified.

The first step has been to develop an operative code known as SOLPENCO (SOLar Particle ENgineering COde). In its present status, rather than a complete operational code for engineering purposes, this code has to be seen as a tool to analyze the aspects of both the theory and modeling of SEP events that must be improved in order to produce useful space weather predictions. Nevertheless, this code can also be used as an engineering tool to predict SEP events only after validation of its procedures and outputs is performed but always keeping in mind its limitations. The complexity of the physical processes involved in generating such SEP profiles makes their simulation especially difficult.

The computational time required to simulate particle flux profiles (from which

fluences can be derived) makes necessary to develop an appropriate tool for space weather prediction and forecasting, particularly if, eventually, we would like to forecast SEP intensities in real time (i.e. be able to predict SEP intensities as a solar event, either a flare or a CME, occurs). The diagram of Figure 3.1 of the shock-and-particle model illustrates the situation: for a given SEP event, instead of computing all procedures indicated in each block of Figure 3.1 (i.e. MHD simulation of shock propagation plus SEP modulation of particle injection and transport), the operational code performs an interpolation of fluxes and fluences of different fiducial pre-built SEP events contained in the data base of SOLPENCO. Thus, the operational tool has two interfaces: the input or initial interface that asks for values of different variables ('proxies' in Figure 3.1) and the output, which yields either a graphic or a set of numeric arrays of the flux and fluences for each given case chosen as input.

A preliminary version of the code (Aran et al. 2001, 2005a) considers a data base containing synthetic proton fluxes at 0.5 MeV and 2 MeV for 288 scenarios where the observer is located at 1.0 AU and 96 cases where the observer is at 0.4 AU. The number of scenarios considered at 0.4 AU represents a first step toward 'exploring and modeling' the main features of SEP events in the innermost region of the interplanetary medium. Instead of expanding our results outward to 1.5 AU, we decided to focus our action on the inner most part of the interplanetary medium because: (i) SEP flux profiles derived for observers located at 0.4 – 0.7 AU could be useful for future ESA and NASA missions such as the Solar Orbiter (Marsden & Fleck 2003), the Inner Heliospheric Sentinels (Szabo 2005) and missions to Mercury or Venus (e.g. Messenger[1] or BepiColombo[2]).(ii) Observations beyond the orbit of Mars are complex to interpret since large SEP events rarely occur in isolation but in a sequence of repetitive events (within intervals ranging from a few hours to 4 – 5 days). SEP transport processes make that separate events at 1.0 AU become merged at large heliocentric distances, and thus individual particle sources are difficult to identify (Lario et al. 2000a). Rosenqvist (2003a) used this preliminary version to check different aspects and outputs of the code; the conclusions of this study[3] have been used to improve several features of the code.

[1]Messenger, http://messenger.jhuapl.edu/the_mission/Messenger.

[2]BepiColombo, http://www.rssd.esa.int/index.php?project=BEPICOLOMBO&page=index.

[3]A main conclusion of the study was: *"It is stressed that no meaningful quantitative information can be derived yet until a fully validated propagation model is available"*. This is not strange because, due to the complexity of the SEP scenario and without performing large and systematic computing runs, it is necessary a large number of simplifying assumptions to derive any significant result, which frequently is rather meaningless.

5.2 The Data Base

The primary purpose of the present version of SOLPENCO is to provide the capabilities to quantitatively predict proton fluxes and fluences of SEP events generated by CME-driven shocks. The energy of the protons ranges from 125 keV to 64 MeV and the velocities of the input pulse that generates the CME-driven shock at 18 $R_\odot$ range from 750 km s^{-1} to 1800 km s^{-1}. The present outputs of SOLPENCO refer to observers located at either 0.4 AU or 1.0 AU from the Sun. The heliolongitude of the parent solar event as seen from the Sun-observer line ranges from E75 to W90 (particularly, a central meridian event, CM or W00, is defined as that directed toward the observer located at either 1.0 AU or 0.4 AU). Four choices for interplanetary particle propagation conditions are also considered: a combination of two possible mean free paths, and the presence or absence of a turbulent region ahead of the propagating shock (foreshock). The set of parameters employed to generate the data base have been selected from the range of values used to model actual SEP events, such as the events described in the former chapter, assuming averaged properties for shock propagation and particle transport.

5.2.1 Basic variables

Flux and fluence values have been calculated using the shock-particle model described in Chapter 3, for each one of the following possibilities:

5.2.A Initial shock pulse speed, v_s: 750, 900, 1050, 1200, 1350, 1500, 1650 and 1800 (km s^{-1}).

5.2.B Initial shock pulse width, ω: 140° (fixed).

5.2.C Observer's heliocentric distances, r: 0.4 AU and 1.0 AU.

5.2.D Heliolongitude of the parent solar activity: W90, W75, W60, W45, W30, W22.5, W15, W00, E15, E22.5, E30, E45, E60 and E75.

5.2.E Solar wind speed: 400 km s^{-1}

5.2.F Mean free paths (at 0.5 MeV), $\lambda_{\parallel 0}$: 0.2 AU and 0.8 AU.

5.2.G Foreshock region: Yes/No option.

5.2.H Proton energies, E: 0.125, 0.250, 0.500, 1.0, 2.0, 4.0, 8.0, 16.0, 32.0 and 64.0 MeV.

For a given observer located at a certain position in space (either 0.4 AU or 1.0 AU), the data base contains 14 values for the heliolongitude of the parent solar event, 8 values for the initial shock speed and 4 values for the energetic particle transport conditions; that correspond to 448 possibilities for the combined shock-particle scenario. Adding the 10 energy channels we have 4480 flux and fluence profiles in the data base. These profiles are stored in two sets (one for 1.0 AU and the other for the 0.4 AU scenarios) of two 6-dimensional arrays with 4480 points. The first contains the flux and the second the cumulative fluence profiles in the upstream region of the shock. Each flux and cumulative fluence profile at 1.0 AU is represented by a vector of 10000 elements, and by 5000 elements for the 0.4 AU case, with a resolution of 1 point every 36 seconds in all cases. Since stored SEP events extend for a period of time that oscillates from ∼10 hours to ∼100 hours, depending on the scenario, only part of these vectors have a non-zero value. The differential flux is given in protons $(\text{cm}^2\ \text{sr}\ \text{s}\ \text{MeV})^{-1}$ and the fluence in protons $(\text{cm}^2\ \text{sr})^{-1}$.

5.2.2 Comments on the adopted values

5.2.A In Chapter 3 we have commented on the indicators of solar activity that can be used as proxies for the initial conditions of the generated coronal-interplanetary shock. The variable that can provide some information about the initial speed of the shock is the mean transit velocity of the shock to travel from the Sun to the measurement location[4], $<v>$. But $<v>$ is not an adequate variable for our purposes since its value can only be determined a posteriori (i.e. once the shock has passed by the observer). Therefore, we have replaced $< v >$ by the initial speed of the pulse, v_s. By looking at the values of $< v >$ derived for a given initial pulse velocity, v_s (Table 5.2, to be commented later), it is possible to derive a simple relation between $< v >$ and v_s for each angular position. This relationship will depend on the angular location of the observer with

[4]Dryer et al. (2004) analyze four different models for real-time shock arrival predictions performed during the SEP events of October-November 2003 based on estimations of the shock speed from metric Type II radio bursts and preliminary CME leading-edge speeds in the plane of the sky. A conclusion of that work is: *"The limitation of this small data set demonstrates, of course, that even with the extreme test presented by the events during this epoch, more of the physics has yet to be learned. Perhaps this can be done with more sophisticated numerical and hybrid 3D MHD models currently under development..."*. For a guideline on how to derive shock speeds from solar coronal radio and white light observations, we refer to Smith et al. (2005) and Manoharan (2006).

respect to the parent solar activity site, since shocks move faster close to their central part than to their flanks (Cane et al. 1988; Smith & Dryer 1990). For example, for an observer located at 1.0 AU and at CM (or W00), $<v>$ is about 85 – 90% of v_s. However, such a relation does not hold for angular positions westward of W60 and eastward of E45 (because there $<v>$ strongly depends on the initial shock speed; see a wider discussion in Appendix F).

The lowest value taken for v_s (750 km s^{-1}) should be considered as a lower limit for the CME to be able to drive an interplanetary shock that will produce a SEP event (i.e. Kahler 2001a and Kahler 2005)[5].

5.2.B Other sets of MHD shocks could be generated with different values of ω ranging, for instance, from 60° to 160°, to take into account both narrow and wide CME-driven shocks. Nevertheless, we have fixed the width of the input pulse, ω, at 140° because: (i) observations of interplanetary shocks at 1 AU estimate a maximum width, only occasionally surpassed, of 180° (Cliver & Cane 1996). (ii) The majority of interplanetary shocks able to produce SEP events are driven by wide CMEs that have the plane-of-sky widths $\geq$ 120° (Gopalswamy et al. 2004, 2005). (iii) The actual limited knowledge about the width of the shocks close to the Sun (that might vary from event to event) turns this exercise useless for space weather purposes[6]. (iv) The numerical grid used for solving the MHD equations has a limited angular extension (180°). And (v) each run of the 2.5D MHD code requires a large amount of computing time and of data storage, which is a technical limitation for exploring different choices of these parameters. This is the main reason why we have also fixed the piston driven duration of the initial shock pulse, τ. It is set to 2 hours, a value used for most of the SEP events we have modeled. See Smith & Dryer (1990) for a description of the influence of these parameters.

5.2.C Other distances could also be considered (1.5 AU, for example) for studying radial gradients; this would have required extra computing time and data

[5]It is worth to consider a comment of this author that reflects the status of knowledge on this topic: *"However, the importance, if any, of CME acceleration in the production of SEP events is still an open question."*

[6]In fact, there is no study devoted to the widths of interplanetary shocks at few ($> 18\ R_\odot$) solar radii. To have an estimation of this parameter, we have to rely on the distribution of CME widths. For instance, half of 144 SEP events studied by Kahler (2005) are associated with Halo CMEs, and 38 of the remaining events have widths > 140°. This author concludes: *"...CME width seems to play a significant role in the production of SEP events, but until we have a better way of determining those widths, we cannot quantify that relationship."*

storage.

5.2.D The range of heliolongitudes of the parent solar activity was extended with respect to the preliminary version of the code and taking into account the extension of the numerical grid of the MHD code. In order to have a homogeneous data base, the same values of heliolongitude are considered at 1.0 AU and 0.4 AU. Hereafter, W22 and E22 will mean W22.5 and E22.5, respectively. Note that the heliolongitudes are measured with respect to the observer regardless of its heliocentric radial distance (either 0.4 or 1.0 AU).

5.2.E The version of the 2.5D MHD shock propagation model used to simulate the CME-driven shocks for the data base of SOLPENCO does not allow us to simulate different solar wind regimes. Consequently, to generate the whole set of proton intensities we have considered a fixed value for the background solar wind speed, according to the solar wind used in the MHD simulations (see details in Smith & Dryer 1990).

5.2.F The mean free path, $\lambda_{\parallel}$, scales with the energy of the particles through its rigidity, R; assuming the QLT approximation. This dependence takes into account the IMF turbulence that we characterize by a spectral index $q = 1.5$ (see Section 3.3). Thus, the mean free path scales with the proton rigidity as $\lambda_{\parallel}(R) = \lambda_{\parallel 0}\ (R/R_0)^{+0.5}$ where $R_0 = 30.635$ MV that corresponds to the rigidity of 0.5 MeV protons and $\lambda_{\parallel 0}$ is either 0.2 AU or 0.8 AU.

5.2.G The turbulent foreshock region is characterized by a mean free path $\lambda_{\parallel 0c} = 0.01$ AU at $E = 0.5$ MeV, and a width of 0.1 AU[7]. This mean free path also scales with the energy as $\lambda_{\parallel c}(R) = 0.01(R/R_0)^{-0.6}$ where $R_0 = 30.635$ MV. The turbulent foreshock region starts acting 20.0 hours prior the shock arrival. This time is the average starting time among the values derived from the actual SEP events modeled. If the duration of the SEP event is shorter than 20.0 hours the foreshock region is assumed to act from the beginning of the event.

5.2.H The reference energy, E_0, is 0.5 MeV. The energy channels corresponding to each energy value are Emin (the minimum energy value) and Emax (the maximum energy value); they are listed in Table 5.1.

The influence of the parameters describing the characteristics of the initial shock pulse (v_s, ω and τ), the heliolongitude of the parent solar event, and the parameters

[7]Bamert et al. (2004) estimates a foreshock 0.11 AU wide for the 14 – 16 July 2000 SEP event.

Table 5.1: Energy bins of SOLPENCO

Energy (MeV)										
E	0.125	0.250	0.500	1.000	2.000	4.000	8.000	16.000	32.000	64.000
Emin	0.088	0.177	0.354	0.707	1.414	2.828	5.657	11.314	22.627	45.255
Emax	0.177	0.354	0.707	1.414	2.828	5.657	11.314	22.627	45.255	90.510

describing the particle transport conditions ($\lambda_{\parallel}$, $\lambda_{\parallel c}$) has been analyzed elsewhere (e.g. Lar98 or Aran et al. 2004).

Tables 5.2 and 5.3 summarize the scenarios depicted for observers at 1.0 AU and 0.4 AU, respectively, as a function of the initial pulse velocity, v_s. Each table lists, for a selected angular position (heliolongitude) of the observer with respect to the parent solar activity, the following information:

(a) Observer's heliolongitude with respect to the parent solar event, or equivalently the heliolongitude of the parent solar event for an observer located on the Sun – Observer line (in degrees).

(b) The connecting time, t_c (in hours), after the occurrence of the parent solar event. That is the time when (i) the magnetic connection between the front of the simulated shock and the observer is established along the nominal IMF, and (ii) the initial cobpoint can be determined (i.e. when VR > 0.1, Lar98).

(c) The heliocentric distance of the initial cobpoint, r_c (in $R_{\odot}$).

(d) The transit time of the shock to travel from the Sun up to 1.0 AU or 0.4 AU, t_s (in hours).

(e) The heliocentric radial distance of the shock, r_s (in $R_{\odot}$), at the time t_s. Its accuracy is determined by the integration grid used in the 2.5D MHD model.

(f) The mean transit velocity of the shock to travel from the Sun to the observer, $<v>$ (in km s^{-1}).

Table 5.2 Shock values derived at 1.0 AU

Table 5.2.1: Initial shock speed, v_s = 750 km s^{-1}

Observer	W90	W75	W60	W45	W30	W22	W15	W00	E15	E22	E30	E45	E60*	E75*
t_c (h)	5.9	5.9	5.9	5.9	5.9	5.9	5.9	6.6	10.6	15.1	20.4	36.9	53.4	77.6
r_c ($R_\odot$)	24.0	24.5	24.5	24.5	24.5	24.0	24.0	25.5	35.5	47.5	61.0	102.1	142.7	202.7
t_s (h)	99.57	91.34	80.73	72.40	66.56	64.40	63.06	61.57	62.23	63.23	64.74	69.07	72.89	80.39
r_s ($R_\odot$)	213.0	213.0	213.0	213.0	213.0	213.0	213.0	213.0	213.0	213.0	213.0	213.0	213.0	213.0
$<v>$ (km s^{-1})	414	451	511	570	620	641	654	670	663	652	637	597	566	513

Table 5.2.2: Initial shock speed, v_s = 900 km s^{-1}

Observer	W90	W75	W60	W45	W30	W22	W15	W00	E15	E22	E30	E45	E60*	E75*
t_c (h)	5.0	5.0	5.0	5.0	5.0	5.0	5.0	5.2	7.9	11.2	15.5	27.3	41.5	62.7
r_c ($R_\odot$)	23.5	24.0	24.5	24.5	24.5	24.0	24.0	23.5	30.4	39.0	50.0	80.1	115.8	169.6
t_s (h)	95.17	82.99	70.99	62.16	56.34	54.34	53.00	51.67	52.34	53.34	55.00	59.50	63.67	72.17
r_s ($R_\odot$)	213.0	213.0	213.0	213.0	213.0	213.0	213.0	213.0	213.0	213.0	213.0	213.0	213.0	213.0
$<v>$ (km s^{-1})	433	497	581	664	732	759	778	798	788	773	750	693	648	572

Table 5.2.3: Initial shock speed, v_s = 1050 km s^{-1}

Observer	W90	W75	W60	W45	W30	W22	W15	W00	E15	E22	E30	E45	E60*	E75*
t_c (h)	4.5	4.5	4.5	4.5	4.5	4.5	4.5	4.5	7.7	9.8	13.0	22.4	34.0	52.4
r_c ($R_\odot$)	24.0	24.6	25.0	25.0	25.0	24.5	24.5	23.5	32.3	37.2	45.1	69.0	99.2	145.1
t_s (h)	89.14	74.32	62.15	53.82	48.49	46.64	45.32	44.15	44.81	45.81	47.32	51.82	55.82	64.48
r_s ($R_\odot$)	213.0	213.0	213.0	213.0	213.0	212.6	212.6	213.0	213.0	213.0	213.0	213.0	213.0	213.0
$<v>$ (km s^{-1})	463	555	664	766	851	883	908	934	920	900	872	796	739	639

Table 5.2.4: Initial shock speed, v_s = 1200 km s^{-1}

Observer	W90	W75	W60	W45	W30	W22	W15	W00	E15	E22	E30	E45	E60*	E75*
t_c (h)	4.1	4.1	4.1	4.1	4.1	4.1	4.1	4.1	6.3	8.3	10.5	18.8	28.2	45.0
r_c ($R_\odot$)	24.5	25.0	25.5	25.5	25.5	25.0	24.5	23.5	29.2	34.1	39.0	61.1	85.8	128.4
t_s (h)	82.59	66.47	54.59	47.25	42.42	40.76	39.59	38.43	39.08	39.93	41.43	45.43	49.25	57.43
r_s ($R_\odot$)	212.7	213.0	212.7	213.0	213.0	213.0	213.0	212.6	213.0	212.4	213.0	212.2	213.0	213.0
$<v>$ (km s^{-1})	499	624	755	873	972	1012	1042	1071	1055	1030	996	904	837	718

Table 5.2.5: Initial shock speed, v_s = 1350 km s^{-1}

Observer	W90	W75	W60	W45	W30	W22	W15	W00	E15	E22	E30	E45	E60*	E75*
t_c (h)	3.8	3.8	3.7	3.6	3.8	3.8	3.8	3.8	4.6	7.0	9.3	16.3	24.7	39.1
r_c ($R_\odot$)	25.0	25.5	25.0	25.0	26.0	25.5	25.0	24.0	24.9	31.0	36.6	55.6	77.1	115.1
t_s (h)	74.78	58.78	48.61	41.77	37.44	35.94	34.95	33.95	34.44	35.44	36.60	40.44	43.78	51.44
r_s ($R_\odot$)	213.0	213.0	213.0	213.0	212.6	213.0	213.0	212.4	213.0	213.0	213.0	213.0	213.0	213.0
$<v>$ (km s^{-1})	551	702	849	987	1102	1146	1180	1215	1194	1164	1123	1020	942	802

Table 5.2.6: Initial shock speed, v_s = 1500 km s^{-1}

Observer	W90	W75	W60	W45	W30	W22	W15	W00	E15	E22	E30	E45	E60*	E75*
t_c (h)	3.4	3.4	3.4	3.4	3.4	3.4	3.4	3.6	4.6	6.6	8.7	14.7	21.9	35.1
r_c ($R_\odot$)	24.5	25.0	25.5	25.5	25.0	25.0	24.5	24.5	25.5	31.0	36.6	53.3	72.3	107.2
t_s (h)	67.36	52.70	43.53	37.36	33.53	32.21	31.20	30.36	30.87	31.70	32.71	36.20	39.36	46.37
r_s ($R_\odot$)	213.0	213.0	213.0	212.7	213.0	213.0	213.0	213.0	213.0	213.0	212.2	213.0	213.0	213.0
$<v>$ (km s^{-1})	612	783	947	1102	1230	1281	1322	1358	1136	1301	1256	1139	1048	889

Table 5.2.7: Initial shock speed, v_s = 1650 km s^{-1}

Observer	W90	W75	W60	W45	W30	W22	W15	W00	E15	E22	E30	E45	E60*	E75*
t_c (h)	3.2	3.2	3.2	3.2	3.2	3.2	3.2	3.4	3.5	5.7	7.9	13.2	19.5	31.4
r_c ($R_\odot$)	25.0	25.5	26.0	26.0	25.5	25.5	25.0	24.5	23.0	28.6	34.7	50.0	66.7	99.4
t_s (h)	60.67	47.67	39.35	33.83	30.17	29.00	28.17	27.34	27.84	28.67	29.67	32.84	35.68	42.00
r_s ($R_\odot$)	213.1	213.0	213.0	213.0	212.6	212.6	213.0	212.5	212.4	213.0	213.0	213.0	213.0	211.9
$<v>$ (km s^{-1})	680	865	1048	1219	1365	1420	1464	1505	1477	1439	1390	1256	1156	977

Table 5.2.8: Initial shock speed, v_s = 1800 km s^{-1}

Observer	W90	W75	W60	W45	W30	W22	W15	W00	E15	E22	E30	E45	E60*	E75*
t_c (h)	3.0	3.0	3.0	3.0	3.0	3.0	3.0	3.0	4.0	5.4	7.4	12.0	17.9	28.2
r_c ($R_\odot$)	25.0	26.0	26.5	26.5	26.0	25.5	25.0	24.0	25.6	28.5	34.7	47.6	64.4	91.6
t_s (h)	55.02	43.34	35.84	30.84	27.51	26.51	25.67	25.01	25.34	26.01	27.00	29.85	32.52	38.51
r_s ($R_\odot$)	213.1	213.0	213.0	213.0	212.6	213.0	213.0	213.0	212.0	212.2	212.4	212.2	213.0	214.1
$<v>$ (km s^{-1})	750	952	1151	1337	1496	1556	1607	1650	1620	1580	1523	1377	1269	1077

Table 5.3 Shock values derived at 0.4 AU

Table 5.3.1: Initial shock speed, v_s = 750 km s^{-1}

Observer	W90	W75	W60	W45	W30	W22	W15	W00	E15	E22	E30	E45	E60*	E75*
t_c (h)	7.4	5.9	5.9	5.9	5.9	5.9	5.9	5.9	5.9	5.9	5.9	8.1	15.4	27.3
r_c ($R_\odot$)	19.8	22.5	23.5	24.5	24.5	24.5	24.5	24.5	24.0	24.0	23.5	29.0	48.5	78.0
t_s (h)	48.72	33.41	29.22	26.06	23.72	22.89	22.40	21.89	22.06	22.55	23.06	24.89	26.57	29.73
r_s ($R_\odot$)	85.6	86.0	86.0	86.0	86.0	86.0	86.0	86.0	85.5	86.0	86.0	86.0	86.0	86.0
$<v>$ (km s^{-1})	345	499	570	639	702	728	743	761	751	739	722	669	627	560

Table 5.3.2: Initial shock speed, v_s = 900 km s^{-1}

Observer	W90	W75	W60	W45	W30	W22	W15	W00	E15	E22	E30	E45	E60*	E75*
t_c (h)	6.4	5.2	5.0	5.0	5.0	5.0	5.0	5.0	5.0	5.0	5.0	6.2	11.7	20.4
r_c ($R_\odot$)	19.7	23.0	23.5	24.5	24.5	24.0	24.0	23.5	24.0	23.5	23.5	25.9	40.5	62.1
t_s (h)	35.50	30.17	25.67	22.16	20.00	19.34	18.82	18.33	18.49	19.00	19.50	21.32	22.99	26.67
r_s ($R_\odot$)	86.0	86.0	86.0	86.0	86.0	86.0	86.0	86.0	85.5	86.0	86.0	86.0	86.0	86.0
$<v>$ (km s^{-1})	469	552	649	752	833	861	885	909	896	877	854	781	724	625

Table 5.3.3: Initial shock speed, v_s = 1050 km s^{-1}

Observer	W90	W75	W60	W45	W30	W22	W15	W00	E15	E22	E30	E45	E60*	E75*
t_c (h)	5.4	4.9	4.5	4.5	4.5	4.5	4.5	4.5	4.5	4.5	4.5	4.5	10.0	16.7
r_c ($R_\odot$)	19.2	24.0	24.0	24.5	25.0	25.0	25.0	25.0	24.5	24.0	23.5	22.5	37.6	54.1
t_s (h)	33.30	27.31	22.48	19.30	17.32	16.65	16.15	15.80	15.98	16.32	16.98	18.48	20.15	23.81
r_s ($R_\odot$)	86.0	86.0	86.0	86.0	86.0	86.0	85.6	86.0	85.5	85.5	86.0	85.4	86.0	86.0
$<v>$ (km s^{-1})	500	610	741	863	962	1001	1027	1054	1036	1015	981	895	827	700

Table 5.3.4: Initial shock speed, v_s = 1200 km s^{-1}

Observer	W90	W75	W60	W45	W30	W22	W15	W00	E15	E22	E30	E45	E60*	E75*
t_c (h)	4.8	4.1	4.1	4.1	4.1	4.1	4.1	4.1	4.1	4.1	4.1	5.1	8.6	14.1
r_c ($R_\odot$)	19.2	23.0	24.3	25.0	25.0	25.5	25.5	25.5	25.0	24.5	24.0	26.5	35.1	48.6
t_s (h)	30.92	24.56	19.92	16.91	15.25	14.58	14.25	13.92	14.08	14.42	14.92	16.42	17.91	21.25
r_s ($R_\odot$)	86.0	86.0	86.0	85.6	86.0	85.5	85.6	86.0	85.5	85.5	86.0	86.0	86.0	85.4
$<v>$ (km s^{-1})	539	678	836	980	1092	1136	1163	1196	1176	1148	1116	1015	930	778

Table 5.3.5: Initial shock speed, v_s = 1350 km s^{-1}

Observer	W90	W75	W60	W45	W30	W22	W15	W00	E15	E22	E30	E45	E60*	E75*
t_c (h)	4.3	3.8	3.8	3.6	3.8	3.8	3.8	3.8	3.8	3.8	3.8	4.0	7.5	12.5
r_c ($R_\odot$)	19.2	23.5	24.5	25.5	25.0	25.0	25.0	25.0	25.5	25.0	24.5	23.5	32.7	45.5
t_s (h)	28.44	22.11	17.95	15.27	13.61	13.11	12.77	12.44	12.61	12.95	13.44	14.77	16.11	19.28
r_s ($R_\odot$)	86.0	86.0	85.6	86.0	85.6	86.0	86.0	85.6	85.5	86.0	86.0	86.0	86.0	86.0
$<v>$ (km s^{-1})	586	753	932	1091	1218	1280	1305	1332	1314	1287	1240	1128	1034	864

Table 5.3.6: Initial shock speed, v_s = 1500 km s^{-1}

Observer	W90	W75	W60	W45	W30	W22	W15	W00	E15	E22	E30	E45	E60*	E75*
t_c (h)	3.9	3.6	3.6	3.4	3.4	3.4	3.4	3.4	3.4	3.4	3.6	3.6	6.6	11.3
r_c ($R_\odot$)	19.1	23.5	25.0	25.0	25.5	25.5	25.5	25.5	25.0	24.5	25.0	23.0	30.2	43.1
t_s (h)	26.04	19.87	16.20	13.70	12.37	11.86	11.54	11.20	11.37	11.71	12.20	13.37	14.54	17.54
r_s ($R_\odot$)	86.0	85.6	86.0	85.6	86.0	85.6	85.6	85.0	85.0	85.5	86.0	85.4	85.4	86.0
$<v>$ (km s^{-1})	640	834	1028	1210	1347	1398	1437	1470	1448	1415	1365	1237	1138	950

Table 5.3.7: Initial shock speed, v_s = 1650 km s^{-1}

Observer	W90	W75	W60	W45	W30	W22	W15	W00	E15	E22	E30	E45	E60*	E75*
t_c (h)	3.7	3.4	3.2	3.2	3.2	3.2	3.2	3.4	3.2	3.2	3.2	3.4	6.0	10.5
r_c ($R_\odot$)	19.2	23.5	24.5	25.5	26.0	26.0	26.0	26.0	25.0	24.7	24.1	23.5	29.6	43.7
t_s (h)	23.84	18.17	14.67	12.66	11.33	10.83	10.50	10.33	10.50	10.67	11.17	12.33	13.34	16.01
r_s ($R_\odot$)	85.7	86.0	85.6	86.0	86.0	85.5	85.2	86.0	85.5	85.0	86.0	86.0	85.4	86.0
$<v>$ (km s^{-1})	696	917	1130	1316	1470	1529	1573	1612	1578	1543	1492	1351	1240	1041

Table 5.3.8: Initial shock speed, v_s = 1800 km s^{-1}

Observer	W90	W75	W60	W45	W30	W22	W15	W00	E15	E22	E30	E45	E60*	E75*
t_c (h)	3.4	3.0	3.0	3.0	3.0	3.0	3.0	3.0	3.0	3.0	3.0	3.2	5.7	9.6
r_c ($R_\odot$)	19.1	23.5	24.5	25.5	26.0	26.5	26.5	26.0	25.5	25.0	24.5	23.5	29.6	41.2
t_s (h)	22.00	16.67	13.51	11.68	10.34	10.00	9.67	9.50	9.67	9.84	10.17	11.34	12.34	14.84
r_s ($R_\odot$)	86.1	85.6	85.6	86.0	85.2	85.5	85.0	85.5	85.5	84.8	84.8	85.5	85.4	86.0
$<v>$ (km s^{-1})	758	995	1227	1427	1596	1656	1703	1743	1713	1670	1615	1459	1340	1123

Note that for observers separated the same angular distance with respect to the parent solar event but in opposite directions, i.e. eastward or westward (e.g. E15 and W15, a single shock arrives first in the case of the eastern events (e.g. E15). This asymmetry is due to the fact that the 2.5D MHD model considers the solar rotation while the shock is injected. Consequently, the energy injected into the interplanetary medium is not symmetrically distributed (Smith & Dryer 1990). The asterisk in the events E60* and E75* indicates that for these events the associated interplanetary shocks are only partially simulated since the domain of integration of the 2.5D MHD model covers only 180° in the ecliptic plane and, because of the angular value adopted for ω, the angular distance between the observer's connection and the farthest flank of the shock is larger than 180°.

5.3 The source of accelerated particles

To produce synthetic flux and anisotropy profiles, the model assumes that the injection rate of shock-accelerated particles is given by $\log Q(t) = \log Q_0 + k\mathrm{VR}(t)$, with $Q_0(E) = C\ E^{-\gamma}$. The applicability of this $Q(\mathrm{VR})$ relation to produce synthetic flux profiles for 'typical' SEP events has been explored by Lario et al. (1995b). The values of k and γ modify the shape and values of the synthetic flux profiles, as well as other variables that define the event (those variables have been studied, for example, by Lario et al. 1995a and Lario 1997 or Sanahuja & Lario 1998). Note that k and γ might be different at different ranges of energy. The energy spectrum measured *in situ* at different times during a SEP event depends on the combined effects of acceleration, injection and transport of the energetic particles that are both energy and time dependent. Therefore, the energy spectrum changes not only from event to event but also throughout the development of a single event, from its onset up to the arrival of the shock and throughout the downstream region of the event (Tylka et al. 2000). In this section we will analyze how the variations of the values of k affect the shape of the flux profiles, we will determine both the average energy spectrum and the parameterization of the injection rate of shock-accelerated particles used to produce the data base of SOLPENCO.

5.3.1 Influence of the k-values in the flux profile

The range of values of k derived from the Q(VR) relation is not well established yet because the number of SEP events already modeled is small. The values of k can also vary with the energy (see Appendix G of Lario 1997 and Chapter 4). Lar98 discusses this point, concluding that most probably this is a consequence of not having a more precise description of the MHD conditions at the front of the shock (a limitation imposed by the performance of the MHD code) and that this relation only partially describes the influence of the MHD conditions at the cobpoint (see discussion in Section 3.5.4). Unfortunately, the value adopted for k can have a strong influence in the profile of the synthesized fluxes, specially its variation with energy and the in the shape of the late phases of the event. This is an important issue to cope with in space weather modeling because in many SEP events the high energy fluxes start decreasing at some point before the arrival of the shock, while the low-energy fluxes keep increasing until its passage (see, e.g. Figures 2.3 and 2.4). The situation is even worse at high energies ($\geq$ 10 MeV) because the difficulties in getting reliable anisotropy measurements that would increase the number of constraints to use when determining the parameters of the model to simulate actual SEP events. The straightforward conclusion is that the possible range of values for the coefficient k should be thoroughly analyzed. Our contribution to shed light on this point has been studying and modeling a number of SEP events (Chapter 4) to gain insights on the role of k, but further analysis is needed. Appendix D shows three examples that illustrate the dependence of the intensity-time profiles on the values of k, from low to high energies.

5.3.2 The spectral index γ

The energy spectra of the differential flux, $j(E)$, measured *in situ* at different times during a SEP event, is often characterized by either a double power law with a knee[8] energy (see Section 2.1.5), or a Bessel function or an exponential-potential law[9] (Tylka et al. 2001). The energy spectra measured *in situ* throughout a SEP events are the result of a combination of acceleration, injection and transport processes.

[8]Also refereed as rollover energy or energy turnoff, depending on the functional dependence assumed.

[9]Exponential-potential law: $j(E) = j_0 E^{-\gamma} exp(-E/E_0)$, where E_0 is the e-folding energy and j_0 a normalization constant (Jones & Ellison 1991).

Theories of diffusive shock acceleration predict that energetic particle distributions in the vicinity of the shock tend to form a power-law in energy (Lee 1983). However, particles that propagate beyond a free escape boundary upstream of the shock leak onto the upstream IMF lines and they do not undergo further acceleration.

The energy spectra of the escaping particles when they arrive at the spacecraft depend on the transport processes they undergo. Since the escape of a particle from the shock is governed by the scattering processes (that depend on the energy of the particle), the effects of shock acceleration are limited in energy. Higher energy particles escape more easily from the shock than lower energy particles, which remain near the shock and hence get accelerated more efficiently. The consequence is that spectra observed close to the shock have power-law dependences at low-energies whereas particle intensities decay faster as we move to higher energies. The knee-energy where this energy dependence changes varies from event to event but it is usually observed above 10 MeV (Tylka et al. 2000) whereas at lower energies ($E < 2$ MeV) the energy spectra is well described by a power law, $j(E) = j_0 E^{-\gamma}$, in particular around the arrival of the shock (van Nes et al. 1984). Therefore, if we want to use reasonable values for the spectral index of the injection rate Q, we should compare the synthetic spectra derived from SOLPENCO with those of energetic particle intensities observed around the shock passage, and basically not affected by transport processes (for details on how the transport processes affect the spectrum of the proton flux at shock see an example in Aran et al., 2004). At low energies and for typical shock-associated SEP events this is -approximately- the time when the particle flux reaches its maximum intensity.

Since the SEPs energy spectrum varies from event to event, we have preferred to assume a reasonable dependence of the flux with the energy, that is, to determine the spectral index, γ. The main difficulty is to understand and define what 'reasonable' in the present scenario means. A thorough literature survey (up to 2003) of proton energy spectra observations around the shock passage has given the following meager results:

(a) At low-energy ($E < 2$ MeV)

- van Nes et al. (1984): $\gamma = 2.05$; this is an average value over 46 proton events observed by ISEE-3, for energies between 35 keV and 1600 keV.
- Reames et al. (1997a): $\gamma = 2.33$; IMP-8 observation; one proton event, for energies between 0.1 MeV and 2 MeV.

(b) At high-energy ($E \geq 2$ MeV)

- Reames et al. (1997a): $\gamma = 2.46$; IMP-8 observation; one proton event, for energies between 24MeV and 80 MeV.
- Torsti et al. (1999): $\gamma = 2.30$; SOHO observation; one proton event, at energies < 85 MeV.

At energies higher than 10 MeV, there are a number of studies that analyze the spectral index at proton peak intensities for several SEP events:

- Cane et al. (1988) reported a wide range of values for the spectral index for $24 < E < 81$ MeV derived at the peak intensity for 235 proton events from May 1967 to the end 1985 (data from IMPs 4, 5, 6, 7 and 8 and ISEE-3)[10]. Figure 5.1 (Figure 14 of Cane et al. 1988) shows that the spectral index varies from 1.5 to 7.1, from event to event as a function of the position (longitude) of the observer with respect to the solar parent activity. Figure 5.1 is comparable to Figure 10 of van Hollebeke et al. (1975). These authors studied the spectral index as a function of the heliolongitude for 20 – 80 MeV protons of 125 events in the period from May 1967 to December 1972. Both studies show similar trends: most of western events and far eastern events have values of the spectral index, γ, that vary from 2 to 4 and central meridian events show the steepest spectra.

- Kahler (2001b) analizes the peak integral intensities for protons with $E >$ 10 MeV and $E > 60$ MeV for 71 SEP events (GOES data) in the period from 1986 – 2000. This author derives a differential energy power law with $\gamma = 3.0$.

The values derived from these studies, although indicative, are not applicable to use as the spectral index around the shock, since in most of the events, the peak flux is achieved at different times for different energies, and do not necessarily coincide with the shock arrival.

As far as we know, these are the clearest values found in the literature useful to our purposes. After years of study, the situation is far from being clear and there is not a definitive single expression to depict the energy spectra[11]. It is hard to define

[10]The peak intensity may occur at different times for different energies; specially at high energies, it may occur at or well before the shock passage.

[11]For example, Freier & Webber (1963) conclude that the particle rigidity exponent is the best way to describe the energy spectra. van Hollebeke et al. (1975), however, show that a power-law

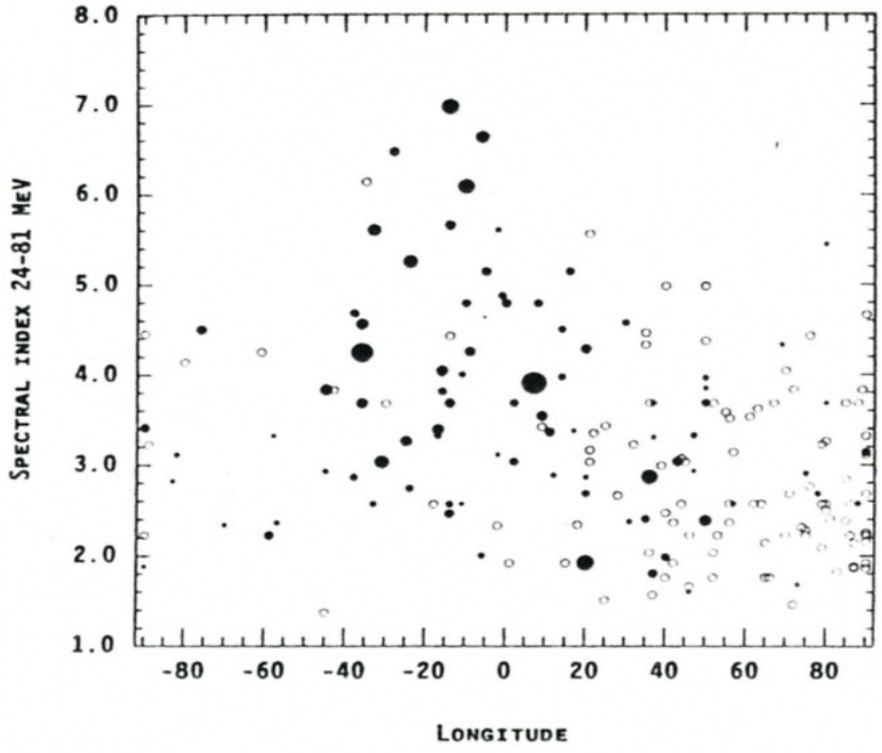

Figure 5.1: Spectral indices derived for proton event, derived from comparing observed fluxes in the 24 − 81 MeV range (from Cane et al. 1988).

an average value for the spectral index at high energy because of the disparity of values. It is worth to visualize with a simple example what are the implications of this indefinition when forecasting. Assuming a turnoff energy between 5 and 10 MeV, the injection rate of 100 MeV-particles is $\sim 8 \times 10^3$ times smaller than the injection rate of 5 MeV-particles if $\gamma = 5$ instead of $\gamma = 2$. Hence for, it is clear that a more elaborated statistical analysis of the spectral indices of SEP events is needed. Such study should consider the possible variation of the spectral index with the strength of the shock and heliolongitude of the solar parent activity (as can be inferred from Figure 5.1).

From the first models (He952) up to now, we have already modeled sixteen

on the energy also gives a suitable quantitative description. Mazur et al. (1992) conclude that the spectra can be reasonably well described by a modified Bessel function (and not so well by a power-law energy function with exponential energy turnoff, below 10 MeV). Mottl & Nymmik (2003) indicate that this dependence is a power-law function of the particle momentum with a varying spectral index which also depends on the energy (see also Section 2.1.5).

SEP events. The conditions or assumptions made in these simulations have not been always the same, especially with respect to the MHD modeling of the shock propagation. In that sense, we have evaluated which ones of these simulations represent a coherent set of events. We have remodeled a few of these SEP events in order to see the robustness of the simulations under different assumptions, and we have simulated new SEP events under the same assumptions (Chapter 4). At present, this set is formed by the following events: (a) using data from ISEE-3 (see details in Appendix B (Lar98): 18 February 1979 (Feb79, an E59 event), 24 April 1979 (Apr79, E10), 8 December 1981 (Dec81, W40) and 26 April 1981 (Apr81, W50); (b) from ACE (see details in Chapter 4): 6 April 2000 (Apr00, W66), 15 September 2000 (Sep00, W09), 2 October 1998 (Oct98, W81). The values of the spectral index of these simulated events at low and high energy yield an average value at the shock of $\gamma = 1.64$ for $0.1 < E < 2$ MeV, and $\gamma = 3.13$ from 2 MeV to $\sim$20 MeV.

By combining our experience in modeling SEP events and the results of the literature survey, we decide to assume two power-laws with the following spectral indices:

$$\gamma = \begin{cases} 2.0 & E < 2 \text{ MeV} \\ 3.0 & E \geq 2 \text{ MeV} \end{cases}$$

Hereafter we will refer to 'low-energy particles' those with energies < 2 MeV and to 'high-energy particles' those with energies ≥ 2 MeV; otherwise, the particle energy will be indicated. We are aware that we are probably over/under-estimating the fluence at high energies, because $\gamma = 3.0$ is not necessarily a representative value of the whole set of possibilities. Looking at Figure 5.1, a variant to explore in the future is to assume for SEP events with heliolongitudes between E40 to W90 (from -40 to +90, in Figure 5.1) a dependence of the spectral index with the heliolongitude, particularly at high energies ($>$ 20 MeV; Mottl & Nymmik 2003). Alternatively, other expressions such as those derived by Jones & Ellison (1991) or Xapsos et al. (2000) can be taken into account.

5.3.3 Injection rate of accelerated particles. Calibration

In the shock-and-particle model, the injection rate of shock-accelerated protons into a given flux tube is represented by the function G (Section 3.3). This function is related to the injection rate $Q(t, E)$ by $G(t, r, E) = A(r)\ Q(t, r, E)$, where $A(r)$ is

the area of the flux tube at the distance r where the injection of particles occurs (i.e. the cobpoint, see Lario 1997 or Lar98 for details). The energy dependence of the computed flux profiles results not only from the energy dependence of the injection function $G(t, r, E)$, but also, from the transport processes included in our transport equation (i.e. the adiabatic deceleration effect, see Section 3.3). As commented in Section 3.6, the particle transport model provides proton intensities in arbitrary values. Therefore, to translate the intensity values into physical units it is necessary to calibrate them with measurements (a procedure that we call normalization). The procedure we use to normalize the particle intensities in the simulation of real SEP events is described in Appendix A. The differential particle intensities in physical units are given by: $j(E) = K(E)j^{arbi}(E)$, where $j^{arbi}(E)$ is the differential intensity of protons at the given energy, E, provided by the simulation and $K(E)$ is the 'constant' of normalization, which can be energy dependent. In fact, the value of this constant can change from event to event; i.e. it depends on the specifics of the event. This 'constant' allows us to translate the injection rate of particles into physical units:

$$Q(t, r, E) = \frac{K(E)}{A(r)} G(t, r, E).$$

Since $K(E)$ may depend on the particle energy, the energy dependence of the computed fluxes in physical units is affected not only by the energy spectra assumed for $G(t, r, E)$ and the processes of adiabatic deceleration, but also by $K(E)$[12]. As a 'first order' approach we have considered a unique constant of normalization for all heliocentric distances, angular positions and transport conditions. We assume that this constant of normalization depends on the proton energy as E^{-1} since this is the energy dependence between the differential flux and the particle columnar density provided by a simulation (i.e. the distribution function). This approach demands a statistical analysis of many SEP events to determine the average value or values needed to assure the most reliable scaling of the flux and fluence profiles of the data base (see discussion in Chapter 6)[13].

[12] In next versions of the code we plan to assume the same value of the constant of normalization, K, for all energies. In this way the dependence of Q on the energy will be considered solely through the function G.

[13] The assumption of a unique constant of normalization and the particle injection rate dependence on the energy described in this section are different from those formerly considered in Aran et al. (2001). Some of the assumptions made in that preliminary code led to partial inconsistent features (Rosenqvist 2003a) on the flux profiles among events of different heliolongitudes. As discussed in Aran et al. (2004) the present procedure removes all these inconsistences.

The values of Q_0 and k (defined in Section 3.4) derived from the actual SEP events already simulated are listed in Tables 4.1, 4.2 and 4.3 and, in Appendix E for those events formerly modeled. In the following discussion we will refer only to the values derived from the simulations performed without including the modifications of the MHD code described in Chapter 4. According to the range of values covered by k and VR in each case, it is possible to classify the modeled SEP events into two wide categories. The first category includes the following events: E10 Apr79, W81 Oct98, W50 Apr81, W40 Dec81, and W66 Apr00 events. The second category only has two events at this moment: the E59 Feb79 and W09 Sep00 events. The events of the first category have VR values that decrease a factor of 10 to 20 from the time of connection, t_c, to the shock arrival. Further the values of k derived from the simulation are small and with a limited range of variation. Events from the second category show a much shorter range of values of VR, they only vary by a factor of $\sim$2, and the k-values are between 10 and 15 times larger than those of the first category. Furthermore, the values of k at high-energy are larger than at low-energy, by factor of $\sim$2.5 in both events. Roughly speaking, we could say that for the first type of SEP events, k is constant or weakly dependent on the energy, while for the second type of events, k is strongly dependent on the energy. Nevertheless, we have to be cautious with such a division because of the small number of SEP events considered: it is just a working hypothesis that has to be further investigated by modeling a larger number of events.

Taking into account that the majority of the SEP events modeled belong to the first category we decided to build the data base assuming that the energy dependence of the injection rate for all events behave as if all of them belong to this category. This assumption translates into: (i) The use of a unique (averaged) value of k for all energies since k slightly varies with the energy for this type of SEP events, and (ii) the adoption of Q_0-values 'typical' of these events. In this way, the temporal and spatial dependence of Q is determined by VR through the $\log Q(t) = \log Q_0 + k\mathrm{VR}(t)$ relation and the energy dependence is specified through Q_0. Therefore, the next step to perform is the analysis and quantification of the variation of Q_0 with the energy.

The spectral indices derived from the fitting of Q_0 for all the energies modeled (up to 20 MeV in the case of ISEE-3 data) for each event are shown in Figure 5.2; these indices have been labeled 'α' to differentiate them from the values adopted in SOLPENCO (γ).

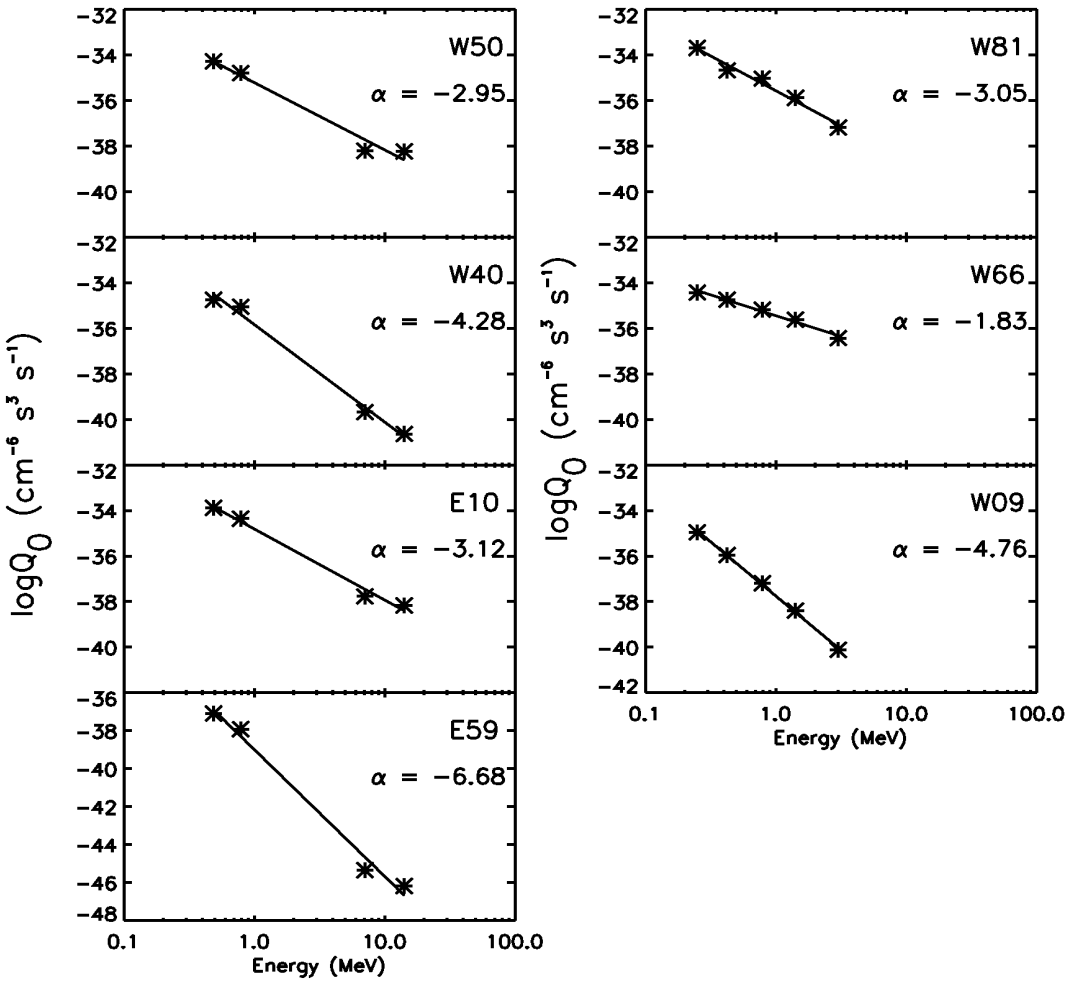

Figure 5.2: Spectral indices derived from fitting Q_0 for all energy channels; the fitted spectral index is labeled 'α' (see text for details).

The fact that the events of the second category (W09 Sep00 and E59 Feb79) show the steepest spectra might mean that either: (i) the associated shocks are inefficient particle-accelerators at high energies (which translates into a large variation of k with energy); (ii) there is a strong dependence of k on the energy due to the fact that the injection rate may depend not only on VR but also on other MHD properties of the shock at the cobpoint, like for instance θ_{B_n}; or (iii) a combination of both possibilities.

As can be seen in Figure 5.2, the spectral index of Q_0 varies from event to event. Therefore, in order to assure a reasonable dependence of the proton fluxes

with the energy, and taking into account that the energy spectrum of SEP events at the shock arrival might be compared to that of the injection rate (see discussion in Section 5.3.2), we assume that Q_0 scales with the energy as a power law with the averaged values of the spectral index obtained in the previous section: $\gamma = 2.0$ at low energies (< 2 MeV) and $\gamma = 3.0$ at high energies (≥ 2 MeV). Therefore, we have to fit Q_0 with these constraints; Figure 5.3 shows the results. The fittings are good[14] for the E10 Apr79, W50 Apr81, W66 Apr00 and W81 Oct98 events and not so good for the E59 Feb79 and W09 Sep00 events (as expected). It is hard to decide how 'good' the fit for the W40 Dec81 event is, because the spectral index γ is the highest when compared with the other events of the first type.

The final step of this process is the selection of the event from which the values of Q_0 and k will be used to build the data base. Among E10 Apr79, W50 Apr81 and W66 Apr00 events, in order to make a first evaluation of the resulting flux and fluence profiles, we decided to use the values of k and Q_0 corresponding to the W50 Apr81 event. We chose this event instead of the W66 Apr00 because it has two high energy channels modeled over 2 MeV while there is only one for the W66 Apr00 event. We also preferred the W50 Apr81 event instead of the E10 Apr79 event because k displays a more regular behavior (E10 Apr79 shows negative values of k, as can be seen in Appendix E).

Consequently, we have built the data base by taking $k = 0.5$, for all energies, and the dependence of Q_0 on the energy as derived from the fitting shown in the top left panel of Figure 5.3. Table 5.4 lists the values of Q_0 for each of the proton energies simulated in the data base of SOLPENCO.

This rather elaborated procedure has allowed us to introduce the dependence of the shock-accelerated particles injection rate with energy through Q_0, without considering any other dependence on the particle energy. An example of the resulting flux profiles can be seen in Figure 5.4. Note that the number of orders of magnitude covered by the flux is similar to what is usually observed from actual SEP events.

For those observers magnetically well connected to the site of the parent solar event, the flux tubes that sweep over the spacecraft are filled with energetic particles from the very beginning of the event (even before the connection time given by the

[14] Within the uncertainties due to the reduced number of events modeled and taking into account that the low-energy channels of the W81 Oct98 event are contaminated (Section 4.3).

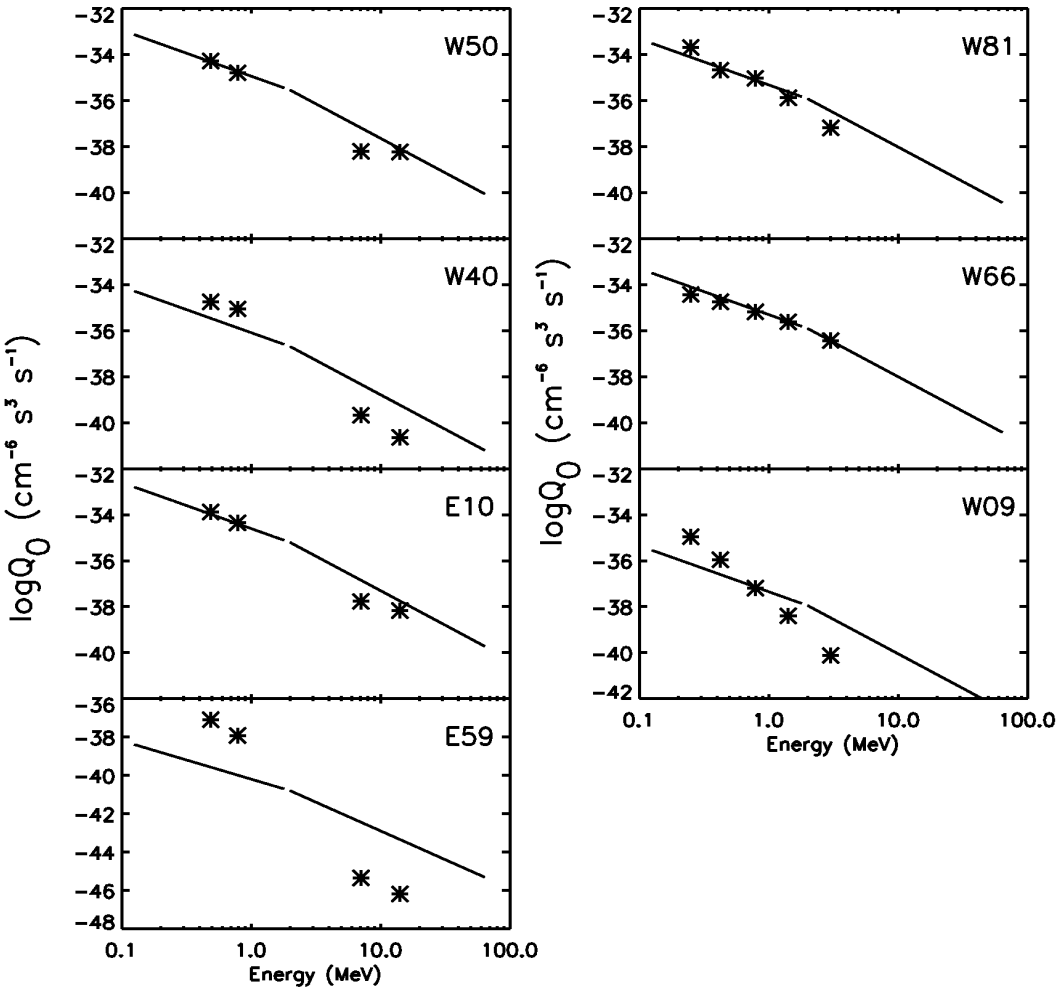

Figure 5.3: Fittings of Q_0 with the energy, forcing the spectral index to be $\gamma = 2.0$ for $E < 2$ MeV, and $\gamma = 3.0$ for $E \geq 2$ MeV.

Table 5.4: Values of Q_0 for the energy bins of SOLPENCO

E (MeV)	0.125	0.250	0.500	1.000	2.000
Q_0 $(cm^{-6}s^3s^{-1})$	7.3×10^{-34}	1.81×10^{-35}	4.6×10^{-35}	1.2×10^{-35}	2.9×10^{-36}
E (MeV)	4.000	8.000	16.000	32.000	64.000
Q_0 $(cm^{-6}s^3s^{-1})$	3.6×10^{-37}	4.5×10^{-38}	5.6×10^{-39}	7.0×10^{-40}	8.6×10^{-41}

MHD simulation). To take into account this fact, it is necessary to introduce an injection of solar particles from the onset of the event up to the connecting time, t_c

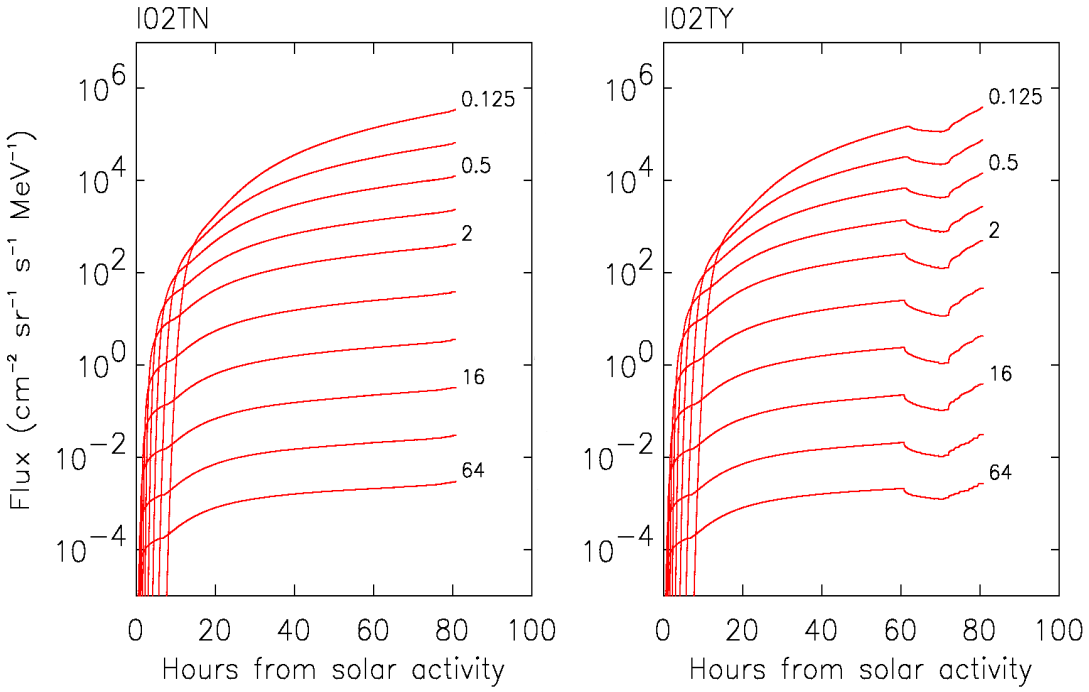

Figure 5.4: Two sets of computed proton flux profiles for ten energies between 0.125 MeV and 64 MeV, for a W60 event associated with a slow shock, generated by an initial shock pulse velocity of 750 km s^{-1}. Right panel flux profiles have been derived assuming the presence of a high turbulent region ahead of the front of the shock; left panel shows the equivalent profiles without the foreshock. The origin of time marks the development of the solar event.

(Sections 3.3 and 5.2). This injection accounts for SEPs accelerated by the shock prior its arrival to the inner boundary of the MHD simulation (i.e. 18 $R_\odot$) and permits to take into consideration the effects of a possible coronal shock (Section 2.1.3), or the existence of an impulsive injection of particles (e.g. "CME/eruptive flare"; Cliver 1995). The time profile of this injection can be constant or follow the time profiles proposed by Reid-Axford; more details of this procedure can be found in He925 and Lar98.

In order to avoid an increase of the number of parameters defining the data base of SOLPENCO, we have assumed in all well-connected events a constant solar injection rate of protons[15]. This is the case for all observers at 1.0 AU located from

[15]As the inner condition of the MHD shock model is located at 18 $R_\odot$, in the western well-connected events we cannot discern the real value of t_c, since the injection of shock-accelerated

W90 to W00 (thus, for all western events). Because of the nominal Parker spiral assumed for the upstream IMF, an observer located at 0.4 AU is considered to be well-connected for heliolongitudes ranging from W75 to E30. We assume that this first injection of particles is constant throughout the short time interval from the onset of the event up to t_c. To derive the constant value of this injection rate for each event of the data base, we have assumed that there is no discontinuity between the injection rate of energetic particles before t_c and that assumed once the observer and the shock establish magnetic connection.

Finally, just to recall that we are implicitly assuming that the effect of corotation[16] is not important. It has not been considered when computing the flux profiles of the data base of SOLPENCO. Lar98 demonstrates that in some cases – at 1.0 AU for western events – this effect could modify the computed flux by a factor of 1.4 at maximum. The corotation effect will be minimal for short-duration events ($\lesssim$ 1 day) and at 0.4 AU where the events last shorter than at 1.0 AU.

5.4 SOLPENCO's procedure

5.4.1 The initial user interface

The initial interface of the code is a graphic interacting window where the user can select the characteristics of the SEP event to be studied. Figure 5.5 shows an example of this interface. The user specifies there the values of the variables described in Section 5.2.1, except the initial shock pulse width, ω, and the solar wind speed:

- The initial velocity of the shock, v_s: between 750 km s^{-1} and 1800 km s^{-1} (the internal code name for this variable, VELOS)
- The location of the spacecraft:
  (i) The heliocentric radial distance, r: 0.4 AU or 1.0 AU (DISTRAD)

starts before than this connecting time.

[16] An Earth-orbiting observer (for example) will scan different magnetic flux tubes, filled with shock-accelerated protons injected from eastern regions of the front. This yield to changes in the flux as a result of the spatial evolution of the IMF. This effect is generally ignored and only has been discussed or considered by Lario (1997), Kallenrode & Wibberenz (1997) and Lar98 (e.g. their Figure 14).

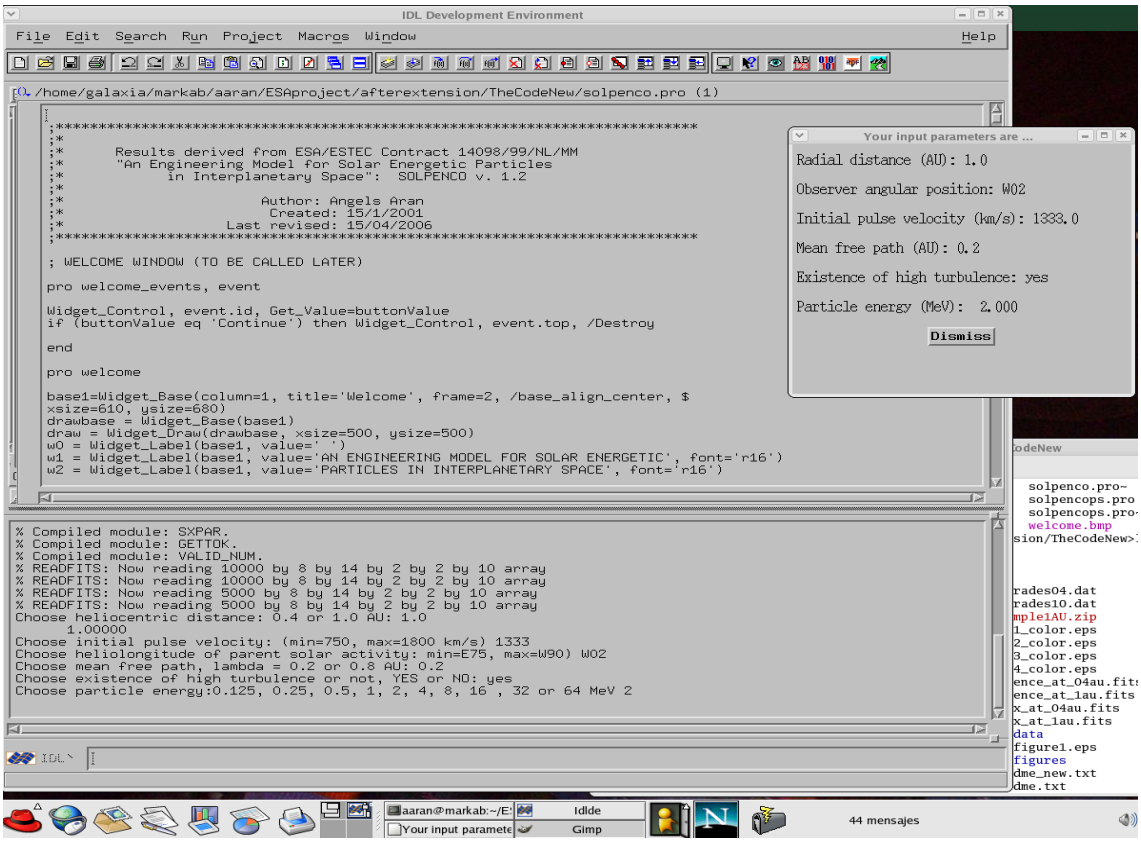

Figure 5.5: The initial interface of SOLPENCO.

(ii) The relative angular position with respect to the parent solar event: between W90 and E75 (POSANG)

– The proton mean free path: $\lambda_{\|0}$: 0.2 AU or 0.8 AU (LAMBDA)

– The presence of a turbulent region ahead of the shock front: Y/N option (TURB)

– The energy channel, E: 0.125, 0.25, 0.50, 1.0, 2.0, 4.0, 8.0, 16.0, 32.0 or 64.0 MeV (ENERG)

SOLPENCO software is written in IDL (5.4 version) language, which is also used as interface language. The code also runs successfully under IDL 6.0. A summary of SOLPENCO's technical characteristics and procedures is given in Appendix H together with a list of modifications and improvements done to the code from 2001 to present day. SOLPENCO is available on request at the website of the Solar-Terrestrial Physics and Space Weather Group of the University of Barcelona[17] and

[17]http://www.am.ub.es/~blai

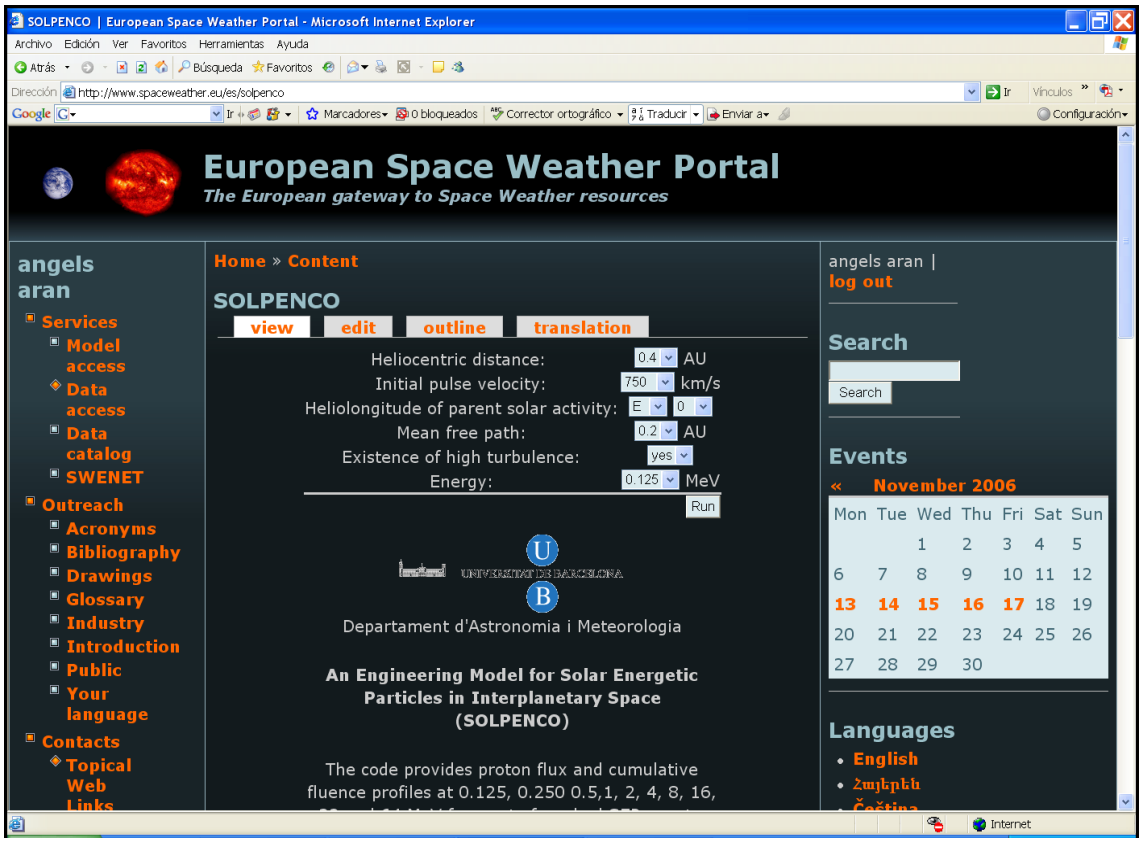

Figure 5.6: The initial interface of SOLPENCO at the European Space Weather Portal.

an it can be run on-line the web of the European Space Weather Portal[18]. Figure 5.6 shows an example of this interface.

The program can detect wrong or out of range input values for any variable; in this case, it asks for a new input value. Once all values have been correctly selected within the possible choices, the program shows a small display summarizing the user's selected input data. Once the values of the input variables have been fixed by the user, the IDL subroutine INT3.PRO interpolates the calculated data out of four arrays in FITS format. The main program is SOLPENCO.PRO, and the following non-standard IDL routines are needed: readfits.pro, gettok.pro, ieee_to_host.pro, strnumber.pro, sxaddpar.pro, sxdelpar.pro, sxpar.pro and wherenan.pro. All of them are part of the public IDL Astronomy User's Library[19]. Finally the code permits to save the selected event in a graphical and/or text (ascii) file. The name of these files

[18]European Space Weather Portal. The European gateway to Space Weather resources (an initiative of the COST724 Action), http://www.spaceweather.eu/es then register and go to 'Model access' and to SOLPENCO.

[19]Available at http://idlastro.gsfc.nasa.gov/ or under request.

identifies the event by means of a coded label that displays the values of VELOS, POSANG, (initial angular width, ω), DISTRAD, LAMBDA, TURB and ENERG. For example: W450750W10l02TNE3 refers to a SEP event defined by POSANG = W45, VELOS = 750 km s^{-1}, the following 'W', means that this is a wide shock (ω is fixed, thus it always appears in this version of SOLPENCO), DISTRAD = 1.0 AU, LAMBDA = 0.2 AU, TURB = No and ENERG[20] = 1 MeV. In this report we usually refer to a SEP event using the first four variables, that is, without specifying the transport conditions and the energy of the particles (i.e. W450750W10 in this example).

5.4.2 Internal structure of the data base

The internal structure of the flux and fluence arrays is as follows:
for the flux (array 'F')
F04 (j1, j2, j3, j4, j5, j6) = fltarr (5000, 8, 14, 2, 2, 10)
F10 (j1, j2, j3, j4, j5, j6) = fltarr (10000, 8, 14, 2, 2, 10)
for the cumulative fluence (array 'fl')
fl04 (j1, j2, j3, j4, j5, j6) = fltarr (5000, 8, 14, 2, 2, 10)
fl10 (j1, j2, j3, j4, j5, j6) = fltarr (10000, 8, 14, 2, 2, 10)
where j1, j2,..., j6 vary as
j1 = flux or cumulative fluence values
j2 = initial pulse velocity:
VELOS = [0750, 0900, 1050, 1200, 1350, 1500, 1650, 1800] km s^{-1}
j3 = heliolongitude of the parent solar activity
POSANG = [W90, W75, W60, W45, W30, W22, W15, W00, E15, E22, E30, E45, E60, E75]
j4 = mean free path
LAMBDA = [0.2, 0.8] AU at 0.5 MeV
j5 = existence of a turbulent foreshock region
TURB = [TY, TN] (Yes or No)
j6 = proton energy
ENERG = [0.125, 0.250, 0.500, 1.0, 2.0, 4.0, 8.0, 16.0, 32.0, 64.0] MeV

[20]The first symbol is an 'E' (standing for 'energy', variable ENERG) while the second is a digit between 0 and 9; then E0, E1, ..., E9 respectively stand for 0.125 MeV, 0.25 MeV, ..., 64 MeV.

5.4.3 The interpolation procedure

For a given set of parameters defining the event, the program calculates the particle fluxes and fluences by interpolating between the respective values previously calculated and stored for the grid elements defined in the data base. Once the program has identified the input values (for DISTRAD, LAMBDA, TURB, ENERG a unique fixed value, and for VELOS and POSANG, any value within a defined range), the procedure is as follows:

Step 1. The program looks at the data base for POSANG values (here identified as WP) and VELOS values (here identified as VS) that closely bound them:

(a) WP1 $\leq$ WP $\leq$ WP2, with WP1 and WP2 being the closest values of the solar event longitude, WP, in the data base, and
(b) VS1 $\leq$ VS $\leq$ VS2, with VS1 and VS2 being the closest values of the initial pulse speed, VS, in the data base.

Step 2. There are four possible situations:

(a) WP = WP1 = WP2 and VS = VS1 = VS2. In this case the selected event is already contained in the data base and the code delivers the precalculated particle flux and/or fluence profiles without performing any interpolation.
(b) WP = WP1 = WP2 and VS1 $<$ VS $<$ VS2. The program performs a single interpolation of values for VS.
(c) VS = VS1 = VS2 and WP1 $<$ WP $<$ WP2. The program performs a single interpolation of values for WP.
(d) In any other case, which is the most frequent situation, the program performs a double interpolation of values for WP and VS.

'Performing an interpolation' here means that the code calculates the flux profile for a (VS, WP) pair, from the flux profiles contained in the data base, performing a simple linear interpolation, as described below, from the four cases: (VS1, WP1), (VS1, WP2), (VS2, WP1) and (VS2, WP2).

The basic problem with these interpolations is that the duration of each event (i.e. the time elapsed from the onset of the event until the arrival of the shock) is different for each of these four events. Each flux profile has been built up with particles accelerated by a shock (it can also have an initial solar component, but this makes no difference here). The shocks of the events to interpolate have different

velocities or different transit times from the Sun to the observer and, moreover, the observers of the events to interpolate are located at different positions with respect to the front of the shocks. For example, for two observers at 1.0 AU located at W45 and W22, the transit time of the shock to travel from its origin to the observer is shorter for the W22 observer (Table 5.2) than for the W45. Consequently, it is not possible to make a straightforward identification among the values of the particle flux at a given time, or in a given position in space, from which we can derive the interpolated value. To reasonably solve this question, we can imagine a dense grid of POSANG (WP) and VELOS (VS) values. The differences between adjacent points of this grid would be small. The corresponding points of the flux for the four cases (VS, WP) would be easily identified, within small errors. Thus, the first thing to do is to build up a (VS, WP)-grid of values dense enough to reduce the errors; the main constraint is, of course, the final size of the data base.

In order to calculate the shock transit time from the Sun to the observer for the required event, it is necessary to estimate its transit shock velocity, $<v>$, from the values of $<v>$ obtained when running the MHD code for each one of the eight shocks (as commented in Section 5.2.2). We consider two different cases: (i) the pair of events to be interpolated have the same initial shock speed, VS or (ii) the pair of events have the same heliolongitude, WP. Figure 5.7 shows the values of $<v>$, derived for each one of the eight shocks used to generate the data base (identified by their initial pulse velocity, VS; symbol coded), for each of the fourteen observers located at 1.0 AU with angular positions ranging from E75 (WP = -75) to W90 (WP = +90). We have fitted the transit velocity of the different angular positions for each one of the eight MHD shocks with a fourth degree polynomial. This fitting allows us to calculate the transit time of the interpolated event between two events with the same VS but different longitudes, case (i), with better accuracy than when calculated by a simple linear interpolation between the values of their respective time of arrival. As can be seen in this figure there is a slight east-west asymmetry in the $<v>$ -values derived from the MHD code (see Section 5.2 and Appendix F). Therefore, we performed two fittings for each observer located 1.0 AU, one for the western events (from 0 to 90) and another for eastern events (from -75 to 0), thus, both including the central meridian event.

Figure 5.8 shows the set of fits of the shock transit velocity for the observers of the data base located at 0.4 AU. These fittings are obtained by following the same procedure as the 1.0 AU case. As can be seen, both sets of curves display similar

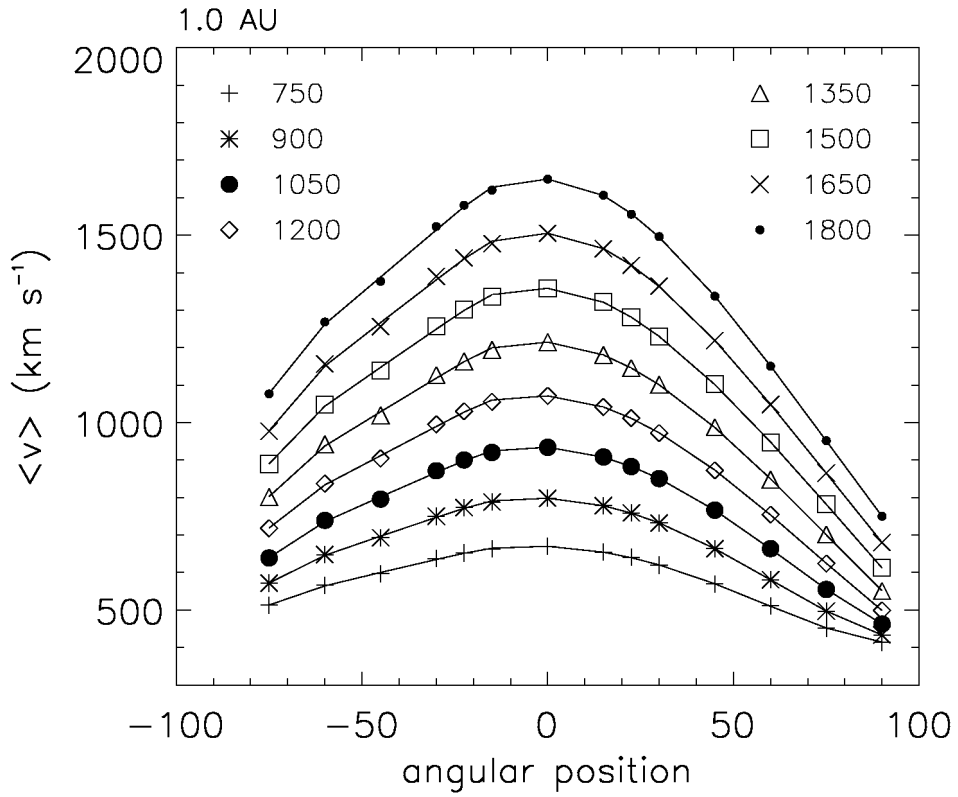

Figure 5.7: The resulting fits of the transit velocity at 1.0 AU, $< v >$ for each shock, as a function of the angular position and the initial pulse velocity, from eastern events (E75 = -75) to western limb events (W90 = +90). Curves from top to bottom represent the polynomial fittings performed.

shapes, except for farthest western angular position (W90) of the slowest shock. In this interplanetary scenario, the cobpoint of the observer located at 0.4 AU scans the most distant part of the weak right wing of the shock front. The debilitation of the slowest shock in its weakest flank produces a larger reduction of its transit speed than that obtained for the rest of the shocks. The coefficients of the polynomial fits shown in Figures 5.7 and 5.8 are given in Appendix F.

When the pair of events to be interpolated have the same angular position but different speed, case (ii), we estimate the transit speed of the interpolated event by performing a linear interpolation between the values of the transit speed of each of

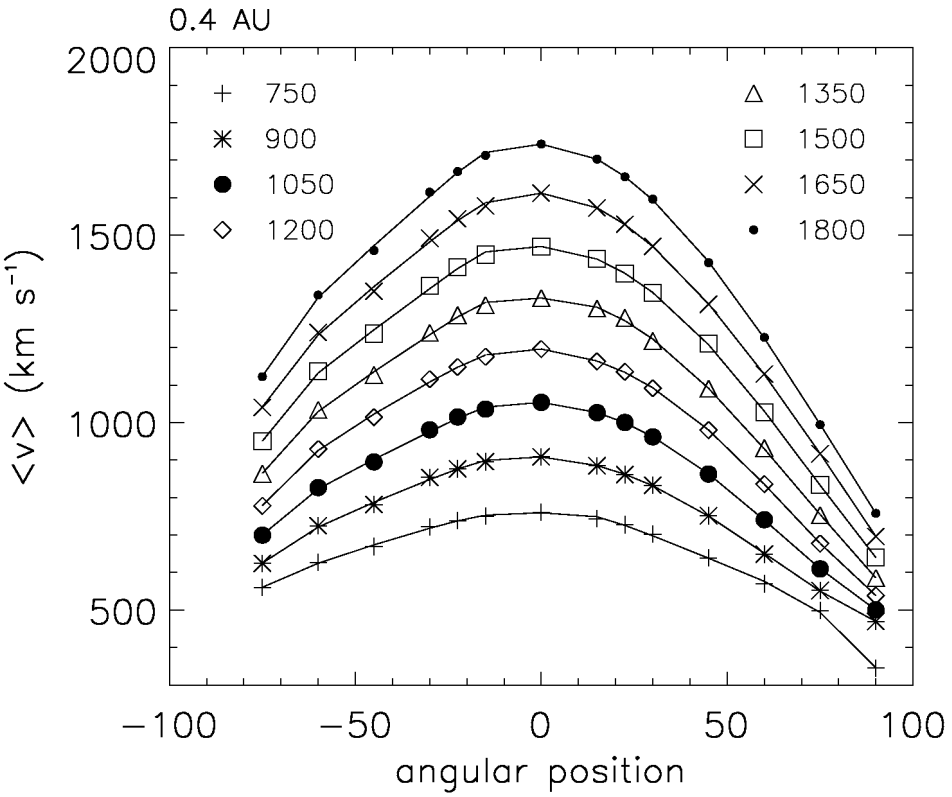

Figure 5.8: The resulting fits of the transit velocity at 0.4 AU, $< v >$ for each shock, as a function of the angular position and the initial pulse velocity. Legend is the same as in Figure 5.7.

the two events, $<v>_1$ and $<v>_2$:

$$<v>=<v>_1 \frac{\mathrm{VS2}-\mathrm{VS}}{\mathrm{VS2}-\mathrm{VS1}}+ <v>_2 \frac{\mathrm{VS}-\mathrm{VS1}}{\mathrm{VS2}-\mathrm{VS1}}$$

The code reads the values of the variables needed to perform the estimations of the transit speeds for the interpolated events from the file 'entrades10.dat' or the file 'entrades04.dat', either for the 1.0 AU or the 0.4 AU choices, respectively. Each one of these files contains:

- The initial pulse velocity,
- the time of the shock passage by the observer's position,
- the shock transit velocity, and

– the five coefficients of the fourth degree polynomial fitting of the transit speed for each shock. First, those corresponding to the western events and, second, those to the eastern events.

The algorithm developed to automatically identify the point of each flux of a given pair of (VS, WP)-values to be used in the interpolation procedure consists of three steps:

Step 1. We multiply the duration of each event by the adequate factor to equate them to the time of the selected event (i.e. a homothetic correction of the time scale). This factor is $< v > / < v >_i$ where $< v >_i$ is the transit shock speed of each of the events to be interpolated.

Step 2. We interpolate the flux between pairs of events. When the required event (VS, WP) is the result of the interpolation among four events in the data base we first produce two intermediate fluxes corresponding, respectively to the pair (VS1, WP1) - (VS1, WP2), identified as (VS1, WP), and to the pair (VS2, WP1) - (VS2, WP2), identified as (VS2, WP).

Step 3. Finally, in the last case, we interpolate the flux between the fluxes derived in step 2, associated with the pairs (VS1, WP) and (VS2, WP); this yields the flux profile which corresponds to the required event (VS, WP).

There are three critical points where this procedure can be incorrectly rated (by a few time points, but enough for generating errors): (1) at the onset of the SEP event, (2) at the shock-connecting time, t_c, and (3) at the time when the leading edge of the foreshock (if exists) reaches the observer's position. As already commented, the errors due to these misidentifications can be reduced by making the size of the grid of the data base smaller (see Section 5.4.4).

5.4.4 Checking the interpolated values

To check how accurately the algorithm for interpolation works, we can compare the flux profiles derived from the interpolation among SEP events contained in the data base to obtain a given intermediate event (also contained in the data base) with the flux profiles directly obtained when running the code for the intermediate SEP event. For example, if we take the cases VS = 1050, 1200 and 1350 and WP =

W15, W30 and W45, it is possible to compare the interpolated flux profile values for VS = 1200 and WP = 30 with the profiles directly obtained from the data base. Figure 5.9 shows the results of such comparison. The two top plots show the two intermediate interpolations between the pair of events with the same VS and the bottom plot the final interpolation (as described in steps 2 and 3 of the previous section). Each plot shows the 0.5 MeV proton intensities (top panel) of the events used to do the interpolation (blue and orange traces), of the interpolated event (black trace) and of the pre-calculated event (red trace) to be compared with the interpolated event. The bottom panels show the relative difference between the flux profiles of the interpolated and pre-calculated events. The vertical solid lines in these plots indicate the time of the shock passage corresponding to the interpolated event. As can be seen, one of the boundary fluxes does not reach this line while the other goes beyond it, also note that these values are different among the plots. The differences between interpolated values and the respective values coming from the data base can be significant at the onset of the event. It must be noted that:

(i) The flux scale (top panel) is logarithmic while the differences (bottom panel) are displayed in a linear scale;

(ii) the differences at the onset of the event that correspond to the lower flux values of the SEP event rapidly decrease (therefore, their influence in the cumulative fluence is even smaller than in the particle intensity);

(iii) the relative differences represent an upper limit of the differences obtained when running the code because the interpolation is performed between non-correlative events (too separate) in the grid of the data base. Appendix G shows more examples of interpolations performed for flux profiles at 0.5 MeV, for a shock with an initial pulse speed of 1450 km s^{-1}.

To summarize, the basic conclusion is that for reasonable situations, and with an adequate grid size, the errors will not be large and, in any case, they will not be relevant to the outputs of the code. Nevertheless, they could be large when the interpolation has to be performed between too different flux profiles, either in duration or intensity, and therefore, it is essential to build up a dense grid of synthetic events.

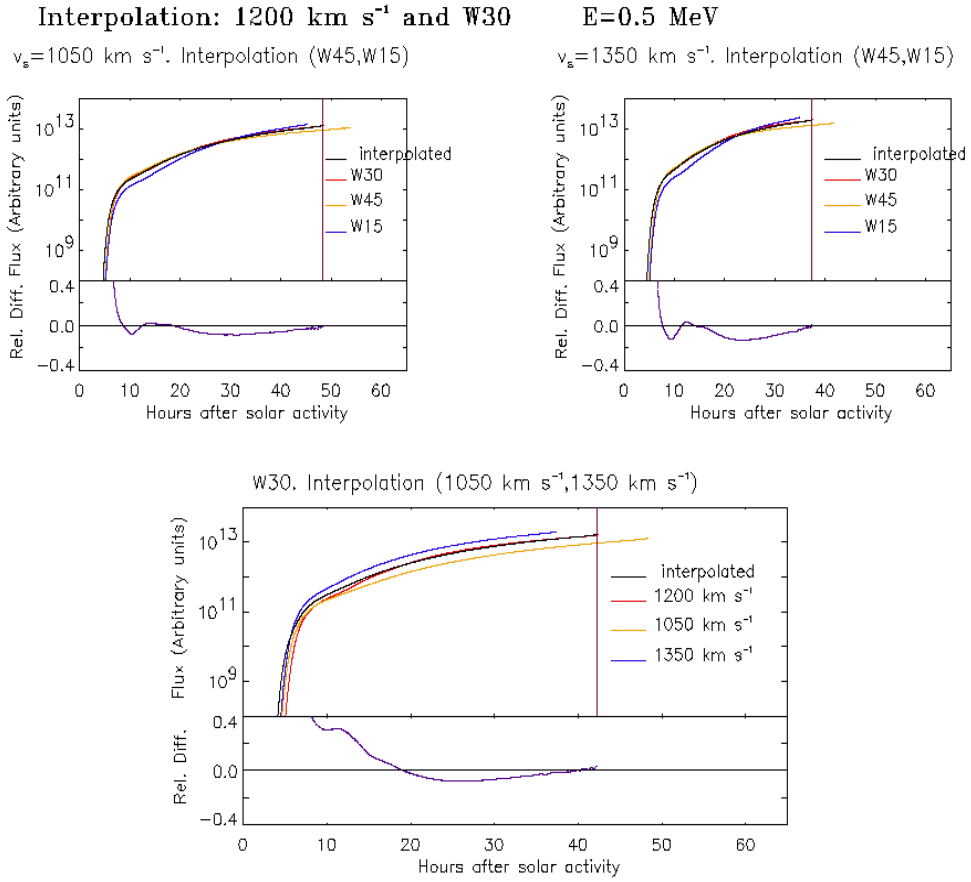

Figure 5.9: Interpolation procedure for the SEP event characterized by v_s = 1200 km s^{-1} and W30. Each plot shows the 0.5 MeV proton flux profiles (top panel) and the relative differences (bottom panel) between interpolated (black trace) and computed (red trace) flux profiles. Vertical solid line indicates the time of the shock passage by the spacecraft of the interpolated event.

5.4.5 Computing the fluence and the peak flux

The cumulative fluence is defined as the integrated fluence from the onset of the SEP event up to a given time and above a given energy. The total fluence of an event is computed from the onset of the event up to the shock arrival. Therefore the last value in time of the cumulative fluence corresponds to the total event fluence. An issue to be addressed in the future (or whenever is possible!) is how to evaluate the contribution to the fluence from the downstream region of the shock, since the shock-and-particle model description stops at the shock passage. Models assuming

particle propagation along Parker spiral field lines in the downstream region of the shocks are wrong because IMF is distorted in this region (Lario et al. 1999). In many cases the downstream contribution to the cumulative fluence is small in front of the upstream contribution (see Section 3.5.3), but this is not always the case. It would be possible to evaluate the contribution of the downstream part by using some empirical approach, but this is beyond our present objectives. Note that in SOLPENCO the fluence is given in [protons $(\mathrm{cm}^2\ \mathrm{sr})^{-1}$]; to translate to [protons cm^{-2}] it is necessary to multiply the values in [protons $(\mathrm{cm}^2\ \mathrm{sr})^{-1}$] by the value of solid angle covered by the detector.

To obtain the grid of fluences for each time, t, and threshold energy, E (one of the ten energies, from 0.125 MeV to 64 MeV), we have integrated the fluxes from the onset of the event, t_0, to t and for all energies above E. The input for this double integration is the calculated set of fluxes of the data base. By using these values, a numerical integration between t_0 and t, and between the threshold energy and 90.51 MeV (which corresponds to the upper limit of highest energy included in the code, see Table 5.1) is performed. Particle flux above 90.51 MeV is also taken into account by assuming a power spectrum for the flux, $\gamma = 3$, according to the discussion in Section 5.3.2 and extrapolating to higher energies. As for the fluxes, the final step is the interpolation of cumulative fluence given from the closest points of the data base. This interpolation is done following the same procedure used to obtain interpolated fluxes.

Together with the total fluence of a given SEP event, a relevant magnitude from the space weather point of view is the peak flux of the event (e.g. Feynman & Gabriel 2000). The peak flux or peak intensity at a given energy is defined as the maximum of the particle differential flux at that energy. Therefore, for each selected event, SOLPENCO scans for the maximum value of the flux and the time when it is reached.

Finally, SOLPENCO converts the resulting flux and cumulative fluence arrays of the chosen SEP event to physical units. As discussed in Section 5.3.3, the normalization constant is given by:

$$K(E) = \frac{j^{obs}(t_a, r_0, E_0)}{F^{arbi}(t_a, r_0, E_0)} \frac{A(r_0)}{mE}$$

where $j^{obs}(t_a, r_0, E_0)$ is the observational value of the proton differential flux at the energy E_0, measured at an heliocentric distance, r_0 at a given time t_a; $F^{arbi}(t_a, r_0, E_0)$

is the value of the columnar density given by the model (in arbitrary units) of E_0–MeV protons at the same distance and time as the measured differential flux; $A(r_0)$ is the cross section of the magnetic tube flux at r_0, m is the proton mass at rest and E is the considered proton kinetic energy. The mathematical approach applied is given in Appendix A and in the quotations given there[21]. Therefore, to normalize the flux profiles is necessary to know, at least for one event, the quotient between the observed and the modeled value of the flux for a given time and energy (quotient that we call 'scaling factor'). To derive a scaling factor demands a statistical study of a large set of SEP events that is beyond the scope of this work (see Section 5.3.3). Therefore, in the present version of the code, we use, as a first approach, a scaling factor derived from the 0.5 MeV flux measured at the time of arrival of the shock associated with the SEP event on September 12 – 15, 2000 at 1.0 AU. For this case, j^{obs}(63.3 hours, 1.0 AU, 0.424 MeV) = 15.98×10^4 (cm^2 sr s MeV)$^{-1}$, F^{arbi}(62.2 hours, 1.0 AU, 0.5 MeV) = 4.31×10^{13} (arbitrary units). Hence, the constant of normalization used in SOLPENCO is

$$K(E) = \frac{2.4 \times 10^8}{E[\text{MeV}]}$$

5.4.6 Outputs of the code

After running SOLPENCO, a graphic display of the interpolated fluxes and cumulative fluences versus time, for the chosen input parameters is shown. It also provides two panels with different information. The first panel summarizes the input values chosen by the user (the variables listed in Section 5.4.1): radial distance, angular position of the observer, initial shock pulse velocity, existence of a turbulent foreshock region, and mean free path and energy of the particles for which the differential flux and cumulative fluence have been calculated. The second panel gives the transit time and transit speed of the shock, to travel from the Sun to the observer's location, and the total fluence at the shock arrival (for the energies equal and higher than the input energy value) as well as the time and value of the peak intensity of the input energy. The interface also offers other display possibilities: only the flux profile (option 1), the fluence profile (option 2) or both of them (option 3).

The plots presented in Figures 5.10 and 5.11 show four different SEP events of

[21] We are implicitly assuming that for the range of energy values considered in SOLPENCO the relation $E = p^2/(2m)$ is valid, where p is the particle momentum and m the particle mass at rest.

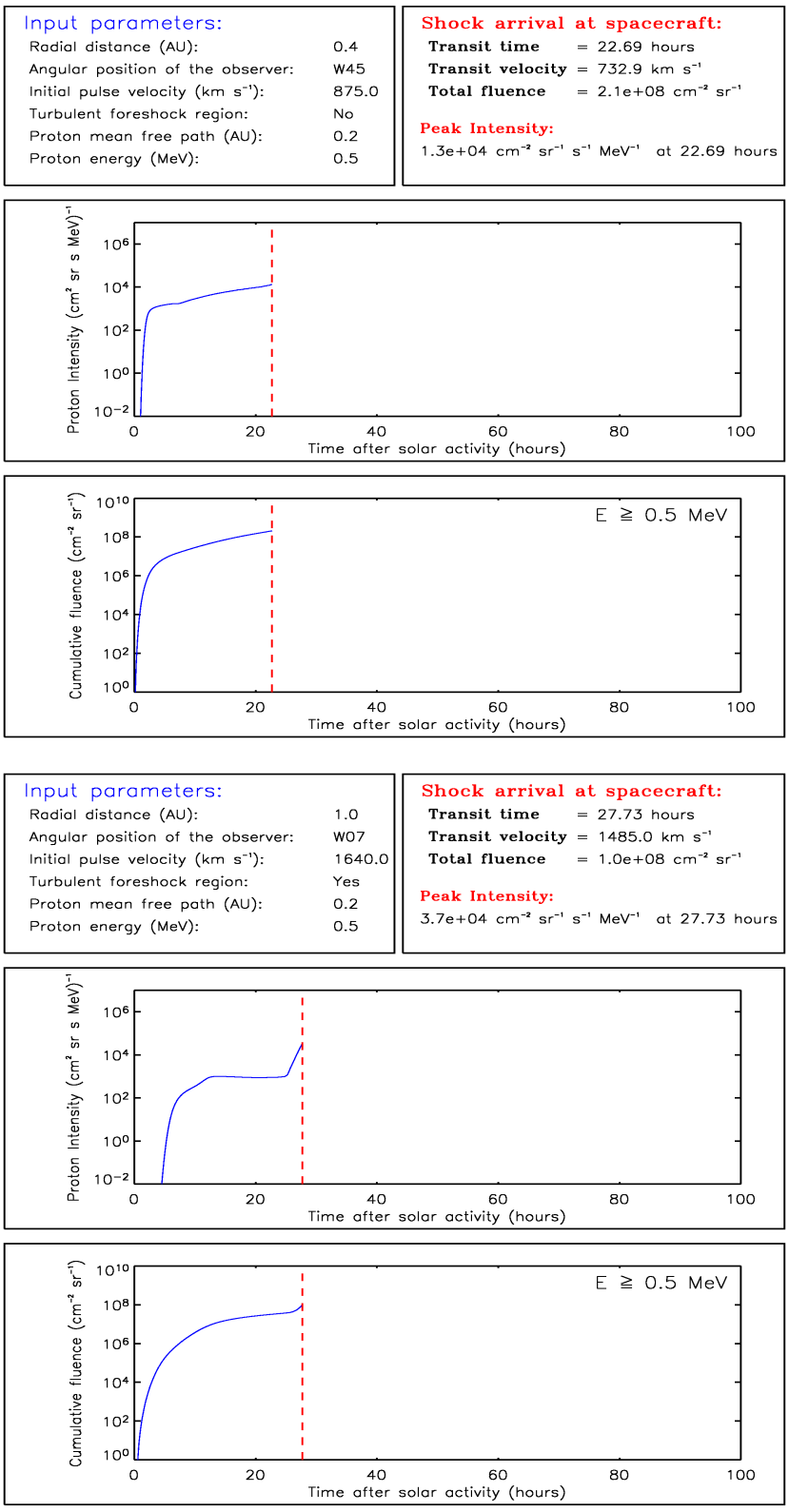

Figure 5.10: 5.10A (Upper plot) and 5.10B (lower plot). Outputs of the code for the cases W450875W04[l02TN] (top four panels) and W071640W10[l02TY] (bottom four panels), respectively.

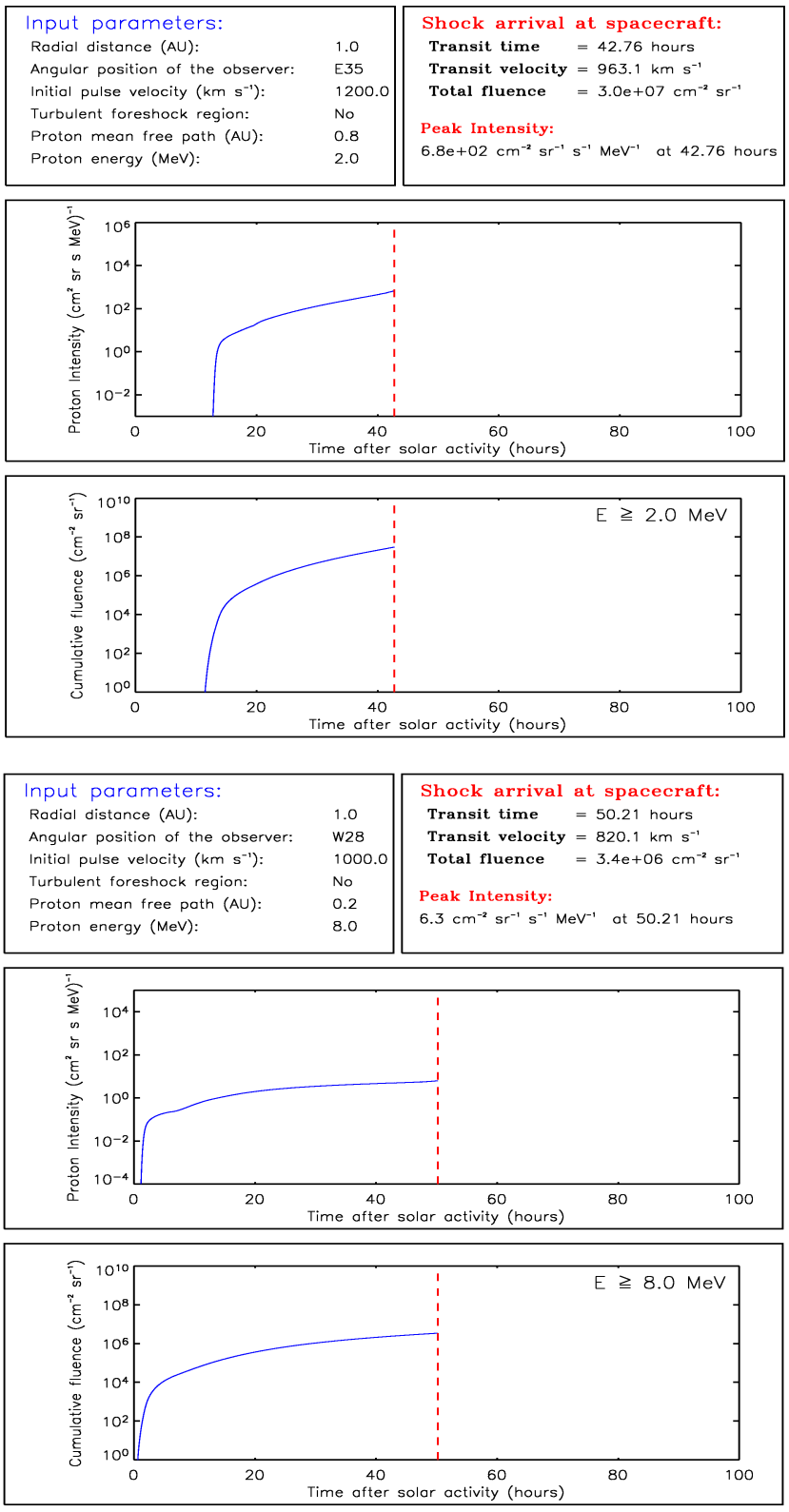

Figure 5.11: 5.11A (Upper plot) and 5.11B (lower plot). Cases E351200W10[I08TN] (top) and W281000W10[I02TN] (bottom), respectively.

the output flux and cumulative fluence profiles built by SOLPENCO. This is not a complete set of examples, but enough to give an overall idea of the outputs that the code can produce.

Figure 5.10A. It shows the 0.5 MeV-proton flux and cumulative fluence profiles for a W45-event, with initial pulse velocity equal to 875 km s^{-1}, as observed at 0.4 AU, a particle mean free path of 0.2 AU, and no foreshock region. Descriptor: W450875W04[l02TN]. Remember (Section 5.4.1) that W45 stands for the angular position of the observer, 0875 the initial pulse velocity of the shock, W means that this is a wide shock, the '04' for this event, means that the observer is at 0.4 AU ('10' for an observer at 1.0 AU); inside the brackets, the 'l02' identifies the mean free path of the particles (only '02' or '08' digits, standing for 0.2 AU or 0.8 AU, respectively), and the 'TN' (or 'TY') refers to the absence (or presence) of a foreshock region.

Figure 5.10B. 0.5 MeV-proton flux and cumulative fluence profiles for a W07-event, with initial pulse velocity equal to 1640 km s^{-1}, as observed at 1.0 AU, a particle mean free path of 0.2 AU, and no foreshock region. Descriptor: W071640W10[l02TY].

Figure 5.11A. 2.0 MeV-proton flux and cumulative fluence profiles for an E35-event, with initial pulse velocity equal to 1200 km s^{-1}, as observed at 1.0 AU, a particle mean free path of 0.8 AU, and no foreshock region. Descriptor: E351200W10[l08TN].

Figure 5.11B. 2.0 MeV-proton flux and cumulative fluence profiles for a W28-event, with initial pulse velocity equal to 1000 km s^{-1}, as observed at 1.04 AU, a particle mean free path of 0.2 AU, and no foreshock region. Descriptor: W281000W10[l02TN].

The origin of time (in hours) marks the development of the parent solar event, the last point of each curve the arrival of the shock at the observer's location, also indicated by the vertical dashed line. As expected, the onset of the western events occurs earlier than for the eastern events; this simply reflects the time elapsed until the shock connects with the observer through the IMF lines. The foreshock keeps shock-accelerated particles close to the front while the shock propagates in the interplanetary medium. Once the shock is near the observer, particle flux increases more or less rapidly, depending on the size of the turbulent foreshock region; the result is a depleted plateau and a larger ESP spike (as the case shown in Figure 5.10B).

W661445W10l02TYE3.dat

```
# Output file from SOLPENCO.
# Author: A. Aran
# University of Barcelona. December 2005
#
# First row is an array which gives for the selected SEP event: the proton
# energy (MeV), the transit time (hours) and speed (km s^-1), the total
# fluence (cm^-2 sr^-1), the peak intensity (cm^2 sr s MeV)^-1 and time (hours).
# Each one of the following rows represent a time step. Each row contains the
# time in hours, the proton intensity in (cm^2 sr s MeV)^-1 and the
# cumulative fluence in  cm^-2 sr^-1 . Format is:(1x,f5.2,3x,g10.4,3x,g10.4)
#
1.0 48.50 849.1 2.3e+08 4.1e+03 48.50
  0.010         0.000    4.615e-18
  0.019         0.000    1.213e-16
  0.033         0.000    5.843e-15
  ...           ...      ...
  4.242         9.146    1.667e+05
  4.252         9.354    1.686e+05
  4.270         9.808    1.721e+05
  ...           ...      ...
 12.221         550.1    9.623e+06
 12.231         551.2    9.648e+06
  ...           ...      ...
 24.242         1840.    6.955e+07
 24.256         1841.    6.965e+07
  ...           ...      ...
 36.212         1248.    1.489e+08
 36.217         1247.    1.489e+08
  ...           ...      ...
 48.488         4068.    2.313e+08
 48.498         4073.    2.315e+08
```

Figure 5.12: Example of an output data file from SOLPENCO. The header explains the format of the data contained in the file. First data row indicates the values of the energy selected, the transit time and velocity, the total upstream fluence of the event above that energy and the maximum (peak) intensity and time. Afterward, first, second and third columns respectively contain time (hours), differential flux (cm^{-2} sr^{-1} s^{-1} MeV^{-1}) and cumulative fluence (cm^{-2} sr^{-1}) for each time step.

SOLPENCO allows the user to save the selected display as an image file in Potable Network Graphics (png) format, as Figures 5.10 and 5.11. It is also possible to store the values of the resulting profiles in a data file for further use; Figure 5.12 shows an example of the output format. Each output data file is identified by means of the same descriptor aforementioned. The example shown in Figure 5.12 corresponds to the case W661445W10l02TYE3.dat; therefore it corresponds to the flux of 1 MeV and cumulative fluence of protons with $E \geq 1$ MeV.

6 Fluxes and Fluences derived from SOLPENCO

The outputs provided by SOLPENCO vary according to the values adopted to describe the interplanetary scenario where SEP events develop. By 'interplanetary scenario' we mean both [1] the conditions for injection and propagation of shock-accelerated particles and [2] the relative position in space of the observer with respect to the parent active region. The first conditions are characterized by the input variables listed in Section 5.4.1 that quantify the proton mean free path (LAMBDA), the turbulent region (TURB), the proton energy (ENERG), and the initial speed of the shock (VELOS). The position of the observer is described by its heliocentric radial distance (DISTRAD) and the heliolongitude of the solar activity associated with the origin of the SEP event (POSANG). This heliolongitude also defines the direction of propagation of the shock in interplanetary space by assuming that the nose of the shock is centered at the angular position given by the heliolongitude. Other possible relevant factors, such as the presence of an energy-dependent seed particle population (Kahler 2001b) or the presence of preceding CMEs (Gopalswamy et al. 2004), have not been taken into account in SOLPENCO because it does not exist yet any procedure that allows us to quantify their influence.

The aim of this chapter is twofold: [1] To study the influence of the aforementioned input variables in the proton intensity-time profiles produced by SOLPENCO; and [2] to study the coherence and behavior of the set of synthetic flux and fluence profiles that constitutes its data base, as a function of the input variables most relevant to space weather applications. For mission design, and in order to evaluate the radiation that satellites and humans might experience in space, two main features of SEP events have to be predicted: the peak flux at a given energy and the total fluence that could be attained above a given threshold energy (e.g. Feynman &

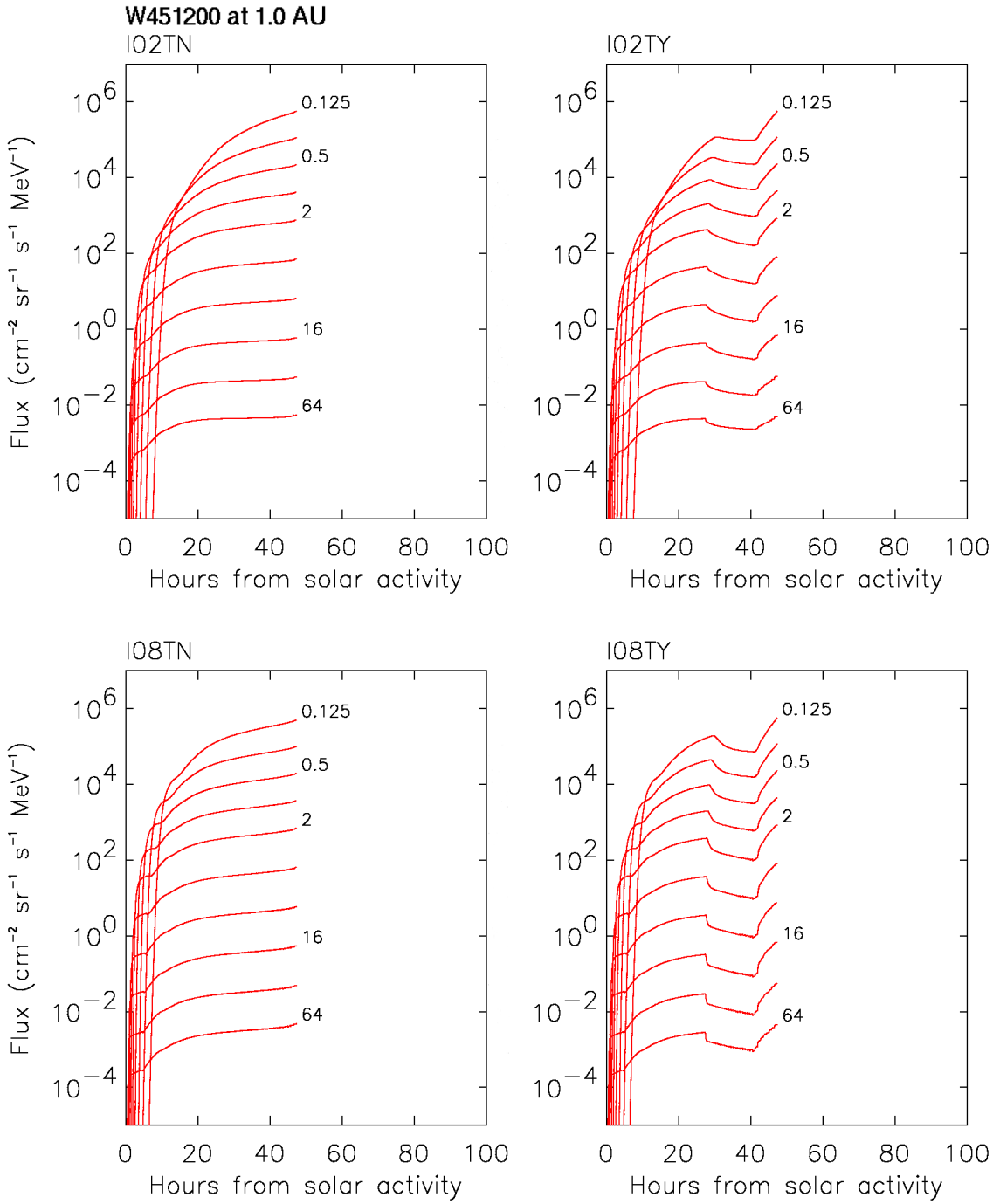

Figure 6.1: SEP event W451200W10. Energy dependence of the proton flux profiles for the four input transport conditions: mean free path: 0.2 AU (top panels) and 0.8 AU (bottom panels) and with the absence (TN, left panels)and presence of a high turbulent foreshock region (TY, right panels). Proton energies are from top to bottom: 0.125, 0.25, 0.50, 1.0, 2.0, 4.0, 8.0, 16, 32 and 64 MeV.

Gabriel 2000; Turner 2001; Xapsos et al. 1998, 2004). Therefore, we study the peak intensity and the total fluence of the SEP events provided by SOLPENCO by analyzing their variations with the strength of the interplanetary shock, the heliolongitude and heliocentric distance of the observer, as well as the particle energy.

Each event of the data base is identified by its longitude, initial pulse velocity, the observer's distance, the value of the mean free path and the presence/absence of a turbulent foreshock (Section 5.4), and it is given as a function of the energy of the particles. For instance, Figure 6.1 illustrates the case of a W45 event detected by an observer located at 1.0 AU and generated by a shock which initial pulse speed is 1200 km s^{-1} (W451200W10). Each one of the four panels of the figure shows a set of flux profiles corresponding to the ten possible values of the variable ENERG (from 0.125 MeV to 64 MeV; for clarity, only five are labeled in the figure). The intensity-time profiles are computed in the shock-upstream region, therefore, they start at the onset of the event and stop at the time of the shock passage by the observer's position. The top (bottom) panels show the output profiles assuming a mean free path of 0.2 (0.8) AU for the 0.5 MeV protons; the left (right) panels show the corresponding flux profiles assuming the absence (presence) of a foreshock. In this chapter we complete and correct when necessary the analysis of the data base of SOLPENCO published in Aran et al. (2004, 2005b) as commented below.

6.1 Flux profiles: influence of the input variables

6.1.1 Energy and mean free path

The processes of particle-acceleration by interplanetary shocks are more efficient at low than at high energies (i.e. Lee 2005). Therefore, under nominal conditions, the lower the energy of the particles the larger the SEP fluxes. Moreover, if there is a permanent magnetic connection between the observer and the source of particles, the proton flux profiles will show a velocity dispersion effect at the onset of the event. Besides, at a given energy, larger particle mean free paths must yield a prompt and faster onset of the flux profiles. Figure 6.1 is an illustrative example of how the proton profiles of the SOLPENCO data base fulfill these features.

Figure 6.2 shows the intensity-time profiles of the E300750W10 event obtained for

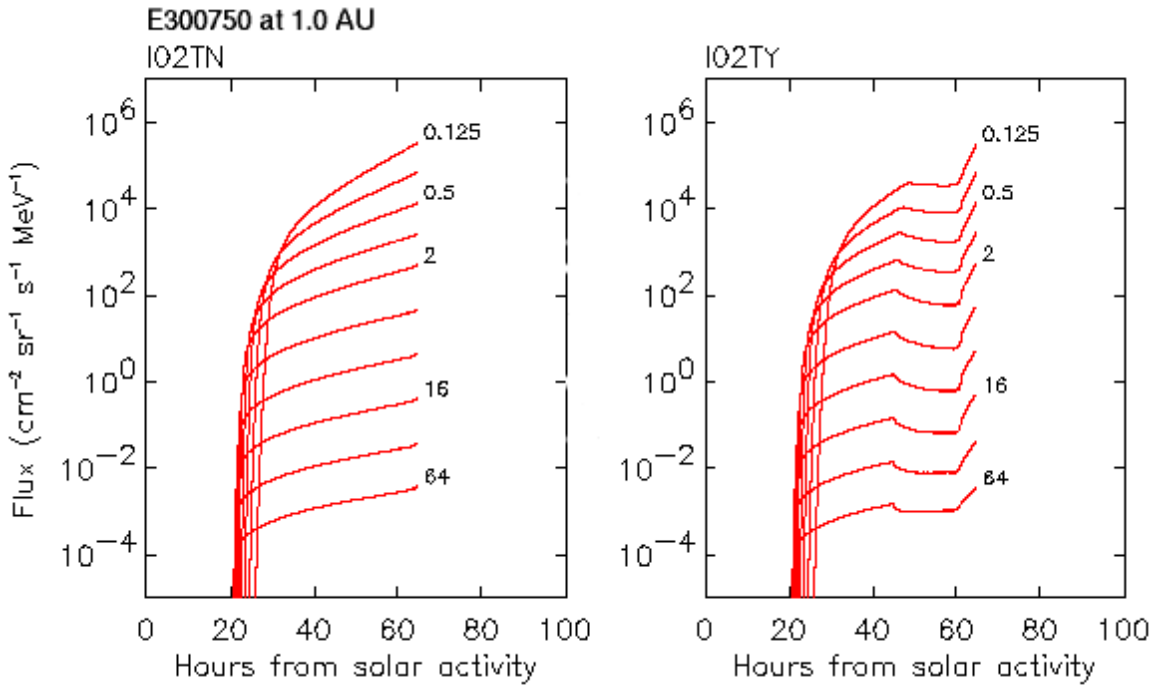

Figure 6.2: SEP event E300750W10. Different shapes of the proton flux profile as a function of the energy (see Figure 6.1 for the energy values).

the case $\lambda_{\|0} = 0.2$ AU. As can be seen, the proton fluxes start to increase later than those shown in Figure 6.1 because for this event the magnetic connection between the shock front and the observer was established later. Such a delay in the connection time is due to the higher longitudinal separation between the observer and the leading edge of the shock (or the site of the parent solar activity) and, the lower speed of the associated traveling shock. The comparison between the profiles shown in Figure 6.1 and in Figure 6.2 illustrates the fact that the influence of the proton mean free path in shaping the synthetic flux profiles is less important (within the range of values considered, $0.2 \leq \lambda_{\|0} \leq 0.8$ AU at 0.5 MeV) than the heliolongitude of the parent solar event and the speed of the associated interplanetary shock.

In the cases shown in Figures 6.1 and 6.2, the particle intensity profiles attain their maximum intensity at the shock arrival, regardless of the proton energy considered. This is the case for most of the flux profiles in the SOLPENCO data base (see discussion in Section 6.2). Nevertheless, observed western SEP events (e.g. westward than ∼W30) usually reach the maximum intensity at high-energies (e.g. $E > 4$ MeV) during the prompt or the plateau phase before the arrival of the shock

(i.e. Cane et al. 1988; Tylka et al. 2000; Lario & Simnett 2004). In order to accurately reproduce this behavior, future versions of SOLPENCO should consider [1] an MHD model allowing us to simulate the contribution of shock-accelerated particles starting at $\sim 4\ R_{\odot}$ from the Sun (Chapters 7 and 8) and [2] at high-energies, a higher value of k in the Q(VR) relation than the value currently adopted ($k = 0.5$)[1].

Finally, it is appropriate to point out that the observational velocity dispersion at the onset of the event can be blurred out (totally or only at low-energies) because of (i) the presence of pre-event background particles populating the flux tube, (ii) the contamination of low-energy channels by particles of higher energies and/or by electrons, (iii) instrumental saturation of the detector, or (iv) spatial inhomogeneities such as discontinuities in the IMF, that might suddenly change the flux tube that sweeps the observer. Therefore, a number of well-connected SEP events may not necessarily display such a clear velocity dispersion as that of the synthetic events provided by SOLPENCO (Figure 6.1). Poor connected SEP events (eastern events at 1.0 AU), might display a sort of "inverse" velocity dispersion; see for example the E18 event on 6 – 8 June 2000 (Figure 2.6) and the E69 event on 6 – 8 March 1989 (Figure 8.4). The reason is that high-energy protons ($E > 15$ MeV in these events) are not efficiently injected by the shock at the cobpoint, located at the weak western flank of the shock front, in such a way that their intensity-time profiles raise above the background later than those of low-energy particles. This behavior is not seen in the event of Figure 6.2 since SOLPENCO does not assume any pre-event background at any energy in the flux profiles. This assumption could be implemented in future versions of the code but a previous statistical analysis of observations is needed in order to decide which representative values should be taken.

[1] As it was considered by Aran et al. (2001, 2005a), see also Chapter 5, provided that a consistent normalization method could be found and that this did not increase the number of parameters of the code (Aran et al. 2006).

6.1.2 Turbulent foreshock region

The turbulent foreshock region stores particles ahead of the shock front. Then, by simulating the existence of such a trapped-particle zone it is possible to reproduce the local peak flux enhancements observed at the arrival of the shock in many SEP events, i.e. the ESP component of SEP events (Section 2.2). The main effect of a foreshock region is the confinement of part of the shock-accelerated particle population, impeding their journey along the IMF lines up to the observer's position. This effect is translated, first, into a reduction of the measured particle flux and later, when the foreshock is only within ∼0.1 AU (in the case of SOLPENCO) from the spacecraft, into a sudden flux increase which frequently peaks at the shock passage.

In order to illustrate the influence that the adopted turbulent foreshock region can have in the shape of the computed flux profiles, Figure 6.3 shows the profiles of four events, assuming either its presence (red traces) or absence (black traces). These are representative cases of the data base of fast (a and b) and slow (c and d) propagating shocks, for western (a and c) and eastern (b and d) SEP events. Figure 6.3a shows the flux profiles for a W451200W10[l02] event, at 2 MeV (the same event shown in Figure 6.2). Plots (b), (c) and (d), respectively, show flux profiles for events E301350W10[l08], W300750W10[l08], and E300750W10[l02], at 0.5 MeV protons. The differences between the two profiles in each plot are consequence of the effect of the foreshock region, able to store particles ahead of the shock owing to the higher rate of scattering processes between the particles and the MHD waves generated by the shock-accelerated particles themselves (represented by a small local mean free path, $\lambda_{\parallel c}$; see Lar98, Appendix B).

As can be seen in Figure 6.3, in many simulated flux profiles the maximum proton intensity at shock passage is only slightly larger when there is a foreshock region than when this region is absent. The reason is the assumption of a inner absorbing boundary, located just behind the shock front, as the shock approaches to the observer. The large number of scattering processes undergone by the particles trapped within the foreshock region reduces the anisotropy of the particle population almost to isotropy. This means that more particles interact with the shock and, as a consequence, the number of particles absorbed by the boundary is greater than when no foreshock region is assumed. A more elaborated calibration of the flux profiles must include a deep study of the influence of the absorbing or reflecting boundary conditions considered (with a large number of particles returning toward

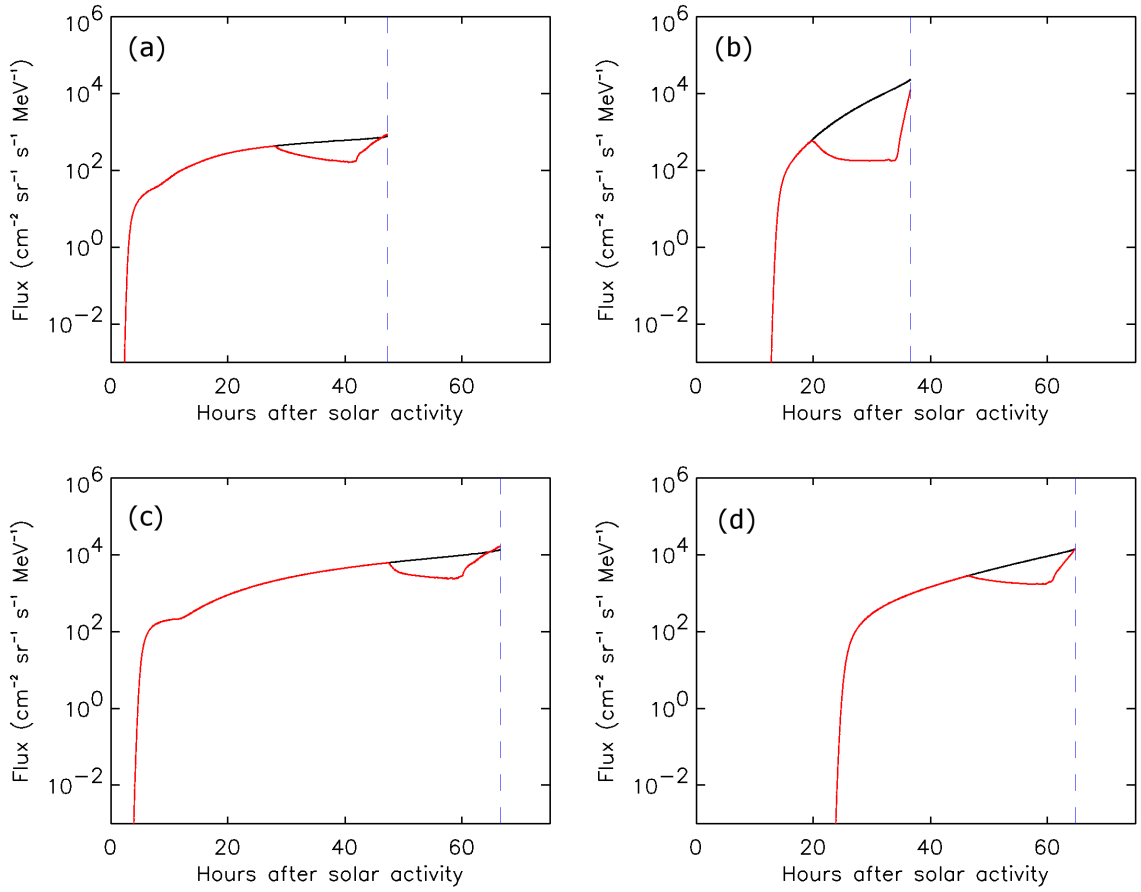

Figure 6.3: SEP flux profiles for different events considering the presence (TY, red traces) and absence (TN, black traces) of a turbulent foreshock region. Vertical dashed lines indicate the passage of a shock. (a) Event W451200W10[l02] at 2.0 MeV; (b) event E301350W10[l08] at 0.5 MeV; (c) event W300750W10[l08] at 0.5 MeV; and (d) event E300750W10[l02] at 0.5 MeV. See details in the text).

the upstream part of the shock) in the particle transport code.

6.1.3 Initial shock speed and heliolongitude

The faster the propagating interplanetary shock the higher its MHD strength and, in principle, the higher its efficiency in particle acceleration. Therefore, for a given observer, we should expect higher fluxes for faster shocks. But the shape of the intensity-time profiles of SEP events is also highly dependent on the relative geometric position of the observer with respect to the parent solar activity (Chapter

2). Figure 6.4 shows an example of the shapes of the flux profiles generated by 8 shocks with different initial velocities (between 750 and 1800 km s^{-1}, color coded), for two different observers located at 1.0 AU: W45 (top panels) and E30 (bottom panels). These events are representative of the synthetic flux profiles provided by SOLPENCO. These profiles have been computed by taking $\lambda_{\parallel 0} = 0.2$ AU[2]. The left panels of this figure do not assume the presence of a foreshock, while right panels do (like in Figure 6.1). The transit time of each shock is indicated by a vertical dashed line. As can be seen, in general, the faster the shock the higher the fluxes (few exceptions are commented in Section 6.2). Thanks to the parametric Q(VR) relation, the speed of the shock translates (via the value of VR at the cobpoint) into an injection rate of shock-accelerated particles, in such a way that the faster the shock the more efficient at particle acceleration[3].

The flux profiles shown in the panels of Figure 6.4 display a regular behavior. The difference between the profiles corresponding to the same initial shock speeds in the top and bottom panels is a direct consequence of the different conditions for particle acceleration and injection in the regions scanned by the cobpoint. As the shock moves away from the Sun, the cobpoint moves along the shock front and scans different regions of it depending on the longitude of the observer with respect to the parent solar activity site. Western events (W45 top panels) display a rapid rise to a maximum because, at the onset of the event, the cobpoint is close to the nose of the shock which is near the Sun. As the shock expands, the cobpoint moves along the eastern wing of the shock and injects less accelerated particles than at the onset. For eastern events (bottom panels), the magnetic connection between the observer and the shock is established later in the event, hence the delayed onset. In addition, the cobpoint moves closer to the nose of the shock and consequently yields the rising intensity-time profiles shown in the bottom panels. As already commented, the presence of a foreshock region confines energetic particles in front of the traveling shock. This is the reason of the lower fluxes observed in the prompt component of the events but, the increase in the particle intensities just before the arrival of the shock (right panels of Figure 6.4).

Figure 6.5 shows the proton flux profiles derived with the same input values as

[2]The flux and fluence profiles do not show relevant differences if we consider $\lambda_{\parallel 0} = 0.8$ AU, instead.

[3]Therefore, hereafter, we identify a fast shock as a strong shock, that is, a shock efficient at particle acceleration and injection.

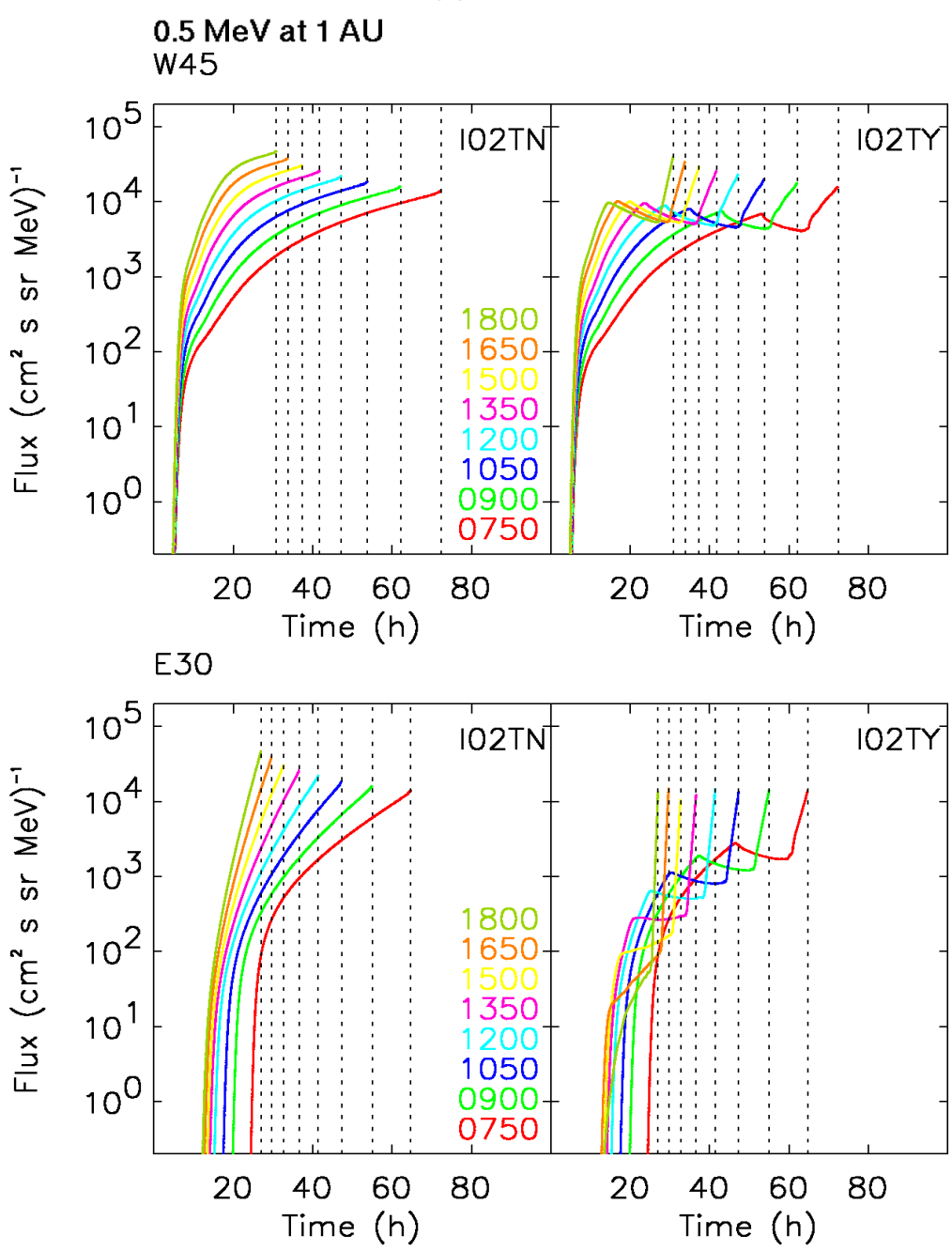

Figure 6.4: Synthetic 0.5 MeV proton flux profiles for two observers located at 1.0 AU and at heliolongitudes of W45 and E30 (two top and two bottom panels, respectively). The initial velocity of the eight simulated shocks is color coded (from top to bottom, v: 1800, 1650, 1500, 1350, 1200, 1050, 900, and 750 km s^{-1}, as indicated in the inset of the left panel. The flux profiles have been computed by assuming $\lambda_{\parallel 0} = 0.2$ AU, and the absence (right panels) or the presence (left panels) of the foreshock region. Vertical dashed lines mark the arrival time for each shock at the observer's location.

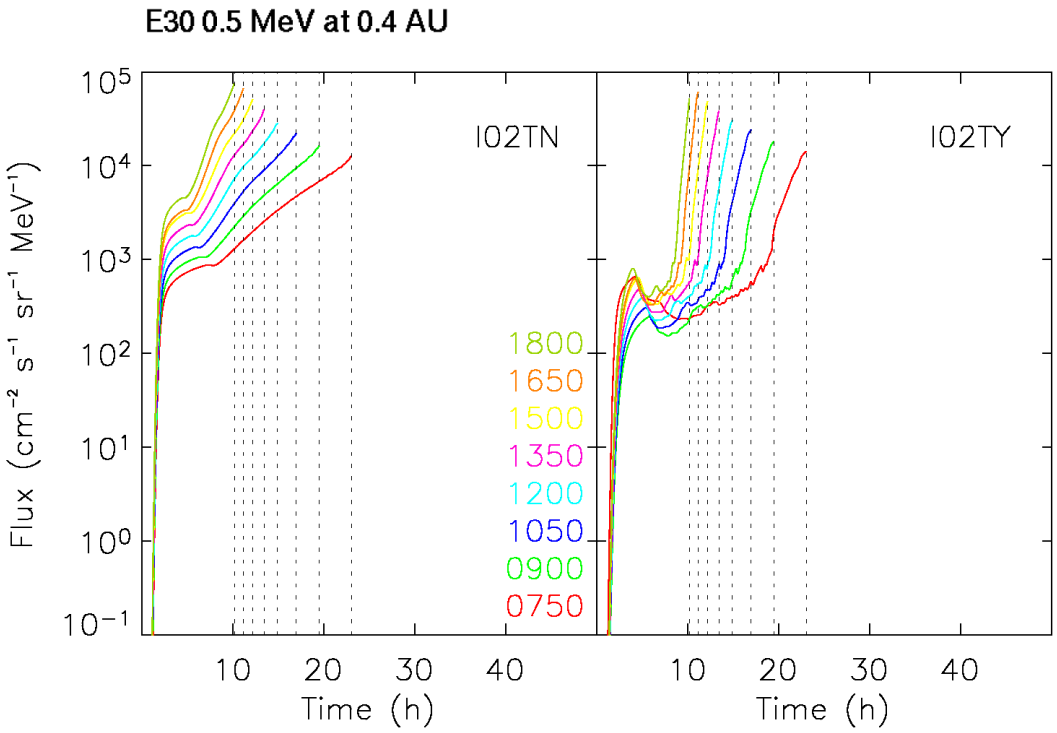

Figure 6.5: 0.5 MeV proton flux profiles at as seen by an E30 observer located at 0.4 AU. Same inset description as in Figure 6.4.

those shown in bottom panels of Figure 6.4 but for a spacecraft located at 0.4 AU. The differences between the set of flux profiles obtained at 1.0 AU and at 0.4 AU are mainly due the longer duration of the SEP events at 1.0 AU, and the different magnetic connection established between the shock front and the observers. Since the model assumes that the IMF is a nominal Parker spiral with a constant solar wind speed of 400 km s^{-1}, an observer located at 0.4 AU is connected to the Sun 35° eastward than an observer at 1.0 AU with the same heliolongitude. That is, the E30 observer at 0.4 AU shares the same IMF line (thus, the same history of the cobpoint displacement along the shock front) that a W05 observer located at 1.0 AU. Therefore, for each shock, the cobpoint of the E30 observer at 0.4 AU scans a region along the shock front more efficient at accelerating particles than the cobpoint of the E30 observer at 1.0 AU; hence, the higher intensities attained at 0.4 AU.

In addition, the interplanetary shocks simulated in SOLPENCO are wide shocks; then, at 1.0 AU, an observer located in western longitudes near the central meridian (such a W05 observer) is connected to the shock at the beginning of the event.

Therefore, the E30 observer at 0.4 AU is well-connected, while the E30 observer at 1.0 AU is not. That is the reason why the flux profiles shown in Figure 6.5 display a prompt phase while this phase is absent in the profiles of the bottom panels of Figure 6.4.

In fact, the SEP events shown in Figure 6.5 have a similar shape as those of a central meridian event at 1.0 AU, except for the effect of the turbulent foreshock region (right panel of this figure). This region is defined to be active from the beginning of the event for those events where the transit time of the shock is less than 20 hours (Section 5.2). This is the case for all but one (that associated with the slowest shock, 750 km s^{-1}) of the events shown in Figure 6.5. The effect of the foreshock region at so early stage translates into a substantial reduction of the initial flux, as can be seen by comparing the corresponding flux profiles in both panels of the figure. This effect is not observed either in central meridian events at 1.0 AU or in the slowest shock at 0.4 AU (red trace in Figure 6.5), because the foreshock region starts to act later (20 hours before the shock passage by the observer).

6.2 The peak flux

The maximum intensity of the differential flux profiles (the 'peak flux' or 'peak intensity') of SEP events usually appears either shortly after the onset of the event or around the shock arrival. Its timing and value in each SEP event largely depend on the solar-interplanetary scenario where the event develops. Here, we describe the main features of the peak flux of the events in the data base of SOLPENCO (characterized by the initial pulse velocity of the shock and the heliolongitude). Otherwise indicated, in this section we will work with the average value of the peak flux over the four cases l02TN, l02TY, l08TN and l08TY. At present, the presence or absence of a foreshock region (variable TURB) is a factor hard to be identified in observations and the influence of the mean free path (variable LAMBDA) on the particle intensity profiles is of less importance than the shock speed or the event helilongitude, as discussed in the previous section. Thus, for space weather purposes, an average case is representative enough for the discussion.

6.2.1 Dependence on the initial shock speed and the location of the observer

For a given angular position of the observer, either 1.0 AU or 0.4 AU, the peak flux increases with the initial shock speed, that is, with the strength of the shock. This trend can be easily seen in Figures 6.6 and 6.7, where the peak flux is represented versus the initial speed of the shock for the fourteen angular positions. In each plot, the heliolongitudes range from W90 to E75 (color coded) and sorted from higher (top) to lower (bottom) peak flux values. Western events (from W90 to W45) are indicated by dashed lines, central meridian events (from W30 to E30) by solid lines, and eastern events (from E45 to E75) by dotted lines.

Figure 6.6 shows the 1.0 MeV proton peak flux values at 1.0 AU. Extreme scenarios display a few exceptions to the aforementioned trend. For E75 events the peak flux decreases as the initial speed increases from 1200 km s^{-1} to 1650 km s^{-1}. For these far-eastern events, the observer establishes magnetic connection with the shock just a few hours before the shock-arrival, and hence the duration of the shock injection is the shortest among the events of the data base. In addition for these events, the cobpoint is located on the distant western flank of the shock front, and thus it scans a region of weak efficiency in terms of particle acceleration. The combination of these two facts translates into a more gradual increase (with the initial shock speed) of the peak flux than the increase obtained for the rest of heliolongitudes, when the absence of the turbulent region is assumed. When the turbulent foreshock region is present, the peak fluxes decrease with the initial shock speed for values ranging from 900 km s^{-1} to 1650 km s^{-1}. The foreshock is already active when the shock starts injecting particles. It begins to store particles when the flux is still low; thus, making the effect of the inner absorbing boundary behind the shock to become noticeable (Lario et al. 1995a). As the injection rate of shock-accelerated particles increases, more particles remain trapped in the foreshock region. Then, the amount of particles absorbed by the inner boundary is greater for rapid shocks than for slow shocks, hence, the decrease of the peak flux. The sum of these effects when averaging over the four transport conditions makes the peak flux to decrease for shocks with initial speeds between 1200 km s^{-1} to 1650 km s^{-1}. For the other longitudes the particle injection at the cobpoint is of longer duration and the effects of the foreshock region with respect the events without it are less noticeable.

The majority of the computed SEP flux profiles peaks at the shock passage (like

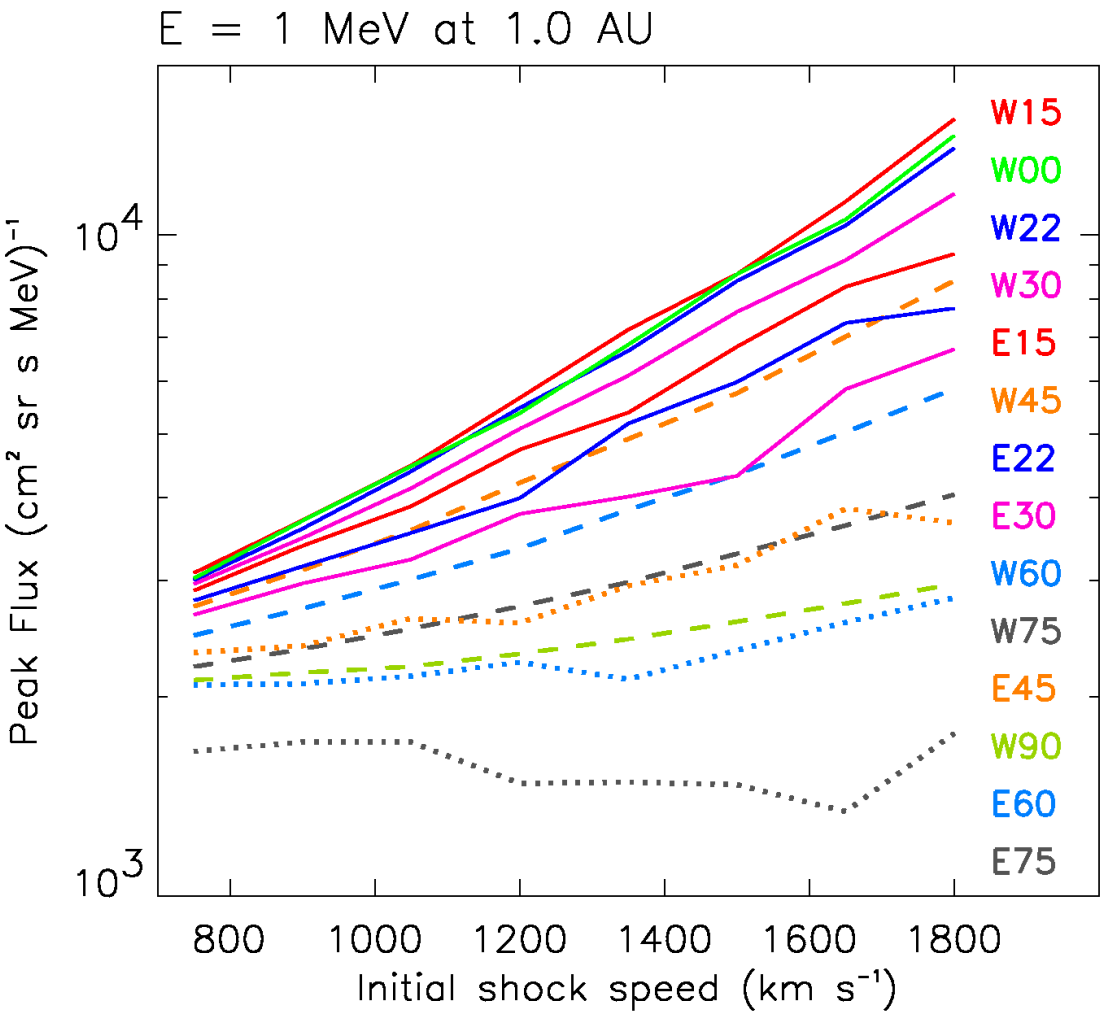

Figure 6.6: Variation of the 1.0 MeV proton peak flux as a function of the initial shock speed and the heliolongitude of the observers located at 1.0 AU. The 14 heliolongitudes are color coded from top (higher peak flux values) to bottom (lower values) as indicated. To make the plot clear, the lines have been binned in three traces: dashed lines for western events (from W90 to W45), solid lines for central meridian events (from W30 to E30) and dotted lines for eastern events (from E45 to E75).

the events shown in Figure 6.6): 100% of the SEP events (4480 cases) at 0.4 AU and 97% at 1.0 AU, this later value increases to 99.9% when energies below 32 MeV are considered. In 94 of the remaining 134 cases, the peak flux is attended between 1 and 25 minutes before the shock arrival; in the other 40 cases, the peak flux appears shortly after the onset of the event or several hours before the arrival of the shock. All these cases correspond to western events with heliolongitudes westward of W30 and for high-energies (24 events at 64 MeV, 12 events at 32 MeV, 2 events at 16 MeV, and 2 events at 8 MeV). This is the same behavior found in the observed flux profiles of many western SEP events at similar energies (Cane et al. 1988).

Figure 6.7 shows the variation of the peak intensity with the initial shock speed at energies 0.125 MeV (top panels), 1.0 MeV (middle panels) and 8.0 MeV (bottom panels), and for each of the fourteen angular positions of the spacecraft at 1.0 AU (left panels) and at 0.4 AU (right panels). Note that the middle left panel is the Figure 6.6, included here in order to compare the peak intensities attained at 1.0 AU with those obtained at 0.4 AU.

The highest peak fluxes at 1.0 AU correspond to observers located at W00, W15 and W22. For these events, the cobpoint moves along the central part of the shock front (its strongest part), and the connection is usually established at the beginning of the event (i.e. the events are magnetically well-connected). For a given angular position, the peak flux increases with the initial speed of the shock, for all energies. The exception are E60 events at $E < 0.5$ MeV and E75 events at $E < 8$ MeV due to the effects of the foreshock region already commented for 1 MeV protons (Figure 6.6). At higher energies, however, the peak intensity increases because the effects of the transport conditions (i.e. the net balance between the effect the mean free path, the efficiency of the foreshock region and the effect of the inner boundary of the model) are less important than at lower energies.

The most intense peak fluxes at 0.4 AU are obtained for the same observers as at 1.0 AU adding the case E15 (right panels of Figure 6.7). At 0.4 AU, an E15 event is well-connected to the spacecraft. Regardless of the considered proton energy, peak fluxes increase with the initial shock speed. In contrast to the case at 1.0 AU, they do not show any deviation (except for punctual cases) due to transport conditions because the shorter duration of the events at 0.4 AU does not allow transport effects at the foreshock region to become important and, because eastern events are better

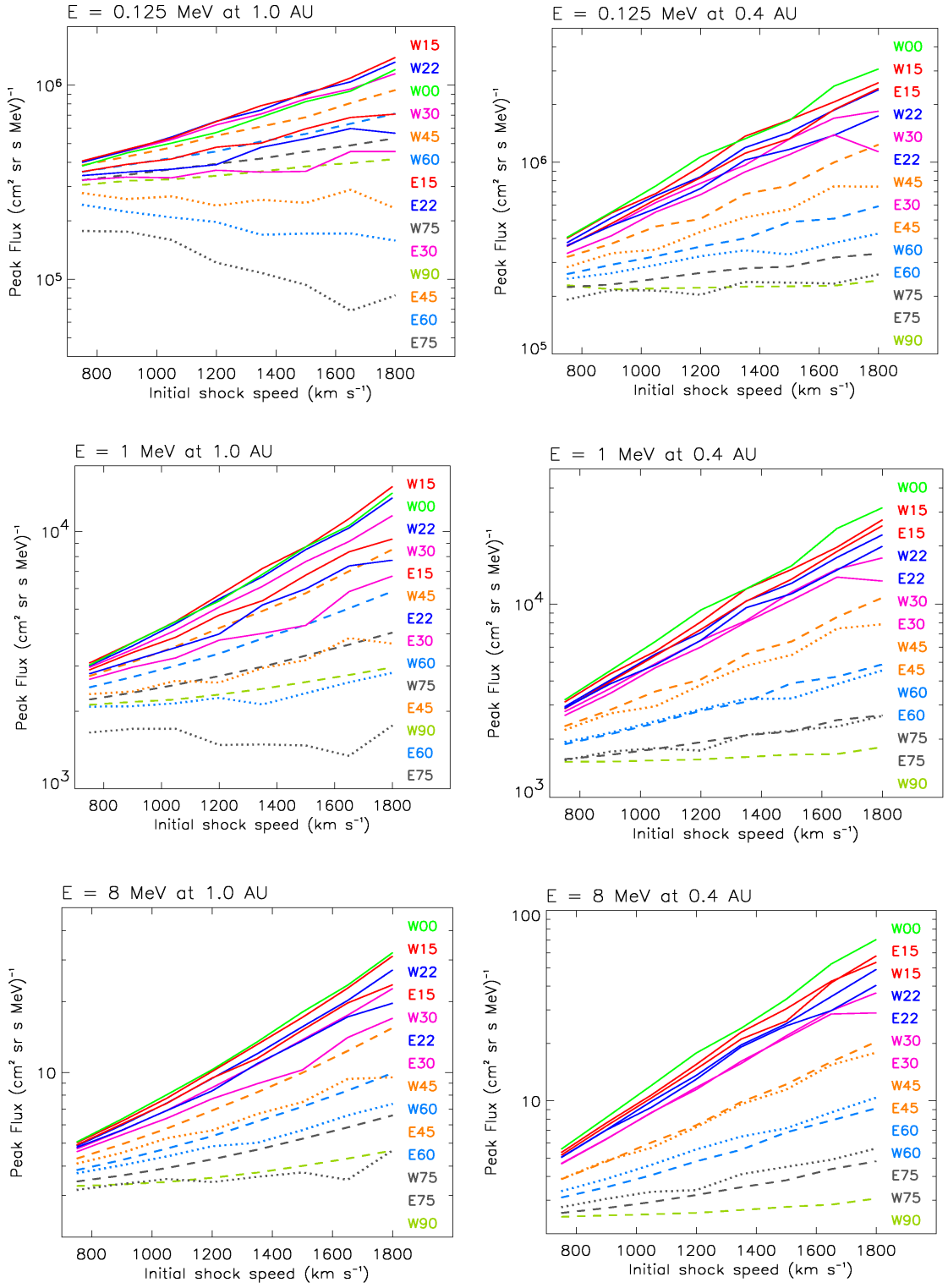

Figure 6.7: Variation of the peak flux as a function of the initial shock speed and the heliolongitude of the observers located at 1.0 AU (left panels) and at 0.4 AU (right panels) for 0.125 MeV protons (top panels), 1 MeV protons (middle panels) and 8 MeV protons (bottom panels). Color and line-style codes are the same as in Figure 6.6.

connected than at 1.0 AU[4].

When comparing both radial positions at a given energy, the values of the peak flux observed at 0.4 AU are higher, about a factor 2, than those at 1.0 AU, but only for the fastest shocks and for the angular positions where the maximum peak fluxes are attained (e.g. W00, W15, E15 and W22). The reason is twofold:

[1] The shock weakens as it propagates out from the Sun, therefore it is stronger when it reaches these observers at 0.4 AU than at 1.0 AU.

[2] The observers close to Central Meridian are connected closer to the nose of the shock (i.e. the cobpoint is closer to the most effective region at accelerating particles) at 0.4 AU than at 1.0 AU.

For the remaining cases, the peak flux may or may not increase with the heliocentric distance depending on the initial speed of the shock, the way the observer establishes connection with the shock front, and the proton energy. We will discuss this in the last section of this chapter.

6.2.2 Correlation with the initial shock speed

A correlation between observed proton peak fluxes and speeds of the associated CMEs, as seen from coronagraph images from SOHO/LASCO and SOLWIND, was studied by Reames (2000). This author derived a power-law dependence between the peak intensity and the observed projected velocity of the associated CME[5]. Although we are not dealing with CME velocities, we have studied the possibility that the same type of functional dependence exists between the peak flux, f, and the initial shock speed given by SOLPENCO, v (input variable VELOS), for each angular position of the observer at 1.0 AU. Therefore, following the idea of Reames (2000), by assuming that $f \propto v^{\alpha}$, it is possible to compute linear fits for the different sets of interplanetary scenarios and energies contained in the data base.

[4]In the case of E30 SEP events, the peak flux attained for the speed 1650 km $s^{-1}$is higher than that for the speed 1800 km s^{-1}. Again, the reason is the combined effects of the presence of the turbulent foreshock region, the inner absorbing boundary located behind the shock and the duration of the SEP event.

[5]But without distinguishing whether the peak intensity was observed in association with the shock passage or during the prompt component of the event.

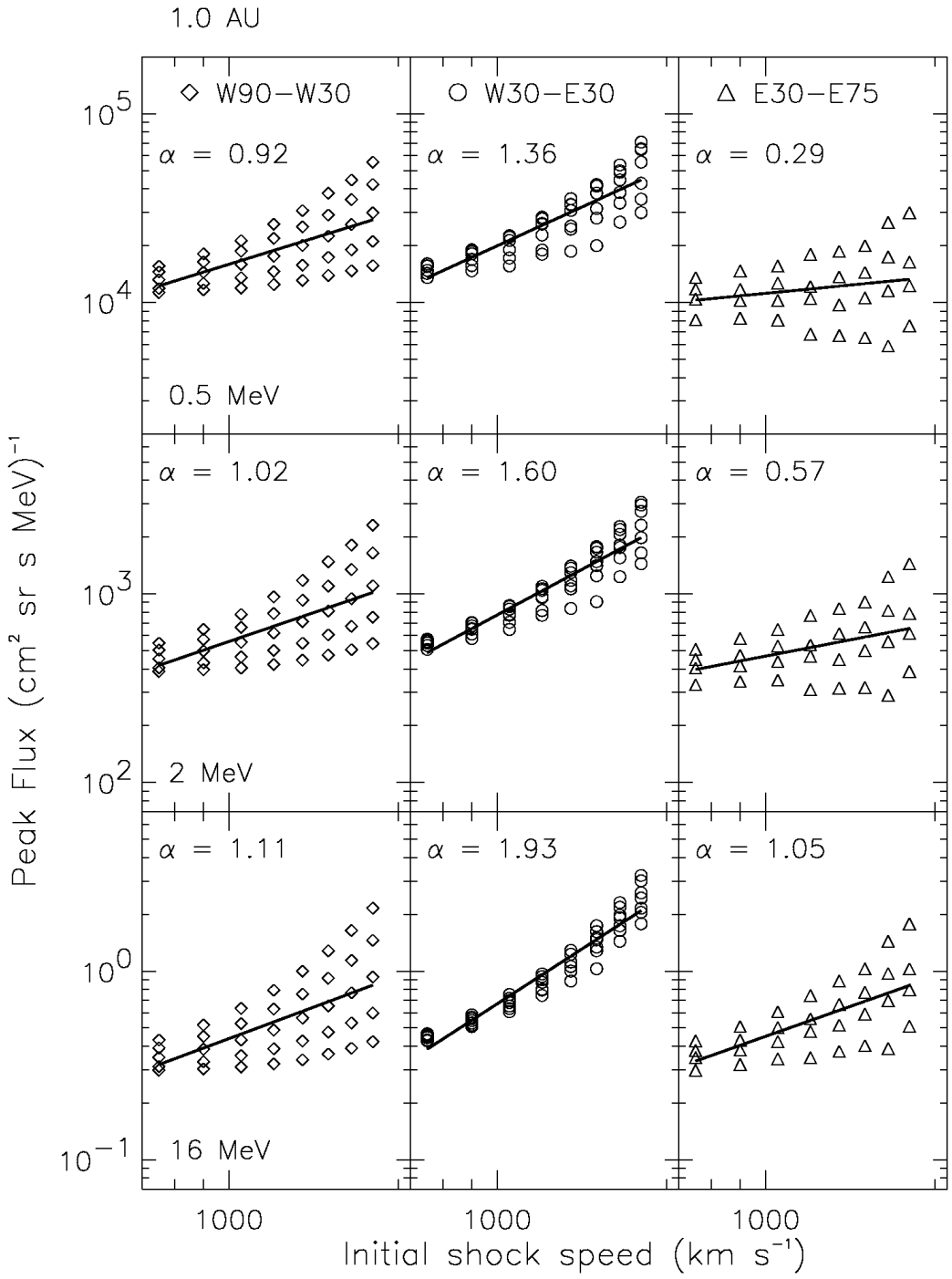

Figure 6.8: Correlation between the computed peak flux, f, at 1.0 AU and the initial shock speed, v, for 0.5 MeV, 2 MeV and 16 MeV (top, middle and bottom panels, respectively) proton SEP events. Each row displays three plots: western, central meridian and eastern events. The black line in each plot depicts the best linear fit to these points and, the index α of the derived dependence is shown at the top.

Table 6.1: Dependence of the computed peak flux, f, and the initial shock speed, v, at 1.0 AU, for three energies, as a function of grouped heliolongitudes. Each row shows the values of the index α and the coefficient of correlation, ξ (in parentheses), of the fits shown in Figure 6.8. The fourth row shows the values derived from the fit of the whole set of heliolongitudes.

Heliolongitude	0.5 MeV	2 MeV	16 MeV
W90-W30	0.92 (0.65)	1.02 (0.63)	1.11 (0.63)
W30-E30	1.36 (0.88)	1.60 (0.93)	1.93 (0.96)
E30-E75	0.29 (0.21)	0.57 (0.41)	1.05 (0.68)
W90-E75	0.93 (0.49)	1.13 (0.58)	1.42 (0.67)

Figure 6.8 shows the values of the peak fluxes for each initial shock speed, v, derived for three energies (from top to bottom: 0.5 MeV, 2 MeV and 16 MeV) and for spacecraft located at 1.0 AU. Each row has three panels displaying the peak flux value grouped by heliolongitude: "western events" (from W90 to W30, diamond symbols), "central meridian events" (from W30 to E30, open circles) and "eastern events" (from E30 to E75, open triangles). The value of the index α derived from a least-square fitting to the peak fluxes is indicated in each panel of this figure[6]. Table 6.1 displays the value of α derived for each set of locations as well as the correlation coefficient, ξ (in parentheses), for each energy. The last row of Table 6.1 gives the results of the fitting applied to the overall set of longitudes.

The relation between the initial shock speed, v, and the speed of the leading edge of the CME is not known, because a number of factors such as coronagraph image projections or the location of the shock in the CME white-light images (used when computing the CME speed) are difficult to quantify[7]. Therefore, the values of α are not directly comparable to those deduced by Reames (2000): 4.36 at ∼2 MeV and of 4.83 at ∼20 MeV.

Table 6.1 shows the correlation coefficients increase with particle energy when the whole set of heliolongitudes are taken into account. This reproduces the same

[6]In a double logarithmic plot, the $f \propto v^{\alpha}$ dependence should be represented as a straight line, like those of Figure 6.8.

[7]In fact, it does not exist yet any trustful procedure (e.g. Wen et al. 2007).

trend of the correlations of the peak flux with the CME speed found by Reames (2000). The reason is that the higher the energy of the particles, the less effect of the interplanetary transport processes on the final flux profiles and, thus a more direct relationship between the shock parameters and the peak fluxes. The correlation coefficients also increase with the energy for the specific sets of central meridian and eastern events. For western events, these coefficients keep constant with the energy. The reason is that these events have the largest transit times and, shock-accelerated particles are mostly injected at the onset of the event. Therefore, for western events, the transport processes have a stronger effect on the high-energy particle flux profiles considered in SOLPENCO than for central meridian and eastern cases. Note that only 40 western events show the peak flux near the onset whereas for the rest of events the peak flux occurs close to the shock passage.

Central meridian events display a much better correlation between the initial shock speed and the peak flux than western and eastern events. This is a consequence of the fact that for central meridian events the cobpoint is connected to the strongest region of the shock front when the shock arrives at the spacecraft. Hence, transport effects are less relevant with respect to the efficiency of the shock at injecting particles in the interplanetary medium. Fig. 6.7 shows that the faster the shock, the higher the peak flux for central meridian events. For eastern events the cobpoint scans only a small portion of the western wing of the shock front and the shock only establishes magnetic connection for a few hours before its arrival to the observer. These two facts, together with the influence of the foreshock region, explain the poor correlation obtained between the peak flux and the initial speed of the shock for these events.

The correlation coefficients for central meridian and eastern events increase when fitting only the peak fluxes derived from the two cases without assuming a turbulent foreshock region (Table 6.2). On the contrary, the correlation decreases when the presence of such a region is assumed (Table 6.3). The reason is a consequence of the effects of transport conditions within the foreshock region and those caused by the inner boundary of the transport model; hence, the higher correlation with the initial speed of the shock when there is no foreshock region. In the case of western events the correlation found in both scenarios is similar since the foreshock region is only active when the cobpoint scans the eastern wing of the shock toward its flank. Consequently, the effect of the foreshock region in western events is less important than in central meridian events, which are connected to the central part of the

Table 6.2: Dependence of the computed peak flux, f, and the initial shock speed, v, as for Table 6.1 but considering only the cases that do not assume the presence of a foreshock region.

Heliolongitude	0.5 MeV	2 MeV	16 MeV
W90-W30	1.03 (0.63)	1.09 (0.63)	1.14 (0.63)
W30-E30	1.77 (0.95)	1.90 (0.96)	2.00 (0.96)
E30-E75	0.84 (0.57)	1.04 (0.67)	1.18 (0.73)

Table 6.3: Same as in Table 6.2 but assuming the presence of the foreshock region.

Heliolongitude	0.5 MeV	2 MeV	16 MeV
W90-W30	0.81 (0.66)	0.85 (0.64)	1.08 (0.63)
W30-E30	0.77 (0.56)	1.25 (0.82)	1.87 (0.96)
E30-E75	−0.75 (0.40)	−0.09 (0.06)	0.94 (0.62)

shock while the foreshock is active. The same is true for eastern events, which are connected to a region of increasing efficiency (Heras et al. 1995).

In summary, both the particle injection history and the transport conditions have influence on the variation of the peak intensity with the initial shock speed. Simulations allow us to conclude that eastern SEP events contribute to the spread of peak intensities to lower values with decreasing energy, whereas central meridian events are those for which the higher peak fluxes are achieved[8].

Kahler & Vourlidas (2005) studied 20 MeV proton peak intensities associated with 116 CMEs with heliolongitudes ranging from W30 to >W90; their Figure 1 displays the peak intensities as a function of the CME speed. It is possible to compare this figure with the bottom left panel of Figure 6.8 by assuming that the range of CME speeds (< 2000 km s^{-1}) is comparable to the initial shock speeds considered in SOLPENCO and, that the computed high-energy peak fluxes scale with the

[8]The majority of the highest peak fluxes ($E > 10$ MeV) are derived for central meridian events (see e.g. http://www.sec.noaa.gov/ftpdir/indices/SPE.txt or Watari et al. 2001).

energy as a power law of spectral index $\gamma = 3$. Then, we can compare the 16 MeV proton peak intensities with those shown in their Figure 1 for 20 MeV protons by dividing the first by a factor 1.95. Under these assumptions, the computed peak values agree with those derived by Kahler & Vourlidas (2005) for the set of SEP events that show the highest peak fluxes. This result is also in agreement with the finding of these authors that these SEP events are associated with CMEs that tend to be wide[9] and bright, since all SEP events of SOLPENCO are associated with wide shocks.

6.3 The Fluence

The cumulative fluence of a SEP event is calculated by integrating the flux above a threshold energy, E, and throughout the duration of the upstream part of the SEP event up to a given time, t. The total fluence, F, is the cumulative fluence computed up to the arrival of the shock at the observer. Otherwise specified, hereafter, we will use the terms "total fluence" and "fluence" indistinctly. In this section we focus the analysis on the total fluence of the events in the data base of SOLPENCO. Two main factors determine the fluence:

[1] The duration of the injection of shock-accelerated particles, as the shock propagates from the Sun to the observer's position.

[2] The efficiency of the shock as a particle accelerator, which in turn depends on the position and evolution of the cobpoint.

Consequently, we have studied the dependence of the total fluence with the initial shock speed and the heliolongitude of the solar parent activity. We will not discuss each individual SEP profile obtained for each scenario of SOLPENCO, because all of them present a regular evolution of the cumulative fluence profiles from low to high energies (and, as expected, the lower the threshold energy E the higher the fluence). Since the aforementioned factors largely contribute to a greater difference on the total fluence from event to event, we will discuss the evolution of the total fluence by taking the average value over the four cases l02TN, l02TY, l08TN and l08TY.

[9] That is, significantly broader in longitude and latitude than CMEs associated with the particle events of lower peak intensities (Kahler & Vourlidas 2005).

6.3.1 Dependence on the initial shock speed and the location of the observer

Figure 6.9 plots the total upstream fluences computed at 1.0 AU (left panels) and at 0.4 AU (right panels) for the energy thresholds: 1 MeV, 4 MeV, and 32 MeV (top, middle and bottom rows, respectively). From this figure it is easy to notice that the highest fluences correspond to those observers that are magnetically connected to the shock front at the beginning of the event. That is, western and west-central meridian SEP events as seen at 1.0 AU (from W90 to W00), and central meridian and western SEP events (except W90) at 0.4 AU (i.e. from W75 to E30). Furthermore, the fluence for each event at a given energy is higher at 1.0 AU than at 0.4 AU because the shock injects particles for longer period of time before arriving at the spacecraft.

At 1.0 AU (left panels of Figure 6.9), the longer the time the shock injects particles the higher the fluence. Therefore, W45 events show the highest fluences for all energies and for each shock, and it is followed by W30, W22, W15 and W00 events[10]. For these observers, the cobpoint scans the most efficient regions along the shock front. As expected, the fluences for these five angular positions increase with the strength (the speed) of the shock, except for the W00 event at energies lower than 0.5 MeV and initial speeds lower than 1400 km s^{-1}. In these particular scenarios, the contribution of the duration of the event to the total fluence counteracts the contribution of the efficiency of the shock at accelerating particles. It is worth noting that at high energies, the total fluences of well-connected SEP events remain high as long as the shock is still able to accelerate particles when it arrives at 1.0 AU.

The connection time, t_c, increases from central meridian to eastern angular positions. Thus, the period of time during which the shock injects particles decreases as the observer is located farther east. For this reason the total fluence decreases when moving toward eastern heliolongitudes, for a given shock speed (left panels of Figure 6.9).

[10]For W75 and W90 observers, the cobpoint slides from about 17° westward of the nose of the shock toward its eastern flank. Therefore, the capability of the shock to accelerate particles is weaker than for the rest of western events; hence, the lower or similar fluences for faster shocks, in spite of their long duration.

W60 events behave similarly as W45 events at $E < 1$ MeV; but as higher energies are considered, the more the behavior of the fluence resembles that of the W75 events.

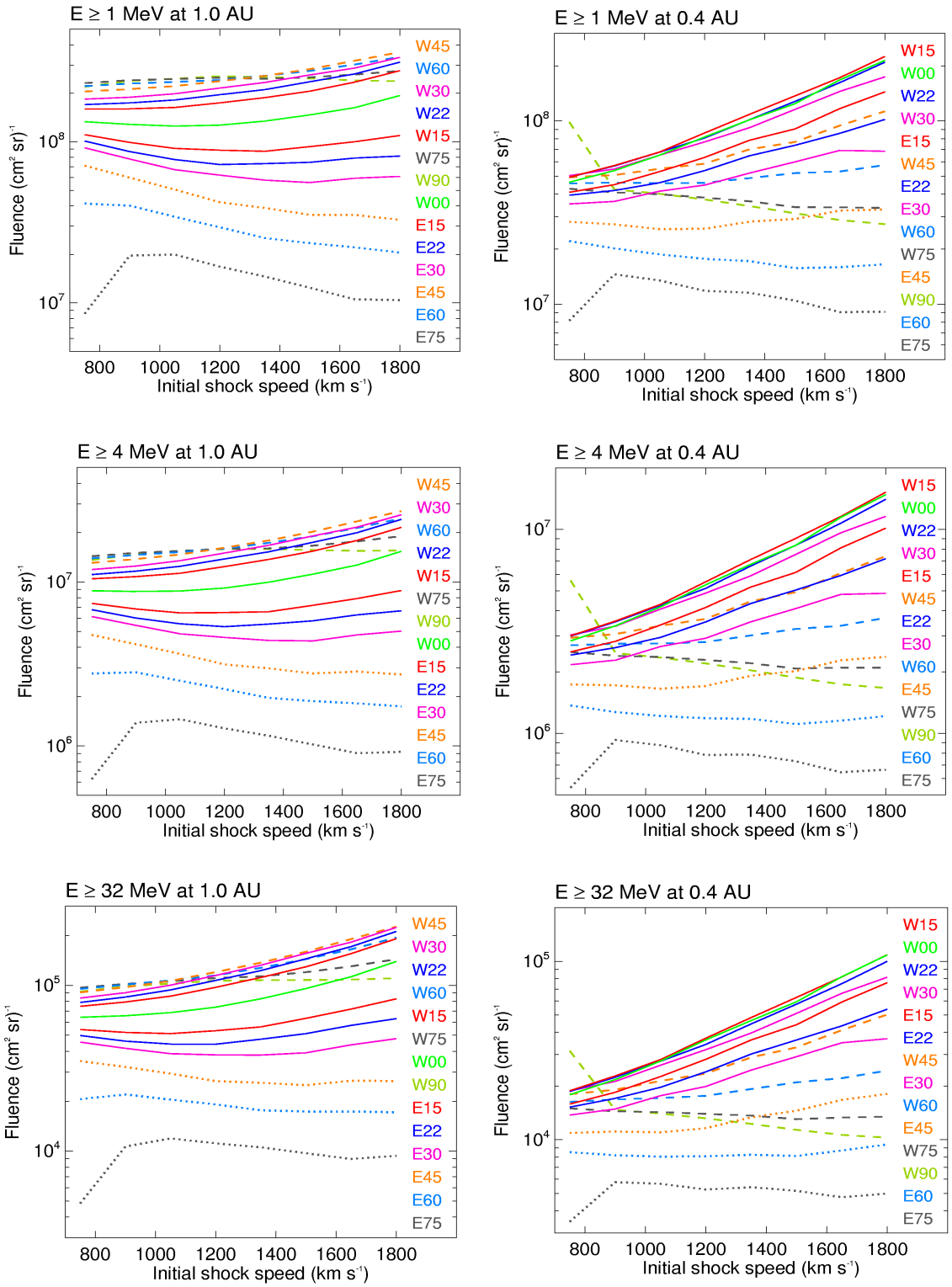

Figure 6.9: Total upstream fluence of SEP events observed at 1.0 AU (left panels) and at 0.4 AU (right panels) as a function of the initial shock speed and heliolongitude (color coded as in Figure 6.6). The fluence is shown for $E \geq 1$ MeV protons (top row), $E \geq 4$ MeV (central row) and $E \geq 32$ MeV protons (bottom row).

The behavior of the fluence with the speed of the shock, shows a smooth transition from central meridian to eastern events. The fluence starts to decrease with increasing shock speeds for E45 and E60 observers, at all energies. In these type of events, the cobpoint is connected to weak parts of the left wing of the shock; thus, the prevailing factor is the duration of the events (the faster the shock the less time it is injecting particles)[11]. This decrease diminishes with increasing proton energies because of the sum of the effects of the low efficiency of slow shocks and the transport conditions at high energies.

At 0.4 AU the influence of the duration of the shock-particle injection in the fluence is less important than at 1.0 AU due to the short transit times of the shock and, the fact that most observers (from E30 to W75) are connected at the beginning of the event. Therefore, the dependence of the total fluence[12] with the heliolongitude (left panels in Figure 6.9) is basically determined by the efficiency at accelerating particles of the region scanned by the cobpoint. Consequently, the higher fluences are measured by the W15 and W00 observers: for W15, the cobpoint is connected to the central part of the shock throughout the event and, the highest peak fluxes are attained by W00.

For well-connected events (except for W75) at 0.4 AU, the total fluence increases with the initial shock speed, that is, the stronger the shock the higher the fluence[13]. In the case of W75 events, the cobpoint scans the eastern flank of the shock[14]. Then, the dominant factor is the time that the shock injects particles; hence, the decrease of the fluence with the initial shock speed. The same reasoning applies for W90 and, for E60 and E75 observers, whose cobpoint moves along the western flank.

[11]The slowest E75 event shows the lowest fluence because the shock is injecting particles only for 3 hours.

[12]The total fluence of the SEP events calculated at 0.4 AU had been corrected by the flux tube cross section factor $A(1.0\text{ AU})/A(0.4\text{ AU})$ with respect to those shown in Figure 5 of Aran et al. (2005b). That is the reason why the values of the total fluence shown in the top right panel of Figure 6.9 are higher than those shown in Figure 5 of Aran et al. (2005b) and Figure 4.24 of Aran et al. (2004). The radial indices also change with respect to those shown in Figure 6 of Aran et al. (2005b), see next section.

[13]Two apparent odd features can be found in Figure 6.9: [1] The slowest W90 event has a total fluence remarkably higher than that of the remaining shocks because its long duration: it lasts 48.7 hours while the following slowest shock (900 km s^{-1}) only lasts 35.5 hours. [2] The slowest E75 event has the lowest fluence because the shock is injecting particles during only 2.4 hours, as happens at 1.0 AU.

[14]These observers are connected to the same IMF line that W110 observers at 1.0 AU.

To summarize, the main conclusions from this analysis are:

[1] For the same shock, the better the connection between shock and observer the higher the fluences either at 1.0 AU and 0.4 AU.

[2] For the same heliolongitude, the faster events that are well-connected from the beginning show the higher fluences.

[3] For the events that are initially poorly connected to the shock or not connected at all at the onset of the event, the events with higher fluences are those whose shock injects particles for a longer time.

6.3.2 Influence of the normalization constant

Statistical models for solar proton fluence predictions use event fluences measured above a given threshold energy (in particles cm^{-2}). In order to compare the total fluences provided by SOLPENCO with those estimated by statistical models (e.g. Gabriel & Feynman 1996 or Feynman & Gabriel 1996, and references therein), we multiply the values of the SOLPENCO synthetic fluences by a factor 4π sr to obtain the omni-directional fluences (e.g. Goswami et al. 1988). As can be seen in Table 6.4 the range of ≥ 1 MeV and ≥ 4 MeV fluences obtained at 1.0 AU are in accordance with the fluence values attained by the 70% of the events in the JPL proton fluence model by Feynman et al. (1993), $< 6.0 \times 10^9$ and $< 4.0 \times 10^8$ cm^{-2}, respectively. This model is based on proton data gathered by the IMP spacecraft fleet during active years between 1963 and 1991. For energies > 30 MeV SOLPENCO provides fluences in the range $6.3 \times 10^4 < F < 2.8 \times 10^6$ cm^{-2} (Table 6.4). In the JPL model only the 20% of the events at these energies have fluences in this interval, while the 70% of the events have higher fluences (up to 2.0×10^7 cm^{-2}). According to Smart et al. (2006), however, common > 30 MeV proton events have fluences in the range of $10^5 - 10^6$ cm^{-2}. This discrepancy may come from the fact that the JPL model only considers active years of the solar cycle, reducing the actual number of small events within this range of fluence values.

The output values of the flux and fluence profiles of SOLPENCO have been calculated using a scaling factor derived from analysis of the 12 – 15 September 2000 event (W09 Sep00, Section 5.4.5). To have an idea on how the value of the total fluence varies with the normalization constant, we select two simulated SEP events and calculate their correspondent scaling factors. These events are the 4 – 7 April

Table 6.4: SOLPENCO data base: minimum and maximum total fluences, F (cm^{-2}), derived at 1.0 and 0.4 AU for three energy thresholds.

	$F(\geq 1$ MeV)	$F(\geq 4$ MeV)	$F(\geq 32$ MeV)
1.0 AU	$1.0 \times 10^8 - 4.4 \times 10^9$	$7.5 \times 10^6 - 3.4 \times 10^8$	$6.3 \times 10^4 - 2.8 \times 10^6$
0.4 AU	$1.0 \times 10^8 - 2.8 \times 10^9$	$6.5 \times 10^6 - 1.9 \times 10^8$	$4.1 \times 10^4 - 1.9 \times 10^6$

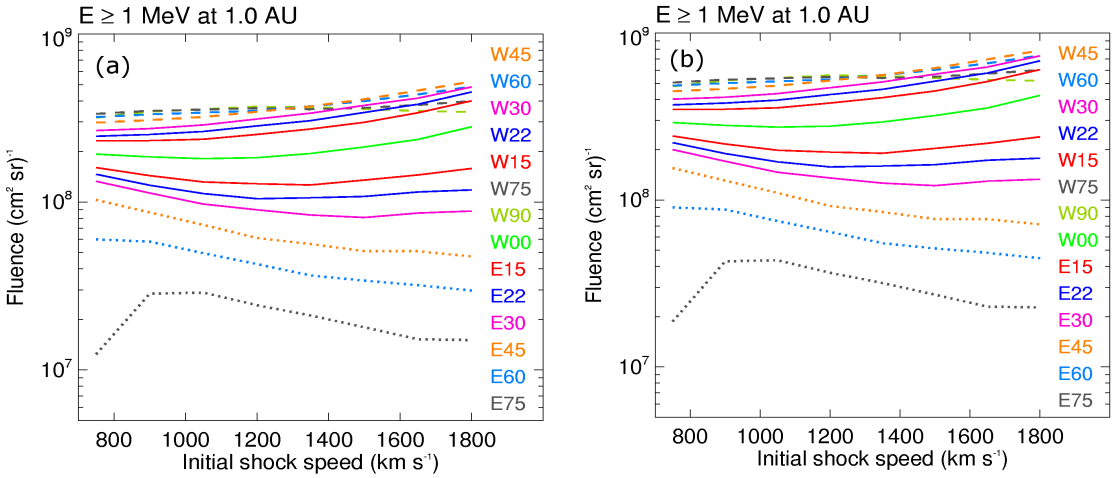

Figure 6.10: Total upstream fluence $E \geq 1$ MeV protons for SEP events observed at 1.0 AU using a normalization constant derived from (a) the Apr00 event (left panel) and from (b) the Jun00 event (right panel). Details and color code as in Figure 6.6.

2000 (W66 Apr00) and the 6 – 8 June 2000 (E18 Jun00) events (Vainio et al. 2007). Both events yield a normalization constant larger than the one used in SOLPENCO by a factor 1.5 and 2.2, respectively. Figure 6.10 shows the ≥ 1 MeV fluences at 1.0 AU obtained using the scaling factor from the Apr00 event (left panel) and from the Jun00 event (right panel).

Note that both Sep00 and Jun00 events are associated with central meridian solar sources and they lead to a noticeable different range of fluence values. This can be seen by comparing Figure 6.10b and the top left panel of Figure 6.9. The fluences shown in Figure 6.10b extend from 2.2×10^8 to 9.7×10^9 cm^{-2}. This increment (by a factor 2.2) of the total fluence represents that the 80% of the events in the fluence

distributions given by JPL model (Feynman et al. 1993) is within the range of values of the SOLPENCO data base. The same is obtained for ≥ 4 MeV fluences, whereas for ≥ 32 MeV the use of the Jun00 normalization constant accounts for $\gtrsim 40\%$ of the JPL model events.

To compute the total fluence of a given SEP event, the particle intensity above a given energy, E, is integrated throughout the time interval that the particle intensity is above a certain intensity threshold (e.g. Feynman et al. 1993). Therefore, such a definition may count compound SEP events as a sole event, like for instance, the series of events from 19 October to 9 November 1989 (Jun et al. 2007). The synthetic events of the SOLPENCO data base are created with the aim to predict isolated gradual events, therefore the fluence an event provided by SOLPENCO is expected to be lower than the total fluence measured over a compound SEP event. This fact can account for part of the large events considered in the JPL model that SOLPENCO cannot reproduce. On the other hand, occasionally, large isolated gradual SEP events may have > 30 MeV fluences exceeding $> 1.0 \times 10^9 \mathrm{cm}^{-2}$, like for example, the 24 March 1991 SEP event (Smart et al. 2006). Several factors may explain the difference of $\sim$3 orders of magnitude between the largest observed fluences and those predicted by SOLPENCO: (i) part of these SEP events may be associated shocks that move faster than the shocks simulated in SOLPENCO (as for example, the 4 August 1972 SEP event Smart & Shea 2003) , thus, presumably more efficient injectors of shock-accelerated particles; (ii) the larger SEP events usually show powerful particle injections close to the Sun that we cannot model due to the location at $18R_\odot$ of the inner boundary of the MHD shock propagation model; and (iii) the energy spectrum at high-energies is harder than the average spectrum assumed in SOLPENCO[15]. In addition, the code does not take into account the contribution of the downstream region, that in these events might be important.

After all these considerations, we conclude that SOLPENCO may predict fluences of not-too-large SEP events and mainly at low-energies. Further, scaling factors derived from statistics over as many SEP events as possible are needed in order to obtain reliable fluences. Furthermore, the contribution of the downstream region could be important for certain type of events.

Finally, we would like to draw the attention on the fact that the fluences derived

[15]In Chapter 7 we compare several characteristics of the proton flux profiles of a set of large gradual SEP events with respect to the corresponding synthetic profiles produced by the code and we make a first analysis of these factors.

at 0.4 AU have similar or lower values than those derived at 1.0 AU (Table 6.4). In the study by Lario et al. (2006) only 9 of the 72 SEP events were measured when Helios spacecraft were within the range of heliocentric distances 0.40 ± 0.05 AU. Their fluences at 4 – 13 MeV range from 2.3×10^6 to 1.9×10^8 cm^{-2} and, at 27 – 37 MeV, from 5.0×10^3 to 1.2×10^6 cm^{-2}. Therefore, compared to these 9 SEP events, SOLPENCO yields similar values of the total fluence for $\geq$ 4 MeV and $\geq$ 32 MeV proton events as measured at 0.4 AU (Table 6.4).

6.4 Radial and longitudinal variations

By comparing the fluences derived from SOLPENCO at 1.0 AU and 0.4 AU, we conclude that the contribution of the interplanetary shock as a particle accelerator to the total fluence of the SEP event is relevant. Fluences observed at 1.0 AU are larger than the corresponding fluences measured at 0.4 AU, by a factor between $\gtrsim$1 and 10 times depending on the shock speed and the heliolongitude of the parent solar event. This conclusion contrast with the usually recommended inverse square law dependence with the heliocentric distance, r (e.g. Feynman et al. 1993)[16]. The recent work by Lario et al. (2006) is the sole thorough observational study performed over a large number of SEP events simultaneously observed either by IMP-8 and by Helios-1 or Helios-2. The statistical analysis of a selected ensemble of 72 events determines that the dependence of the event fluence on r is $r^{-2.1}$ at 4 – 13 MeV and $r^{-1.0}$ at 27 – 37 MeV. Therefore, the obtained radial dependence is less steep than r^{-2} for 27 – 37 MeV protons, thus suggesting that the r^{-2}-law may be relaxed.

We have compared the total fluence, F, of the SEP events within the SOLPENCO data base for several pairs of observers at 0.4 and 1.0 AU which are approximately located along the same upstream magnetic field line[17]. These pairs are: E75 – E45, E60 – E30, E45 – E15, E30 – W00, E15 – W15, W00 – W30, W15 – W45, W30 – W60,

[16] As commented in Section 2.4, this dependence is largely based on two superseded ideas: (i) that particle acceleration is mainly confined at the flare site or nearby, neglecting the contribution due to the interplanetary shock; (ii) and that the particle transport is diffusive (Chapter 2, last section). Rosenqvist (2003b) reported that the data from Helios spacecraft do not support the inverse square law hypothesis for the fluence and they suggested that it could vary from $r^{-1.1}$ to $r^{-0.05}$.

[17] Their respective magnetic footpoints are separated by 5°, assuming a Parker spiral for the upstream IMF topology and a background solar wind speed of 400 km s^{-1}(Section 6.1).

W45 – W75 and W60 – W90. Where the first longitude refers to the event at 0.4 AU and the second to the event at 1.0 AU. Assuming a dependence $F(r)$ given by $F \propto r^{\beta}$, we can calculate for each pair of observers the ratio of fluences $F(0.4)/F(1.0)$ and deduce the radial index, β, as: $F(0.4)/F(1.0) = 0.4^{\beta}$. Since both observers are sitting almost on the same IMF line, their respective cobpoints are close and, therefore, they share the same particle injection history. In this way, we eliminate the contribution of different conditions for particle injection along the shock front from the analysis of the radial dependence for each pair of observers.

Figure 6.11 shows, the values of β derived for the pairs of SEP events described above, as a function of the initial shock speed, for $\geq$ 2 MeV (left panel) and $\geq$ 32 MeV (right panel) protons (for sake of clarity, only seven pairs have been plotted). The duration of the shock-accelerated particle injection is longer for the observer at 1.0 AU than for the observer at 0.4 AU (from 12 to 70 hours), thus resulting in larger fluences at 1.0 AU than at 0.4 AU. This is the reason why the obtained radial index is always positive: $0.5 < \beta < 1.8$ at $E \geq 2$ MeV and $0.7 < \beta < 2.0$ at $E \geq 32$ MeV. For the energy thresholds considered in SOLPENCO, β increases with the energy. This suggests that the ratio of fluence at high-energy over fluence at low-energy increases with increasing distance of the observer from the Sun. This energy dependence behavior agrees with that of the radial indices derived by Lario et al. (2006) from observations[18] and with the simulations performed by Lario et al. (2007).

As can be seen in Figure 6.11, β decreases as the initial shock speed increases for those observers magnetically connected to the central regions of the shock front throughout the event. This behavior is basically due to two facts:

[1] The faster the shock the shorter the difference of duration of the particle injection between both observers and thus, the less difference between the fluence of the SEP event at 1.0 AU and 0.4 AU.

[2] The higher peak fluxes attained at 0.4 AU with increasing shock speed contribute to reduce the difference between the fluences calculated at both radial distances.

For events connected to the flanks of the shock (pairs W60 – W90 and E60 – E30 in

[18] Lario et al. (2006) comments: *"Particle intensities and event fluences decrease faster with radial distance at low than at high energies. One possible explanation is that transport processes such as pitch-angle scattering, and indirectly energy loss, are more effective at low than at high energies..."*.

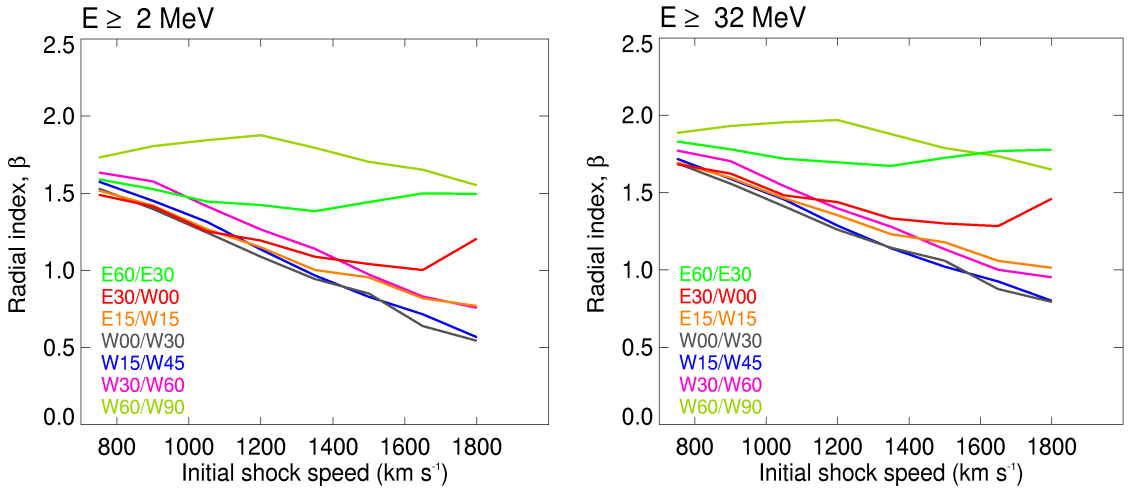

Figure 6.11: Radial dependence, r^{β}, of the upstream fluence for $E \geq 2$ MeV (left panel) and $E \geq 32$ MeV (right panel) plotted as a function of the initial speed of the shock. Each line represents one pair of SEP events at 0.4 AU and at 1.0 AU, respectively indicated in the inset, that approximately share the same IMF line.

Figure 6.11) β remains almost constant with the initial shock speed. In the case of western events this is a consequence of the long duration of the particle event seen at 1.0 AU. In the case of eastern events, the higher peak flux attained at 1.0 AU, with respect to that at 0.4 AU, counteracts the effect of the shorter difference of the duration of the injection of particles between both locations.

The values of the radial index derived from fluences do not match with those derived by Lario et al. (2006). This is not strange because (i) SOLPENCO does not take into account either the contribution of the downstream region to the total fluence or the injection of high-energy particles by the shock when it is close to the Sun. And (ii) we are comparing the radial indices derived from SOLPENCO with the observational indices derived from spacecraft measurements in interplanetary scenarios quite different from those computed with SOLPENCO: Only two of the 72 SEP events of the statistical study by Lario et al. (2006) have the two observers sitting on the same nominal IMF line[19] and are located at different radial distances ($\Delta r > 0.1$ AU) and only 9 events of this set are measured at 0.40 ± 0.05 AU and at 1.0 AU locations (i.e, directly comparable with the scenarios provided by SOLPENCO).

[19]The average angular separation between IMP-8 and the closest Helios spacecraft is $73° \pm 44°$.

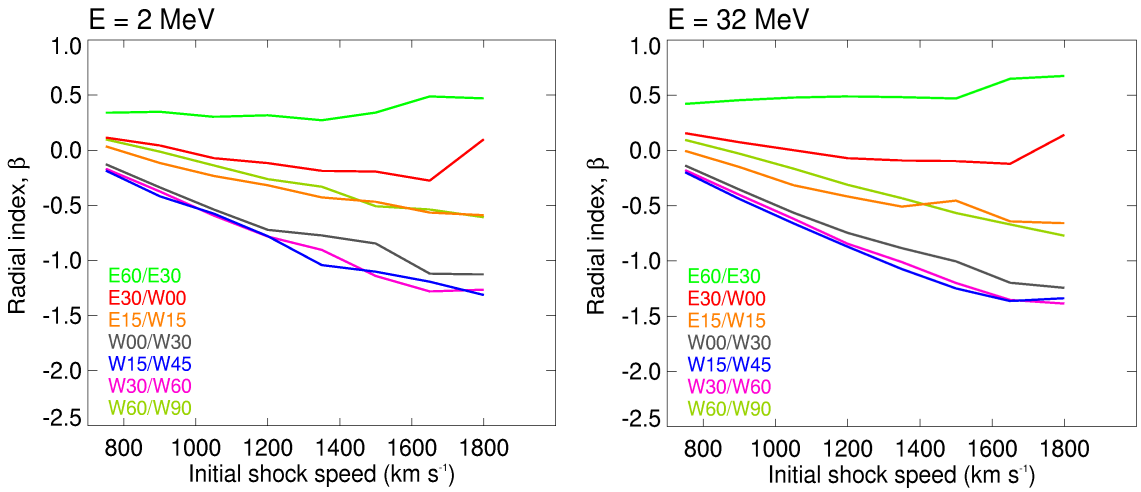

Figure 6.12: Radial dependence, r^{β}, of the peak intensity for $E = 2$ MeV (left panel) and $E = 32$ MeV (right panel) plotted as a function of the initial shock speed like in Figure 6.11.

Two events reported by Lario et al. (2006) where the fluences for the two energy channels are measured and the angular distance between magnetic footpoints is $< 20°$ show different behaviors for the radial dependence: $r^{-1.6}$ and $r^{-0.71}$ at 4 – 13 MeV and $r^{-1.6}$ and $r^{+0.99}$ at 27 – 37 MeV (Figure 4 and 5 of this paper, respectively).

Figure 6.12 shows the radial dependence of the peak intensity for the same set of events shown in Figure 6.11. As for the case of fluences, well-connected events show decreasing values of the radial index with increasing speed. The lower values of the radial indices are obtained for those pairs formed by central meridian events[20], as seen at 0.4 AU, because they have the higher peak fluxes (Figure 6.7). For eastern pairs (E60 – E30 in Figure 6.12), the obtained radial indices are positive because the cobpoint moves toward a stronger region of the shock front, and consequently, the highest peak flux is attained at 1.0 AU.

The energy dependence of the radial index derived for peak intensities is not as clear as for the fluence. Figure 6.12 shows that the range of values of β seems to spread with increasing energy. Taking minimum and maximum values, β varies within the following intervals: $-1.2 < \beta < 0.3$ at 0.125 MeV, $-1.3 < \beta < 0.5$

[20]The pairs E15 – W15 and E30 – W00 show higher values of β than those of west-central meridian events because the W15 and W00 observers show the highest peak intensities attained at 1.0 AU.

at 2 MeV and $-1.4 < \beta < 0.7$ at 32 MeV. Thus, the average values increase with the energy, but for specific cases it may decrease, as for well-connected events associated with slow shocks. Lario et al. (2006) studied three events with close magnetic footpoints, their Figures 4, 5 and 6, that yield a variation of the radial dependence from $r^{-1.2}$ to $r^{-1.6}$ at 4 – 13 MeV and a dependence of $\sim r^{0}$ at 27 – 37 MeV. Therefore, the values of β match with the radial variation derived from these observations.

The main conclusion of this chapter is that it cannot be derived an universal radial dependence valid for all types of gradual SEP events, neither for fluences nor for peak intensities. The variation of these quantities with the heliocentric distance depends on:

[1] The efficiency of the shock, at injecting shock-accelerated particles, in the region scanned by the cobpoint along the shock front (that is, on the angular separation in heliolongitude between the observer and the nose of the shock).

[2] The strength of the shock, here characterized by its initial speed.

[3] The kinetic energy of the particles[21].

The first factor agrees with the main conclusion by Lario et al. (2006) that the azimuthal distance between the magnetic footpoint of the spacecraft and the site of the flare associated with the SEP event's origin is more important than the heliocentric radial distance of the spacecraft when determining the peak intensity and the fluence of SEP events.

In order to indicate how the peak intensity varies with the angular position of the observers and the initial speed of the shock, we have considered the synthetic flux profiles of events triggered by three different shocks which are measured by three spacecraft located along, approximately, the same IMF line at 0.4, 0.7 and 1.0 AU for two different magnetic connections:

[Case A] The spacecraft are connected to the nose of the shock at the beginning of the event (i.e. the heliolongitude of the leading edge of the shock is W60 as seen from 1.0 AU) and their cobpoints slide along the right wing of the shock as it propagates outward, hence the observers are connected to less efficient regions of the shock front as it approaches them.

[21] Ruzmaikin et al. (2005) analyzed the variation with the radial distance of the maximum intensity attained at the front of a strong shock. They obtained that the radial index decreases with the energy. This is an expected result because, in fact, it only reflects that the shock becomes less efficient at injecting high-energy particles as it propagates away from the Sun.

[Case B] The spacecraft are sit along the IMF line that passes through the central meridian observer (W00) at 1.0 AU. In this case, the observers establish magnetic connection with the shock front at some point on its left wing and their cobpoints move toward the nose of the shock as it expands.

Figure 6.13 illustrates the Case A. The top right plot sketches the scenario. The shock expands into the interplanetary medium in a direction 60° to the west from the Sun – spacecraft-at-1.0 AU line. Color squares mark the location of the three spacecraft at 1.0 AU (black), 0.7 AU (blue) and 0.4 AU (red). Their respective angular positions are W60, W45 and W30; hence, they share almost the same IMF line. The brown arch is a sketch of the shock front when it reaches 0.3 AU. Each of the three pair of plots correspond to a different shock: a fast shock, $v_s = 1800$ km s^{-1} (top left panels), an intermediate-speed shock, $v_s = 1350$ km s^{-1} (bottom left panels), and a slow shock, $v_s = 750$ km s^{-1} (bottom right panels). The transit speed of the shock up to each observer is indicated in brackets with the same color code as for spacecraft. For each shock, the left panel shows the computed flux profiles of 8 MeV and 32 MeV protons observed by each spacecraft (color coded, as well) assuming $\lambda_{\parallel 0} = 0.2$ AU (for 0.5 MeV protons, and scaled with energy, see Section 5.2) and the absence of the turbulent foreshock region. The value of the mean free path assumed at the two energies is indicated in each plot. Vertical dashed lines indicate the time of the shock arrival at each observer. Right panels show the peak intensity (solid circles) and differential fluence (solid squares) as a function of the heliocentric distance (denoted by R in the plots) at the same energies, 8 MeV (black) and 32 MeV (red).

For the fast shock, the flux profiles for the observer at 0.4 AU continuously increase and peak at the shock arrival. For the observer located at 1.0 AU, the flux starts to decrease once the traveling shock is beyond 0.7 AU. The reason is that the cobpoint is located in the strong central part of the shock front (i.e. most effective at injecting particles); but when the shock approaches 1.0 AU, the cobpoint is already on the eastern wing of the shock front (thus, in a weaker region). In this case, peak intensities decrease with radial distance as $r^{-1.28}$ at 8 MeV and $r^{-1.21}$ at 32 MeV. As the initial speed of the shock decreases, the difference between the jump speed (VR) at the shock front (at its nose and flanks) reduces, thus reducing the difference of the injection rate, Q, between both regions. Consequently, the peak intensities at the three spacecraft become more similar, thus obtaining flatter radial dependences ($r^{-0.04}$ at 8 MeV and $r^{-0.09}$ at 32 MeV, for the slowest shock).

Figure 6.14 shows with the same format as Figure 6.13 the case of shocks directed toward the observer located at 1.0 AU (case B). Now, the angular positions of the three spacecraft are W00, E15 and E30 at 1.0, 0.7 and 0.4 AU, respectively. In this case the cobpoint moves from the western wing toward the nose of the shock front as the shock travels and decelerates up to 1.0 AU. In terms of the efficiency of the shock at accelerating particles, this means that VR (and thus, the injection rate, Q) increases until the shock arrives to a certain distance between 0.4 AU and 0.7 AU (depending on the speed of the shock) and afterward, it starts to decrease up to 1.0 AU.

The increase of the peak intensities due to the motion of the cobpoint toward the central part of the shock front is compensated by the weakening of the shock as it expands. Consequently, similar peak intensities are attained at the three spacecraft; thus showing almost flat power-laws with the radial distance for the three shocks. The variation of the peak intensities is more noticeable in the case of the fast shock because the range of values of VR is the largest among the shocks considered, and VR reaches its maximum value close to 0.7 AU. Hence, the highest peak flux is observed by the spacecraft located at this distance. As the shock speed decreases, the range of values of VR reduces. This yields flat radial dependences for the mid-speed shock ($r^{+0.10}$ at 8 MeV and $r^{+0.08}$ at 32 MeV). For the slow shock, VR is almost constant throughout the event. In this case, the peak intensity increases with r because of the combined effects of the longer time that the shock is injecting particles in the interplanetary medium, as it travels toward 1.0 AU, and the transport processes undergone by these particles.

In summary, the main conclusion derived from the analysis presented in this section is that even in the case of observers located in the same flux tube, the heliolongitude of the parent solar event, and the way each observer establishes magnetic connection with the traveling shock, determines the radial variation of the peak fluxes and of the upstream fluences. Consequently, it makes no sense to derive a general law for the radial dependence because of the wide variation of behavior from event to event. The possible exception are events connected to the central region of the shock front, for which the derived range of radial indices is narrow (see Figures 6.11 and 6.12). It is also clear that the results obtained here must be revisited after including in SOLPENCO the contribution to the fluence of the downstream region of each event and the extension of the particle shock-injection below $18R_{\odot}$. Furthermore, we cannot forget that other factors, like the particle transport con-

ditions, may contribute to the heliocentric variations of peak intensities and event fluences (Lario et al. 2007).

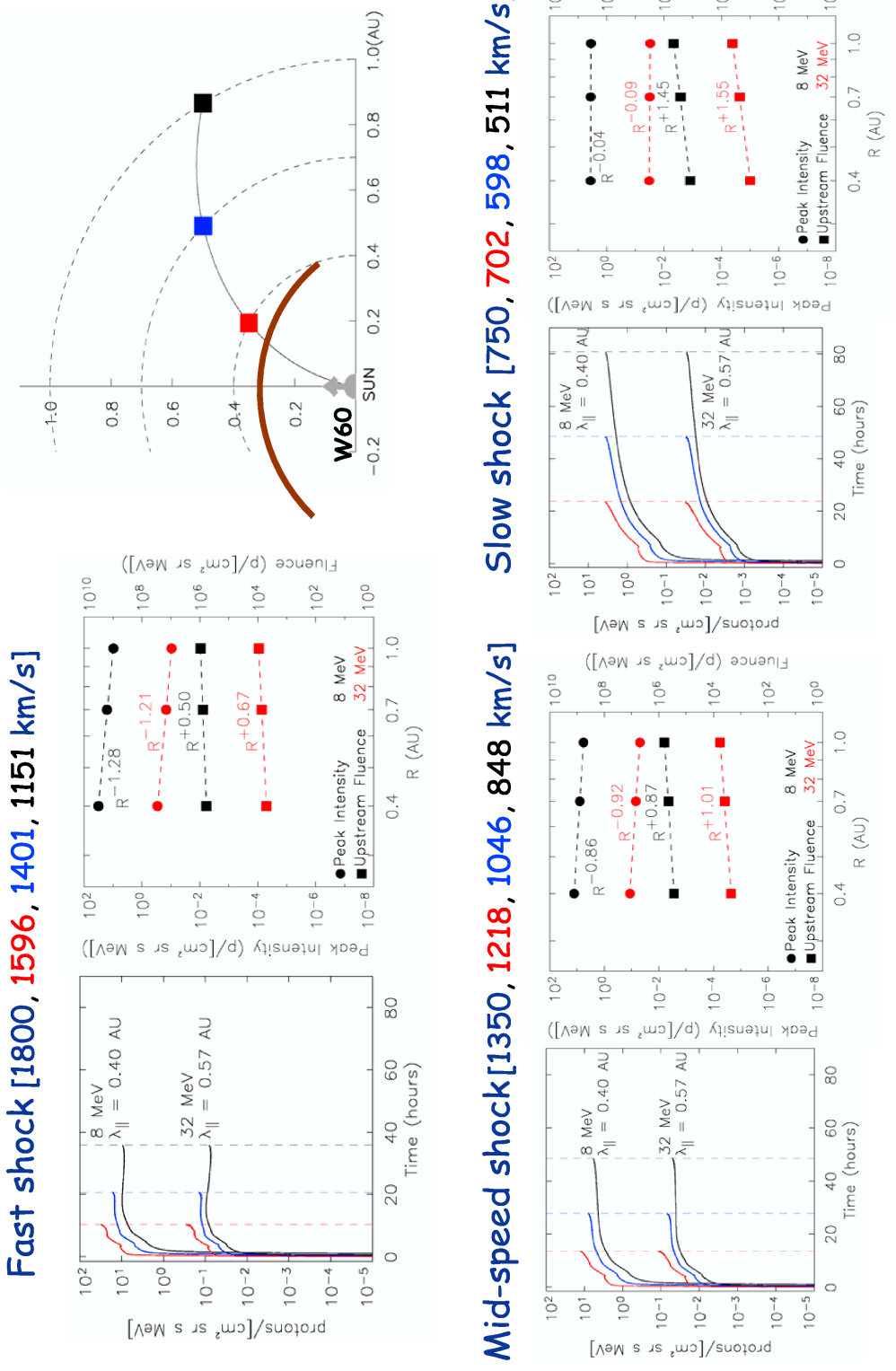

Figure 6.13: 8 MeV and 32 MeV proton flux profiles of SEP events measured at 0.4 AU (red), 0.7 AU (blue) and 1.0 AU (black) by observers located on almost the same IMF line and connected to the nose of the associated shocks at the beginning of the event. Case A. See text for details.

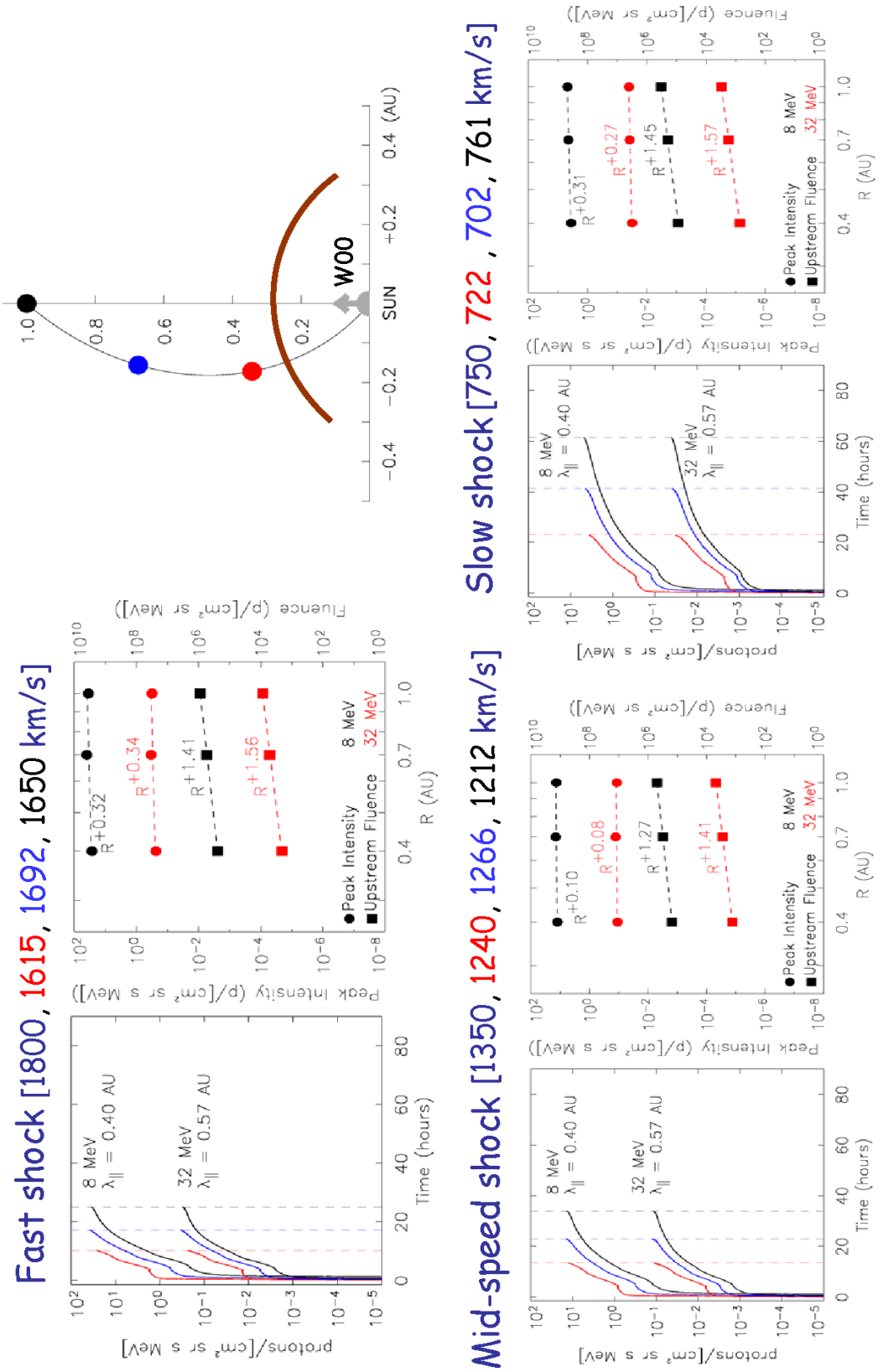

Figure 6.14: Same as Figure 6.13 but for shocks directed toward the 1.0 AU spacecraft, Case B (see text for details).

7 Observations and Predictions

In order to use SOLPENCO as an operative tool it is necessary to verify[1] that it has been built right. This means to compare the outputs of the code with observed and modeled SEP events. Nevertheless, as already commented, modeling gradual SEP events is a hard task due to the complexity of processes involved and the number of variables and observables to handle. As a consequence, verification becomes an extended and long-term procedure. Here we will focus on two aspects of this process. First we will analyze the synthetic intensity-time profiles provided by SOLPENCO for two SEP events already modeled. This comparison will allow us to understand the influence of the values adopted on the outputs of the code. Second, we will evaluate the performance of SOLPENCO at predicting the peak intensity of SEP events, one of the key factors of SEP event induced space weather effects. We will compare the peak flux values derived by SOLPENCO with the observed peak intensities of SEP events characterized by the initial speed of the associated shock and the heliolongitude of the parent solar event.

As a reminder, we summarize here the main parameters used to build the data base of SOLPENCO. The injection rate has been calculated from the evolution of the normalized speed ratio (VR) at the cobpoint position for each case, taking $k = 0.5$ for all energies and Q_0 derived from the simulation of the Apr81 W50 SEP event. The energy dependence of Q_0 has been considered to be a power law with index $\gamma = 2$ for $E < 2$ MeV and $\gamma = 3$ for $E \geq 2$ MeV. The initial parameters describing the shock simulation are the pulse shock speed ($750 \leq v_s \leq 1800$) km s^{-1}, its angular width (fixed, $\omega = 140°$) and the piston-driven duration ($\tau = 2$ hours). The proton energies considered are: 0.125, 0.25, 0.5, 1.0, 2.0, 4.0, 8.0, 16.0, 32.0 and 64.0 MeV.

[1] Verification ('to build right') is a previous step to validation ('to build the right thing'); see footnote 4 in Chapter 1.

7.1 Comparing SOLPENCO with modeled SEP events

7.1.1 The 4 –6 April 2000 event (Apr00)

Apr00 is a western event[2] (N18 W66), with a shock transit time of 48.82 hours and speed of 843 km s^{-1} (see Section 4.2 for more details). The parameters derived from the simulation of this event are (see Appendix C): VR $\in (0.5, 2.8)$ (Figure C.2); $v_s = 1445$ km s^{-1} ($\omega = 140°$, $\tau = 2$ hours); the values for the mean free path, Q_0 and k can be found in Section 4.2 and Table 44.1.

The values of the input variables needed to reproduce this event with SOLPENCO are the following:

- Radial distance: 1.0 AU.
- Initial shock speed: 1445 km s^{-1}.
- Heliolongitude: W66.
- Proton mean free path: 0.2 AU.
- Turbulence: YES.

The outputs from SOLPENCO are:

- Shock transit time: 48.5 hours, 19 minutes shorter than the actual transit time.
- Shock transit speed: 849 km s^{-1}(less than 1% faster than the actual average transit speed).
- The proton flux profiles shown in Figure 7.1.

Figure 7.1 shows the flux profiles obtained by SOLPENCO (black traces) and proton intensities measured by the EPAM instrument on board ACE (red traces, Gol98). The seven panels (a-g) compare similar energy channels (88 keV$< E <$ 5.7 MeV). The observational values are the same that those shown in Figure 4.5. Table 7.1 lists the energy channels compared in Figure 7.1. The second and the

[2]The comparison of the proton intensity profiles provided by SOLPENCO for this event with those measured by ACE/EPAM has been published in Aran et al. (2006).

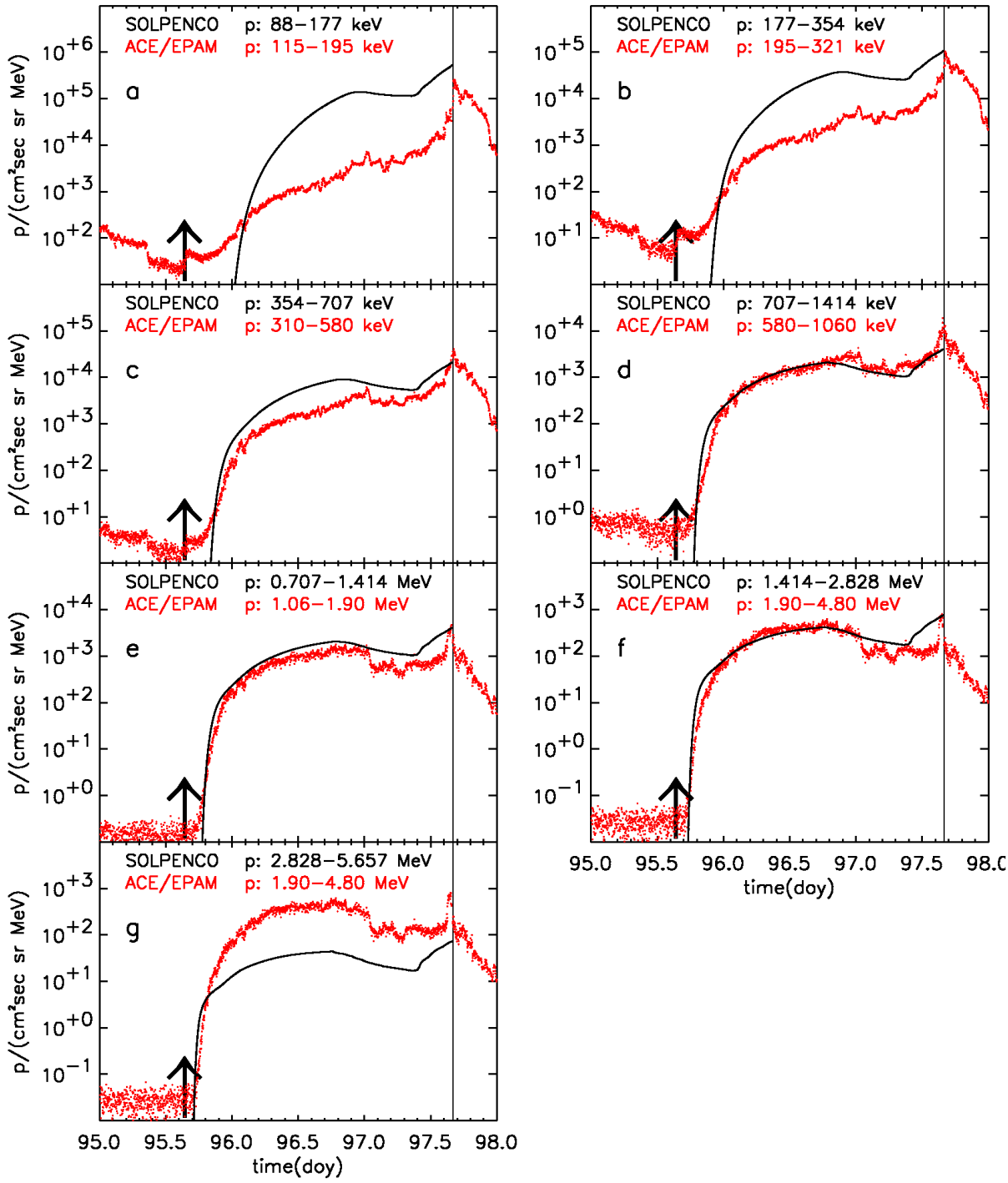

Figure 7.1: Flux profiles for the 4−6 April 00 event. Comparison between synthetic flux profiles produced by SOLPENCO (black solid line) and those observed by the ACE/EPAM (red dotted trace), for seven energy ranges, as indicated in the top of each panel. The thin vertical line marks the time of the shock arrival at the spacecraft and the arrow indicates the onset of the parent solar activity.

Table 7.1: Energy (in MeV) channels shown in Figure 7.1

Plots	SOLPENCO		ACE/EPAM	
	Energy interval[a]	$< E >$	Energy channel	$< E >$[b]
a	0.09 – 0.18	0.125	0.16 – 0.20	0.150
b	0.18 – 0.35	0.250	0.20 – 0.32	0.250
c	0.35 – 0.71	0.500	0.32 – 0.58	0.424
d	0.71 – 1.41	1.000	0.58 – 1.06	0.784
e	0.71 – 1.41	1.000	1.06 – 1.90	1.419
f	1.41 – 2.83	2.000	1.90 – 4.80	3.020
g	2.83 – 5.66	4.000	1.90 – 4.80	3.020

[a]These energy intervals have been calculated by assuming that the simulated proton energy (next column) is the geometric mean of the interval (see Table 5.1).

[b]Geometric mean energy of each channel.

fourth columns give the energy windows of SOLPENCO and ACE/EPAM, respectively; whereas the third and the fifth columns show the corresponding geometric mean value of each energy window. The energy channels of SOLPENCO do not coincide with those of ACE, therefore, Figure 7.1 compares the flux profiles for the most similar channels available.

Figure 7.1 shows that:

- The simulated peak flux reaches values similar to the observed ones for most of the energy channels (panels b, c, e and f).
- The synthetic flux profiles at high energies (> 700 keV) match the observations (panels d, e and f).
- The predicted flux for the highest channel (plot g) is smaller than the observed flux profile. This result is expected because the ACE/EPAM flux includes protons with $E > 1.9$ MeV (Table 7.1), whereas SOLPENCO's profile is derived assuming only $E > 2.8$ MeV. The contribution of low-energy particles represents a noticeable fraction of the observed flux depending on the spectral energy dependence[3]. Note that the observed flux is fitted better when a mean

[3]For example, when considering the spectral index observed at the shock arrival ($\gamma = 1.59$), protons of $1.9 < E < 2.8$ MeV account for the 60% of the flux of the 1.9 – 4.8 MeV ACE/EPAM channel.

energy of 2.0 MeV is assumed, as displayed in Figure 7.1f.

– The flux profiles are overestimated at low energies (panels a, b, and c).

Despite the simplifying assumptions made to build the synthetic flux profiles, SOLPENCO performs well in predicting the peak fluxes of this SEP event and the flux for the intermediate and high energy channels. The overestimation of the flux at low energies is due to the average values of k and Q_0 used in the equation $\log Q = \log Q_0 + k\mathrm{VR}$. SOLPENCO uses $k = 0.5$ for all energies; this value is slightly higher than the values of k derived from the modeling of this event at different energies. For instance, the simulation yields a value $k = 0.26$ for the 0.25 MeV channel. Since VR at the cobpoint decreases from 2.8 to 0.5 throughout the event (see Chapter 4, for example), the difference between the values of k in the simulation and in SOLPENCO leads to consider an overestimated injection rate of shock accelerated particles at low-energy. In addition, for western events the cobpoint slides from the strongest central part of the shock front (the region most efficient in particle acceleration) at the onset of the event, to the weaker (less efficient) eastern wing of the shock late in the event. Therefore this extreme variation of VR makes our results sensitive to our selection of k. A second factor which has an important influence is the initial injection rate, Q_0; the value adopted in SOLPENCO for 0.25 MeV protons is 1.8×10^{-34} cm^{-6} s^3 s^{-1}, while the simulation of the event yields 3.7×10^{-35} cm^{-6} s^3 s^{-1}.

The combination of these two factors results in a clear overestimation of Q at low-energy (i.e. a factor 23 at the beginning of the event which reduces to 6 at the shock arrival, for the 0.25 MeV channel). These differences largely reduce when comparing energy channels better adjusted; for example, to a factor 5 and 2, at the time of connection and at the shock arrival, when comparing the 1 MeV channel of SOLPENCO with the 0.789 MeV channel of ACE/EPAM. The dependence of the injection rate of shock-accelerated particles, Q, on the energy can also produce differences between the synthetic and observed flux profiles. SOLPENCO assumes a constant spectral index for the energy dependence of Q throughout the event, which is an over-simplification. Figure 7.2 shows how the spectral index of Q deduced from the simulation of the event evolves from the beginning of the event up to the shock arrival. It is easy to see that the spectral indices assumed in SOLPENCO are almost the same as those derived from the modeling of this event at the shock arrival (for example, if t >40 hours, $\gamma_e = 1.85$ for $E < 2$ MeV and $\gamma_e = 2.77$ for $E \geq 2$ MeV); nevertheless, they are quite different at the beginning of the event (if

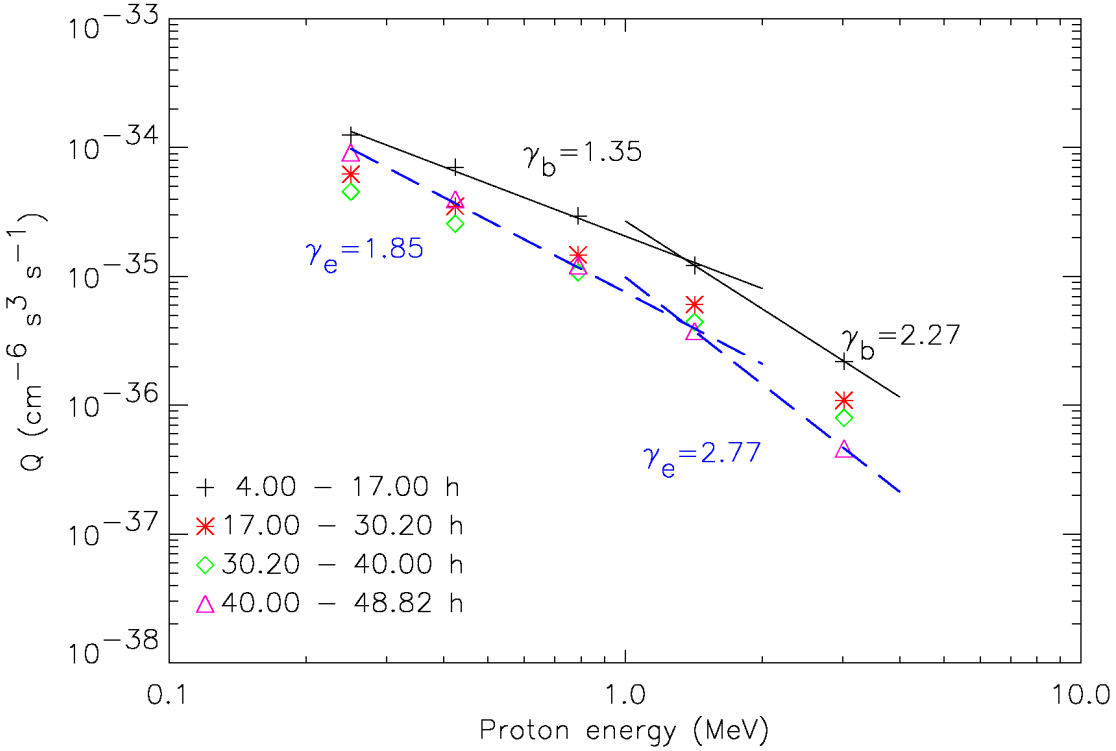

Figure 7.2: Spectra of Q as derived from the modeling of the Apr00 SEP event using the form of the initial shock pulsation used in SOLPENCO (Smith & Dryer 1990). Each point is the average value of Q over the time interval indicated for each energy channel. The solid line shows the fit at low ($E < 2$ MeV) and at high ($E \geq 2$ MeV) energy for the first period and the dashed line shows the fit for the last period (ending at the shock arrival). The values of the spectral index, at the beginning, γ_b, and at the end, γ_e, of the event derived from the fittings are also shown.

$t \geq 17$ hours, then $\gamma_b = 1.35$ for $E < 2$ MeV and $\gamma_b = 2.27$ for $E \geq 2$ MeV). For the 0.25 MeV energy interval (panel b of Figure 7.1), these variations lead SOLPENCO to use at the beginning of the event a value of Q that is 2.5 times higher than that derived from the modeling. This factor decreases to 1.2 at the shock arrival. It is worth noting that the changes in the spectral index are less significant than those of k and Q_0.

7.1.2 The 22 – 24 April 1979 event (Apr79)

This event was generated from a central meridian longitude (S20E10). A detailed description of this SEP event can be found in Sanahuja et al. (1983), Heras (1989), Heras et al. (1992) and Lario (1997). The shock transit time to 1 AU is 48.0 hours thus, its transit speed is 856.5 km s^{-1}. The parameters derived from the simulation of this event are: VR $\in (0.1, 1.0)$; $v_s = 900$ km s^{-1} ($\omega = 72°$, $\tau = 12$ hours). At 1.0 MeV, the derived mean free path is: 0.075 AU for $t < 20$ hours, 0.33 AU for $20 \leq t < 35$ hours, 0.30 AU for $35 \leq t < 39$ hours, and 0.20 AU for $t \geq 39$ hours (Lario 1997). The values of Q_0 and k are given in Table E.2 of Appendix E.

SOLPENCO flux profiles are obtained selecting the following inputs for all energies:

- Radial distance: 1.0 AU.
- Initial shock speed: 965 km s^{-1}.
- Heliolongitude: E10.
- Proton mean free path: 0.2 AU.
- Turbulence: YES for $E < 2$ MeV and NO for $E \geq 2$ MeV.

The outputs from SOLPENCO are:

- Shock transit time: 48.0 hours, the same time elapsed by the actual shock to arrive at ISEE-3.
- Shock transit speed: 857.9 km s^{-1}.
- Proton flux profiles: see Figure 7.4.

The different initial width and duration of the pulse of the shock derived from modeling this event and the value of these parameters used in SOLPENCO forced us to choose among the possible shocks in SOLPENCO that have an initial speed that better reproduces the time of the shock arrival at ISEE-3, $v_s = 965$ km s^{-1}. The difference between this speed and the speed derived from the modeling of the event (900 km s^{-1}) mainly comes from the six times longer duration of the initial pulse considered in the actual MHD models of the event ($\tau = 12$ hours). The longer the pulse duration, for $\tau \in (0.5, 12)$ hours, the larger the energy during the shock, and thus the shorter the transit time of the shock even though the initial speed and width remain fixed (Smith & Dryer 1990). The effect of the different width

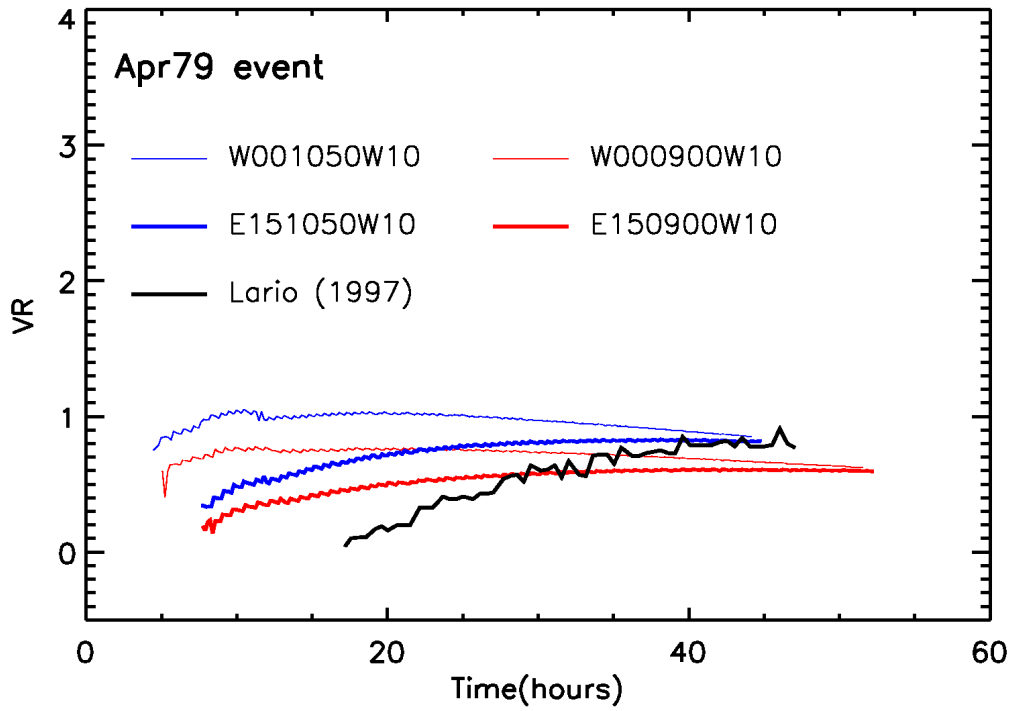

Figure 7.3: Evolution of VR for the four shock simulations of the data base of SOLPENCO (color lines) used to compute the Apr79 event and that derived from the modeling of this SEP event by Lario (1997) (black trace).

translates also into a delayed connection (t_c = 18 hours) for the narrow simulated shock (Lario 1997).

Figure 7.3 shows the evolution of the normalized speed jump across the shock front, VR, derived by Lario (1997) (black trace) and the evolution of VR for each of the four shocks in the data base from which the April79 flux profiles are computed (color traces). Each curve starts at the connection time and ends at the shock arrival at the spacecraft. As can be seen the wide shocks considered in SOLPENCO establish connection before the modeled shock. This difference between connection times determines the lack of match between the predicted and modeled evolution of VR in the first half of the event. In spite of this, the early connection established in SOLPENCO leads to a good fitting of the rising phase of the flux profiles for all the energy channels shown in Figure 7.4 except for the energy window displayed in panel f.

Figure 7.4 shows the comparison between proton differential intensity-time profiles measured by ISEE-3 and those provided by SOLPENCO for seven energy

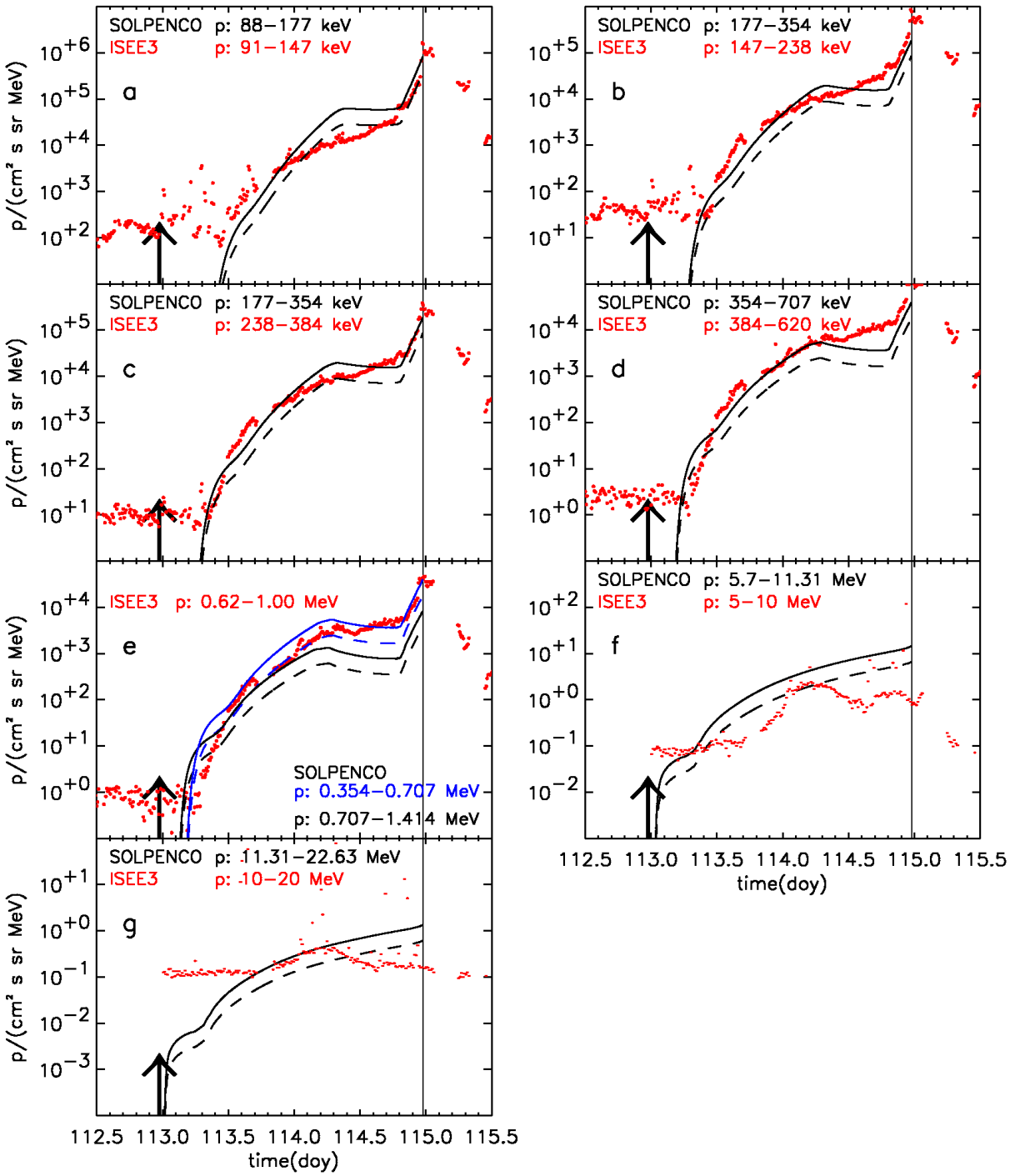

Figure 7.4: Flux profiles for the 22−24 April 79 event. Comparison between the particle intensity profiles measured by ISEE-3 (red dots) and the synthetic flux profiles produced by SOLPENCO using the Sep00 normalization constant (black dashed lines) and the Jun00 normalization constant (black solid lines), for seven energy ranges, as indicated in the top of each panel. See text for details.

Table 7.2: Energy (in MeV) channels shown in Figure 7.4

Plots	SOLPENCO		ISSE-3	
	Energy interval[a]	$< E >$	Energy channel	$< E >$[b]
a	0.09 – 0.18	0.125	0.09 – 0.15	0.116
b	0.18 – 0.35	0.250	0.15 – 0.24	0.187
c	0.18 – 0.35	0.250	0.24 – 0.39	0.302
d	0.35 – 0.71	0.500	0.39 – 0.62	0.488
e	0.71 – 1.41	1.000	0.62 – 1.00	0.787
f	5.7 – 11.3	8.000	5.0 – 10.0	7.071
g	11.3 – 22.6	16.000	10.0 – 20.0	14.142

[a]These energy intervals have been calculated by assuming that the simulated proton energy (next column) is the geometric mean of the interval (see Table 5.1).

[b]Geometric mean energy of each channel.

ranges. Table 7.2 gives the energy channels compared in each of the seven plots (a-g) of this figure, following the same pattern described for Table 7.1. In panels b and c, we compare the flux profiles measured by the 0.15 – 0.24 MeV and the 0.24 – 0.39 MeV energy channels of the detector DFH onboard ISEE-3 with the same synthetic profiles from SOLPENCO at 0.25 MeV because both channels include this energy and overlap part of the energy interval described by this energy, 0.18 – 0.35 MeV (Table 7.2, panels b and c). For each channel two synthetic profiles are displayed: black dashed and black solid lines. The black dashed dashed traces are the flux profiles provided by SOLPENCO (i.e. by calibrating the intensities with the normalization constant derived from the Sep00 SEP event, see Chapter 5). The black solid traces are the flux profiles provided by SOLPENCO scaled using the normalization constant derived from Jun00 SEP event (Chapter 6). As can be seen in Figure 7.4, for this event, the election of the Jun00 normalization constant yields better predictions of the flux profiles at low-energies (plots a – e).

From the intensity-time profiles displayed in Figures 7.4 we can see that:

– The rising phase of this event is well fitted for all energies below 1.0 MeV. The main difference with respect to the observed profiles arises from the characteristics of the foreshock region. The fitting could be improved by introducing a thinner foreshock region whose effects should start earlier than that considered

by SOLPENCO.

- Using the calibration factor derived from the Jun00 event, the peak flux is reasonably well fitted for the lowest energies (plots a, c and d). It is not the case for plot b where the ISSE-3 energy channel has the contribution of protons of lower energies than those considered by SOLPENCO.
- The mean energy of the 0.62 – 1.00 MeV channel of ISEE-3, i.e. 0.788 MeV (Table 7.2 and plot e), lays between the mean energies of the two SOLPENCO channels plotted in this figure, i.e. 0.5 MeV (blue trace) and 1 MeV (black trace). We can conclude from this comparison that if SOLPENCO could interpolate between these two energies, the rising phase and the peak flux would be much better fitted.
- For the highest energies (> 5 MeV), SOLPENCO fails to reproduce the evolution of the observed flux profiles (plots f and g).

Two factors are responsible for the differences obtained at high energies (> 5 MeV): the value of $k = 0.5$ and the energy spectrum of the injection rate ($\gamma = 3$) assumed in SOLPENCO. VR softly increases throughout the event; hence the injection rate Q(VR) also increases with time. However, from the modeling of this event, Lario (1997) derived that Q decreases with time for the energies > 5 MeV (those considered in plots f and g of Figure 7.4) and, consequently he derived a negative value of k at these high energies (see Appendix E). On the other hand, the spectral index of Q derived by Lario (1997) is steeper ($\gamma = 4.37$) than the value assumed in the code; hence, the higher intensities attained by SOLPENCO at these energies.

7.1.3 Summary

The two SEP events analyzed in this section are representative of the problems that arise when comparing SOLPENCO outputs with real SEP events. From this analysis, we conclude that despite the simplicity of the assumptions made in the generation of the data base and the small number of real SEP events compared, SOLPENCO can predict with relative accuracy the intensity-time profiles of different energy channels for a variety of SEP events. However, there are no two SEP events alike and there is a diversity of factors that can determine the final shape and values of the fluxes observed by spacecraft. The assumptions and simplifications adopted in our model are only a crude approximation of the multiple actual processes involved

in the development of the SEP events, ranging from the particle transport, the shock propagation and the dynamic evolution of the shock-acceleration mechanisms and particle injection into the interplanetary medium.

The main factors responsible for the differences between the observed and the synthetic flux profiles, are the values of k, Q_0, the spectral index of the injection rate and the value of the normalization constant. Consequently, to improve this engineering code it would be necessary to (i) further investigate the dependence of the k-parameter with the energy, as well as the dependence of Q with other MHD-shock parameters at the cobpoint position; (ii) model the shock propagation of western events starting closer to the Sun at a few solar radii above the solar surface due to the sensitivity of Q(VR) relation to the value of k in the early stages of western events; and (iii) derive an 'average' value of the normalization constant between observed and synthetic fluxes by using a larger number of modeled SEP events.

7.2 Central meridian SEP events

In this section we extend the comparison between observations and the outputs of SOLPENCO to a number of gradual SEP events observed at 1.0 AU between January 1998 and October 2001, for proton energies higher than 5 MeV. In the first section, we describe the data sets used for the present study and the criteria established to select the SEP events. Two features relevant to space weather predictions are the event fluence and peak intensity attained at different energies (e.g. Feynman & Gabriel 2000; Lario et al. 2006). In the present work we have focused on the analysis of the event peak fluxes. First we present the comparison of both the measured peak fluxes and their energy spectra with those predicted by SOLPENCO for the subset of central meridian SEP events[4] (i.e. events originated by solar events associated with solar flares occurring at heliolongitudes spanning from E30 to W30). Further, we extend the study to the remaining heliolongitudes and finally, we give the conclusions.

[4]Aran, Sanahuja & Lario, *Comparing proton fluxes of central meridian SEP events with those predicted by SOLPENCO*, Adv. Space Res., doi:10.1016/j.asr.2007.08.003, in press (2007).

7.2.1 Observational data

We have identified the solar origin of 115 forward interplanetary shocks associated with SEP events detected by ACE and IMP-8 between January 1998 and October 2001. The energy range of the investigated proton intensities extends from 47 keV to 440 MeV. The shock passages by ACE were obtained from the preliminary list available at the web site of the ACE Lists of Disturbances and Transients[5]. We also inspected the solar wind velocity and the interplanetary magnetic field components throughout the whole period using ACE/SWEPAM (McComas et al. 1998) and ACE/MAG (Smith et al. 1998) data available at the ACE Science Data Center, respectively ([w4] and [w5], Section 2.5).

In order to compare the fluxes at the energies provided by SOLPENCO with observations, we have used low energy (< 5 MeV) particle data from the LEMS120 telescope of the ACE/EPAM instrument, with a time resolution of 96s (Gol98). Specifically, we have analyzed the proton LEMS120 data from channels P'3 to P'8 that cover energies from 0.115 MeV to 4.8 MeV ([w3] in Section 2.5). At higher energies, we have used 330s-averaged data collected by the IMP8/CPME instrument (Sar76)[6]. The IMP8/CPME proton energy channels examined for comparison with the outputs of the code are P5, P7, P8 and P9, that extend from 4.6 MeV to 96 MeV ([w7], Section 2.5).

In order to identify the parent solar event that originated the SEP event and the accompanying transient interplanetary shock, we have proceeded in two ways: [1] we have carried out a literature survey of previous studies that already established the origin of both SEP events and shocks; and [2] we have searched for flares and CMEs occurring before the onset of the event in the solar activity reports of the Solar Geophysical Data (SGD) and the LASCO-CME Catalog ([w9] in Section 2.5) assembled by Yashiro et al. (2004). A table with the solar origin identification of each of the 115 interplanetary shocks associated with SEP events is presented in Appendix I.

[5] http://www-ssg.sr.unh.edu/mag/ace/ACElists/obs_list.html

[6] Available at http://hurlbut.jhuapl.edu/IMP/data/imp8/cpme/cpme_330s/protons/.

7.2.2 Selection of events and procedure

We define a central meridian event as that generated by a solar event taking place within 30° of the Sun-Earth line, i.e. from E30 to W30 locations. We have started by studying central meridian events because these SEP events are expected to produce the highest values of peak flux intensities and fluences (e.g. Smart et al. 2006). Therefore, from the initial set of 115 shock-associated SEP events we have chosen those that fulfill the following criteria:

[1] the association between the shock and the parent solar activity is well established and unique;

[2] the longitude of the solar event lies between E30 and W30;

[3] the proton intensity-time profiles show a significant increase of the flux profiles for $E < 25$ MeV and a noticeable enhancement up to 96 MeV; and

[4] the SEP event is not superimposed on a preceding event (i.e. we require small particle pre-event background intensity).

The final output is a set of 8 SEP events whose main features are shown in Table 7.3. The first column indicates the number of the selected event. Columns 2 – 5 give the year, day of year, month/day, and time in UT of the shock passage by ACE, respectively. Columns 6 – 12 describe the main characteristics of the associated solar events. Columns 6 – 9 show the date, and the time of the first appearance of the associated CME by the C2 SOHO/LASCO coronagraph, the derived linear speed and type (H = Halo) of the CME. Column 10 gives the class of the associated X-ray and H_α flare, column 11 provides the onset time of the 1 – 8 Å X-ray emission, and column 12 the H_α flare location. Finally, the last column indicates the references where the associations between the solar origin and the interplanetary shock have been established.

In order to generate the synthetic flux profiles corresponding to each one of the selected SEP events it is necessary to determine the initial speed of the shock. At present, it does not exist any observational proxy that can provide a reliable estimation of the shock speed at the distance of the inner boundary of the MHD model (see Section 3.2). The initial input shock speeds for the shocks at 18 $R_\odot$ listed in Table 7.3 have been derived from the transit speed of the shock[7] and the heliolongitude

[7]Transit speed of the shock: Sun-ACE distance divided by the shock transit time (the time elapsed from the onset of the X-ray flare up to the shock arrival time at ACE).

Table 7.3: List of selected SEP events

	Interplanetary Shock				Solar Origin							
No.	Year	Doy	Date (mm/dd)	Time at ACE (UT)	CME Date (mm/dd)	Time (UT)	V_{CME} (km/s)	Type	Peak Flare (Xray/H_α)	Onset Time	H_α Location	Ref
1	1998	238	08/26	06:21	08/24	Data Gap			X1.0/3B	21:48	N35 E09	1,2
2	1998	267	09/24	23:13	09/23	Data Gap			M7.1/3B	06:44	N18 E09	2
3	2000	160	06/08	08:41	06/06	15:54	1119	H	X2.3/3B	14:58	N20 E18	3,4
4	2000	197	07/15	14:15	07/14	10:54	1640	H	X5.7/3B	10:03	N22 W07	5
5	2000	259	09/15	04:00	09/12	11:54	1550	H	M1.0/2N	11:31	S17 W09	3,6,7
6	2001	090	03/31	00:23	03/29	10:26	942	H	X1.7/2N	09:57	N16 W12	8,9
7	2001	101	04/11	15:28	04/10	05:30	2411	H	X2.3/3B	05:06	S23 W09	5,8,9
8	2001	268	09/25	20:02	09/24	10:30	2402	H	X2.6/2B	09:32	S16 E23	10

1, Bale et al. (1999); 2, Lario et al. (2000a); 3, Gopalswamy et al. (2004); 4, Cane & Richardson (2003); 5, Lario et al. (2004b); 6, Aran et al. (2005a); 7, SGD679; 8, Sun et al. (2002); 9, Manoharan et al. (2004); 10, Lario et al. (2003b).

of the associated solar event (column 12) by interpolating among the polynomial fittings, as described in Section 5.4. The values obtained for each SEP event following this method are: 1399, 1136, 1131, 1615, 740, 1222, 1348, 1387 km s^{-1}, from events #1 to #8 of Table 7.3, respectively. Since the lowest value for the possible input initial shock velocities in SOLPENCO is 750 km s^{-1}, we have set the initial speed of the event #5 to this value.

To identify the proton maximum intensity measured at a given energy channel, we have smoothed the intensity-time profile by running a time-window of 22 minutes, in order to skip punctual data irregularities. We have searched for the maximum intensity by scanning the smoothed flux profile from the onset of the event up to the time that either the flux decreases to the pre-event level or another SEP event starts. The top panel of Figure 7.5 shows the proton differential intensity-time profiles of the ten studied energy channels (between 0.1 and 96 MeV) for the 12 – 15 September 2000 event (#5 in Table 7.3). The peak intensities found are marked by black crosses. The short left vertical line (W09) indicates the onset of the associated X-ray flare and the vertical thick line marks the time of the shock passage by the ACE spacecraft. The vertical dashed line indicates the time up to which the peak flux has been searched for. The occurrence of another central meridian (W07) solar event early on doy 260 is indicated by a short small thick vertical line as well as the

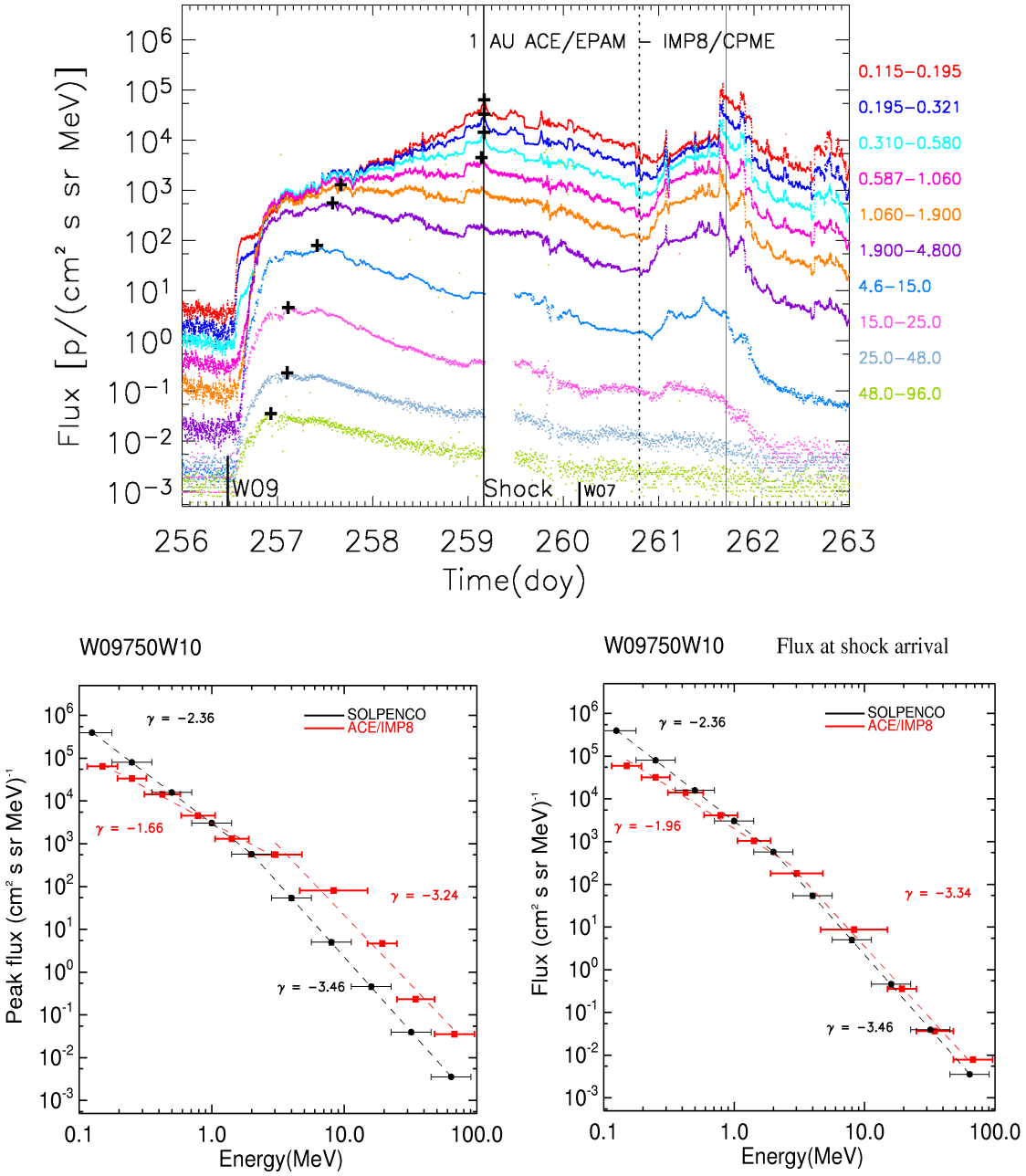

Figure 7.5: 12 – 15 September 2000 SEP event. Top panel: Differential intensity-time profiles measured by ACE/EPAM (0.12 – 4.8 MeV) and IMP-8/CPME (4.6 – 96.0 MeV), color coded. Peak intensities are marked by black crosses. A short vertical line on doy 256 indicates the onset of the solar parent event. A thick vertical line marks the time of the shock arrival at ACE. Bottom panels: Computed and observed peak flux (left panel) and flux values at the shock arrival (right panel)shown as a function of the particle energy; observed values are marked by red squares and predicted values by black circles. See text for details.

associated interplanetary shock arrival by a thin vertical line on day 261. This SEP event (#56 in Appendix I) was discarded because it does not meet the conditions [3] and [4] of the selection criteria.

As discussed in Chapter 6, it is difficult to know a priori the transport conditions undergone by the particles during a given SEP event. Therefore, we have taken as the predicted peak flux the average value over the synthetic peak intensities when calculated for each of the four particle transport conditions considered in SOLPENCO[8]. Since the space weather community is interested in predictions of the value of the peak flux at different energies, we have calculated the spectra of the peak flux regardless of the time at which it is attained[9]. In order to test the average energy spectra assumed in SOLPENCO for the injection rate of shock accelerated particles, we have also calculated the energy spectra at the shock arrival (see details in Section 5.3).

Following the same criteria as in Chapter 5 we assume that the energy dependence of the proton intensity (either at the peak flux or at at the shock passage) behaves as a double power law, $E^{-\gamma}$, with one spectral index for low energies (from 0.12 MeV to 4.8 MeV) and another one for high energies (from 1.9 MeV to 96 MeV). The bottom panels of Figure 7.5 show the energy dependence of the peak intensity (left panel) and of the intensity at the shock arrival (right panel). Observational values are indicated by red squares and predicted values by black circles. The horizontal error bars mark the width of each energy channel. The small vertical error bars of the predicted peak fluxes (barely discernable) indicate the range of variation of the peak flux value with the particle transport conditions. The peak intensities do not significantly vary with transport conditions; thus, for this comparative study it is reasonable to take the average peak intensity as the peak flux of the event. The dashed lines in the bottom panels of Figure 7.5 are the obtained log-log linear fits, and the values of the corresponding spectral indices at low and high energies are also indicated. As for the SEP event shown in this figure, the flux at the shock arrival is generally better predicted by SOLPENCO than the peak flux.

[8]Two values of the mean free path and the existence/absence of the turbulent foreshock region (Section 5.2).

[9]This is frequently done among the scientific community as well, for instance, when calculating either the event-average spectra of particle intensities (e.g. Tylka & Lee 2006) or the spectra of event fluences (e.g. Mewaldt et al. 2005), or when analyzing observed peak intensities (c.f. Figure 14 Cane et al. 1988). By analogy, the corresponding value is known as the 'spectral index' of the peak flux.

7.2.3 Peak fluxes: intensity and time

For each SEP event and for any energy channel, we have calculated the ratio between the synthetic and the observed peak flux. Table 7.1 lists the pairs of synthetic/observational energy intervals used when comparing ACE/EPAM data with SOLPENCO outputs, whereas Table 7.4 gives the pairs of compared energy intervals when comparing IMP-8/CPME data. The left panels of Figure 7.6 show this ratio for six pairs of energy channels, from low (~ 0.4 MeV, top panel) to high (~ 67 MeV, bottom panel) energy. Since the energy channels of ACE/EPAM and IMP-8/CPME and those of SOLPENCO do not fully coincide, we compare in the second and third panels the observed 1.9 – 4.8 MeV and 4.6 – 15.0 MeV peak fluxes with the peak fluxes of two channels of SOLPENCO. As can be seen, peak flux predictions fit much better with the observations at low than at high energy. For $0.3 < E < 0.7$ MeV (top panel), the average ratio between the derived and observed values is 0.44 and for $45 < E < 96$ MeV (bottom panel) this ratio is 0.08. The worst cases are: (1) the Bastille Day event, the event #4, (W07, 1615 km s^{-1}) and (2) the event #8, (E23, 1387 km s^{-1}) of Table 7.1. Contrary to what is expected for central meridian events (e.g. Cane et al. 1988; Smart et al. 2006), these two events display both an intense high-energy prompt component, observed up to 440 MeV, and a 48 – 96 MeV proton flux profile that remains elevated and almost constant up to the shock arrival. For the remaining six events of Table 7.1, the average peak flux ratio over all energy ranges shown in Figure 7.6 is 0.66.

The second left panel of Figure 7.6 compares the peak fluxes observed at 1.9 – 4.8 MeV (geometric mean energy of the channel: 3.0 MeV) with the synthetic fluxes derived at 2.0 MeV (open diamonds) and 4.0 MeV (solid circles). It is clear that the 2.0 MeV-peak fluxes are closer to the observed peak fluxes (average ratio = 0.67) than the corresponding values at 4.0 MeV (average ratio = 0.07). Similarly, the third panel compares the peak intensities measured by the 4.6 – 15.0 MeV channel of IMP-8/CPME (geometric mean energy: 8.3 MeV) with the synthetic fluxes derived at 4.0 MeV (open diamonds) and 8.0 MeV (solid circles). The predictions obtained at 4.0 MeV (closer to the low energy bound of the observational channel) overestimate the observed peak intensities (average ratio = 1.60) whereas those obtained at 8 MeV underestimate the observed values (average ratio = 0.16).

The observed peak fluxes at the energy channels 1.9 – 4.8 MeV and 4.6 – 15.0 MeV compare better with the synthetic value computed using the minimum energy of the

Table 7.4: Compared high-energy channels (in MeV)

SOLPENCO		IMP-8/CPME	
Energy interval[a]	$< E >$	Energy channel	$< E >^b$
2.8 – 5.7	4.0	4.6 – 15.0	8.3
5.7 – 11.3	8.0	4.6 – 15.0	8.3
11.3 – 22.6	16.0	15.0 – 25.0	19.4
22.6 – 45.3	32.0	25.0 – 48.0	34.6
45.3 – 90.5	64.0	48.0 – 96.0	67.9

[a]These energy intervals have been calculated by assuming that the simulated proton energy (next column) is the geometric mean of the interval (see Table 5.1).

[b]Geometric mean energy of each channel.

channel than with that computed using the mean energy (as it is usually done). If we assume that the proton intensities scale with the energy as a power law, $E^{-\gamma}$, the energy channels are more populated with protons of lower energies than with protons of the corresponding mean energy. For these two observational channels, for example, if we assume a value for the spectral index of $\gamma = 3$, the contribution of the 1.9 – 3.02 MeV protons to the particle intensity of the 1.9 – 4.8 MeV window is 79%, whereas the contribution of the 4.6 – 8.3 MeV protons to the 4.6 – 15.0 MeV channel is of 85%. This is the reason why peak intensities computed with the lowest energy value of the observational channel better predict the measured peak intensities specially for those events showing an average spectral index close to 3 (see bottom panel of Figure 7.7 below). Nevertheless, before drawing a firm conclusion about whether the observed peak flux has to be compared with the synthetic value derived from either the mean energy or the minimum energy of the channel, a comparative study with a much larger number of SEP events is required. At high energy (> 45 MeV, bottom left panel of Figure 7.6), if events #4 and #8 are not taken into account, the average ratio is 0.32, which is acceptable considering the constraints of SOLPENCO already commented. It is clear that a necessary and important improvement to incorporate into the model is to start the MHD modeling of the shock propagation from distances closer to the Sun than $18\,R_\odot$. These simulations will allow us to include the continuous contribution of shock-accelerated particles to the high energy particle intensities at these distances.

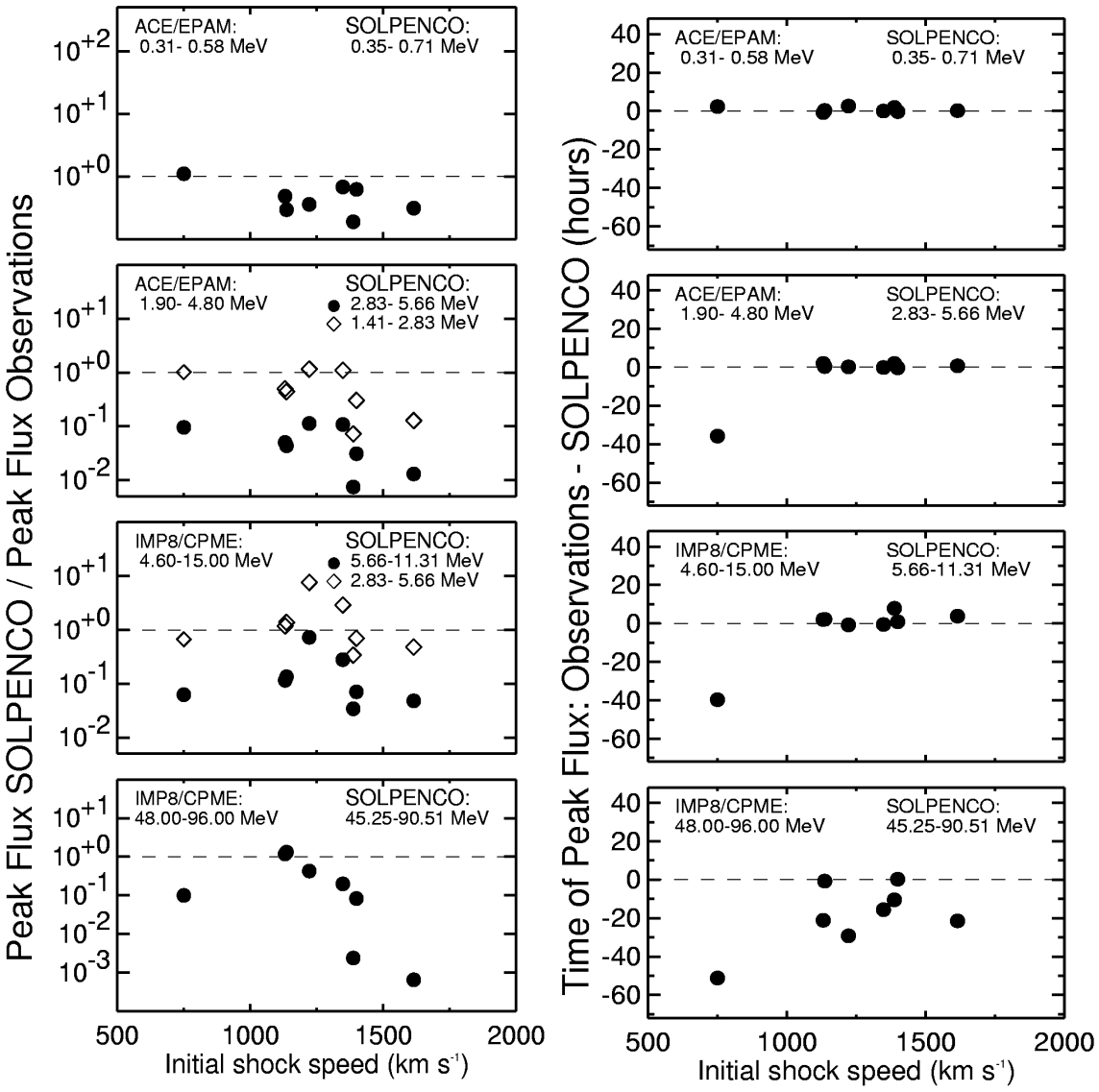

Figure 7.6: Left panels: Ratio between the peak flux derived from SOLPENCO predictions and the peak flux measured, for each SEP event of Table 7.3, as a function of the initial speed of the associated shock. These peak flux ratios are shown for four different energy channels, as indicated in the inset at the top of each panel. The two middle panels show the ratio for two possible energy choices from SOLPENCO (see discussion in the text). Right panels: Difference between the observational and predicted peak time corresponding to the cases shown in left panels.

Another relevant feature to space weather purposes is the time at which the peak flux is reached. In the right panels of Figure 7.6 we have plotted the difference between the observed and the predicted time of the peak flux, for the same events and energies displayed in the left panels of this figure. The second and third right panels show one energy channel of SOLPENCO because all synthetic proton fluxes in the 0.09 – 11.3 MeV energy range are always reached at the time of the shock arrival. At low energy ($\sim$ 0.4 MeV, top panel), the prediction of the peak flux occurrence is correct (from 0 to less than 5 hours with an average of 0.8 hours). The same is true at $\sim$ 3 MeV (second panel), and at $\sim$ 8 MeV (third panel), except for the September 2000 SEP event (event #5 in Table 7.3) for which the difference is ~ -40 hours. At energies above 2 MeV, the event #5 shows flux profiles that rapidly decrease after the prompt phase suggesting a strong contribution of particles accelerated early in the event when the shock is still close to the Sun, but not when the shock approaches the observer. Thus, this contribution decreases as the shock propagates, suggesting a less efficient acceleration of particles to high energies at later stages of the event. Excluding this event, the average time differences are 0.7 hours and of 2.2 hours at $\sim$3 MeV and $\sim$8 MeV, respectively. For the highest energy channel (geometric mean average $\sim$67 MeV, bottom right panel), the differences are important (-14.1 hours in average) even excluding the event #5. The main reason for this large difference at high energies is the fact that the high-energy proton intensity profiles are dominated by particles accelerated in the early phase of the event, when the shock is still in the corona or just leaving it. As commented, the inner boundary of the MHD shock propagation model prevents us from a more accurate continuous modeling of such an early high-energy particle injection.

Figure 7.7 compares the values of the observational (open diamonds) spectral index γ (measured at the peak flux) with those predicted by SOLPENCO (solid circles), as function of the initial speed of the shock. The top and bottom panels show the spectral index derived at low (from 0.12 MeV to 4.8 MeV) and high (from 1.9 MeV to 96 MeV) energies, for each SEP event. SOLPENCO predicts an almost constant spectral index with the shock speed either at low or at high energy. The reason is that the code assumes, for all the events, the same energy spectra for the injection rate of the shock-accelerated protons, regardless of the heliolongitude or the initial speed of the shock. From the events studied here it seems that the faster the shock, the harder the energy spectrum (i.e. the less steeper it is or the smaller the value of γ). However, it is not possible to derive any reliable function of the spectral index at low energy in terms of the initial speed of the shock. At high

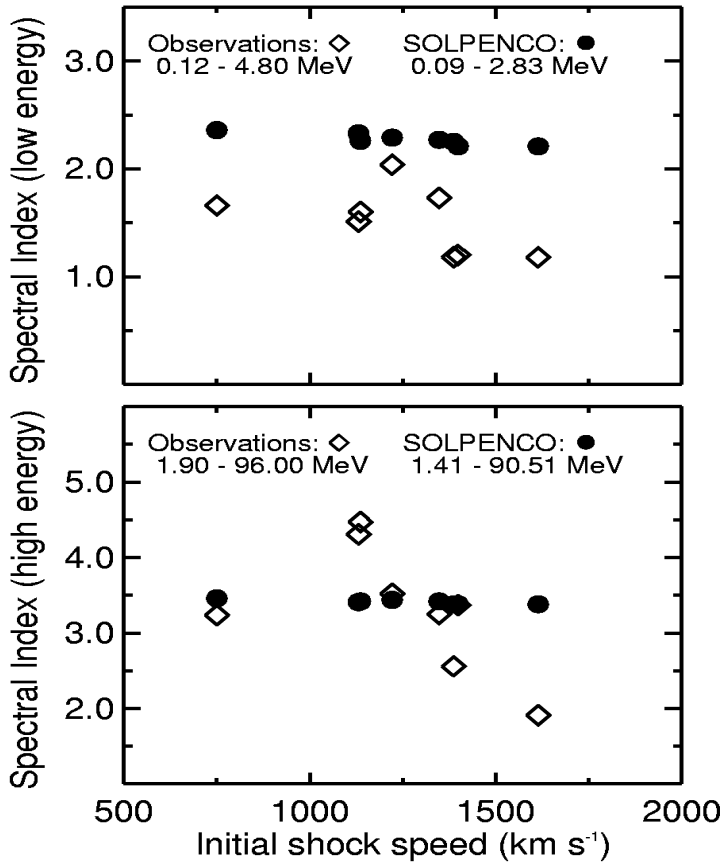

Figure 7.7: Spectral indices of the peak flux derived from observations (open diamonds) and from SOLPENCO (solid circles) at low energy (top panel) and at high energy (bottom panel), as a function of the initial shock speed.

energy, the events with the highest initial velocities display the hardest spectra, i.e. a less steep energy spectrum, indicating a powerful injection of shock-accelerated particles at high energies.

7.3 Western SEP events

The highest peak fluxes recorded at the prompt phase of SEP events are obtained for western ('well-connected') SEP events (Chapter 2, Shea & Smart (1996); Smart et al. (2006)). Usually, SEP events associated with solar events with heliolongitudes within W20 and W90 are considered to be 'well-connected' (e.g. Cliver & Ling 2007). We do not expect that the peak intensity ($E > 5$ MeV) for part of this type of events

would be fairly predicted by the SOLPENCO because, as commented in Chapter 6, most of the events provided by the code peak at the shock passage. Therefore, our aim now is to compare the outputs of SOLPENCO with actual western SEP events in order to quantify the deviation of the predicted peak intensities, analyze the ways to improve the model and thus provide more reliable predictions for these scenarios.

7.3.1 Selection of events

We have searched in the data set described in Section 7.2.1 for those SEP events that have associated solar events in heliolongitudes ranging from W30 to W90 and that fulfill conditions [1], [3] and [4] depicted in Section 7.2.2. Table 7.5 gives the same characteristics of the interplanetary shock and solar origin associated with each SEP event as described in Table 7.3. (Additionally, we have also included the sole eastern event (E46, #16 in Table 7.3) in the studied period that meets the aforementioned conditions).

The values of the initial shock speed obtained for each event in Table 7.5 (from top to bottom) are: 1249, 2248, 782, 1394, 2584, 1007, 2102 and 1566 km s^{-1}. Since the maximum initial shock speed in SOLPENCO is 1800 km s^{-1}, we have set the initial speed of events #10, #12 and #14 to this value. Consequently, the transit time of the shock provided by SOLPENCO for the three events is longer (by 6.5, 12.0 and 4.4 hours, respectively) than the actual transit time. Note that the event #10 is the Set98 event (modeled in Chapter 4). The derived initial speed of the MHD simulation of the interplanetary shock of this event is $v_s = 2065$ km s^{-1} when the initial pulse conditions are as those used in SOLPENCO (Smith & Dryer 1990), while $v_s = 1300$ km s^{-1} when the 'off-center' initial pulse described in Chapter 4 is used instead. As commented in Chapter 4, different initial pulsations lead to different values of VR (mainly close to the inner boundary) and hence different values of the injection rate of shock-accelerated particles. Therefore, in these extreme scenarios of very fast shocks with leading-edge longitudes westward than W75, the outputs of the MHD code near 18 $R_\odot$ should be handled carefully since they could significantly depend on the initial conditions assumed.

The association of the SEP event #11 with the solar source indicated in Table 7.5 deserves a detailed description since there is no complete agreement on its origin. At the onset of the solar event there were no H_α observations. Gopalswamy

Table 7.5: List of selected SEP events

	Interplanetary Shock				Solar Origin							
No.	Year	Doy	Date (mm/dd)	Time at ACE (UT)	CME Date (mm/dd)	Time (UT)	V_{CME} (km/s)	Type	Peak Flare (Xray/H_α)	Onset Time	H_α Location	Ref
9	1998	113	04/23	17:28	04/20	10:07	1863	H	M1.4	09:38	S43 W90	3,11
10	1998	275	10/02	06:53	09/30	Data Gap			M2.8/2N	14:02	N23 W81	2
11	2000	302	10/28	09:08	10/25	08:26	770	H	C4.0	08:45	W50	12
11'	2000	302	10/28	09:08	10/25	08:26	770	H	C4.0	08:45	N17 W90[a]	10, 14
12	2000	315	11/10	06:04	11/8	23:06	1738	P	M7.4/1N	22:42	N10 W75	5,13
13	2001	031	01/31	07:22	01/28	15:54	916	P	M1.5/1N	15:40	S04 W59	3,14
14	2001	094	04/04	14:23	04/02	22:06	2505	P	X20/?	21:32	N17 W78	5
15	2001	108	04/18	00:04	04/15	14:06	1199	P	X14.4/2B	13:19	S20 W85	5,11,12
16	2001	023	01/23	10:06	01/20	21:30	1507	H	M7.7/2B	21:06	S07 E46	4,12

1, Bale et al. (1999); 2, Lario et al. (2000a); 3, Gopalswamy et al. (2004); 4, Cane & Richardson (2003); 5, Lario et al. (2004b); 6, Aran et al. (2005a); 7, SGD679; 8, Sun et al. (2002); 9, Manoharan et al. (2004); 10, Lario et al. (2003b); 11, Tylka et al. (2005); 12, Kahler (2005); 13, Nitta et al. (2003); 14, Cane et al. (2002).

[a]Lario et al. (2003b) reported that this flare was located beyond west limb. Thus, the heliolongitude assumed here has to be considered as an approximation. Cane et al. (2002) estimated its location at W120.

et al. (2002) uses movies from SOHO's Extreme-ultraviolet Imaging Telescope (EIT) and the soft X-ray telescope (SXT) of Yohkoh to identify the origin of the eruption accompanying this event. They establish that this SEP event is associated with the Halo CME on October 25 at 08:26 UT originated from N10W66. Zhang et al. (2003) identify the location of the CME source at N18W23 by using SOHO/LASCO and EIT images, whereas Kahler (2005) using SOHO/EIT and Yohkoh/SXT estimates its solar source location at W50. Zhang et al. (2003) and Gopalswamy et al. (2004) associate this SEP event and the CME with a C4.0 1 – 8 Å X-ray flare at 08:45 UT on the same day, in agreement with Cane et al. (2002) who previously established the same association among the particle event, CME and X-ray flare and estimated the H_α location at S W120 (i.e. behind the west limb). Lario et al. (2003b) associate the particle event observed by ACE with the same CME and X-ray flare whose location is set beyond W90. Furthermore, Zhang et al. (2003) and Cane & Richardson (2003) establish the same CME – ICME identification. Consequently, all these authors relate the SEP event #11 to the same activity. However, the identification of the solar site where this event originated is different: if we trust the CME-based location the heliolongitude of the event should be ∼W50 but if we trust the flare lo-

cation the heliolongitude should be W90, instead. Therefore, we decided to compute the synthetic flux profiles using to both heliolongitudes, therefore using the inputs: W500782W10 and W901394W10 of SOLPENCO (#11 and #11' in Table 7.5).

The top panel of Figure 7.8 shows the timing of the peak intensity (black crosses) for the ten ACE and IMP-8 energy channels (color coded) of the event #11 in Table 7.5. The bottom panels of this figure display, as a function of the energy, the values of the peak flux derived from observations (red squares) and those obtained from SOLPENCO (black circles) for the W50 event (left panel) and the W90 event (right panel). The corresponding log-log linear fits below and above 2 MeV are indicated by dashed lines and the values of the slope γ derived from these fittings are indicated for each case, with the same color code and format as in Figure 7.5. As can be seen, the derived energy dependence in both cases is practically the same and the difference between the values of the peak intensity at each energy are not significant (the average peak ratio is 0.91 and the average peak time difference is 0.03 hours). Therefore in the following analysis the heliolongitude of the event #11 is assumed to be W50, since SOLPENCO assumes that the CME-driven shock is the main source of accelerated particles (we only count once this SEP event in the comparative study).

7.3.2 Peak fluxes: intensity and time

As for the case of central meridian events, we have calculated the ratio of the predicted over the observed peak intensities, the time difference between both peak fluxes and the energy dependence of the peak fluxes for the SEP events listed in Table 7.5. Figure 7.9 shows the peak flux ratios for the same energy channels as in Figure 7.6 and for the whole ensemble of selected SEP events: the eight central meridian events listed in Table 7.3 (indicated by circles), the seven western events (diamonds) and the eastern event (a triangle) listed in Table 7.5. Open symbols mark those events whose calculated initial shock speed value is larger (events #10, #12 and #14) or smaller (event #5) than the values assumed in SOLPENCO. For these three western events (#10, #12 and #14), the predicted peak intensities are smaller than the peak values that would be attained if the data base of SOLPENCO had provided fast shocks as the ones required for these events (as shown in Chapter 6, the faster the shock the higher the peak intensity of the resulting synthetic SEP event). Consequently, the peak fluxes predicted by SOLPENCO should be con-

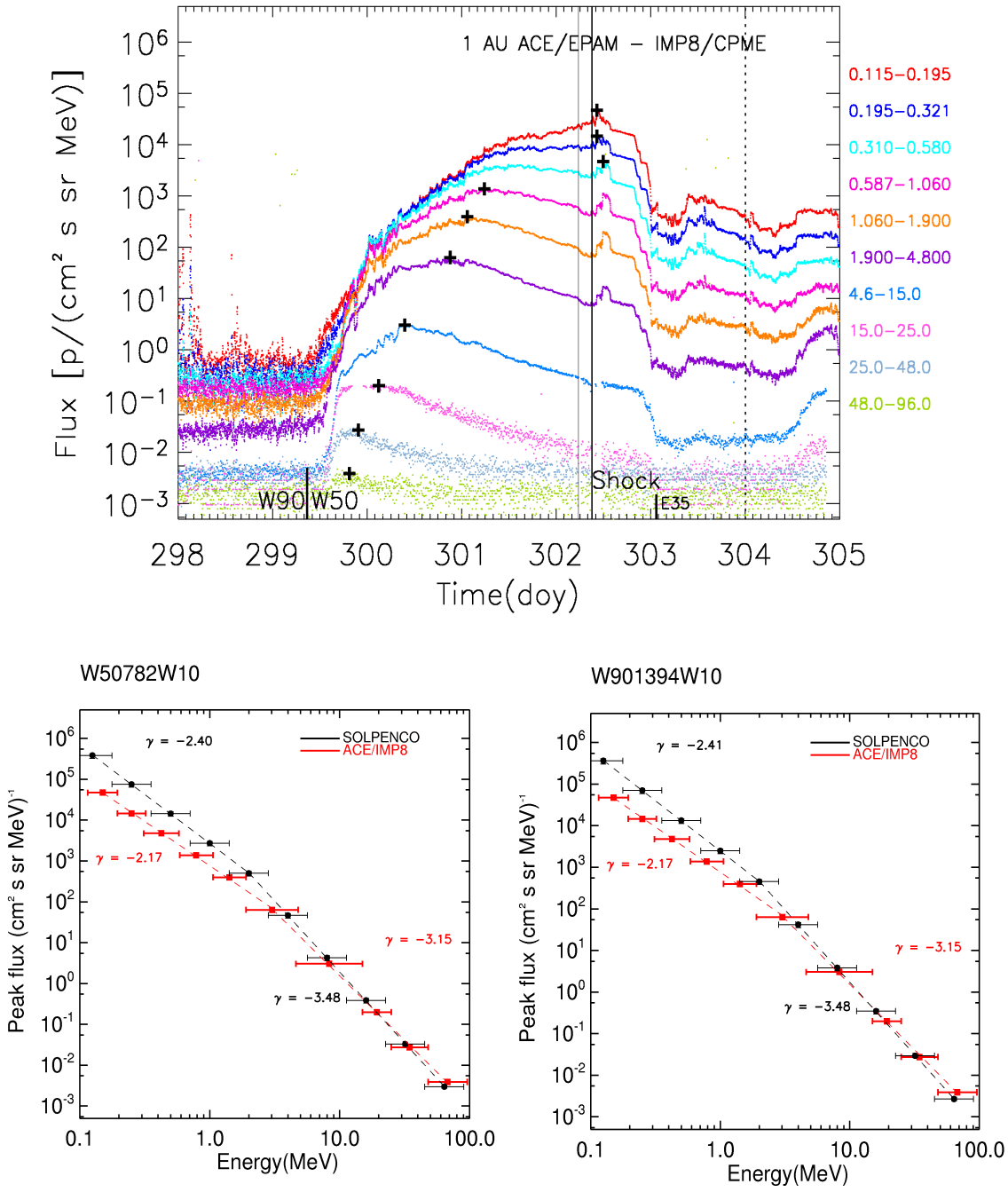

Figure 7.8: 25 – 28 October 2000 SEP event. Top panel as in Figure 7.5. Bottom panels: Peak flux for the W500782W10 synthetic event (left panel) and for the W901394W10 event shown as a function of the particle energy. Observed values are marked by red squares and predicted values by black circles. The values of the observed (red) and predicted (black) spectral indices derived at low and at high energies also shown. See text for details.

sidered as a lower limit of the actual peak flux. Since for these events, the predicted values are always lower than the measured values, we have included them in this comparative analysis. The similarity of the calculated and used ($v_s = 735$ km s^{-1} and $v_s = 750$ km s^{-1}, respectively) initial shock speeds for event #5 warrants its inclusion in the present study.

As can be seen in Figure 7.9, for western events, peak fluxes are better predicted at low than at high energies, as for central meridian events. For $0.3 < E < 0.7$ MeV (top panel) and for $45 < E < 96$ MeV (bottom panel) the average ratio over the western events are 1.49 and 0.008, respectively. At low energies, the predictions for western events are as correct as for central meridian events; whereas at high energies the average ratio is worse by an order of magnitude. This is an expected result because, for all the western events of this study, the 48 – 96 MeV proton peak intensity is reached during the prompt phase; SOLPENCO (as commented for events #4 and #8) is not able to account for the contribution of high-energy shock-accelerated particles when the shock is still close to the Sun. The average peak flux ratio when considering the whole set of 16 SEP events is 0.83 for protons of $0.3 < E < 0.7$ MeV and 0.03 for protons of $45 < E < 96$ MeV.

As for central meridian events, the peak intensities of both energy intervals are better predicted by the particle flux profiles computed using an energy value close to the low limit of the channels than by the intensity-time profiles calculated using the corresponding geometric mean energy. This can be seen in the second and third panels of Figure 7.9. In these panels we compare the ACE/EPAM 1.9 – 4.8 MeV and the IMP-8/CPME 4.6 – 15.0 MeV channels with the predictions provided by SOLPENCO at 2.0 (green symbols) and 4.0 MeV (orange) and, at 4.0 MeV (black) and 8.0 MeV (blue), respectively. The average peak ratios are 1.26 (0.12) when comparing with the low energy bound (mean energy) of the 1.9 – 4.8 MeV channel; and 1.12 (0.10) at 4.6 – 15.0 MeV. Globally, these values are similar to those obtained for central meridian events.

For the western SEP events of this study, the predicted time of the peak intensity deviates from observations above 2 MeV. Figure 7.10 shows this time difference for the 16 SEP events, with the same format as Figure 7.9. The timing of the 1.9 – 4.8 MeV and 4.6 – 15.0 MeV proton peak fluxes are compared with only one prediction of SOLPENCO 4.0 MeV and 8.0 MeV respectively (two middle panels of Figure 7.9), because for the events studied here and in this energy range, the

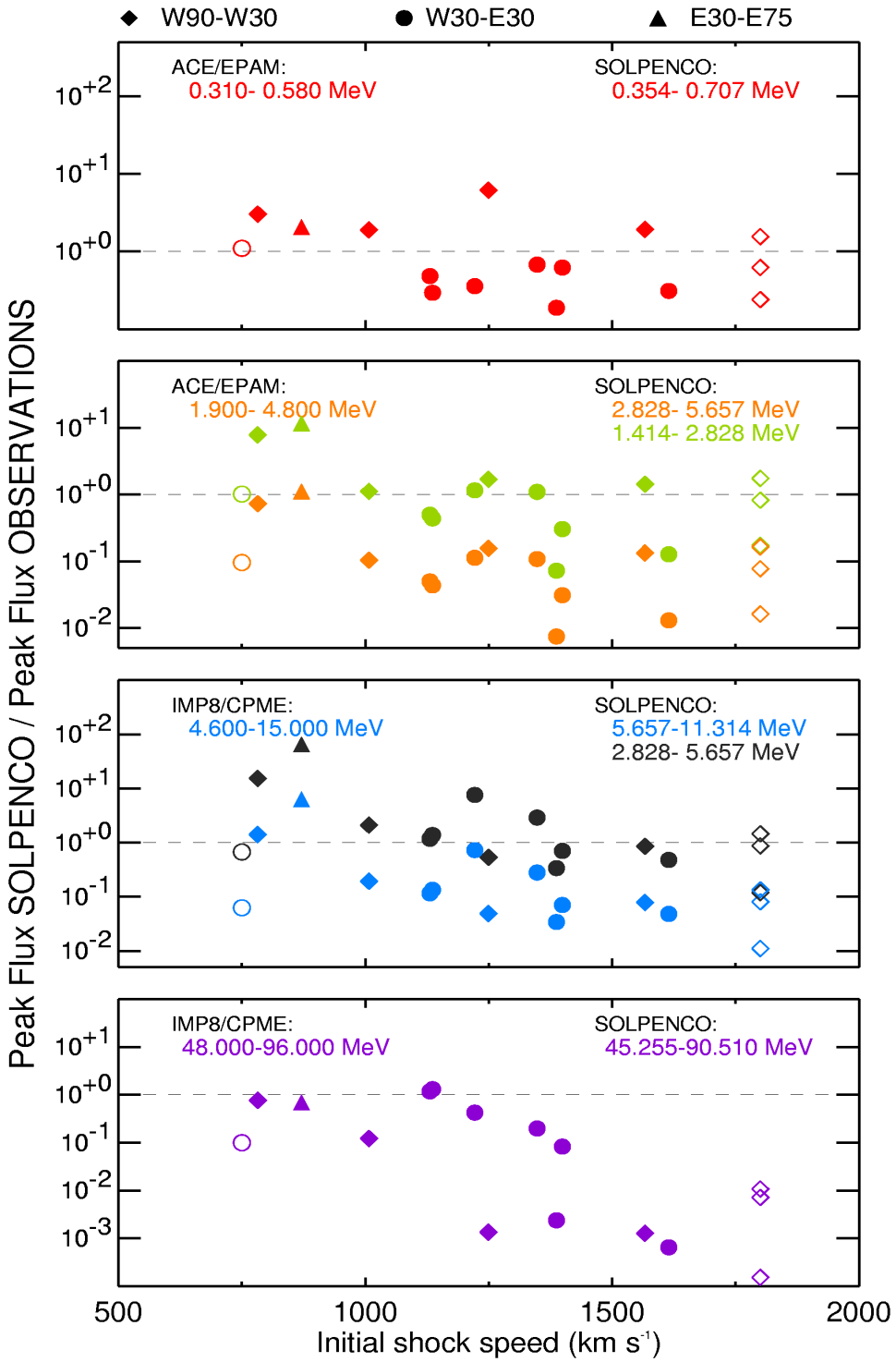

Figure 7.9: Ratio of the predicted over the observed peak flux for each SEP event listed in Tables 7.3 and 7.5, as a function of the initial speed of the associated shock and the heliolongitude: western events (diamonds), central meridian events (circles) and the eastern event (triangle). These ratios are shown for four different energy channels (color coded) from low (top) to high (bottom) proton energies. See text for details.

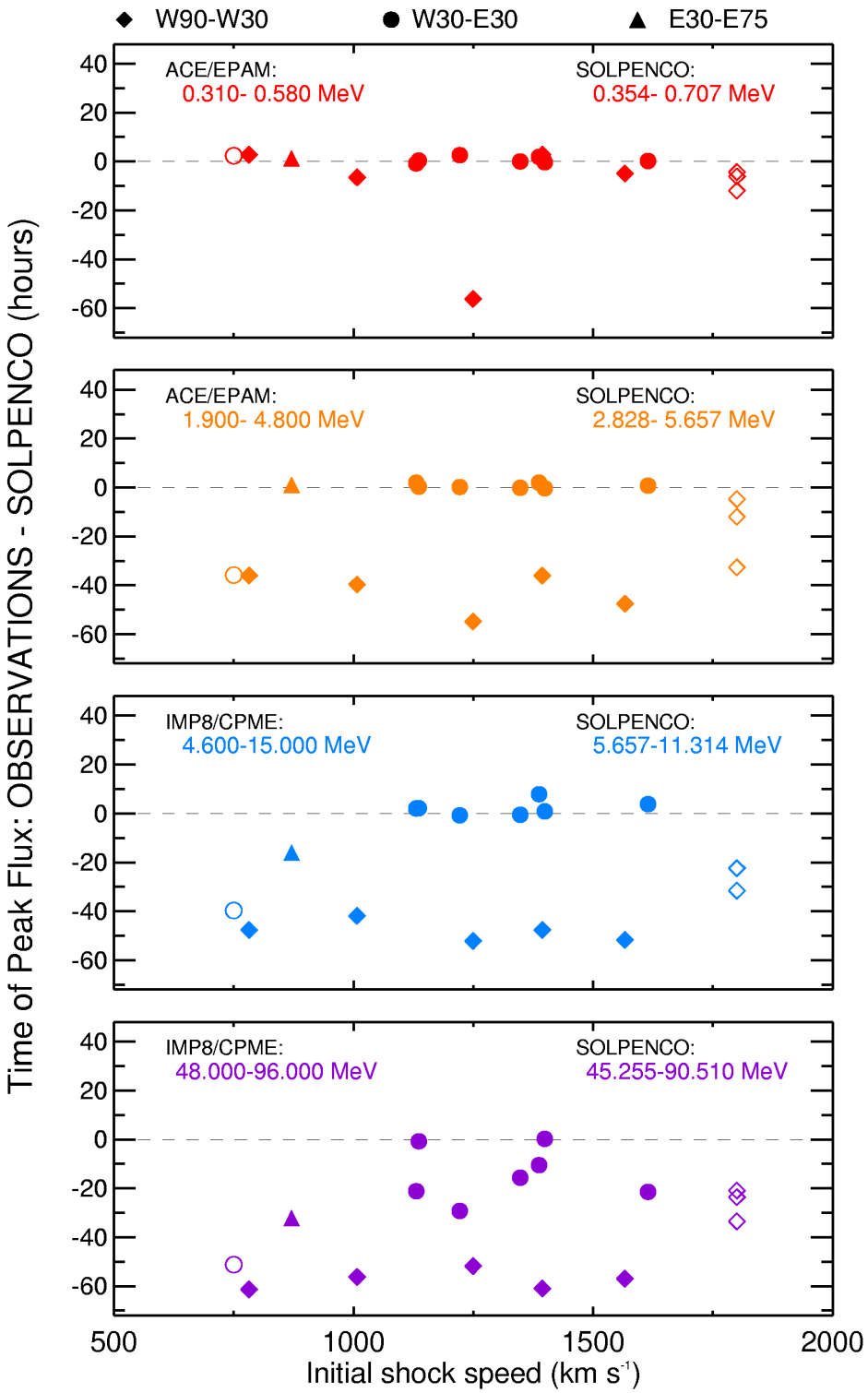

Figure 7.10: Difference between the observed and predicted peak time occurrence corresponding to the cases shown in Figure 7.9.

derived peak intensities are always attained at the time of the shock arrival at the spacecraft. For western events, the average difference of the timing between predicted and observed peak fluxes are -32.5, -38.5 and -43.5 hours for the 1.9 – 4.8 MeV, 4.6 – 15.0 MeV and 48 – 96 MeV energy channels, respectively. For the events #10, #12 and #14 (indicated by open diamonds in Figure 7.10) the peak intensity of the 0.31 – 0.58 MeV flux profile is attained at the shock arrival at ACE as in the corresponding predicted proton flux profiles. Therefore, the time difference shown in the top panel of Figure 7.10 comes from the approximated initial shock speed used in the prediction of the three events. Excluding these events, and the 20 – 23 April 1998 SEP event (#9 in Table 7.5), the time difference varies from -6.5 hours to +2.8 hours (average -2.9 hours). Hence, the prediction of the peak occurrence at 0.31 – 0.58 MeV is clearly better than at higher energies, and slightly less correct than for central meridian events (average 0.8 hours) at 0.31 – 0.58 MeV[10].

Figure 7.11 shows, for the 16 SEP events, the spectral index[11] γ derived at the time of the peak flux for the low-energy interval (0.12 – 4.8 MeV, top panel) and the high-energy interval (1.9 – 96.0 MeV, bottom panel) as a function of the heliolongitude of the associated solar event. The symbols used in this figure bin the events in three subsets of longitudes as in the preceding figures. The values of γ derived from observations are marked by red symbols and the predicted values by black symbols. For western events at low-energies, the energy dependence of the peak intensities behaves similarly as that of central meridian events: the predicted spectral index is almost constant (average value, $\gamma = 2.4$) and steeper than the index derived from observations (average, $\gamma = 1.7$). At higher energies (bottom panel of Figure 7.11), the predictions of events with heliolongitudes westward than W75 deviate from the observational values. These SEP events have either very fast associated shocks (events, #10, #12 and #14) or a strong prompt phase (events, #9

[10]The peak flux ratio for the eastern event (#16 in Table 7.5) is better predicted at the highest energy channel 48 – 96 MeV (ratio 0.70) than for the lowest 0.31 – 0.58 MeV (ratio 2.07) as can be seen in the bottom and top panels, respectively, of Figure 7.9. In addition, the peak intensities of both the 1.9 – 4.8 MeV and 4.6 – 15.0 MeV channels are better estimated when using the closest energy value to the geometric mean energy of the channel to compute the corresponding synthetic proton flux profile, rather than using the closest value to the low limit. The peak time occurrence is correctly predicted below ~ 5 MeV (average time difference 1.3 hours). At higher energies, the predicted peak occurrence increasingly deviates from observations: the time differences are -16.0 hours and -32.1 hours for ~ 8 MeV and ~ 67 MeV protons, respectively (the third and the bottom panels of Figure 7.10).

[11]As commented in Section 7.2.2, this is not a true spectral index.

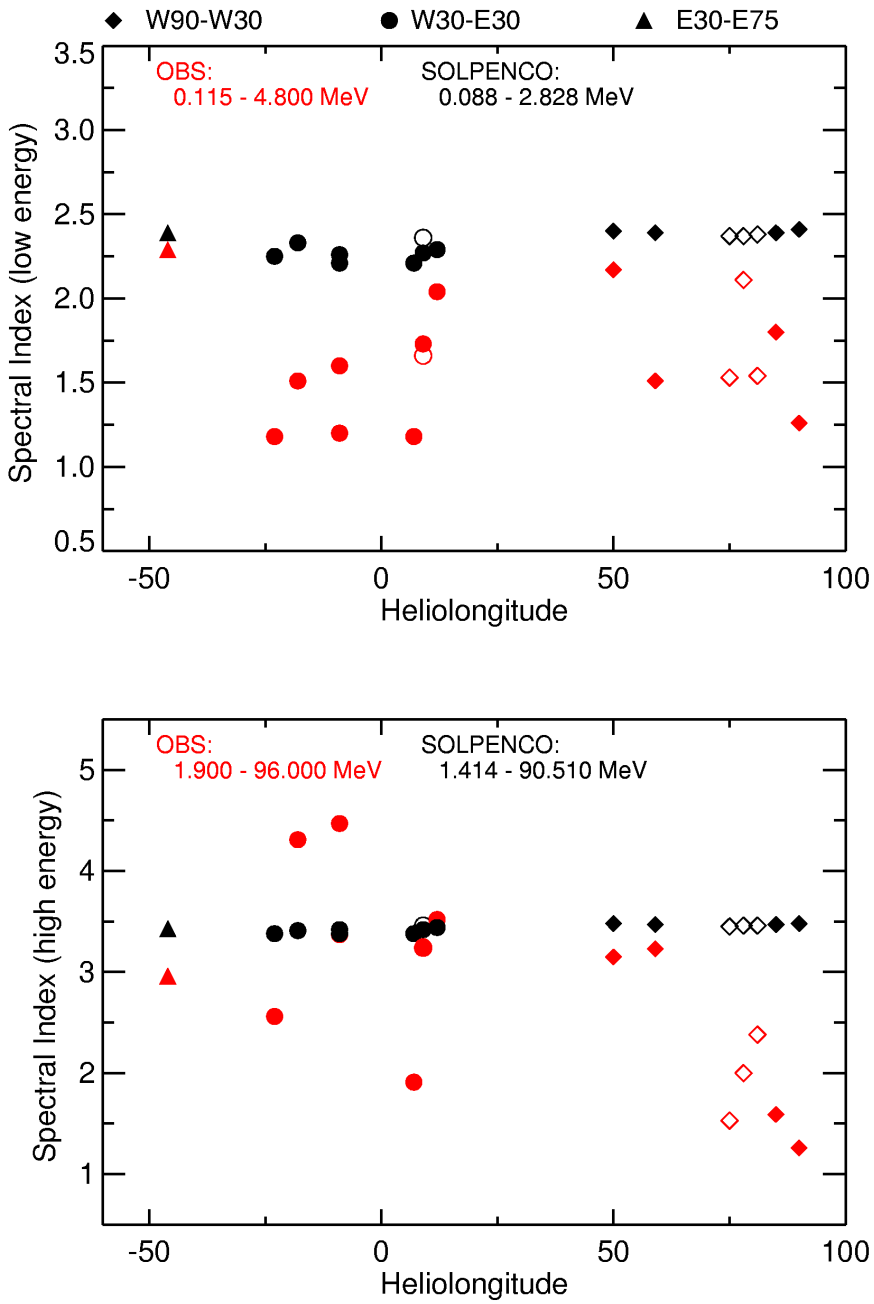

Figure 7.11: Values of the spectral indices calculated at the peak intensities for low (top panel) and high (bottom panel) energies, as a function of the heliolongitude of the event. The observed (red symbols) and predicted (black symbols) values are obtained for each of the SEP events listed in Tables 7.3 and 7.5. Western events (diamonds), central meridian events (circles) and the eastern event (triangle).

and #15); indicating in both cases a strong injection of shock-accelerated particles at high energies early in the event that SOLPENCO cannot reproduce. The value of the spectral index for the remaining two western events and for the eastern events are well predicted both at low and high energies.

7.3.3 The Q(VR) relation between 4 and 18 $R_\odot$

The location at 18 $R_\odot$ of the inner boundary of the MHD shock prevents us from determining the position of the cobpoint when the shock is still close to the Sun and hence, from characterizing the continuous contribution of shock-accelerated particles to the particle intensities at the prompt phase of the SEP events. In order to show how the evolution of the proton intensities would change if we knew the evolution of the radial speed jump across the shock (the values of VR) from distances close to the Sun (i.e. starting at 3 or 4 $R_\odot$), we have revisited the Sep98 SEP event (#10 in Table 7.5). Figure 7.12 shows the proton flux profiles of this SEP event measured by ACE/EPAM and IMP-8/CPME. Black crosses mark the time at which the peak intensity is attained, for each of the energy channels considered.

From the simulation of this event (Chapter 4 and Appendix C), we know the cobpoint position and the values of VR from the time that the magnetic connection between the observer and the simulated shock front is established ($t_c = 2.8$ hours at $r_c = 26\,R_\odot$) up to the shock arrival at 1.0 AU. As can be seen in left panel of Figure C.3, VR monotonically decreases from 3.6 (at 26 $R_\odot$) to 0.6 at (1.0 AU). Then, using the same Q(VR) relation applied to generate the data base of SOLPENCO, and transport conditions characterized by a proton mean free path, $\lambda_{\parallel 0} = 0.2$ AU (scaled with the energy as described in Section 5.2), and without assuming a foreshock region, we compute the synthetic proton intensity-time profiles corresponding to this event for the same set of energies of SOLPENCO. Black traces in the left panel of Figure 7.13 show these flux profiles obtained by SOLPENCO.

Now assuming that [1] the values of VR decrease linearly from 3VR(t_c) at 4 $R_\odot$ to VR(t_c) at 26 $R_\odot$, [2] the shock travels at a constant speed ($v_s = 2065$ km s^{-1}) from 4 to 26 $R_\odot$, and [3] the Q(VR)-relation and transport conditions hold as in the preceding case, we are able to compute the contribution of particles accelerated and injected by the shock early in the event into the flux profiles at 1 AU. The resulting intensity-time profiles are shown in the left panel of Figure 7.13 (red traces). As can

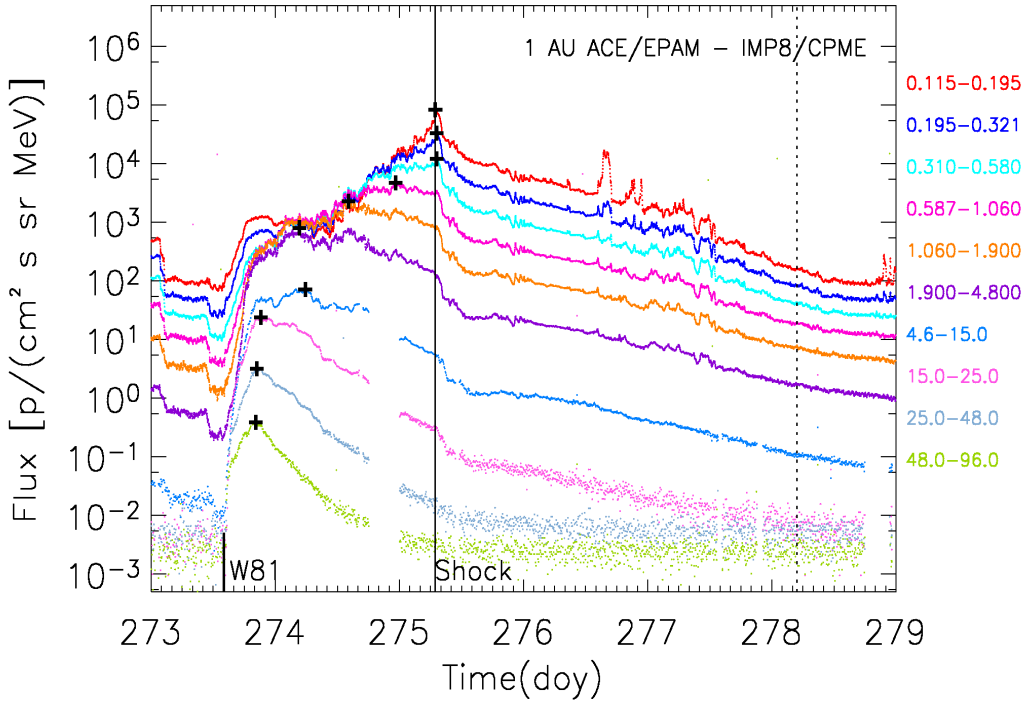

Figure 7.12: Same as in top panel Figure 7.5 for the 30 September – 2 October (Set98 W81) SEP event.

be seen, the flux profiles computed by assuming a near Sun shock injection (hereafter, 'SOLPENCO-4 $R_\odot$') display a more intense prompt phase (a factor $\sim$ 100) than the flux profiles computed as in SOLPENCO. The result of including such early injection is the fact that peak intensities above 0.5 MeV are attained early in the event during its prompt component such as the actual observed intensities above 1.9 MeV (Figure 7.12).

The right panel of Figure 7.13 shows the energy dependence of the peak intensities (red circles) as derived from measurements both at low and high energies. The black circles correspond with the peak fluxes calculated from the black flux profiles shown in the left panel of this figure. The blue triangles mark the peak fluxes derived from the red profiles of the same panel. Their corresponding fittings (dashed lines) are shown with the same color code as the symbols. The values of the peak fluxes at $E > 3$ MeV obtained from the simulation SOLPENCO-4 $R_\odot$ are closer to the observational values than those derived from SOLPENCO (black circles). The SOLPENCO-4 $R_\odot$ simulation also predicts better the values of the spectral indices at both low and high energies.

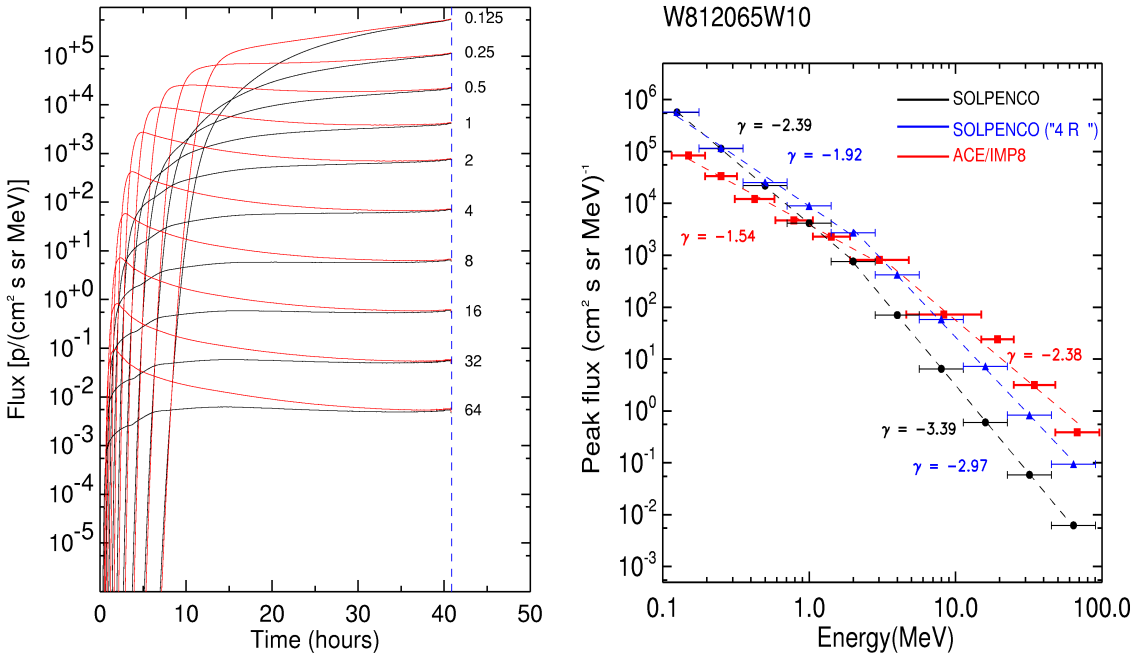

Figure 7.13: Set98 SEP events. Left panel: Synthetic proton flux profiles computed by using the same $Q(\mathrm{VR})$ relation and proton mean free path as in SOLPENCO (black traces) and by considering an ad hoc injection of shock-accelerated particles close to the Sun (red traces). The profiles are shown for the ten proton energy values (in MeV) assumed in SOLPENCO. The vertical dashed line marks the time of the shock arrival at ACE. Right panel: Same as left bottom panel of Figure 7.5 including the spectral index prediction derived by using the ad hoc shock-particle injection (in blue). See text for more details.

Consequently, we conclude that an MHD shock propagation model with a inner boundary closer to the Sun (3 or 4 $R_\odot$) could provide a notable improvement of the present version of SOLPENCO.

7.4 Discussion and conclusions

We have started the verification of SOLPENCO by comparing part of its outputs with observations, for the large isolated SEP events measured at 1.0 AU by ACE and IMP-8, at different energies between $\sim$0.1 MeV and $\sim$96 MeV, in the period from

January 1998 to October 2001. We have presented a comparative analysis of the values of the maximum proton differential flux intensity (the 'peak flux') regarding three factors: the initial speed of the shock, the heliolongitude of the parent solar event and the energy dependence.

The parameters selected to generate the database of SOLPENCO are basically derived from modeling individual SEP events, by carefully fitting simultaneously both the upstream proton flux and the first order anisotropy profile for various (usually eight) energy channels between $\sim$0.1 MeV and $\sim$5 MeV. In several cases, SEP modeling extends up to $\sim$50 MeV, but with the limitation of wide energy channels and no observational anisotropies to compare with. Therefore, the number of spectral indices of the injection rate of shock-accelerated particles derived from modeling at high-energy is really scarce; this casts doubts on the representativeness of the deduced values. Observations (e.g. Cane et al. 1988) show that, at high energies (> 24 MeV), SEP events display a wide range of spectral indices (from 1.5 to 7.1), even without taking into consideration their parent solar heliolongitude (neither the fact that the energy windows of these energy channels are usually too wide to perform a full reliable comparison). Furthermore, at these energies, the majority of the particles is generally injected when the shock is still close to the Sun (i.e. below the inner boundary of the simulation of the shock propagation used here). The combination of these factors makes SOLPENCO predictions less reliable at high than at low energies).

The peak fluxes of the analyzed central meridian SEP events are well predicted by SOLPENCO at low energies (< 2 MeV); the average ratio of the predicted over the measured peak flux is 0.72 and the average difference of the peak time is -0.4 hours. At these energies the main contributor of accelerated particles is the CME-driven shock as it propagates through interplanetary space, therefore, SOLPENCO provides good predictions. The predicted values are still valid at high energies for the events with a relatively poor contribution of a particle population accelerated at the early phase of the event, i.e. when the shock is still close to the Sun (average ratio 0.60 and average time difference -4.5 hours). For events displaying a strong prompt component (events #4, #5 and #8 in Table 7.3), predictions deviate from observations at $E > 2$ MeV (average ratio 0.04 and average time difference -17.1 hours). For western events, the predictions of the peak flux ratio are still correct below 2 MeV (average ratio 2.33) but the predicted peak time occurrence deviates from observations even excluding the event #8 (average time difference -11.5 hours).

The reason is that for these events the > 0.5 MeV-proton peak intensities are attained before the shock passage by spacecraft. At high energies ($E > 2$ MeV), the predictions for western events do not match the observations. The average peak intensity ratio is 0.09 and the average time difference is -41.43 hours.

Hence, western and central meridian events with a strong prompt phase, the present version of SOLPENCO is not able to predict the time and intensity of the peak flux for $E > 2$ MeV. The reason is twofold: [1] The initial conditions of the MHD code are placed at $18\,R_{\odot}$, thus above the region where the injection of the high-energy particles is assumed to take place; and [2] the constant of proportionality between Q and VR ($k = 0.5$) has been derived from modeling actual SEP events only at low energies.

In order to analyze the evolution of the peak flux with the particle energy, we have derived the spectral indices by fitting the peak flux by a power law. At low energies (0.12 – 4.8 MeV) the predicted spectral index (with an average value over the 16 SEP events, $\gamma = 2.3$) is steeper than the observed (average $\gamma = 1.6$). If we only take into account the analyzed events, the average value of the spectral index adopted for Q should be less steep than $\gamma = 2$ in order to improve the predictions of SOLPENCO at low energies. For this range of energies and from the 16 SEP events studied here, it is not possible to derive any reliable function of the spectral index in terms of either the heliolongitude of the solar parent event or the initial speed of the shock.

For higher energies (from ~ 2 to 96 MeV), spectral indices are well fitted by SOLPENCO for central meridian events with small or medium (< 1300 km s^{-1}) initial shock speeds (average spectral index: predicted $\gamma = 3.4$ and observed $\gamma = 3.3$) as well as for the slow western events (#11 and #13 in Table 7.5) and for the eastern event (#16 in Table 7.5). The predicted average spectral index over these three events is $\gamma = 3.5$ while the observed average value is $\gamma = 3.1$. The events either associated with fast interplanetary shocks or with solar events with heliolongitudes westward than W75 show a harder spectral index (less steep) than that predicted by SOLPENCO, pointing out a more powerful injection than for the remaining events. For this type of events, the spectral index adopted in SOLPENCO for Q should be less steep than $\gamma = 3$.

The two eastern-central meridian events (events #2 and #3 in Table 7.3) with initial shock speeds about $\sim$1130 km s^{-1} are the only two selected SEP events show-

ing a spectrum steeper than that predicted at high energies. In general, spectral indices show a wider range of variation for eastern events than for western events (e.g., see Fig. 14 in Cane et al. 1988). Thus, the average value for the spectral index at high energy assumed in SOLPENCO ($\gamma = 3$) is expected to fit better western events than eastern events. For eastern events, the spacecraft is magnetically connected to the western wing of the shock front. Consequently, the cobpoint scans a less efficient region on the shock front in terms of particle shock-acceleration and injection than that scanned in western-central meridian events (for which the cobpoint moves along the leading edge of the shock front at the beginning of the event, i.e. the most efficient region at accelerating). For this reason, the energy spectrum derived at high-energies in several eastern-central meridian events is expected to be steeper than the spectrum of western-central meridian events.

The number of events analyzed here is still small to derive any statistically significant conclusion. We have drawn conclusions about the usefulness of SOLPENCO that must be revisited in the future after:

[1] Analyzing more SEP events, including those that do not show intensity increases at high (> 50 MeV) energies.

[2] Studying spectral indices and other features of flux profiles at high energies, as a function of the heliolongitude and shock speed.

[3] Analyzing more carefully the way the synthetic flux profiles at a given energy are created and compared with observations.

8 Modeling and forecasting solar energetic particle events at Mars: The event on 6 March 1989

8.1 Introduction

Large solar energetic particle (SEP) events are an important element in assessing the radiation hazards in space. The objective of sending humans to Mars must be accompanied by basic protection rules (Lanzerotti 2004). To ensure astronaut safety, it is important to know how intense an episode of enhanced radiation will be; when it will reach dangerous levels; when its maximum intensity will be attained and how long it will last. In terms of SEPs, all these parameters depend on the location, speed, strength and extent of the energetic particle source relative to the observer, as well as on the complexity of the heliospheric magnetic field at the time of the SEP event (Turner 2000). As already commented, forecasting the arrival of solar generated shocks and solar energetic particle events anywhere in the heliosphere presents an awesome challenge in space weather. The major part of observations of solar wind plasma, interplanetary magnetic fields and energetic particles are collected at the L1, the Sun-Earth libration point located at $\sim$245 Earth radii sunward from our planet. Such observations might provide to Earth systems a warning time of less than one hour (SRH06 Report). This approach however is not enough for interplanetary missions.

The scenario of a mission to Mars addresses interplanetary issues that have not been figured out until recently (i.e. Foullon et al. 2005; Baker et al. 2006). It is reasonable to assume that the earth/L1-based solar-monitoring network will support

a Mars mission with SEP event forecast and alerts, but there are two substantial differences with respect the Earth environment: (i) Earth is not always in a position to directly monitor critical regions on the Sun and (ii) the radial distance of the Earth and Mars (or a spacecraft) and, specially their angular separation are important parameters when dealing with SEP events. Particularly, in the frame of the shock-and-particle model, the injection rate of shock-accelerated particles depend on the value of VR at the cobpoint, and the cobpoint position of an observer located at (or close to) the Earth could be quite different from the cobpoint position of an observer located at (or close to) Mars (see for example, Figure 23 of Foullon et al. 2004).

In addition, observational data for radial distances different than 1.0 AU is scarce (see Section 2.4). Hence, only for a bunch of SEP events it is possible to compare model predictions with spacecraft observations. At present, there are few observational analyses on the dependence of particle flux and fluences with radial distance (a summary can be found in Lario et al. 2006). Recommendations for radial extrapolation of SEP intensities from measurements at 1.0 AU (Feynman & Gabriel 1988) have been proven to be unsuccessful, especially when traveling interplanetary shocks dominate the evolution of the particle intensity time profiles (Smart & Shea 2003). The situation is even worst when trying to perform simultaneously multi-spacecraft studies and modeling, for example, by using one spacecraft as baseline to fix the parameters of a model and performing predictions of the SEP event observed by another spacecraft, in order to be checked with the measurements collected by this latter spacecraft. In this chapter we study one of the few cases of multi-spacecraft configuration that allows us to test the Q(VR) relation, by using SEP observations from near Earth spacecraft to derive predictions that can be compared with the corresponding SEP observations by a Mars-orbiting spacecraft[1]. To our knowledge no studies dealing with forecasting individual SEP events at Mars' orbit from SEP Earth-orbit observations have been reported.

We apply the shock-and-particle model to one of the few SEP events that, fortunately, was observed by the IMP-8 spacecraft (orbiting around the Earth) and by the Phobos-2 spacecraft (orbiting around Mars) (Marsden et al. 1990; McKenna-Lawlor et al. 1991, 2005). For this event, the upstream solar wind had not been disturbed by any former interplanetary transient event. While the observation of SEP events at the orbit of the Earth has been routinely performed for the last three solar cycles (Lario & Simnett 2004, and references therein), the observation of SEP events at

[1]The contents of this chapter has been published (Aran et al. 2007).

Mars has only been possible in a few rare occasions. Missions such as Phobos-2 and Mars-Odyssey have offered us only a slight clue of the SEP environment at Mars (e.g. Marsden et al. 1991; McKenna-Lawlor et al. 1991; Cleghorn et al. 2004).

In this chapter we use energetic particle data from the Low Energy Telescope (LET) on board Phobos-2 (Marsden et al. 1990) and the Charged Particle Measurement Experiment (CPME) on board IMP-8 (Sarris et al. 1976) to compare the SEP environment at the Earth and Mars during an intense SEP event of solar cycle 22. Phobos-2 was launched on 12 July 1988 and reached Mars on 29 January 1989. It was inserted into orbit around Mars and, after several orbit corrections, it was lost on 27 March 1989 due to a failure of the on board control electronics (Sagdeev & Zakharov 1989). Therefore, the opportunity to study this particle event is quite unique even though this is not a text-book case for modeling: Phobos-2 particle data contains a relevant gap after the onset of the SEP event and there are no particle anisotropy measurements. In addition, the accuracy of the solar wind data available is low and there is a lack of useful observations of the IMF because of the orbit of Phobos-2 around Mars.

In Section 8.2 we present the characteristics of this event as seen by IMP-8 and Phobos-2. In Section 8.3 we apply the shock-and-particle model to describe the SEP event measured by each of the two spacecraft. We discuss the predictions of SEP profiles in the Martian environment in Section 8.4 and the predicted maximum particle intensities and fluences in Section 8.5. Finally, we give a discussion and conclusions in Section 8.6.

8.2 The solar energetic particle event on 6 March 1989

The SEP event analyzed in this paper was the first in a series of events detected in March 1989 (McKenna-Lawlor et al. 2005). The transit of the NOAA Active Region 5395 over the solar disk was marked by an intense level of solar activity including the occurrence of at least 10 X-class X-ray flares (Feynman & Hundhausen 1994). This large and complex active region rotated onto the visible disk of the Sun (as seen from the Earth) on 6 March 1989. This same day the second largest X-ray flare in solar cycle 22 (estimated to be a class X15) occurred (Watari et al. 2001). An optical 3B

class flare took place at N35E69 with onset at 1354 UT. The 1-8 Å X-ray emission began at 1350 UT and reached maximum flux at 1405 UT. A fast coronal mass ejection (CME) was seen by the Solar Maximum Mission (SMM) over the northeast limb of the Sun at 1415 UT (Feynman & Hundhausen 1994). At the time of the X15 flare on 6 March 1989, Phobos-2 was in circular equatorial orbit at an altitude of ∼2 Martian radii, and located 72° to the East of the Earth at a heliocentric distance of 1.58 AU (McKenna-Lawlor et al. 2005). We have limited this study to the first SEP event because only before the arrival of the first interplanetary shock at both spacecraft was the solar wind stable enough to allow a reasonable modeling of the existing upstream interplanetary conditions, both for shock propagation and interplanetary magnetic field topology.

Several authors (e.g. Marsden et al. 1990; Kurt et al. 2004) have associated the SEP event observed by IMP-8 on 6 of March and later by Phobos-2, with the X15/3B flare at N35E69. We agree with this identification (see below), in spite that McKenna-Lawlor et al. (2005) associated the particle intensity enhancement at IMP-8 with a C5.2/SF flare that occurred at 2356 UT on 5 March from S20W61 (see their paragraph [25]). Figure 1 of McKenna-Lawlor et al. (2005) shows that 4.6 – 15.0 MeV proton intensities at IMP-8 started to increase above the background at ∼2000 UT on 6 March, whereas the 48 – 96 MeV proton intensity enhancement at IMP-8 was not detected until the end of a data gap at ∼1200 UT on 7 March. The nominal Parker spiral magnetic field connection between IMP-8 and the Sun implies that the site of the C5.2/SF flare was well connected to IMP-8. However, SEP events originating from activity at western longitudes have rapid intensity rises shortly after the occurrence of the solar flare (Cane et al. 1988), whereas in the case of this event the intensity enhancement was gradual and with a significant delay with respect to the parent solar event as typically observed in eastern events. In addition, the low-energy proton intensities measured by IMP-8 started to increase earlier than the higher energy intensities contrary to what is expected from well-connected western events. Although the correlation found between solar flare X-ray integrated fluxes and peak fluxes of > 10 MeV protons is weak (cf. Figure 1 of Balch 1999), it seems reasonable to expect that the solar event associated with an X15/3B flare was more productive in terms of energetic particles than the events associated with the C5.2/SF flare. Hence, we will assume that this X15/3B flare was temporally associated with the SEP event observed by both spacecraft.

IMP-8 observed the passage of an interplanetary shock at ∼1800 UT on 8 March

with a local increase of the low-energy (<15 MeV) proton intensities. The passage of this shock was associated with the occurrence of a Sudden Storm Commencement (SSC) at 1755 UT on 8 March (Marsden et al. 1990) and a decrease of the Dst index to ∼−100 nT. A later SSC was also observed at the Earth at 1900 UT on 9 March, and the Dst that was already low, decreased again to −100 nT. McKenna-Lawlor et al. (2005) attributed the SSC on March 9 to the solar event associated with the X15/3B. This association implies an average transit speed for the associated plasma disturbance to travel from the Sun to the Earth of $< v > = 539$ km s^{-1}. According to these authors the shock observed by IMP-8 at 1800 UT on 8 March was probably originated during the C5.2/SF flare, implying an average transit speed for the associated solar wind disturbance of $< v > = 629$ km s^{-1}.

Fast CMEs tend to occur in association with intense solar flares (Feynman & Hundhausen 1994; Dryer 1996; Gopalswamy et al. 2004), therefore, it is reasonable to assume that the CME that occurred in temporal association with the X15/3B was faster than the presumed CME associated with the C5.2/SF (if any). Since the longitudinal separation between the Earth and the sites of the X15/3B and C5.2/SF flares were similar (E69 and W61, respectively), it is reasonable to assume that the shock associated with the X15/3B flare was faster and had stronger effects on the Earth's environment than the presumed shock associated with the C5.2/SF flare. In view of all these facts, we consider that the shock at 1800 UT on 8 March at IMP-8 was originated during the solar event associated with the X15/3B flare. By using this association we deduce that the time interval between the occurrence of the solar flare and the shock passage at 1.0 AU is 52.1 hours implying an average transit speed of $< v > = 798$ km s^{-1}.

Marsden et al. (1990) identified the passage of a shock at Phobos-2 at 2015 UT on 9 March, in coincidence (within the precision of the solar wind data available) with the highest flux values of a SEP event measured by the Phobos-2/LET instrument. According to these authors, this shock originated from the solar events occurring in association with the X15/3B flare. The time interval between the occurrence of this solar flare and the shock passage at Phobos-2 was 78.4 hours, thus implying an average transit speed from the Sun to 1.58 AU of $< v > = 837$ km s^{-1}. The longitudinal separation between the site of the solar flare and the Phobos-2 location was only 3°. Because of the motion of Mars, the longitudinal separation between the location of Mars on 9 March and the site of the X15/3B flare on 6 March was only 2°. The assumption made by McKenna-Lawlor et al. (2005) that the shock

originated at the time of the X15/3B flare reached IMP-8 at ∼1900 UT on 9 March and Phobos-2 at ∼ 2015 UT on 9 March implies a shock that moves very fast in the direction toward Mars ($< v >$ = 837 km s^{-1}) but extremely slowly toward the Earth ($< v >$ = 539 km s^{-1}). We argue that the shock originated in association with the X15/3B flare had an approximate uniform radial expansion over at least 72° in longitude being able to reach IMP-8 at 1800 UT on 8 March ($< v >$ = 798 km s^{-1}) and Phobos-2 at 2015 UT on 9 March ($< v >$ = 837 km s^{-1}). Therefore, we consider that the solar event associated with the X15/3B flare generated not only the SEP event under study but also a wide and fast shock recorded aboard both IMP-8 and Phobos-2.

8.3 Modeling the particle event

8.3.1 MHD simulation of the shock propagation

Similar to the SEP events modeled in Chapter 4, we use the 2.5-dimensional MHD time-dependent code developed by Wu et al. (1983) to simulate the propagation of the interplanetary shock in the ecliptic plane. As described by Smith & Dryer (1990), the initialization parameters for the MHD model are the initial disturbance speed, v_s, at the inner boundary of the model (located at 18 $R_\odot$, 0.08 AU, from the center of the Sun); its longitudinal angular width, ω; and the temporal duration of the input pulse driving time, τ. In contrast to the Smith & Dryer (1990) study, we have extended the outer boundary of the computation domain to 2 AU and modified the prior steady-state background medium where the disturbance propagates allowing for a better description of both plasma and magnetic field observations prior to the shock arrival. We have considered that solar wind speed, density, and magnetic field magnitude at 18 $R_\odot$ are 252 km s^{-1}, 1 197 cm^{-3} and 504 nT, respectively. The resulting values at 1.0 AU are 434 km s^{-1}, 4.8 cm^{-3}, 6.9 nT; and at 1.58 AU are 435 km s^{-1}, 1.9 cm^{-3}, and 4.0 nT, respectively, for these variables. Using the same functional form of the input pulse assumed by Smith & Dryer (1990) we inject a pulse centered at E69 with v_s = 1 260 km s^{-1}, ω = 131° and τ = 1 hour. The resulting plasma disturbance reaches IMP-8 in 51.1 hours ($< v >$ = 813 km s^{-1}) and Phobos-2 in 77.4 hours ($< v >$ = 848 km s^{-1}). The transit times are measured from the onset of the X15/3B flare. Since the inner boundary of the MHD code is at

0.08 AU from the center of the Sun, we add to the time when the MHD simulation starts the transit time spent by the input pulse to move from the solar surface to the inner boundary of the MHD code assuming that it moves at the speed v_s.

Figure 8.1 shows the solar wind speed, density and magnetic field magnitude observed by IMP-8 (top panel) and Phobos-2 (bottom panel) together with the results of the simulation. The simulated shock not only reproduces the arrival time but also the jump observed in solar wind speed and density; however the simulated magnetic field shows a discontinuous jump larger than observed. The magnetic field magnitude measured by Phobos-2 (cf. third panel of Figure 5 of McKenna-Lawlor et al. 2005) shows periodic structures due to the spacecraft circular orbit around Mars that makes the shock identification difficult.

Figure 8.2 is a snapshot of the modeled shock propagation 40.7 hours after the occurrence of the X15/3B flare. The shock front is located within the steep gradient of the density isocontours and indicated by a white arch. The locations of IMP-8 and Phobos-2 are indicated by asterisks, and IMF lines are plotted as white lines. Red and orange dots indicate the points of the shock front that magnetically connect to Phobos-2 and IMP-8, respectively; each of these points is named "cobpoint" (Connecting with the OBserver POINT), after Heras et al. (1995). As the shock expands, the cobpoints of both observers scan different regions of the shock front. The two top panels of Figure 8.3 show the cobpoint locations versus time for both observers: panel (a) displays the heliocentric radial distance, panel (b) the azimuthal angle as measured from the Sun-IMP-8 line. Since the shock had an approximate radial expansion in all longitudes, heliocentric radial distances of the two cobpoints were very similar throughout the event (Figure 8.3a); however the IMP-8 cobpoint was always more toward the west than the Phobos-2 cobpoint (Figure 8.3b) at the same time.

We have also computed the downstream-to-upstream ratios of the magnetic field magnitude BR $= |B|_d/|B|_u$ (Figure 8.3c) and the normalized plasma velocity ratio VR $= (V_{r_d} - V_{r_u})/V_{r_u}$ (Figure 8.3d) at the cobpoint (where u and d stand for upstream and downstream of the shock, respectively). These parameters give a local measure of the strength of the shock at the cobpoint. Since the IMP-8 cobpoint is always more toward the western flank of the shock than the Phobos-2 cobpoint (Figure 8.2), both parameters BR and VR are always lower for IMP-8 than for Phobos-2. In addition BR and VR increase with time for IMP-8, whereas for Phobos-

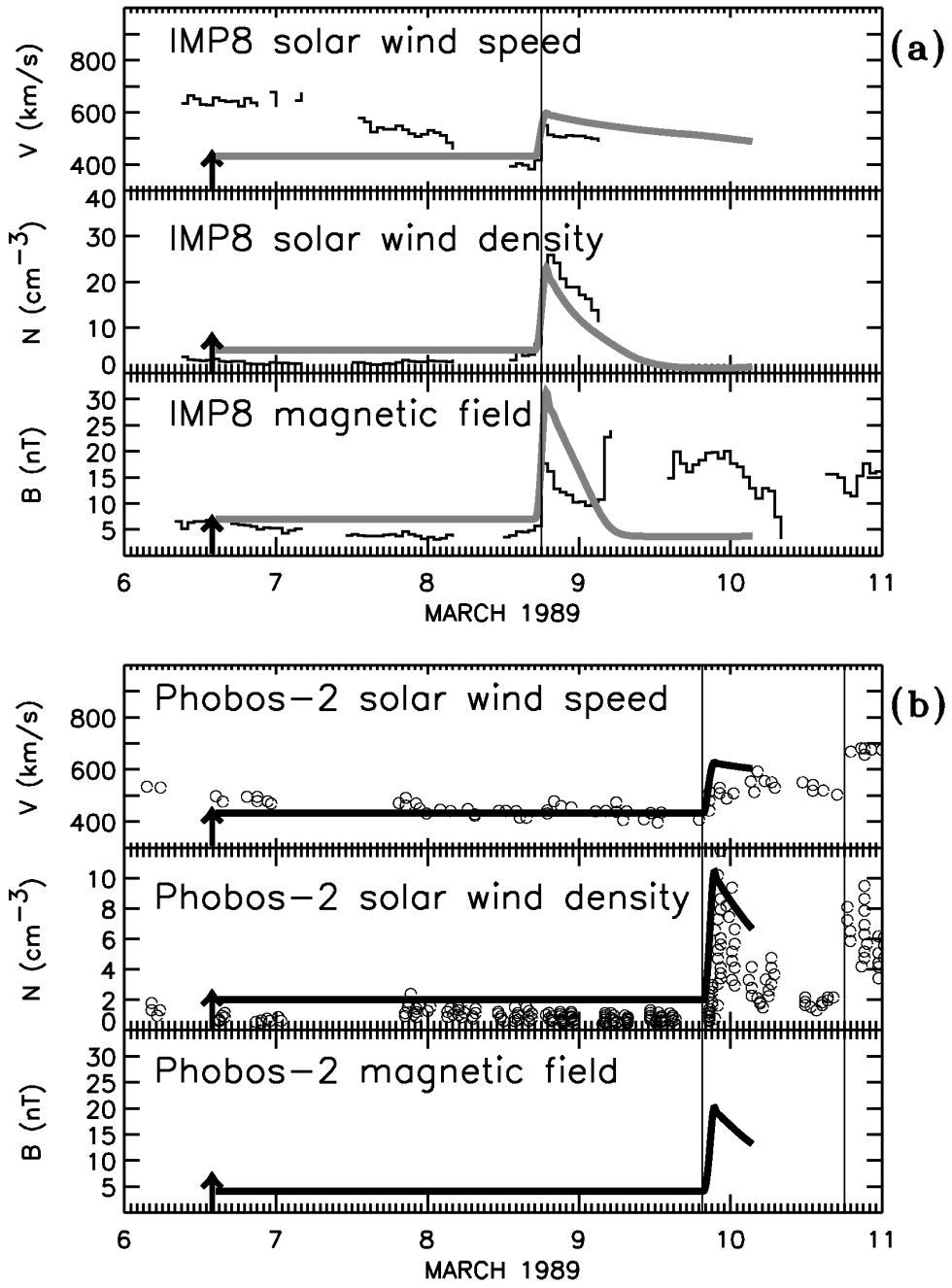

Figure 8.1: (a; top panels) Solar wind speed, density and magnetic field magnitude observed by IMP-8 from 6 to 11 March and the result of the MHD shock simulation (gray line) for a hypothetic observer at the IMP-8 location. (b; bottom panels) Solar wind speed and density as measured by Phobos-2 (cf. Figure 5 of McKenna-Lawlor et al. 2005) and the results of the MHD shock simulation (black thick line) for an observer at the Phobos-2 location. The vertical arrows indicate the onset time of the X15/3B solar flare. The first vertical lines mark the time of the shock passage as inferred from solar wind observations at each spacecraft.

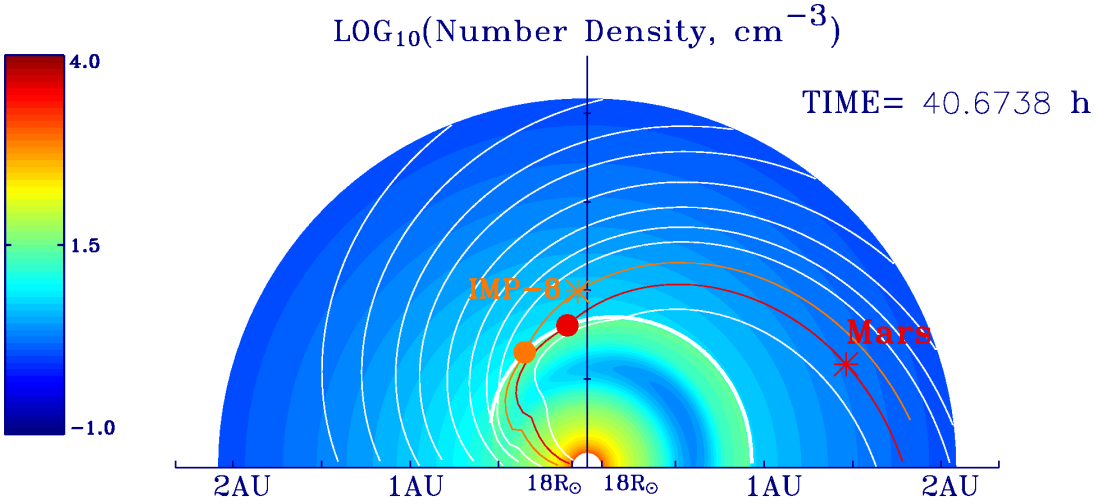

Figure 8.2: Snapshot of the shock propagation simulation 40.7 hours after the parent solar event. The density contours $\log(n\ [\mathrm{cm}^{-3}])$ and some IMF lines are represented. The locations of IMP-8 and Mars are indicated by asterisks and their cobpoints by orange and red dots, respectively. The input pulse of the MHD shock modeling was centered at E69 (as seen from IMP-8).

2 they initially increase until the end of 8 March and then keep approximately constant or decrease until the shock arrival. The evolution of VR and BR is a consequence of (1) the cobpoint displacement along the shock front (moving from the weak western flank toward the nose of the shock), and (2) the weakening of the shock as it propagates outward in the interplanetary medium.

Comparison of Figure 8.3 with Figure 3 of Heras et al. (1995) allows us to state that the event at Phobos-2 has the characteristics of a central meridian event whereas the event at IMP-8 has the characteristics of an eastern event, in agreement with the heliolongitude of the X15/3B flare and the location of both observers. Vertical arrows in Figure 8.3 mark the onset of the X15/3B flare and, otherwise indicated, the time origin. The time interval between these arrows and the onset of the lines is the propagation time of the shock from the Sun to the inner boundary of the MHD model, plus the time necessary for the observers to establish magnetic connection with the simulated shock. From the MHD simulation, we deduce this time to be 14.4 hours for IMP-8 and 10.4 hours for Phobos-2. The inner boundary of the MHD code at 0.08 AU precludes our determining of either the evolution of the actual shock from its formation closer to the Sun or its possible propagation through the solar corona (Cliver et al. 1995). The connecting time, t_c = 21.6 hours for IMP-8

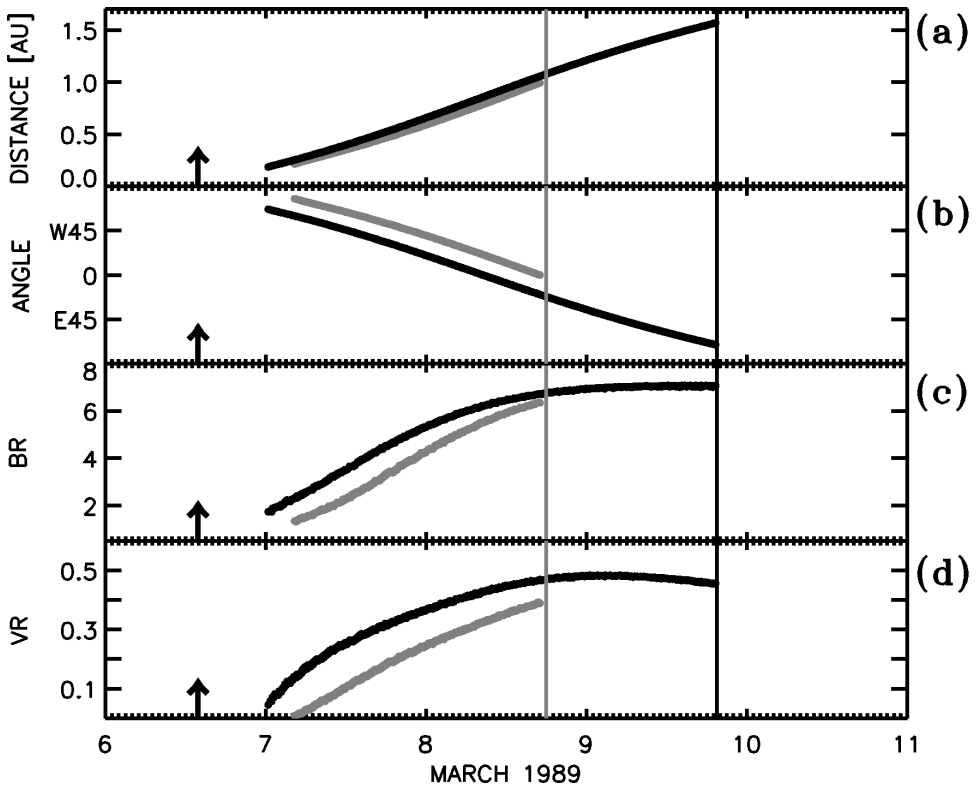

Figure 8.3: Evolution of the IMP-8 (gray) and Phobos-2 (black) cobpoint; (a) heliocentric radial distance, (b) cobpoint heliolongitude, and parameters (c) BR and (d) VR measured at the cobpoints. The vertical arrows indicate the onset time of the X15/3B solar flare and the vertical lines the time of the shock passage as inferred from solar wind observations at IMP-8 (gray) and Phobos-2 (black).

and $t_c = 12.6$ hours for Phobos-2, is determined from the time that the observer establishes magnetic connection with the part of the shock front where VR ≥ 0.1. This is the limit where we assume that the simulated shock starts to be an efficient injector of shock-accelerated protons (Lario et al. 1998).

8.3.2 Simulation of the particle event at 1 AU

In order to reproduce the particle intensities observed by IMP-8 we have followed the procedure described by Lario et al. (1998). We assume that shock-accelerated particles are injected from the cobpoint onto the IMF line that connects the shock front with the observer. The injection rate of shock-accelerated particles is described by

the function $Q(t, r)$ [cm^{-6} s^3 s^{-1}], see equation 1 of Lario et al. (1998). This injection rate evolves in time and space as the shock expands in the interplanetary medium and the cobpoint scans different regions of the shock front. The model assumes that Q scales with energy as a power law of spectral index γ: $Q(E) = Q_0(E_0)(E/E_0)^{-\gamma}$. Here, we will consider $E_0 = 3.03$ MeV, the mean energy of the 2.0 – 4.6 MeV proton channel of the IMP8/CPME instrument. Energetic particles propagate along the IMF line undergoing processes of pitch-angle scattering, adiabatic focusing, solar wind convection and adiabatic deceleration (Ruffolo 1995).

The pitch-angle scattering is modeled by a process of diffusion in pitch-angle described by a constant mean free path, $\lambda_{\parallel 0} = 0.6$ AU, with an energy dependence given by $\lambda_{\parallel} = \lambda_{\parallel 0}(R/R_0)^{2-q}$ (Hasselmann & Wibberenz 1970), where R is the particle rigidity ($R_0 = 75.52$ MV, for 3.03 MeV protons) and where q is the power index of the magnetic field fluctuations spectrum (we take $q = 1.5$; see, for example Kunow et al. 1991). We also consider the existence of a turbulent region 0.07 AU wide in front of the shock where particles undergo a higher frequency of pitch-angle scattering processes characterized by a mean free path $\lambda_{\parallel c} = 0.03$ AU for 3.03 MeV protons, that scales in rigidity as $(R/R_0)^{-0.8}$ (see simulations of foreshock regions in Heras et al. 1992 and Beeck & Sanderson 1989).

Figure 8.4 shows the observed proton intensities in six energy channels (0.5 MeV $< E <$ 48 MeV) of the IMP-8/CPME instrument together with the fit obtained by the model, as well as the evolution of one of the computed first-order parallel anisotropies, A1/A0 (see Section 2.2.1). As can be seen in the top panel, the onset of the energetic proton intensity enhancement at $E <$15 MeV occurred before the connection time t_c (short solid vertical line on 7 March). However, this increase was delayed with respect to the time expected from the propagation of particles injected at the time of the X15/3B flare and transported along the nominal IMF Parker spiral line connected to IMP-8. For example the 4.6 – 15.0 MeV proton intensities started to increase at ∼2000 UT on 6 March, ∼6 hours after the solar flare. The increase of particle intensities at higher energies occurred presumably later than t_c since it was not observed until ∼1200 UT on 7 March after a data gap, but not before 0400 UT on the same day.

The inverse velocity dispersion effect suggests that the initial particle source that magnetically connected to IMP-8 was only efficient at accelerating particles at low-energies as expected from an injection produced at the weakest part of the

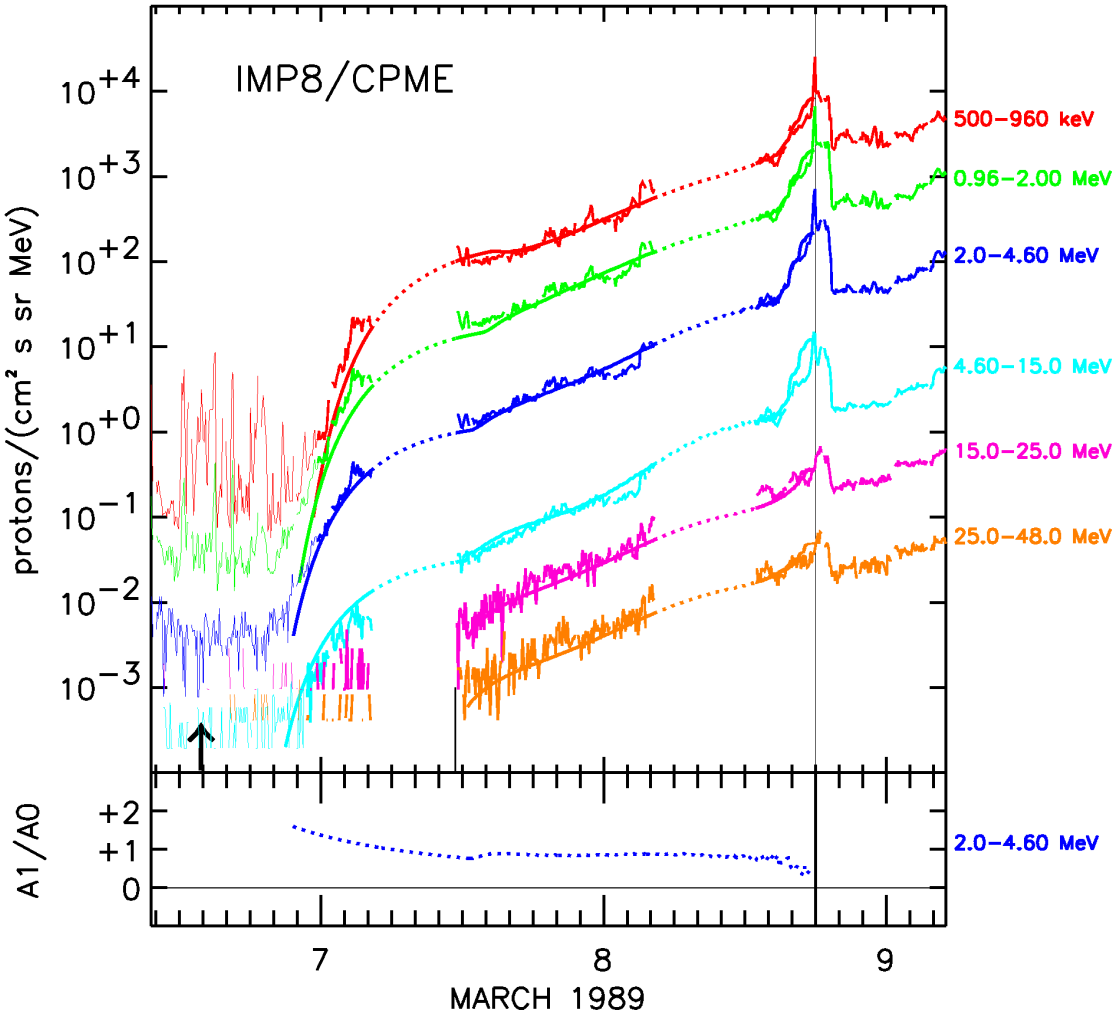

Figure 8.4: Top panel: Observed and simulated (lines) particle intensities for six energy channels of the IMP-8/CPME instrument, from 0.5 MeV to 48 MeV. The arrow marks the time of the onset of the X-ray flare. The vertical line indicates the time of the shock arrival at the spacecraft and the small vertical line marks the time of connection, t_c. Bottom panel: Example of the evolution of the first order anisotropy parallel component, A1/A0, in the upstream region, that is, from the onset of the event up to shock arrival.

Table 8.1: Spectral index, γ, of the injection rate of shock accelerated particles, Q, derived from the modeling of proton intensities at IMP-8.

	γ		
Time (hours)	$E \leq 1$ MeV	$1 < E \leq 15$ MeV	$E > 15$ MeV
$t \leq 36.75$	3.4	4.0	4.0
$t > 36.75$	3.1	3.5	4.0

flank of the shock front. The inner boundary of the MHD code does not allow us to simulate the propagation of shocks in the solar corona. Therefore, we assume that particles observed before t_c are accelerated by a coronal shock that only injects protons of energies below 15 MeV. The time delay between flare occurrence and particle injection onto an IMF field line connecting to IMP-8 may be interpreted as the time that the shock takes to form and to intercept at a few solar radii ($\sim$6 $R_\odot$) the IMF line that connects to IMP-8 (whose nominal footpoint is located at $\sim$W53) (e.g. Mann et al. 2003). In order to reproduce the gradual release of low-energy particles from a traveling coronal shock, we assume that the particle injection before t_c depends on time as $Q \propto 1/t \exp(-\beta/t - t/\tau)$ where $\beta = 50$ hours and $\tau = 15$ hours (i.e. a Reid-Axford profile, Reid 1964) and that it scales with energy as $E^{-4.3}$.

The bottom panel of Figure 8.4 displays the evolution of the normalized first-order parallel anisotropy; we have only plotted the case corresponding to the 2.0–4.6 MeV energy channel for clarity and because there are no anisotropy observations to compare with. Particle population evolves from a collimated distribution (A1/A0$>$ 1.0) at the onset of the event to a much less anisotropic (< 0.2) distribution at the shock arrival. This kind of evolution can be tracked in other eastern events (e.g. Lario et al. 1998), specially when the traveling shock continues to inject particles and the peak fluxes appear slightly after the shock passage (e.g. Sanahuja & Domingo 1987). The values derived for the spectral index γ of the Q function are given in Table 8.1. We have considered three energy ranges, below 1 MeV, from 1 to 15 MeV and above 15 MeV. As can be seen, the spectra become steeper with increasing energy and as longer upstream distances ahead of the shock arrival are considered (Lee 2005). The top panel of Figure 8.5 shows the evolution of the injection rate of shock-accelerated particles, Q, for each energy channel. The cobpoint corresponding to IMP-8 slides along the shock front from the weak western flank toward the strong nose of the shock (Figure 8.3), therefore Q is expected to steadily

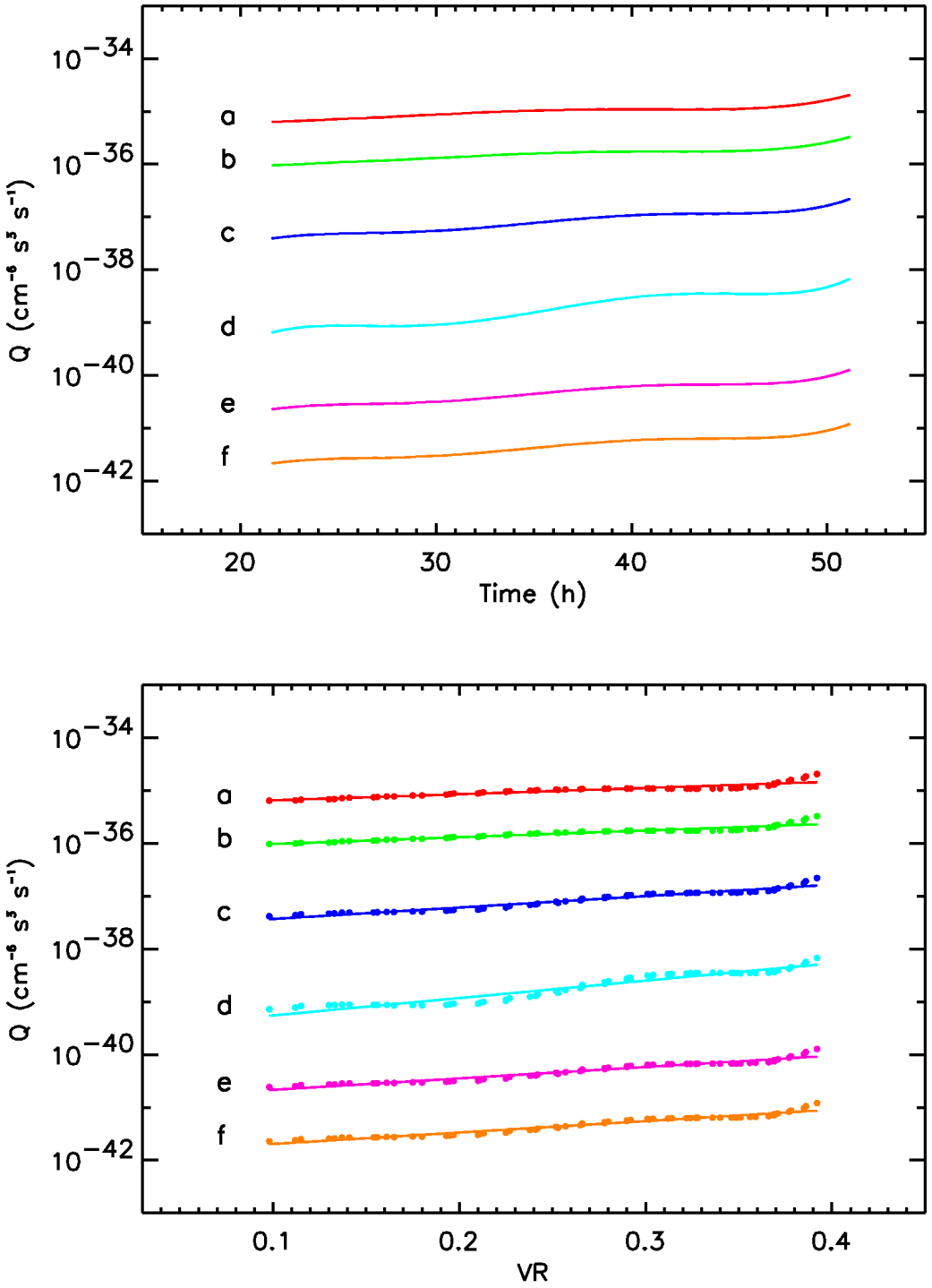

Figure 8.5: Evolution of the injection rate of shock-accelerated protons, Q (top panel) and correlation between Q and VR (bottom panel) for the six modeled energy channels (a: 0.50 – 0.96 MeV; b: 0.96 – 2.00 MeV; c: 2.0 – 4.6 MeV; d: 4.6 – 15.0 MeV; e: 15.0 – 25.0 MeV and f: 25.0 – 48.0 MeV). In the bottom panel, time runs from left to right.

Table 8.2: Q_0 and k coefficients values for the $Q(\mathrm{VR})$ relation, $\log Q = \log Q_0 + k\mathrm{VR}$, derived from the modeling of proton intensities at IMP-8.

E (MeV)	$\Delta E/<E>$	Q_0 (cm^{-6} s^3 s^{-1})	k	ξ^a
0.50 – 0.96	0.66	4.91×10^{-36}	1.18	0.93
0.96 – 2.00	0.72	7.10×10^{-37}	1.30	0.95
2.0 – 4.6	0.86	2.20×10^{-38}	2.19	0.98
4.6 – 15.0	1.25	2.48×10^{-40}	3.33	0.97
15.0 – 25.0	0.52	1.28×10^{-41}	2.19	0.98
25.0 – 48.0	0.66	1.20×10^{-42}	2.19	0.98

[a]Regression coefficient of the linear fit.

increase with time. The bottom panel of Figure 8.5 shows the correlation between Q and VR, derived from the evolution of Q (top panel) and VR (bottom panel of Figure 8.3); time runs from left to right. The straight line represents the fitted function $\log Q = \log Q_0 + k\mathrm{VR}$. This is the $Q(\mathrm{VR})$ relationship deduced by Lario et al. (1998). Table 8.2 gives the values of Q_0 and k, and the regression coefficient, ξ, obtained from each energy channel. Since VR also increases with time (Figure 8.3d) all the slopes, k, are positive.

As can be seen in Table 8.2, the value of k derived for the 4.6 – 15.0 MeV channel is significantly larger than any other value deduced for the other energy channels. This fact can have consequences when predicting Phobos-2 particle data, so, it deserves a short comment. The mean energy ($< E >$) of this energy channel is 8.3 MeV and its energy window (ΔE) is 10.4 MeV. The second column of Table 8.2 shows that the relative width of this channel ($\Delta E/ < E >$) is the largest of all energy channels. This is the reason why the derived value of k is so high, because particle transport simulations assume 8.3 MeV protons as representative of the entire energy channel whereas this energy channel detects protons with energies between 4.6 and 15.0 MeV. That means that we are implicitly assuming that 8.3 MeV protons undergo the same scattering processes as the 4.6 MeV protons or the 15.0 MeV protons (at the foreshock, for example). In fact, when modeling such a wide 4.6 – 15.0 MeV channel we are forcing the shock to be more efficient at accelerating the high-energy protons of the channel than in reality it is, hence, the high value of k derived.

8.3.3 Modeling of the particle event at Mars

Interplanetary conditions for energetic particle transport are usually derived from modeling SEP fluxes and first order anisotropies. As neither IMP-8/CPME nor Phobos-2/LET detectors provide particle anisotropy measurements, it is possible to derive different evolutions of the injection rate Q and of the mean free path by fitting solely proton intensities. Moreover, both spacecraft are separated in radial distance (0.58 AU) and angular position (72°); therefore, it may be that the values derived from the fitting of the corresponding fluxes at one spacecraft were different from those deduced using the other spacecraft measurements. In particular, the magnetic connection between Phobos-2 and the shock front (Figure 8.3) is established earlier than with IMP-8, this means that the cobpoint of Phobos-2 scans the shock front hours in advance than the cobpoint of IMP-8 and, therefore, under different conditions for particle acceleration. Direct modeling of the SEP event observed by Phobos-2 can provide insights about the transport conditions and accelerated-particle injection up to the Mars orbit, within the context of the limitations of both the shock propagation and the particle transport models (see Section 3.5).

Figure 8.6 shows the proton differential intensities (small solid circles) derived from the measured count rates for four (P1: 0.9 – 1.2 MeV, P3: 1.8 – 3.8 MeV, P4: 3.8 – 8.0 MeV and P5: 9.0 – 19.0 MeV) of the five detector channels of the Phobos-2/LET instrument (Marsden et al. 1991). We have not considered the P2 detector channel (1.2 – 3.0 MeV) because its energy range largely overlaps with that of P3. The telemetry nominal period is 20 minutes. The geometric factor for P3, P4 and P5 detectors is 0.58 cm^2 sr, while for P1 it is not well determined due to partial obscuration of the detector field of view by components of the spacecraft; we have assumed that P1 has a geometrical factor of 9.1 cm^2 sr, the same as that of the identical LET instrument aboard Ulysses (Simpson et al. 1992). Under these circumstances, we have used the P1 data just to extend the energy coverage of the study.

The proton flux profiles resulting from the modeling are shown in Figure 8.6 (solid and dotted lines). There is a considerable data gap at the beginning of the SEP event, from ∼2120 UT on 6 March to ∼2045 UT on 7 March, that prevents the fitting of the earlier stages of the SEP event. The flux profile shown by dotted traces is the profile that better fits the scarce data available at the onset of the event and that later softly fits the observed and modeled flux profiles.

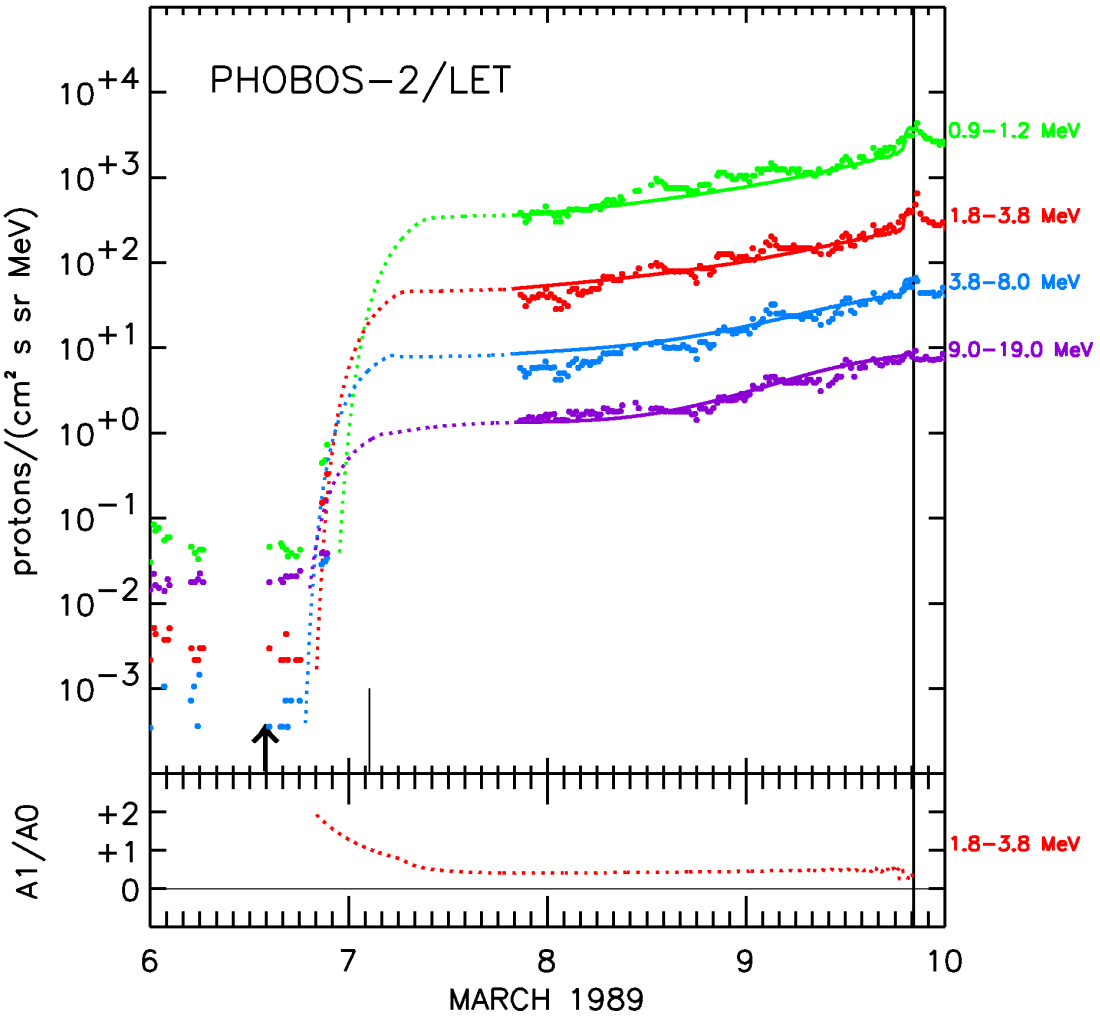

Figure 8.6: Top panel: Observed (small solid circles) and fitted (solid lines) particle intensities at Phobos-2/LET instrument, for four energy channels between 0.9 MeV and 19.0 MeV(from top to bottom: P1, P3, P4 and P5). The fitted profiles are direct output of the application of the shock-and-particle model (see text). The arrow marks the time of the onset of the X-ray flare. The vertical thick line indicates the time of the shock arrival at the spacecraft and the small vertical line marks the time of connection, t_c. Bottom panel: Anisotropy evolution, described as in Figure 8.4.

Table 8.3: Spectral index, γ, of the injection rate of shock accelerated particles, Q, derived from the modeling of proton intensities observed at Phobos-2.

	γ	
Time (hours)	$E < 1.8$ MeV	$E \geq 1.8$ MeV
$t \leq 53.00$	3.1	3.4
$t > 53.00$	3.0	3.0

The solid vertical line indicates the shock arrival at Phobos-2 and the short vertical line marks when shock-accelerated particles start being injected at the Phobos-2 cobpoint (t_c = 12.6 hours). The magnetic connection is established closer to the Sun ($\sim$25 $R_\odot$) than for the IMP-8 cobpoint.

The injection rate, Q, derived from this fitting follows a power law; the values of the spectral index γ are given in Table 8.3. A comparison with the values of Table 8.1, corresponding to similar energies, shows that the energy spectrum derived at 1.6 AU is less steep (specially, above 1.8 MeV) than that derived at 1.0 AU. In other words, the part of shock front connected with Phobos-2 is able to inject more efficiently shock-accelerated particles at high energies than the region scanned by the cobpoint of IMP-8. This is an expected result because the SEP event is a central meridian event as seen by Phobos-2, but an eastern event as seen by IMP-8 (e.g. Heras et al. 1995).

To simulate the particle injection before t_c we have assumed a Reid-Axford time profile as for the simulation of the SEP event at IMP-8, but with β = 20 hours and τ = 15 hours and an energy dependence of $E^{-3.4}$. Such injection allows us to fit the scarce data available at the onset of the event for the three higher energy channels (dotted traces). This initial particle injection is stronger than the one assumed for IMP-8; in fact, we should expect such behavior because the magnetic connection of Phobos-2 with the Sun is $\sim$40° closer to the center of the leading edge of the shock than that of IMP-8 (assuming a solar wind speed of 434 km s^{-1} and a nominal Parker spiral for the IMF). In fact it may be possible that the coronal shock traveled from its origin site (presumably close to the flare site E69) to the foot of the IMF line ($\sim$1.5 $R_\odot$) connecting to Phobos-2, nominally located at $\sim$W13 as seen from the Sun-Earth line (e.g. Krucker et al. 1999; Lin & Hudson 1976).

The derived proton mean free path and its dependence on the rigidity are the

same as those from the modeling of the SEP event at IMP-8. In order to reproduce the Energetic Storm Particle (ESP) component observed at $E < 8$ MeV, just before the shock passage, we assume a turbulent foreshock region that becomes operative 12 hours after the onset of the event ($\sim$10 hours earlier than for IMP-8). This assumption reflects the fact that the cobpoint of Phobos-2 is located in a region of the shock front whose MHD strength is larger than the equivalent region for the IMP-8 cobpoint (displaced toward the left wing of the shock front). The particle mean free path within the foreshock is the same as that of the SEP event at IMP-8, but the dependence on the rigidity has to go as $R^{+0.2}$ to fit the flux ramp before the shock arrival (such positive values of the rigidity exponent have been derived for other SEP events, Beeck & Sanderson 1989). The bottom panel of Figure 8.6 shows the first order normalized parallel anisotropy of 2.62 MeV protons that slowly decreases as the shock approaches the spacecraft as usually observed in western and central meridian events (Heras et al. 1994; Lario et al. 1998).

8.4 Forecasting the particle event at Mars

The injection rate Q at Phobos-2 can be predicted assuming that the Q(VR) relation derived from the modeling of the SEP event detected by IMP-8 (bottom panel of Figure 8.5) holds throughout the entire event and all along the shock front, because the evolution of VR at the Phobos-2 cobpoint is known (derived from MHD shock-modeling; Figure 8.3d). Consequently, it becomes possible to synthesize particle flux profiles at 1.58 AU and compare them with the intensity profiles observed by the Phobos-2/LET instrument. Since we cannot know a priori the transport conditions of the particles en route to Mars, in order to avoid any extra assumption, we have considered that the mean free path of the parameters characterizing the turbulent foreshock region are those obtained from the modeling of the SEP event at IMP-8. The only difference is that, because of the different magnetic connection of Phobos-2 to the Sun, the initial injection (for $t < t_c$) of accelerated particles is the injection derived from the modeling at Phobos-2. As already commented, the particle injection at the earlier stages of the event is expected to be stronger for Phobos-2 than that derived from the fitting of the SEP event at IMP-8.

The energy channels of the Phobos-2/LET instrument are different from those of the IMP-8/CPME instrument. Therefore, Q_0 and k have to be calculated with

Table 8.4: Q_0 and k coefficients values for the $Q(\mathrm{VR})$ relation to be applied to Phobos-2 forecasting, derived from the modeling of proton intensities at IMP-8.

E (MeV)	Q_0 (cm^{-6} s^3 s^{-1})	k
P1: 0.9 – 1.2	1.63×10^{-36}	1.30
P3: 1.8 – 3.8	4.25×10^{-38}	2.19
P4: 3.8 – 8.0	2.02×10^{-39}	3.33/2.19
P5: 9.0 – 19.0	5.90×10^{-41}	3.33

respect to the energy channels of LET from the values derived at IMP-8 (Table 8.2). We assume a power law dependence with the energy for Q_0 and that the value of the slope k adopted for each energy channel of the Phobos-2/LET instrument corresponds to the most similar energy channel of the IMP-8/CPME instrument.

Table 8.4 shows the values derived for Q_0 and k for each energy. For the 3.8 – 8.0 MeV (P4) channel we have considered two possible choices of k because this energy channel partially overlaps with the 2.0 – 4.6 MeV and 4.6 – 15.0 MeV channels of IMP-8. If the dependence of particle intensity with the energy scales as a power-law, the contribution of the 3.8 – 4.6 MeV protons to the intensity of the 3.8 – 8.0 MeV channel is about 45%. For the same reason, we have only considered the value of k derived from the 4.6 – 15.0 MeV channel of the CPME instrument for the 9.0 – 19.0 MeV (P5) channel of the LET instrument; the contribution of the 9.0 – 15.0 MeV protons to the intensity of the energy channel is ∼85%.

Taking into account the aforementioned considerations we have performed three particle intensity predictions at Phobos-2, respectively named "Fc1", "Fc2" and "Fc3".

Forecast Fc1. Figure 8.7 displays the two predictions of the synthetic flux profiles for the 3.8 – 8.0 MeV channel: the dashed line profile has been computed assuming the values of k corresponding to the 2.0 – 4.6 MeV energy channel of IMP-8 (k = 2.19) and the solid line that of the 4.6 – 15.0 MeV channel (k = 3.33). There are also two predictions for the 9.0 – 19.0 MeV flux profile, both calculated with the same value for k (see Table 8.4) but assuming the absence (solid line) or presence (dotted-dashed line) of the foreshock region. The reason is that for this energy interval it is not clear whether the foreshock is active, because it partially overlaps the 4.6 – 15.0 MeV and the 15.0 – 25.0 MeV channels of IMP-8/CPME.

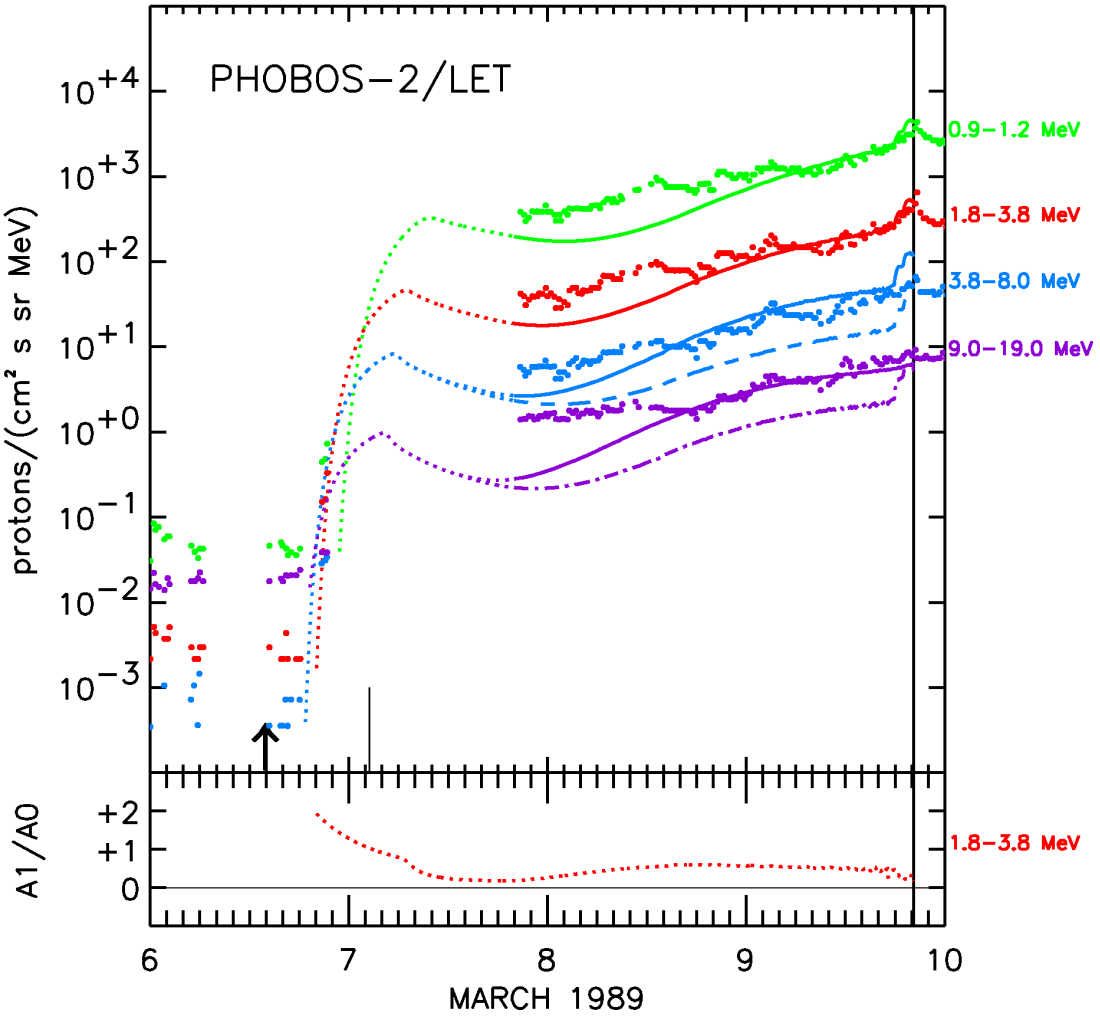

Figure 8.7: *Forecast Fc1*. Top panel: Observed (small solid circles) and predicted (solid, dashed and dotted lines) particle intensities at Phobos-2/LET instrument, for the four energy channels between 0.9 MeV and 19.0 MeV (from top to bottom: P1, P3, P4 and P5. The two synthetic profiles (solid and dashed traces) for the 3.8 − 8.0 MeV channel and for the 9.0 − 19.0 MeV channel (solid and dotted-dashed traces) refer to different modeling conditions (see text for details). Other displayed features are as in Figure 8.6.

As can be seen in Figure 8.7, observations and synthetic profiles show good agreement ∼27 hours before the shock arrival (∼15 hours for the lowest energy channel). Just after the data gap, the computed intensities (the four solid lines) underestimate the flux observations by a factor 2.0, 2.3, 2.2 and 8.0, for channels P1, P3, P4 and P5, respectively (we call these synthetic profiles "forecast Fc1"). Several factors may be responsible for these differences:

1. The influence of the MHD conditions on the efficiency of the shock as a particle accelerator is only partially reflected in the Q(VR) relation (Lario et al. 1998; Sokolov et al. 2006). It might not take into account, for example, the influence of the changes of the angle θ_{Bn} as the cobpoint moves along different regions of the shock front (Tylka & Lee 2006).

2. As the shock expands and the cobpoint moves toward the nose of the shock, the geometry of the shock may change to an oblique configuration allowing processes of particle scattering by self-generated Alfvén waves to become efficient and thus enhancing the injection rate of shock-accelerated particles (e.g. Lee 2005).

3. Particle transport conditions from the shock to IMP-8 and from the shock to Phobos-2 may be different, due to the radial and angular separation between these spacecraft.

4. The magnetic field configuration was not the nominal Parker spiral assumed here, then Phobos-2 would have been magnetically connected to locations closer to the central part of the shock front more efficient as particle-accelerators (Cane et al. 2006).

5. A local pre-existing seed particle population could make the injection rate of shock-accelerated particles more efficient at the early stages of the shock propagation from a quasi-perpendicular geometry (Tylka et al. 2005).

Factor [2] assumes the formation of a foreshock in quasi-parallel or oblique shocks (Tsurutani et al. 1983; Lee 2005), although the efficiency of the particle injection does not necessarily depend on the geometry of the shock. The ESP component of the SEP event observed by IMP-8 below ∼15 MeV clearly indicates that accelerated particles are trapped near the shock front at 1.0 AU and thus the presence of a turbulent foreshock; the same applies with respect to the SEP event recorded at

Phobos-2 below 8 MeV but acting earlier and probably not so strongly (see comments in the previous section). These differences can imply higher values of Q at Phobos-2 than those derived from the modeling at IMP-8.

Forecast Fc2. In order to check factors [2] and [3] we have computed the proton flux profiles at Phobos-2 by using the transport conditions derived from the modeling of the SEP event at Mars that differ from those derived at IMP-8 only by the rigidity dependence of the foreshock region and the time at which this region starts to act. The values of Q_0 and k are the same as those used in the prediction shown in Figure 8.7. The resulting proton-intensity profiles ("forecast Fc2") are not shown in a figure because they are similar to those displayed in Figure 8.7. They only show a slight improvement with respect to forecast Fc1 from ∼28 hours before the shock passage, whereas, after the data gap, the intensities derived are underestimated by the same factors. Therefore, the possible influence of the foreshock region and the particle transport conditions acting differently on the particle population detected by IMP-8 and Phobos-2 cannot account for the discrepancy between observations and predictions at the beginning of the SEP event.

Forecast Fc3. Flare particle population can be an important source of seed particles in large SEP events, especially at high energies either from prior or accompanying flares (e.g. see Tylka & Lee 2006; Cane et al. 2006). The latter could be the case, the case [5], for the present scenario. The X15/3B flare seen in conjunction with the CME on the 6 of March was located at one of the legs of the CME (Feynman & Hundhausen 1994); then it is likely that energetic protons produced at the flare site could escape and reach the leading edge of the CME and experience further acceleration and injection there (Li & Zank 2005). Furthermore, note that an observer located at the Earth distance on the same IMF line that connects at the beginning Mars with the Sun would have seen this event as an E29 event. Although not usual, eastern events with similar longitudinal locations have exhibited a significant prompt phase of high energy (up to 400 MeV) protons. For instance, this is the case of the 24 September 2001 event (Lario et al. 2003b). Moreover, since IMP-8 is magnetically connected to the Sun ∼40° westward than Phobos-2, this seed population could more easily fill the magnetic flux tubes connecting to Mars and not those (if any) to the Earth. In fact, no high energy (> 15 MeV) particle fluxes were observed by IMP-8 at the onset of the SEP event. This assumption is supported by the fact that heavy-ion abundance measurements of the ESP component are consistent with the acceleration of an ambient population of solar flare

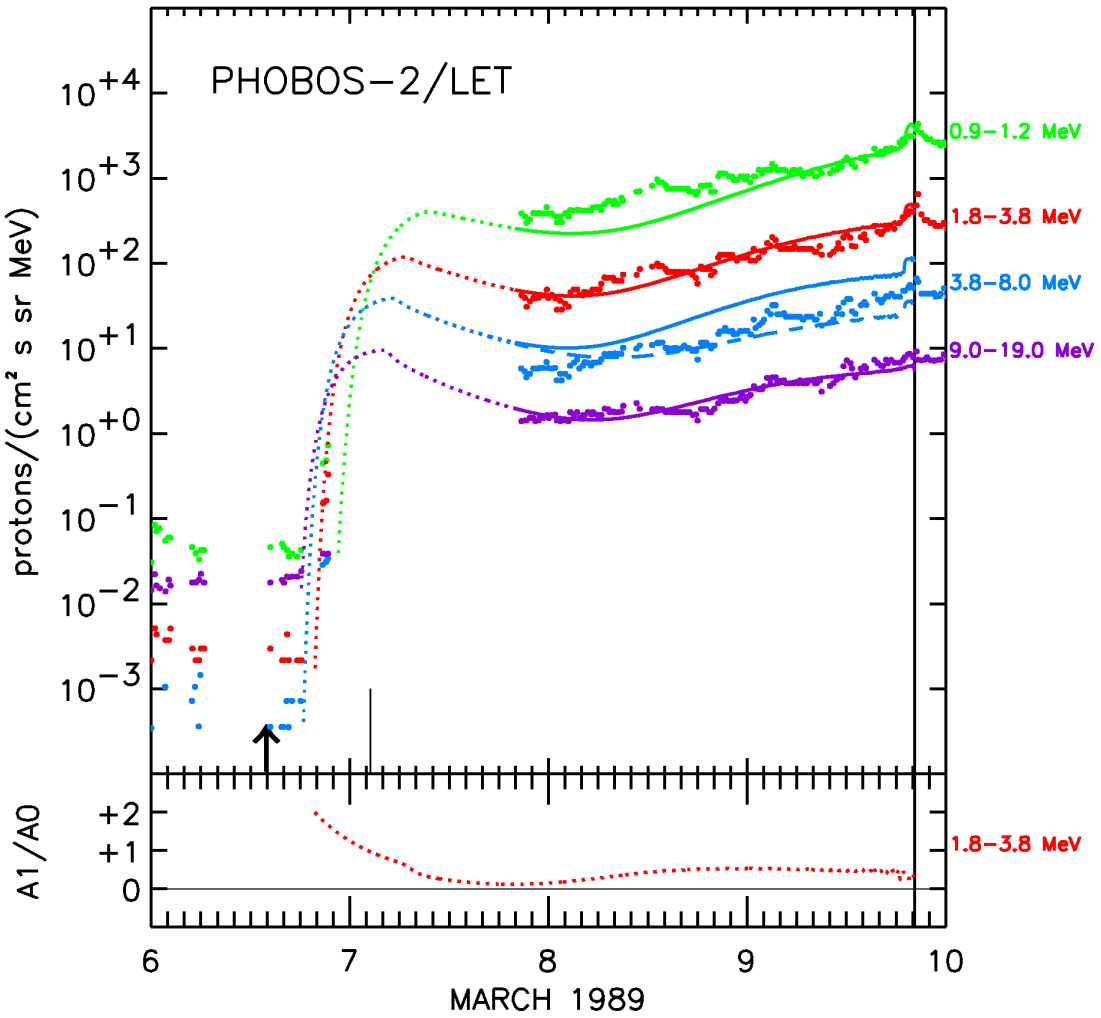

Figure 8.8: *Forecast Fc3*. Top panel: Observed (small solid circles) and predicted (solid, dotted and dashed lines) particle intensities at Phobos-2. Interplanetary propagation conditions assumed are those derived at 1.6 AU but considering a more powerful injection before the time of magnetic connection (see text for more details).

particles (Marsden et al. 1991).

In order to simulate such an enhanced population of seed particles, and their presumably acceleration and injection by the shock closer to the Sun than the inner grid boundary allowed by our MHD shock simulation, we have assumed an injection of accelerated particles with a Reid-Axford profile characterized by $\beta = 20$ hours and $\tau = 5$ hours, that scales with the energy as $E^{-2.5}$ (from $f \propto p^{-5}$, i.e. Sokolov et al. 2006). Figure 8.8 shows the predictions for the particle intensities obtained using such a stronger near-Sun particle injection rate ("forecast Fc3"), assuming the same transport conditions and Q(VR) relations as for the forecast Fc2.

As can be seen in Figure 8.8, the predictions fit the measurements of the 1.8-3.8 MeV and 9.0-19.0 MeV channels. The two possible predictions for the 3.8-8.0 MeV channel (depending on the adopted value of k) closely contour the observations. The flux prediction for the lowest energy channel has also improved with respect to forecasting Fc1 (Figure 8.7) and Fc2, although it still underestimates the proton intensity from the data gap up to one day before the shock arrival. This discrepancy would disappear if a less steep spectrum were considered for the injection of low energy (< 1.8 MeV) protons near the Sun (as it happens with the injection rate of shock-accelerated particles, Q, derived from modeling the SEP event; see Table 8.3).

In spite of the gaps present in the particle data of IMP-8 and Phobos-2, and the lack of anisotropy measurements that do not permit the derivation of more accurate proton transport conditions (and hence allowing us just to assume average conditions for the proton mean free path and the foreshock region), we can conclude that: (1) shock-accelerated particles en route to different observers may encounter different interplanetary transport conditions (although for this specific SEP event this effect is almost negligible); and (2) different pre-existent seed particle populations can affect differently the flux predictions of SEP events for observers in locations other than 1.0 AU.

This study is a clear example that there is not a comprehensive model able to account for all the factors at work in the generation and development of SEP events, and that SEP flux predictions out of 1.0 AU from measurements at 1.0 AU are not free of uncertainties. In fact, it would be difficult to obtain precise predictions, with absolute values in physical units of the particle intensities (relative values or predictions in arbitrary units are frequently useful enough for scientific purposes)

Table 8.5: Fluences at Mars: observed, modeled and forecasted (Fc1, Fc2 and Fc3) values; see text for details. Units are: p $(cm^2\ sr\ MeV)^{-1}$.

E (MeV)	Observed	Modeled	Fc1	Fc2	Fc3	
P1: 0.9 – 1.2	1.8	1.5	1.5	1.4	1.5	$(\times 10^8)$
P3: 1.8 – 3.8	2.1	2.0	1.8	2.1	2.3	$(\times 10^7)$
P4: 3.8 – 8.0	3.1	3.4	*2.4*	*3.2*	*3.8*	$(\times 10^6)$
P5: 9.0 – 19.0	5.5	5.8	*1.7*	1.4	2.2	$(\times 10^5)$

because average values derived at 1.0 AU are not necessarily representative for other angular locations and heliocentric distances. This point can be illustrated with some numbers for the peak flux and the fluence derived from the intensity profiles fitted and forecasted for this SEP event at Mars.

8.5 Fluences and peak fluxes at Mars

In the following, "peak flux" stands for the maximum intensity of the particle directional differential intensity (or flux, as defined in E-10-04 2000). The fluence is defined here as the time integral of the differential intensity; hence, it is expressed in particles $(cm^2\ sr\ MeV)^{-1}$. To compute the fluence of a SEP event for a given energy channel, we first subtract the background intensity measured before the onset of the event. Afterward, we integrate the resulting differential fluxes (either derived from observations or simulated) from the end of the initial data gap (2045 UT, March 7) up to shock arrival (2015 UT, March 9). Due to this data gap, we do not intend to derive fluence values for operational purposes but just to compare results from modeling and prediction with observations.

Table 8.5 lists different fluence values, for the four considered energy channels of the Phobos-2/LET instrument. The first column gives the energy range of the channel, second and third columns show the values of the fluence derived from observations and from the modeling of the flux profiles (small circles and solid lines in Figure 8.6), respectively. The three following columns give the values of the fluence predicted for each case, Fc1, Fc2 and Fc3, respectively, as described in the previous section. When the model gives two predictions for the same energy channel, the average value has been calculated and listed (in italics). From the comparison

between the values of the modeling of the event (column 3) and those derived from the measurements (column 2), we can conclude that the simulation fits well the observed values, slightly underestimated (∼10%) for low energies (< 3.8 MeV) and slightly overestimated (∼7%) at higher energies. It is worth to note that we have not tried to produce better fittings of the proton flux profiles to the observed values, for example, by assuming a radial dependence of the proton mean free path, or by trying to achieve a more precise determination of the peak flux by better tuning the injection rate spectrum.

As already commented, the data gaps, the absence of anisotropies and the small number of channels available at Phobos-2 avoid any further real improvement for prediction. As a consequence, small logarithmic differences between the output values (factors between 0.990 and 1.006, frequently enough for modeling) translate into non desirable absolute differences (∼10%) for forecasting purposes. From the last three columns of Table 8.5, it is easy to realize, that on average the predictions of the fluence are accurate for channels P3 and P4, correct for P1 (the observed fluence is underestimated by 17%) and less accurate for the highest energy channel, P5 (underestimated by 70%). When averaging over the four energy channels, the case Fc3 yields more accurate predictions than cases Fc2, and Fc1 (in spite of the fact that case Fc3 underestimates the observed values by a factor ∼0.8).

Predictions globally improve when the presence of an early powerful injection of energetic particles is assumed (case Fc3). Particularly, at high energy (P5 channel), the difference with respect to observations reduces to 40% (see Table 8.5). This means that predictions can be improved by using a model able to simulate the shock propagation closer to the Sun (e.g. < 5 $R_\odot$). Nevertheless, the discrepancy at high energy still is large (P5 energy channel in Figure 8.8) because the predicted profile underestimates the observed intensity by a factor ∼1.4 during the 8 hours prior to the shock arrival. This results from the fact that the predictions for the P5 energy channel are based on the values derived from modeling the 4.6 – 15.0 MeV channel of IMP-8, which has a wide energy window (see discussion in Section 8.3). Therefore, the higher energy protons detected ($\lesssim$ 15 MeV) may undergo different conditions than those of lower energies ($\gtrsim$ 4.6 MeV). For example, the efficiency of a shock as a particle-accelerator can start to decrease rapidly at some (unknown) energy between ∼5 MeV and ∼20 MeV (e.g. Tylka et al. 2000; Lario et al. 1998); or the efficiency of the foreshock as temporal storage of accelerated particles can also start to diminish rapidly in the same energy range. Thus particle detectors with

Table 8.6: Peak Fluxes at Mars: observed, modeled and forecasted (Fc1, Fc2 and Fc3) values; see text for details. Units are: p $(cm^2\ sr\ s\ MeV)^{-1}$.

E (MeV)	Observed	Modeled	Fc1	Fc2	Fc3
P1: 0.9 – 1.2	3 412.7 (4 361.3)[a]	3 713.6	4 266.6	3 903.4	3 909.0
P3: 1.8 – 3.8	443.8 (650.6)[b]	400.0	487.0	451.8	453.4
P4: 3.8 – 8.0	66.4	63.9	*64.3*	*58.4*	*58.9*
P5: 9.0 – 19.0	9.2	8.6	*6.8*	6.8	6.8[b]

[a]Values at the time of the shock passage and, between parentheses, values observed in the downstream region of the shock.

[b]Value at the time of the shock passage.

relatively wide energy windows in the 5 – 20 MeV range may not be well suited for a simultaneous and precise prediction of the fluence and the peak flux of a SEP event.

Table 8.6 gives the values of the peak flux measured or derived for the same cases described in Table 8.5. For P1 and P3 channels, the peak flux was reached 24 minutes after the time of the shock passage by Phobos-2. Our model does not allow us to simulate the downstream part of the SEP event, hence we miss the opportunity to fit the value of the peak flux for these two energy channels (these values are given between parentheses in Table 8.6). Instead, the observed values listed are those measured proton intensities at the shock passage. This difference is not relevant for the prediction of particle fluences ($<4\%$) but it is important for peak flux prediction since the flux value at the shock passage is, on average, $\sim$27% smaller than the real peak value. For channels P4 and P5 the observed peak fluxes are attained at the time of the shock passage. The peak flux given for the highest energy channel (P5) in forecast Fc3 (Table 8.6) is the maximum particle intensity obtained after the data gap, in order to compare it with the available data. The peak flux values derived from the modeling of the SEP event (third column) are 15% (P1 channel), 38% (P3), 4% (P4) and 7% (P5) smaller than the observed values. The three forecasts (Fc1, Fc2 and Fc3) underestimate the observed peak flux values (at the shock passage) by similar percentage as the values derived from modeling, although the percentage is larger, 26%, for the P5 channel (the reason is the same as that argued in the case of the fluences).

From the results shown in Tables 8.5 and 8.6, we can conclude that the differences between observational flux measurements with respect to modeled flux profiles and

those differences with respect to the predicted synthetic proton flux profiles, are of the same order. Therefore, the use of the Q(VR) relation allows us to predict the proton flux of the SEP event observed at Mars from the fitting to the measurements gathered at 1.0 AU of the SEP event triggered by the same interplanetary shock.

8.6 Discussion and conclusions

The dependence assumed between the injection rate of shock-accelerated particles, Q, and the normalized downstream-to-upstream solar wind speed, VR, at the cobpoint (Lario et al. 1998) allows us to build up synthetic intensity-time profiles for different observers in interplanetary space. The extension of SOLPENCO to Mars depends on the validity of the hypotheses made, the most relevant being the assumption that the Q(VR) relation holds for a wide variety of SEP events that may develop in a variety of solar-interplanetary scenarios (different locations of the parent solar event with respect to the observer, different shock speeds, and different conditions for particle acceleration and propagation in interplanetary space). Studies of the type presented in this work have not been regularly performed, basically because measurements of SEP events from different spacecraft at different distances and angular positions suitable to be modeled are still scarce, either closer to the Sun (Venus or Mercury orbits) or at larger (Mars orbit) heliocentric distances. In that sense, STEREO can provide data that will help us to determine the longitudinal dependences of SEP events and the dependence of Q on the shock strength and geometry at two different regions of its front but not with respect to the radial distance. Up to now few works dealing with modeling SEP events observed by different spacecraft have been performed (e.g. Kallenrode 1997; Lario et al. 1998). Moreover, it is not possible to exclude that the functional dependence between the injection rate Q on the MHD strength of the shock at the cobpoint can solely rely on the variable VR (i.e. a dependence on BR or θ_{Bn} is suggested in several cases, but the MHD modeling of the shock does not allow us to draw firm conclusions).

After all these caveats that give an idea of the present limitations of any prediction, once a SEP is observed at 1.0 AU and a Q(VR) relation is derived, in order to extend it to Mars, we have to be sure that the Mars orbiting spacecraft is observing the same shock as that observed at near-Earth. Unfortunately, with the present available data and the limitations for modeling, this 6 March 1989 SEP event is

the only case for which we can produce such a prediction. As it can be easily understood, the Earth and Mars will not always be well located to observe the same shock, and to detect particles accelerated by the same shock but injected into the interplanetary medium from different locations ("the cobpoint" when connected to the observer) on the shock front; these are two strong constraining conditions. Furthermore, intense SEP events tend to occur in series, i.e. when a complex active group crosses the solar disk. In this case, the identification of the solar origin of each shock is not straightforward, especially at large heliocentric distances. Moreover, when a SEP event develops in the downstream region of a previous shock, the interplanetary conditions can largely differ from the assumptions commonly made by modelers. This is the reason why we applied the model only to the first event observed in the series of March 1989 events.

We have simulated both the propagation of the interplanetary shock and the time-intensity profiles observed by IMP-8 and Phobos-2 during the event on 6 March 1989 associated with one of the most intense X-ray flares of solar cycle 22. By assuming the validity of the Q(VR) relation at the cobpoint derived from the simulation of the SEP event at IMP-8, we have predicted the proton differential flux profiles observed at Phobos-2. The comparison between predicted, modeled and measured profiles at Mars yields the conclusion that the Q(VR) relation performs well in forecasting the peak flux and the differential fluence at each energy channel. Unfortunately, the singularity of this SEP event prevents us from drawing any general conclusion about the validity of this assumption. We have discussed the limitations of our model and the Sun-Earth-Mars scenarios where it can provide predictions of proton flux profiles of SEP events. At present, there is no other model able to forecast proton flux profiles of SEP events at Mars from another SEP event observed at Earth, such as that presented here. We expect that future measurements of SEP events gathered by STEREO will give us the opportunity to model more events in order to evaluate the applicability of our model to forecast SEP events in the Martian environment.

9 Summary and future perspectives

9.1 Summary

We have developed SOLPENCO, an engineering tool for rapid predictions of flux and fluences of SEP events. This is the first predictive code that takes into account the contribution of the expanding interplanetary shock to the SEP flux. It is based on the Shock-and-Particle model of Lario et al. (1998). SOLPENCO is a new step toward a fully and reliable operational tool able to produce quantitative predictions of radiation hazards in space. We have presented the main characteristics of SOLPENCO and start checking part of its outputs, comparing them with measurements made by the ACE, IMP-8 and ISEE-3 spacecraft. For first time ever, SEP observations at 1.0 AU (by IMP-8) have been used as a baseline to model and predict the proton flux profiles, fluences and peak fluxes at 1.6 AU (recorded by Phobos-2, orbiting Mars) by using the Q(VR)-relation. We found a good agreement between predictions and observations, and we have discussed the main difficulties appeared in the process. This study is a clear example of how powerful this empirical relation can be for space weather purposes.

Specifically,

1. We have developed a data base, the core of SOLPENCO, consisting on a large number of pre-calculated energetic particle flux profiles. This database allows a rapid computation, by interpolation, of particle fluxes and fluences of other possible scenarios for gradual SEP events, under user's demand. The data base contains the synthetic flux and fluence profiles for a set of 448 different

interplanetary scenarios, calculated throughout the upstream part of the SEP event (i.e. from the event onset up to the shock passage by the spacecraft) for proton energies ranging from 0.1 to 90 MeV. These scenarios are basically defined by (i) the solar longitude of the parent solar activity (from E75 to W90); (ii) two heliocentric radial positions of the observer, either 0.4 AU or 1.0 AU; (iii) the transit speed of associated interplanetary shocks (from ~ 400 km s^{-1} to ~ 1700 km s^{-1}); and (iv) four conditions for particle transport (parallel mean free path of 0.5 MeV protons, either 0.2 AU or 0.8 AU, scaled with the proton rigidity as $R^{+0.5}$ and either the existence or absence of a turbulent foreshock region.

We have developed a user-friendly interface for SOLPENCO that permits a rapid acquisition of the flux and cumulative fluence profiles in the upstream part of a SEP event for a given scenario (outputs are provided as ascii or graphic files). This interface also gives an estimate for the transit time and speed of the CME-driven shock, as well as, of the upstream peak intensity and fluence. SOLPENCO can be run on-line at http://www.spaceweather.eu/es/-model_access_interface and it is available under request.

2. We have modeled three gradual SEP events, by using the shock-and-particle model, in order to test the Q(VR) relation in scenarios different from those of the former modeled SEP events. The simulation of these events clarifies and supports the values of Q_0 and k of the Q(VR) relation finally adopted in SOLPENCO. However, the number of SEP events modeled is still small. It is necessary to model a much large number of events (and it take times to accurately model each one of them), then average the particularities of each specific event and find representative synthetic profiles of the flux that will predict the main characteristics of the SEP events.

   However, textbook SEP events to model are hard to find. The attempt to put together too many variables of different type that should behave 'reasonably well' (even just for the upstream region) for the application of the shock-and-particle model is a tricky task. It is necessary a background solar wind relatively constant, an IMF not varying too much in direction and/or magnitude, a scenario not perturbed by former interplanetary shocks or corotating interaction regions, a low background energetic particle intensity allowing a precise definition of the onset of the event, no contributions from the Earth's magnetosphere, no rapid variations in the flux particle intensity, a precise identification of the CME features relevant for modeling, etc. It is even bet-

ter if there are several spacecraft continuously operating at the time of the SEP event, in order to constraint as much as possible the simulations. These reasons do obligate us to first analyze the shock-and-particle interplanetary scenario and then apply the model to understand the processes at work in the development of the SEP event (and even then difficulties may arise).

3. We have performed a thoughtful review of the existing literature in order to clarify the range of values that different variables involved in SOLPENCO encompass, and thus define the 'average values' to be implemented into the code. We have selected representative values for such variables, being the most relevant the spectral index of the injection rate of shock accelerated particles, γ (at low- and high-energy), and the coefficient k of the Q(VR)-relation.

   We have discussed in detail the influence of k and γ in the flux profile, as well as how to compute the absolute values of the particle intensity.

   In this review we have also identified the weak points of the shock-and-particle model (many of them also applicable to other published models), as well as those specific of SOLPENCO.

4. We have studied how the synthetic proton flux profiles produced by SOLPENCO depend on the input variables, since these output profiles can show a variety of shapes and specific features. Therefore, we have studied their dependence on: (i) the particle energy and mean free path; (ii) the presence or absence of a turbulent foreshock region; (iii) the initial speed of the shock; and (iv) the heliolongitude of the solar parent activity with respect to the observer.

   As a general result, we can say that it is not possible to write down a simple conclusion of the influence of all these factors together, since the relative contribution of each one to the final profiles for a given SEP event is different and can change as a function of the evolution of the cobpoint. The result is a variety of SEP flux profiles that reproduce many features of the different types of observed profiles.

5. We have analyzed the dependence of both the initial shock speed and on the heliolongitude on the peak flux and total (upstream) fluence of the SEP events in the data base of SOLPENCO.

   For the peak flux we draw the following conclusions. (i) The majority (100% at 0.4 AU and 97% at 1.0 AU) of the flux profiles peak at the shock passage. (ii) The highest peak fluxes at 1.0 AU correspond to observers located between

W22 and W00, while this latter limit extends to E15 for observers located at 0.4 AU. (iii) The peak fluxes attained at 0.4 AU are higher than those at 1.0 AU, for faster shocks and for heliolongitudes between W22 and E15. (iv) For a given angular position of the observer, peak intensities increase with the initial shock speed, except for events eastward than E60 at energies $E < 8$ MeV. (v) There is a correlation between the peak intensity and the initial shock speed, and this correlation is high ($\xi > 0.95$) for central meridian events without the presence of the turbulent foreshock region. And (vi) both the particle injection history and the transport conditions have a significant influence on the correlation between the peak intensity and shock speed.

For the fluence, the conclusions are the followings. (i) Two factors determine the fluence, the time that the observer is connected to the shock front and the efficiency of the shock at injecting shock-accelerated particles (that depends on the position and evolution of the cobpoint). (ii) For a given shock, the better the connection between the observed and the shock the higher the fluence at either 1.0 AU or 0.4 AU. (iii) For the same heliolongitude, events well-connected from the beginning of the events and associated with fast shocks present the higher fluences. And (iv) for those events where the observer is initially poorly or not connected to the shock, the longer the connection between the observer and the shock the higher the fluence of the event.

6. The radial dependences of event fluences derived from the analysis of the 0.4 AU and 1.0 AU simulations does not support the hypothesis that the fluence scales with heliocentric distances as the inverse square law of the radial distance. The contribution of shock-accelerated particles to the upstream fluence of the SEP events in the interplanetary region between 0.4 AU and 1.0 AU is important, by a factor ranging between $\gtrsim$1.0 and 10, depending on the shock speed and the observer's heliolongitude.

   The comparison of the peak intensity derived for pairs of spacecraft located at 0.4 AU and 1.0 AU and sitting on the same IMF line, yields a decrease of the peak intensity with both the radial heliocentric distance for well connected events; furthermore, this decrease accentuates with the initial shock speed. For eastern events, the derived radial indices are positive, indicating larger peak intensities at 1.0 AU than at 0.4 AU; this results from the cobpoint's displacement along the shock front. In the case of the upstream fluence, for these pairs of observers, we always obtain positive radial indices because of the shock is continuously injecting particles as it travels toward 1.0 AU.

The main conclusion we draw is that a general (valid for all type of SEP events) radial dependence either for upstream fluences or peak intensities cannot be derived. Even in the case of observers located in the same magnetic flux tube, the radial variation of these magnitudes depends on the heliolongitude of the parent solar event and the way each observer establishes magnetic connection with the traveling shock, as well as on the particle energy.

We also want to point out that the analysis presented here must be resumed once both (i) the contribution of the downstream region to the fluence (and in some cases to the peak intensity) and (ii) the extension of the particle shock injection below $18\,R_{\odot}$ have been included into the code.

7. We have analyzed and discussed two SEP events (4 – 6 April 2000 and 22 – 24 April 1979) in order to show the problems that may arise when comparing SOLPENCO outputs with real SEP events. This analysis allow us to conclude that the code can predict with relative accuracy the intensity-time profiles of different energy channels for a variety of SEP events despite the simplicity of the assumptions made in the generation of the data base and the small number of actual SEP events compared with.

   The main differences between both synthetic and observed profiles arise from the range of energies compared, from the average values of the parameters k and Q_0 adopted to compute the injection rate of shock accelerated particles, and from the value of the normalization constant. There is a diversity of factors that determine the final shape and values of the fluxes observed by spacecraft; hence, average values may not be necessarily representative of any possible solar-interplanetary scenario.

   In general, SOLPENCO predictions may be improved by modeling more SEP events in order to further investigate the dependence of k with the energy, to obtain the spectrum of the injection rate, and to derive an average value for the normalization constant.

8. We have started the verification of SOLPENCO by comparing part of its outputs with observations, for the large isolated SEP events measured at 1.0 AU at different energies between ~ 0.1 MeV and ~ 96 MeV, in the period from January 1998 to October 2001. We have made a comparative analysis of the values of the maximum proton differential flux intensity regarding three factors: the initial speed of the shock, the heliolongitude of the parent solar event and the energy dependence.

For the analyzed central meridian events, the peak fluxes and the time of their occurrence are well predicted by SOLPENCO at low energies (< 2.0 MeV). Predictions are still valid at high energies (> 2.0 MeV) for the events that show a relatively poor contribution of the particle population accelerated when the shock was still close to the Sun (i.e. slow shocks and/or not magnetically well connected events). For western events, the predictions of the peak flux magnitude for $E < 2.0$ MeV are correct but the occurrence of the peak flux is not well predicted for $E > 0.5$ MeV.

For western and central meridian events with a strong prompt phase, the present version of SOLPENCO is not able to predict the time and intensity of the peak flux for $E > 2.0$ MeV mainly because: (i) the initial conditions of the MHD code are placed above the region where the bulk part of the high-energy particle injection is assumed to take place, and (ii) the adopted value of k has been derived from modeling actual SEP events at low energies.

In short, the conclusion is that in order to improve the predictions at high energies it is necessary to use an MHD code with initial shock conditions closer to the Sun as well as different values of k in the Q(VR) relation.

9. We have simulated both the propagation of the interplanetary shock and the intensity-time profiles of the major SEP event on 6 March 1989 observed by both IMP-8 (orbiting the Earth) by Phobos-2 (orbiting Mars). This event was associated with one of the most intense X-ray flares of solar cycle 22. By assuming that the Q(VR) relation derived from the simulation of the SEP event at IMP-8 is also applicable to the region of the shock front scanned by the cobpoint of Phobos-2, we have predicted the proton flux observed by Phobos-2. This is the first time that this type of analysis is performed.

   The comparison between predicted, modeled and measured profiles at Mars leads to the conclusion that the Q(VR) relation performs well in forecasting the peak flux and the upstream fluence. We have discussed the limitations of our model and the set of Sun-Earth-Mars scenarios where the model can provide predictions of SEP flux profiles.

   Nevertheless, we can not draw a general conclusion about the validity of the Q(VR) relation because of the singularity of this SEP event. At present, there is no other model able to forecast proton flux profiles of SEP events at Mars from another SEP event observed at Earth.

9.2 Future perspectives

There are important open issues about shocks, particles, CMEs as well as their propagation and acceleration in interplanetary space. Several of these issues have been already tackled in this study and the others will be undertaken in an immediate future:

1. Study and simulation of a large number of SEP events.
2. Application of both the shock-and-particle model and SOLPENCO to multi-spacecraft observations.
3. Research of improved interplanetary models, where the evolution of the coronal/interplanetary shock closer to the Sun can be taken into account.
4. Improvement of the algorithms used to determine numerically the position of the shock front and the plasma parameters at the cobpoint.
5. Extension of the shock-and-particle model to a 3D scenario.
6. Calculation of the flux profiles in the downstream region of a shock for space weather purposes.
7. Analysis of particle flux observations as function of the energy in order to determine (wherever is possible) the energy dependence of the flux as a function of the longitude of the parent solar event.
8. Implementation of the heavy ion population evolution in our code.
9. Modeling the variation of the SEP event fluence and peak flux as a function of both the longitudinal and the radial heliocentric distances.

Items 1 and 2 are needed in order to strengthen the plausibility and reliability of the Shock-and-Particle model (in fact of any model) and to provide more cases to support and discuss (and whenever possible to extend) the Q(VR) relation[1].

Items 3 and 4 are necessary to produce an improved version of SOLPENCO. Since September 2006 we are working on this objective in the context of a two-years ESA contract, integrated in an international consortium formed by research groups

[1] Although SOLPENCO is the only existing model that can produce quantitative predictions (good enough or not, more or less limited), this is a key point; see for example the comment about SOLPENCO in the U.S National Research Council SRH06 report, p. 47 'Models for Coronal Mass Ejections and Flares and for Solar Energetic Particles'.

of the K.U. Leuven, the University of Southampton, the Belgian Institute for Space Aeronomy (BIRA), the enterprise QinetiQ, and our STP/SW group (University of Barcelona). Our specific objective, in close collaboration with K.U. Leuven group, is to build SOLPENCO2. SOLPENCO2 is the core of the 'Solar Energetic Particle Environment Modelling' (SEPEM) project (http://www.oma.be/SEPEM/) in the sense that it will be used to derive non 1.0 AU SEP event predictions.

Overall SEPEM objectives are multiple. (i) We will create standardized (with community consensus) and easily updating tools that will produce new types of space weather products, for example, including peak flux statistics, durations of high or arbitrary flux periods, and corresponding error and uncertainty estimates. (ii) We will take advantage of new data to re-consider recent advances in understanding the generation mechanisms of SEP events. (iii) We will integrate data bases of ion species into tools for the analysis of SEP events. And (iv) we will examine the limited available data collected out of 1.0 AU and improve the models to predict the event time profiles at non-Earth locations (e.g. near-Sun, Mercury, Venus, Mars,...) and thus avoid potentially over-severe environment specifications. Large part of these objectives has been already discussed in this dissertation. Recommendations formulated by the 'Helio-radial variations and Physical Modelling Group' during the roundtable about SEPEM project held at Southampton in February 2007, have been included (although not all of them) in the SEPEM project[2].

The updated version of SOLPENCO, SOLPENCO2, will have a data base of synthetic SEP flux and fluences that encompasses radial distances as close as 0.1 AU of the Sun and beyond the orbit of Mars (up to 1.7 AU). In this way, under the assumptions that define the shock-plus-particle model, we would be able to derive radial dependences for the flux and fluences and produce input for predictive statistical models. The grid of the database of SOLPENCO2 will be defined by seven variables (the six in SOLPENCO plus, most probably, a choice between slow or fast solar wind regimes). We will use a new MHD model (produced by the K.U. Leuven group) for the shock propagation, with the input pulse at $3\,R_\odot$ or $5\,R_\odot$. SOLPENCO2 data base will contain flux profiles for seven radial distances (from 0.1 to 1.7 AU); the range of heliolongitudes will also be larger than in SOLPENCO,

[2]They read: *'In the spirit of future improvements of the various modules of the model, we recommend the following improvements to SOLPENCO: (1) Extend the MHD and particle calculation close to the Sun (optimally back to $3\,R_\odot$); (2) include a simple calculation of the intensity downstream of the shock; and (3) include a spectral rollover at high energies in the shock injection.'*

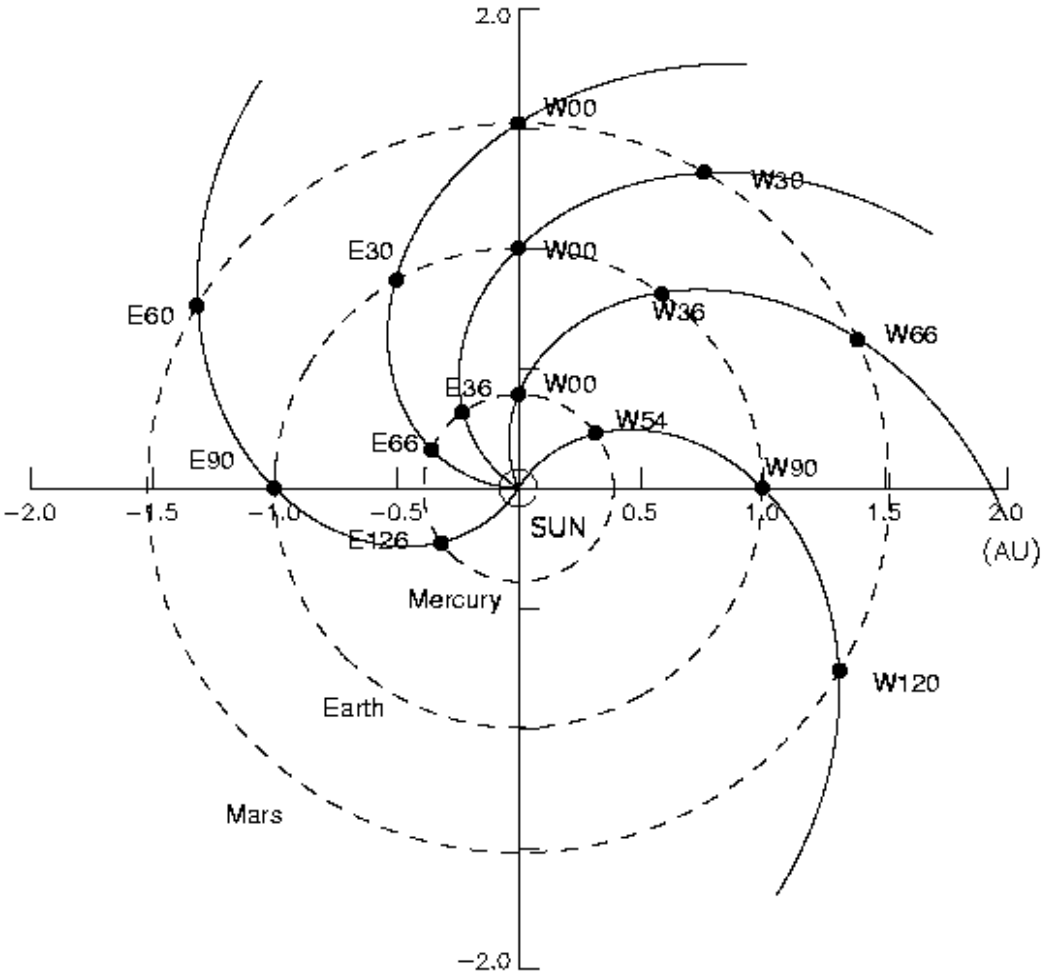

Figure 9.1: Magnetic field lines connecting spacecraft at different radial distances from the Sun (assuming a solar wind velocity of 400 km/s).

14 values from E60 to W120 for an observer at 1.0 AU, and similarly for other radial distances (see Figure 9.1). The energy range will consider 11 channels from 0.125 MeV to 128 MeV.

The range of applications of the study indicated in item 5 includes data from the Ulysses spacecraft and the future mission Solar Orbiter that envisages a spacecraft at 0.2 AU from the Sun and at 22° in heliolatitude. The full 3D picture of the propagation shock and the IMF will have to be taken into account.

Item 6 is not an easy task when the entire involved physical scenario is considered. But, for space weather purposes, a simple physical hypothesis (such the assumption that the population of the tube is only affected by adiabatic cooling) would probably provide a rough description of the flux profiles in this region, useful enough for evaluating the contribution of the downstream region to the time integrated fluence of the event[3] .

Items 7, 8 and 9 are important too to improve particle models and, hence, physics-based predictive codes. But it is a matter of time, human resources and opportunity to cope with (and afford) them in an immediate future.

Finally, we would like to comment that the starting era of the STEREO mission is interesting because it will be possible to perform again (after the Helios-1 and -2 era) multi-spacecraft analysis of SEP events in a systematic way. However, STEREO will not be able to give insights into the variation of SEP events with the heliocentric distance. To estimate these variations, physics-based models and tools such as the shock-and-particle model and SOLPENCO are needed. We need fresh data from the generation of spacecraft that will explore the interplanetary space at distances other than 1.0 AU, and for periods of time large enough to produce significant enough data records. Among these new missions we include the Inner Heliospheric (and near-Earth) Sentinels, the Solar Dynamic Orbiter, the Solar Orbiter (if finally approved), the Solar Probe and the KuaFu-A (if finally approved).

[3]However, the changing magnetic connection between observer and shock, as well as the possibility that the shock still injects particles into the downstream region, complicates the scenario and its implementation into the code.

A Differential flux and anisotropy

A.1 Transformation of units (from Lario 1997)

The function $F(t, \mu, r, p)$ for a given momentum p_0, time t_0, and radial distance r_0, can be expressed in terms of orthogonal Legendre functions as

$$F(t_0, \mu, r_0, p_0) = \sum_{i=0}^{\infty} A_{i0} P_i(\mu) = A_0 + A_{10}\mu + A_{20}\frac{1}{2}(2\mu^2 - 1) + \cdots \tag{A.1}$$

The isotropic part of the μ–distribution is given by A_0

$$A_0 = \frac{1}{2}\int_{-1}^{+1} F(t_0, \mu, r_0, p_0) d\mu \tag{A.2}$$

which is proportional to the omnidirectional intensity defined by

$$I(t_0, r_0, p_0) = \frac{1}{2}\int_{-1}^{+1} f(t_0, \mu, r_0, p_0) d\mu\,, \tag{A.3}$$

where $f(t, \mu, r, p)$ is the particle distribution function in the phase space. The proportional constant between A_0 and I is determined by the cross-sectional area of the flux tube at r_0. Although the omnidirectional intensity and the function $F(t, \mu, r, p)$ are suitable for a theoretical interpretation of the behavior of the energetic particles,

it is measured only indirectly. The measurements used in this work provide the differential directional flux of particles within a range of solid angles Ω, and within an energy band of width ΔE around E, where E is the kinetic energy of the particles. Representing this flux as $J(t, r, E)$ we have

$$J(t_0, r_0, E_0) = p_0^2 \, I(t_0, r_0, p_0) \tag{A.4}$$

and its units are $\left[\frac{\text{particles}}{\text{energy sr time area}}\right]$.

For a given momentum p_0, the only difference between the omnidirectional intensity and the differential flux is a constant of proportionality, so when intensity and flux are given in arbitrary units, talking of flux or intensity is completely equivalent.

The anisotropy of the particle distribution in the solar wind frame parallel to the IMF, is defined as the quotient between the second and the first term of the Legendre polynomials expansion. That is,

$$\xi(t_0, r_0, p_0) = 3\frac{\int_{-1}^{+1} \mu F(t_0, \mu, r_0, p_0) d\mu}{\int_{-1}^{+1} F(t_0, \mu, r_0, p_0) d\mu} = \frac{A_{10}}{A_0} \tag{A.5}$$

which is equivalent to the anisotropy calculated from the observations of the DFH on-board ISEE-3 spacecraft (see Sanderson et al., 1985a), and to the anisotropy calculated from the observations of other detectors.

In order to compare the results of the model with the observations, it is necessary to convert them into differential flux with its correct units. The model gives the temporal evolution of the isotropic part of the $\mu-$distribution of $F(t, \mu, r, p)$, i.e.,

$$\mathcal{R}^{arbi}(t, r_0, p_0) = \frac{1}{2}\int_{-1}^{+1} F(t_0, \mu, r_0, p_0) d\mu \tag{A.6}$$

for a given momentum p_0, and at the observer position r_0. $\mathcal{R}^{arbi}(t, r_0, p_0)$ is expressed in arbitrary units, therefore it is necessary to normalize it to the observed values. Let $J^{arbi}(t, r_0, p_0)$ be the differential flux, in arbitrary units, corresponding to $\mathcal{R}^{arbi}(t, r_0, p_0)$, i.e.,

$$J^{arbi}(t, r_0, p_0) = p_0^2 \, \mathcal{R}^{arbi}(t, r_0, p_0)/A(r_0) \tag{A.7}$$

where $A(r_0)$ is the cross sectional area of the IMF flux tube at r_0. The normalization lies in the translation from arbitrary units to physical units

$$J(t, r_0, p_0) = K(r_0, p_0) \, J^{arbi}(t, r_0, p_0) \tag{A.8}$$

$K(r_0, p_0)$ is the constant of normalization, which is chosen as

$$K(r_0, p_0) = \frac{J(t_1, r_0, p_0)}{J^{arbi}(t_1, r_0, p_0)} \tag{A.9}$$

where $J(t_1, r_0, p_0)$ is the differential flux observed at t_1 and $J^{arbi}(t_1, r_0, p_0)$ is the differential flux derived from the model at t_1. It is required that t_1 is within a period of time during which the flux does not oscillate sharply. Note that $K(r_0, p_0)$ is different for each energy considered.

Assuming that the constant of normalization is the same at any distance, it is possible to translate the values of the isotropic part, $G_0^{arbi}(t, r, p)$, of the term $G(t, \mu, r, p)$, to the isotropic part, $Q_0(t, r, p)$, of the injection rate of shock-accelerated particles $Q(t, \mu, r, p)$ in physical units,

$$Q_0(t, r, p) = K(r_0, p_0) \, G_0^{arbi}(t, r, p)/A(r) \tag{A.10}$$

where $A(r)$ is the cross sectional area of the IMF flux tube at the radial distance r. Using equations A.9 and A.7, equation A.10 becomes

$$Q_0(t, r, p_0) = \frac{J(t_1, r_0, p_0)}{p_0^2 \, \mathcal{R}^{arbi}(t_1, r_0, p_0)} \, \frac{A(r_0)}{A(r)} \, G_0^{arbi}(t, r, p_0) \tag{A.11}$$

The radial distance r indicates the position where shock-accelerated particles are injected, which is given by the MHD simulation of the shock propagation.

A.2 Observations

A.2.1 Proton anisotropies, from Heras et al. (1994)

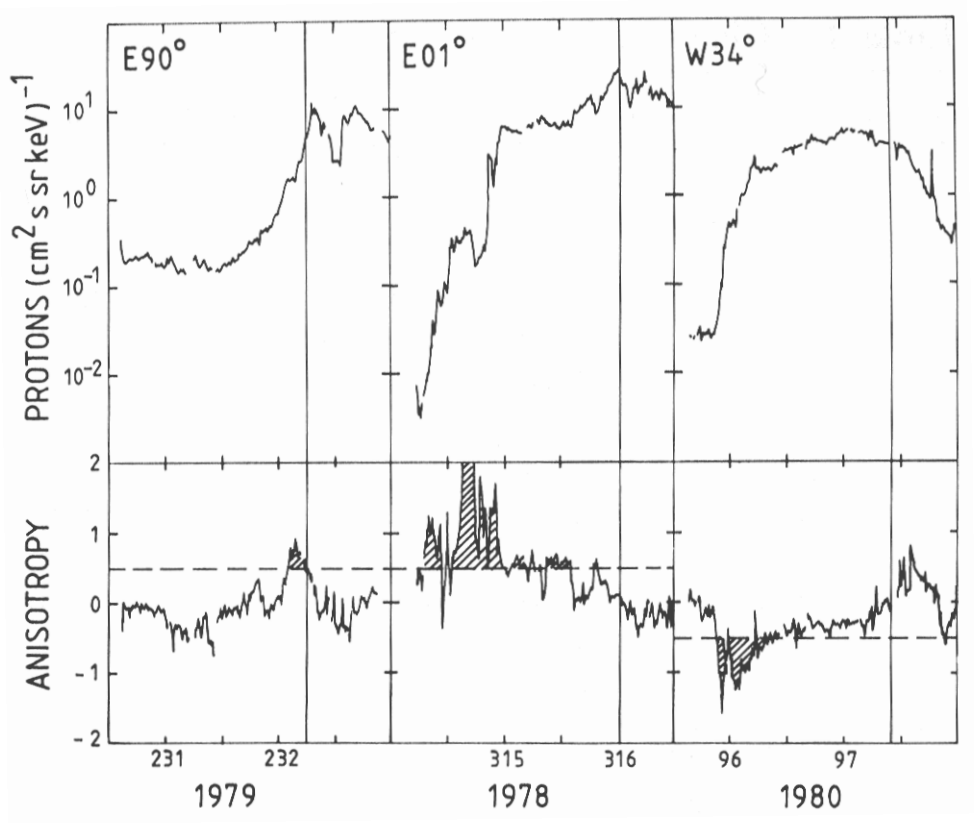

Figure A.1: Flux and anisotropy profiles of three events originated in the east, central meridian, and west solar hemisphere, respectively. The vertical line indicates the passage of the shock; the time during which the anisotropy is greater than 0.5 is represented by a striped pattern.

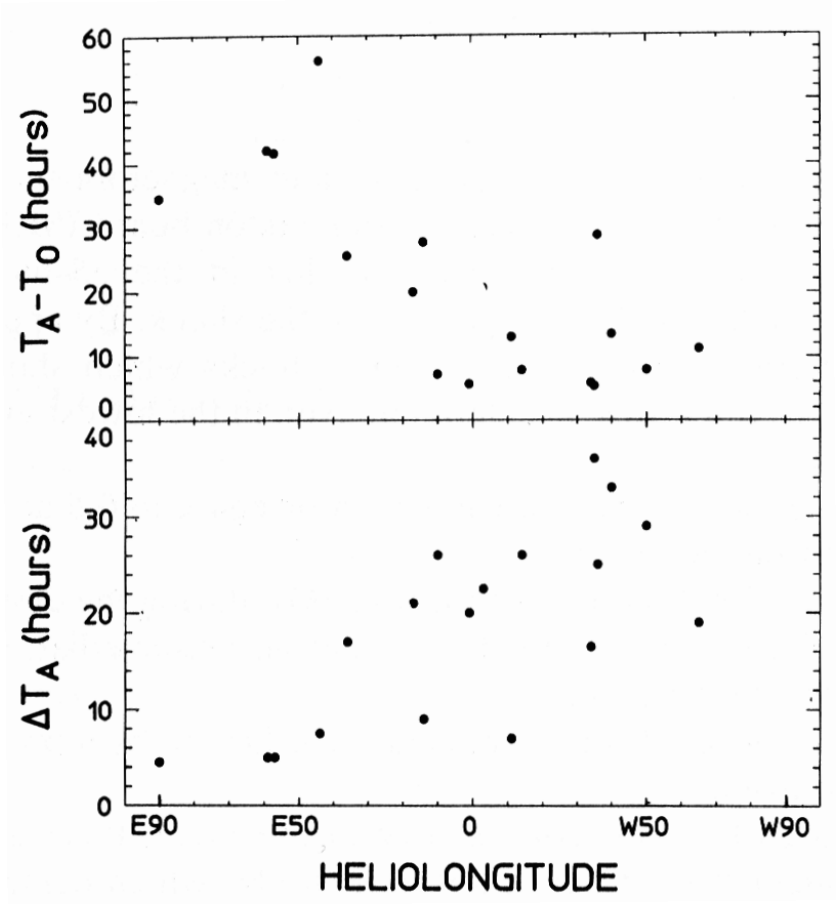

Figure A.2: Two anisotropy parameters calculated for each event as a function of the solar source heliolongitude. Top: delay between the occurrence of the solar parent activity and the large-anisotropy onset. Bottom: interval of time during which the particle anisotropy is greater than or equal to 0.5.

A.2.2 Proton anisotropies, from Heras et al. (1995)

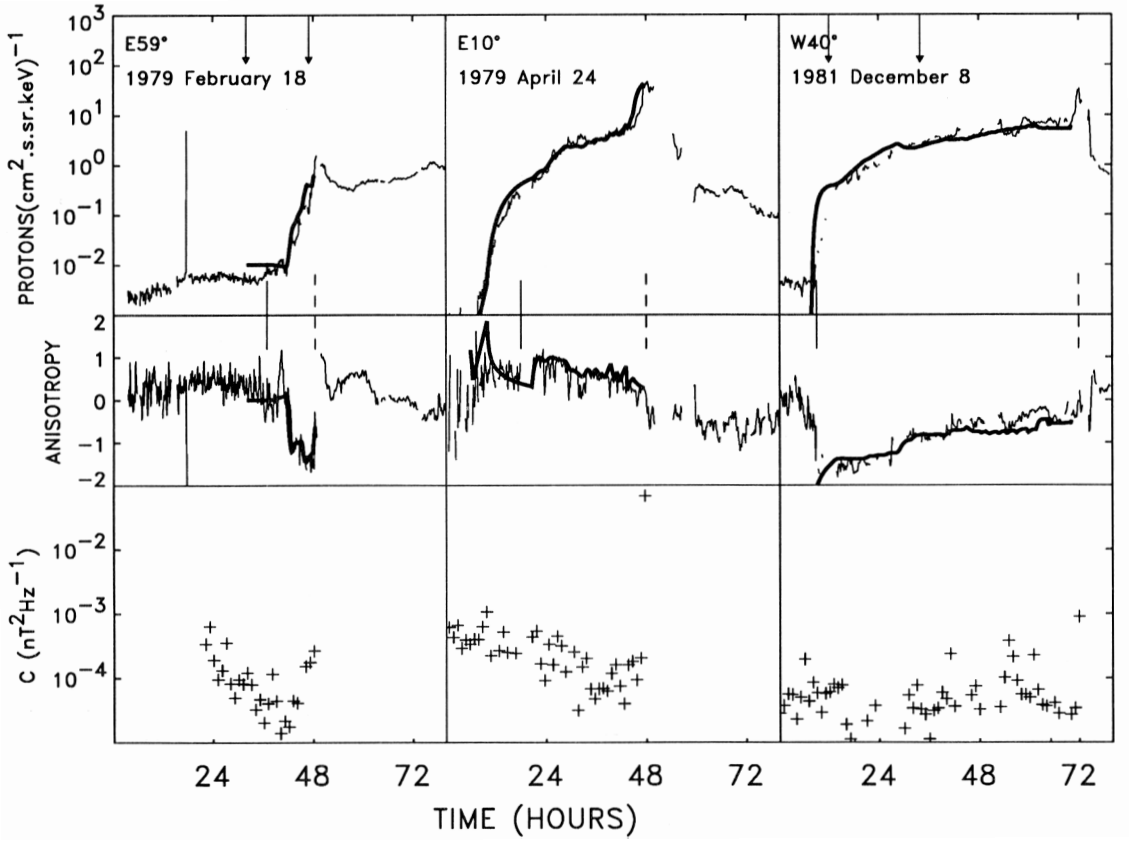

Figure A.3: Upper and middle panels: flux and anisotropy observations at 620 - 1000 keV (thin lines) and the corresponding fits obtained with the model (thick lines) for the three selected events. The solid vertical lines indicate the initial time of the connection between the shock and the observer, and the dashed vertical lines the passage of the respective shocks at ISEE-3. Lower panel: magnetic field spectral density at 1 Hz. The origin of time is set at the occurrence of the solar parent activity.

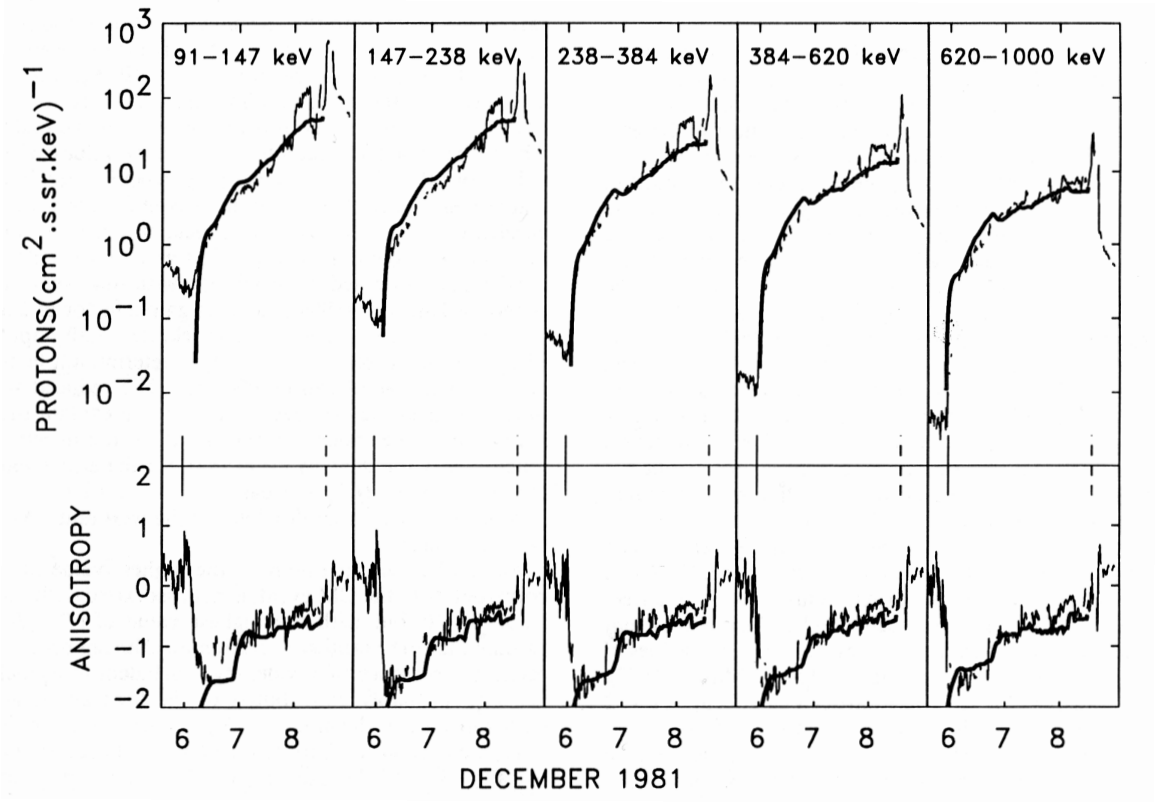

Figure A.4: Observed flux and anisotropy profiles during the West event of December 1981 at five energy channels (thin lines), and the corresponding fits derived from the model (thick lines). The solid vertical line indicates the initial time of connection between the shock and the observer, and the dashed vertical line the time of the shock passage at ISEE 3. The origin of time is set at the occurrence of the solar parent activity.

B Lario et al. (1998) paper. [Lar98]

THE ASTROPHYSICAL JOURNAL, 509:415–434, 1998 December 10

ENERGETIC PARTICLE EVENTS: EFFICIENCY OF INTERPLANETARY SHOCKS AS 50 keV < E < 100 MeV PROTON ACCELERATORS

D. LARIO[1] AND B. SANAHUJA[2]
Departament d'Astronomia i Meteorologia, Universitat de Barcelona, Avinguda Diagonal 647, 08028 Barcelona, Spain
AND
A. M. HERAS
ESA Space Science Department, VILSPA, ESA Satellite Tracking Station, P.O. Box 50727, Villafranca del Castillo, E-28080 Madrid, Spain
Received 1997 February 21; accepted 1998 July 16

ABSTRACT

We have studied the injection rate of shock-accelerated protons in long-lasting particle events by tracing back the magnetohydrodynamic conditions at the shock under which protons are accelerated. This tracing back is carried out by fitting the observed flux and anisotropy profiles at different energies, considering the magnetic connection between the shock and the observer, and modeling the propagation of the shock and of the particles along the interplanetary magnetic field. A focused-diffusion transport equation that includes the effects of adiabatic deceleration and solar wind convection has been used to model the evolution of the particle population. The mean free path and the injection rate have been derived by requiring consistency with the observed flux and anisotropy profiles for different energies, in the upstream region of the events. We have extended the energy range of previous models down to 50 keV and up to ~100 MeV. We have analyzed four proton events, representative of west, central meridian, and east scenarios. The spectra of the injection rate of shock-accelerated protons derived for these events show that for energies higher than 2 MeV the shock becomes a less efficient proton accelerator. We have related the derived injection rates to the evolution of the strength of the shock, particularly to the normalized downstream-upstream velocity ratio (VR), the magnetic field ratio, and the angle θ_{Bn}. As a result, we have derived an empirical relation of the injection rate with respect to the normalized velocity ratio (log $Q \propto$ VR), but we have not succeeded with the other two parameters. The Q(VR) relation allows us to determine the injection rate of shock-accelerated particles along the shock front and throughout its dynamical expansion, reproducing multispacecraft observations for one of the simulated events. This relation allows us to analyze the influence of the corotation effect on the modeled particle flux and anisotropy profiles.

Subject headings: acceleration of particles — interplanetary medium — MHD — shock waves — Sun: particle emission

1. INTRODUCTION

Modeling energetic proton events associated with interplanetary shocks requires two basic components: a suitable description of the propagation of protons through the interplanetary medium and an adequate simulation of the evolution of the interplanetary shock where protons are accelerated. Heras et al. (1992, 1995; hereafter He92 and He95, respectively) have developed a quantitative model that accounts for the main features of these events in the upstream region of the shock. This model is based on the concept of the "cobpoint" (Connecting with the OBserver point), the point at the front of the shock that connects with the observer through the IMF (interplanetary magnetic field) lines; the model has two basic parameters: the mean free path of the protons, $\lambda_{\parallel}$, and the injection rate of shock-accelerated protons into the interplanetary medium, $Q(r, t)$. From the fitting of the observed flux and first-order anisotropy profiles, for a fixed energy, it is possible to determine Q and $\lambda_{\parallel}$, as well as their evolution until the shock passes the spacecraft. Specifically, it allows us to relate the evolution of Q, for energies between ~200 keV and 1.5 MeV, to the evolution of various physical parameters at the shock front. Hereafter, we will use the terms "proton" or "particle" indistinctly, and unless otherwise indicated, "high-energy" will mean $E \gtrsim 2$ MeV.

The transport equation used by He92 and He95 to describe the propagation of energetic protons along the IMF is the focused-diffusion equation derived by Roelof (1969). The diffusion-convection approximation (Parker 1965) is not applicable to the description of large particle events associated with strong interplanetary shocks, because these often show high anisotropies in the upstream region, not only at the onset but also for many hours before the shock passage. These high anisotropies imply that protons are injected continuously into the interplanetary medium after being accelerated at the shock (Heras et al. 1994 and references therein). The injection rate is described

[1] Now at the Space Science Department of ESA, ESTEC, P.O. Box 299, 2200 AG Noordwijk, The Netherlands.
[2] Also at the Institut d'Estudis Espacials de Catalunya. Gran Capità 2, Nexus-201, 08034-Barcelona, Spain.

in the model by adding a source term to the transport equation, the function Q mentioned above. Q is identified with the "efficiency" of the shock as a particle accelerator, which comprises the effectiveness of the shock in accelerating protons plus the efficiency of injecting these protons into the interplanetary medium. The injection factor depends on the conditions around the shock; for example, the presence of a turbulent wavy region upstream of the shock or a large background of protons acting as a seed population. The model uses a magnetohydrodynamic (MHD) code to simulate the expansion and propagation of interplanetary shocks, up to 1.1 AU, triggered by solar activity (i.e., Dryer 1994). The evolution of the injection rate Q can be analyzed as a function of the MHD conditions at the shock front and as a function of the assumptions considered by the MHD code to describe the interplanetary shock.

It is generally accepted that interplanetary shocks accelerate particles more efficiently at low than at high energies (Forman & Webb 1985 give a comprehensive review of the acceleration of energetic particles). It is quite usual to see a small peak, if any, on the 1 MeV proton flux at the shock passage, while a jump from 1 to 3 orders of magnitude is observed in the flux at 50 keV. One basic limitation of the focused-diffusion equation used in He92 and He95 is that it does not take into account the effects of adiabatic deceleration or convection by the solar wind; these effects may be important below 800 keV. If, for example, the injection rate at 100 keV is derived by means of this equation, substantial uncertainty is introduced in the values of Q found, because it might include arbitrarily positive (high-energy) or negative (low-energy) contributions due to adiabatic deceleration. A similar discussion involving $\lambda_{\|}$ is given by Ruffolo (1995, hereafter Ru95). Solar wind convection may also have an important influence in determining the onset of an event and the occurrence of the maximum of flux, especially at low energies. For that reason, the focused-diffusion equation should be used judiciously below 500 keV. Ru95 has developed an explicit formula for the focused-diffusion transport of solar cosmic rays, including adiabatic deceleration and solar wind convection effects (a first-order approximation). This equation is more appropriate for describing the transport of low-energy particles than the Roelof (1969) approximation; with it, Ru95 models the transport of solar flare protons (from a fixed source, the Sun). For particle events associated with interplanetary shocks, however, it is necessary to assume that the source of accelerated particles is moving jointly with the shock, which demands a different approach for the numerical resolution of the transport equation.

The acceleration of low-energy protons is reasonably well understood in terms of either shock drift acceleration or diffusive shock acceleration (with MHD turbulence). Nevertheless, how these processes work above a few MeV is not clear, since it is expected that the efficiency of the shock decreases rapidly with the energy (e.g., Kallenrode 1996 and references therein). Since the He92 model can evaluate this efficiency, it is worth extending the range of applicability of the model in order to analyze what happens at such high energies. Furthermore, based on these results, Lario et al. (1995b) suggest that the large-scale features of the flux and anisotropy profiles for different events can be easily adjusted, assuming a reasonable functional dependence of the injection rate at the cobpoint. Consequently, we have developed a model that allows us to extend the range of applicability to energies between 50 keV and 100 MeV, with a more reduced set of parameters.

The observed flux and anisotropy profiles of energetic particle events depend on both how efficiently protons are accelerated, and how the IMF irregularities modulate this population during its journey. Lario, Sanahuja, & Heras (1995a) show examples of particle flux profiles that can be adjusted in different ways if only one of those aspects is considered. Moreover, the efficiency of the acceleration depends on the MHD strength of the shock at the cobpoint. This strength could either diminish, because of the shock expansion in the interplanetary medium (or because the cobpoint slides clockwise to the right wing of the shock), or increase, when the cobpoint moves from the left wing to the central region of the shock. It is then possible that a region of the shock could accelerate protons up to 20 MeV at 0.1 AU, but only to 500 keV when it reaches 1 AU. This scenario for particle acceleration at the shock and their further propagation upstream has already been qualitatively depicted using statistical studies and multispacecraft analysis of specific events (e.g., Cane, Reames, & von Rosenvinge 1988; Domingo, Sanahuja, & Heras 1989; Reames, Barbier, & Ng 1996). Although there is an extended consensus about it, the details of how the MHD conditions at the front of the shock translate into an "efficiency" in particle acceleration, and of how it evolves as the shock expands, are neither completely clear nor quantified as yet. Therefore, we would like to focus on an analysis of the efficiency of the shock as an accelerator of protons, $Q(r, t)$. The other main parameter of the model, the mean free path, is tuned to fit the observations and theoretical predictions, but the values obtained will not be discussed in detail. We refer to other studies on the influence of $\lambda_{\|}$ on the interplanetary transport of protons (e.g., Beeck et al. 1990). Our aim is to deconvolve the effects of particle transport on the flux, in order to derive the efficiency of the shock as an injector of protons into the interplanetary medium.

Kallenrode & Wibberenz (1997) have extended a model formerly used to analyze solar particle events (see, for example, Beeck & Wibberenz 1986 and references therein) to describe the influence of the shock as a moving accelerator of particles. The physical basis of this model is the same as in He92 and He95, since they use Roelof's transport equation to describe particle propagation, and include a source term for particles moving along the IMF line; furthermore, this source term is derived by fitting the flux profile independently at each energy. The main differences are the handy separation of the source term in two contributions, radial and azimuthal along the shock front, the assumption that particles propagate downstream spiraling in an Archimedian IMF, and the assumption that the shock can be represented by a segment of a circle propagating at a constant speed, which allows the unhindered motion of the particles across it. There is also an arbitrary parameter (r_{start}) used to fix the connecting time of the observer with the shock front when high-energy particles arrive with too much delay. Nevertheless, the shock does not evolve at constant velocity, and its central part does not propagate at the same speed as the wings; the IMF downstream of the shock cannot be represented by an Archimedian spiral, and particles cannot propagate freely across the shock, especially at low energy. This model cannot be adequately applied to low energies, since the particle transport equa-

tion does not take into account adiabatic deceleration and solar wind convection.

The main justification for the set of assumptions made by Kallenrode & Wibberenz (1997) is the result of the statistical study of 44 particle events (Kallenrode 1997a), and individual analysis of several of these events (Kallenrode 1997b). This statistical study cannot yield clear quantitative conclusions about the injection rate, its energy spectrum, or its evolution. The most probable reasons for this are that (1) shock-accelerated particles come from different regions along the front of the shock, showing different MHD conditions due to shock expansion that this model ignores; (2) statistical analysis is not able to cancel out the specificity of each event; and (3) the source term cannot always be unequivocally described by a combination of radial and azimuthal dependence, as stated by Kallenrode (1997b). On the other hand, the evolution of the injection rate derived for a large portion of the events presented by Kallenrode (1997b) should be taken with caution, because many of the fits performed for the flux and anisotropy profiles display large discrepancies (more than 1 order of magnitude) with observations, for long periods (i.e., Figs. 1, 5, or 8 of that paper). There is also no discussion or justification of how these discrepancies affect the injection rate derived and its evolution.

The improvements now included in the transport equation over that of He95 allow us to reduce the parameters of the model and to improve the description of particle propagation. We also propose a different way to relate the evolution of the injection rate of shock-accelerated particles to the dynamic properties of the shock. The new model yields a quantification of the injection rate, its energy spectrum, and its evolution. We will discuss the assumptions of the model and the influence of the shock modeling on the results. We will proceed as follows: in § 2 we briefly describe the new numerical procedure for solving the transport equation, how we proceed to derive the injection rate of shock-accelerated particles from the fitting of flux and anisotropy profiles, and the role of the shock front as a source of particles. In § 3 we briefly review the observational features of the four particle events to be modeled. In § 4 we present the fits performed for these events and discuss the mean features of the injection rate and of its energy spectrum derived from those fittings. In § 5 we relate the evolution of the injection rate to the strength of the shock. We discuss this dependence and other aspects of the depicted scenario that could make the interpretation of these results or their comparison with the observations difficult. We also discuss the influence of corotation. Finally, in § 6 we present the conclusions of the paper.

2. THE NUMERICAL MODEL

2.1. *Propagation of Particles*

Our goal is to study the evolution of the injection rate of protons accelerated at the front of interplanetary shocks, for a wide range of energies from 50 keV to 100 MeV. Shock-accelerated particles are considered to propagate in a magnetic flux tube from the shock front up to the observer. Their transport is modulated by the characteristics of the IMF and of the solar wind, which have different effects depending on the energy of the particles. We describe particle propagation by means of the following transport equation (Ru95), written in mixed coordinates:

$$\frac{\partial F(t,\mu,r,p)}{\partial t} = -\cos\psi\,\frac{\partial}{\partial r}\times\left\{\left[v\mu+\left(1-\mu^2\frac{v^2}{c^2}\right)v_{sw}\sec\psi\right]F(t,\mu,r,p)\right\}$$
$$-\frac{\partial}{\partial\mu}\left\{\left[\frac{v}{2L(r)}\left(1+\mu\frac{v_{sw}}{v}\sec\psi-\mu\frac{v_{sw}v}{c^2}\sec\psi\right)+v_{sw}\left(\cos\psi\frac{d}{dr}\sec\psi\right)\mu\right](1-\mu^2)F(t,\mu,r,p)\right\}$$
$$+\frac{\partial}{\partial\mu}\left\{D_{\mu\mu}\frac{\partial}{\partial\mu}\left[\left(1-\mu\frac{v_{sw}v}{c^2}\sec\psi\right)F(t,\mu,r,p)\right]\right\}$$
$$+\frac{\partial}{\partial p}\left\{pv_{sw}\left[\frac{\sec\psi}{2L(r)}(1-\mu^2)+\cos\psi\frac{d}{dr}(\sec\psi)\mu^2\right]\times F(t,\mu,r,p)\right\}+G(t,\mu,r,p)\,, \quad (1)$$

where p denotes the particle momentum, μ is the cosine of the pitch angle, v is the velocity of the particles, r is the heliocentric distance, t the time, ψ is the angle between the radial direction and the magnetic field $\boldsymbol{B}$, L is the focusing length, $D_{\mu\mu}$ is the diffusion coefficient in μ-space, and v_{sw} is the radial solar wind velocity relative to a fixed frame. The particle phase-space distribution function, f, is related to the distribution function of protons inside the flux tube, F, by $F(t, \mu, r, p) = A(r)f(t, \mu, r, p)$ (Ng & Wong 1979), where $A(r)$ is the cross-sectional area of the magnetic flux tube. G represents a local source of protons, directly related to the injection rate of protons in the phase-space, Q, by $G(r, t) = A(r)Q(r, t)$, with $A(r)$ estimated at the point where the injection of protons is occurring.

The coordinates p, v, and μ refer to the local solar wind frame comoving with the inhomogeneities of the IMF, while z, r, and t refer to a frame fixed at the Sun. The first term on the right-hand side of equation (1) represents the streaming and convection, and the second term is the usual expression for adiabatic focusing. The third term represents the pitch-angle scattering, and the fourth term represents the adiabatic deceleration. The two main differences between equation (1) and equation (11) of Ru95 are the inclusion of the source term $G(t, \mu, r, p)$, which gives the injection of protons at the cobpoint, and the use of the r coordinate instead of the distance z along the magnetic field line ($dr = dz \cos\psi$). The use of the radial coordinate is forced because the MHD simulation provides the radial position of the shock and the structure of the IMF lines with its own r-grid. Using r instead of z allows us to couple the grid of the MHD simulation for the shock propagation and the grid used to solve equation (1).

Assuming a Parker field, we have $L = r/\cos\psi(1+\cos^2\psi)$, $\tan\psi = \Omega r/v_{sw}$, and $A = A(r_0)r^2/(1+\tan^2\psi)^{1/2}$, where Ω is the angular velocity of the solar rotation and r_0 is a given radial distance. For other magnetic field configurations, these equations would require more complicated expressions; in fact, they would require a complex numerical description. Therefore, this approximation can only be applied when the upstream solar wind is not highly perturbed.

To describe the interaction between energetic particles and IMF irregularities, we adopt the approximation of

pitch-angle scattering. For the pitch-angle diffusion coefficient we use the standard model (Jokipii 1971), $D_{\mu\mu} = \mathscr{A}|\mu|^{q-1}(1-\mu^2)$. $\mathscr{A}$ is a constant that depends on the particle charge, mass, and velocity, and on the level of the IMF fluctuations, and q is the spectral index of the field power spectrum. Following the quasi-linear theory (QLT) approximation (Jokipii 1966), we take $\mathscr{A} = 3v/2\lambda_{\parallel}(4-q)(2-q)$, and for consistency we assume for $\lambda_{\parallel}$ a dependence on the rigidity, $\lambda_{\parallel} \propto R^{2-q}$ (Hasselmann & Wibberenz 1970). For each event, the value of q is derived from *ISEE 3* IMF data; a frequently quoted value is $q = 1.6$ (Kunow et al. 1991). This approximation might be subject to correction or improvement, but this would have little influence on the fit performed to the particle flux and anisotropy profiles. Several corrections have recently been suggested. For example, Ng & Reames (1995) suggest an extended QLT that takes into account the distribution of the medium-scale background magnetic field, eliminating the resonance gap for very low energy protons (<25 keV) at pitch angles around 90°. Since our lowest energy channel considered is above 25 keV and our numerical scheme does not evaluate the coefficient $D_{\mu\mu}$ at $\mu = 0$, we do not consider this extension. Bieber, Wanner, & Matthaeus (1996) show that the turbulence regime observed in the IMF is a composite of the slab turbulence and the two-dimensional turbulence; this second component contributes to the level of turbulence measured, but it does not contribute to resonant scattering of the particles. This is an important result, but we have not included this variable in our modeling because possible changes in q have small influence on the anisotropy derived, and thus on the mean free path (see, e.g., Fig. 5 of He92). Furthermore, the ratio between those components of the turbulence can largely change between different events (Bieber et al. 1996). In our model, this variable would simply be an extra parameter, without leading to any significant real improvement in the results.

The transport equation (1) is solved by applying a time-splitting method that separates this equation into four one-dimensional equations (Lario 1997 describes the numerical procedure in detail). The grid of integration extends in time, space, pitch angle, and momentum, (t, μ, r, log p). This grid has absorbing outer and inner boundaries in radial distance (RE and RI, respectively); therefore, particles are allowed to flow out, but the influx is set to zero; that is, $F(t, \mu, r, p) = 0$ when $\mu \leq 0$ (at RI) and when $\mu \geq 0$ (at RE). The outer boundary is set $\gtrsim 3$ AU from the inner boundary, sufficiently far from the Sun and from the observer's position so that it has no effect on the distribution of particles. The four one-dimensional equations are solved using a number of finite-difference methods (first- and second-order, centered/not centered, and upwind/downwind schemes), depending on the characteristics of each equation at each time step. The procedure has been corrected for numerical diffusion by means of a weighted average of the flux computed by a lower order scheme and a higher order scheme (Zalesak 1979). Zalesak's technique of antidiffusion flux correction largely reduces the effects of numerical diffusion.

To compute the effect of adiabatic deceleration, it is necessary to interpolate the distribution function at two adjacent energies (see details in Ru95). Ru95 discusses two ways to compute this, depending on the physical situation: (1) interpolating at equal distance traveled by the particles, or (2) interpolating at a given time. In our case, the continuous injection of particles from the shock leads to the second possibility, since the distribution functions $F(t, \mu, r, p)$ at two different energies are more similar at a given time than at equal distance traveled. For the simulations shown in § 4, we have adopted a time step of 0.01 hr, an r-grid spacing of 0.01 AU, a μ-grid spacing equal to $\frac{1}{8}$, and a momentum step of 0.104 (p in MeV/c). To assess the method, we have tested the code under different conditions and in the diffusion limit. Lario, Sanahuja, & Heras (1997) give a brief description of the performed tests; a full explanation of them can be found in Lario (1997).

To fit the particle flux and anisotropy profiles observed by the spacecraft, it is assumed that the protons are injected from the cobpoint and propagate along the magnetic flux tube connecting the observer to the cobpoint. As the shock expands, the observer establishes magnetic connection to different regions of the shock front; therefore, the cobpoint slides along the shock front. The successive injections of particles from the cobpoint fill the magnetic flux tube where the observer is located. We consider that this flux tube is unique throughout the event; that is, the particles injected from the cobpoint as it moves along the shock front become part of the particle population within the same magnetic flux tube. The inclusion of different flux tubes filled with particles coming from different parts of the shock front and crossing the observer position will be considered in § 5.3.

The procedure for fitting the particle and anisotropy profiles is as follows. We fit particle flux and anisotropy profiles in the upstream region for one energy channel, usually at ~ 1 MeV. This yields the $\lambda_{\parallel}$ and G values for this energy, as well as their evolution. Then, assuming that the functional dependence of G on the energy is a power law ($G \propto E^{-\gamma}$), we use the spectral index γ to obtain the best fit for fluxes and anisotropies at lower energies. The injection rate Q is calculated through the dependence on $A(r)$ and the change to differential flux units. In all cases, the mean free path at different energies is directly given by the QLT dependence of $\lambda_{\parallel}$, provided that the value of q is known from the magnetic field observations. At high energy, each channel has been fitted independently, without assuming any energy dependence for G. In § 4 we will see that the spectral index at high energy must be greater than at low energy. Therefore, this model requires only four basic parameters to fit nine or ten energy channels between 100 keV and 100 MeV, while the number of free parameters is much higher when the profiles are adjusted independently for each energy channel modeled (as is usually done). It is worth pointing out that for some events (see discussion in § 4.2), a turbulent foreshock region is required in order to simultaneously fit particle flux and anisotropy profiles. This is represented by a region of a certain width in front of the shock, characterized by a mean free path ($\lambda_{\parallel c}$) smaller than the mean free path in the rest of the upstream medium. The significance of $\lambda_{\parallel c}$ is discussed in He92 and in Beeck & Sanderson (1989). This represents an additional parameter of the model necessary to simulate simultaneously particle and anisotropy profiles in some particle events.

The low-energy profiles ($\lesssim 1.5$ MeV) have been calculated using a momentum grid that corresponds to the geometric mean energy of each channel. At these energies, the channels are narrow enough that the geometric mean of the window gives a good description of the whole channel. Since the energy windows at high energy are considerably wider than at low energy, we have adopted a wider momentum spacing, also taking into consideration the geometric mean energy of each channel. This implies that the fit at high energy is less accurate than at low energy. This is a

source of uncertainty, because in a west event, for example, the fit to the flux for an energy channel extending from 4 to 57 MeV corresponds to a 15 MeV proton flux. Nevertheless, at the onset of the event, the profile is dominated by the faster 57 MeV protons, while later the 4 MeV protons shape the profile because they are more abundant. It is possible to use a finer grid of momenta, but this would require knowing, a priori, the energy spectrum of Q. An alternative is to postulate in advance an energy spectrum for this energy window, but the injection rate is very sensitive to such an assumption, and there is no way to determine how much more abundant the 4 MeV protons are with respect to the 57 MeV protons. We have preferred to fit the profiles at high energy independently, channel by channel; then the derived spectral index results from a simple fit of the points at high energy and at ~ 1 MeV independently.

2.2. *Evolution of the Shock*

The MHD model used for the shock propagation is the same as in He92. This model reproduces the plasma and magnetic field data supplied by the spacecraft, as well as the arrival time of the shock at different positions. It has been clearly and extensively laid out in the literature, with all its assumptions. We refer the reader to former studies (He92) for details of the procedure (see also Smith & Dryer 1990). Recently, this model has been compared to another numerical code (Vandas et al. 1997) and found to be in good agreement. This code gives a dynamical description of the propagation of an interplanetary shock between 18 $R_\odot$ and 220 $R_\odot$ from the Sun, the main uncertainties coming from the initial conditions taken at the inner boundary. Gopalswamy et al. (1998) suggest that the proxy used to specify the initial conditions of the input pulse (metric type II shock velocity) that drives the shock is not valid. Transient interplanetary shocks are driven by coronal mass ejections (CMEs) (Cane, Sheeley, & Howard 1987); however, the behavior of these shocks in the corona is different (or is thought to be different) from their behavior in the interplanetary medium (Cliver et al. 1995; Cane 1997). Since the transition of these shocks from the corona to the interplanetary medium is not clear, it is difficult to establish the initial conditions of a shock below 18 $R_\odot$. At this distance, we characterize the shock by a pulse of a certain width, velocity, and duration, where the Rankine-Hugoniot conditions are satisfied. What happens below this boundary remains masked to our model. The assumptions considered to initiate the simulation of the shock are the time of the injection (given by the time of the solar activity associated with the event plus the time spent by the shock to travel up to 18 $R_\odot$) and the direction of injection (given by the solar activity site). Plasma and magnetic field observations from the *ISEE 3*, *Helios 1*, or *Helios 2* spacecraft, depending on their location and the availability of the data, are used to secure adequate initial conditions for the shock propagation, reproducing the time of the shock arrival at the spacecraft and the plasma discontinuity values at the shock passage.

From the simulation of the propagation of the shock, we can estimate its MHD strength at each point of the front, and particularly at the cobpoint. We characterize this strength by the downstream/upstream normalized velocity ratio, $\mathrm{VR} = [V_r(d) - V_r(u)]/V_r(u)$, and the magnetic field ratio, $\mathrm{BR} = |\boldsymbol{B}(d)|/|\boldsymbol{B}(u)|$, where u and d stand for the values upstream and downstream of the front, respectively, measured in a frame fixed at the Sun. Another relevant variable is θ_{Bn}, the angle between the IMF upstream of the shock and the normal to the shock front. The evolution of VR, BR, and θ_{Bn} is followed once the magnetic connection with the observer is established at $t = t_c$ (t_c being the connecting time), up to the passage of the shock by the observer's position. The determination of the shock parameters at the wings or when the shock is weak (i.e., when BR $\simeq 1$ or VR is small) has been improved over former works (He95). In these situations, it is not easy to identify the zones in which the variables should be evaluated, because of the small jump on plasma parameters that the shock represents. The upstream zone has been located at the radial positions where plasma values start to increase from the background, while the downstream region has been located at the point where plasma values stop increasing (see Lario 1997 for details). The identification of the limits of the shock and its effects on particle population are not easy to define. The interaction of a particle with a plasma discontinuity depends on the energy of the particle. As a consequence, it is possible that a shock could efficiently accelerate low-energy particles at its wings while becoming an inefficient accelerator at high energy. Or, a low-energy particle could "see" a discontinuity on the plasma and magnetic field as a shock, while a high-energy particle will "see" just a small irregularity. In these conditions, the evolution of the cobpoint that this dynamical model yields (i.e., where the wings could deform or slow down) has more physical significance than an evolution derived solely by assuming a half-circumferential shock propagating at the mean transit speed, with ad hoc locations for the starting and ending injection of particles, and is, physically, much better than any description based on cartoons.

3. OBSERVATIONAL FEATURES OF THE EVENTS

We have applied the model to four intense particle events detected by *ISEE 3*. Three of them have already been modeled (He95), but now the energy range explored has been extended down to ~ 50 keV and up to ~ 100 MeV (the precise values depending on the observational data available). More important, the fitting will directly yield the energy spectra of the injection rate of shock-accelerated particles. In this way, we can compare the results obtained with those derived for the 0.1–1 MeV range. The fourth particle event is associated with an interplanetary shock observed by the *ISEE 3* spacecraft at 0748 UT on 1981 April 26. We will refer to these particle events as the "WF event" (West Fast event, 1981 April 26), the "WS event" (West Slow event, 1981 December 8), the "E event" (East event, 1979 February 18), and the "CM event" (Central Meridian event, 1979 April 24). Hereafter, we will designate the shocks associated with each of these events as the WF, WS, E, and CM shocks, respectively. Modeling the WF event will permit us to compare the evolution of Q over a long time (1.5–2.5 days), and to analyze the influence on Q of different hypotheses of the model.

Among the large energetic particle west events observed by *ISEE 3* between 1978 September and 1982 February, the WF event is one of the few for which the anisotropy has been computed for a large number (seven) of low-energy channels, that shows a relatively stable IMF in the upstream region, and that shows signatures of both coronal and interplanetary accelerated matter. This event is associated with a 2B flare located 18° north, 50° west, on 1981 April 24, between 1355 UT and 1408 UT (Sanahuja & Domingo 1982), showing a long-duration X-ray event and

type II radio emission (Cane 1985). No CME has been reported around that time, although Solwind observed a CME 2 hr earlier, located at 10° south (R. Howard 1996, private communication). The interplanetary shock is associated with an interplanetary type II event (Pinter et al. 1982; Cane 1985). This hectometric radio emission seems to originate at about 10 $R_\odot$ (Cane 1997 and references therein); particularly for this event, Pinter et al. (1982) found an average velocity of propagation of 2030 km s^{-1} at 0.05 AU, and of 1480 km s^{-1} at 0.1 AU. These values should be taken as approximate, because of the simplifications assumed when derived (see Pinter's comments). The average velocity of propagation of the shock, between the Sun and *ISEE 3*, is 970 km s^{-1}; consequently, the shock undergoes significant deceleration during its journey to 1 AU.

The WF event is a well-connected event, showing an enrichment of the Fe/O ratio (2–12 MeV amu^{-1}; Reames, Cane, & von Rosenvinge 1990) in the early phase of the event. This ratio stays high until the high-energy (4–6 MeV) proton flux reached its maximum, ~5 hr after the onset of the event (a signature of impulsive events; Reames 1990); later, it decreases to the value found in gradual events. Klecker (1983) and Cane, Reames, & von Rosenvinge (1991) interpret this evolution as a composite of flare-associated ion populations at the onset phase, followed by an interplanetary shock-accelerated population (see also Miller & Viñas 1993). This event is one of the few cases identified (Reames et al. 1990) that has impulsive and gradual components; following Cliver's (1996) terminology, it is a mixed-impulsive event. Finally, a particular characteristic of this event is that between 50 and 500 keV, it shows magnetic flux tubes with a background proton population of magnetospheric origin (highly anisotropic flux spikes), and also from a former event (quasi-isotropic).

While the WF event was developing, *Helios 1* (located at ~0.8 AU, ~105° east) observed two proton (5–10 MeV) flux enhancements at the beginning of April 26. In principle, one of them might be related to the shock observed by *ISEE 3*, because *Helios 1* should be magnetically connected to the Sun at ~60° east. This is highly improbable, except if the shock was really huge ($\gtrsim$220°, twice from 50° west to 60° east), and strong enough to maintain active shock-particle acceleration at its right wing for an extended period of time. It is more reasonable to assume that the particle events observed by *Helios 1* were associated with one of the several solar active phenomena developing between 10° and 90° east at that time (Woo & Schwenn 1991); in particular, there were two intense flares erupting at 0633 UT (54° east) and at 0718 UT (58° east) on April 26. Otherwise, such a wide shock ought to be related to a large CME, for which there is no observational evidence (i.e., Sheeley et al. 1985). Furthermore, Woo & Schwenn (1991) report Doppler scintillation observations by *Pioneer Venus* for this period, and relate them to the interplanetary disturbances detected by *Helios 1*. Looking at these observations, it is clear that the scintillation transient observed in early April 25 has no relation to the shock observed by *Helios 1* (except if it propagates very fast at ~0.7 AU), and it is even more improbable that this could be the same shock as observed by *ISEE 3* on April 26.

Low-energy data come from the DFH instrument on board the *ISEE 3* spacecraft (Balogh et al. 1978; Sanderson, Reinhard, & Wenzel 1981). High-energy data have been extracted from the *ISEE 3* data pool, except for the flux in the 26.5–147 MeV channel, for which the raw *ISEE 3* data were kindly provided by D. Ruffolo (1994, private communication). The anisotropy of low-energy fluxes is derived as described in Sanderson et al. (1985), while at high energy it is calculated from the sector count rates, taking into account the characteristics of the detector. It has not been possible to compute all the anisotropies at high energy, because either the fluxes were too low, the integration time was too long (from which unreasonable values result), or the counts per sector were not available. For the E event, anisotropy profiles have been calculated using the count rates in a very wide energy range (26.5–147 MeV) and an integration time of 10 minutes. The method used is an application of Sanderson et al. (1985) for one detector with eight sectors on a plane, and correcting for the Compton-Getting effect (Lario 1997).

4. DERIVING THE INJECTION RATE AND ITS SPECTRUM

4.1. *Evolution of the Shocks*

The shocks associated with the CM, E, and WS events have been modeled as in He92 and He95. The propagation of the WF shock from the Sun to 1.1 AU has been simulated assuming initial conditions for the MHD pulse that reproduce the plasma velocity and magnetic field values observed by *ISEE 3*. Unfortunately, at this time *Helios 1* was not adequately located to be able to further constrain these conditions; *Prognoz 8* also detected this shock, but it was orbiting the Earth and thus was too close to *ISEE 3* to provide supplementary useful information. The hectometric type II radio emission observed in association with this event gives clues as to how the shock propagates, but it does not help us to decide how wide (ω) the initial pulse should be. We have assumed two different initial conditions for the initial shock: WF1 (V_s = 1775 km s^{-1}, ω = 60°), and WF2 (V_s = 1350 km s^{-1}, ω = 168°), with the time duration of the shock pulse τ = 2 hr in both cases. The WF1 shock better reproduces the values of the velocity associated with the type II emission, while the WF2 shock more accurately fits the magnetic jump ratio observed at *ISEE 3*; at 1 AU, WF2 produces a shock front wider than the shock for the WF1 case. It would be possible to merge both conditions into one case, but as the shock data cannot be checked by another spacecraft in this event, we have considered both cases for the evolution of this shock. This will also allow us to study how the topology of the shock front influences the evolution of Q, and its dependence on the input shock conditions.

Figure 1 shows one snapshot of the simulation of the propagation for the WF1 and WF2 shocks, 25 hr after the maximum of the solar activity (t = 0) that originated the event. The shock front is located within the steep density gradient of the isocontours [$\log_{10}$ (density) cm^{-3}]. The inner boundary only permits us to establish an upper limit for the moment at which the magnetic connection between *ISEE 3* and the shock front was established, t_c, although the expected value should be zero, or very close. We have considered t_c = 5 hr; in this way, we make sure that the shock has enough time to reach the inner boundary of the MHD simulation, and a stable magnetic connection perfectly delineated by the MHD model is established. The transit time from the Sun to *ISEE 3* given by the model is 42.00 hr for the WF1 shock, and 41.43 hr for the WF2 shock. The evolution of VR and BR at the cobpoint for these two cases is shown in the two upper panels of Figure 2. The lower panels give the position of the cobpoint at the shock front, identified by its distance to the Sun and the angle with

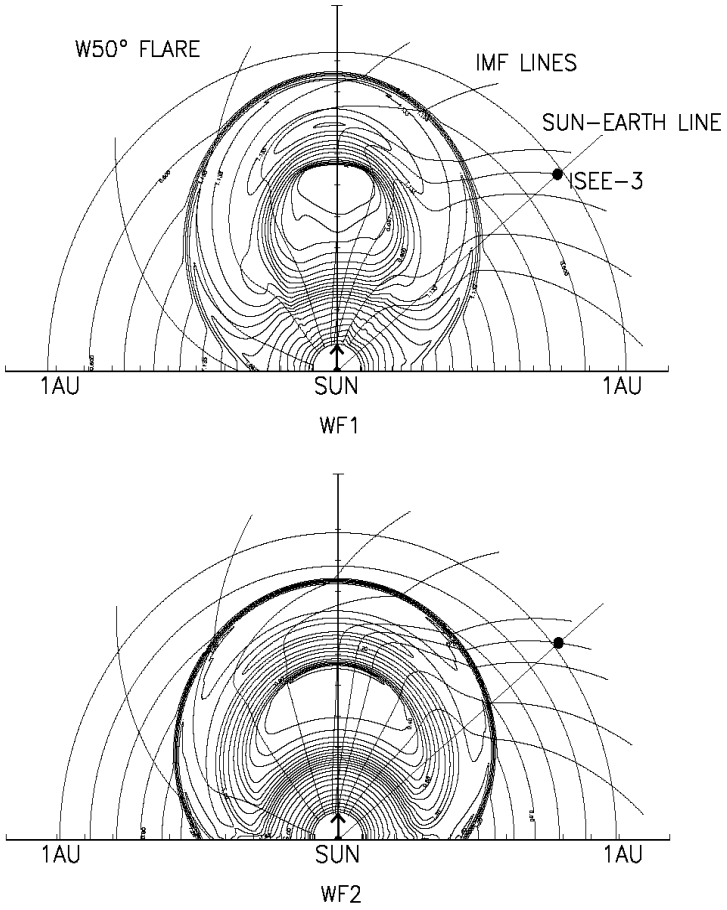

FIG. 1.—Snapshots of the simulation of the propagation of the WF1 (*upper panel*) and WF2 (*lower panel*) cases for the WF event. The log (density) contours (particles cm^{-3}) and some IMF lines are represented. The shock is located within the steep gradients. The arrow indicates the position of the solar source.

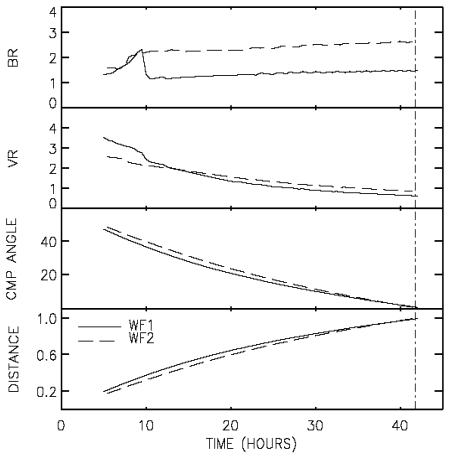

FIG. 2.—WF event. Evolution of the conditions at the cobpoint, as derived from the simulation of the shock propagation (WF1 and WF2) between t_o and the passage of the shock at *ISEE 3* (*vertical dot-dashed line*). Panels from top to bottom: BR, VR, the CMP angle (degrees) and the distance (AU) of the cobpoint to the Sun.

respect to the central meridian position (CMP). As can be seen, the differences in the cobpoint positions between the two cases are small. For low-energy particles, these differences will result in a small change in Q, because particles are injected from slightly different positions. For high-energy particles, which travel much faster than the shock, the differences between the two cobpoints become insignificant. Consequently, the fitting of the flux and anisotropy profiles in this event are practically independent of the topology assumed for the shock front. Nevertheless, the BR values (also in VR at the beginning) are different, because the WF2 shock is much wider than the WF1 shock. This would imply that any functional dependence that could appear between the injection rate and VR or BR, will depend on the modeling of the shock propagation. This is why it is very important to fix the initial conditions by using other spacecraft plasma data, as we did for the CM, E, and WS events; we will come back to this point in § 5.

4.2. *Fitting the Flux and Anisotropy Profiles*

As we discussed in the former section, we first fit the flux and anisotropy profiles in the upstream region of the 620–1000 keV channel, assuming that protons propagate along a

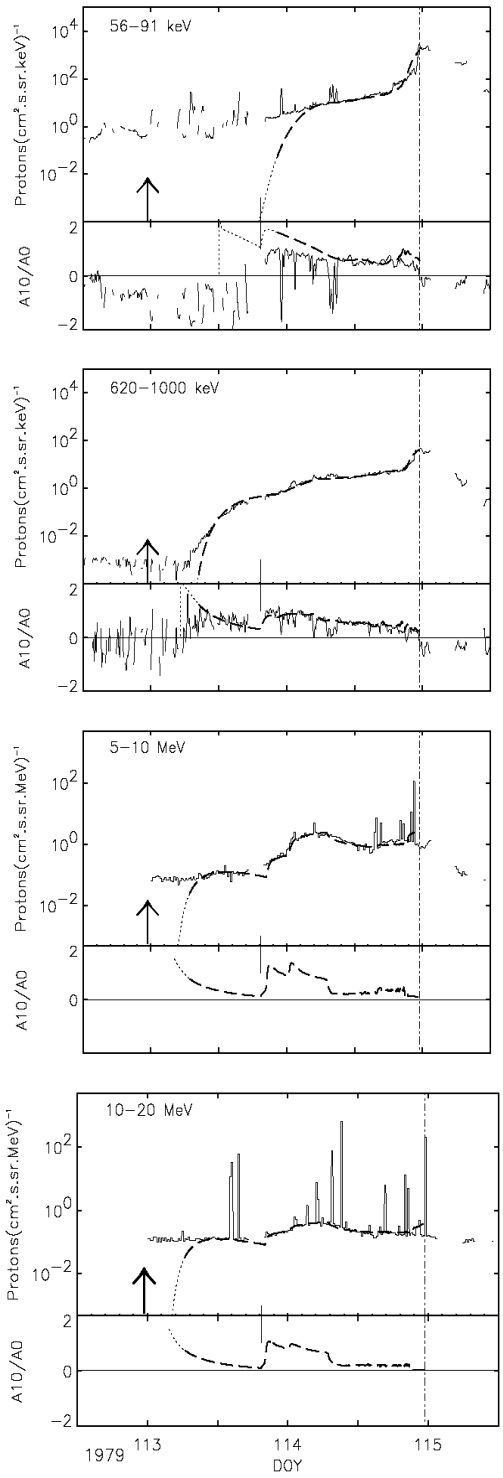

FIG. 3.—1979 April 24 event (CM event). Observed (*thin lines*) and fitted (*thick dashed lines*) flux and first-order anisotropy profiles. The thick arrow indicates the time of the solar activity, the dot-dashed vertical line indicates the passage of the shock, and the short solid vertical line shows t_c, the initial connecting time between the shock and the observer. The part of the profiles plotted as a dotted line (at the onset) is not physically meaningful; the background overwhelms the flux associated with the event.

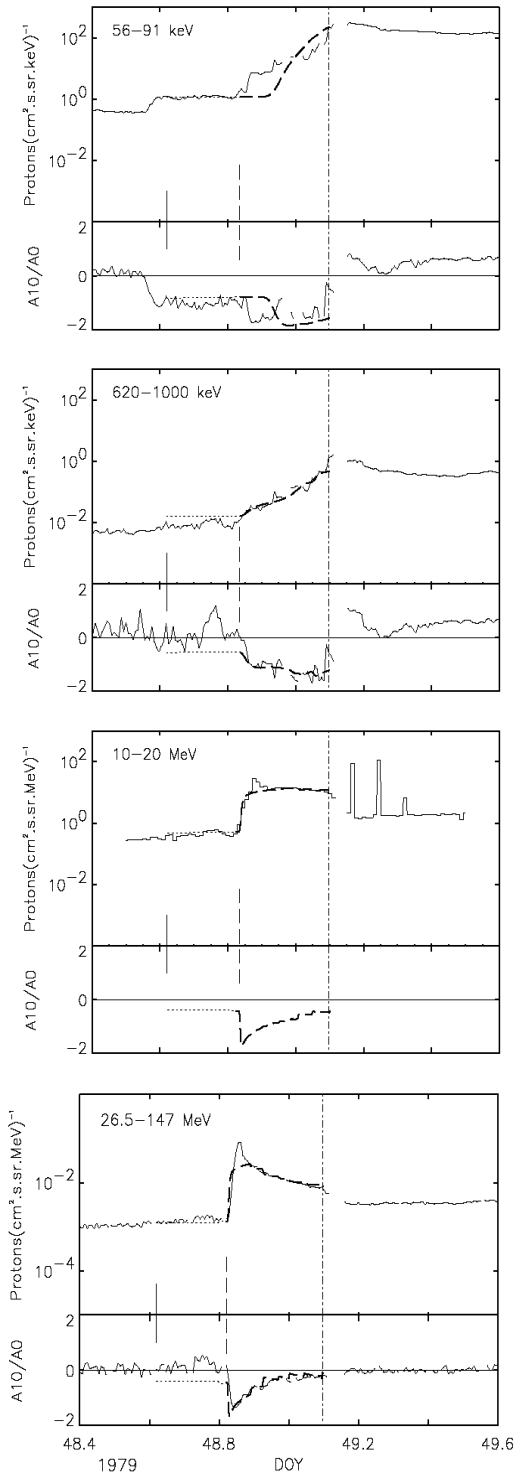

FIG. 4.—1979 February 18 event (E event). Lines are as in Fig. 3. Dashed vertical line marks the discontinuity commented on in the text.

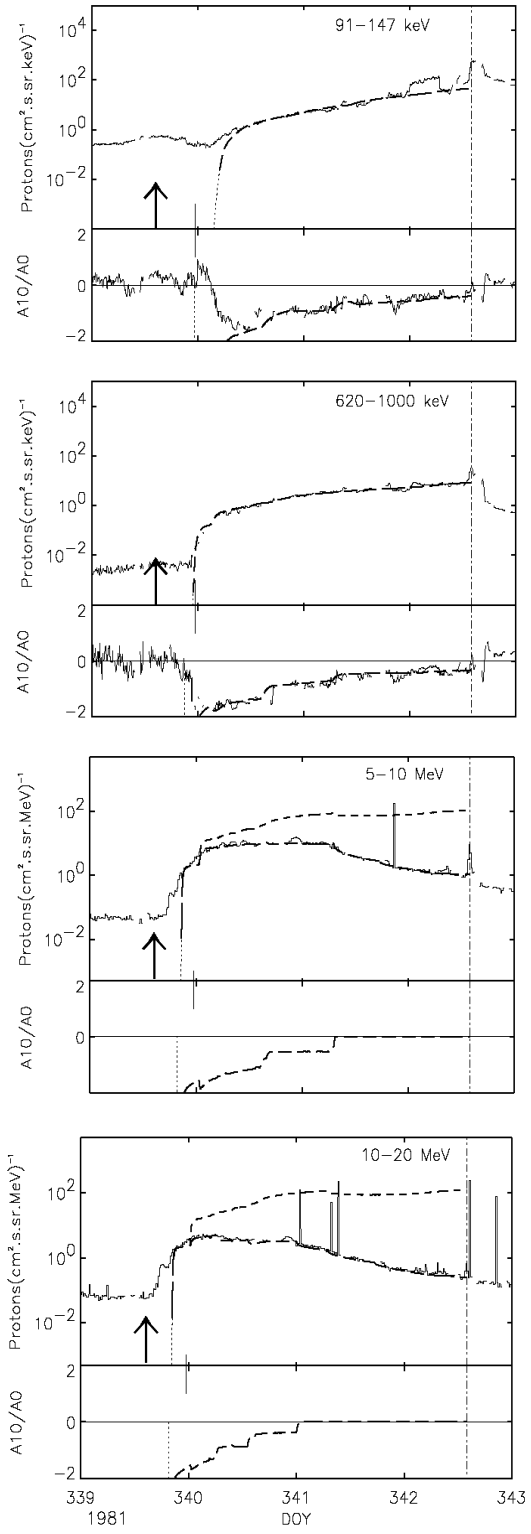

FIG. 5.—1981 December 8 event (WS event). Lines are as in Fig. 3. The extra flux profiles plotted (*dashed line*) at 5–10 MeV and at 10–20 MeV have been calculated assuming the same γ as at low energy.

magnetic flux tube associated with the cobpoint. This yields the $\lambda_{\parallel}$ and G values for this energy. Then we use the spectral index γ to obtain the best fit for fluxes and anisotropies at lower energies. Figures 3, 4, and 5 show the fitting performed for the CM, E, and WS events at energies lower and higher than in He92 and He95, plus the fit at ~ 1 MeV from which the others at lower energies are derived (the total number of channels fitted is nine or ten for each event). Figure 6 shows the fitting performed for the WF event (taking $q = 1.4$); only the results for the WF1 shock are shown because the profiles for the WF2 shock are practically coincident.

The thick arrow in each panel indicates the time of the solar activity, the dot-dashed vertical line indicates the passage of the shock, and the short solid vertical line shows t_c, the initial connecting time between the shock and the observer. There is no arrow in Figure 4 (E event) because it should be out of the frame, more than 2 days to the left; the timescale for this event (~ 10 hr) is much shorter than for the other events modeled ($\gtrsim 40$ hr). The part of the profiles plotted as a dotted line (at the onset) is not physically meaningful; this part corresponds to the first particles arriving at the spacecraft, which cannot be seen because the background overwhelms the flux associated with the event. None of these figures display the lowest energy channel of *ISEE 3* (35–56 keV); at these energies there is always a large background population, which makes comparison with the observations rather difficult. Because of this contamination, the flux emerges from the background only a few hours before the shock passage. We will discuss this point when commenting on the WF event.

The CM event (Fig. 3) shows hardly any shock-accelerated protons for $E \gtrsim 10$ MeV, and the particle flux for $t < t_c$ results in a contribution that is below the background; at low energy, this initial component is more relevant. This event was associated with the disappearance of a quiescent filament (Sanahuja et al. 1983) and with a CME (Cane, Kahler, & Sheeley 1986), and did not show any signature of intense flaring activity (X-rays, type II emission, etc.). The lack of a satisfactory model for the formation of coronal shocks and its evolution to interplanetary (Cane 1997 and references therein), together with the location of the inner boundary of the shock model, obliges us to assume, in some cases, an injection of particles below this boundary and before t_c. The CM event requires a long-lasting injection, and it is clear that these are non–flare-accelerated particles.

Figure 4 shows the profiles for the E event. Because of a weak discontinuity several hours after t_c (Fig. 4, *short dashed line*), the model can only give an approximate fit of the profiles in this period, which in turn affects the overall upstream profile adjusted for the lowest energy channel. This is a consequence of trying to fit the profiles for several energy channels simultaneously; the fit can be improved by assuming slightly different solar wind conditions ahead of this point, or a different initial population in the magnetic flux tube to which the observer is connected. Nevertheless, we have preferred to keep the fits for all the events at the same level of complexity. Assuming the same conditions as at lower energies, for example, it is not possible to model the initial peak of the flux observed above 10 MeV.

Figure 5 shows the fits and observational profiles of flux and anisotropy for the WS event. The shock travels slowly, which implies a long-lasting injection of shock-accelerated

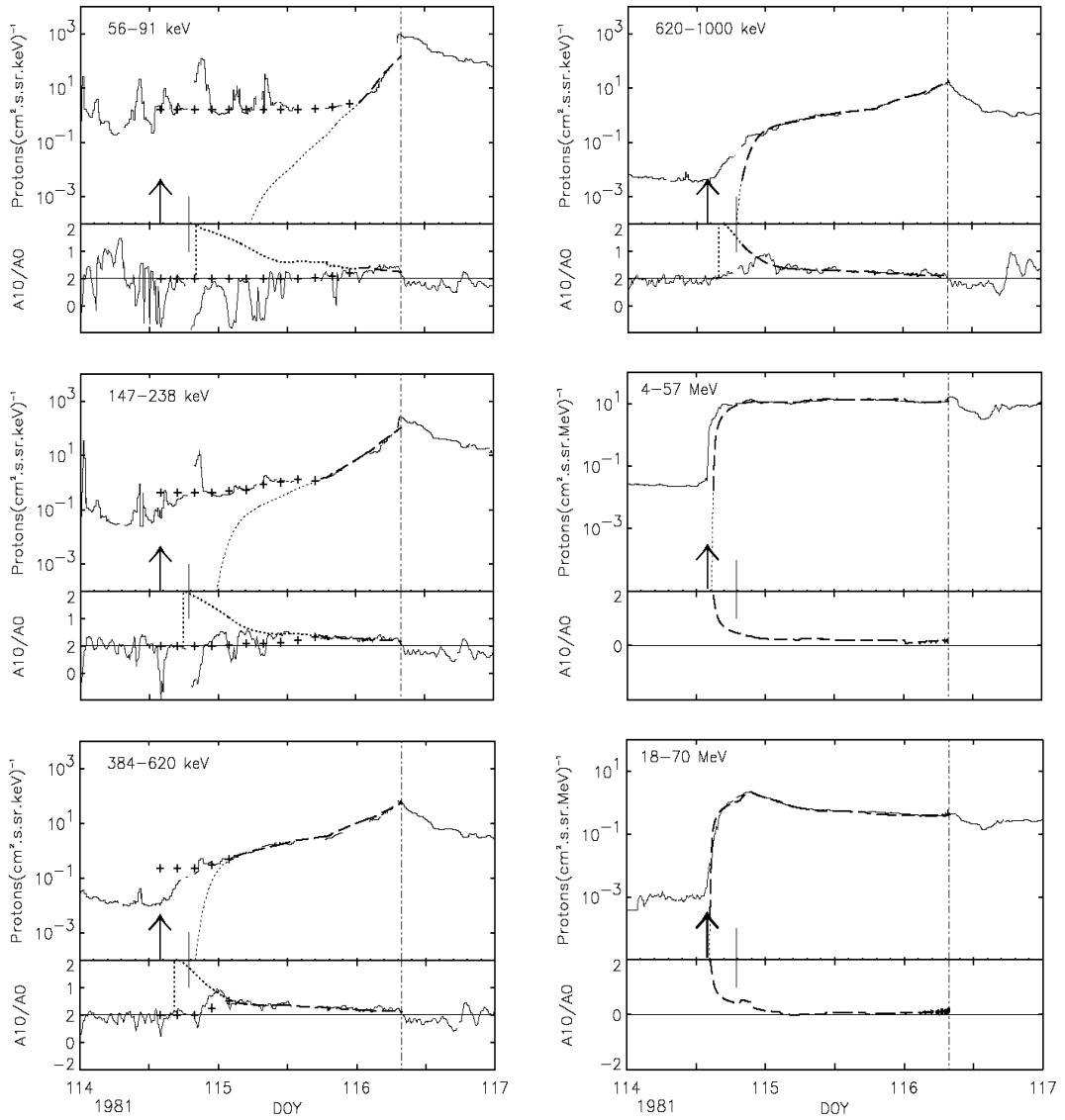

FIG. 6.—1981 April 26 event (WF event). Lines are as in Fig. 3. The line of crosses shows the flux profile obtained after including an isotropic population that simulates the preexisting background. Note the change in the anisotropy. The spikes at low energy correspond to the magnetospheric contributions (not simulated).

protons. The anisotropy decreases very slowly, and the fit does not require any region of increased magnetic turbulence ahead of the shock front. Looking at the evolution of the flux in the upstream region (i.e., ~30 hr ahead of the shock passage), we can see that the shock is still able to accelerate low-energy protons, but it has become very inefficient at high energy.

Figure 6 shows the profiles for the WF event. The flux and anisotropy profiles have been fitted assuming a constant injection of particles before t_c, as for the WS event, and a region of enhanced scattering upstream of the shock, characterized by a smaller mean free path, as for the CM event (see He92). We also assume that such a region has no effect on high-energy protons; although this is a reasonable hypothesis (Kallenrode 1996), we cannot test it because the anisotropy profiles are not available (or derivable) at these energies. In this event, the IMF tubes were filled with an abundant low-energy population (a quasi-isotropic distribution) produced by a former event, and with spiky contributions of magnetospheric origin (highly anisotropic). These two populations mask the real anisotropy of the shock-accelerated population; below ~500 keV, the fits do not agree with the profiles observed until 10 or 20 hr (depending on the energy channel) before the shock passage. If we add to the fits a small isotropic population simulating this background (Fig. 6, *line of crosses*), the anisotropy is largely reduced, even to zero at the onset of the event, as the observations indicate. We cannot consistently introduce the

effect of the magnetospheric population that produces the antisunward flow (large negative anisotropies) when there is a good magnetic connection between *ISEE 3* and the bow shock of the Earth. Sanderson et al. (1981) present magnetospheric events of this type and discuss how they affect the values (and sign) of the anisotropy when riding upon larger energetic particle events. These contributions vanish as higher energies are considered.

The mean free path derived from the flux and anisotropy profiles observed in the 620–1000 keV channel for the CM and WS events are nearly identical to those found in He92 and He95. For the E event, we found $\lambda_{\parallel} = 1.3$ AU, and the fittings in the WF event yields $\lambda_{\parallel} = 0.1$ AU for the whole event in both WF cases. As commented on in § 2, the mean free path for other energies scales as R^{2-q}; all the values obtained are within the accepted range (i.e., Valdés-Galicia 1993). The inclusion of the solar wind effects at low energies leads to lower $\lambda_{\parallel}$ values than when those effects are not considered (see the discussion in Ru95). Furthermore, since we assume a $\lambda_{\parallel}(R)$ dependence in order to simultaneously fit the profiles for several energy channels, the mean free paths derived are not identical (although they are very similar) to those obtained using the focused-diffusion transport equation (Roelof 1969). These differences do not have any significant consequence for our analysis. The foreshock regions for the CM and WF events are characterized by $\lambda_{\parallel e}(\ll \lambda_{\parallel})$. The reduction of the integration grid allows us to take smaller mean free paths than the ones found in He92 for the fit (0.01 AU for the CM event, 0.02 AU for both WF cases), as well as thinner foreshock regions (0.04 and 0.2 AU, respectively). The smaller the grid, the more accurately the increase in the flux can be fitted at the shock passage.

4.3. *The Injection Rate*

Figure 7 displays the evolution of the injection rate of shock-accelerated protons, Q, for the four events. These values are derived directly from equation (1), after correcting for the cross-sectional area of the magnetic flux tube. The first point of each curve represents the injection at the connecting time, while the last point is the injection just before the shock passage at *ISEE 3*. The MHD model gives $t_c(\mathrm{E}) > t_c(\mathrm{CM}) > t_c(\mathrm{WS}) \gtrsim t_c(\mathrm{WF})$. The longest elapsed time for the injection of protons corresponds to the WS event. The values of Q, computed through the dependence on $A(r)$, have been evaluated at the points of the grid given by the MHD simulation where protons are injected. Small jumps in Q caused by the discrete nature of $A(r)$ have been smoothed. The injection rate has an intrinsic radial dependence as r^{-2} (distance of the Sun to the cobpoint) through $A(r)$; thus, it should show a tendency to decrease with time as the shock moves away from the Sun. Nevertheless, it increases for CM and E events. The reason for this is that the evolution of Q depends basically on the quantity of particles available to be accelerated (not only from the solar wind but also from the particle population previously accelerated by the same shock or by other earlier events), the strength of the shock, and its ability to accelerate and to inject particles into the interplanetary medium.

The top panel of Figure 7 shows the evolution of Q for the 620–1000 keV channel. At lower energies, the values of Q are scaled according to the values of the spectral index γ discussed below. Curves labeled CM, WS, and E in the top panel of Figure 7 can be compared to the respective ones shown in Figure 8 of He95, showing that the evolution is

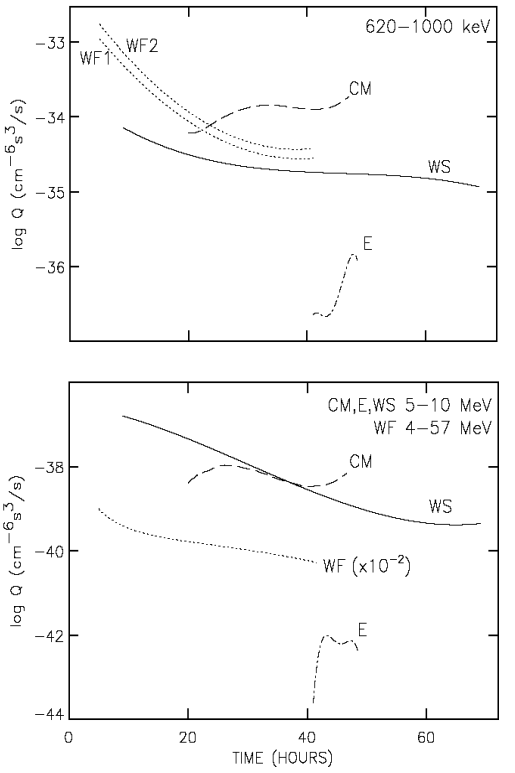

FIG. 7.—Evolution of the injection rate of shock-accelerated protons, Q, for the four events studied, at 620–1000 keV (*top panel*) and 5–10 MeV (*bottom panel*). The high-energy profile for the WF event displays the values for the 4–57 MeV channel. Each curve extends from t_c to the time of the shock passage by *ISEE 3*. The curves WF1 and WF2 shown in the top panel correspond to the WF event (see text).

essentially the same. This is a remarkable result, since the transport equation and the method used to integrate it are quite different; there are, however, small quantitative differences. Below 1 MeV, for example, the injection rate can be about twice as large as in He95. We attribute this difference to the combined effects of the solar wind convection and adiabatic deceleration; this is small at $\sim$1 MeV, but increasingly important at lower energies. Solar wind convection makes protons reach the observer sooner; therefore, in order to keep the flux high, a greater injection of fresh protons is required. Adiabatic deceleration demands large injections of protons because part of the flux decays to lower energies; this effect becomes important in impulsive injections. For a continuous strong injection from the shock, these effects are attenuated because protons travel shorter distances (as the shock is approaching the observer). Furthermore, the energy channels are populated in such a way that at the same distance and at the same time, the distribution of protons as a function of energy depends only on the spectrum of the injection, but not on the distance traveled (Lario et al. 1997). Therefore, the cumulative effect of deceleration becomes smaller. The top panel of Figure 7 shows two curves for the injection rate, corresponding to the evolution in the WF1 and WF2 cases. As discussed above, the differences between the injection rates derived are small at low energy and insignificant at high energy, and

they are derived from the position of the cobpoint at the front shock, which is very similar but not identical in both cases (Fig. 2, *two lower panels*).

The bottom panel of Figure 7 shows the evolution of Q at high energy: the 5–10 MeV channel for the E, CM, and WS events, and the 4–57 MeV channel for the WF event. At high energy, the particle fluxes have been fitted independently for each energy, because it is not possible to obtain results in agreement with the observations if we maintain the spectral index derived at low energy, even without knowing the anisotropy. For example, Figure 5 shows one extra curve for the two highest energy channels; these represent the flux profiles derived assuming the same spectral index as at low energy. At the shock passage, the discrepancy with respect to the observed flux is greater than 2 orders of magnitude, and it is practically independent of the $\lambda_{\parallel}$ assumed (even under scatter-free conditions); in fact, it is a consequence of the continuous injection of protons from the approaching shock. Therefore, the efficiency of the shock as particle accelerator decreases more rapidly when higher energies are considered; as Kallenrode (1996) pointed out, a high efficiency of particle acceleration at some MeV is not necessarily expected. Reames et al. (1997a) also suggest that in larger events, the efficiency for the acceleration of high-energy ions may decrease more rapidly than those at low energies as the shock expands outward from the Sun.

In broad outline, the evolution of Q at high energy (Fig. 7, *bottom panel*) is similar to the evolution at low energy; we will come back to this point in the next section. In the E event, the behavior of Q with respect to the energy is not the same at low and high energies; this may be due to the sudden connection, after the IMF discontinuity, to a magnetic flux tube containing a rich population of high-energy protons. The model can reproduce this feature by assuming a strong injection of protons coming from the shock after t_c. However, we suspect that this energetic population is associated with a 1B flare, located 10° east, erupting at 1439 UT on February 17 (Behannon, Burlaga, & Hewish 1991). In particular, the model cannot reproduce the flux peak observed above 10 MeV (which does not appear at lower energies). This contribution alters the Q values at this energy in this particular case. At low energy (<1.5 MeV), the evolution of the anisotropy after the discontinuity (day of year 48.8) removes the possibility of particle contamination from any other event: it is large and increases or keeps constant, then decreases sharply when the shock is approaching.

The spectra of the injection rates derived for the four events can be seen in Figure 8; the insets in the panels indicate the periods of time over which the injection rate has been averaged (from t_c to the passage of the shock). The energy assumed for each channel is the geometric mean of the interval; the error bars reflect the time dispersion, which means different injection rates at different energies for different intervals, and the change to differential flux units taken independently at each energy channel when computing Q. As can be seen, Q depends only slightly on the time considered, except for the WS event at high energy, and for the first interval of the WF event (these correspond to the WF1 case, and are nearly identical for the WF2 case). The first interval of the WF event is affected by the background population, which prevents a better fit to the profiles, without introducing further ad hoc assumptions. The

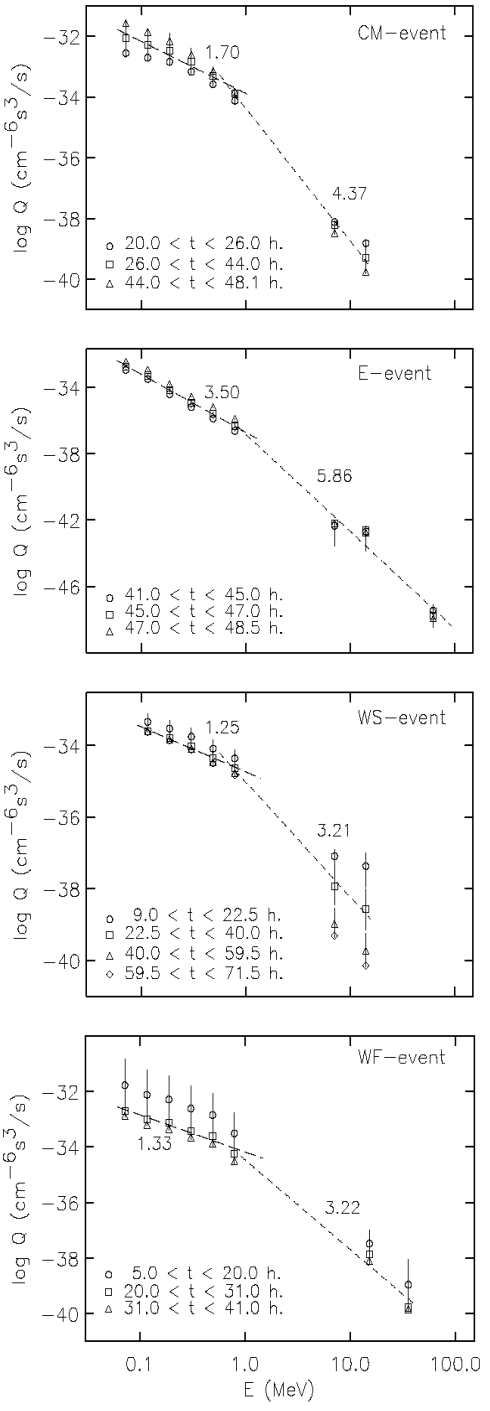

FIG. 8.—Spectra of the particle injection rate for the four events. Each point is the average value of Q over the period indicated in the inset, for each energy channel. The dashed line shows the fit to the points at low ($E < 2$ MeV) and high ($E > 1$ MeV) energy for the second period; the number is the corresponding spectral index, γ. The highest time value in each inset corresponds to the passage of the shock.

straight lines drawn in Figure 8 correspond to the best fit for the points of the second period plotted for each event, at low ($\lesssim$2 MeV) and high ($\gtrsim$1 MeV) energy, where the numbers are the respective spectral indices (absolute value of the slope). At low energy, the small dispersion guarantees that the values are representative of the whole set; the slope could change significantly at high energies, as indicated by the error bars. However, even taking into account this uncertainty, it is clear that the efficiency of the shock as an injector of accelerated protons decreases sharply above 2–5 MeV.

The low-energy spectral indexes can be compared with those given in Figure 8 of He92, and Figures 5 and 7 of He95. For the CM event, we assume that shock-accelerated particles start filling the flux tube of the cobpoint at t_c; this tube has already been populated by particles accelerated at the corona. Since equation (1) includes the solar wind effects, when the shock starts injecting particles into the tube, most of the solar-accelerated population is farther away than if the transport equation neglects the solar wind terms. Therefore, the shock starts filling a less populated flux tube, and consequently, higher injection rates are required to obtain a high and prolonged increase of the flux. The rigidity dependence assumed for the mean free path in the foreshock region ($\lambda_{\|_c} \propto R^{-0.4}$) implies a more abundant population of $\sim$1 MeV protons than that of $\sim$100 keV protons. This dependence was also found by Beeck & Sanderson (1989), who analyzed several foreshock regions. Part of this energetic population feeds the lower energy levels, which does not happen if the transport equation does not consider the deceleration terms: in this latter case, the fitting of the profiles requires higher Q values at low energy, leading to a higher spectral index (a softer energy spectrum). In the WS event, the continuous injection of particles into the cobpoint magnetic flux tube makes the solar wind influence less perceptible; for that reason, the spectral index derived and that formerly estimated are similar. Once the magnetic connection is established, the E event shows a power-law spectrum with a slight softening when the shock is close to the observer. For this short event, the spectral index is very sensitive to how the fit is performed.

TABLE 1

THE SPECTRAL INDEX

Time (hr)	γ
CM event	
$t_c \le t < 26$	1.51
$26 \le t < 44$	1.71
$t \ge 44$	2.21
E event	
$t_c \le t < 45$	3.61
$45 \le t < 47$	3.47
$t \ge 47$	3.37
WS event	
$t_c \le t < 40$	1.21
$t \ge 40$	1.41
WF event	
$t_c \le t < 20$	1.70
$20 \le t < 31$	1.28
$t \ge 31$	1.50

The spectral indexes γ used in $G \propto E^{-\gamma}$ to obtain the fits of fluxes and anisotropies are given in Table 1. Note that the values displayed in Figure 8 correspond to the fit to the points of the second period plotted for each event, after computing the injection rate Q. The small differences between the values in Table 1 and those in Figure 8 do not affect the derived flux or anisotropy profiles. Figure 9 shows a representative example, the WS event in the energy channel 91–147 keV. The top and bottom panels display, respectively, the differences between the values of the flux and anisotropy profiles shown in Figure 6, and those calculated taking the slope displayed in Figure 8. When both profiles are coincident, the values shown in these panels should be zero; as can be seen, the solid line is close to zero. We have included in this figure two more lines in order to illustrate the sensitivity of the fit to the spectral index. These curves show the same magnitudes, but for spectral indexes equal to $\gamma + 0.25$ and $\gamma + 0.5$ (*dashed and dotted lines, respectively*); the first case produces a steady increase in the flux up to a factor of 1.5, while for the second the factor is 2.5.

We have seen in this section that a lower efficiency of the shock as a high-energy particle accelerator translates into a steepening of the energy spectrum of Q. This spectrum has usually been computed by measuring the intensity of particles at the moment of the shock passage, but not throughout the period during which the injection of particles from the shock lasts. Klecker, Scholler, & Hovestadt (1983) studied the variations of intensity, energy spectra, and composition of ions in the energy range 0.3–20 MeV for an event observed by *ISEE 3* on 1978 September 29. About 2 hr before the shock passage, the spectrum of the differential flux of protons (their Fig. 6) has a slope of 1.9 for $E \lesssim 1$ MeV; the spectrum above this energy softens as the slope changes to 4.1. Nevertheless, this is not a clear example, because the energy range covered only extends up to 2 MeV, and they were implicitly assuming that the transport of protons during these 2 hr had not modified the spectrum.

Reames et al. (1997a) reported spectral invariance during a 3 day period for a gradual particle event on 1995 October 20, starting almost 1 day before the shock arrival. Their

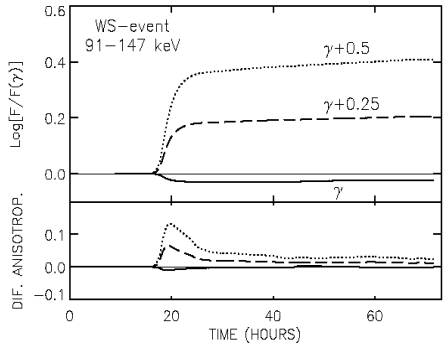

FIG. 9.—1981 December 8 (WS) event, $\sim$100 keV channel. Differences between the flux and anisotropy profiles shown in Fig. 5 and those calculated assuming that the spectral index estimated in Fig. 8 applies to the whole event (*solid line*). The top panel shows the logarithm of the flux ratio; bottom panel shows the subtraction between both anisotropies. The other two curves in each panel show the same magnitudes, but assuming two arbitrary slopes, as labeled.

Figure 7 shows that the slope of the proton flux spectrum is between 2.5 and 3.1; there is a slight softening above 10 MeV. We think that it is not immediately apparent to relate these values to the slope of our distribution function source term, Q, either because of the possible presence of a turbulent foreshock region ahead the shock (as suggested by the different evolution of fluxes immediately ahead of the shock; see their Fig. 6), or because of the transport effects of the IMF on the particle population, especially when the shock is farther away from the observer. Reames, Kahler, & Ng (1997b) point out that the slope of the differential flux spectrum in the invariant region largely varies among different events (between 1.7 and 4.1), with many spectra steepening at high energy. If the downstream population is a reservoir population for later shock acceleration, we should expect a softer spectrum at low energy immediately ahead of the shock, because the acceleration process is more efficient at low energy than at high energy. Nevertheless, in the upstream region the shock-accelerated particles can interact with the magnetic field, thereby further modifying the spectrum. Thus, the spectrum measured in the upstream region results from competition among three factors: the initial spectrum of the seed population, the efficiency of the shock as a particle accelerator, and the modulation due to the IMF. These factors, as well as their energy dependence, can be different from event to event. They could yield a variety of spectra, softening in different degrees and at different energies.

5. EVOLUTION AND FEATURES OF THE INJECTION RATE

5.1. *Evolution of the Injection Rate of Shock-Accelerated Particles*

This is the first time that the quantitative evolution of the injection rate and its spectrum for long-lasting energetic particle events have been modeled at energies higher than 2 MeV; He95 presented similar results at low energy, although the evolution of Q was only schematically described because the transport equation and the hypotheses assumed did not permit a link of the fits performed at different energies. The evolution of Q for the WS and WF events (Fig. 7) shows that these shocks inject more particles into the interplanetary medium when they are close to the Sun than when they are approaching a distance of 1 AU. The injection rate decreases more than 1 order of magnitude at all energies in both events (in some cases even up to 2.5). This decreasing efficiency of the shock as a particle accelerator results from the combination of two effects: the evolution of the cobpoint along its front (moving clockwise, as seen from the Sun), and the expansion of the shock (weakening its MHD strength). When a west shock is still close to the Sun, its cobpoint is located in the central part of the front, where the shock is stronger (the highest VR values). However, when this shock is near 1 AU, the cobpoint has slipped $\sim 50°$ away from the central part of the front to the right flank (which means lower VR values).

In contrast to what happens in the west events, the injection rate at low energy increases with time in the CM and E events. The evolution of VR also shows a monotonic increase in both cases. The magnetic compression increases monotonically in the E event, while in the CM event it grows until the cobpoint reaches 0.4 AU, and then remains stable and high (~ 3.5) for the rest of the upstream event. It seems that for the CM event, Q increases until BR reaches its maximum value (at $t \sim 24$ hr). This behavior reflects the approach of the cobpoint to the nose of the shock, and thus the increase in Q. At high energy, for the same event, Q decreases slightly, showing a weakening of the shock as a high-energy particle accelerator. Nevertheless, we cannot attach much significance to this conclusion, since the flux at 10 MeV scarcely stands out over the background.

It is clear from Figure 8 that the Q spectrum does not extend smoothly from low energies (~ 50 keV) to high energies (100 MeV or, as a more conservative limit, 50 MeV) in any of the four events modeled. From these limited results (because of the small number of points and events), we cannot conclude that the diffusion mechanism does not work above ~ 2 MeV, or whether the shock-acceleration processes have not yet reached the steady state regime (Forman & Webb 1985). To obtain more accurate results at high energy demands more sophisticated observations (better spatial and temporal resolution), which should allow us to apply the same procedure at high energy as at low energy to fit the flux and anisotropy profiles.

As can be seen in Figure 7, the injection rate at low energy decreases more slowly in the WS event than in the WF event. However, the opposite happens at high energy; the WS event decreases by 2 orders of magnitude, while the WF event decreases by 1. Both events have a similar heliolongitude, and the magnetic compression shows a similar evolution at the cobpoint. The most significant differences are their respective durations (or, equivalently, the velocity of propagation of the shock), and the evolution of the velocity compression, VR, at the cobpoint. VR is about twice as large for the WF event as for the WS event. Furthermore, the WS event develops over a normal isotropic background of protons, and it is not necessary to assume a high-scattering region at any energy, while the WF event grows over a former particle event, and its simulation requires a foreshock turbulent region active at low energy. In addition to the influence of the foreshock region, the presence of a seed population also favors the acceleration of particles (Tan et al. 1989). The combined influence of both factors may explain the differences between the injection rates of the two events, leading to higher Q values in the WF event.

We have already mentioned that the injection of particles before t_e constitutes the component of those particles accelerated close to the corona. The temporal evolution of this injection is given by a constant injection (west events), by a Reid-Axford profile (CM event), or is not considered (E event). This is a useful way to represent an injection of particles from the corona, which allows us to include the effects of a possible coronal shock propagating close to the Sun, or the existence of an impulsive injection of particles. The effects of this injection close to the corona frequently appear in the literature; for example, when Cane (1996) defines "eruption" or "CME/eruptive flare." The current state of shock modeling does not allow us to simulate this contribution within the global scenario of our combined shock-particle model. In the west events, we cannot discern the exact value of t_e because the inner boundary of the MHD model does not permit us to go closer than 18 $R_\odot$. For such magnetically well-connected events, an observer is connected to the particle source from the time of the occurrence of the solar activity that triggers the event. At that time, the newly formed shock accelerates large quantities of particles because it propagates in a dense medium with strong embedded fields. Although a realistic model for

this scenario has not yet been proposed (Kahler 1992), the best approach was taken by Lee & Ryan (1986), who investigated the acceleration and propagation of particles at an expanding coronal shock, presenting different time profiles at 1 AU. Nevertheless, as they commented, these profiles cannot be directly compared with the observations. For our purposes, a more serious flaw of this model is that it neglects the role of the magnetic field and uses a diffusive equation. Another example of the existence of a strong component of particles accelerated close to the Sun is the WF event, which shows an impulsive and a gradual component (§ 3). In particular, the Fe/O ratio is high until ~ 5 hr after the onset of the event, which coincides with the connecting time, t_c, derived from the MHD simulation. The first phase of the injection is closely associated with type III bursts, and it has also been inferred indirectly from the absence of an associated coronal shock in different events (Cane & Reames 1990). On the other hand, the WS event does not show any change in chemical abundances (Kahler et al. 1986), which suggests a unique agent for the particle acceleration. Kahler, Reames, & Sheeley (1990) examined several injection profiles (for 175 MeV protons) between 2 and 10 $R_\odot$, suggesting that these particles are accelerated in shocks driven by CMEs. Unfortunately, there are few west events for which the impulsive and gradual components have been reasonably well identified; their analysis would be very helpful to understanding the evolution of the shocks from the corona to the inner interplanetary medium.

5.2. *Dependence of Q on the MHD Strength of the Shock*

The injection rate can now be evaluated during the evolution of the event, since the effect of the interplanetary transport has been removed (at least to a first approximation) by making allowances for the boundary conditions of the model and the size of the MHD grid. Figures 10, 11, and 12 show the evolution of Q as a function of VR, BR, and θ_{Bn} at the cobpoint for the four events modeled. The two upper panels in Figure 10 display the evolution of Q for the CM and E events (*top*) and the WS and WF events (*middle*) at low energy (two channels); the two curves that appear at each energy for the WF event represent the fittings for the WF1 and WF2 cases. The lower panel shows high energy (one energy for each event). Each point represents a time step of the numerical integration at which particle injection occurs. The thin arrows in the top two panels indicate the direction of increasing time. In the top panel, the points to the left correspond to MHD conditions of the shock when it is still close to the Sun, and the points to the right indicate when the shock is close to 1 AU. The opposite is true for the middle panel; in the bottom panel each set tracks the evolution of the corresponding event in the upper panels. This time evolution is a straightforward consequence of the evolution of Q discussed above. The dashed line shows the result of a simple linear regression to each set of points (black dots); when the coefficient of the regression, ξ, is less than 0.75, the values are represented by open circles (only the E event at high energy). The statistical analysis yields the following values for the coefficient ξ at ~ 100 keV, ~ 1 MeV, and $\gtrsim 4$ MeV, respectively: CM event, 0.88, 0.86, and 0.94; E event, 0.75, 0.75, and 0.52; WS event, 0.76, 0.94, and 0.98; WF1 event, 0.99, 0.94, and 0.98; and WF2 event, 0.98, 0.99, and 0.99. For the intermediate energy channels not represented in Figure 10, ξ is around the corresponding values given here. The ξ values found for the E event are

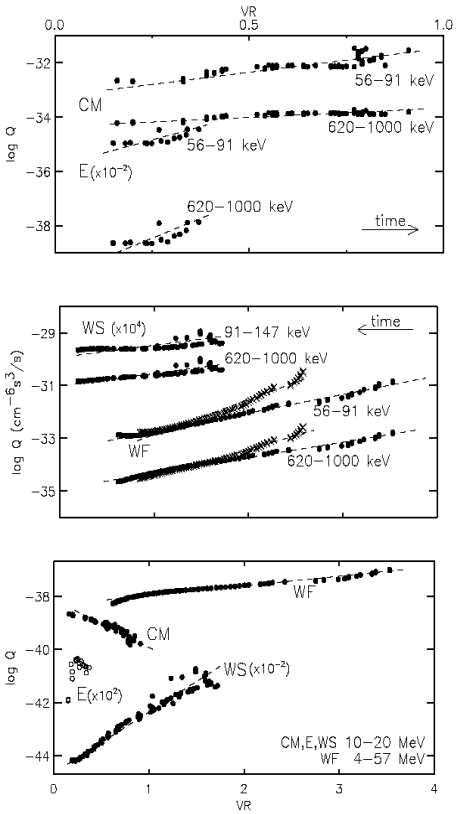

FIG. 10.—Representative examples of the dependence of the injection rate, Q, on the normalized velocity ratio, VR. *Top panel*: low-energy fits for the CM and E events. *Middle panel*: low-energy fits for the WS and WF events (filled circles in the WF event represent the WF1 case, crosses represent the WF2 case). *Bottom panel*: high-energy fits for the four events. The top scale of VR only applies to the top panel. Straight dashed lines follow a log $Q \propto$ VR dependence. Open circles represent the cases for which the linear regression has a correlation coefficient lower than 0.76. The arrows indicate increasing time in each case (see text).

lower because this event develops rapidly, less than half a day between t_c and the passage of the shock, which limits the evolution of VR.

Table 2 gives the coefficients found for the relation $\log Q = \log Q_0 + k\mathrm{VR}$, and the e-folding, $\mathrm{VR}_e = \log e/k$, for each event at low energy. The values derived from these lineal regressions have physical meaning only for the range

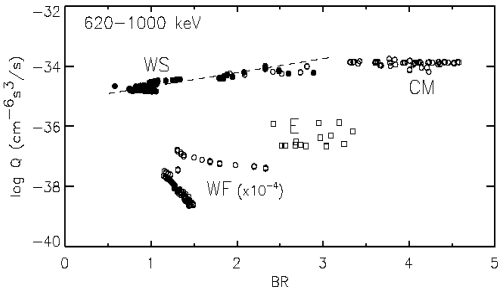

FIG. 11.—Dependence of the injection rate, Q, on the magnetic field ratio, BR. Plots are as in Fig. 10.

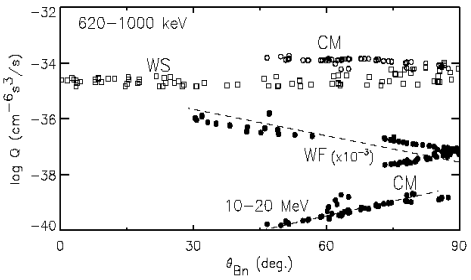

FIG. 12.—Dependence of the injection rate, Q, on the angle θ_{Bn}. Plots are as in Fig. 10. The points associated with the E events have not been included, for clarity.

of VR values found; VR ≥ 0.10 is the lower limit from which the injection has been considered active. Thus, Q_0 should be understood as the injection rate of accelerated particles when the shock-acceleration process starts. For the WF event, for example, VR decreases from 3 or 4 to 1 (the shock is strong close to the Sun, but much weaker at 1 AU), which represents a reduction of Q by 2 orders of magnitude at low energy. The values of these coefficients at high energy must be taken with caution, because of the uncertainty involved in their derivation; we include them in Table 2 so that they can be compared to the coefficients at low energy. Lario et al. (1995b) have modeled the evolution of the flux at $\sim$1 MeV for four particle events, assuming this dependence for the injection rate of shock-accelerated particles, and assuming an average MHD shock obtained from a set of shocks producing large gradual particle events. In spite of these drastic simplifications, the fits obtained are surprisingly good. The different slopes found for the two cases considered in the WF event reflect the different evolution of VR; thus, to correctly quantify the dependence of Q

TABLE 2

COEFFICIENTS FOR THE RELATION $\log Q = \log Q_0 + k\mathrm{VR}$ (FOR VR > 0.10)

Energy	Q_0 (cm^{-6} s^3 s^{-1})	k	VR$_c$
CM event			
90 keV	5.3×10^{-34}	1.52	0.29
1 MeV.....	4.4×10^{-35}	0.69	0.63
$\sim$15 MeV.....	6.8×10^{-39}	−1.76	−0.25
E event			
90 keV	3.6×10^{-35}	4.29	0.10
1 MeV.....	1.2×10^{-38}	5.84	0.07
WS event			
90 keV	1.4×10^{-34}	0.40	1.08
1 MeV.....	1.0×10^{-35}	0.46	0.94
$\sim$15 MeV.....	2.0×10^{-41}	2.40	0.18
WF Event: WF1			
90 keV	1.8×10^{-34}	0.68	0.64
1 MeV.....	1.2×10^{-35}	0.59	0.74
$\sim$15 MeV.....	4.5×10^{-39}	0.36	1.19
WF event: WF2			
90 keV	4.2×10^{-35}	1.26	0.34
1 MeV.....	3.2×10^{-36}	1.04	0.42
$\sim$15 MeV.....	1.5×10^{-39}	0.72	0.60

on VR it is necessary that the MHD code model reproduces the real evolution of the shock as best as possible.

We have proceeded with BR and θ_{Bn} in the same way as with VR. Figures 11 and 12 show the results, which are completely different from those obtained for VR (we only present one energy channel for each event). The linear regression performed for the magnetic field compression ratio only gives significant results in the WS event ($\xi = 0.83$). Nevertheless, we cannot extract any clear conclusion from these data because most of the points group around BR $\sim$ 1, which is a typical value of BR during most of the event (except at the onset). Thus, if there is any dependence of Q on BR, it is too weak to be detected at this stage of our modeling. The same conclusion holds for other energies of the same event, and for the WF event. The argument given in the preceding paragraph for the E event is valid here (and is also valid for θ_{Bn}). The CM event is a different case, because BR is high about 1 day after the onset of the event, and it remains high until the passage of the shock. But it also shows important fluctuations (Fig. 3 of He95), while the injection rate varies slowly. Looking at the points associated with this event (Fig. 11), the injection rate does not appear to depend on BR, or else the dependence is too weak for our model to discern it.

A similar conclusion can be drawn for the dependence of Q on θ_{Bn} (Fig. 12); in this case, the dispersion of the values is even larger than for BR. The E event has not been plotted, for clarity; all points cluster around 82° because the E shock is quasi-perpendicular. The points plotted in this figure do not reflect any time sequence (as in Fig. 10); ξ is lower than 0.20 for the WF and WS events. In both events, the cobpoint stays for a long time in a region of the respective shocks where the magnetic field presents a low downstream/upstream ratio (BR $\sim$ 1). To derive θ_{Bn}, we apply the coplanarity theorem, following Chao & Hsieh (1984), which implies a number of interpolations upstream and downstream of the shock front as a result of the discrete nature of the MHD grid. When the magnetic compression is low, the oscillations of the components of the magnetic field (upstream and downstream) yield important variations in the values derived for θ_{Bn} (Balogh et al. 1995), even if the front is perfectly identified by the jump of the hydrodynamic variables (velocity or density). In short, we cannot draw any conclusion about the functional dependence of Q on θ_{Bn}, because of the uncertainties in the determination. The only significant result corresponds to the CM event at high energy; ξ is 0.84 and 0.87, respectively, for the 5–10 MeV and 10–20 MeV channels (0.59 for the 620–1000 keV channel). In this case, Q decreases with θ_{Bn} (this shock evolves from quasi-perpendicular to quasi-parallel conditions), which means that the efficiency of the shock as an accelerator diminishes when the condition of perpendicularity is lost. This evolution seems to indicate that the shock-drift process works efficiently at high energy, but that at low energy the shock-diffusion mechanism is more efficient.

It is possible to synthesize the flux and anisotropy profiles that should be observed by another spacecraft, provided that it is magnetically connected with the front of the shock. The evolution of the cobpoint associated with this second spacecraft can be easily evaluated from the simulation of the shock, and therefore it is possible to derive the values of the MHD variables at that point. Accepting that there is a dependence of the injection rate of shock-accelerated par-

ticles on these variables at the cobpoint (VR in our case), it is straightforward to build up the flux and anisotropy profiles that this second spacecraft would observe. The most favorable situation for such a prediction appears when the cobpoint associated with the second spacecraft moves through the region of the shock front already covered by the cobpoint of the spacecraft already simulated, or nearby. The worst situation appears when the cobpoint is at the wings of the shock, or, for the East events, where the evolution of Q only extends for a short period. Among the four events studied, only the CM event offers an adequate scenario; Figure 5 of Sanahuja et al. (1983) shows the position of *Helios 1* and *Helios 2* with respect to the shock and *ISEE 3*, and Figure 1 of He92 shows the evolution of the shock modeled. The cobpoint of *Helios 2* moves in a region of the shock that is later scanned by the cobpoint of *ISEE 3*; therefore, it is easy to derive the values of Q associated with the cobpoint of *Helios 2* taking into account the VR values given by the MHD simulation. Figure 13 shows the observed flux profiles at low energy for two similar channels of *Helios 2* and *ISEE 3*. The dashed lines show the flux profile fitted to *ISEE 3* flux data (the third energy channel, not shown in Fig. 3), as described in § 4, and the flux buildup for *Helios 2*; we have assumed the same mean free path for the particles at the same time. As can be seen, the observed and synthesized profiles fit closely. We can proceed in the same way at high energy, particularly with the 4–6 MeV channel of *Helios 2*, and we can obtain similar good fits. Unfortunately, for this energy range there are only two or three observational points in the upstream region of *Helios 2* (I. Richardson 1996, private communication; see also Fig. 2 of Richardson 1997), therefore, the result at high energy is not especially relevant, since there are a wide range of power laws that can yield good fits.

The model also predicts that *Helios 1* should observe a large low-energy particle event, because it is magnetically connected to the central part of the shock, and as the shock propagates the cobpoint slips towards its right wing. But the observations reveal nothing (Sanahuja et al. 1983). Burlaga, Behannon, & Klein (1987) describe the scenario of this event in detail (see their Figs. 8–12); there is a corotating stream perturbation progressing counterclockwise that modifies the conditions of the ambient solar wind and the IMF topology assumed by the model. The front of such a discontinuity modifies the magnetic connection between the spacecraft and the front of the shock, and most probably prevents the arrival of the low-energy particles accelerated by the shock. It is also possible that the front of the stream interacts with the right wing of the progressing shock, preventing the formation there of a true shock front. Watanabe & Kakinuma (1984) depict such a scenario from radio-scintillation observations. The MHD code for the shock is not prepared to take into account a highly perturbed solar wind; thus, we cannot describe what really happens in the right wing of the shock. Nevertheless, the presence of this stream does not modify our conclusions about the injection rate of particles for this event, since *Helios 2* and *ISEE 3* are not affected by the presence of this stream until after the passage of the shock by *ISEE 3*.

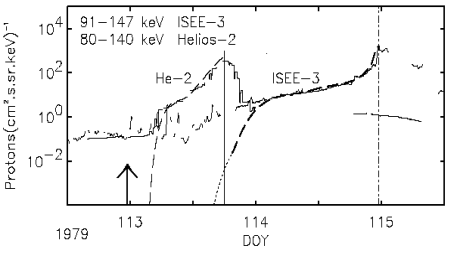

FIG. 13.—CM event. Low-energy flux profile derived for *Helios 2*, assuming log $Q \propto$ VR. Thin lines show the flux profiles measured by *ISEE 3* and *Helios 2*. Thick dashed line shows the fit for *ISEE 3* derived from the fit performed at ~1 MeV. The thin dashed line shows the flux profile synthesized for *Helios 2*, under the assumptions commented on in the text. Vertical lines represent the shock passage, and the arrow indicates the time of the filament disappearance.

An interesting point to note is the dependence of the injection rate on the radial distance to the Sun, r, and on the angular distance to the nose of the shock, the azimuthal distance (i.e., Reames et al. 1996 and references therein). As the position of the cobpoint and the value of Q are known throughout the event, it is easy to fit the evolution of Q as a function of r. Assuming a power law like $Q \propto r^{\alpha}$, the exponent α should characterize the evolution of the injection rate. For the CM event, the values of α found vary between 2.0 (56–91 keV) and 0.7 (620–1000 keV); the difference in the exponents reflects the fact that Q increases with the distance and the spectrum weakens as the shock approaches the observer. At high energy, Q decreases with distance ($\alpha = -0.8$ at 5–10 MeV and $\alpha = -2.4$ at 10–20 MeV), a behavior also expected from the weakening of the shock. For the two west events, α ranges between -4.8 and -0.6 (depending on the energy); Q decreases with distance, reflecting the weakening of the shock and the movement of the cobpoint away from its nose. Another possibility, explored by Kallenrode (1996), is to assume an exponential decrease for Q along the shock front, and to derive the e-folding angle, Φ, for each event. At low energy, the values found for Φ range between 9° and 58° for the four events; large values mean that the injection rate is less dependent on the azimuthal distance. At high energy, the fits yield negative values for the CM event, and angles between 7° and 34° for the west events. According to these results, any possible azimuthal dependence of Q along the shock front should be different at different energies, and not necessarily constant during the evolution of the event. The injection rate may not be completely represented by a radial or an azimuthal dependence alone; Kallenrode (1997a) refers to similar situations. We must bear in mind that the injection rate depends not only on the movement of the cobpoint due to the expansion of the shock, but also on the MHD conditions for the shock acceleration and injection of particles at this point, and on the shape of the shock, which changes during its interplanetary journey.

5.3. *The Influence of Corotation*

The scenario adopted for modeling the four particle events assumes a stable solar wind regime, and thus an Archimedial structure for the IMF upstream of the shock. Consistently, we can only interpret the quantitative evolution of Q correctly in terms of the evolution of the shock, if the topology of the upstream IMF does not change significantly during the event. But even under such favorable conditions, the corotation of the magnetic field tubes (and of the particle population filling them) could affect the conclusions. This "corotation effect" is a consequence of the solar

rotation: while the shock is propagating out from the Sun, the background medium is rotating westward at a rate of $\sim 13.^{\circ}6$ per day. An Earth-orbiting observer located at ~ 1 AU will scan different magnetic flux tubes, filled with shock-accelerated protons injected from eastern regions of the front (to the right, as seen from the Sun). For that reason, corotation might lead to changes in the flux as a result of the spatial evolution of the tubes, and the more slowly the shock propagates, the more flux tubes will sweep the spacecraft before the shock arrival.

Until now, the observer was considered to be in a unique flux tube, which, as the shock expanded, remained connected to different regions of the shock front (cobpoint). The particles injected from the cobpoint filled the same magnetic flux tube. The inclusion of the corotation effect involves the simulation of different flux tubes, each one connected to different parts of the shock. Therefore, it is necessary to fill the several flux tubes that, one after the other, will sweep across the observer, and to study the temporal dependence of the particle population in each flux tube. A direct consequence of including corotation in the model is that the CPU time needed to produce a fit is greatly increased, because it is necessary to include the contribution to the flux coming from different IMF tubes. It is possible to analyze the influence of corotation, assuming a functional dependence of the injection rate with respect to the position of the cobpoint along the shock front. There have been qualitative suggestions for such dependence (Reinhard et al. 1983; Sarris, Decker, & Krimigis 1985, among others), but up to now, only Kallenrode & Wibberenz (1997) have explicitly taken it into account, assuming that the flux intensity decays exponentially from the central part of the shock toward its flanks. In our case, assuming that $\log Q \propto \mathrm{VR}$, we are implicitly considering the influence of the angular distance from the central part of the shock, as well as the temporal evolution due to its propagation.

The thick solid line in Figure 14 shows the difference between the flux profile obtained for the WF event (at ~ 1 MeV, Fig. 6) and the profile that results after including the corotation effect, assuming $\log Q \propto \mathrm{VR}$ (for the WF2 case). We have computed the evolution of the 36 magnetic flux tubes ($0.^{\circ}33$ wide) to the right of the formerly original tube. We have replaced the contribution of each tube by the contribution of the next one to the right when the magnetic connection (the cobpoint) changes due to corotation. The

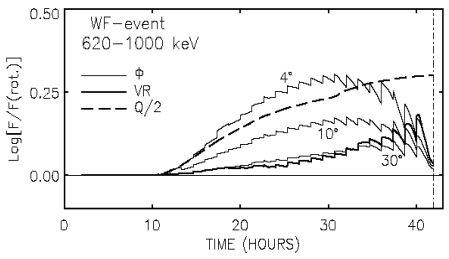

FIG. 14.—1981 April 26 (WF) event, ~ 1 MeV channel, showing the influence of corotation. *Thick line*: difference between the flux calculated without corotation and the resulting flux that includes this effect. *Thick dashed line*: the same difference, but assuming an injection rate equal to half that obtained without considering corotation. *Thin lines*: differences found assuming an exponential decay for Q, with $\Phi = 4^{\circ}$, 10°, and 30°, as labeled.

global influence of corotation is small, in spite of the shock taking nearly two days to reach 1 AU. It is also clear, however, that for certain periods, corotation could modify the injection rate derived by a factor of 1.4 at the maximum, depending on the geometry of the scenario (position of the observer with respect to the shock) and the velocity of propagation (strength) of the shock. The thick dashed line shows the same difference computed assuming that the injection rate taken is one-half the value needed to fit the profiles in Figure 6 (the WF1 case yields the same conclusion). The net effect of corotation, in this case, is to underestimate Q by a factor of 0.5 between 18 and 25 hr after the onset of the event. These differences are smaller for the E and CM events, and similar for the WS event; in the latter case, the shock propagates more slowly than in the other events, but Q and VR also vary slowly.

The jumps that appear in the curves of Figure 14 correspond to changes from one flux tube to another. These discontinuities can be smoothed using a finer grid of tubes, but we have preferred to keep the same grid used to compute all the flux and anisotropy profiles, since increasing the number of tubes implies modifying the MHD grid used for the simulation of the shock. We have not explored the importance of this effect at distances greater than 1.2 AU, since it is beyond the present possibilities of our code. The effect of corotation should be kept in mind, since it might be important when the shock velocity is low, when the observer has a proper motion with respect to the shock, or when the injection rate of shock-accelerated particles is strongly dependent along the shock front. Kallenrode & Wibberenz (1997) discuss the importance of corotation in similar terms for shocks with increasing or decreasing efficiency with radial distance, also depending on the observer's position with respect to the central part of the shock.

Kallenrode (1996) suggests that the flux intensity decays exponentially from the central part of the shock toward its flanks. The e-folding decay is characterized by an angle $\Phi = 10^{\circ}$. This is an interesting result, but it must be taken with caution, because the set analyzed is small and it encompasses values between 4° and 180°; consequently, the coefficients of correlation found are not significant (see discussion in Kallenrode 1996). Nevertheless, it is reasonable to explore the influence of such a dependence in the corotation effect. We can assume that Q behaves like the intensity, having its highest value at the nose of the shock, with a symmetric decay toward the flanks. Note that this angular dependence is not directly related to that suggested for the intensity, and there is no clear evidence of the symmetry of the decay. Figure 14 includes three curves (thin lines) showing the differences between the profile obtained in Figure 6 and those obtained assuming $\Phi = 4^{\circ}$, 10°, and 30°, respectively. The differences are large for the lowest value, and they are practically independent on Φ above 30°. This is an expected result, since for a given shock an ad hoc azimuthal evolution of Q (i.e., an appropriate Φ) could mimic the evolution of Q due to the shock expansion. As can be seen in this figure, the effect of the corotation in this event can be reasonably modeled assuming $\Phi = 30^{\circ}$, but when the WF1 case is considered, $\Phi = 10^{\circ}$ is a more appropriate value (the thick VR line tracks closer to the 10° curve, instead of the 30° curve). The reason is clear: the WF2 shock has a wider front than the WF1 one, whereas the Q-values derived from the fittings of flux and anisotropy are very similar; consequently, the e-folding angle must be

larger for the wide front shock than for the narrow one. Therefore, it is not clear that assuming that all shocks have a semicircular shape could result in a characteristic *e*-folding angle representative of a large fraction of the events.

6. CONCLUSIONS

We have presented an improved version of a numerical code for studying energetic particle events associated with interplanetary shocks. The major improvement over the former version of the model is in the transport equation describing the particle propagation along the IMF, which now includes the effects of solar wind convection and adiabatic deceleration. In order to minimize the parameters of the model, we have assumed a dependence of the injection rate ($\propto E^{-\gamma}$) and of the mean free path ($\propto R^{2-q}$) on the energy of the particles. In this way, by fitting the observed particle flux and anisotropy profiles at only one energy channel, we obtain simultaneously all the other low-energy channels, reducing the arbitrariness of fitting each energy channel on its own. We have used this model to reproduce the observed flux and first-order anisotropy profiles for four particle events, extending the energy range between $\sim$50 keV and 100 MeV. The results have been compared with former results (He95), explaining the differences and/or the good agreement between them. From the fits performed for each event, we have been able to derive the injection rate of shock-accelerated particles and its energy spectrum at the cobpoint, while the shock is propagating from near the Sun to 1 AU. We have quantified this injection and have found that the efficiency of the shock as a particle accelerator decreases more rapidly above $\sim$2 MeV than at lower energies.

We have related the evolution of the injection rate to the evolution of the MHD strength of the shock at the cobpoint. We have found a linear relation between log Q and VR, but not for BR or θ_{Bn}. This relation is energy dependent, since the log Q–VR slope smoothly changes from low to high energy. We cannot explain this energy dependence, because we have only modeled four events and because it varies from event to event. Our suspicion is that this relation only reflects part of the influence of the MHD variables at the cobpoint on the efficiency of the shock in the particle acceleration mechanisms. We expect that future improvements in the modeling of shock propagation and the study of a larger number of events will allow us to confirm (or reject) the existence of such relations. We have used the Q(VR) dependence derived to build up a synthetic flux profile to be compared with *Helios 2* observations, resulting in a very good agreement. We have discussed the influence of the corotation of the IMF tubes, concluding that depending on the type of particle event and the location of the observer, this effect cannot be ruled out in advance. Within 1 AU, however, it is not relevant in most situations.

The concept of the cobpoint allows us to quantify the evolution of the injection rate, Q, and the results derived confirm previous qualitative descriptions of its evolution (Kallenrode et al. 1993; Reames et al. 1996). We emphasize that the evolution of Q found is smoother than in previous studies. The dynamic evolution of the strength of the shock and in which part of the shock front the observer establishes magnetic connection throughout its expansion seem to be the main factors that determine the structure and shape of the particle events. Moreover, since the particle flux and anisotropy profiles are different at different energies, any azimuthal dependence for Q along the shock front should be dependent on the energy and time. We have clearly established the influence of the shock (and of its evolution) on the flux profiles observed at different energy ranges by removing the effects of the particle transport.

Recently, some criticism regarding the adoption of the shock simulation has appeared (Kallenrode 1997b; Gopalswamy et al. 1998). We would like to point out that the shocks used in this work were chosen in such a way that the plasma conditions observed at different spacecraft were reasonably adjusted by the MHD modeling, and that a dynamical description of the shock (given by a MHD code) is better than a simple kinetic one. We have studied the influence of the initial shock conditions on the evolution of the injection rate, showing that the precise position of the cobpoint has a small influence on the evolution of Q, but that it can modify its quantitative dependence on VR. In our model, the shock is not described as a pressure pulse, and it does not need a flare explosion to drive it. On the contrary, we consider an explicit shock satisfying the computed Rankine-Hugoniot conditions. Moreover, it is not possible to have a flare explosion driving the shock and the CME, because, for example, two of the events (CM event and WS event, both well-known in the literature; i.e., Kahler 1992) are associated not with flare activity but with filament disappearances. We have assumed in all cases, regardless of the shock's solar origin and explicit formation, its existence at a certain distance (18 $R_\odot$), and further assumed that its shape and velocity fit plasma and IMF observations by two or more spacecraft. This fact does not exclude the acceleration of particles near the Sun by a coronal shock or in front of the CMEs; on the contrary, in some events they must coexist. In that sense, Cane (1997) comments: "Multispacecraft observations support the fact that in large events, particles are seen rather promptly from widespread regions. The widespread acceleration is difficult to reconcile in terms of latitudinal extents of CMEs and the longitudinal extents of interplanetary shocks at 1 AU." We plead for the existence of an injection of particles near the Sun, and an injection of particles from an expanding shock in the interplanetary medium, whose origin is probably the same shock propagating in a different medium and in a different way, or two shocks (Cane 1997). In some events, it is clear that the magnetic connection between the shock and the observer is established at some time (call it t_c or r_{start}; He95; Kallenrode 1997b) after the interplanetary shock has started to propagate, while the magnetic flux tubes may have been filled with energetic particles accelerated near the Sun.

To conclude these comments, we would like to point out that if for west events the magnetic connection between the observer and the shock exists from the beginning, while for east events this connection is established shortly before the passage of the shock (at 1 AU), a spectrum of values for the connecting time between zero and a few hours before the shock arrival must exist. The accuracy of its determination relies on how good the MHD simulation of the shock is, and on the details of how the coronal shock is produced and how it evolves to an interplanetary shock. Until such time as current ambiguities in shock modeling (such as the initial conditions and the width of the coronal shock) are removed, we rely on the observations of two or more spacecraft to fix the main characteristics of the propagating shock. A MHD model with the inner boundary conditions

set at 1 $R_\odot$, which we expect to be available within the next few years, will be of great help to remove these uncertainties and to obtain more accurate values for the initial connecting time in west and central meridian events. In addition, it is necessary to study more individual events observed from different spacecraft, and to perform statistical analyses to confirm or reject our suggestion that the Q(VR) relation, plus the cobpoint concept, provides a reliable tool for reproducing particle fluxes in this type of event.

We are in debt to D. Ruffolo and J. Sánchez for their assistance and valuable suggestions. We thank T. R. Sanderson for providing the low-energy particle flux and anisotropy data, and D. Ruffolo for part of the raw high-energy data of *ISEE 3*. We thank I. Richardson for sending us high-energy *Helios* data. We have also benefited from useful comments offered by M. Vandas, M. Dryer, Z. Smith, M. Lee, D. Smart, M. Shea, and S. T. Wu. B. S. and D. L. acknowledge the support of the Spanish DGYCIT project PB93-0821 (Ministerio de Educación y Ciencia), the DGU project 1995/SGR569 (Generalitat de Catalunya), and computational support provided by the Centre de Supercomputació de Catalunya (C^4); D. L. also acknowledges financial support from the CIRIT of Catalunya.

REFERENCES

Balogh, A., et al. 1978, IEEE Trans. Geosc. Elec., G-16, 176
Balogh, A., González-Esparza, J. A., Forsyth, R. J., Burton, M. E., Goldstein, B. E., Smith, E. J., & Bame, S. J. 1995, Space Sci. Rev., 72, 171
Beeck, J., Mason, G. M., Marsden, R. G., Hamilton, D. C., & Sanderson, T. R. 1990, J. Geophys. Res., 95, 10279
Beeck, J., & Sanderson, T. R. 1989, J. Geophys. Res., 94, 8769
Beeck, J., & Wibberenz, G. 1986, ApJ, 311, 437
Behannon, K. W., Burlaga, L. W., & Hewish, A. 1991, J. Geophys. Res., 96, 21213
Bieber, J. W., Wanner, W., & Matthaeus, W. H. 1996, J. Geophys. Res., 101, 2511
Burlaga, L. F., Behannon, K. W., & Klein, L. W. 1987, J. Geophys. Res., 92, 5725
Cane, H. V. 1985, J. Geophys. Res., 90, 191
———. 1996, J. Geophys. Res., 101, 15533
———. 1997, AGU Geophys. Mono., 99, 205
Cane, H. V., Kahler, S. W., & Sheeley, N. R. 1986, J. Geophys. Res., 91, 13321
Cane, H. V., & Reames, D. V. 1990, ApJS, 73, 253
Cane, H. V., Reames, D. V., & von Rosenvinge, T. T. 1988, J. Geophys. Res., 93, 9555
———. 1991, ApJ, 373, 675
Cane, H. V., Sheeley, N. R., & Howard, R. A. 1987, J. Geophys. Res., 92, 9869
Chao, J. K., & Hshieh, K. C. 1984, Planet. Space Sci., 32, 641
Cliver, E. W. 1996, in High Energy Solar Physics, ed. R. Ramaty, N. Mandzhavidze, & X.-M. Hua (Woodbury: AIP), 45
Cliver, E. W., Kahler, S. W., Neidig, D. F., Cane, H. V., Richardson, I. G., Kallenrode, M.-B., & Wibberenz, G. 1995, Proc. 24th Int. Cosmic-Ray Conf. (Rome), 4, 257
Domingo, V., Sanahuja, B., & Heras, A. M. 1989, Adv. Space Res., 9(4), 195
Dryer, M. 1994, Space Sci. Res., 67, 363
Forman, M. A., & Webb, G. M. 1985, AGU Geophys. Mono., 34, 91
Gopalswamy, N., et al. 1998, J. Geophys. Res., 103, 307
Hasselmann, K., & Wibberenz, G. 1970, ApJ, 162, 1049
Heras, A. M., Sanahuja, B., Lario, D., Smith, Z. K., Detman, T., & Dryer, M. 1995, ApJ, 445, 497 (He95)
Heras, A. M., Sanahuja, B., Sanderson, T. R., Marsden, R. G., & Wenzel, K.-P. 1994, J. Geophys. Res., 99, 43
Heras, A. M., Sanahuja, B., Smith, Z. K., Detman, T., & Dryer, M. 1992, ApJ, 391, 359 (He92)
Jokipii, J. R. 1966, ApJ, 146, 480
———. 1971, Rev. Geophys. Space Phys., 9, 27
Kahler, S. W. 1992, ARA&A, 113, 197
Kahler, S. W., Cliver, E. W., Cane, H. V., McGuire, R. E., Stone, R. G., & Sheeley, N. R., Jr. 1986, ApJ, 302, 504
Kahler, S. W., Reames, D., & Sheeley, N. R., Jr. 1990, 21st Int. Cosmic-Ray Conf. (Adeleide), 5, 183
Kallenrode, M.-B. 1996, J. Geophys. Res., 101, 24393
———. 1997a, J. Geophys. Res., 102, 22335
———. 1997b, J. Geophys. Res., 102, 22347
Kallenrode, M.-B., & Wibberenz, G. 1997, J. Geophys. Res., 102, 22311
Kallenrode, M.-B., Wibberenz, G., Kunow, H., Müller -Mellin, R., Stolpovskii, V., & Kontor, N. 1993, Solar Phys., 147, 377
Klecker, B. 1983, Adv. Space Res. 2, 11, 285
Klecker, B., Scholler, M., & Hovestadt, D. 1983, ApJ, 251, 393
Kunow, H., Wibberenz, G., Green, G., Müller-Mellin, R., & Kallenrode, M. B. 1991, in Physics of the Inner Heliosphere II, ed. R. Schwenn & E. Marsch (Berlin: Springer), 243
Lario, D. 1997, Ph.D. thesis, Univ. Barcelona
Lario, D., Sanahuja, B., & Heras, A. M. 1995a, Proc. II SOLTIP Symp., Step GBRSC News, 5, 235
———. 1997, Adv. Space Res., 20, 1, 115
Lario, D., Sanahuja, B., Heras, A. M., Smith, Z., & Dryer, M. 1995b, Proc. 24th Int. Cosmic-Ray Conf. (Rome), 4, 385
Lee, M. A., & Ryan, J. M. 1986, ApJ, 303, 829
Miller, J. A., & Viñas, A. F. 1993, ApJ, 412, 386
Ng, C. K., & Reames, D. V. 1995, ApJ, 453, 890
Ng, C. K., & Wong, K.-Y. 1979, Proc. 16th Int. Cosmic-Ray Conf. (Kyoto), 5, 252
Parker, E. N. 1965, Planet. Space Sci., 13, 9
Pinter, S., Grigorieva, V. P., Kecskeméty, K., & Kudela, K. 1982, Proc. STIP Symp. on Solar/Interplanetary Intervals, ed. M. A. Shea, D. F. Smart, & S. M. P. McKenna-Lawlor (Huntsville: Book Crafters), 119
Reames, D. V. 1990, ApJ, 358, L63
Reames, D. V., Barbier, L. M., & Ng, C. K. 1996, ApJ, 446, 473
Reames, D. V., Barbier, L. M., von Rosenvinge, T. T., Mason, G. M., Mazur, J. E., & Dwyer, J. R. 1997a, ApJ, 483, 515
Reames, D. V., Cane, H. V., & von Rosenvinge, T. T. 1990, ApJ, 357, 259
Reames, D. V., Kahler, S. W., & Ng, C. K. 1997b, ApJ, 491, 414
Reinhard, R., van Nes, P., Sanderson, T. R., Wenzel, K.-P., Smith, E. J., & Tsurutani, B. 1983, Proc. 18th Int. Cosmic-Ray Conf. (Bangalore), 3, 162
Richardson, I. 1997, AGU Geophys. Mono., 99, 189
Roelof, E. C. 1969, in Lectures in High Energy Astrophysics, ed. H. Ögelman & J. R. Wayland (NASA SP-199), 111
Ruffolo, D. 1995, ApJ, 442, 861 (Ru95)
Sanahuja, B., & Domingo, V. 1982, Proc. STIP Symp. on Solar/Interplanetary Intervals, ed. M. A. Shea, D. F. Smart, & S. M. P. McKenna-Lawlor (Huntsville: Book Crafters), 311
Sanahuja, B., Domingo, V., Wenzel, K.-P., Joselyn, J. A., & Keppler, E. 1983, Sol. Phys., 84, 321
Sanderson, T. R., Reinhard, R., van Nes, P., & Wenzel, K.-P. 1985, J. Geophys. Res., 90, 19
Sanderson, T. R., Reinhard, R., & Wenzel, K.-P. 1981, J. Geophys. Res., 86, 4425
Sarris, E. T., Decker, R. B., & Krimigis, S. M. 1985, J. Geophys. Res., 90, 3961
Sheeley, N. R., Jr., Howard, R. A., Koomen, M. J., Michels, D. J., Schwenn, E., Muhlhauser, K. H., & Rosenbauer, H. 1985, J. Geophys. Res., 96, 163
Smith, Z. K., & Dryer, M. 1990, Sol. Phys., 129, 387
Tan, L. C., Mason, G. M., Klecker, B., & Hovestadt, D. 1989, ApJ, 345, 572
Valdés-Galicia, J. F. 1993, Sol. Phys., 62, 67
Vandas, M., Fischer, S., Odstrcil, D., Dryer, M., Smith, Z., & Detman, T. 1997, AGU Geophys. Mono., 99, 169
Watanabe, T., & Kakinuma, T. 1984, Adv. Space Res., 4(7), 331
Woo, R., & Schwenn, R. 1991, J. Geophys. Res., 96, 21227
Zalesak, S. T. 1979, J. Comput. Phys., 31, 335

C Details of the SEP event modeling

C.1 Evolution of VR and BR from the two MHD shock simulations

As commented in Chapter 4, the original ('Sun-centered') version of the MHD model assumes an input pulse to initialize the interplanetary shock that is a semicircle centered at the Sun. Since the IMF is assumed to be radial at the inner boundary of the model (located at $18\,R_{\odot}$), this means that the initial shock is parallel to the upstream IMF all along its front[1] and thus the shock input pulse does not represent a change in the magnetic field. This condition leads to simulated IMF intensity jumps at 1.0 AU lower than those observed, especially for western events. Figure C.1 illustrates this situation, it shows the evolution of VR (top panel) and BR (bottom panel) obtained for the Apr00 event when using the Sun-centered initial shock pulse (Smith & Dryer 1990). As can be seen, the jump in magnetic field is not fitted at all, whereas the off-center simulation reproduces the observed jump (bottom panel of Figure 4.3). The reason is that by placing the center of the input semicircle at a few solar radii from the center of the Sun, each point of the initial pulse front has a different obliquity; that is, each point has a different value of θ_{Bn}. By solving the Rankine-Hugoniot conditions along the shock front (Wu et al. 1983) we can obtain magnetic field increases larger than those derived with the Sun-centered MHD simulation. This *ad hoc* assumption allows us to better reproduce the observed shock discontinuities at arrival at the spacecraft.

[1]The angle between the shock normal and the upstream magnetic field is $\theta_{Bn} = 0°$.

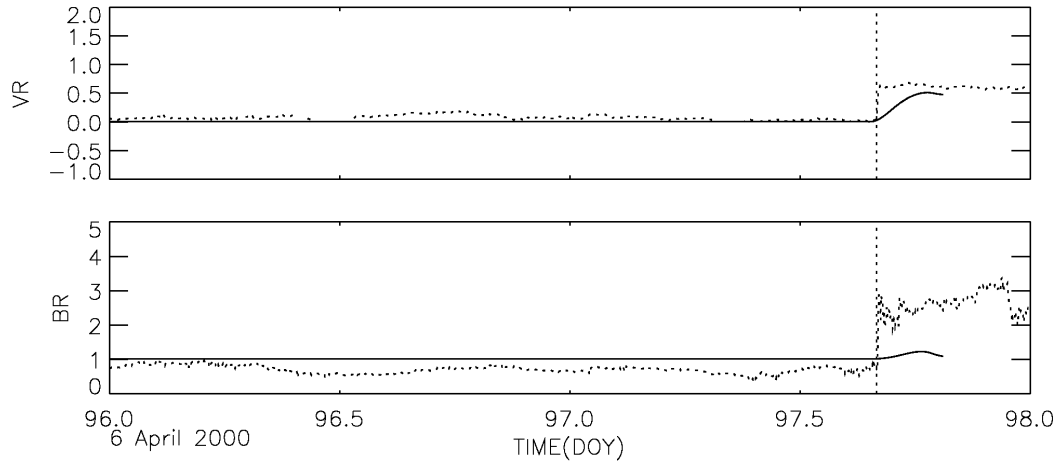

Figure C.1: Apr00 event. Observed (dotted lines) and computed (solid lines) radial velocity and the magnetic field downstream-to-upstream ratios, VR (top panel) and BR (bottom panel), respectively.

At present, the uncertainty in the characteristics of the initial pulse used in the MHD models and the unrealistic definition of the downstream magnetic field precludes us from deriving conclusions about a possible Q(BR) relation, as suggested in some events (Apr00, for example). The Apr00 event is illustrative of the other events modeled in Chapter 4 (see also Lar98).

The value of the parameters used in the simulation of the Apr00 SEP event with the Sun-centered MHD model are: $v_s = 1445$ km s^{-1}, $\omega = 140°$ and $\tau = 1$ hour. The simulated transit time is 48.62 hours and the shock establishes magnetic connection with the observer located at 1.0 AU at $t_c = 3.5$ hours from the onset of the event (the values used in the off-center simulation are given in Chapter 4). Figure C.2 compares the evolution of VR (left panel) and BR (right panel) at the cobpoint, from t_c up to the shock arrival time for both MHD simulations. The red traces are the values obtained from the Sun-centered simulation, whereas the blue traces represent the values from the off-center simulation. For this event, the evolution of VR derived from both simulations is similar. By contrast, the evolution of BR confirms that the magnetic field aspect of the MHD model requires the improvement of both the initial conditions and the numerical treatment of the magnetic field.

Figure C.3 shows the comparison of the evolution of VR derived from the off-center MHD simulation (blue traces) and the Sun-centered simulation (red traces) for the Sep98 event (left panel) and the Sep00 event (right panel). For the Sep98

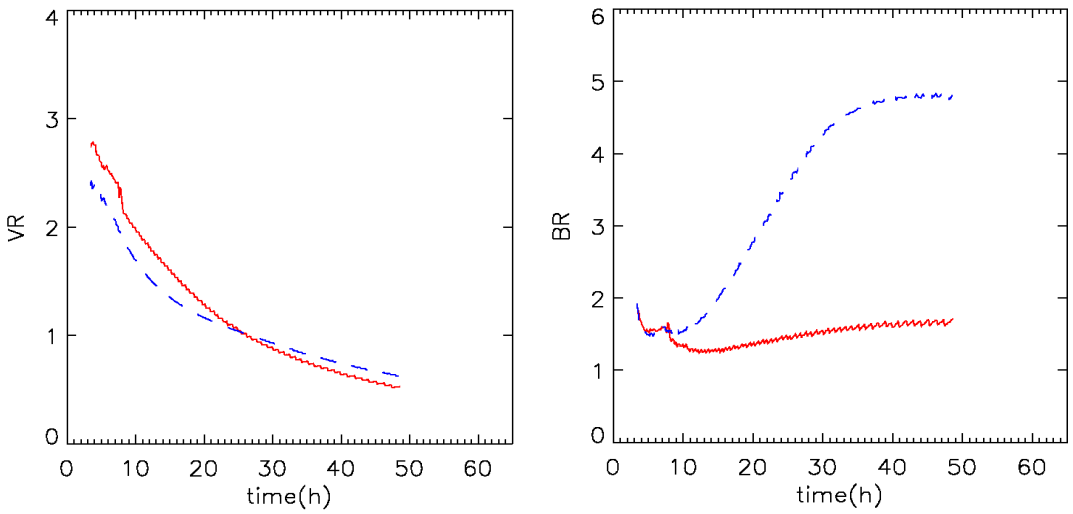

Figure C.2: Apr00 event. Left panel: comparison between the evolution of VR at the cobpoint's position resulting from the Sun-centered input pulse shock simulation (red traces) and the off-center simulation (blue traces). Right panel: The same as left panel but for BR.

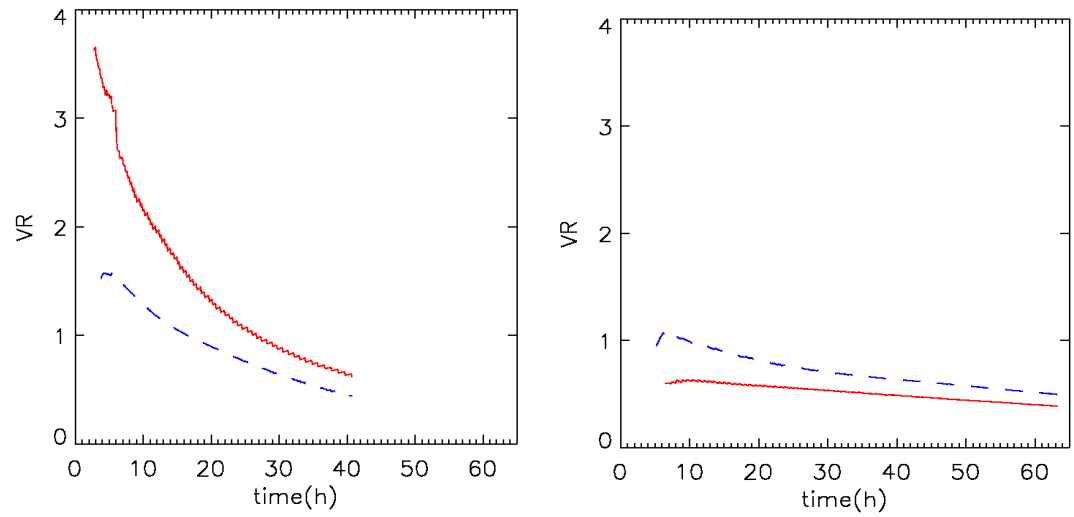

Figure C.3: Sep98 (left panel) and Sep00 (right panel) events. Comparison between the evolution of VR at the cobpoint's position resulting from the original input pulse shock simulation (red trace) and the off-center simulation (blue trace).

SEP event, the input pulse parameters using the Sun-centered MHD shock model are: $v_s = 2065$ km s^{-1}, $\omega = 140°$ and $\tau = 1$ hour. The derived connection time is $t_c = 2.8$ hours. As can be seen in the left panel of this figure, the values of VR obtained from both simulations are different because of the large difference between both initial input speeds (2065 km s^{-1} versus 1300 km s^{-1} for the Sep98 event). For far western events like this, the observer is connected to the flank of the shock at the shock arrival. The numerical determination of the position of a forward shock (i.e. to determine where the shock front is and where the downstream region ends) is specially difficult at the flanks of the shock wave. In these regions the changes of the velocity and of the magnetic field magnitude can be small. Hence, small variations on the numerical treatment of the jump conditions, can lead to rather different results (as those presented here).

The initial input pulse parameters that fit the shock arrival at 1.0 AU when using the Sun-centered pulse are: $v_s = 735$ km s^{-1}, $\omega = 140°$ and $\tau = 1$ hour for the Sep00 event. From this simulation, the observer establishes magnetic connection with the shock front at $t_c = 6.5$ hours. The values of VR derived from the off-center simulation are larger than those from the Sun-centered simulation (right panel of Figure C.3). The modified background solar wind speed ($v_r = 317$ km s^{-1} at 1.0 AU instead of the original corresponding value, $v_r = 360$ km s^{-1}) allows for a better fit of the jump in velocity at the shock passage by the spacecraft.

C.2 Apr00 event. Proton population from different IMF flux tubes

The time interval over which a gradual SEP event is observed frequently is larger than two days, from the parent solar activity that triggers the event up to the shock arrival. This extended duration implies that a large portion of the solar wind sweeps over the spacecraft carrying with the frozen magnetic field. Therefore, during a SEP event the spacecraft detects particles that propagate along different flux tubes. This effect requires a separate analysis to understand its possible influence on the outputs and has required a decision about how to further proceed.

This effect is significant for the Apr00 event for $E > 1.06$ MeV. The lower left panels of Figure 4.5 show a change in the magnetic field orientation that took place

shortly after doy 97.0 up to doy 97.3, and another one from then up to the shock passage. As can be seen, the high-energy (> 1.06 MeV) ion intensity fluctuates in accordance to the rapid changes in the orientation of the IMF. We interpret that this behavior implies that the cobpoint location at the shock front does not smoothly move and, consequently, that the observer detects magnetic flux tubes with different low- and high energy particle populations. At low-energy, this effect is tempered because the shock-acceleration processes work more efficiently throughout the shock propagation filling equally neighboring flux tubes. On the other hand, the efficiency of the shock as a high energy (> 1.06 MeV) shock-accelerated particle injector may be dependent on the region of the shock front where the cobpoint is located. The point is to evaluate how important is a precise modeling of those profiles for this period and how it may influence the injection rate of shock accelerated particles derived from the fittings and, consequently, how this affects the value of the coefficient k of the Q(VR) relation.

We have redone the fittings of the proton flux and anisotropies of this event by reproducing the high-energy proton intensity-time profile from doy 97 up to the shock arrival. Figure C.4 shows the resulting fittings (black dashed lines) with the same format as Figure 4.5. As can be seen, the three lower energy channels (left panels of Figure C.4) show near identical fittings as the corresponding energy windows in Figure 4.5. At higher energies (right panels) the computed flux profiles fit the decrease in the particle intensity seen after doy 97. The only change in the parameters of the particle modeling with respect to the simulation presented in Chapter 4 is the value of the spectral index of the injection rate, G, for $E > 1.06$ MeV that is assumed to be $\gamma = 2.75$ for $t > 28.6$ hours.

Figure C.5 shows the resulting evolution of the injection rate of shock-accelerated particles. The only significant difference with respect to Figure 4.6 is the evolution of Q for the $1.06-1.90$ MeV and $1.90-4.80$ MeV channels. For these energies, the injection rate decreases to lower values than those shown in the top panel of Figure 4.6. During four hours before the shock arrival there is an increase of the values of Q. This reflects the fact that the injection rate has to slightly increase just before the shock passage in order to account for the observed sharp increase at that time. The change in the evolution of Q translates into obtaining of higher values of the k coefficient than those shown in Table 4.1: 0.46 at $1.06-1.90$ MeV and 0.60 at $1.90-4.80$ MeV. It is worth noting that this change in the values of k has a small influence on the fluence of the SEP event computed in its upstream region ($\lesssim 10\%$).

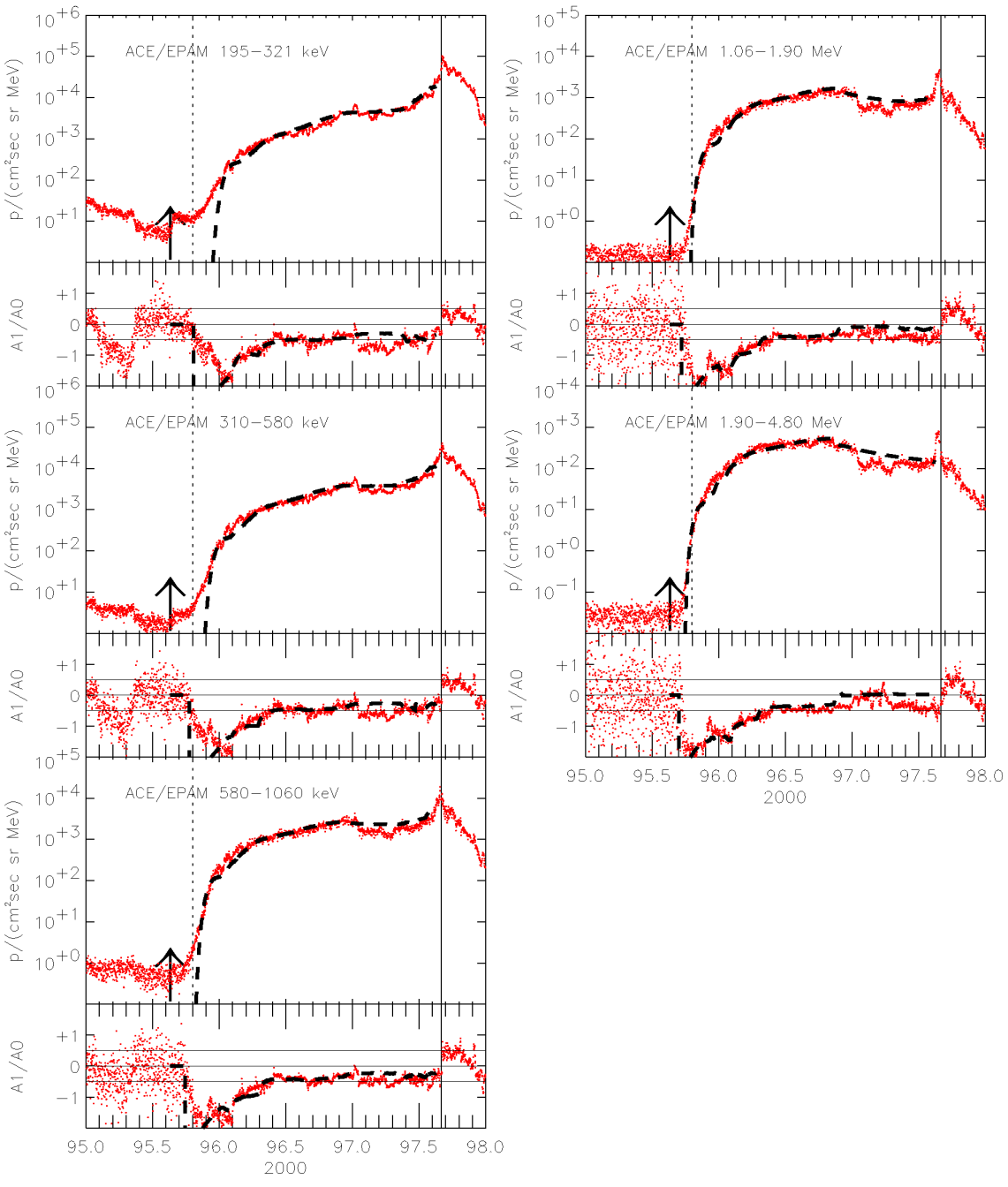

Figure C.4: Apr00 event. Flux and anisotropy profiles in the upstream region of the event, for five energy channels, from 195 keV to 4.8 MeV. Observed values are shown as red dots, computed values are represented by black dashed lines. To be compared with Figure 4.5.

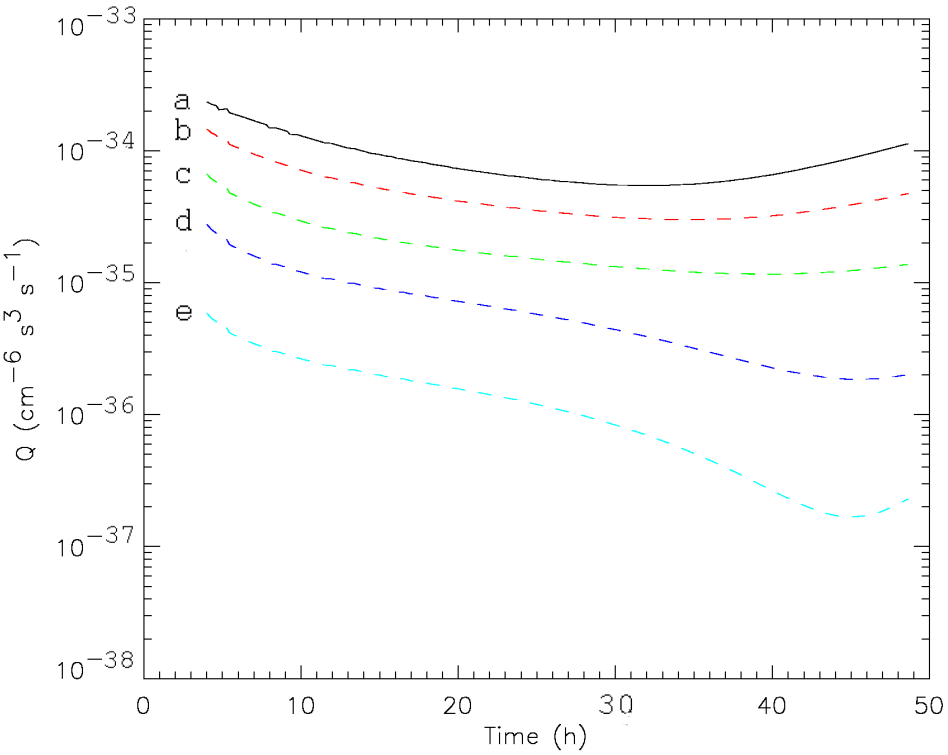

Figure C.5: Apr00 event. Evolution of the particle injection rate, Q, for five energy channels: a, 195 – 321 keV; b, 310 – 580 keV; c, 580 – 1060 keV; d, 1.06 – 1.9 MeV and d, 1.9 – 4.8 MeV. To be compared with top panel of Figure 4.6.

D Influence of the k-value in the flux profiles

Depending on the adopted value for k, the proton flux can show different profiles at low and high energies. Since k is a determinant variable to define a flux profile, the uncertainty of its value demands an evaluation of its influence on the generation of synthetic flux profiles. Here we show several examples that illustrate the dependence of the output profiles on k.

Figures D.1, D.2 and D.3 show computed flux and anisotropy profiles for six values of the energy between 0.250 MeV and 8.0 MeV, for three interplanetary scenarios. The upper panel of each plot displays the computed flux profile for a set of values of k; the corresponding lower panel shows the evolution of the first order anisotropy ('A10/A0'). The vertical dashed line marks the limit of the injection of solar-accelerated particles, that is, the time, t_c, when particles start being injected from the cobpoint at the front of the shock. The maximum value of the anisotropy at the onset of the events is 3, the theoretical value corresponding to the arrival to the position of the observer of 'the first particle'[1](with $\mu = 1$). Then, the anisotropy gradually decreases to zero up to the arrival of the shock[2]. In some cases, new injections of particles from the cobpoint yield to an increase of fluxes and anisotropy values as seen by an observer. The behavior of the anisotropy does not change significantly from case to case; therefore, we will not make any further comment on it.

Figure D.1 displays the flux profiles computed for a W45 event, with initial shock speed, $v_s = 900$ km s^{-1} and for an observer located at 1.0 AU (event W450900W10).

[1]This 'first particle' is never observed indeed, because of the existing background of particles.

[2]Although not for all events, see, for example, Sanahuja & Domingo 1987 and Heras et al. 1994.

The four profiles shown in this figure correspond to k = 0.5, 1.0, 2.0 and 2.5 (from top to bottom), a set of reasonable range of possible values for k derived from modeling SEP events of this type. The mean free path adopted for 0.5 MeV protons is $\lambda_{\parallel 0}$ = 0.8 AU (t < 35 hours) and $\lambda_{\parallel 0}$ = 0.2 AU (t > 35 hours) and with the energy dependence described in Section 5.2. The connecting time for this event is 5.0 hours and the transit time from the Sun to the spacecraft is 62.2 hours. These flux profiles present an initial maximum followed by a slow decrease, similar to the observed profiles at high energy (E > 2 MeV), for values of $k \geq 2$.

Figure D.2 displays the flux profiles obtained under the same conditions as in Figure D.1, but for v_s = 750 km s^{-1} (W450700W10). The 0.5 MeV proton mean free path taken is $\lambda_{\parallel 0}$ = 0.8 AU through the event and the presence of a turbulent region after 35 hours is assumed. This foreshock region is set as 0.06 AU wide and $\lambda_{\parallel 0c}$ = 0.01 AU for 0.5 MeV protons, producing the flux increase observed a few hours before the passage of the shock. The transit time of the shock is 72.4 hours. In this case the particle flux profile shows a decrease only for $k \geq 2.5$.

Figure D.3 shows the profiles for the same scenario as for the middle plot, but assuming $\lambda_{\parallel 0}$ = 0.2 AU. The conclusion in this case is that the mean free path does not play a relevant role in shaping the flux profiles. In fact, this is a valid conclusion for many interplanetary scenarios. This is the reason why: (i) SOLPENCO only considers two possible choices for the proton mean free path and (ii) when we analyze the distribution of the peak intensities and fluences provided by SOLPENCO in heliolongitude and initial shock speed we average the four transport conditions ($\lambda_{\parallel 0}$ = 0.2 AU and 0.8 AU and foreshock, Yes/No).

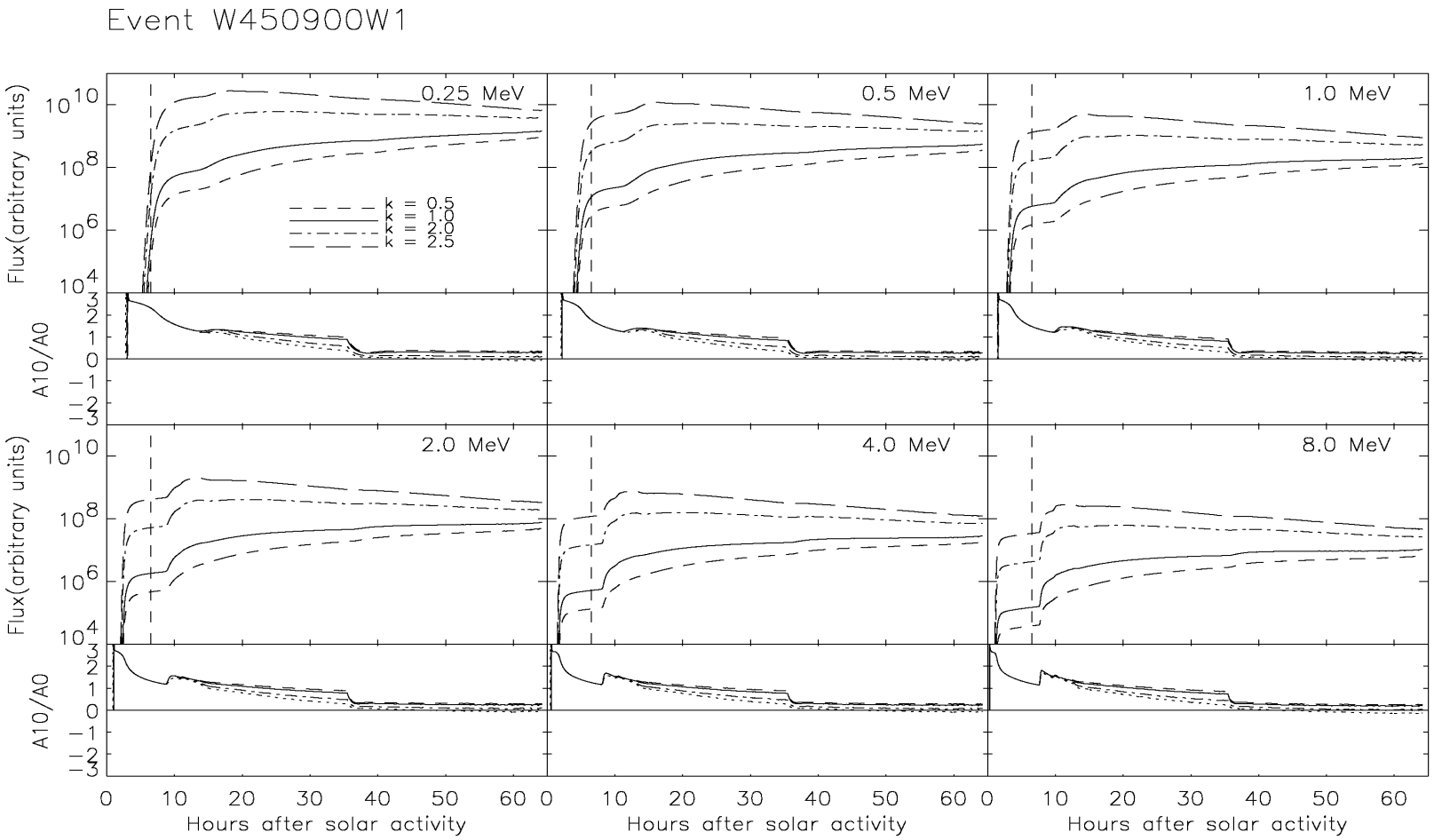

Figure D.1: Influence of k in the proton flux and first order anisotropy profiles under different scenarios at 1.0 AU for the event W450900W10 considering two values for the proton mean free path and without a foreshock region (see text for details).

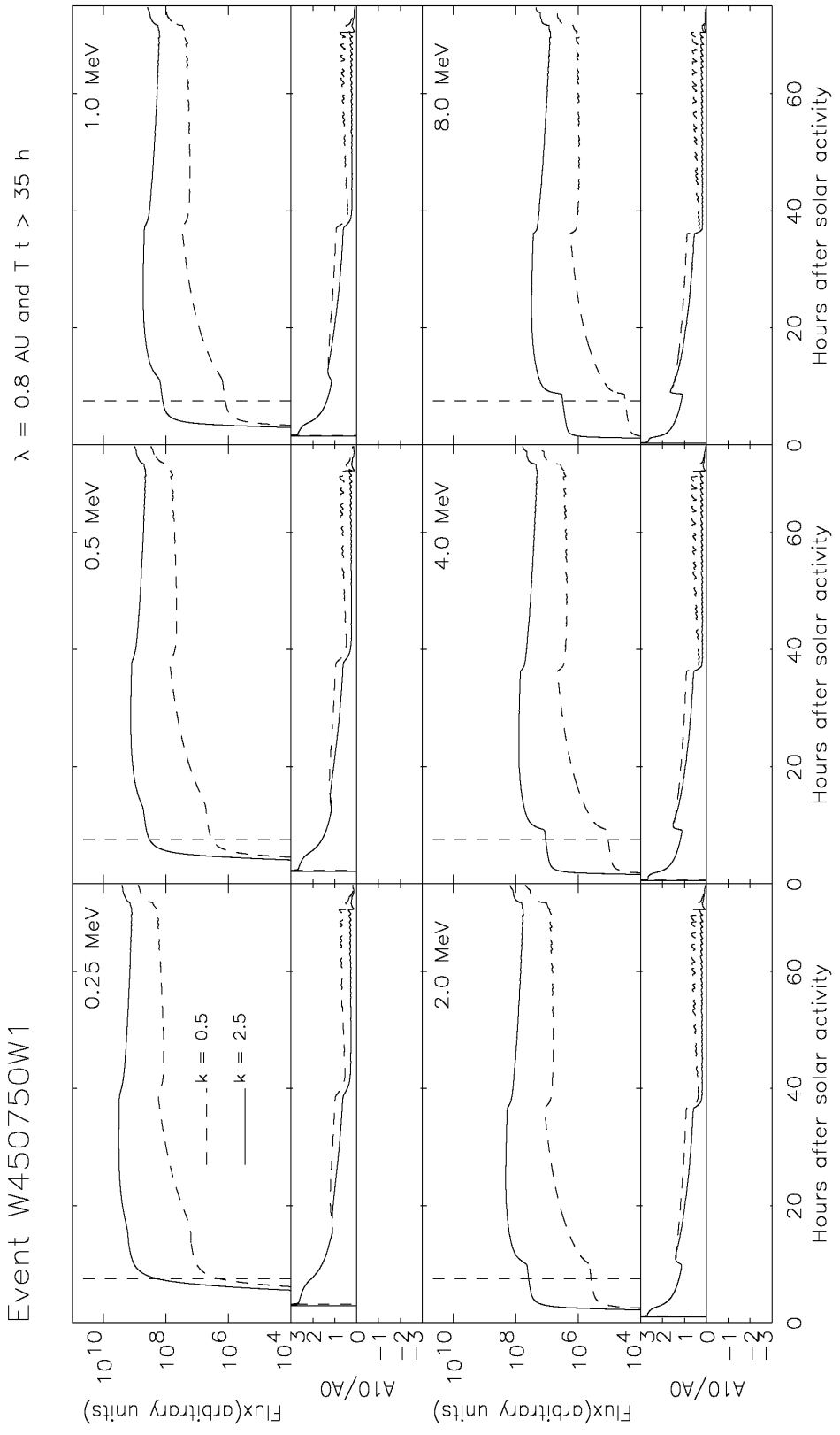

Figure D.2: Same as for Figure D.1 but for an event triggered by a slower shock, W450750W10, assuming a constant mean free path, $\lambda_{\parallel 0} = 0.8$ AU and an active foreshock from $t > 35$ hours.

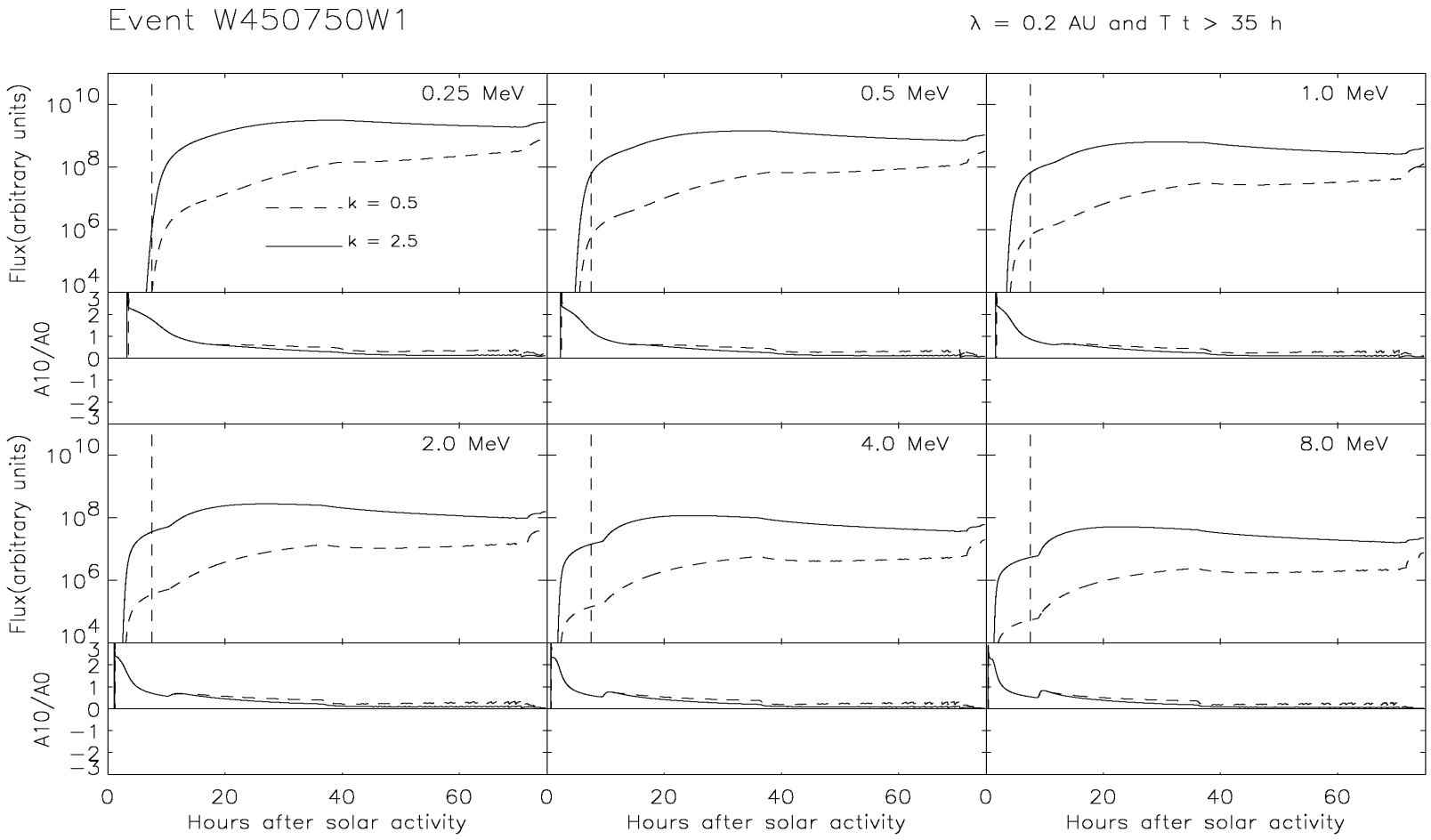

Figure D.3: Same as Figure D.2 but assuming $\lambda_{\|0} = 0.2$ AU.

E Values of Q_0 and k derived from formerly modeled SEP events

The simulation of these four SEP events was performed by Lario (1997), therefore the values of k and Q_0 are taken from that report (as well as the values of the initial conditions for the MHD simulation of the associated interplanetary shock). The description of each of these variables can be found in chapters 3 and 4. The observational data used to model the proton differential flux profiles of the energy channels presented here come from the DFH instrument aboard the ISEE-3 spacecraft (see section 2.5).

E.1 Feb79: 16 - 18 February 1979

E59 Feb79 VR $\in$ (0.2,0.4) $v_s = 1500$ km s^{-1} ($\omega = 90°$, $\tau = 1.5$ hours)

Table E.1: Feb79 SEP Event

Energy (MeV)	Q_s (cm^{-6} s^3 s^{-1})	k
0.384 – 0.620	8.1×10^{-38}	5.45
0.620 – 1.0	1.2×10^{-38}	5.84
5 – 10	4.5×10^{-46}	11.69
10 – 20	6.6×10^{-47}	13.38

E.2 Apr79: 22 - 24 April 1979

E10 Apr79 VR $\in$ (0.1,1.0) $v_s = 900$ km s^{-1} ($\omega = 72°$, $\tau = 12$ hours)

Table E.2: Apr79 SEP Event

Energy (MeV)	Q_s (cm^{-6} s^3 s^{-1})	k
0.384 – 0.620	1.3×10^{-34}	0.85
0.620 – 1.0	4.4×10^{-35}	0.69
5 – 10	1.7×10^{-36}	-0.77
10 – 20	6.8×10^{-39}	-1.76

E.3 Dec81: 5 - 8 December 1981

W40 Dec81 VR $\in$ (0.2,1.8) $v_s = 1000$ km s^{-1} ($\omega = 54°$, $\tau = 24$ hours)

Table E.3: Dec81 SEP Event

Energy (MeV)	Q_s (cm^{-6} s^3 s^{-1})	k
0.384 – 0.62	1.8×10^{-35}	0.48
0.620 – 1.0	8.8×10^{-36}	0.51
5 – 10	2.1×10^{-40}	1.83
10 – 20	2.3×10^{-41}	2.28

E.4 Apr81: 24 - 26 April 1981

W50 Apr81 VR $\in$ (0.5,4.2) $v_s = 2000$ km s^{-1} ($\omega = 30°$, $\tau = 2$ hours)

Table E.4: Apr81 SEP Event

Energy (MeV)	Q_s (cm^{-6} s^3 s^{-1})	k
0.384 – 0.62	5.2×10^{-35}	0.56
0.620 – 1.0	1.6×10^{-36}	0.52
5 – 10	6.1×10^{-39}	0.30
10 – 20	5.8×10^{-41}	0.56

F Input pulse and transit shock speeds in SOLPENCO

Smith & Dryer (1990) perform a 2.5D MHD parametric study of numerically simulated shocks using the MHD code developed by Wu et al. (1983). They conclude that the transit time to 1.0 AU of a shock can be obtained from a power-law dependence on the net input energy[1] into the solar wind when 'modest' initial angular widths, ω, (from 18° to 54°) and piston-driven durations, τ (0.5 to 2 hours) are taken into account and that this kind of dependence no longer holds for larger initial angular widths. The initial angular width, $\omega = 140°$, fixed to run the shock simulations of the data base of SOLPENCO is much larger than those values, therefore it is not possible to obtain a simple algebraic relation between the net input energy (i.e. the initial shock speed, v_s) and the transit time of the shock to 1.0 AU (i.e. the transit speed of the shock, $<v>$).

Figure F.1 shows the percentage of $<v>$ with respect to v_s for every observer's angular position and initial shock speed (symbol coded) considered in the data base of SOLPENCO at 1.0 AU (left panel) and at 0.4 AU (right panel). As can be seen, the relation between both speeds strongly depends on the angular position of the observer. This is a consequence of the fact that the shock strength diminishes as the angular separation from the leading position of the shock front (the nose of the shock) increases. This effect is shown in Figure 6 of Smith & Dryer (1990) for the 1.0 AU location and in Figures 5.7 and 5.8 of this report. For angular positions near the central meridian (that is, the observer intercepts the shock near its nose), it is possible to estimate the transit speed of the shock by simply using a percentage of the initial shock speed with an error of 5 – 10%. But the scatter of values shown

[1]The dominant input parameter is the initial pulse speed of the shock (usually referred as initial shock speed), v_s, because the net input energy is primarily kinetic energy (Smith et al. 2005).

for angular positions longer than ∼45° from central meridian does not allow us to obtain a simple relation between $< v >$ and v_s for the events described by those longitudes. This type of dispersion between the input energy and the transit time with the angular position of the observer is also reported by Smith & Dryer (1990).

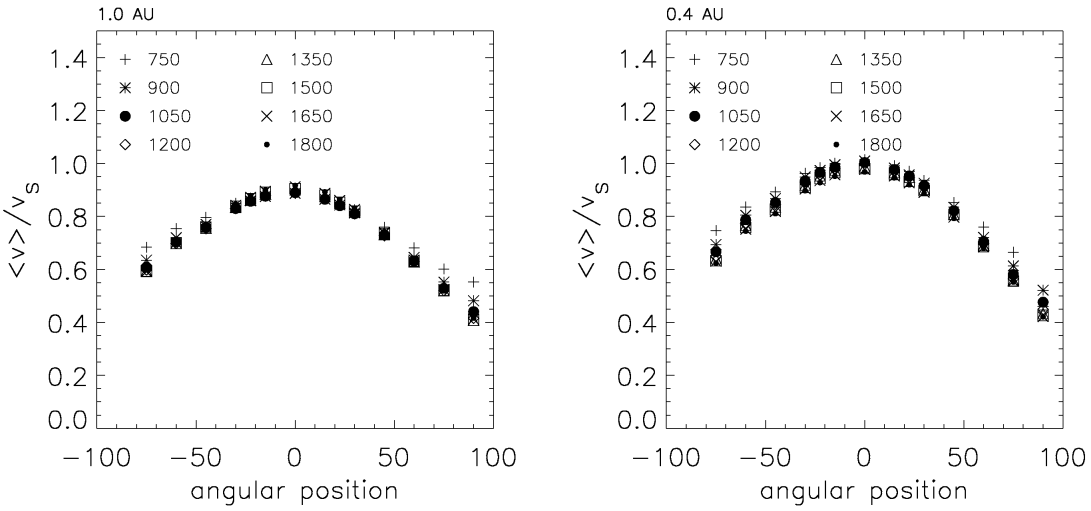

Figure F.1: Percentage of the transit speed of the shock ($< v >$) over the initial shock speed (v_s) for every observer's angular position considered in the data base of SOLPENCO. Left panel shows the values for observers located at 1.0 AU and the right panel those obtained for the observers at 0.4 AU. Each simulated shock initial pulse speed (in km s^{-1}) is indicated by a different symbol.

Taking into account this remarkable dependence of the transit speed of the shock (i.e. the transit time of its travel from the Sun up to the location of the spacecraft) with the heliolongitude from a given input energy (i.e. a given v_s) we decided to fit the transit velocities of the events contained in the data base of SOLPENCO as a function of the angular positions of the observers for each shock of the data base. In this way, it is possible to obtain the transit time of the interpolated events characterized by intermediate values of the angular position.

The transit time of an eastern event is shorter than that of the western event with an equidistant angular separation from the nose of the shock because of the effect of the solar rotation during the injection of the input pulse (see Chapter 5). To take into account this asymmetry two fittings have been performed for each initial shock speed: (i) for the western events (from W90 to W00) and (ii) for eastern events (from W00 to E75). Tables F.1 and F.2 give the coefficients of these two

Table F.1: Coefficients of the polynomial fitting at 1.0 AU.

v_s (km s^{-1})	Heliolongitude	a_0	a_1	a_2 (x10^{-1})	a_3 (x10^{-3})	a_4 (x10^{-5})
750	W90-W00	669.86	-0.50037	-0.32425	-0.32659	0.44191
	W00-E75	669.45	-1.30190	-1.39000	-2.33331	-1.44203
900	W90-W00	798.31	-0.50086	-0.52501	-0.27164	0.46241
	W00-E75	797.79	-1.90684	-2.04416	-3.46137	-2.14694
1050	W90-W00	934.20	-0.76638	-0.63515	-0.25712	0.45601
	W00-E75	933.40	-2.54097	-2.72559	-4.66654	-2.90733
1200	W90-W00	1071.47	-0.48238	-1.05680	0.37514	0.08085
	W00-E75	1070.57	-3.22181	-3.41769	-5.92135	-3.69455
1350	W90-W00	1214.75	-0.50557	-1.26237	0.55534	-0.00102
	W00-E75	1213.94	-3.35223	-3.76806	-6.53372	-4.10714
1500	W90-W00	1358.48	-0.30165	-1.59329	0.95180	-0.18651
	W00-E75	1357.49	-3.85004	-4.29880	-7.45251	-4.68371
1650	W90-W00	1505.08	-0.29453	-1.76248	0.99298	-0.14424
	W00-E75	1504.01	-4.09703	-4.74693	-8.27141	-5.22316
1800	W90-W00	1649.61	-0.15314	-2.01710	1.23823	-0.23558
	W00-E75	1648.24	-4.80410	-5.36666	-9.32527	-5.83460

polynomial fittings for observers located at 1.0 AU and at 0.4 AU, respectively. Each row displays the five coefficients of the fourth degree polynomial fit,

$$P_{v_s}(x) = a_0 + a_1 x + a_2 x^2 + a_3 x^3 + a_4 x^4,$$

where x is the heliolongitude of the associated solar event expressed in degrees, from 0° to 90° for western events and from -75° to 0° for eastern events. $P_{v_s}(x_j)$ gives the transit velocity, $<v>$, of an event characterized by the angular position x_j and initial shock speed, v_s. The units of the coefficient a_i is km $s^{-1}/[(^\circ)]^i$. Each table contains eight pairs of lines, corresponding to the coefficients for the eight pairs of curves shown in Figures 5.7 (upper line) and 5.8 (lower line), respectively; and from the lowest (first pair) to the highest (last pair) initial pulse velocity of the shocks, the value of which is indicated in the first column.

Table F.2: Coefficients of the polynomial fitting at 0.4 AU.

v_s (km s^{-1})	Heliolongitude	a_0	a_1	a_2 (x10^{-1})	a_3 (x10^{-3})	a_4 (x10^{-5})
750	W90-W00	759.48	1.73892	-2.10052	3.40557	-2.05915
	W00-E75	760.20	-1.13517	-1.34068	-2.00614	-1.19143
900	W90-W00	908.28	-0.54760	-0.62242	-0.31354	0.52311
	W00-E75	907.84	-2.01198	-2.23705	-3.70712	-2.33621
1050	W90-W00	1054.00	-0.62036	-0.73939	-0.42435	0.62504
	W00-E75	1053.12	-2.71531	-3.05875	-5.35052	-3.45483
1200	W90-W00	1196.34	-1.05795	-0.60333	-0.91110	0.89954
	W00-E75	1195.56	-2.45711	-3.01177	-5.07177	-3.30732
1350	W90-W00	1332.31	0.68220	-1.63516	0.60182	0.11786
	W00-E75	1331.41	-4.12910	-4.22852	-7.32766	-4.70668
1500	W90-W00	1469.94	-0.36575	-1.22948	-0.19778	0.52262
	W00-E75	1468.68	-4.68949	-4.88041	-8.58671	-5.52077
1650	W90-W00	1612.15	-0.12995	-1.76660	0.77940	-0.06347
	W00-E75	1610.74	-3.51069	-4.44843	-7.63722	-4.90436
1800	W90-W00	1743.04	-0.04537	-1.83831	0.64185	0.06063
	W00-E75	1741.68	-4.83791	-5.43829	-9.44831	-6.02887

G Checking the interpolation procedure

For a given set of parameters, we can compare the interpolated flux data, using the values previously calculated and stored, with the flux values directly derived when using the input SEP event parameters. These are extreme cases since real cases are interpolated among two values contained in the data base. That means that here we now interpolate cases using a grid twice less dense than the one used by SOLPENCO. In this way we can estimate the accuracy of the fit performed. We have tested many cases, those shown here display and summarize the main features of the procedure.

The first example, shown in Figure G.1, considers a flux profile generated by a W45-event, for three input velocities of 750, 825 and 900 km s^{-1}, with a turbulent foreshock region, and the observer located at 1.0 AU (W450825W10). The upper panel shows the interpolated flux (thick line) for $v_s = 825$ km s^{-1}, the corresponding computed profile (dotted line) which acts as fiducial event, as well as the two profiles from which the interpolation is performed (dashed and dashed-dotted lines). The lower panel shows the relative difference between the interpolated and the computed flux with $v_s = 825$ km s^{-1}; as can be seen the differences are below 10%. The peak differences occur when the flux profiles of the cases $v_s = 750$ km s^{-1} and $v_s = 900$ km s^{-1} show a different evolution at a given time. In this case around $t = 40$ hours when the effects of the foreshock regions are noticeable at 1.0 AU at different times due to the change in the slope of the interpolating profiles, which does not occur simultaneously.

The second example (Figure G.2) shows a shock with transit velocity of 750 km s^{-1}, but generated from three different longitudes with respect to the observer; in par-

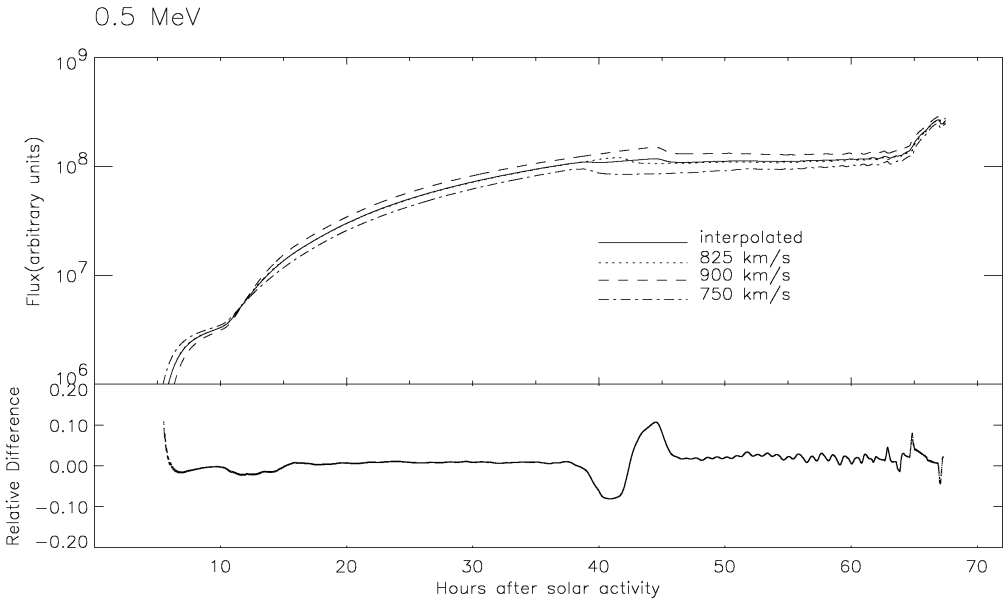

Figure G.1: Particle flux profiles and relative differences for a W45-event associated with a shock with an initial speed of 825 km s^{-1}. The interpolated flux is derived from the corresponding 750 and 900 km s^{-1} events of the data base.

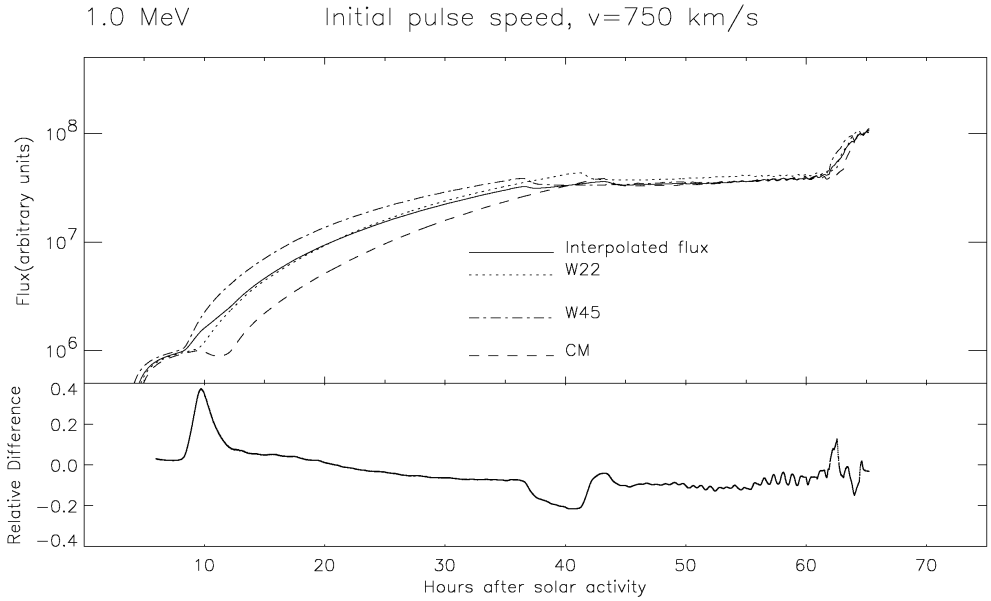

Figure G.2: Particle flux profiles and relative differences for a W00-event associated with a shock with an initial speed of 750 km s^{-1}. The interpolated flux is derived from the corresponding W22 and W45 events of the data base.

ticular W45 (dashed-dotted line), W22 (dotted line) and central meridian (CM or W00, dashed line). In the bottom panel the difference between the simulated W22 flux profile (W220750W10) and the flux profile obtained by interpolating the cases W45 and W00 (CM, represented by a solid line in the top panel) is shown. This difference is large at the onset of the event due to the combination of two factors: (i) the W45-event is connected to the shock 1 hour earlier than the W00-event and hence the flux of shock-accelerated particles starts to increase earlier and (ii) the western shock is connected to the nose of the shock early in this event, the most efficient region on the shock front in accelerating particles, while at the same time the central meridian event is connected to the eastern wing of the shock front. Therefore, at the very beginning of the connection, VR is higher for the western event than for the central meridian, and hence the injection rate, Q, allowing the flux profile of the W45-event to increase faster than that of the W00-event. It is worth to remark that this example represents the worst situation that could take place since we are using two events (W45 and CM) that are three times more distant in angular position that those of the data base of SOLPENCO between which the interpolation is performed. There are also peak differences ($< 20\%$) around $t = 40$ and 62 hours due to the effects of the foreshock region, as already commented in the previous case.

To better illustrate how the double interpolation is performed (i.e. the interpolation using different shock speeds and different observer's longitudes), the following figures show a typical case of a flux profile for 0.5 MeV protons. The selected initial velocity of the shock is 1200 km s^{-1} and the observer is at 1.0 AU, in W30 position (W301200W10). Figures G.3 and G.4 display the interpolated flux assuming a mean free path $\lambda_{\|0} = 0.2$ AU, Figure G.3 without considering the foreshock [l02TN] and Figure G.4 taking it into account [l02TY]. Figures G.5 and G.6 display the two same cases but with $\lambda_{\|0} = 0.8$ AU; [l08TN] and [l08TY], respectively. Each figure contains three plots with two panels. All plots show an upper panel with two flux profiles, and a lower panel displaying the differences between these profiles. The solid line is the flux profile resulting from the interpolation among profiles of the data base, whereas the dashed profile is the flux computed directly by the SEP model with the required parameters (neither interpolated nor from the data base).

The left upper panel in Figure G.3 shows the flux profile interpolated for W30 (solid line). It has been calculated from the fluxes picked up in the data base for the cases W45 and W15, and $v_s = 1050$ km s^{-1}, as well as the computed profile

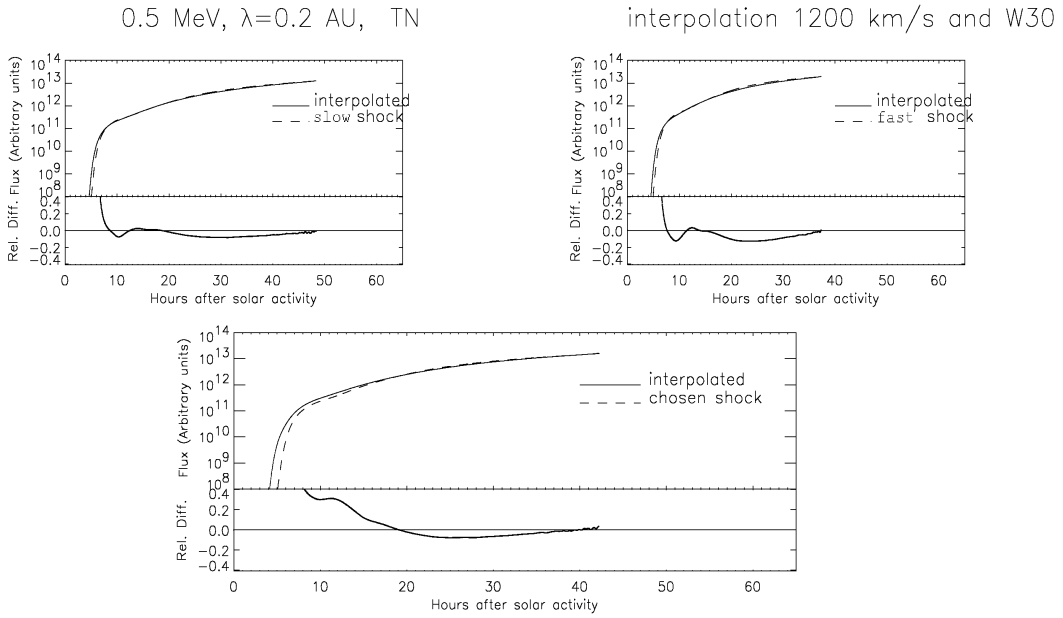

Figure G.3: Double interpolation for a W301200W10[l02TN] SEP event. Top left: interpolated flux profile using W45 and W15 to derive W30, and an initial shock speed of 1050 km s^{-1}(slow shock). Top right: the same as the left plot but for an initial speed of 1350 km s^{-1}(fast shock). Bottom: second interpolation using the two top profiles to derive the 1200 km s^{-1}case.

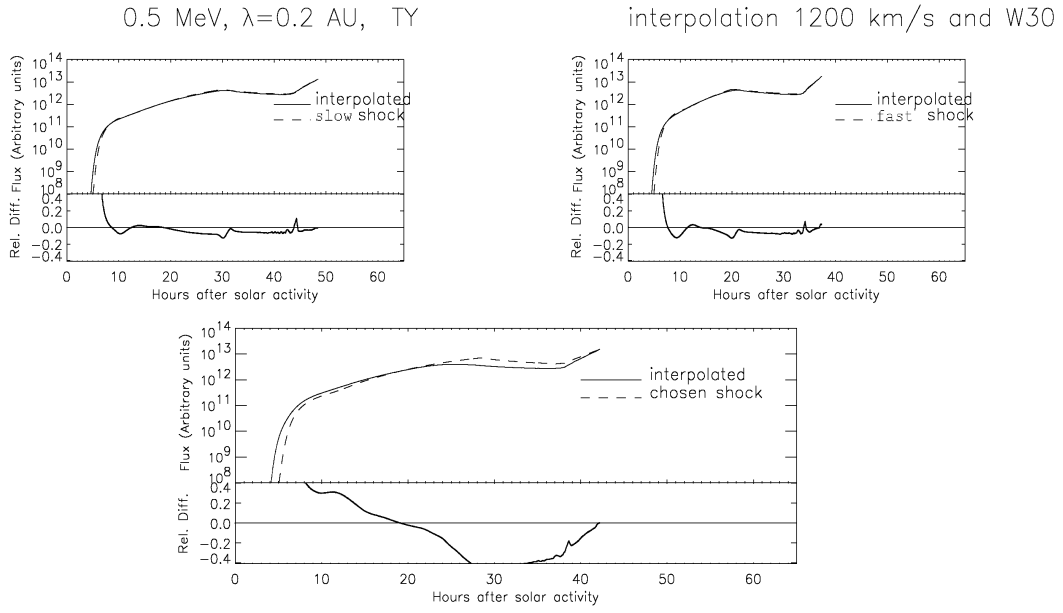

Figure G.4: The same as in Figure G.3 but with foreshock, event W301200W10[l02TY] for 0.5 MeV protons.

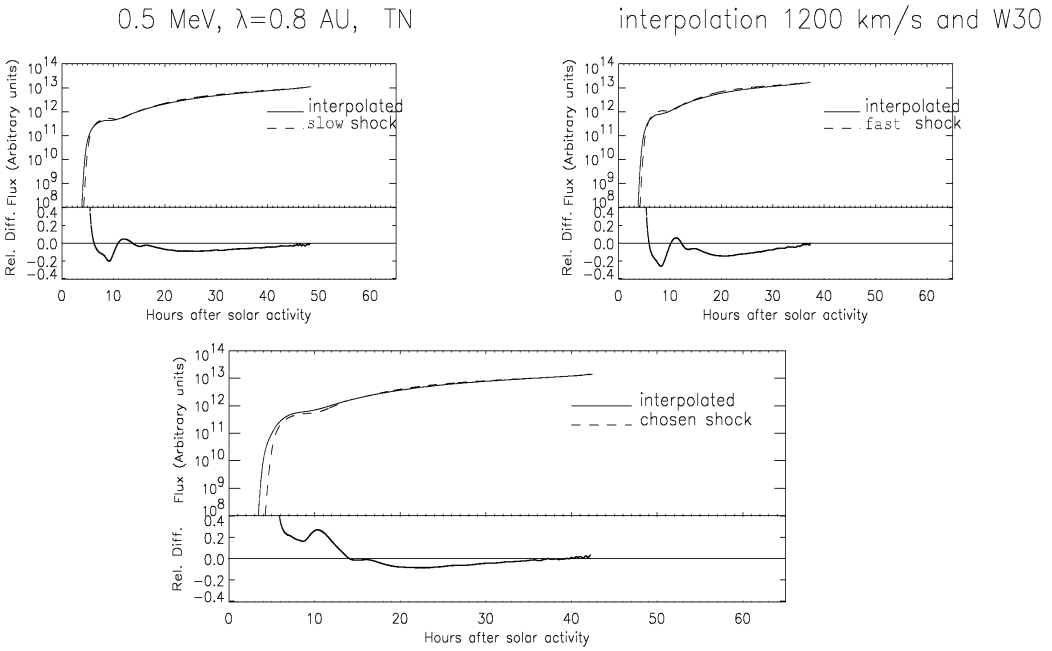

Figure G.5: The same as in Figure G.3 but for a particle mean free path of 0.8 AU, event W301200W10[l08TN] for 0.5 MeV protons.

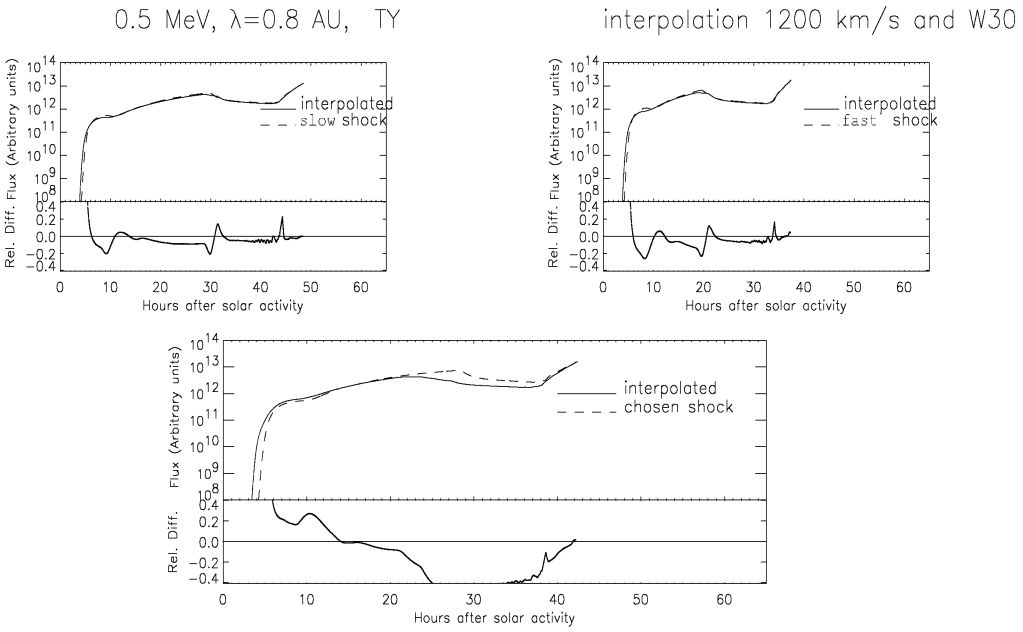

Figure G.6: The same interpolated as in Figure G.5 but with foreshock, event W301200W10[l08TY] for 0.5 MeV protons.

(dashed line). The difference among them is similar to those commented for events in Figure G.1; and the same is true for the profiles shown in the right upper plot, a W30 flux profile generated from the cases W45 and W15, but now with v_s = 1350 km s^{-1}. Finally, the lower plot displays the result obtained from interpolating the two upper flux profiles, which yields the interpolate flux profile for a W30 event and v_s = 1200 km s^{-1}(chosen shock).

As can be seen in these figures, the relative differences at the onset of the event increases from top to bottom: the connecting time differs due to the heliolongitude of the observers (top), and to the different speed of the shocks, which affects the connecting time, t_c (bottom). The differences at the arrival of the shocks are caused by the fact that the length of the profiles is not the same. The transit time for the v_s = 1050 km s^{-1} event (slow shock) is larger than for the 1350 km s^{-1} event (fast shock). Results shown in Figure G.4 essentially differ from those shown in Figure G.3 because of the presence of the turbulent region ahead of the front of the shock. In addition to the factors discussed for the case without turbulence, the foreshock keeps particles stalled in front of the shock, thus depleting the profile of the plateau. Since the effect that this region produces in the particle population depends on how fast the shock propagates, it translates into a supplementary source of differences between the interpolated flux profile and the profile directly computed. Figures G.5 and G.6 only differ from the former plots in the value of the particle mean free path (0.8 AU). They essentially show the same features (even slightly increased) that draw to the same conclusions.

The eight following plots, grouped in Figures G.7 and G.8 show different flux profiles obtained from the code, for the same energy (0.5 MeV), the same type of shock (the initial shock speed is 1450 km s^{-1}) and the same observer's location (at 1.0 AU). The indicators for events in Figure G.7 are W451450W10; for the top plots of Figure G.8 they are W001450W10, and E301450W10 for the bottom plots of Figure G.8. The differences among them arise from considering different heliolongitudes of the parent solar activity with respect to the observer (W45, CM and E30), the mean free of the particles (0.2 or 0.8 AU), and the presence or absence of a foreshock region ahead the shock (TY or TN). This is not a complete set of examples, but enough to give an overall idea of the outputs that the code can produce. In addition to the result of the interpolation obtained from the code (solid line), the top panel of each figure displays the flux derived directly from computing the same profile (dashed line). The bottom panels of each plot show the relative

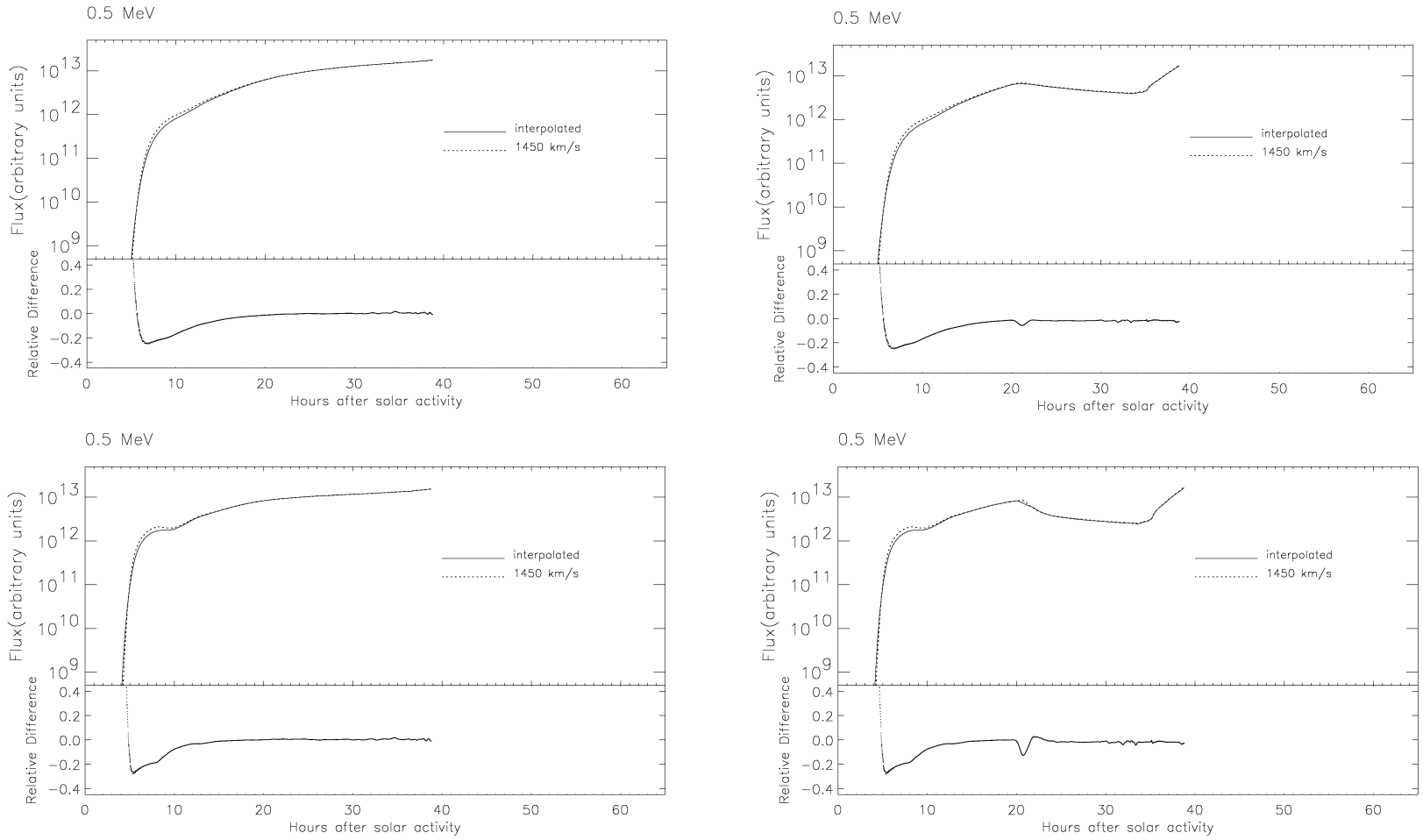

Figure G.7: Four different flux profiles obtained from the code and compared with the corresponding value of the data base. The bottom panel of each plot shows the relative difference between both flux profiles. The four cases correspond to a W451450W10 SEP event, where top left plot is [l02TN], top right [l02TY], bottom left is [l08TN] and bottom right is[l08TY].

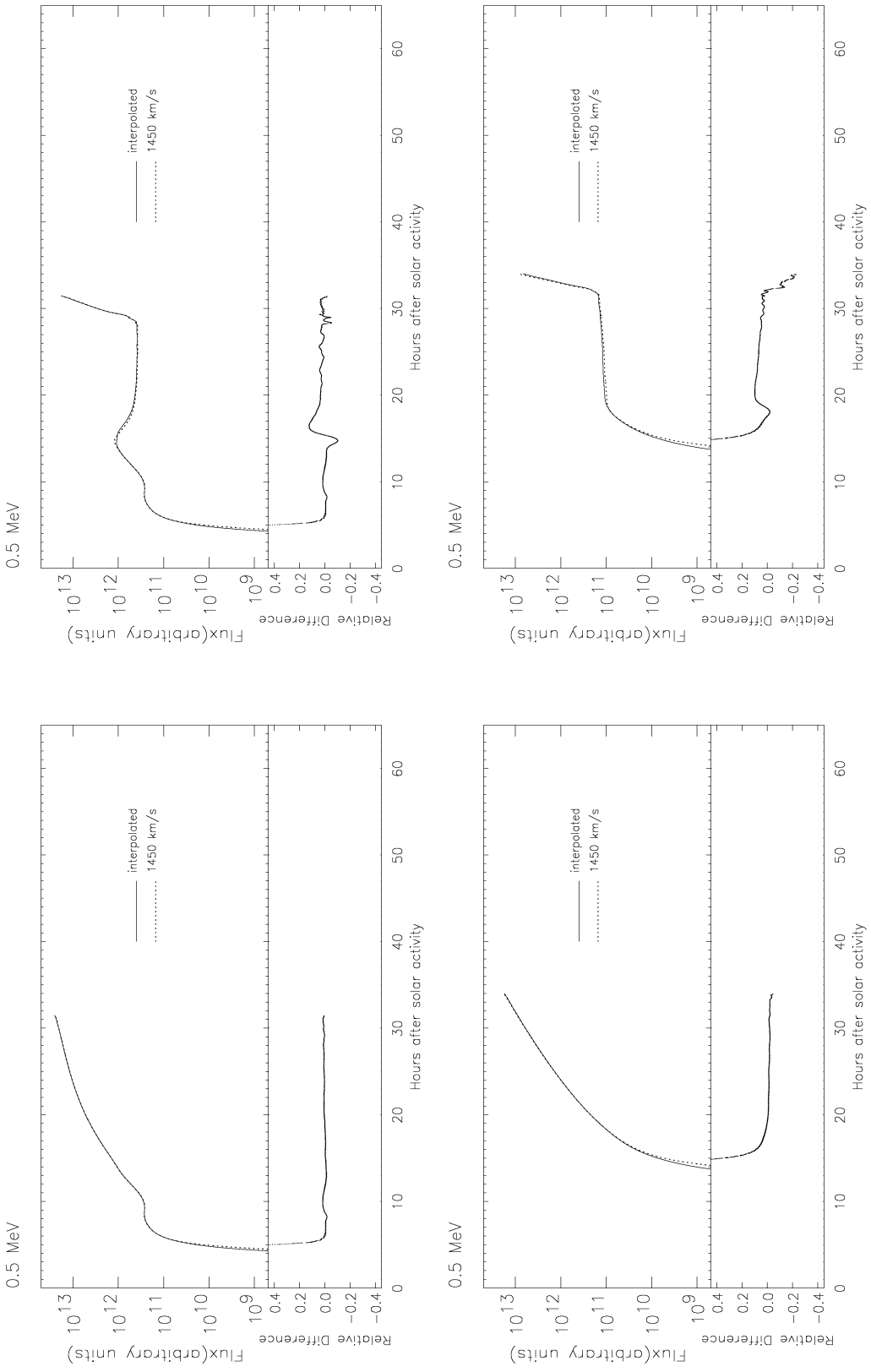

Figure G.8: Top plots are of the same type as in Figure G.7 for the case W001450W10; top left is [I08TN] and top right is [I08TY]. Bottom plots are alike top plots for the case E301450W10.

difference among these two values (from 40% to -40%).

The origin of time (hours) marks the onset of the parent solar activity, the last point of each curve the arrival of the shock at 1.0 AU. Note that the W45 events are longer than the CM events, and that those are longer than the E30 events. Furthermore, the onset of the W45 events occurs much earlier than for the eastern events; this simply reflects the time elapsed until the shock connects with the observer through the IMF lines.

The foreshock region keeps shock-accelerated particles close to the front while the shock propagates in the interplanetary medium. Once the shock is near enough to the observer the particle flux increases more or less rapidly, depending on the size of the foreshock region; the result is a depleted plateau and a larger ESP spike. This can be seen by comparing the pairs of plots TY/TN in these figures. The presence of a foreshock region of different characteristics for the two profiles, from which the interpolation is performed, increases the differences at certain points. This is even clear for the E30 event (Figure G.8). In spite of the small visual difference between both profiles (remember that this is a logarithmic scale), the error increases at the shock arrival. This suggests the possibility of a logarithmic instead of a linear interpolation, but there is no physical argument to proceed that way; the most evident choice is, however, the reduction of the grid-size when necessary (i.e. increase the number of events in the database from which to perform interpolations).

H Basic information about SOLPENCO

This document is the file 'Readme.txt' enclosed in SOLPENCO's program and data files package. The main features of the code are described in this file together with complementary references. This document is updated as the last updates and modifications of SOLPENCO are performed. These improvements are listed and specified at the beginning of the file.

```
*************************************************************************
*            "An Engineering Model for Solar Energetic Particles        *
*                    in Interplanetary Space (SOLPENCO)"                *
*************************************************************************
Created: 15/01/2001; Last Revised: 15/04/2006
Author: Angels Aran (e-mail:aaran@am.ub.es)
        Departament d'Astronomia i Meteorologia
        Universitat de Barcelona


SOLPENCO v1.2 Supported by
Ministerio de Educación y Ciencia. Spain. Project AYA2004-03022
Ministerio de Ciencia y Tecnologia. Spain. Project AYA2001-03304

SOLPENCO v1.0 and v1.1 Supported by
ESTEC/ESA Contract 14098/99/NL/MM
Ministerio de Ciencia y Tecnologia. Spain. Project AYA2001-03304
Centre de SuperComputacio de Catalunya (CESCA)

*************************************************************************
Modification: 15/04/2006 - SOLPENCO v1.2

1) New output: The maximum intensity of the SEP event (the peak flux) has
been included as output information, both in the graphical display and in
the ascii data file. The time at which the peak flux is reached is also
indicated.

2) Correction of 0.4 AU output data:  A missing factor was localized in the
normalization of the data at 0.4 AU. The quotient between the cross sections
of the magnetic flux tube at 1.0 and 0.4 AU has been added, to translate
from columnar intensities to intensities in the phase space.

3) SOLPENCO is thought to be run under a LINUX OS. If it is run in Windows
OS a few things have to be changed in the code: a) Replace set_plot,'x' by
set_plot,'WIN' and b) replace in every file path '/' by '\' .
*************************************************************************
References: 15/12/2005
Updated information about SOLPENCO's results can be found at:

1) Aran A., B. Sanahuja and D. Lario, Fluxes and fluences of SEP events
derived from SOLPENCO, Annales Geophysicae, 23, 3047-3053, SRef-ID:
1432-0576/ag/2005-23-3047 (2005)

2) Aran A., B. Sanahuja and D. Lario, SOLPENCO: A SOLar Particle
ENgineering COde, Advances in Space Research, In Press, Corrected Proof,
Available online 2 November (2005)
*************************************************************************
Modification: 15/12/2004 - SOLPENCO v1.1

1) Change in the output graphic display: From now is saved in Portable
Network Graphics (PNG) format; not in the JPEG format used in the previous
version.

2) Output images files and ascii data files are stored in the folders
"outfigures" and "outdata", respectively. They have to be created by the
user before running the code and in the folder where SOLPENCO is executed.

3) The code runs successfully under IDL 6.0
*************************************************************************
Reference update: 15/07/2004

Final Report (FR): Aran A., B. Sanahuja and D.Lario,
'An Engineering Model for Solar  Energetic Particles in Interplanetary
Space'. ESA Final Report Contract (April 2004),
http://space-env.esa.int/Final_Presentations/esa_contract.html and/or
http://www.am.ub.es/~blai/grupospacew_UB.html for the Final Report and the
```

Appendices.
****
Revised: 05/12/2003- SOLPENCO v1.0
---

1. Introduction

This code is written in IDL language. It runs successfully under IDL version 5.4. Not yet proved in more recent IDL versions.

The code provides proton flux and cumulative fluence profiles at 0.125, 0.250 0.5,1, 2, 4, 8, 16, 32 and 64 MeV for a set of gradual SEP events, and for observers located at either 1.0 AU or 0.4 AU. The code also gives the transit time and velocity of the shock from the Sun to the observer and the total fluence of the SEP event computed from the onset of the event up to the arrival of the associated transient CME-driven shock.

We have built up a data base containing synthetic proton flux and cumulative fluence profiles for 448 scenarios for spacecraft located either 1.0 AU or at 0.4 AU (see details in FR). This code is based on the model by Lario et al. (1998) assuming a series of supplementary hypotheses. The simulation of the evolution of particle injection and propagation, and the characteristics of the code used to produce the data base are described in Lario (1997). We use the 2 1/2-D MHD code by Wu et al. (1983) to simulate the propagation of the CME-driven shock by assuming an initial input pulse at 18 solar radii from the Sun.

2. Brief Description of the Code

The code is described in the section 3 of the Final Report ('SolpencoI_7.pdf', hereafter FR). Below we summarize the basic procedures of the programme and provide some additional useful information.

The main programme is SOLPENCO.PRO. It reads the data base and allows the user to choose several characteristics of the event. The database is composed of four arrays: 'flux_at_1au.fits', 'flux_at_04au.fits', 'fluence_at_1au.fits', and 'fluence_at_04au.fits'. To read these files the following non-standard IDL routines from the public IDL Astronomy Library are needed: READFITS(), GETTOK(), IEEE_TO_HOST, STRNUMBER(), SXADDPAR, SXDELPAR, SXPAR() and WHERENAN(). They are included in the attached folder named 'IDLroutines'.

The subroutine INT3.PRO carries out the following procedures:

a) It interpolates among the calculated scenarios of the database when necessary (see section 3.5.3 of FR for details). To perform the interpolation the code needs some additional information of the shock which is read from the files 'entrades10.dat' and 'entrades04.dat'. Both files contain: the shock initial pulse velocity; the time of the shock passage by the observer's location and the averaged shock transit velocity at that position. Additional information contained in these two files is the coefficients of the four order polynomial fitting to the shock transit velocities at each angular position for each shock. First, those corresponding to the set of western observers and second, those for eastern observers. These coefficients are required in order to to obtain better interpolated shock transit times when the interpolation is performed between events with different heliolongitudes (we refer the user to section 3.5.3 of FR for a details).

b) It normalizes the obtained flux profiles to physical units. Thus, the units of the proton intensity profiles delivered by the code are: flux in (cm^2 sr s MeV)^-1 and fluence (cm^2 sr)^-1. To translate to units of cm^-2, the fluence values should be multiplied by the solid angle covered by the detector.

c) It calculates the transit time and velocity of the shock and the total

fluence of the event.

d) It produces the graphical display of the results. And

e) It generates ASCII/JPEG files to store the results.

3. Using the code

3.1. When running the code for the first time a welcome window pops up. The programme starts when the user clicks on the "continue" button.

3.2. Then the code asks the user to select the input parameters that describe the wanted SEP event:
- The heliocentric distance of the observer (0.4 AU or 1.0 AU).
- The initial pulse velocity of the associated shock (from 750 km/s to 1800 km/s).
- The heliolongitude of the parent solar activity with respect to the Sun-Observer line: (from E75 to W90)
- The proton mean free path for 0.5 MeV protons (0.2 AU or 0.8 AU)
- The existence of a turbulent 'foreshock' region, (YES/NO).
- The proton energy (0.125,0.25,0.5,1,2,4,8,16,32 or 64 MeV).

After that, the code displays a window listing the parameters introduced by the user. The code continues when clicking the "dismiss" button.

3.3. Next, the code indicates the velocity and heliolongitude of the closest events contained in the database. After computing the proton flux and fluence of the selected event, the programme allows the user to choose the display of the results: (option 1) only the flux profile; (option 2) only the cumulative fluence profile; (option 3) both flux and cumulative fluence profiles. Then the programme shows a window with the selected plot (flux or cumulative fluence vs time) and two panels at the top. The left panel lists the parameters selected by the user, and the right panel contains the transit time and velocity of the shock as well as the total fluence (in the upstream region) of the event.

3.4. Next, the code allows the user to save the window display in JPEG format and/or to save the results in a data ASCII file.

3.5. Finally, the code allows the user to either run another case with a new set of parameters or exit.

4. WARNING!

This is not an operative code for prediction, because:
- It has not been validated yet.
- The interplanetary scenarios in the database are limited in number.
- The interpolation algorithm and the initial database grid are subject of constant improvement.
- The empirical relationship Q(VR) used to describe the particle injection along the shock front and throughout the SEP event must be checked for more solar/interplanetary particle events.
- The initial conditions near the Sun are not related to proxy indicators of solar activity.
- The input/output interfaces have not been fully developed to provide an easy interaction for external users.

Consequently, this code has to be taken as a first step towards full proton flux prediction useful for space weather - not as an operational tool.

Any suggestion or comments are welcomed.

5. References:

- Lario D.: 'Propagation of low-energy particles through the interplanetary medium: modeling their injection from interplanetary shocks'. Ph.D. Thesis, University of Barcelona (1997).

- Lario D., B. Sanahuja, and A.M. Heras: Astrophys. J. 509, 415 (1998).

- Wu, S.T., M. Dryer, and S.M. Han: Solar Phys. 84, 395 (1983).

I Table of IP Shocks - Solar Origin

No.	Doy	Interplanetary Shock Date (mm/dd)	Time at ACE (UT)	Solar Origin CME Date (mm/dd)	Time (UT)	V_{CME} (km/s)	Type	Peak Flare (Xray/H_α)	Onset Time	H_α Location	Ref
				1998							
1	049	02/18	07:52	02/14	06:55	123	P	n. id.	- -	S24 E23	1,2,3a
2	063	03/04	10:58	02/28	12:48	176	H	B1.1	11:38	S24 W01	1,2,3b,4
3	097	04/07	16:51	04/02	18:30	155	P	C1.8/SF	16:43	S23 E23	1,3c
4	113	04/23	17:28	04/20	10:07	1863	H	M1.4	09:38	S43 W90	3d,5,6,7,8,9,10
5	120	04/30	08:43	04/27	08:56	1039	H	X1.0/2B	08:55	S16 E50	3e,11,12
6	121	05/01	21:22	04/29	16:58	1374	H	C6.8/3B	16:05	S18 E20	1,2,4,10,13
7	123	05/03	17:00	05/02	14:06	938	H	X1.1/3B	13:31	S15 W15	1,2,7,11,14,15
8	135	05/15	13:57	05/11	21:35	1100	H	n. id.	- -	N32 W90	2,12
9	149	05/29	15:04	05/27	13:45	910	P	n. id.	13:13	S21 W83	10,13
10	168	06/17	20:46	06/16	18:27	1612	P	M1.0	18:03	S17 W90*	10,15,16,17
11	176	06/25	15:43	06/21	05:35	192	P	C2.7/SF	04:59	N17 W25	1,2,3f
12	238	08/26	06:21	08/24	Data Gap			X1.0/3B	21:48	N35 E09	2,11,13,18, 19,20a,21
13	267	09/24	23:13	09/23	Data Gap			M7.1/3B	06:44	N18 E09	2,11,13
14	275	10/02	06:53	09/30	Data Gap			M2.8/2N	14:02	N23 W81	11
15	291	10/18	19:01	10/15	10:04	262	H	EIT/DF	- -	N22 W01	1,2,16
16	312	11/08	04:21	11/05	20:44	1128	H	M8.4/2B	19:50	N22 W18	2,10,11,16,22
17	334	11/30	04:18	11/28	08:30	805	P	X3.3/3N	06:05	N17 E32	11
				1999							
18	013	01/13	09:58	01/11	Data Gap			C1.2/SF	17:52	S28 W03	3g
				01/10	Data Gap			C1.0/SF	02:45	S28 E10	3h
19	022	01/22	19:48	01/19	Data Gap			C2.5/SF	01:28	S24 E01	3i

Interplanetary Shock			Solar Origin							
No. Doy	Date (mm/dd)	Time at ACE (UT)	CME Date (mm/dd)	Time (UT)	V_{CME} (km/s)	Type	Peak Flare (Xray/H_α)	Onset Time	H_α Location	Ref
			1999							
			01/20	Data Gap			M5.2/SF	21:23	S24 W25	3i,15
			01/20	Data Gap			M5.2/-	19:06	S99 W90	14
			01/20	Data Gap			M5.2/-	19:06	S99 E95	13
20 049	02/18	02:09	02/16	Data Gap			M3.2/SF	02:49	S23 W14	2,13,14,23
21 069	03/10	00:40	03/07	05:54	835	P	n. id.	- -	S20 E15	1,16
22 106	04/16	10:35	04/13	03:30	291	H	n. id.	- -	N16 W00	1,2,4
			04/13	03:30	293	P	n. id.	- -	N20 E10	24,25
23 125	05/05	14:59	05/03	06:06	1584	H	M4.4/2N	05:36	N15 E32	5,10,14
24 177	06/26	02:17	06/22	18:54	1133	H	M1.7/1N	18:18	N22 E37	2,3j,12
25 177	06/26	19:25	06/24	13:31	975	H	C4.1/1F	13:21	N29 W13	2,3j,21,25
26 183	07/02	00:24	06/29	07:31	634	H	C3.0/SF	06:25	N19 E02	1,3k,10
27 187	07/06	14:17	07/03	19:54	536	P	C7.5/1F	20:00	N16 W55	2,3k
28 216	08/04	01:16	08/01	19:27	1133	P	SF	18:21	N25 E13	1,20b
29 220	08/08	17:44	08/04	06:26	383	P	M6.0/1N	05:45	S16 W64	20b,25,26
30 234	08/22	22:49	08/20	13:26	265	P	M1.8	12:36	S29 E75	20b,25,26
31 265	09/22	11:46	09/20	06:06	604	H	n. id.	- -	S20 W05	1,2,20c
			09/20	06:06	604	H	C2.2	- -	S24 E13	22
32 294	10/21	01:38	10/18	00:06	247	P	n. id.	- -	S30 E15	1,2,16
			10/18	00:06	371	P	C1.2	- -	S40 E05	22
33 301	10/28	11:26	10/25	14:26	511	P	C1.2	- -	S20 E05	1,20d
			2000							
34 022	01/22	00:22	01/18	17:54	739	H	M3.9/1N	17:07	S19 E11	1,2,10,12,13
35 042	02/11	02:13	02/08	09:30	1079	H	M1.3/1B	08:42	N25 E26	1,2,16,20e
36 042	02/11	23:19	02/10	02:30	944	H	C7.3/1N	01:40	N31 E04	1,2,20e
			02/09	19:54	910	H	C7.4/2F	19:15	S17 W40	20e,21,22
37 045	02/14	06:57	02/12	04:31	1107	H	M1.7/1N	03:51	N26 W23	1,2,10,12,13,20e
38 051	02/20	20:47	02/17	20:06	600	H	M1.3/2N	20:17	S29 E07	2,4,10,12,13,20e
			02/17	20:06	600	H	M2.5/1B	18:41	S25 W12	1,2,20e
39 097	04/06	16:04	04/04	16:32	1188	H	C9.7/2F	15:12	N16 W66	2,5,10,13,14,16,27
40 156	06/04	14:23	05/31	08:06	396	H	n. id.	- -	N28 E04	2,16
			06/02	10:30	442	H	C2.4/SF	09:00	N10 E23	1,10,20f
41 160	06/08	08:41	06/06	15:54	1119	H	X2.3/3B	14:58	N20 E18	2,5,10,20f,28,29

No.	Interplanetary Shock Doy	Date (mm/dd)	Time at ACE (UT)	Solar Origin CME Date (mm/dd)	Time (UT)	V_{CME} (km/s)	Type	Peak Flare (Xray/H_α)	Onset Time	H_α Location	Ref
				2000							
42	175	06/23	12:27	06/20	09:10	464	P	n. id.	- -	S30 W30	1,20f
43	192	07/10	05:58	07/07	10:26	453	H	C5.6/SF	08:42	N17 E10	1,2,20g
				07/07	10:26	453	H	M1.3/SF	10:56	N23 W41	2,20g,30
44	193	07/11	11:23	07/08	23:50	483	P	-/SF	23:28	N18 W12	1
45	195	07/13	09:19	07/10	21:50	1372	P	M5.7/2B	21:05	N18 E49	20g,25,31,32,33
				07/11	13:27	1078	H	X1.0 2N	13:20	N18 E27	2,10,12,20g,21,25
				07/11	13:27	1078	H	X1.0/1B	11:33	N16 E40	2,20g,30
46	197	07/15	14:15	07/14	10:54	1640	H	X5.7/3B	10:03	N22 W07	31
47	201	07/19	14:49	07/17	08:54	788	116	C5.3/1F	08:24	S10 E36	2,20g,33
48	208	07/26	17:55	07/23	05:30	631	P	C2.8/SF	05:34	S12 W44	2,3l,20g
49	210	07/28	05:43	07/24	23:54	320	P	n. id.	- -	N05 W10	1,20g
50	210	07/20	09:10	07/25	03:30	528	H	M8.0/2B	02:43	N06 W08	1,20g
51	223	08/10	04:07	08/06	23:06	597	P	n. id.	- -	S20 W30	1
				08/06	18:30	233	P	n. id.	- -	S99 E90	22
52	224	08/11	18:11	08/09	16:30	702	H	C2.3/SF	15:19	N11 W11	1,2,4,20h,22,24
53	227	08/14	21:35	08/12	14:54	876	P	C3.2/SF	13:48	N13 W46	10,20h,25
				08/12	10:35	662	P	M1.1/SF	09:45	S17 W79	2-20h,10
54	250	09/06	16:13	09/04	06:06	849	P	DSF	05:01	N12 W37	3m,20i,25
55	259	09/15	04:00	09/12	11:54	1550	H	M1.0/2N	11:31	S17 W09	1,2,5,20i 25,34,35,36
56	261	09/17	16:57	09/16	05:18	1215	H	M5.9/2B	04:06	N14 W07	1,13,20i,22
57	277	10/03	00:08	09/30	18:06	703	P	M1.0/SF	17:38	S20 E42	4,20i
58	278	10/04	13:37	10/02	03:50	525	H	C4.1/SF	02:48	S09 E07	20j
59	279	10/05	02:40	10/02	20:26	569	H	C8.1/F	19:59	S09 W00	1,2,20j,22
60	286	10/12	21:45	10/09	23:50	798	H	C6.7/1F	23:19	N01 W14	1,2,10,20j
61	302	10/28	05:41	10/25	08:26	770	H	C4.0	- -	N18 W23	22
	302	10/28	09:08	10/25	08:26	770	H	C4.0	08:45	N17 W66	2,10,17
62	305	10/31	16:30	10/29	Data Gap			M4.4/2B	01:28	S25 E35	3n,13,20j,37
63	309	11/04	01:35	11/01	16:26	801	H	C2.2/SF	15:51	N06 E24	20k,25
64	311	11/06	09:15	11/03	18:26	291	H	C3.2/SF	18:35	N02 W02	1,4,20k
65	315	11/10	06:04	11/08	23:06	1738	P	M7.4/1N	22:42	N10 W75	31, 48
66	331	11/26	05:00	11/24	05:30	994	H	X2.0/3B	04:55	N20 W05	1,4,10,14,20k
67	331	11/26	11:24	11/24	15:30	1245	H	X2.3/2B	14:51	N22 W07	1,2,10,14, 17,20k,38

Interplanetary Shock			Solar Origin							
No. Doy	Date (mm/dd)	Time at ACE (UT)	CME Date (mm/dd)	Time (UT)	V_{CME} (km/s)	Type	Peak Flare (Xray/H_α)	Onset Time	H_α Location	Ref
			2000							
68 333	11/28	04:57	11/26	17:06	980	H	X4.0/2B	16:34	N18 W38	17,20k,22,39
69 338	12/03	03:21	11/30	Data Gap			M1.3/SF	20:27	S14 E23	20k
			2001							
70 013	01/13	01:42	01/10	00:54	832	H	C5.9/1N	00:34	N13 E36	3o-20l,13
71 023	01/23	10:06	01/20	21:30	1507	H	M7.7/2B	21:06	S07 E46	2,10,13,14,20l
72 031	01/31	07:22	01/28	15:54	916	P	M1.5/1N	15:40	S04 W59	5,6,10,13
73 051	02/20	00:54	02/15	13:54	625	H	EF/B8.8	13:08	N07 E12	1,3p,20m,25,40
74 062	03/03	10:39	02/28	14:50	313	P	EIT EF	- -	S02 W12	1,2,40
75 078	03/19	10:22	03/16	03:50	271	P	EIT EP	- -	N11 W09	1,2,4,24
76 081	03/22	12:43	03/19	05:26	389	H	EIT EF	- -	S05 W00	1,3g,40
77 086	03/27	01:09	03/24	20:50	906	H	M1.7/2N	19.37	N15 E22	10,20n-25,31
78 086	03/27	17:15	03/25	17:06	677	H	C9.0/1F	16:25	N16 E25	2,17,20n,31
79 089	03/30	21:52	03/28	12:50	519	H	M4.3/SF	11:21	N18 E02	20n,25,41
			03/28	01:27	427	H	C5.6/SF	01:29	N20 E22	20n,25
80 090	03/31	00:23	03/29	10:26	942	H	X1.7/2N	09:57	N16 W12	1,5,10,20n,24,41
			03/28	12:50	519	H	M4.3/SF	11:21	N18 E02	2,31
81 090	03/31	22:56	03/29	10:26	942	H	X1.7/2N	09:57	N16 W12	2,10,13,31
82 094	04/04	14:23	04/02	22:06	2505	P	X20/?	21:32	N17 W78	2,5,6,10,13,31,41
83 097	04/07	16:59	04/05	17:06	1390	H	M5.1/2N	16:57	S24 E50	20o,25,30,41
84 098	04/08	10:33	04/06	19:30	1270	H	X5.6/SF	19:10	S21 E31	2,20o,25,39
85 101	04/11	13:15	04/09	15:54	1192	H	M7.9/2B	15:20	S21 W04	1,10,13,17 20o,41,42
86 101	04/11	15:28	04/10	05:30	2411	H	X2.3/3B	05:06	S23 W09	1,10,27,31,41,42
87 103	04/13	07:14	04/11	13:31	1103	H	M2.3/1F	12:56	S22 W27	1,2,20o
88 108	04/18	00:04	04/15	14:06	1199	P	X14.4/2B	13:19	S20 W85	5,6,10,13,24 25,31,41,43–46
89 111	04/21	15:06	04/18	02:30	2465	H	C2.2	02:12	S20 W120	10,13,20o, 31,41,45
			04/19	12:30	392	P	DSF/EIT	- -	N20 W20	1,4
90 118	04/28	04:32	04/26	12:30	1006	H	M7.8/2B	11:26	N17 W31	2,4,5,10,13,31
91 126	05/06	07:06	05/03	09:30	434	114	C2.9/SF	07:54	N13 W21	3r-20p
92 132	05/12	09:24	05/10	01:31	1056	P	C5.6/1N	01:05	N24 W65	20p
93 147	05/27	14:17	05/24	20:26	387	P	M1.2/1N	19:30	N07 E29	3s-20p
			05/25	04:06	569	P	n. id.	- -	S09 E04	4
94 158	06/07	08:53	06/04	16:30	464	P	C3.2/SF	16:25	N24 Wf59	10,17,20q

No.	Interplanetary Shock Doy	Date (mm/dd)	Time at ACE (UT)	Solar Origin CME Date (mm/dd)	Time (UT)	V_{CME} (km/s)	Type	Peak Flare (Xray/H_α)	Onset Time	H_α Location	Ref
				2001							
				06/05	05:06	836	P	M2.5/2N	04:44	S18 E44	20q
95	169	06/18	01:55	06/15	15:56	1701	H	n. id.	15:24	SXX W120	4,10,34
96	215	08/03	06:26	07/31	Data Gap			DSF	09:38	S39 E07	3t,20r
97	224	08/12	10:49	08/09	10:30	479	P	n. id.	- -	N05 W05	1,10,20s
98	229	08/17	10:16	08/14	16:01	618	H	EIT EF	13:19	N20 W05	2,10,24,31
99	239	08/27	19:19	08/25	16:50	1433	H	X5.3/3B	16:23	S17 E34	2,20s,25,31
100	256	09/13	01:40	09/11	14:54	791	H	C3.2/SF	14:00	N13 E35	20t,25,31,39
101	257	09/14	01:18	09/11	21:30	646	P	n. id.	- -	S00 E05	1,20t
102	268	09/25	20:02	09/24	10:30	2402	H	X2.6/2B	09:32	S16 E23	37
103	272	09/29	09:06	09/27	04:54	509	P	C3.8/SF	04:22	S20 W27	1,2,20t
104	273	09/30	18:47	09/28	08:54	846	H	M3.3/2N	08:10	N10 E18	1,2,20t,31
105	281	10/08	12:20	10/05	10:06	1537	H	n. id.	- -	Backside	40
106	284	10/11	16:20	10/09	11:30	973	H	M1.4/2F	10:46	S28 E08	1,2,10,20u,37,39
107	294	10/21	16:12	10/19	16:50	901	H	X1.6/2B	16:13	N15 W29	1,2,10,20u,27,47
108	298	10/25	08:02	10/22	15:06	1336	H	M6.7/2N	14:27	S21 E18	1,10,20u,27,37
109	301	10/28	02:42	10/25	15:26	1092	H	X1.3/2B	14:42	S16 W21	1,2,20u,37
110	304	10/31	12:53	10/29	11:50	598	P	M3.6/1F	10:56	N12 E25	1,20u
111	319	11/15	13:55	11/12	03:50	180	P	SF	03:47	N13 E71	25
112	323	11/19	17:35	11/17	05:30	1379	H	M2.8/1N	04:49	S13 E42	2,10,20v,27,47
113	334	11/30	17:28	11/28	17:30	500	H	M6.9/1B	16:26	N04 E16	20v,25
114	363	12/29	04:48	12/26	05:30	1446	P	M7.1/1B	04:32	N08 W54	2,6,10,20w,27,38
115	364	12/30	19:31	12/28	20:30	2216	H	X3.4	20:02	S26 E90	5,10,20w,25

References

1, Manoharan, P. K. et al., JGR, 109, A06109, doi:10.1029/2003JA010300, 2004

2, Cane, H. V., and I. G. Richardson, JGR, vol. 108, A4, 1156, doi:10.1029/2002JA009817, 2003.

3, PRF[1], a: 1172, b: 1174, c: 1179, d: 1182, e: 1183, f: 1190, g: 1219, h: 1218, i: 1221, j: 1243, k: 1244, l: 1299, m: 1036, n: 1313, o: 1324, p: 1329, q: 1334, r: 1340; s: 1343, t: 1353.

[1]Prelinimary Report and Forecast of Solar Geophysical Data, fom NOAA/SEC, http://www.sec.noss.gov/weekly/index.html

4, Gopalswamy, N., et al., Adv. in Space Research, doi:10.1016/j.asar.2004.07.014, 2005 in press.
5, Gopalswamy, N., et al., JGR, vol. 109, A12105, doi:10.1029/2004JA010602, 2004.
6, Tylka, A.J. et al., ApJ, 625, 474-495, 2005.
7, Cane, H.V. et al., GRL, vol. 30, 12, 8017, doi:10.1029/2002GL016580, 2003.
8, Maia, D., et al., ApJL, 528, 49-51, 2000.
9, Bastian, S. T., et al., ApJL, 558, 65-69, 2001.
10, Kahler, S. W. ApJ, 628, 1014, 2005.
11, Lario, D., et al., JGR, vol. 105, A8, 18,251-18,274, 2000.
12, Gopalswamy, N., et al., JGR, vol. 106, A12, 29,219-29,229, 2001.
13, Cane, H.V., et al., JGR, vol. 107, A10, 1315, doi:10.1029/2001JA000320, 2002.
14, von Rosenvinge, T. T., et al., Proceedings of ICRC 2001, 3126, 2001.
15, Reames, D. V., et al., ApJ, 550, 1064-1074, 2001.
16, Gopalswamy, N., et al., JGR, vol. 106, A12, 29,207-29,217, 2001.
17, Gopalswamy, N., et al., ApJL, 572, 103-107, 2002.
18, Bale, S. D., Reiner, M. J., Bougeret, J.-L., et al., GRL, 26, 11, 1573-1576, 1999.
19, Tylka, A. J. et al., GRL, 26, 14, 2141-2144, 1999.
20, SGD[2], a: 649, b: 666, c: 667, d: 668, e: 672, f: 676, g: 677, h: 678, i: 679, j: 680, k: 681, l: 683, m: 684, n: 685, o: 686, p: 687, q: 688, r: 689, s: 690, t: 691, u: 692, v: 693, w: 694.
21, Smith, Z., et al., JGR, vol. 109, A01110, doi:10.1029/2003JA010044, 2004.
22, Zhang, J. et al., ApJ, 582, 520-523, 2003.
23, Lario, D., Haggerty, D. K., Roelof, E.C., et al., Space Science Reviews, 97, 277-280, 2001.
24, Cid, C., et al., Solar Physics, 223, 231-243, 2004.
25, url1[3].
26, Kim, Y.-H., Moon Y.-J., Cho, K.-S., et al., ApJ, 622, 1240-1250, 2005.
27, Aran, A., et al., accepted in Adv. Space Research, 2005.
28, Gopalswamy, N., GRL, 30, 12, 8013, doi:10.1029/2003GL017277, 2003.
29, Deng, N., Liu, C., Yang, G., et al., ApJ, 623, 1195-1201, 2005.
30, Dryer, M., Fry, C. D., Sun, W., et al., Solar Physics, 204, 267-286, 2001.
31, Lario, D., Livi, S., Roelof, E. C., et al., JGR, 109, A09S02, doi:10.1029/2003JA010107, 2004.
32, Bieber, J. W., Dröge, W., Evenson, P. A., et al., ApJ, 567, 622-634, 2002.
33, Smith, C. W., Ness, N. F., Burlaga, L. F., et al., Solar Physics, 204, 229-254, 2001.
34, Cane, H. V., and Erickson, W. C., JGR, vol. 108, A5, 1203, doi:10.1029/2002JA009488,

[2]Solar Geophysical Data Reports, from NOAA/SEC, ftp://ftp.ngdc.noaa.gov/STP/SOLAR_DATA/SGD_PDFversion

[3]http://cdaw.gsfc.nasa.gov/CME_list/

2003.
35, Aran, A., et al., Adv. Space Res., doi:10.1016/j.asr.2004.06.023, 2005 (Available online from 15 June 2005).
36, Qiu, J., Wang, H., Cheng, C.Z., et al., ApJ, 604, 900-905, 2004.
37, Lario, D., Roelof, E.C., Decker, R. B., et al., Adv. Space Res., 32, 4, 579-584, 2003.
38, Cane, H.V., von Rosenvinge, T. T., Cohen, C. M. S. et al., GRL, 30, 12, 8017, doi:10.1029/2002GL016580, 2003.
39, Michalek. G., Gopalswamy, N., Lara, A., et al., A&A, 423, 729-736, 2004.
40, url2[4];
41, Sun, W., Dryer, M., Fry, C. D., et al., Annales Geophysicae, 20, 937-945, 2002.
42, Reames, D. V. and Tylka, A. J., ApJL, 575, 37-39, 2002.
43, Tylka, A.J., Boberg, P. R., Cohen, C. M. S., et al., ApJL, 581, 119-123, 2002.
44, Lario, D., Decker, R. B. and Armstrong, T. P., Proceed. ICRC 2001, 3254, 2001.
45, Johnson, A. S., Golightly, M. J., Lin, T., et al., Adv. Space Res.,
doi:10.1016/j.asr.2005.04.083, 2005, in press.
46, Bieber, J. W., Evenson, P. A., Dröge, W., et al., ApJL, 601, 103-106, 2004.
47, Lario, D., Decker, R. B., Roelof, E. C., et al., JGR, 109, A01107,
doi:10.1029/2003JA010171, 2004.
48, Nitta, N.V., Cliver, E.W. and Tylka, A.J., ApJ, 586, L103, 2003.

[4]http://lasco-www.nrl.navy.mil/cmelist.html

Bibliography

Agueda, N., Vainio, R., Lario, D., & Sanahuja, B. 2007, ApJ, Submitted

Antiochos, S. K., DeVore, C. R., & Klimchuk, J. A. 1999, ApJ, 510, 485

Anttila, A., Kocharov, L. G., Torsti, J., & Vainio, R. 1998, Ann. Geophys., 16, 921

Aran, A., Lario, D., Sanahuja, B., et al. 2007, A&A, 469, 1123

Aran, A., Sanahuja, B., & Lario, D. 2001, in ESA SP-493: Solar encounter. Proceedings of the First Solar Orbiter Workshop, ed. B. Battrick, H. Sawaya-Lacoste, E. Marsch, V. Martinez Pillet, B. Fleck, & R. Marsden, 157–160

Aran, A., Sanahuja, B., & Lario, D. 2004, Final Report ESA/ESTEC Contract 14098/99/NL/MM.
(http://space-env.esa.int/Final_Presentations/esa_contract.html)

Aran, A., Sanahuja, B., & Lario, D. 2005a, Adv. Space Res., 36, 2333

Aran, A., Sanahuja, B., & Lario, D. 2005b, Ann. Geophys., 23, 3047

Aran, A., Sanahuja, B., & Lario, D. 2006, Adv. Space Res., 37, 1240

Armstrong, T. P., Chen, G., Sarris, E. T., & Krimigis, S. M. 1977, in Study of Travelling Interplanetary Phenomena 1977, ed. M. A. Shea, D. F. Smart, & S. T. Wu, 367–388

Armstrong, T. P., Pesses, M. E., & Decker, R. B. 1985, Geophys. Monogr. Ser., Vol. 35, Shock Drift Acceleration, ed. B. T. Tsurutani & R. G. Stone (Whashington, D.C.: AGU), 271–286

Aschwanden, M. J. 2002, Space Sci. Rev., 101, 1

Baker, D. N., Braby, L. A., Curtis, S., et al. 2006, Space Radiation Hazards and the Vision for Space Explortion: Report of a Workshop (Washington DC: The National Academies Press), (SRH06)

Balch, C. 1999, Radiat. Meas., 30, 231

Bale, S. D., Reiner, M. J., Bougeret, J.-L., et al. 1999, Geophys. Res. Lett., 26, 1573

Balogh, A., Hynds, R., van Dijen, G., et al. 1978, IEEE Trans. on Geoscience Electronics, 16, 176

Bamert, K., Kallenbach, R., Ness, N. F., et al. 2004, ApJ, 601, L99

Barouch, E. & Raguideau, J. 1970, A&A, 9, 146

Beeck, J., Mason, G. M., Hamilton, D. C., et al. 1987, ApJ, 322, 1052

Beeck, J. & Sanderson, T. 1989, J. Geophys. Res., 94, 8769

Berezhko, E. G., Petukhov, S. I., & Taneev, S. N. 2001, in 27th ICRC, 3215–3218

Brueckner, G. E., Howard, R. A., Koomen, M. J., et al. 1995, Sol. Phys., 162, 357

Burlaga, L. F., Lepping, R. P., & Jones, J. A. 1990, Geophys. Monogr. Ser., Vol. 58, Global configuration of a magnetic cloud (Whashington DC: AGU), 373–377

Campeanu, A. & Schlickeiser, R. 1992, A&A, 263, 413

Cane, H. V. 1988, J. Geophys. Res., 93, 1

Cane, H. V. 1997, Geophys. Monogr. Ser., Vol. 99, The current status in our understanding of energetic particles, coronal mass ejections, and flares, ed. N. e. a. Crooker (Whashington, D.C.: AGU), 205–215

Cane, H. V. & Erickson, W. C. 2003, J. Geophys. Res., 108, 8

Cane, H. V. & Erickson, W. C. 2005, ApJ, 623, 1180

Cane, H. V., Erickson, W. C., & Prestage, N. P. 2002, J. Geophys. Res., 107, 1315

Cane, H. V. & Lario, D. 2006, Space Sci. Rev., 123, 45

Cane, H. V., McGuire, R. E., & von Rosenvinge, T. T. 1986, ApJ, 301, 448

Cane, H. V., Mewaldt, R. A., Cohen, C. M. S., & von Rosenvinge, T. T. 2006, J. Geophys. Res., 111, 6

Cane, H. V., Reames, D. V., & von Rosenvinge, T. T. 1988, J. Geophys. Res., 93, 9555

Cane, H. V. & Richardson, I. G. 2003, J. Geophys. Res., 108, 6

Cane, H. V., Sheeley, Jr., N. R., & Howard, R. A. 1987, J. Geophys. Res., 92, 9869

Cane, H. V., von Rosenvinge, T. T., Cohen, C. M. S., & Mewaldt, R. A. 2003, Geophys. Res. Lett., 30, 5

Cargill, P. J. & Schmidt, J. M. 2002, Ann. Geophys., 20, 879

Chané, E., Jacobs, C., van der Holst, B., Poedts, S., & Kimpe, D. 2005, A&A, 432, 331

Chané, E., van der Holst, B., Jacobs, C., Poedts, S., & Kimpe, D. 2006, A&A, 447, 727

Chao, J. K. & Hsieh, K. C. 1984, Planet. Space Sci., 32, 641

Chen, J. & Krall, J. 2003, J. Geophys. Res., 108, 1410

Cleghorn, T. F., Saganti, P. B., Zeitlin, C. J., & Cucinotta, F. A. 2004, Adv. Space Res., 33, 2215

Cliver, E. W. 1995, Sol. Phys., 157, 285

Cliver, E. W. 1996, in American Institute of Physics Conference Series, ed. R. Ramaty, N. Mandzhavidze, & X.-M. Hua, 45

Cliver, E. W. 2000, in AIP Conf. Proc. 528: Acceleration and Transport of Energetic Particles Observed in the Heliosphere, ed. R. A. Mewaldt, J. R. Jokipii, M. A. Lee, E. Möbius, & T. H. Zurbuchen, 21–31

Cliver, E. W. & Cane, H. V. 1996, J. Geophys. Res., 101, 15533

Cliver, E. W. & Cane, H. V. 2002, EOS Trans. AGU, 83, 61

Cliver, E. W. & Hudson, H. S. 2002, J. Atmos. Solar-Terr. Phys., 64, 231

Cliver, E. W., Kahler, S. W., Neidig, D., et al. 1995, in Proc. 24^{th} Int. Cosmic Ray Conf., Vol. 4, 257–260

Cliver, E. W., Kahler, S. W., & Reames, D. V. 2004, ApJ, 605, 902

Cliver, E. W., Klecker, B., Kallenrode, M.-B., & Cane, H. 2002, EOS Trans. AGU, 83, 132

Cliver, E. W. & Ling, A. G. 2007, ApJ, 658, 1349

Cohen, C. M. S., Mewaldt, R. A., Leske, R. A., et al. 1999, Geophys. Res. Lett., 26, 2697

Daly, E., Nieminen, P., Hilgers, A., & et al. 2005, Technical Note, TEC-EES/2005.265/ED, ESA

Davis, A. J., Mewaldt, R. A., Cohen, C. M. S., et al. 2001, J. Geophys. Res., 106, 29979

Desai, M. I., Mason, G. M., Dwyer, J. R., et al. 2001, ApJ, 553, L89

Domingo, V., Sanahuja, B., & Heras, A. M. 1989, Adv. Space Res., 9, 191

Domingo, V., Sanahuja, B., & Wenzel, K.-P. 1981, in 17th ICRC, Vol. 3, 109–112

Dryer, M. 1994, Space Sci. Rev., 67, 363

Dryer, M. 1996, Sol. Phys., 169, 421

Dryer, M., Smith, Z., Fry, C. D., et al. 2004, Space Weather, 2, 9001

E-10-04, E. 2000, European Cooperation for Space Environment Standards. ESA publication

Ellison, D. C. & Ramaty, R. 1985, ApJ, 298, 400

Feynman, J., Armstrong, T. P., Dao-Gibner, L., & Silverman, S. 1988, in Interplanetary Particle Environment, ed. J. Feynman & S. Gabriel, JPL Publication 88-28, JPL, California Institute of Technology, Pasadena, CA, 58–71

Feynman, J. & Gabriel, S. 1988, Interplanetary Particle Environment, JPL Publication 88-28 (JPL, California Institute of Technology, Pasadena, CA)

Feynman, J. & Gabriel, S. B. 1996, IEEE Trans. Nucl. Sci., 43, 344

Feynman, J. & Gabriel, S. B. 2000, J. Geophys. Res., 105, 10543

Feynman, J. & Hundhausen, A. J. 1994, J. Geophys. Res., 99, 8451

Feynman, J., Ruzmaikin, A., & Berdichevsky, V. 2002, J. Atmos. Solar-Terr. Phys., 64, 1679

Feynman, J., Spitale, G., Wang, J., & et al. 1993, J. Geophys. Res., 98, 13281

Fisk, L. A. 1971, J. Geophys. Res., 76, 1662

Forbes, T. G., Linker, J. A., Chen, J., et al. 2006, Space Sci. Rev., 123, 251

Forman, M. A. & Webb, G. M. 1985, Geophys. Monogr. Ser., Vol. 34, Acceleration of energetic particles, ed. R. G. Stone & B. T. Tsurutani (Whashington, D.C.: AGU), 91–114

Foullon, C., Crosby, N., & Heynderickx, D. 2005, Space Weather, 3, 7004

Foullon, C., Holmes-Siedle, A., Crosby, N. B., & Heynderickx, D. 2004, Radiation Hazard and Space Weather Warning System, work package in Radiation Exposure and Mission for Interplanetary Manned Missions (REMSIM) (Noorwidjk, The Netherlands: European Space Agency)

Freier, P. S. & Webber, W. R. 1963, J. Geophys. Res., 68, 1605

Gabriel, S. B. & Feynman, J. 1996, Sol. Phys., 165, 337

Giacalone, J. & Jokipii, J. R. 1999, ApJ, 520, 204

Gloeckler, G., Fisk, L. A., Zurbuchen, T. H., & Schwadron, N. A. 2000, in AIP Conf. Proc. 528: Acceleration and Transport of Energetic Particles Observed in the Heliosphere, ed. R. A. Mewaldt, J. R. Jokipii, M. A. Lee, E. Möbius, & T. H. Zurbuchen, 221–224

Gold, R. E., Krimigis, S. M., Hawkins, III, S. E., et al. 1998, Space Sci. Rev., 86, 541, (Gol98)

Golightly, M., Barth, J., Bieber, J., et al. 2005, Radiation Working Group Report, Greenbelt, MD, (RWG05)

Gopalswamy, N. 2004a, Astroph. and Space Science Libr., Vol. 314, , ed. D. Gary & C. U. Keller (Kluwer Academic Publishers), 305

Gopalswamy, N. 2004b, Astroph. and Space Science Libr., Vol. 317, , ed. G. Poletto & S. T. Suess (Kluwer Academic Publishers), 201

Gopalswamy, N., Aguilar-Rodriguez, E., Yashiro, S., et al. 2005, J. Geophys. Res., 110, A12S07

Gopalswamy, N., Kaiser, M. L., Lepping, R. P., et al. 1998, J. Geophys. Res., 103, 307

Gopalswamy, N., Lara, A., Kaiser, M. L., & Bougeret, J.-L. 2001, J. Geophys. Res., 106, 25261

Gopalswamy, N., Yashiro, S., Krucker, S., Stenborg, G., & Howard, R. A. 2004, J. Geophys. Res., 109, A12105

Gopalswamy, N., Yashiro, S., Michałek, G., et al. 2002, ApJ, 572, L103

Gordon, B. E., Lee, A. M., Möbius, E., & Trattner, K. J. 1999, J. Geophys. Res., 104, 28263

Goswami, J. N., McGuire, R. E., Reedy, R. C., Lal, D., & Jha, R. 1988, J. Geophys. Res., 93, 7195

Haggerty, D. & Roelof, E. 2001, in 27th ICRC, 3238–3241

Haggerty, D. K. & Roelof, E. C. 2002, ApJ, 579, 841

Hamilton, C. D., Mason, M. G., & McDonald, B. F. 1990, in 21st ICRC, Vol. 5, 237–240

Hamilton, D. C. 1977, J. Geophys. Res., 82, 2157

Hamilton, D. C. 1988, in Interplanetary Particle Environment, ed. J. Feynman & S. Gabriel, JPL Publication 88-28, JPL, California Institute of Technology, Pasadena, CA, 86–90

Harrison, R. A. 1995, A&A, 304, 585

Hasselmann, K. & Wibberenz, G. 1970, ApJ, 162, 1049

Heckman, G. R., Kunches, J. M., & Allen, J. H. 1992, Adv. Space Res., 12, 313

Heras, A. M. 1989, Relación Sol-Tierra: actividad solar, choques y partículas en el medio interplanetario, PhD thesis, University of Barcelona

Heras, A. M., Sanahuja, B., Domingo, V., & Joselyn, J. A. 1988, A&A, 197, 297

Heras, A. M., Sanahuja, B., Lario, D., et al. 1995, ApJ, 445, 497

Heras, A. M., Sanahuja, B., Sanderson, T. R., Marsden, R. G., & Wenzel, K.-P. 1994, J. Geophys. Res., 99, 43

Heras, A. M., Sanahuja, B., Smith, Z. K., Detman, T., & Dryer, M. 1992, ApJ, 391, 359

Hudson, P. D. 1965, MNRAS, 131, 23

Huttunen, K. E. J., Koskinen, H. E. J., Pulkkinen, T. I., et al. 2002, J. Geophys. Res., 107, 15

Jacobs, C., Poedts, S., Van der Holst, B., & Chané, E. 2005, A&A, 430, 1099

Jacobs, C., Poedts, S., Van der Holst, B., & Chané, E. 2006, in SOHO-17: Ten years of SOHO and beyond, ESA-SP617, ed. H. Lacoste, 177

Jokipii, J. R. 1966, ApJ, 146, 480

Jokipii, J. R. 1982, ApJ, 255, 716

Jones, F. C. & Ellison, D. C. 1991, Space Sci. Rev., 58, 259

Jun, I., Swimm, R. T., Ruzmaikin, A., et al. 2007, Adv. Space Res., in press

Kahler, S. 1994, ApJ, 428, 837

Kahler, S. W. 2001a, Geophys. Monogr. Ser., Vol. 125, Origin and properties of solar energetic particles in space (Whashington, D.C.: AGU), 109–122

Kahler, S. W. 2001b, J. Geophys. Res., 106, 20947

Kahler, S. W. 2005, ApJ, 628, 1014

Kahler, S. W., Aurass, H., Mann, G., & Klassen, A. 2005, in IAU Symposium, ed. K. Dere, J. Wang, & Y. Yan, 338–345

Kahler, S. W., Aurass, H., Mann, G., & Klassen, A. 2007a, ApJ, 656, 567

Kahler, S. W., Cane, H. V., Hudson, H. S., et al. 1998, J. Geophys. Res., 103, 12069

Kahler, S. W., Cliver, E. W., Cane, H. V., et al. 1986, ApJ, 302, 504

Kahler, S. W., Cliver, E. W., & Ling, A. G. 2007b, J. Atmos. Solar-Terr. Phys., 69, 43

Kahler, S. W., McAllister, A. H., & Cane, H. V. 2000, ApJ, 533, 1063

Kahler, S. W., Reames, D. V., & Sheeley, Jr., N. R. 2001, ApJ, 562, 558

Kahler, S. W., Simnett, G. M., & Reiner, M. J. 2003, in 28th ICRC, 3415–3418

Kahler, S. W. & Vourlidas, A. 2005, J. Geophys. Res., 110, A12S01

Kallenrode, M.-B. 1995, Adv. Space Res., 15, 375

Kallenrode, M.-B. 1996, J. Geophys. Res., 101, 24393

Kallenrode, M.-B. 1997, J. Geophys. Res., 102, 22347

Kallenrode, M.-B. 2001, J. Geophys. Res., 106, 24989

Kallenrode, M.-B. 2002, J. Atmos. Solar-Terr. Phys., 64, 1973

Kallenrode, M.-B. & Cliver, E. W. 2001, in 27th ICRC, 3318–3321

Kallenrode, M.-B., Cliver, E. W., & Wibberenz, G. 1992, ApJ, 391, 370

Kallenrode, M.-B. & Hatzky, R. 1999, in 26th ICRC, 324–327

Kallenrode, M.-B. & Wibberenz, G. 1997, J. Geophys. Res., 102, 22311

Keeney, A. C. 1999, Energetic particle fluxes of two large solar events using the EPAM instrument: November 1997 and April 1998, Master's thesis, Johns Hopkins Univ., Laurel, Md.

Kennel, C. F., Coroniti, F. V., Scarf, F. L., et al. 1986, J. Geophys. Res., 91, 11917

Kennel, C. F., Coroniti, F. V., Scarf, F. L., Smith, E. J., & Gurnett, D. A. 1982, J. Geophys. Res., 87, 17

Kennel, C. F., Edmiston, J. P., & Hada, T. 1985, Geophys. Monogr. Ser., Vol. 34, , ed. R. G. Stone & B. T. Tsurutani (Whashington, D.C.: AGU)

King, J. H. 1974, J. Spacecraft, 11, 401

Klecker, B., Hovestadt, D., Scholer, M., et al. 1984, ApJ, 281, 458

Klecker, B., Kunow, H., Cane, H. V., et al. 2006, Space Sci. Rev., 123, 217

Klein, K.-L. & Trottet, G. 2001, Space Sci. Rev., 95, 215

Klimchuck, J. A. 2001, Geophys. Monogr. Ser., Vol. 125, , ed. p. Song, H. J. Singer, & G. L. Siscoe (Whashington, D.C.: AGU), 143

Kocharov, G. E., Kovaltsov, G. A., & Kocharov, L. G. 1983, in 18th ICRC, Vol. 4, 105–108

Kocharov, L., Lytova, M., Vainio, R., Laitinen, T., & Torsti, J. 2005, ApJ, 620, 1052

Kocharov, L. & Torsti, J. 2002, Sol. Phys., 207, 149

Koskinen, H., Tanskanen, E., Pirjola, R., & et al. 2001, Study Report, ESWS-FMI-RP-0001, ESA (http://esa-spaceweather.net/spweather/esa_initiatives/spweatherstudies/RAL/ESWS-FMI-RP-0001_2.2.pdf)

Kóta, J., Manchester, W. B., & Gombosi, T. I. 2005, in 29th ICRC, 125–128

Krucker, S., Kontar, E. P., & Lin, R. P. 2004, AGU Fall Meeting Abstracts, A1129

Krucker, S., Larson, D. E., Lin, R. P., & Thompson, B. J. 1999, ApJ, 519, 864

Krucker, S. & Lin, R. P. 2000, ApJ, 542, L61

Kunow, S. W., Wibberenz, G., Green, G., Müller-Mellin, R., & Kallenrode, M.-B. 1991, Energetic particles in the inner heliosphere (Berlin), 243–330

Kurt, V., Belov, A., Mavromichalaki, H., & Gerontidou, M. 2004, Ann. Geophys., 22, 2255

Lanzerotti, L. 2004, Space Weather, 2, 1

Lario, D. 1997, Propagation of Low-Energy Particles through the Interplanetary Medium: Modeling their Injection from Interplanetary Shocks, PhD thesis, University of Barcelona

Lario, D., Aran, A., Agueda, N., & Sanahuja, B. 2007, Adv. Space Res., 40, 289

Lario, D. & Decker, R. B. 2001a, in 27th ICRC, 3485–3488

Lario, D. & Decker, R. B. 2001b, EOS Trans. AGU Fall Meeting Abstracts, 82, SH41B0754

Lario, D. & Decker, R. B. 2002, Geophys. Res. Lett., 29, 32

Lario, D., Decker, R. B., & Armstrong, T. P. 2001, in 27th ICRC, 3254–3257

Lario, D., Decker, R. B., Ho, G. C., et al. 2005a, in AIP Conference Series, Vol. 781, The Physics of Collisionless Shocks: 4th Annual IGPP International Astrophysics Conference, ed. G. Li, G. P. Zank, & C. T. Russell, 180–184

Lario, D., Decker, R. B., Livi, S., et al. 2005b, J. Geophys. Res., 110, A09S11

Lario, D., Decker, R. B., Roelof, E. C., Reisenfeld, D. B., & Sanderson, T. R. 2004a, J. Geophys. Res., 109, A01107

Lario, D., Heras, A. M., & Sanahuja. 1995a, in 2nd SOLTIP Symp. STEP GBRSC News, Vol. 5, 235–238

Lario, D., Ho, G. C., Decker, R. B., et al. 2003a, in AIP Conf. Proc. 679: Solar Wind Ten, 640–643

Lario, D., Hu, Q., Ho, G. C., & et al. 2005c, in ESA SP-592: Solar Wind 11/SOHO 16, Connecting Sun and Heliosphere, 81–86

Lario, D., Kallenrode, M.-B., Decker, R. B., et al. 2006, ApJ, 653, 1531

Lario, D., Livi, S., Roelof, E. C., et al. 2004b, J. Geophys. Res., 109, A09S02

Lario, D., Marsden, R. G., Sanderson, T. R., et al. 2000a, J. Geophys. Res., 105, 18235

Lario, D., Marsden, R. G., Sanderson, T. R., et al. 2000b, J. Geophys. Res., 105, 18251

Lario, D., Roelof, E. C., Decker, R. B., & Reisenfeld, D. B. 2003b, Adv. Space Res., 32, 579

Lario, D., Sanahuja, B., & Heras, A. M. 1998, ApJ, 509, 415, (Lar98)

Lario, D., Sanahuja, B., Heras, A. M., Smith, Z., & Dryer, M. 1995b, in 24th ICRC, Vol. 4, 385–388

Lario, D. & Simnett, G. M. 2004, Geophys. Monogr. Ser., Vol. 141, Solar particle variations (Whashington, D.C.: AGU), 195–216

Lario, D., Vandas, M., & Sanahuja, B. 1999, in Solar Wind Nine. AIP Conf. Proc., ed. S. R. Habbal, R. Esser, J. V. Hollweg, & P. A. Isenberg, Vol. 471, 741–747

Lee, M. A. 1982, J. Geophys. Res., 87, 5063

Lee, M. A. 1983, J. Geophys. Res., 88, 6109

Lee, M. A. 1997, Geophys. Monogr. Ser., Vol. 99, Particle acceleration and transport at CME-driven shocks, ed. N. e. a. Crooker (Whashington, D.C.: AGU), 227–234

Lee, M. A. 2005, ApJS, 158, 38

Lee, M. A. & Fisk, L. A. 1982, Space Sci. Rev., 32, 205

Lee, M. A. & Ryan, J. M. 1986, ApJ, 303, 829

Li, G. & Zank, G. P. 2005, Geophys. Res. Lett., 32, 2101

Li, G., Zank, G. P., & Rice, W. K. M. 2003, J. Geophys. Res., 108, SSH10

Li, G., Zank, G. P., & Rice, W. K. M. 2005, J. Geophys. Res., 110, A06104

Lin, R. P. 1970, Sol. Phys., 12, 266

Lin, R. P. 1974, Space Sci. Rev., 16, 189

Lin, R. P. 2005, Advances in Space Research, 35, 1857

Lin, R. P. & Hudson, H. S. 1976, Sol. Phys., 50, 153

Lionello, R., Linker, J. A., & Mikić, Z. 2003, in AIP Conf. Proc. 679: Solar Wind Ten, ed. M. Velli, R. Bruno, F. Malara, & B. Bucci, 222–225

Lovell, J. L., Duldig, M. L., & Humble, J. E. 1998, J. Geophys. Res., 103, 23733

Luhmann, J. G., Solomon, S. C., Linker, J. A., et al. 2004, J. Atmos. Solar-Terr. Phys., 66, 1243

Luhn, A., Klecker, B., Hovestadt, D., & Moebius, E. 1987, ApJ, 317, 951

Luttrell, A., Richter, A. K., Rosenbauer, H., & Neubauer, F. M. 1984, Advances in Space Research, 4, 327

Mace, R. L., Matthaeus, W. H., & Bieber, J. W. 2000, ApJ, 538, 192

Manchester, W. B., Gombosi, T. I., Roussev, I., et al. 2004a, J. Geophys. Res., 109, A1102

Manchester, W. B., Gombosi, T. I., Roussev, I., et al. 2004b, J. Geophys. Res., 109, A2107

Manchester, IV, W. B., Gombosi, T. I., De Zeeuw, D. L., et al. 2005, ApJ, 622, 1225

Mann, G., Klassen, A., Aurass, H., & Classen, H.-T. 2003, A&A, 400, 329

Manoharan, P. K. 2006, Sol. Phys., 235, 345

Manoharan, P. K., Gopalswamy, N., Yashiro, S., & et al. 2004, J. Geophys. Res., 109

Marsden, R. G., Afonin, V., Erdos, G., & et al. 1990, in Proc. 21^{st} Int. Cosmic Ray Conf., Vol. 5, 121–124

Marsden, R. G. & Fleck, B. 2003, Adv. Space Res., 32, 2699

Marsden, R. G., Wenzel, K.-P., Afonin, V. V., Gringauz, K., & Witte, M. 1991, Planet. Space Sci., 39, 57

Mason, G. M., Mazur, J. E., & Dwyer, J. R. 1999, ApJ, 525, L133

Mason, G. M., Wiedenbeck, M. E., Miller, J. A., et al. 2002, ApJ, 574, 1039

Matthaeus, W. H., Qin, G., Bieber, J. W., & Zank, G. P. 2003, ApJ, 590, L53

Mazur, J. E., Mason, G. M., Klecker, B., & McGuire, R. E. 1992, ApJ, 401, 398

McComas, D. J., Bame, S. J., Barker, P., et al. 1998, Space Sci. Rev., 86, 563

McGuire, R. E. & von Rosenvinge, T. T. 1984, Advances in Space Research, 4, 117

McKenna-Lawlor, S. M. P., Afonin, V. V., Gringauz, K. I., Keppler, E., & Kirsch, E. 1991, Planet. Space Sci., 39, 47

McKenna-Lawlor, S. M. P., Dryer, M., Fry, C. D., et al. 2005, J. Geophys. Res., 110, 3102

Mewaldt, R. A., Cohen, C. M. S., Labrador, A. W., et al. 2005, Journal of Geophysical Research (Space Physics), 110, A09S18

Mewaldt, R. A., Cohen, C. M. S., Leske, R. A., et al. 2002, Adv. Space Res., 30, 79

Mewaldt, R. A., Cummings, A. C., Adams, Jr., J. H., et al. 1988, in Interplanetary Particle Environment, ed. J. Feynman & S. B. Gabriel, JPL Publication 88-28, JPL, California Institute of Technology, Pasadena, CA, 14–32

Michałek, G., Gopalswamy, N., & Yashiro, S. 2003, ApJ, 584, 472

Mikić, Z. & Lee, M. A. 2006, Space Sci. Rev., 123, 57

Miller, J. A. & Viñas, A. F. 1993, ApJ, 412, 386

Morozova, E. I., Pisarenko, N. F., Riedler, W., et al. 1984, Advances in Space Research, 4, 331

Mottl, D. & Nymmik, R. 2003, Adv. Space Res., 32, 2349

Ng, C. K., Reames, D., & Tylka, A. J. 1999a, in 26th ICRC, 151–154

Ng, C. K., Reames, D., & Tylka, A. J. 2001, in 27th ICRC, 3140–3143

Ng, C. K., Reames, D. V., & Tylka, A. J. 1999b, Geophys. Res. Lett., 26, 2145

Ng, C. K., Reames, D. V., & Tylka, A. J. 2003, ApJ, 591, 461

Ng, C. K. & Wong, K.-Y. 1979, in 16th ICRC, Vol. 5, 252–255

Nitta, N. & Akiyama, S. 1999, ApJ, 525, L57

Nitta, N. V., Cliver, E. W., & Tylka, A. J. 2003, ApJ, 586, L103

Nymmik, R. A. 1998, Adv. Space Res., 21, 1689

Nymmik, R. A. 1999, Radiat. Meas., 30, 287

Odstrčil, D. & Pizzo, V. J. 1999, J. Geophys. Res., 104, 493

Odstrčil, D., Riley, P., & Zhao, X. P. 2004, J. Geophys. Res., 109, A02116

Pallavicini, R., Serio, S., & Vaiana, G. S. 1977, ApJ, 216, 108

Parker, E. N. 1965, Planet. Space Sci., 13, 9

Poedts, S. & Arge, N. C. 2005, in Reports on Astronomy 2002-2005, International Astronomical Union, (in press)

Reames, D. V. 1989, ApJ, 342, L51

Reames, D. V. 1990, ApJ, 358, L63

Reames, D. V. 1999a, Space Sci. Rev., 90, 413

Reames, D. V. 1999b, Radiat. Meas., 30, 297

Reames, D. V. 2000, AIP Conference Proceedings, 516, 289

Reames, D. V. 2002, ApJ, 571, L63

Reames, D. V., Barbier, L. M., & Ng, C. K. 1996, ApJ, 466, 473

Reames, D. V., Barbier, L. M., von Rosenvinge, T. T., et al. 1997a, ApJ, 483, 515

Reames, D. V., Kahler, S. W., & Ng, C. K. 1997b, ApJ, 491, 414

Reames, D. V. & Ng, C. K. 1998, ApJ, 504, 1002

Reames, D. V., Ng, C. K., & Berdichevsky, D. 2001, ApJ, 550, 1064

Reames, D. V., Ng, C. K., & Tylka, A. J. 2000, ApJ, 531, L83

Reid, G. C. 1964, J. Geophys. Res., 69, 2659

Rice, W. K. M., Zank, G. P., & Li, G. 2003, J. Geophys. Res., 108

Richardson, I. G. & Cane, H. V. 2004, J. Geophys. Res., 109, 9104

Richardson, I. G., Lawrence, G. R., Haggerty, D. K., Kucera, T. A., & Szabo, A. 2003, Geophys. Res. Lett., 30, 2

Richter, A. K., Hsieh, K. C., Lutrell, A. H., Marsch, E., & Schwenn, R. 1985, Geophys. Monogr. Ser., Vol. 35, Review of Interplanetary Shock Phenomena Near and Within 1 AU, ed. B. T. Tsurutani & R. G. Stone (Whashington, D.C.: AGU), 33–50

Roelof, E. C. 1969, in Lectures in High-Energy Astrophysics, NASA SP-199, ed. H. Ögelman & J. R. Wayland, 111

Rosenqvist, L. 2003a, Assesment of the Barcelona Engineering Model for Solar Energetic Particles in Interplanetary Space, Tech. Rep. TOS-EMA/10-03-2003, ESA, ESTEC, Noordwijk, The Netherlands

Rosenqvist, L. 2003b, Investigation of radial dependence of gradual solar proton flux distribution, Tech. Rep. TOS-EMA/06-03-2003, ESA, ESTEC, Noordwijk, The Netherlands

Rosenqvist, L. & Hilgers, A. 2003, Geophys. Res. Lett., 30, 1865

Rosenqvist, L., Hilgers, A., Evans, H., et al. 2005, J. Spacecraft and Rockets, 46, 1077

Roth, I. & Temerin, M. 1997, ApJ, 477, 940

Roussev, I. I., Sokolov, I. V., Forbes, T. G., et al. 2004, ApJ, 605, L73

Ruffolo, D. 1995, ApJ, 442, 861

Ruffolo, D. 2002, Adv. Space Res., 30, 45

Ruzmaikin, A., Li, G., Zank, G. P., Feynmann, J., & Jun, I. 2005, in ESA SP-592: Solar Wind 11/SOHO 16, Connecting Sun and Heliosphere, 441–444

Sagdeev, R. Z. & Zakharov, A. V. 1989, Nature, 341, 581

Sanahuja, B. & Domingo, V. 1987, J. Geophys. Res., 92, 7280

Sanahuja, B., Domingo, V., Wenzel, K.-P., Joselyn, J. A., & Keppler, E. 1983, Sol. Phys., 84, 321

Sanahuja, B., Heras, A. M., Domingo, V., & Joselyn, J. A. 1991, Sol. Phys., 134, 379

Sanahuja, B. & Lario, D. 1998, in 19th European Cosmic Ray Symposium (Alcalá University Editions), 129–139

Sanderson, T. R., Marsden, R. G., Tranquille, C., et al. 2003, Geophys. Res. Lett., 30, 8036

Sanderson, T. R., Reinhard, R., van Nes, P., & Wenzel, K.-P. 1985a, J. Geophys. Res., 90, 19

Sanderson, T. R., Reinhard, R., van Nes, P., et al. 1985b, J. Geophys. Res., 90, 3973

Sarris, E. T., Krimigis, S. M., & Armstrong, T. P. 1976, J. Geophys. Res., 81, 2341, (Sar76)

Sarris, E. T. & van Allen, J. A. 1974, J. Geophys. Res., 79, 4157

Schlickeiser, R., Campeanu, A., & Lerche, L. 1993, A&A, 276, 614

Scholer, M. 1985, Geophys. Monogr. Ser., Vol. 35, Diffusive Acceleration, ed. B. T. Tsurutani & R. G. Stone (Whashington, D.C.: AGU), 287–301

Schwenn, R., Dal Lago, A., Gonzalez, W. D., et al. 2001, Fall Meeting Suppl., Abs. SH12A-0739, Eos Trans. AGU, 82, 47

Shea, M. A. & Smart, D. F. 1996, Adv. Space Res., 17, 225

Shea, M. A., Smart, D. F., Swinson, D. B., Humble, J. E., & McKinnon, J. A. 1989, Adv. Space Res., 9, 221

Simnett, G. M., Roelof, E. C., & Haggerty, D. K. 2002, ApJ, 579, 854

Simpson, J. A., Anglin, J. D., Balogh, A., et al. 1992, A&AS, 92, 365

Siscoe, G. L., Carlson, C. W., Carovillano, R. L., & et al. 2000, (Whashington, D.C.: National Academies Press), 24

Smart, D. F. & Shea, M. A. 1985, , ed. A. S. Jursa (Bedford MA: AF Geophysics Laboratory)

Smart, D. F. & Shea, M. A. 1989, Adv. Space Res., 9, 281

Smart, D. F. & Shea, M. A. 1992, Adv. Space Res., 12, 303

Smart, D. F. & Shea, M. A. 2003, Adv. Space Res., 31, 45

Smart, D. F., Shea, M. A., Spence, H. E., & Kepko, L. 2006, Adv. Space Res., 37, 1734

Smith, C. W., L'Heureux, J., Ness, N. F., et al. 1998, Space Sci. Rev., 86, 613

Smith, Z. & Dryer, M. 1990, Sol. Phys., 129, 387

Smith, Z., Dryer, M., & Fry, C. D. 2005, Space Weather, 3, 7002

Sokolov, I. V., Roussev, I. I., Fisk, L. A., et al. 2006, ApJ, 642, L81

Sokolov, I. V., Roussev, I. I., Gombosi, T. I., et al. 2004, ApJ, 616, L171

Srivastava, N., Schwenn, R., Inhester, B., Martin, S. F., & Hanaoka, Y. 2000, ApJ, 534, 468

Stassinopoulos, E. G. 1975, NASA STI/Recon Technical Report N, 75, 23451

Stassinopoulos, E. G. & King, J. H. 1974, IEEE Trans. on Aerospace and Electronic Systems, AES-10, 442

Stone, E. C., Frandsen, A. M., Mewaldt, R. A., et al. 1998, Space Sci. Rev., 86, 1

Sun, W., Dryer, M., Fry, C. D., et al. 2002, Ann. Geophys., 20, 937

Szabo, A. 2005, Advances in Space Research, 35, 61

Tan, L. C., Mason, G. M., Gloeckler, G., & Ipavich, F. M. 1989, J. Geophys. Res., 94, 6552

Tan, L. C., Mason, G. M., Lee, M. A., Klecker, B., & Ipavich, F. M. 1992, J. Geophys. Res., 97, 1597

Tan, L. C., Reames, D. V., & Ng, C. K. 2007, ApJ, 661, 1297

Torsti, J., Kocharov, L., Innes, D. E., Laivola, J., & Sahla, T. 2001, A&A, 365, 198

Torsti, J., Kocharov, L. G., Teittinen, M., & Thompson, B. J. 1999, ApJ, 510, 460

Torsti, J., Kocharov, L. G., Vainio, R., Anttila, A., & Kovaltsov, G. A. 1996, Sol. Phys., 166, 135

Tóth, G., Sokolov, I. V., Gombosi, T. I., et al. 2005, Journal of Geophysical Research (Space Physics), 110, 12226

Tsurutani, B., Wu, S. T., Zhang, T. X., & Dryer, M. 2003, A&A, 412, 293

Tsurutani, B. T. & Lin, R. P. 1985, J. Geophys. Res., 90, 1

Tsurutani, B. T., Smith, E. J., & Jones, D. E. 1983, J. Geophys. Res., 88, 5645

Tsurutani, B. T., Zhang, L. D., Mason, G. L., et al. 2002, Ann. Geophys., 20, 427

Turner, R. 2000, IEEE Trans. on Plasma Science, 28, 2103

Turner, R. 2001, Geophys. Monogr. Ser., Vol. 125, What we must know about solar particle events to reduce the risk of astronauts, ed. p. Song, H. J. Singer, & G. L. Siscoe (Whashington, D.C.: AGU), 29–44

Tylka, A. J. 2001, J. Geophys. Res., 106, 25333

Tylka, A. J., Adams, Jr., J. H., Boberg, P., et al. 1997a, IEEE Trans. Nucl. Sci., 40, 2150

Tylka, A. J., Boberg, P. R., Adams, Jr., J. H., Kleis, T., & Beaujean, R. 1995, ApJ, 438, L83

Tylka, A. J., Boberg, P. R., Cohen, C. M. S., et al. 2002, ApJ, 581, L119

Tylka, A. J., Boberg, P. R., McGuire, R. E., Ng, C. K., & Reames, D. V. 2000, in AIP Conf. Proc. 528: Acceleration and Transport of Energetic Particles Observed in the Heliosphere, ed. R. A. Mewaldt, J. R. Jokipii, M. A. Lee, E. Möbius, & T. H. Zurbuchen, 147

Tylka, A. J., Cohen, C. M. S., Dietrich, W. F., et al. 2005, ApJ, 625, 474

Tylka, A. J., Cohen, C. M. S., Dietrich, W. F., et al. 2001, ApJ, 558, L59

Tylka, A. J. & Dietrich, W. F. 1999, Radiat. Meas., 30, 345

Tylka, A. J., Dietrich, W. F., & Boberg, P. 1997b, IEEE Trans. Nucl. Sci., 40, 2140

Tylka, A. J. & Lee, M. A. 2006, ApJ, 646, 1319

US National Space Weather Program: Implementation Plan, FCM-P31. 1997, 8455 Colesville Road, Suite 1500, Silver Spring MD 20910

US Space Weather Architecture Study Transition Plan. 1999, 8455 Colesville Road, Suite 1500, Silver Spring MD 20910

Vainio, R. 2003, A&A, 406, 735

Vainio, R., Agueda, N., Aran, A., & Lario, D. 2007, Astrophys. and Space Sci. Libr., Vol. 344, Modeling of solar energetic particles in interplanetary space, ed. J. Lilensten (Dordrecht: Springer), 27–37

Vainio, R. & Schlickeiser, R. 1998, A&A, 331, 793

Vainio, R. & Schlickeiser, R. 1999, A&A, 343, 303

van Hollebeke, M. A. I., Ma Sung, L. S., & McDonald, F. B. 1975, Sol. Phys., 41, 189

van Nes, P., Reinhard, R., Sanderson, T. R., Wenzel, K.-P., & Zwickl, R. D. 1984, J. Geophys. Res., 89, 2122

van Rooijen, J. J., van Dijen, G. J., Lafleur, H. T., & Lowes, P. 1979, Space Science Instrumentation, 4, 373

Vandas, M., Fischer, S., Dryer, M., Smith, Z., & Detman, T. 1995, J. Geophys. Res., 100, 12285

Viñas, A. F., Goldstein, M. L., & Acuña, M. H. 1984, J. Geophys. Res., 89, 3762

von Rosenvinge, T. T., Cohen, C. M. S., Christian, E. R., et al. 2001, in 27th, ICRC, 3136–3139

Vourlidas, A. 2004, Astroph. and Space Science Libr., Vol. 314, , ed. D. Gary & C. U. Keller (Kluwer Academic Publishers), 223

Watari, S., Kunitake, M., & Watanabe, T. 2001, Sol. Phys., 204, 425

Wen, Y., Maia, D. J. F., & Wang, J. 2007, ApJ, 657, 1117

Wu, S. T., Dryer, M., & Han, S. M. 1983, Sol. Phys., 84, 395

Wu, S. T., Li, B., Wang, S., & Zheng, H. 2005a, J. Geophys. Res., 110, 11102

Wu, S. T., Wang, A. H., & Falconer, D. A. 2005b, in IAU Symposium, ed. K. Dere, J. Wang, & Y. Yan, 291–301

Xapsos, M. A., Barth, J. L., Stassinopoulos, E. G., Burke, E. A., & Gee, G. B. 2004, IEEE Tans. Nucl. Sci., 51, 3394

Xapsos, M. A., Barth, J. L., Stassinopoulos, E. G., et al. 2000, IEEE Tans. Nucl. Sci., 47, 2218

Xapsos, M. A., Summers, G. P., & Burke, E. A. 1998, IEEE Tans. Nucl. Sci., 45, 2948

Yashiro, S., Gopalswamy, N., Michalek, G., et al. 2004, J. Geophys. Res., 109, 7105

Zank, G. P., Li, G., Florinski, V., et al. 2004, J. Geophys. Res., 109, A04107

Zank, G. P., Rice, W. K. M., & Wu, C. C. 2000, J. Geophys. Res., 105, 25079

Zhang, J., Dere, K. P., Howard, R. A., & Bothmer, V. 2003, ApJ, 582, 520

Zhang, J., Dere, K. P., Howard, R. A., Kundu, M. R., & White, S. M. 2001, ApJ, 559, 452

Zhang, J., Dere, K. P., Howard, R. A., & Vourlidas, A. 2004, ApJ, 604, 420

Zhao, X. P., Plunkett, S. P., & Liu, W. 2002, J. Geophys. Res., 107, 1223

Zurbuchen, T. H. & Richardson, I. G. 2006, Space Sci. Rev., 123, 31

Zwickl, R. D., Doggett, K. A., Sahm, S., et al. 1998, Space Sci. Rev., 86, 633